ASME
SETTING THE STANDARD

Transactions of the ASME, Journal of Applied Mechanics (ISSN 0021-8936) is published bimonthly (Jan., Mar., May, July, Sept., Nov.) by The American Society of Mechanical Engineers, Three Park Avenue, New York, NY 10016. Periodicals postage paid at New York, NY and additional mailing offices. POSTMASTER: Send address changes to Transactions of the ASME, Journal of Applied Mechanics, c/o THE AMERICAN SOCIETY OF MECHANICAL ENGINEERS, 22 Law Drive, Box 2300, Fairfield, NJ 07007-2300. **CHANGES OF ADDRESS** must be received at Society headquarters seven weeks before they are to be effective. Please send old label and new address. **STATEMENT from By-Laws.** The Society shall not be responsible for statements or opinions advanced in papers or printed in its publications (B7.1, Para. 3).

Journal of Applied Mechanics

Published Bimonthly by ASME

VOLUME 76 • NUMBER 1 • JANUARY 2009

RESEARCH PAPERS

TECHNICAL BRIEFS

(Contents continued on inside back cover)

This journal is printed on acid-free paper, which exceeds the ANSI Z39.48-1992 specification for permanence of paper and library materials. ♾™
♻ 85% recycled content, including 10% post-consumer fibers.

Journal of Applied Mechanics Volume 76, Number 1 JANUARY 2009

DISCUSSIONS

ERRATA

The ASME Journal of Applied Mechanics is abstracted and indexed in the following:

Alloys Index, Aluminum Industry Abstracts, Applied Science & Technology Index, Ceramic Abstracts, Chemical Abstracts, Civil Engineering Abstracts, Compendex (The electronic equivalent of Engineering Index), Computer & Information Systems Abstracts, Corrosion Abstracts, Current Contents, EEA (Earthquake Engineering Abstracts Database), Electronics & Communications Abstracts Journal, Engineered Materials Abstracts, Engineering Index, Environmental Engineering Abstracts, Environmental Science and Pollution Management, Fluidex, Fuel & Energy Abstracts, GeoRef, Geotechnical Abstracts, INSPEC, International Aerospace Abstracts, Journal of Ferrocement, Materials Science Citation Index, Mechanical Engineering Abstracts, METADEX (The electronic equivalent of Metals Abstracts and Alloys Index), Metals Abstracts, Nonferrous Metals Alert, Polymers Ceramics Composites Alert, Referativnyi Zhurnal, Science Citation Index, SciSearch (Electronic equivalent of Science Citation Index), Shock and Vibration Digest, Solid State and Superconductivity Abstracts, Steels Alert, Zentralblatt MATH

Blocking in the Rotating Axial Flow in a Corotating Flexible Shell

F. Gosselin
LadHyX,
École Polytechnique,
Palaiseau Cedex 91128, France
e-mail: frederick.gosselin@ladhyx.polytechnique.fr

M. P. Païdoussis[1]
Fellow ASME
Department of Mechanical Engineering,
McGill University,
Montréal, QC, H3A 2K6, Canada
e-mail: mary.fiorilli@mcgill.ca

By coupling the Donnell–Mushtari shell equations to an analytical inviscid fluid solution, the linear dynamics of a rotating cylindrical shell with a corotating axial fluid flow is studied. Previously discovered mathematical singularities in the flow solution are explained here by the physical phenomenon of blocking. From a reference frame moving with the traveling waves in the shell wall, the flow is identical to the flow in a rigid varicose tube. When the ratio of rotation rate to flow velocity approaches a critical value, the phenomenon of blocking creates a stagnation region between the humps of the wall. Since the linear model cannot account for this phenomenon, the solution blows up.
[DOI: 10.1115/1.2998486]

1 Introduction

The present study considers the stability of a rotating cylindrical shell containing a corotating axial flow. The system can be thought of as a long thin-walled pipe carrying an internal axial flow while the whole is in a frame of reference rotating at a prescribed rate. Only a handful of studies have been conducted on the problem of shells subjected to a swirling (helical) flow. Païdoussis [1] offered a review of the work performed in this field and on related problems.

Srinivasan [2] undertook the first study that added the complexity of rotation to the problem of a cylindrical shell subjected to axial flow. In this study, motivated by applications involving swirling flow in multispool aircraft jet engines, the stability of a thin infinitely long cylindrical shell exposed to an outer inviscid helical flow is investigated. Through a numerical frequency analysis, it is found that when the critical velocity is reached, the system loses stability by coupled-mode flutter, where the forward and the backward traveling waves coalesce. These results were later confirmed experimentally by Dowell et al. [3] who measured flutter frequencies and critical rotation rates in fair agreement with the theoretical predictions of Srinivasan.

This fluid-structure interaction problem is obviously related to the research done on the stability of rotating fluids. Rayleigh [4] studied the stability of the Couette flow, i.e., the steady azimuthal flow of a fluid between two rotating coaxial cylinders. His analysis led him to propose a general stability criterion, now named after him, which states that a necessary and sufficient condition for stability is that the circulation $K=V_\theta r$ always increases in magnitude with the radius r. This implies that a solid body rotation flow is stable. Rayleigh noted that the stability of a rotating flow with no axial component between two concentric cylinders is analogous to that of a density-stratified fluid at rest under the action of gravity, so long as only axisymmetric perturbations are considered. Building on this observation, Howard and Gupta [5] suggested that, when an axial flow is also present, the effect of the swirl component may be analogous to the effect of density stratification on a parallel shear flow. From this analogy, they defined a "Richardson number" to propose a sufficient condition for the stability of swirling flows to axisymmetric perturbations. According to this criterion, a plug flow subjected to a solid body rotation is stable to infinitesimal axisymmetric disturbances.

By considering any type of perturbations (not only Fourier type) in a finite-length system, Wang and Rusak [6] showed that flows, which were predicted to be stable to axisymmetric perturbations by Howard and Gupta [5], could, at large enough rotation rates, be unstable and responsible for the phenomenon of vortex breakdown. This type of instability is not considered in the present work, as we study an infinitely long system. Moreover, it is understood that in an exhaustive study of the stability of the coupled shell-flow system, both fluid-only and fluid-structure modes of instability should be considered. On the other hand, as the purpose of the current paper is to explain a weakness in the current fluid-structure interaction model, we will focus solely on the coupled fluid-structure modes and leave out the instability modes which are independent of shell-wall deformations.

Chow [7] investigated the swirling inviscid and incompressible fluid flow in cylindrical tubes with axisymmetric deformations. The flow in this varicose-shaped tube is characterized by the Rossby number

$$\mathrm{Ro} = \frac{U}{2R\Omega} \tag{1}$$

where U is the plug flow velocity in the tube, R is the tube diameter, and Ω is the constant rate of swirl of the flow. Chow [7] found that for flows with certain values of Rossby number, the flow near the wall is "blocked." At those critical values of the Rossby number, no flow solution can be found to satisfy the linear boundary conditions. What happens physically is that the fluid cannot go around the humps on the wall and becomes stagnant in that region, hence effectively reducing the cross section of the tube. This phenomenon of blocking is characteristic of stratified fluid flow over obstacles and is discussed in detail, along with analogies to a rotating fluid, by Yih [8]. To visualize the flow pattern when blocking occurs, Chow [7] studied the flow in a convergent-divergent nozzle with a wall shape determined by ring vortices. The streamlines and the flow velocity profile obtained by Chow [7] at the first critical Rossby number are shown in Fig. 1. At a critical Rossby number, the streamlines become parallel with the pipe wall, and the fluid near the wall is stagnant. The findings of Chow [7] are of importance to the present paper because the same flow model is used by Lai and Chow [9] to study the stability of a rotating thin elastic tube containing fluid flow.

Lai and Chow [9] studied a problem related to "the thrust chamber and the pipelines in the liquid propellant feed system of a spinning rocket." They investigated the stability of a rotating

[1]Corresponding author.

Contributed by the Applied Mechanics Division of ASME for publication in the JOURNAL OF APPLIED MECHANICS. Manuscript received August 23, 2007; final manuscript received August 26, 2008; published online October 23, 2008. Review conducted by Nesreen Ghaddar

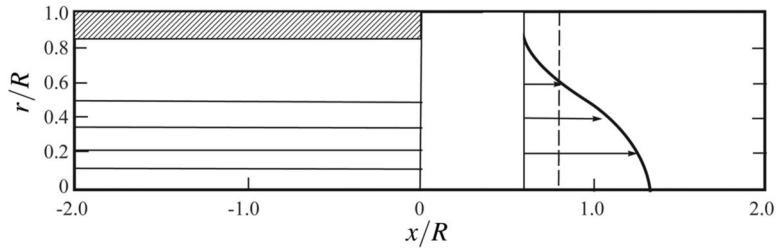

Fig. 1 Streamlines and velocity profile showing the flow pattern of blocking encountered at the first critical Rossby number in a swirling axisymmetric flow in a convergent-divergent nozzle. Figure reproduced from Ref. [7].

thin shell containing inviscid fluid flow where both the fluid and the shell rotate about the axis of the cylindrical shell at a given constant rate. The linear Donnell shell theory was modified to account for the solid body rotation and was coupled to the fluid equations, similar in essence to those derived by Chow [7] for swirling flow in a varicose tube. It was found that the critical flow rate in the shell decreases with increasing angular velocity. Using essentially the same method of solution as Lai and Chow [9], Chen and Bert [10] studied the dynamics of a stationary shell carrying a rotating flow; the latter study differs from Lai and Chow's only in the fact that the shell does not rotate. Once again, it is found that rotation severely decreases the stability of the fluid-shell system.

The present paper is specifically concerned with an issue raised by Cortelezzi et al. [11]. They found it impossible to reproduce the results of Lai and Chow [9] when rotation is present. This led them to question the validity of Lai and Chow's results and also those of Chen and Bert [10] who used the same flow model. Without rotation, the solution for pressure in the fluid is continuous, but in the presence of rotation, the solution is not bounded in particular regions of the parameter space. Cortelezzi et al. mathematically pin-pointed the problem in obtaining the eigenfrequencies of the coupled system to the presence of an infinite number of singularities in the flow solution. The question incidentally raised is then: what is the physical meaning of these mathematical singularities?

By showing that the flow in the spinning shell behaves the same way as in the rigid varicose tube of Chow [7], this paper establishes the link between the mathematical singularities and the physical phenomenon of blocking. This paper is organized as follows. In Sec. 2, the analytical model of Lai and Chow [9] is recalled and the similarities to the flow solution of Chow [7] are highlighted. In Sec. 3, we investigate the dynamics of a nonrotating shell conveying purely axial flow. We also analyze how the solution breaks down when rotation is present and how this breakdown is related to the physical phenomenon of blocking. The main findings of this paper are summarized in Sec. 4.

2 Analysis

We revisit the model developed by Lai and Chow [9] for a rotating shell containing a corotating axial flow. We consider a cylindrical shell of radius R, thickness $h \ll R$, and of infinite length, as shown in Fig. 2. The shell contains an axial incompressible inviscid flow of velocity U, constant across the inner section of the shell. The whole system is in a frame of reference rotating about the axis of the cylinder at rate Ω. The axial, circumferential, and radial time-dependent deformations of the shell are denoted by u, v, and w, respectively. Let ρ_s be the density, E the elastic modulus, and ν the Poisson ratio of the shell material. The motion of the shell is governed by the linear Donnell–Mushtari shell equations (see Ref. [12]) in the rotating frame of reference, i.e.,

$$\mathbf{L}_D \begin{Bmatrix} u \\ v \\ w \end{Bmatrix} = \frac{\gamma^2}{R^2} \begin{Bmatrix} \partial^2 u/\partial t^2 \\ \partial^2 v/\partial t^2 - \Omega^2 v + 2\Omega(\partial w/\partial t) \\ 2\Omega(\partial v/\partial t) + \Omega^2 w - \partial^2 w/\partial t^2 + p_w/\rho_s h \end{Bmatrix} \tag{2}$$

where $\mathbf{L}_D$ is the linear Donnell–Mushtari shell operator given in the Appendix, p_w is the fluid pressure acting on the shell wall, and $\gamma = R\sqrt{\rho_s(1-\nu^2)/E}$ is the structural timescale. In the reference frame rotating at rate Ω about $\vec{e}_x$, the Euler equations in cylindrical scalar form, together with the continuity equation, govern the flow inside the shell

$$\frac{DV_x}{Dt} = -\frac{1}{\rho}\frac{\partial p}{\partial x} \tag{3}$$

$$\frac{DV_r}{Dt} - 2\Omega V_\theta - \frac{V_\theta^2}{r} - \Omega^2 r = -\frac{1}{\rho}\frac{\partial p}{\partial r} \tag{4}$$

$$\frac{DV_\theta}{Dt} + 2\Omega V_r + \frac{V_r V_\theta}{r} = -\frac{1}{\rho}\frac{1}{r}\frac{\partial p}{\partial \theta} \tag{5}$$

$$\frac{\partial V_x}{\partial x} + \frac{1}{r}\frac{\partial}{\partial r}(rV_r) + \frac{1}{r}\frac{\partial V_\theta}{\partial \theta} = 0 \tag{6}$$

in which ρ is the fluid density, V_x, V_r, and V_θ are the fluid velocity components, and D/Dt is the material derivative in cylindrical coordinates, i.e.,

$$\frac{D}{Dt} = \frac{\partial}{\partial t} + V_r\frac{\partial}{\partial r} + \frac{V_\theta}{r}\frac{\partial}{\partial \theta} + V_x\frac{\partial}{\partial x}$$

To be consistent with the derivation of the linear Donnell–Mushtari shell equations, in treating the interface between the shell wall and the flow we assume that the normal to the unde-

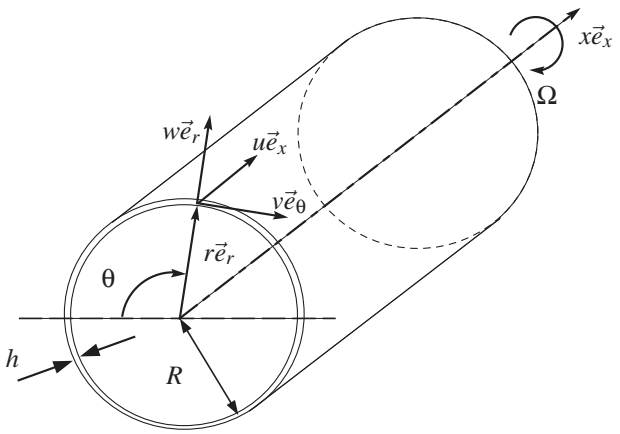

Fig. 2 Schematic of the considered shell

formed shell surface remains unchanged as the shell deforms. This assumption has as a consequence such that only the radial displacement w (not the circumferential and the axial displacements u and v) of the shell influences the flow, since an inviscid fluid cannot transmit shear. We impose a no-penetration condition at the wall by requiring that the radial velocity of the flow matches the radial velocity of the shell wall, i.e.,

$$V_r|_{\text{wall}} = \left.\frac{Dw}{Dt}\right|_{\text{wall}} = \left[\frac{\partial w}{\partial t} + V_r\frac{\partial w}{\partial r} + \frac{V_\theta}{r}\frac{\partial w}{\partial \theta} + V_x\frac{\partial w}{\partial x}\right]_{\text{wall}} \tag{7}$$

We apply a perturbation scheme with a traveling-wave solution of the form

$$p = P(r) + \hat{p}(r)e^{i\alpha} \tag{8}$$

$$\{V_x, V_r, V_\theta\} = \{U,0,0\} + \{\hat{v}_x, \hat{v}_r, \hat{v}_\theta\}e^{i\alpha} \tag{9}$$

$$\alpha = \omega t - kx - n\theta \tag{10}$$

where ω, k, and n are the complex frequency, axial wave number, and circumferential wave number of the system, respectively, and $i=\sqrt{-1}$. Upon substituting Eqs. (8) and (9) into Eq. (4) and keeping only leading order terms, the r-momentum equation is integrated to find the steady pressure distribution

$$P(r) = P_R - \frac{1}{2}\rho\Omega^2(1-r^2) \tag{11}$$

where P_R is the constant pressure at the shell-fluid interface. This term leads to a static deformation and a stiffening of the shell. We take $P_R=0$, as in this linear analysis the static deformation and the stiffening due to pressurization can be modeled by simply using different effective shell properties. Subsequently, the perturbation solutions (Eqs. (8) and (9)) are substituted into the partial differential equations (3)–(6) while making use of Eq. (11) to remove the steady pressure term. By combining the partial differential equations, one can obtain a second-order differential equation of the perturbation pressure

$$r^2\frac{\partial^2\hat{p}}{\partial r^2} + r\frac{\partial\hat{p}}{\partial r} + [r^2k^2(\Lambda^2-1) - n^2]\hat{p} = 0 \tag{12}$$

$$\Lambda = \frac{2\Omega}{kU-\omega} \tag{13}$$

Equation (12) is a variant of Bessel's equation. Its solution takes different forms depending on the values of Λ^2 and n. The perturbation flow is related to the deformation of the shell through the linearized impermeability condition, which is obtained via a Taylor expansion of Eq. (7) about the undeformed wall position and keeping only first-order terms

$$v_r|_{r=R} = i(\omega - kU)\hat{w}e^{i\alpha} \tag{14}$$

where the shell deformation takes the same traveling-wave form as in Eqs. (8) and (9)

$$\{u,v,w\} = \{\hat{u},\hat{v},\hat{w}\}e^{i\alpha} \tag{15}$$

Making use of Eqs. (14) and (15), and solving Eq. (12), the corresponding perturbation pressure solutions are as follows:

For $\Lambda^2<1$,

$$\hat{p} = \frac{\rho\hat{w}R(\omega-kU)^2\sqrt{1-\Lambda^2}I_n(rk\sqrt{1-\Lambda^2})}{RkI_{n-1}(Rk\sqrt{1-\Lambda^2}) - n\dfrac{\sqrt{1-\Lambda^2}}{1-\Lambda}I_n(Rk\sqrt{1-\Lambda^2})} \tag{16}$$

while for $\Lambda^2=1$ and $(n\Lambda)\geq 0$,

$$\hat{p} = \frac{2(kU-\omega)^2\rho(1+|n|)\hat{w}}{n^2+|n|+k^2R^2}\frac{r^{|n|}}{R^{|n|-1}} \tag{17}$$

and for $\Lambda^2>1$,

$$\hat{p} = \frac{-\rho\hat{w}R(\omega-kU)^2\sqrt{\Lambda^2-1}J_n(rk\sqrt{\Lambda^2-1})}{RkJ_{n-1}(Rk\sqrt{\Lambda^2-1}) - n\dfrac{\sqrt{\Lambda^2-1}}{\Lambda-1}J_n(Rk\sqrt{\Lambda^2-1})} \tag{18}$$

where J_n and I_n are the Bessel and modified Bessel functions of the first kind and order n. The pressure exerted by the fluid on the shell surface in Eq. (2) can be expressed linearly by expanding Eq. (8) around the mean wall position and neglecting second order terms of a Taylor expansion

$$p_w = \hat{p}|_{r=R}e^{i\alpha} + \left.\frac{\partial P}{\partial r}\right|_{r=R}\hat{w}e^{i\alpha} \tag{19}$$

Substituting in the steady pressure solution of Eq. (11) into Eq. (19), the pressure of the fluid at the wall can be written as a linear function of the wall displacement

$$p_w = (\hat{p}|_{r=R} + \rho\Omega^2R\hat{w})e^{i\alpha} \tag{20}$$

where $\hat{p}$ is given by Eqs. (16)–(18) depending on Λ and n.

For our analysis, we define the following dimensionless numbers, namely, the reduced velocity, the shell thickness ratio, the density ratio, the dimensionless rate of rotation, shell-wall pressure, axial wave number, complex frequency, coordinates, and shell deformations

$$U_R = \frac{U\gamma}{R}, \quad \bar{h} = \frac{h}{R}, \quad \bar{\rho} = \frac{\rho_s}{\rho}, \quad \bar{\Omega} = \Omega\gamma, \quad \bar{p} = \frac{\gamma^2}{\hat{w}R\rho_s}\hat{p}|_{r=R}$$

$$\bar{k} = Rk, \quad \bar{\omega} = \gamma\omega, \quad \bar{x} = \frac{x}{R}, \quad \bar{r} = \frac{r}{R}, \quad \{\bar{u},\bar{v},\bar{w}\} = \frac{1}{R}\{\hat{u},\hat{v},\hat{w}\} \tag{21}$$

respectively. The equation for the pressure at the wall (Eq. (20)) along with the traveling-wave solution (Eq. (15)) are substituted into the shell (Eq. (2)). With the use of the dimensionless numbers in Eq. (21), the equations of motion of the coupled shell-fluid system can be written as a dimensionless linear homogeneous system of three equations:

$$[\mathbf{L}(\bar{\Omega}, U_R, \bar{\rho}, \bar{h}, \nu, \bar{k}, n, \bar{\omega})]\begin{Bmatrix}\bar{u}\\ \bar{v}\\ \bar{w}\end{Bmatrix} = 0 \tag{22}$$

where

$$[\mathbf{L}(\bar{\Omega}, U_R, \bar{\rho}, \bar{h}, \nu, \bar{k}, n, \bar{\omega})] = \begin{bmatrix} -\bar{k}^2 - \dfrac{1-\nu}{2}n^2 + \bar{\omega}^2 & -\dfrac{1+\nu}{2}\bar{k}n & -i\nu\bar{k} \\ -\dfrac{1+\nu}{2}\bar{k}n & -\dfrac{1-\nu}{2}\bar{k}^2 - n^2 + \bar{\Omega}^2 + \bar{\omega}^2 & -in - i2\bar{\Omega}\bar{\omega} \\ -i\nu\bar{k} & -in - i2\bar{\Omega}\bar{\omega} & 1 + \dfrac{\bar{h}^2}{12}(\bar{k}^2+n^2)^2 - \bar{\Omega}^2 - \bar{\omega}^2 - \dfrac{1}{\bar{h}\bar{\rho}}(\bar{\rho}+\bar{\Omega}^2) \end{bmatrix} \tag{23}$$

We obtain the dispersion relation of the admissible complex frequencies $\bar{\omega}$ with the wave numbers $\bar{k}$ and n by setting the determinant of **L** equal to zero. For given values of $\bar{k}$ and n, the corresponding complex values of $\bar{\omega}$ are found numerically. Each combination of $\bar{k}$, n, and $\bar{\omega}$ satisfying the governing equations of the system corresponds to a mode of the system. For each mode, the complex frequency has a real and an imaginary part, $\bar{\omega}=\bar{\omega}_r+i\bar{\omega}_i$. The real part is the frequency of oscillation and the imaginary part is the rate of damping. If $\bar{\omega}_i<0$, the mode of vibration is unstable and a small perturbation will increase exponentially. On the other hand, if $\bar{\omega}_i>0$, the mode of vibration is stable and a small perturbation will decay. If $\bar{\omega}_i=0$, the mode is neutrally stable.

Two numerical methods are used to obtain the dispersion relation. Without rotation, it is possible to use a Müller iterative procedure to find the complex frequencies, but in the presence of rotation the most suitable numerical scheme is the zero-level contour method. For a given domain of $\bar{\omega}_r$ and U_R, the determinant of **L** is found and a zero-level contour plot is realized, which leads to the admissible neutrally stable frequencies.

Up to here, the derivation of the model is identical to Lai and Chow's. To get an insight of the behavior of the flow near the singularities we consider the relative velocity between the axial velocity of the flow and the traveling waves in the shell

$$V_x^* = \frac{V_x - \omega/k}{U - \omega/k} \tag{24}$$

From Eqs. (3), (9), and (16)–(18), we can obtain the relative axial velocity.

For $\Lambda^2<1$,

$$V_x^* = 1 - \frac{\hat{w}k\sqrt{1-\Lambda^2}I_n(rk\sqrt{1-\Lambda^2})}{I_{n-1}(Rk\sqrt{1-\Lambda^2}) - \dfrac{n}{kR}\dfrac{\sqrt{1-\Lambda^2}}{1-\Lambda}I_n(Rk\sqrt{1-\Lambda^2})}e^{i\alpha} \tag{25}$$

while for $\Lambda^2=1$ and $(n\Lambda)\geq 0$,

$$V_x^* = 1 - \frac{2k^2(1+|n|)\hat{w}}{n^2+|n|+k^2R^2}\frac{r^{|n|}}{R^{|n|-1}}e^{i\alpha} \tag{26}$$

and for $\Lambda^2>1$,

$$V_x^* = 1 + \frac{\hat{w}k\sqrt{\Lambda^2-1}J_n(rk\sqrt{\Lambda^2-1})}{J_{n-1}(Rk\sqrt{\Lambda^2-1}) - \dfrac{n}{kR}\dfrac{\sqrt{\Lambda^2-1}}{\Lambda-1}J_n(Rk\sqrt{\Lambda^2-1})}e^{i\alpha} \tag{27}$$

It can be shown that upon defining a modified Rossby number as

$$\mathrm{Ro}^* = \frac{U-\omega/k}{2R\Omega} = \frac{1}{kR\Lambda} \tag{28}$$

and selecting $n=0$, Eqs. (25)–(27) are identical to Eqs. (7), (9), and (11) in Chow [7] where the waves in the varicose tube are not moving. In other words, if one observes the flow from a reference frame moving with the traveling-wave deformations of the shell, the axial flow in the shell is identical to that in the rigid varicose tube.

3 Results

As in Refs. [9,11], we investigate the stability of a rubber shell containing water flow with $\bar{h}=0.02$, $\bar{\rho}=1.05$, and $\nu=0.49$. We consider first the dynamics of a nonrotating shell carrying a purely axial flow, and then analyze how the solution breaks down when rotation is present and how this breakdown is related to the physical phenomenon of blocking.

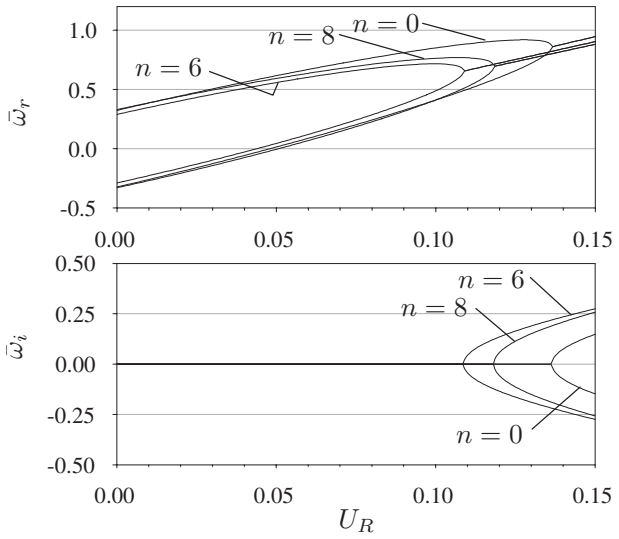

Fig. 3 Evolution of the complex frequencies of the system with $\bar{\Omega}=0$ and $\bar{k}=7.2$

First, for a nonrotating shell, $\bar{\Omega}=0$, the evolution of the frequencies of the system for increasing internal flow velocity is plotted in Fig. 3 for $\bar{k}=7.2$. In each combination of axial and circumferential wave numbers, the system loses stability by coupled-mode flutter when the forward and the backward traveling-wave frequencies coalesce. A mode is said to be unstable when its imaginary frequency becomes negative. For example, in Fig. 3, the circumferential mode $n=6$ becomes unstable at $U_R=0.109$. The curves in Fig. 3 reproduce the results without rotation of Lai and Chow [9] perfectly.

In the presence of rotation, $\bar{\Omega}=0.1$, Lai and Chow [9] obtained the frequency evolution curves in Fig. 4. From these results, it is surmised that, for an axial wavenumber $\bar{k}=10$, the system first loses stability in the $n=3$ mode at $U_R=0.089$, at the "nose" of the curve shown.

However, it is impossible to reproduce any of the curves in Fig. 4. For the typical case $\bar{\Omega}=0.1$, $\bar{k}=10$, and $n=0$, we obtain the dispersion relation curve shown in Fig. 5 superimposed on the contour plot of the absolute value of Λ, which is defined in Eq. (13). This plot is similar to that obtained by Cortelezzi et al. [11]. The "islets where a solution is not feasible" described in Ref. [11] really are numerous infinitely long lines that appear as islets only because of the coarse numerical resolution. These lines of no solution, parallel to the $|\Lambda|$-isolines in the region where $|\Lambda|>1$ in

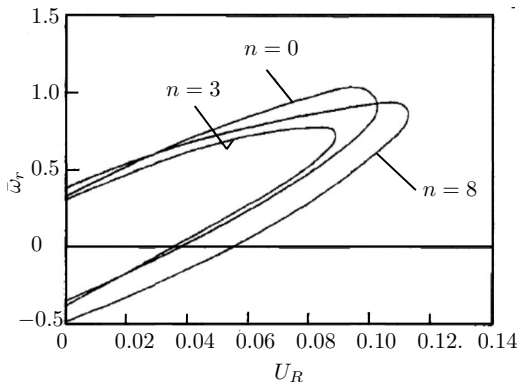

Fig. 4 Stability curve of Lai and Chow [9] for the system with $\bar{\Omega}=0.1$ and $\bar{k}=10$. Figure reproduced from Ref. [9].

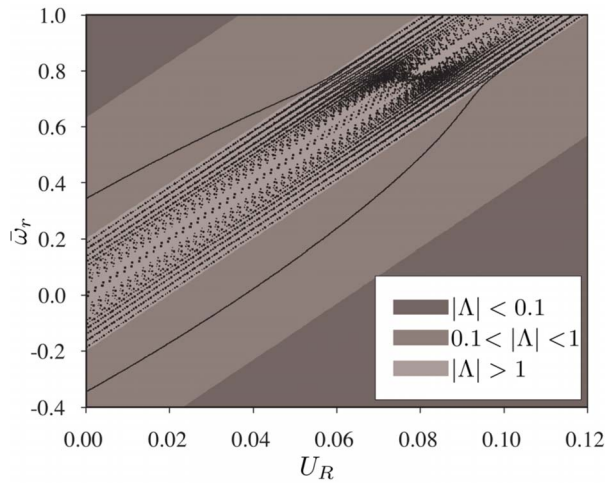

Fig. 5 Evolution of the real frequency of the mode $\bar{k}=10$ and $n=0$ of the system for $\bar{\Omega}=0.1$ over the contour plot of the absolute value of Λ

Fig. 5 arise at every zero of the denominator of the pressure solution, Eq. (18). In the axisymmetric case $n=0$, the singularities happen when $\Lambda^2=1+(\lambda_\ell/\bar{k})^2$, where λ_ℓ designates the ℓth zero of the function $J_1(\lambda)$.

To further our understanding, we take a look at the relative axial velocity profile of Eqs. (25)–(27) for increasing rotation rate. In Fig. 6 we plot the relative axial velocity profile at the throat, $\bar{x}=\pi/\bar{k}$, for the case $\bar{k}=3$ and $\bar{w}=0.1$. As the rotation rate is increased from $\Lambda=0$ to $\Lambda=1.5$, the velocity at the center of the cylinder, V_x^*, keeps increasing. In fact, it keeps increasing with Λ up to $\Lambda=1.6221$, which corresponds to the first singularity $\bar{k}\sqrt{\Lambda^2-1}=\lambda_1$, at which point the velocity and pressure solutions blow up. When $\bar{k}\sqrt{\Lambda^2-1}$ is in the neighborhood of λ_ℓ, a small deformation of the wall, $\bar{w}$, creates a perturbation velocity in the flow, which is not necessarily small when compared with the mean flow velocity U_R. In this case, the linear approximation used in this analysis becomes invalid. As expected from the similitude in the equations, in a reference frame moving with the traveling waves, the axial flow in the deforming shell plotted in Fig. 6 is identical to that in a permanently deformed tube by Chow [7].

Since the flow in the deforming shell and the flow in the permanently deformed tube of Chow [7] are identical when viewed in the appropriate reference frame, we get a physical insight as to what happens to the flow at a critical Λ by reviewing the results of

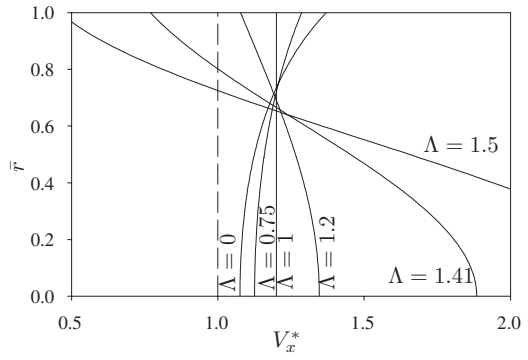

Fig. 6 For small rates of rotation, effect of increasing the rate of rotation on the relative axial velocity profile at the throat $\bar{x}=\pi/\bar{k}$ for $\bar{k}=3$ and $\bar{w}=0.1$

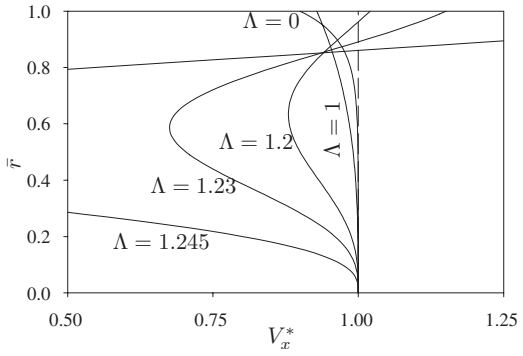

Fig. 7 For small rates of rotation, effect of increasing the rate of rotation on the relative axial velocity profile at $\theta=0$ and $\bar{x}=0$ for $\bar{k}=10$, $n=3$, and $\bar{w}=0.01$

Chow [7] for the behavior of the flow in a converging-diverging nozzle at a critical Rossby number. The streamlines and the flow velocity profile obtained at the first critical Rossby number by Chow [7] are shown in Fig. 1. At a critical Rossby number, the streamlines become parallel to the pipe, and the fluid near the wall is stagnant. What happens to the flow is well described by Chow [7]: "Physically speaking, the fluid cannot go around the humps at the wall, and is expected to become stagnant in that region. This is the phenomenon of blocking, which occurs in a rotating and in a stratified fluid flow." The exact shape of the deformed wall becomes irrelevant, as the fluid close to the wall is stagnant and the effective cross section of the tube is reduced by an amount equal to the height of the constriction.

It is not clear how blocking of the flow would affect the stability of the shell. Since our model is linear and the boundary conditions at the interface between the flow and the deforming wall of the shell are applied at the undeformed position of the wall, blocking cannot be accounted for in the current linear model.

For nonaxisymmetric cases, the behavior is at first sight similar. For any circumferential wavenumber n, the denominator of the pressure solution for $\Lambda^2>1$, Eq. (18), has an infinite number of roots, which lead to an infinite number of critical values of Λ where no flow solution exists. The effect of increasing the rate of rotation on the relative axial velocity profile in a nonaxisymmetric mode for $\bar{k}=10$ and $n=3$ is shown in Fig. 7. The behavior is qualitatively similar to what happens for axisymmetric modes. The flow velocity blows up at a critical Λ. Since no results are available in the literature on the behavior of flow in a permanently spinning nonaxisymmetrically deformed tube, it is impossible to visualize the flow pattern. On the other hand, because the exact shape of the constriction to the flow becomes irrelevant as the fluid close to the wall is stagnant, one is led to believe that dynamics similar to what is shown in Fig. 1 would occur for nonaxisymmetric deformation. This, however, has to be investigated further.

As to how Lai and Chow obtained the closed curves in Fig. 4 in Ref. [9] for the dispersion relation when rotation is present, this question is still open. One possible explanation is that a very limited number of terms were used in a series expansion to represent the Bessel functions, hence reducing the number of roots in the denominator of the pressure function in Eq. (17). By using a finite number of points to trace the curve they could have "skipped" over the singularities and hence got a continuous but numerically incorrect dispersion relation curve (see Ref. [13] for details).

4 Conclusion

When considering the rotating inviscid axial flow inside a corotating cylindrical shell, if one places oneself in a frame of reference moving with the traveling waves in the shell wall, the flow is

identical to that in a rigid varicose tube. By visualizing the flow in a permanently and axisymmetrically deformed tube, as in Chow [7], we can understand that in the shell the phenomenon of blocking creates a stagnation region between the humps of the wall when the Rossby number approaches a critical value. The linear model cannot account for this stagnation region and the solution blows up. The solution also blows up for nonaxisymmetric deformation modes and the physical explanation may be basically the same. In order to correctly model the flow inside the rotating cylindrical shell, accounting for geometric nonlinearities in the boundary conditions and viscous effects in the flow model would be necessary.

Acknowledgment

This research was supported by the Natural Sciences and Engineering Research Council of Canada (NSERC) and the Fonds Québécois de Recherche sur la Nature et les Technologies (FQRNT).

Nomenclature

E = shell-material Young's modulus
h = shell thickness
k = axial wavenumber
n = circumferential wavenumber
R = shell radius
Ro = Rossby number
Ro^* = modified Rossby number
r, θ, x = radial, azimuthal, and axial coordinates
U = mean plug flow velocity
U_R = reduced velocity
u, v, w = shell deformation components
V_r, V_θ, V_x = flow velocity components
V_x^* = dimensionless axial flow velocity relative to the traveling waves in the shell
γ = shell timescale
Λ = dimensionless relative rotation rate
ν = shell-material Poisson's ratio
ρ = fluid density
ρ_s = shell-material density
Ω = rate of rotation
$\omega, \omega_r, \omega_i$ = complex, real, and imaginary frequencies
$\bar{\ }$ = denotes a dimensionless variable

Appendix: Linear Shell Theory

The Donnell–Mushtari thin cylindrical shell equations are derived in detail in Ref. [12]. The simplest available linear cylindrical shell model is based on the following assumptions: the thickness of the shell is small compared with its radius, which implies among other things that shear deformation is negligible; strains and displacements are sufficiently small for quantities of second- and higher-order magnitude in the strain-displacement relations to be neglected in comparison with the first-order terms; the radial normal stress is small compared with the other two normal stress components and may be neglected; at every location on the shell, the normal to the undeformed middle surface remains aligned in the same direction and normal to the deformed middle surface as the shell deforms (this assumption, which is also referred to as the Kirchhoff hypothesis, represents an extension to the case of a thin elastic shell of the familiar Euler–Bernoulli hypothesis of beam theory which states that plane sections remain plane; the assumption of the preservation of the normal implies, among other things, that all of the strain components in the direction of the normal to the reference surface vanish); in the changes in curvature and in the twist of the midsurface, the tangential displacements and their derivatives are neglected (from this simplification, the stretch of the shell only depends on the strain and the transverse displacement); Hooke's law is the constitutive law obeyed by the material; the shell material is isotropic; the stress tensor is symmetric (neglect body couples).

The linear Donnell–Mushtari shell operator used in Eq. (2) can be written as

$$\mathbf{L}_D = \begin{bmatrix} \dfrac{\partial^2}{\partial x^2} + \dfrac{1-\nu}{2R}\dfrac{\partial^2}{\partial \theta^2} & \dfrac{1+\nu}{2R}\dfrac{\partial^2}{\partial x\,\partial\theta} & \dfrac{\nu}{R}\dfrac{\partial}{\partial x} \\ \dfrac{1+\nu}{2R}\dfrac{\partial^2}{\partial x\,\partial\theta} & \dfrac{1-\nu}{2}\dfrac{\partial^2}{\partial x^2} + \dfrac{1}{R^2}\dfrac{\partial^2}{\partial\theta^2} & \dfrac{1}{R^2}\dfrac{\partial}{\partial\theta} \\ \dfrac{\nu}{R}\dfrac{\partial}{\partial x} & \dfrac{1}{R^2}\dfrac{\partial}{\partial\theta} & \dfrac{1}{R^2} + \dfrac{h^2}{12}\nabla^2\nabla^2 \end{bmatrix} \tag{29}$$

where $\nabla^2 = \partial^2/\partial x^2 + (1/R^2)\partial^2/\partial\theta^2$.

References

[1] Païdoussis, M. P., 2004, *Fluid-Structure Interactions: Slender Structures and Axial Flow*, Vol. 2, Elsevier, London.
[2] Srinivasan, A. V., 1971, "Flutter Analysis of Rotating Cylindrical Shells Immersed in a Circular Helical Flowfield of Air," AIAA J., **9**, pp. 394–400.
[3] Dowell, E., Srinivasan, A., McLean, J., and Ambrose, J., 1974, "Aeroelastic Stability of Cylindrical Shells Subjected to a Rotating Flow," AIAA J., **12**, pp. 1644–1651.
[4] Rayleigh, Lord J. W., 1917, "Dynamics of Revolving Fluids," Proc. R. Soc. London, Ser. A, **93**, pp. 148–154.
[5] Howard, L. N., and Gupta, A. S., 1962, "On the Hydrodynamic and Hydromagnetic Stability of Swirling Flows," J. Fluid Mech., **14**, pp. 463–476.
[6] Wang, S., and Rusak, Z., 1996, "On the Stability of an Axisymmetric Rotating Flow in a Pipe," Phys. Fluids, **8**, pp. 1007–1016.
[7] Chow, C. Y., 1969, "Swirling Flow in Tubes of Non-Uniform Cross-Sections," J. Fluid Mech., **38**, pp. 843–854.
[8] Yih, C.-S., 1965, *Dynamics of Nonhomogeneous Fluids*, Macmillan, New York.
[9] Lai, Y.-C., and Chow, C.-Y., 1973, "Stability of a Rotating Thin Elastic Tube Containing a Fluid Flow," Z. Angew. Math. Mech., **53**, pp. 511–517.
[10] Chen, T. L. C., and Bert, C. W., 1977, "Dynamic Stability of Isotropic or Composite-Material Cylindrical Shells Containing Swirling Fluid Flow," ASME J. Appl. Mech., **44**, pp. 112–116.
[11] Cortelezzi, L., Pong, A., and Païdoussis, M., 2004, "Flutter of Rotating Shells With a Co-Rotating Axial Flow," ASME J. Appl. Mech., **71**, pp. 143–145.
[12] Leissa, A. W., 1973, "Vibration of Shells," NASA Report No. SP-288.
[13] Gosselin, F., 2006, "Stability of a Rotating Cylindrical Shell Containing Axial Viscous Flow," M.Eng. thesis, McGill University, Montreal, Canada.

Dynamic Variational-Asymptotic Procedure for Laminated Composite Shells—Part I: Low-Frequency Vibration Analysis

Chang-Yong Lee
Postdoctoral Fellow

Dewey H. Hodges
Professor
Mem. ASME

School of Aerospace Engineering,
Georgia Institute of Technology,
Atlanta, GA 30332-0150

An asymptotically correct dynamic shell theory, valid over a wide range of frequencies and wavelengths, is rigorously derived from an analytical point of view. The derivation provides insight and guidance for the numerical modeling of layered shells. This work is based on three essential theoretical foundations: (a) the concept of decomposition of the rotation tensor, which is to establish the dynamic three-dimensional elasticity problem in a compact and elegant intrinsic form for application to the complex geometry of shells; (b) the variational-asymptotic method, which is to perform a systematic and mathematical dimensional reduction in the long-wavelength regime for both low- and high-frequency vibration analysis; and (c) hyperbolic short-wavelength extrapolation, which is to achieve simple, accurate, and positive definite energy functionals for all wavelengths. Based on these, unlike most established shell theories that are limited to the long-wavelength low-frequency regime, the present theory describes in an asymptotically correct manner not only the low-frequency but also some of the first high-frequency branches of vibrations in the long-wave range. Moreover, it recovers the approximate three-dimensional stress state in both long- and short-wavelength ranges.
[DOI: 10.1115/1.3002761]

1 Introduction

Because laminated composite shells are increasingly being used in various engineering applications that are very sensitive to excessive structural noise and vibration, research covering the dynamic behavior of composite shells has received considerable attention in the past three decades. By the imposition of limits on wavelengths and timescales in question, one can broadly classify the analysis of shell structural dynamic response into three regimes corresponding to various forms of dynamic disturbances: (i) long-wavelength low-frequency vibration analysis (for a low-frequency disturbance), (ii) long-wavelength high-frequency analysis (for a medium-frequency disturbance), and (iii) short-wavelength high-frequency analysis (for a high-frequency disturbance) [1,2]. In general, the short-wavelength low-frequency vibration analysis is not of great interest in dynamics because it is used to determine quasistatic boundary layers localized near the edges of the shell, whereas the other analyses describe disturbances that may extend over the entire shell. Referring to the existing literature, one can easily observe that there has been a tremendous amount of work done on using approximate shell models for the prediction and control of structural dynamic responses under the first regime, i.e., long-wavelength low-frequency vibration conditions [3–8]. However, for the second and third regimes there has been very little work done; see, for example, Refs. [9–12].

Tracking the history of new developments of approximate shell and plate theories, one can observe that there are two main competing methodologies: asymptotic [13] and variational [14]. With the help of these two methods, there have been many attempts to develop dynamic models valid over a wide range of frequencies. First, in order to use variational methods, one needs an a priori kinematical assumption for the distribution of displacements as functions of the through-thickness coordinate. Substituting this assumption into the three-dimensional (3D) energy functional, one can derive the equations determining the dependence of the displacement field on the thickness coordinate by varying the functional obtained after the averaging procedure. The main disadvantage of the variational method is the necessity of a kinematical assumption, while simplicity and brevity are its advantages.

On the other hand in asymptotic methods one expands the displacements in an asymptotic series, so that no ad hoc kinematical assumptions are needed. Indeed, the asymptotic method needs no a priori assumptions; however, it is very cumbersome and restricted from both geometric and material points of view [2,15,16]. Although there are many new theories based on elaborate mathematics or bound up with the phenomenal power of computers in the literature, none of them resolves satisfactorily all the above disadvantages at the same time. This is partly because there are many new models that are constructed for specific problems without generalization in mind (variational method case) and partly because some models are too complicated to be used in design (asymptotic method case). Simple yet efficient and generalized methods of analysis are still needed to predict the structural dynamic response over a wide range of frequencies.

Berdichevsky [14,17,18] first proposed the synthesis of these two methods, called the variational-asymptotic method (VAM), which avoids the disadvantages of both methods described above. It also has proved to be very effective and accurate in formulating theories for a variety of elastic structures, such as theories for the static analysis of both isotropic and composite beams [19] (see also Ref. [20] and the many works cited therein), plates [21], and shells [22], as well as low- and high-frequency theories for vibrations of isotropic beams, plates, and shells [23]. At least some asymptotic methods give results similar to VAM, but they are

Contributed by the Applied Mechanics Division of ASME for publication in the JOURNAL OF APPLIED MECHANICS. Manuscript received September 5, 2007; final manuscript received May 22, 2008; published online October 23, 2008. Review conducted by Edmundo Corona.

more difficult to apply, more awkward in the series substitution into the equations of the 3D theory, and more problematic as far as the subsequent asymptotic derivation of the recurrent system of equations for corresponding terms of the series. Especially for dimensional reduction, the VAM is a quite powerful and systematic mathematical method.

The present development represents a new contribution, as there is no published work on using the VAM for the modeling of composite shells, layers of which possess monoclinic symmetry, that is valid over a wide range of frequencies and expressed in an analytic form. In this first paper of a two-part series, we present the procedure for low-frequency vibration analysis according to the VAM, applicable to shells in which each layer is made of monoclinic composite material. In this procedure, we can define a position vector in the deformed configuration as a result of the primary step under the long-wavelength low-frequency approximations. This is the very beginning point assumption on which most published shell theories are based, whether analytical or numerical. Based on this, one can obtain the total energy functional asymptotically correct up to the zero-order approximation, such as classical laminated shell theories, just as in the static case. In the second paper, high-frequency vibration analysis and hyperbolic short-wavelength extrapolation are undertaken for the same type of shell.

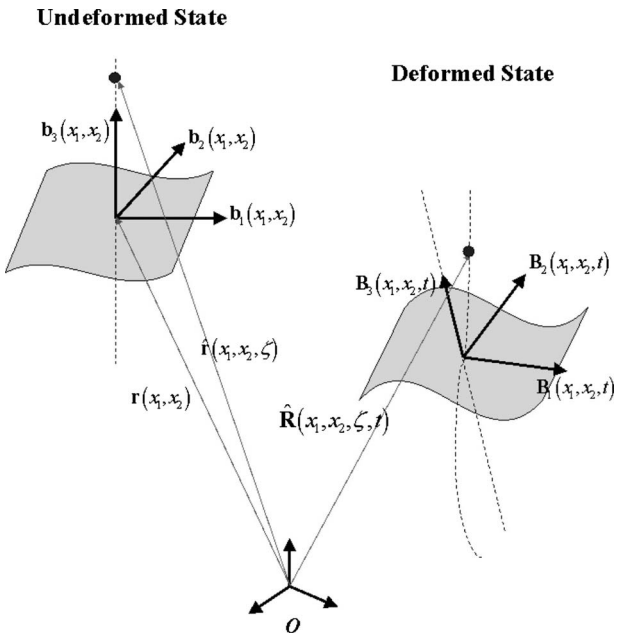

Fig. 1 Schematic of shell deformation

2 Shell Kinematics

A shell may be considered geometrically as a smooth 2D surface S surrounded by a layer of matter with thickness h to form a 3D body with one dimension much smaller than the other two. Let S be called the reference surface of the 3D body, bounded by a smooth closed curve ∂S and mathematically represented by a set of arbitrary curvilinear coordinates, x_α. However, without loss of generality, one may simplify the formulation by choosing the lines of curvature as curvilinear coordinates. In addition, for representing the 3D medium uniquely and following a very natural choice generally, the third coordinate is specified as $x_3=h\zeta$, the coordinate normal to the reference surface. Throughout the analysis, a nondimensional coordinate through the thickness is used $-1/2 \le \zeta \le 1/2$. In fact, almost all published shell theories are based on this choice. Note that here and throughout the rest of the shell development, Greek indices assume values 1 and 2 while Latin indices assume 1, 2, and 3. Repeated indices are summed over their range except where explicitly mentioned. As sketched in Fig. 1, letting $\mathbf{b}_3(x_1,x_2)$ denote the unit vector normal to the reference surface of the undeformed shell, one can then describe the position of any material point in the stress-free undeformed configuration by its position vector $\hat{\mathbf{r}}$ relative to a point O fixed in an inertial frame, such that

$$\hat{\mathbf{r}}(x_1,x_2,\zeta) = \mathbf{r}(x_1,x_2) + h\zeta\mathbf{b}_3(x_1,x_2) \tag{1}$$

where $\mathbf{r}$ is the position vector from O to the point located by x_α on the reference surface.

When the reference surface of the undeformed shell coincides with its middle surface, it naturally follows that

$$\langle \hat{\mathbf{r}}(x_1,x_2,\zeta) \rangle = \mathbf{r}(x_1,x_2) \tag{2}$$

where the angle-brackets $\langle \bullet \rangle$ denote the definite integral through the thickness of the shell $\zeta \in [-1/2, 1/2]$ and will be used throughout the rest of the development for shells.

Typically, let 2D base vectors $\mathbf{a}_\alpha$ associated with x_α be defined as

$$\mathbf{a}_\alpha(x_1,x_2) = \mathbf{r}_{,\alpha} \tag{3}$$

From henceforth, for simplicity, we will avoid including the independent variables on which a function depends unless it is not obvious for the reader to determine what they are. From Eq. (3) one can define the so-called Lamé parameters as

$$A_\alpha(x_1,x_2) = \sqrt{\mathbf{a}_\alpha \cdot \mathbf{a}_\alpha} \tag{4}$$

Let us mention that in Eq. (4), the summation convention is not applied because α is not a dummy index; this same rule will apply to the rest of the development as well. Then, for the computational procedures used later, the 2D unit base vectors $\mathbf{b}_i$ constitute an orthogonal triad system such that

$$\mathbf{b}_\alpha(x_1,x_2) = \frac{\mathbf{a}_\alpha}{A_\alpha}, \quad \mathbf{b}_3 = \mathbf{b}_1 \times \mathbf{b}_2 = \frac{\mathbf{a}_1 \times \mathbf{a}_2}{|\mathbf{a}_1 \times \mathbf{a}_2|} \tag{5}$$

Now by taking the partial derivatives of Eq. (1) with respect to x_α, it is easy to see that the covariant 3D base vectors $\mathbf{g}_i$ associated with the chosen coordinate system are given by

$$\mathbf{g}_1 = \mathbf{a}_1 + h\zeta\mathbf{b}_{3,1}$$

$$\mathbf{g}_2 = \mathbf{a}_2 + h\zeta\mathbf{b}_{3,2}$$

$$\mathbf{g}_3 = \mathbf{b}_3 \tag{6}$$

From the differential geometry of the surface and with the help of Refs. [24,25] one can express the derivative of 2D unit base vectors $\mathbf{b}_{i,\alpha}$ as follows:

$$\mathbf{b}_{i,\alpha} = A_\alpha \mathbf{k}_\alpha \times \mathbf{b}_i \tag{7}$$

with

$$\mathbf{k}_\alpha = (-k_{\alpha 2}\mathbf{b}_1 + k_{\alpha 1}\mathbf{b}_2 + k_{\alpha 3}\mathbf{b}_3) \tag{8}$$

where $\mathbf{k}_\alpha$ is the curvature vector measured in $\mathbf{b}_i$ in which $k_{\alpha\beta}$ refers to out-of-plane curvatures. As mentioned before, because we chose the lines of curvature to be the coordinates, one can easily observe that $k_{12}=k_{21}=0$. Moreover, since we are interested in the interior solution up to the first approximation for regular shells, we can assume that the initial curvatures k_{ij} and Lamé parameters A_α slowly vary or are constant to make our problem more tractable and the procedure simpler. This assumption will result in the neglect of all the derivatives of these quantities with respect to in-plane coordinates x_α in the formulation.

By the standard definition [24], the contravariant base vectors are given by

$$\mathbf{g}^i(x_l) = \frac{1}{2\sqrt{g}} e_{ijk}\mathbf{g}_j \times \mathbf{g}_k \tag{9}$$

where $g = \det(\mathbf{g}_i \cdot \mathbf{g}_j)$ is the determinant of the metric tensor for the undeformed configuration, and e_{ijk} are the components of the permutation tensor in a Cartesian coordinate system.

When the shell is deformed, the particle that had position vector $\hat{\mathbf{r}}(x_1, x_2, \zeta)$ in the undeformed state now has the position vector $\hat{\mathbf{R}}(x_1, x_2, \zeta, t)$ in the deformed configuration. The latter can be uniquely determined by the deformation of the 3D body. A new triad $\mathbf{B}_i(x_1, x_2, t)$ is introduced for the deformed shell. Note that the $\mathbf{B}_i$ unit vectors are just tools to enable one to express vectors and tensors in their component form during the derivation. They are not necessarily tangent to the coordinates of the deformed shell. The relation between $\mathbf{B}_i$ and $\mathbf{b}_i$ can be specified by an arbitrarily large rotation in terms of the matrix of direction cosines $C(x_1, x_2, t)$, so that

$$\mathbf{B}_i = C_{ij}\mathbf{b}_j, \quad C_{ij} = \mathbf{B}_i \cdot \mathbf{b}_j \tag{10}$$

subject to the requirement that $\mathbf{B}_i$ is coincident with $\mathbf{b}_i$ when the structure is undeformed. Without loss of generality, the position vector $\hat{\mathbf{R}}$ can be defined as

$$\hat{\mathbf{R}}(x_1, x_2, \zeta, t) = P_i(x_1, x_2, \zeta, t)\mathbf{B}_i(x_1, x_2, t) \tag{11}$$

where P_i are unknown arbitrary 3D functions to be determined independently at each frequency regime.

Before closing this section, definitions of the 2D generalized curvature and inertial angular velocity measures are introduced for the purpose of formulating this problem in dynamic intrinsic form. Following Ref. [26], they can be defined as

$$\mathbf{B}_{i,\alpha} = A_\alpha(-K_{\alpha 2}\mathbf{B}_1 + K_{\alpha 1}\mathbf{B}_2 + K_{\alpha 3}\mathbf{B}_3) \times \mathbf{B}_i, \quad \dot{\mathbf{B}}_i = \Omega_j \mathbf{B}_j \times \mathbf{B}_i \tag{12}$$

where K_{ij} are the curvatures of the deformed surface, which are the sum of curvatures of undeformed geometry k_{ij} and curvatures introduced by the deformation κ_{ij}. The order of the latter is denoted by $O(\hat{\varepsilon}/h)$, where $\hat{\varepsilon}$ is the order of the maximum strain in the shell. In addition, Ω_i are the inertial angular velocity measures of the deformed shell reference surface, the order of which is denoted by $O(c\hat{\varepsilon}/l)$ with c being the order of the characteristic velocity of plane waves c_0 in the composite material under consideration.

3 3D Formulation

Following Ref. [27], the Jauman–Biot–Cauchy strain components for small local rotation are given by

$$\Gamma_{ij} = \frac{1}{2}(F_{ij} + F_{ji}) - \delta_{ij} \tag{13}$$

where δ_{ij} is the Kronecker symbol, and F_{ij} the mixed-basis component of the deformation gradient tensor such that

$$F_{ij} = \mathbf{B}_i \cdot \mathbf{G}_k \mathbf{g}^k \cdot \mathbf{b}_j \tag{14}$$

Here $\mathbf{G}_i = \partial\hat{\mathbf{R}}/\partial x_i$ is the 3D covariant basis vector of the deformed configuration. With the help of Eqs. (9) and (12)–(14), one can obtain the 3D strain and velocity fields as

$$\Gamma_{11} = \frac{P_{1;1} - \kappa_{13}P_2 + (k_{11} + \kappa_{11})P_3}{1 + h\zeta k_{11}} - 1$$

$$2\Gamma_{12} = \frac{P_{1;2} - \kappa_{23}P_2 + \kappa_{21}P_3}{1 + h\zeta k_{22}} + \frac{P_{2;1} + \kappa_{13}P_1 + \kappa_{12}P_3}{1 + h\zeta k_{11}}$$

$$\Gamma_{22} = \frac{P_{2;2} + \kappa_{23}P_1 + (k_{22} + \kappa_{22})P_3}{1 + h\zeta k_{22}} - 1$$

$$2\Gamma_{13} = \frac{1}{h}P_{1|\zeta} + \frac{P_{3;1} - (k_{11} + \kappa_{11})P_1 - \kappa_{12}P_2}{1 + h\zeta k_{11}}$$

$$2\Gamma_{23} = \frac{1}{h}P_{2|\zeta} + \frac{P_{3;2} - \kappa_{21}P_1 - (k_{22} + \kappa_{22})P_2}{1 + h\zeta k_{22}}$$

$$\Gamma_{33} = \frac{1}{h}P_{3|\zeta} - 1 \tag{15}$$

and

$$\Lambda_1 = \dot{P}_1 - \Omega_3 P_2 + \Omega_2 P_3$$

$$\Lambda_2 = \dot{P}_2 + \Omega_3 P_1 - \Omega_1 P_3$$

$$\Lambda_3 = \dot{P}_3 - \Omega_2 P_1 + \Omega_1 P_2 \tag{16}$$

where $(\bullet)_{;\alpha} = (1/A_\alpha)\,\partial(\bullet)/\partial x_\alpha$, $(\bullet)_{|\zeta} = \partial(\bullet)/\partial\zeta$, and $\dot{(\bullet)} = \partial(\bullet)/\partial t$. Note that unlike most published 2D shell theories, the order of unknown 3D functions P_i is not assumed a priori to derive Eqs. (15) and (16), but rather it is obtained as a result of the minimization procedure in the primary approximation for each range of frequency vibrations. For convenience $\hat{q}$ denotes the order of P_i.

Until now, by using the concept of decomposition of the rotation tensor, we have been trying to keep the analysis both general and simple. However, to make the problem more manageable, we have to make some inevitable approximations that published shell theories have almost universally used. There are several small parameters in most engineering structures, and the existence of small parameters brings about a great variety of possibilities for application of asymptotic methods. In the shell problem considered, three possible small parameters exist: the maximum strain $\hat{\varepsilon}$, the geometric parameter h/R, and the thickness-to-wavelength parameter h/l, where R is the characteristic radius of curvature of the shell reference surface and l is the characteristic wavelength in the in-plane directions. To stipulate the third parameter, as small implies the long-wavelength regime, where the smallest wavelength l of the deformation pattern associated with the in-plane coordinates is considerably greater than the shell thickness h. Moreover, we will introduce one more important physical parameter for a dynamical shell theory

$$\frac{h}{c_0\tau} \tag{17}$$

where c_0 is the characteristic velocity of shear waves in the composite material under consideration, and τ is the characteristic timescale of the change of the deformation with respect to time, which also corresponds to the period of vibrations. Following Ref. [14], if one limits the consideration to the low-frequency vibration of the shell, then τ can be linked to l as

$$\frac{h}{c_0\tau} \ll 1 \Rightarrow \tau \sim O\left(\frac{l}{c_0}\right) \tag{18}$$

On the other hand, for the high-frequency (thickness) vibrations case

$$\frac{h}{c_0\tau} \gg 1 \Rightarrow \tau \sim O\left(\frac{h}{c_0}\right) \tag{19}$$

Therefore, generally speaking, there are three independent small parameters: h/l, h/R, and $\hat{\varepsilon}$. Note that the wavelength of the high-frequency vibrations along the thickness coordinate of the 3D shell is usually smaller than h, but this fact is not an obstacle for the long-wavelength application of the VAM, which is based on the smallness of h/l with l being the wavelength in the in-plane directions.

Following Refs. [25,26], Hamilton's principle for the surface can now be constructed as

$$\int_{t_1}^{t_2}\int_S [\delta\overline{\mathcal{L}} + \overline{\delta\mathcal{W}}]dSdt = \overline{\delta\mathcal{A}} \tag{20}$$

where t_α are arbitrary fixed times, S is the undeformed reference surface, $\overline{\mathcal{L}}$ is the Lagrangian density per unit area, $\overline{\delta\mathcal{W}}$ is the virtual work of the applied loads per unit area, and $\overline{\delta\mathcal{A}}$ is the virtual action at the boundary of shell and at the ends of the time interval. Furthermore, $\overline{\mathcal{L}}$ can be written as

$$\overline{\mathcal{L}} = \overline{\mathcal{K}} - \overline{\mathcal{U}} \tag{21}$$

By definition, $\overline{\mathcal{K}}$ and $\overline{\mathcal{U}}$ are the 3D kinetic energy and strain energy densities per unit area, respectively, of the form

$$\overline{\mathcal{K}} = \frac{1}{2}\langle\rho[\Lambda_e^T\Lambda_e + \Lambda_3^2]\eta\rangle \tag{22}$$

and

$$\begin{aligned}\overline{\mathcal{U}} &= \frac{1}{2}\left\langle\begin{Bmatrix}\Gamma_e\\ 2\Gamma_s\\ \Gamma_3\end{Bmatrix}^T D\begin{Bmatrix}\Gamma_e\\ 2\Gamma_s\\ \Gamma_3\end{Bmatrix}\eta\right\rangle \\ &= \frac{1}{2}\left\langle\begin{Bmatrix}\Gamma_e\\ 2\Gamma_s\\ \Gamma_3\end{Bmatrix}^T\begin{bmatrix}D_e & D_{es} & D_{e3}\\ D_{es}^T & D_s & D_{s3}\\ D_{e3}^T & D_{s3}^T & D_3\end{bmatrix}\begin{Bmatrix}\Gamma_e\\ 2\Gamma_s\\ \Gamma_3\end{Bmatrix}\eta\right\rangle\end{aligned} \tag{23}$$

where

$$\begin{aligned}\Gamma_e &= \lfloor\Gamma_{11} \quad 2\Gamma_{12} \quad \Gamma_{22}\rfloor^T\\ 2\Gamma_s &= \lfloor 2\Gamma_{13} \quad 2\Gamma_{23}\rfloor^T\\ \Gamma_3 &= \Gamma_{33}\\ \Lambda_e &= \lfloor\Lambda_1 \quad \Lambda_2\rfloor^T\\ \Lambda_3 &= \Lambda_3\end{aligned} \tag{24}$$

with

$$\eta = \frac{\mathbf{g}_1\times\mathbf{g}_2\cdot\mathbf{g}_3}{|\mathbf{a}_1\times\mathbf{a}_2|} = 1 + 2h\zeta H + (h\zeta)^2K \tag{25}$$

Here $H=(k_{11}+k_{22})/2$ and $K=k_{11}k_{22}$ are called the mean and the Gaussian curvatures of the surface, respectively, $\rho(\zeta)$ is the mass density of a 3D body and $D(\zeta)$ is the 3D 6×6 material matrix. As one can see, the matrix D_e, the column matrix D_s, and the scalar D_3 refer to extensional, shear, and thickness elasticities. In particular, because we have an interest in modeling composite shells, each lamina of which is made of a material with monoclinic symmetry, D_{es} and D_{s3} always vanish no matter what the layup angle is in Eq. (23). Considering this, we can simplify the strain energy expression, Eq. (23), to the following form:

$$\overline{\mathcal{U}} = \frac{1}{2}\langle[\Gamma_e^TD_e\Gamma_e + 2\Gamma_e^TD_{et}\Gamma_t + 2\Gamma_s^TD_s(2\Gamma_s) + D_3\Gamma_3^2]\eta\rangle \tag{26}$$

If there are surface tractions and body forces applied to the shell, the virtual work can be obtained as

$$\overline{\delta\mathcal{W}} = \delta(\alpha_iP_i^+ + \beta_iP_i^- + \langle\phi_iP_i\rangle) \tag{27}$$

where α_i, β_i, and ϕ_i are the applied loads on the top surface and at the bottom surface and body force through the thickness, respectively, $(\bullet)^+=(\bullet)|_{\zeta=1/2}$, and $(\bullet)^-=(\bullet)|_{\zeta=-1/2}$. Here the loading can be assumed to be of order h/l and h/R, which is acceptable for our level of approximation.

Now, the complete statement of the problem can be presented in terms of the principle of virtual work, such that

$$\delta\overline{\mathcal{K}} - \delta\overline{\mathcal{U}} + \overline{\delta\mathcal{W}} = 0 \tag{28}$$

In spite of the possibility of accounting for nonconservative forces at the starting point of the analysis, the problem that governs the 3D unknown functions turns out to be linear. Hence, any nonconservatism in the applied loads only affects the 2D analysis, and one can pose the problem that governs the functions as the minimization of a total energy functional, viz.,

$$\overline{\mathcal{L}} = \overline{\mathcal{K}} - \overline{\mathcal{P}} \tag{29}$$

with $\overline{\mathcal{P}}=\overline{\mathcal{U}}+\overline{\mathcal{V}}$, so that

$$\delta\overline{\mathcal{L}} = 0 \tag{30}$$

where the work done by applied loads $\overline{\mathcal{V}}$ is

$$\overline{\mathcal{V}} = -\alpha_\parallel^TP_\parallel^+ - \alpha_3P_3^+ - \beta_\parallel^TP_\parallel^- - \beta_3P_3^- - \langle\phi_\parallel^TP_\parallel\rangle - \langle\phi_3P_3\rangle \tag{31}$$

where $(\bullet)_\parallel=\lfloor(\bullet)_1 \quad (\bullet)_2\rfloor^T$.

Below, for simplicity of terminology, we will refer to $\overline{\mathcal{P}}$ as the total potential energy, or the total potential. Here and throughout the rest of the shell development, we assume the mass density to be a constant to make our problem more tractable and the procedure simpler. Introducing nondimensional quantities $\rho/\rho_0=1$ and $D^*=D/\mu_0$ into Eqs. (22) and (26), the total energy functional can be nondimensionalized, so that

$$2\overline{\mathcal{K}} = \rho_0\langle[\Lambda_e^T\Lambda_e + \Lambda_3^2]\eta\rangle \tag{32}$$

and

$$2\overline{\mathcal{U}} = \mu_0\langle[\Gamma_e^TD_e^*\Gamma_e + 2\Gamma_e^TD_{e3}^*\Gamma_3 + 2\Gamma_s^TD_s^*(2\Gamma_s) + D_3^*\Gamma_3^2]\eta\rangle \tag{33}$$

Here ρ_0 and μ_0 are characteristic values of mass density and material constants in the material under consideration (all of which are assumed to be of the same order). Therefore, $c_0=\sqrt{\mu_0/\rho_0}$. Up to this point, this is simply an alternative formulation of the original 3D elasticity problem. If we attempt to solve this problem directly, we will meet the same difficulty as solving any full 3D elasticity problem. Fortunately, as shown below, VAM can be used to calculate the 3D unknown functions asymptotically.

4 Primary Approximation

The dimensional reduction from three dimensions to two cannot be done exactly. The best one can do is to accomplish it asymptotically taking advantage of the small parameters. With h/l, h/R, $\hat{\varepsilon}$, and the additional small parameter in Eq. (18), we are ready to determine the constraints and the orders of the undetermined function for long-wavelength low-frequency vibrations. At the primary step of VAM, since the 3D undetermined functions $P_i(x_1,x_2,\zeta,t)$ have small characteristic lengths along the thickness coordinate ζ, the entire kinetic energy density stemming from Eq. (18) and all derivative terms with respect to in-plane coordinates $(O(\hat{q}/l)^2)$ in the strain energy density can be neglected when compared with derivative terms with respect to the thickness coordinate $(O(\hat{q}/h)^2)$. The latter can be retained as the formally leading terms in Eq. (33); note that one may denote the order of P_i by $O(\hat{q})$. Therefore, from Eq. (29) we obtain the following functional:

$$2\overline{\mathcal{L}} = -\mu_0\left\langle\frac{1}{h^2}P_{\parallel\zeta}^TD_s^*P_{\parallel\zeta} + \frac{1}{h^2}D_3^*P_{3|\zeta}^2\right\rangle \tag{34}$$

It is obvious that the above Eq. (34) is negative definite; its maximum is equal to zero and is reached for functions $\mathbf{R}$ that are independent of ζ, i.e.,

$$\hat{\mathbf{R}}(x_1,x_2,\zeta,t) = \mathbf{R}(x_1,x_2,t) \tag{35}$$

where R_α and R_3 (components of $\mathbf{R}$ in the $\mathbf{B}_i$ basis) are arbitrary functions of x_α and t. Now, in accordance with the variational-asymptotic scheme, the position vector Eq. (11) in the deformed configuration can be redefined in the form

$$\hat{\mathbf{R}}(x_1,x_2,\zeta,t) = \mathbf{R}(x_1,x_2,t) + \bar{P}_i(x_1,x_2,\zeta,t)\mathbf{B}_i(x_1,x_2,t) \tag{36}$$

where $\bar{P}_i$ are unknown 3D functions to be determined later. The formulation in Eq. (36) is six times redundant because of the way unknown functions are introduced; six constraints are needed to make it unique. The redundancy can be removed by choosing appropriate definitions of $\mathbf{R}$ and $\mathbf{B}_i$. The first three constraints can be chosen such that the average of each function through the thickness vanishes. Following Refs. [14,23], if we define $\mathbf{R}$ similarly as Eq. (2) to be the average position through the thickness of the deformed configuration, from it follows that the undetermined functions satisfy the three constraints

$$\langle \bar{P}_\alpha(x_1,x_2,\zeta,t)\rangle = 0, \quad \langle \bar{P}_3(x_1,x_2,\zeta,t)\rangle = 0 \tag{37}$$

According to Eq. (37), $\mathbf{R}$ describes the position vector from point O to the point on the reference surface of the deformed shell, i.e.,

$$\mathbf{R}(x_1,x_2,t) = \mathbf{r}(x_1,x_2) + \mathbf{u}(x_1,x_2,t) \tag{38}$$

where $\mathbf{u}(x_1,x_2,t)$ denote the average shell displacement vector.

Another two constraints can be specified by taking $\mathbf{B}_3$ as the normal to the reference surface of the deformed shell. It is pointed out that this choice is only for convenience in the derivation and has nothing to do with the Kirchhoff assumption.

Definitions of the 2D generalized strain and inertial velocity measures are needed for calculating the undetermined functions asymptotically. Following Refs. [25,26,28], they can be defined as

$$\mathbf{R}_{,\alpha} = A_\alpha(\mathbf{B}_\alpha + \varepsilon_{\alpha\beta}\mathbf{B}_\beta), \quad \dot{\mathbf{R}} = V_i\mathbf{B}_i \tag{39}$$

where $\varepsilon_{\alpha\beta}$ are the 2D in-plane strains, the order of which is denoted by $O(\hat{\varepsilon})$, and V_i are the inertial velocity measures of any material point on the shell reference surface, the order of which is denoted by $O(c\hat{\varepsilon})$. Both $\varepsilon_{\alpha\beta}$ and $\kappa_{\alpha\beta}$ are termed as 2D generalized strains. On the other hand, both V_i and Ω_α are termed as 2D inertial generalized velocities. Here one is free to set $\varepsilon_{12}=\varepsilon_{21}$, i.e.,

$$\frac{\mathbf{B}_1\cdot\mathbf{R}_{,2}}{A_2} = \frac{\mathbf{B}_2\cdot\mathbf{R}_{,1}}{A_1} \tag{40}$$

which can serve as another constraint to specify the global rotation of the triad $\mathbf{B}_i$ and make the formulation in Eq. (36) unique. It is important to emphasize that both generalized strain and velocity measures are nonlinear expressions in terms of 2D displacement and rotation measures and are the source of the geometrical nonlinearities in the 2D shell analysis.

In accordance with the variational-asymptotic scheme, we substitute Eq. (36) again into the total energy functional and neglect all small terms containing $\bar{P}_\alpha$ and $\bar{P}_3$ in the asymptotic sense. Due to the low-frequency assumption Eq. (18), the time derivatives of $\bar{P}_\alpha$ and $\bar{P}_3$ can be removed from the kinetic energy density again. As the result of the foregoing procedure the total potential can be retained as the formally dominant terms in the form

$$2\bar{\mathcal{L}} = -\mu_0\left\langle \frac{1}{h^2}\bar{P}_{\|\zeta}^T D_s^* \bar{P}_{\|\zeta} + 2\varepsilon^T D_{e3}^*\left(\frac{1}{h}\bar{P}_{3|\zeta} - 1\right) + D_3^*\left(\frac{1}{h}\bar{P}_{3|\zeta} - 1\right)^2\right\rangle \tag{41}$$

where

$$\varepsilon = \lfloor \varepsilon_{11} \quad 2\varepsilon_{12} \quad \varepsilon_{22} \rfloor^T$$

The unknown function that maximizes the energy functional expression of Eq. (41), subject to constraint Eq. (37), can be obtained by applying the usual procedure of the calculus of variations with the aid of Lagrange multipliers. The final result is

$$\bar{P}_\alpha = 0, \quad \bar{P}_3 = h\zeta \tag{42}$$

Finally, as a result of the primary step under the low-frequency long-wavelength approximations, the position vector $\hat{\mathbf{R}}$ can be expressed as

$$\hat{\mathbf{R}}(x_1,x_2,\zeta,t) = \mathbf{R}(x_1,x_2,t) + h\zeta\mathbf{B}_3(x_1,x_2,t) + w_i(x_1,x_2,\zeta,t)\mathbf{B}_i(x_1,x_2,t) \tag{43}$$

where the unknown 3D functions w_i represent the general warping displacement of an arbitrary point on the normal line of the deformed shell, subject to the following three constraints:

$$\langle \bar{w}_i(x_1,x_2,\zeta,t)\rangle = 0 \tag{44}$$

According to Eq. (44), the 3D displacement distributions now can be expressed as a series with respect to $h\zeta$ in the case of long-wavelength low-frequency vibration approximations, just as in statics. However, Eq. (43) is the very beginning point assumptions on which most published shell theories are exclusively developed.

Before proceeding to the first approximation, it is convenient to redefine corresponding 3D strain and velocity fields associated with Eq. (43)

$$\Gamma_e = \varepsilon + \zeta(h\kappa) + I_\alpha w_{\|;\alpha} + C_R^e w_3 + h\zeta\bar{C}_R^e[\varepsilon + \zeta(h\kappa)]$$

$$2\Gamma_s = \frac{1}{h}w_{\|\|\zeta} + e_\alpha w_{3;\alpha} + C_R^s w_\|$$

$$\Gamma_3 = \frac{1}{h}w_{3|\zeta} \tag{45}$$

and

$$\Lambda_e = V_\| + \xi(h\Omega_\|) + \dot{w}_\|$$

$$\Lambda_3 = V_3 + \dot{w}_3 \tag{46}$$

with

$$\varepsilon = \lfloor \varepsilon_{11} \quad 2\varepsilon_{12} \quad \varepsilon_{22} \rfloor^T$$

$$h\kappa = \lfloor h\kappa_{11} \quad h(\kappa_{12}+\kappa_{21}) \quad h\kappa_{22} \rfloor^T \tag{47}$$

Here all terms of the type containing $\kappa_{21}-\kappa_{12}$ are neglected due to the compatibility equations for the 2D strains [29]. All the operators are defined as

$$\xi = \begin{bmatrix} 0 & -\zeta \\ \zeta & 0 \end{bmatrix} \tag{48}$$

$$I_1 = \begin{bmatrix} 1 & 0 & 0 \\ 0 & 1 & 0 \end{bmatrix}^T \quad I_2 = \begin{bmatrix} 0 & 1 & 0 \\ 0 & 0 & 1 \end{bmatrix}^T \tag{49}$$

$$e_1 = \lfloor 1 \quad 0 \rfloor^T \quad e_2 = \lfloor 0 \quad 1 \rfloor^T \tag{50}$$

and

$$C_R^e = \lfloor k_{11} \quad 0 \quad k_{22} \rfloor^T \tag{51}$$

$$\bar{C}_R^e = \begin{bmatrix} -k_{11} & 0 & 0 \\ 0 & -\left(\dfrac{k_{11}+k_{22}}{2}\right) & 0 \\ 0 & 0 & -k_{22} \end{bmatrix}^T \quad C_R^s = \begin{bmatrix} -k_{11} & 0 \\ 0 & -k_{22} \end{bmatrix}^T \tag{52}$$

With the help of the methodology in Ref. [21], one can now construct the virtual work done by applied loads, so that

$$\overline{\delta\mathcal{W}} = \overline{\delta q}^T f + \overline{\delta\psi}^T m + \delta(\alpha^T w^+ + \beta^T w^- + \langle\phi^T w\rangle) \tag{53}$$

where $\overline{\delta q}$ and $\overline{\delta\psi}$ are column matrices of the virtual displacement and rotation measures for the reference surface expressed in the $\mathbf{B}_i$ basis, respectively, and

$$f = \alpha + \beta + \langle\phi\rangle$$

$$m = \tilde{e}_3 \left[\frac{1}{2}(\alpha - \beta) + \langle \zeta \phi \rangle \right] \tag{54}$$

with

$$\tilde{e}_3 = \begin{bmatrix} 0 & -1 & 0 \\ 1 & 0 & 0 \\ 0 & 0 & 0 \end{bmatrix} \tag{55}$$

Thus, the work done by applied loads is

$$\bar{\mathcal{V}} = -\alpha_\parallel^T w_\parallel^+ - \alpha_3 w_3^+ - \beta_\parallel^T w_\parallel^- - \beta_3 w_3^- - \langle \phi_\parallel^T w_\parallel \rangle - \langle \phi_3 w_3 \rangle \tag{56}$$

in which only the warping displacement is varied, subject to the constraints Eq. (44).

Using Eqs. (45), (46), and (56), Eq. (29) can be rewritten as a long-wavelength low-frequency vibration of the nondimensional energy functional in terms of

$$2\bar{\mathcal{K}} = \rho_0 \langle \{ [V_\parallel + \xi(h\Omega_\parallel) + \dot{w}_\parallel]^T [V_\parallel + \xi(h\Omega_\parallel) + \dot{w}_\parallel] \quad + [V_3 + \dot{w}_3]^2 \} \eta \rangle \tag{57}$$

and

$$\begin{aligned} 2\bar{\mathcal{P}} = \mu_0 \Bigg\langle \Bigg\{ & \left[\frac{1}{h} w_{\parallel|\zeta} + e_\alpha w_{3;\alpha} + C_R^s w_\parallel \right]^T D_s^* \left[\frac{1}{h} w_{\parallel|\zeta} + e_\alpha w_{3;\alpha} + C_R^s w_\parallel \right] \\ & + \frac{1}{h^2} D_3^* (w_{3|\zeta})^2 + \frac{2}{h} [\varepsilon + \zeta(h\kappa) + I_\alpha w_{\parallel;\alpha} + C_R^e w_3 \\ & + h\zeta \bar{C}_R^e (\varepsilon + \zeta(h\kappa))]^T D_{e3}^* w_{3|\zeta} + [\varepsilon + \zeta(h\kappa) + I_\alpha w_{\parallel;\alpha} + C_R^e w_3 \\ & + h\zeta \bar{C}_R^e (\varepsilon + \zeta(h\kappa))]^T D_e^* [\varepsilon + \zeta(h\kappa) + I_\alpha w_{\parallel;\alpha} + C_R^e w_3 \\ & + h\zeta \bar{C}_R^e (\varepsilon + \zeta(h\kappa))] \eta \Bigg\} \Bigg\rangle - \alpha_\parallel^T w_\parallel^+ - \alpha_3 w_3^+ - \beta_\parallel^T w_\parallel^- - \beta_3 w_3^- \\ & - \langle \phi_\parallel^T w_\parallel \rangle - \langle \phi_3 w_3 \rangle \end{aligned} \tag{58}$$

Now one is ready to use the VAM to solve for the unknown warping field asymptotically.

5 First Approximation (First-Order Warping Field)

The VAM requires one to find the leading terms of the functional according to the different orders. Since only the warping is varied, one needs the leading terms that involve warping only and the leading terms that involve the warping and other quantities (i.e., the generalized strain and velocity and loading). Based on this, the leading terms in Eq. (29) for the first approximation are given by

$$2\bar{\mathcal{L}} = -\mu_0 \left\langle \frac{1}{h^2} (w_{\parallel|\zeta}^T D_s^* w_{\parallel|\zeta} + D_3^* w_{3|\zeta}^2) + \frac{2}{h} [\varepsilon + \zeta(h\kappa)]^T D_{e3}^* w_{3|\zeta} \right\rangle \tag{59}$$

The warping field that maximizes the energy functional expression of Eq. (59), subject to constraint Eq. (44), can be obtained by applying the usual procedure of the calculus of variations with the aid of Lagrange multipliers. The resulting warping is

$$w_\alpha = 0, \quad w_3 = h\bar{D}_1 \varepsilon + h\bar{D}_2(h\kappa) \tag{60}$$

where

$$\bar{D}_{1|\zeta} = -D_{e3}^{*T}/D_3^*, \quad \bar{D}_{2|\zeta} = -\zeta D_{e3}^{*T}/D_3^* \tag{61}$$

with

$$\langle \bar{D}_1 \rangle = 0, \quad \langle \bar{D}_2 \rangle = 0 \tag{62}$$

Here, the solution is the same as that derived by the VAM [22,30].

6 Total Energy Functional for Low-Frequency Vibration Analysis

For performing short-wave extrapolation later, it is convenient to find the total energy functional of low-frequency vibrations in the long-wavelength regime. Substituting Eq. (60) back into the total energy functional Eq. (29), one can obtain the total energy functional asymptotically correct up to the zeroth-order approximation as

$$\bar{\mathcal{L}} = \frac{1}{2}\rho_0 \langle (V_\parallel^T V_\parallel + V_3^2) \rangle - \frac{1}{2}\mu_0 \langle [\varepsilon + \zeta(h\kappa)]^T D_c^* [\varepsilon + \zeta(h\kappa)] \rangle \tag{63}$$

where

$$D_c^* = D_e^* - D_{e3}^* D_{e3}^{*T}/D_3^* \tag{64}$$

The energy functional of this approximation coincides with classical laminated shell theories, just as in statics.

7 Conclusions

Unlike most published work on shell modeling, the present work proposes a new analytic procedure to rigorously construct an accurate geometrically nonlinear model for composite shells that is valid over a wide range of frequencies. The main purpose of this development is to provide insight and guidance for the development of numerical-based shell modeling suitable for a practical procedure to model layered shells. To do this, the concept of decomposition of the rotation tensor introduced by Danielson and Hodges [27] is first used to establish the original three-dimensional elasticity problem in intrinsic form, which helps to avoid unnecessary complexities of the mathematical description. Then, as the most essential and important procedure, the variational-asymptotic method introduced by Berdichevsky [14] and Le [23] is used to perform a rigorous dimensional reduction. This takes advantage of small geometric parameters inherent in the structure. Unlike the static case, however, there is one more important physical parameter in the dynamics case. It is called the characteristic timescale for the change of the deformation with respect to time; it is also used to analyze shell dynamic response for long wavelengths, in both low- and high-frequency vibration regimes. Finally, another logically independent procedure is used, the extrapolation of the foregoing procedures to the short-wavelength regime; this procedure was introduced by Berdichevsky [14] and Le [23].

This paper, which is the first part of a two-part series, presents the low-frequency vibration analysis up to the first approximation. In this procedure, we define a position vector in the deformed configuration as a result of the primary step under the long-wavelength low-frequency approximation. This is the starting point for most published shell theories, whether analytical or numerical. Based on this, we show that the energy functional of this approximation coincides with that of classical laminated shell theories, just as in statics. The present theory is different from the Berdichevsky–Le theory in two aspects. First, the Berdichevsky–Le theory is geometrically linear, while the present theory is based on the intrinsic formulation, which is also valid in the geometrically nonlinear case. Second, the Berdichevsky–Le theory restricted to homogenous and isotropic materials, while the present theory is developed for a layered shell in which each layer is monoclinic. In particular, the velocity and strain measures in Eq. (63) are nonlinear functions of surface displacement and rotation variables [29].

Unlike the low-frequency vibration case, the characteristic timescale is linked to the smallest wavelength of the deformation (shell thickness) as part of the asymptotic procedure. Then, because the frequencies are no longer small, the kinetic energy density must be retained in the primary step of the high-frequency vibration analysis. Therefore, it should also be pointed out that for most published shell theories it is difficult to use the result of the

primary step under the low-frequency vibration analysis even in a primary approximation. In the second part of this work, this issue and another independent procedure, hyperbolic short-wave extrapolation, are further discussed in detail.

References

[1] Langley, R. S., and Bardell, N. S., 1998, "A Review of Current Analysis Capabilities Applicable to the High Frequency Vibration Prediction of Aerospace Structures," Aeronaut. J., **102**, pp. 287–297.

[2] Kaplunov, J. D., Kossovich, L. Y., and Nolde, E. V., 1998, *Dynamics of Thin Walled Elastic Bodies*, Academic, New York.

[3] Leissa, A. W., 1973, "Vibration of Shells," NASA, Report No. SP 288.

[4] Noor, A. K., and Burton, W. S., 1989, "Assessment of Shear Deformation Theories for Multilayered Composite Plates," Appl. Mech. Rev., **42**(1), pp. 1–13.

[5] Qatu, M. S., 2002, "Recent Research Advances in the Dynamic Behavior of Shells, 1989–1999, Part 1: Laminated Shells," Appl. Mech. Rev., **55**(7), pp. 1989–2000.

[6] Qatu, M. S., 2002, "Recent Research Advances in the Dynamic Behavior of Shells, 1989–1999, Part 2: Homogeneous Shells," Appl. Mech. Rev., **55**(5), pp. 415–434.

[7] Reddy, J. N., 2003, *Mechanics of Laminated Composite Plates and Shells: Theory and Analysis*, 2nd ed., CRC, Boca Raton, FL.

[8] Amabili, M., and Païdoussis, M. P., 2003, "Review of Studies on Geometrically Nonlinear Vibrations and Dynamics of Circular Cylindrical Shells and Panels, With and Without Fluid-Structure Interaction," Appl. Mech. Rev., **56**(4), pp. 349–381.

[9] Le, K. C., 1997, "High Frequency Vibrations and Wave Propagation in Elastic Shells: Variational-Asymptotic Approach," Int. J. Solids Struct., **34**(30), pp. 3923–3939.

[10] Kienzler, R., Altenbach, H., and Ott, I., 2004, *Theories of Plates and Shells: Critical Review and New Applications*, Springer, New York.

[11] Braga, A. M. B., and Rivas A, C. E., 2005, "High-Frequency Response of Isotropic-Laminated Cylindrical Shells Modeled by a Layer-Wise Theory," Int. J. Solids Struct., **42**, pp. 4278–4294.

[12] Yang, S., and Yuan, F. G., 2005, "Transient Wave Propagation of Isotropic Plates Using a Higher-Order Plate Theory," Int. J. Solids Struct., **42**, pp. 4115–4153.

[13] Andrianov, I. V., Awrejcewicz, J., and Barantsev, R. G., 2003, "Asymptotic Approaches in Mechanics: New Parameters and Procedures," Appl. Mech. Rev., **56**(1), pp. 87–110.

[14] Berdichevsky, V. L., 1983, *Variational Principles of Continuum Mechanics*, Nauka, Moscow.

[15] Losin, N. A., 1997, "Asymptotics of Flexural Waves in Isotropic Elastic Plates," ASME J. Appl. Mech., **64**, pp. 336–342.

[16] Losin, N. A., 1998, "Asymptotics of Extensional Waves in Isotropic Elastic Plates," ASME J. Appl. Mech., **65**, pp. 1042–1047.

[17] Berdichevsky, V. L., 1979, "Variational-Asymptotic Method of Constructing a Theory of Shells," Prikl. Mat. Mekh., **43**(3), pp. 664–687.

[18] Berdichevsky, V. L., 1980, "Variational-Asymptotic Method of Constructing the Nonlinear Shell Theory," *Theory of Shells*, W. T. Koiter and G. K. Mikhailov, eds., North-Holland, Amsterdam, pp. 137–161.

[19] Yu, W., Hodges, D. H., Volovoi, V. V., and Cesnik, C. E. S., 2002, "On Timoshenko-Like Modeling of Initially Curved and Twisted Composite Beams," Int. J. Solids Struct., **39**(19), pp. 5101–5121.

[20] Hodges, D. H., 2006, *Nonlinear Composite Beam Theory*, AIAA, Reston, VA.

[21] Yu, W., Hodges, D. H., and Volovoi, V. V., 2002, "Asymptotic Generalization of Reissner-Like Composite Plate Theory With Accurate Strain Recovery," Int. J. Solids Struct., **39**(20), pp. 5185–5203.

[22] Yu, W., Hodges, D. H., and Volovoi, V. V., 2002, "Asymptotic Generalization of Reissner-Mindlin Theory: Accurate Three-Dimensional Recovery for Composite Shells," Comput. Methods Appl. Mech. Eng., **191**(44), pp. 5087–5109.

[23] Le, K. C., 1999, *Vibrations of Shells and Rods*, 1st ed., Springer, Germany.

[24] Danielson, D. A., 1997, *Vectors and Tensors in Engineering and Physics*, 2nd ed., Pereus Books, Cambridge, MA.

[25] Hodges, D. H., Atılgan, A. R., and Danielson, D. A., 1993, "A Geometrically Nonlinear Theory of Elastic Plates," ASME J. Appl. Mech., **60**, pp. 109–116.

[26] Hodges, D. H., Yu, W., and Patil, M. J., 2006. "Geometrically-Exact, Intrinsic Theory for Dynamics of Moving Composite Plates and Shells," *Proceedings of the 47th Structures, Structural Dynamics, and Materials Conference*.

[27] Danielson, D. A., and Hodges, D. H., 1987, "Nonlinear Beam Kinematics by Decomposition of the Rotation Tensor," ASME J. Appl. Mech., **54**(2), pp. 258–262.

[28] Libai, A., and Simmonds, J. G., 1998, *The Nonlinear Theory of Elastic Shells*, 2nd ed., Cambridge University Press, Cambridge, New York.

[29] Yu, W., and Hodges, D. H., 2004, "Geometrically Nonlinear Shear Deformation Theory for Composite Shells," ASME J. Appl. Mech., **71**(1), pp. 1–9.

[30] Lee, B. W., 1993. "Application of Variational-Asymptotic Method to Laminated Composite Plates," Ph.D. thesis, Aerospace Engineering, Georgia Institute of Technology, Atlanta, GA.

Dynamic Variational-Asymptotic Procedure for Laminated Composite Shells—Part II: High-Frequency Vibration Analysis

Chang-Yong Lee
Postdoctoral Fellow

Dewey H. Hodges
Professor
Mem. ASME

School of Aerospace Engineering,
Georgia Institute of Technology,
Atlanta, GA 30332-0150

Shell theories intended for low-frequency vibration analysis are frequently constructed from a generalization of the classical shell theory in which the normal displacement (to a first approximation) is constant through the thickness. Such theories are not suitable for the analysis of complicated high-frequency effects in which displacements may change rapidly along the thickness coordinate. Clearly, to derive by asymptotic methods, a shell theory suitable for high-frequency behavior requires a different set of assumptions regarding the small parameters associated with the characteristic wavelength and timescale. In Part I such assumptions were used to perform a rigorous dimensional reduction in the long-wavelength low-frequency vibration regime so as to construct an asymptotically correct energy functional to a first approximation. In Part II the derivation is extended to the long-wavelength high-frequency regime. However, for short-wavelength behavior, it becomes very difficult to represent the three-dimensional stress state exactly by any two-dimensional theory; and, at best, only a qualitative agreement can be expected. To rectify this difficult situation, a hyperbolic short-wave extrapolation is used. Unlike published shell theories for this regime, which are limited to homogeneous and isotropic shells, all the formulas derived herein are applicable to shells in which each layer is made of a monoclinic material. [DOI: 10.1115/1.3002762]

1 Introduction

In the theory of shells, dimensional reduction from the dynamic equations of three-dimensional (3D) elasticity to the approximate two-dimensional (2D) equations is possible only if the displacements change little along the in-plane coordinates over distances of the order of the shell thickness h within the long-wavelength regime. Formally this can be stated as $h/l \to 0$, where l is a characteristic length scale associated with the variation of the deformation of the reference surface, often referred to as the "wavelength" of deformation for the reference surface. However, there is an important physical characteristic τ present in dynamics analysis that is not present in statics. It is called the characteristic "timescale" associated with the change of the deformation with respect to time. Following Ref. [1], one can establish the asymptotic relationships between the characteristic wavelength and timescale, both in the long-wavelength regime. If one limits the consideration to low-frequency vibration of the shell, then τ can be linked to l as

$$\frac{h}{c_0\tau} \ll 1 \Rightarrow \tau \sim O\left(\frac{l}{c_0}\right) \tag{1}$$

where c_0 is in general the characteristic velocity of shear waves in the composite material under consideration. Like the corresponding static shell analysis, Eq. (1) leads, in the first approximation, to classical laminated shell theories for which the displacements are constant through the thickness. See Part I of this paper for a detailed presentation procedure of the low-frequency vibration analysis.

However, the above condition that published shell theories are almost universally used is not suitable for analyzing complicated high-frequency effects. This is because the displacements rapidly oscillate along the thickness coordinate and an infinite variety of displacement distributions along the shell thickness (branches) are possible. Based on this physical behavior, τ can be linked to h instead of l, so that

$$\frac{h}{c_0\tau} \gg 1 \Rightarrow \tau \sim O\left(\frac{h}{c_0}\right) \tag{2}$$

Moreover, for problems with zero displacement at the edge, it turns out that the branches have the quality that they are orthogonal with respect to kinetic and strain energies up to the first approximations. This makes it possible to independently investigate vibrations corresponding to different branches [2,3].

On the other hand, within the short-wavelength range, where $l \gg h$, it is very difficult to represent the 3D stress state exactly by a 2D theory. Therefore, at best, only a qualitative agreement can be expected; it is thus more natural to apply the other operator into the equations of the theory of shells-henceforth referred to as the hyperbolic short-wave extrapolation procedure. The hypothesis assumed here is that it needs to be done by using changes of variable that are motivated by the necessity to match the dispersion curves associated with the 2D theory with those of the 3D theory [4].

Here in this paper, Part II, we present the whole procedure covering the high-frequency vibration analysis and hyperbolic short-wavelength extrapolation procedure in detail. Figure 1 shows a flowchart for the overall process. The work is an extension of certain works of Berdichevksy and Le [2–5], which were restricted to the linear theory and homogeneous isotropic materi-

Contributed by the Applied Mechanics Division of ASME for publication in the JOURNAL OF APPLIED MECHANICS. Manuscript received September 5, 2007; final manuscript received May 22, 2008; published online October 23, 2008. Review conducted by Edmundo Corona.

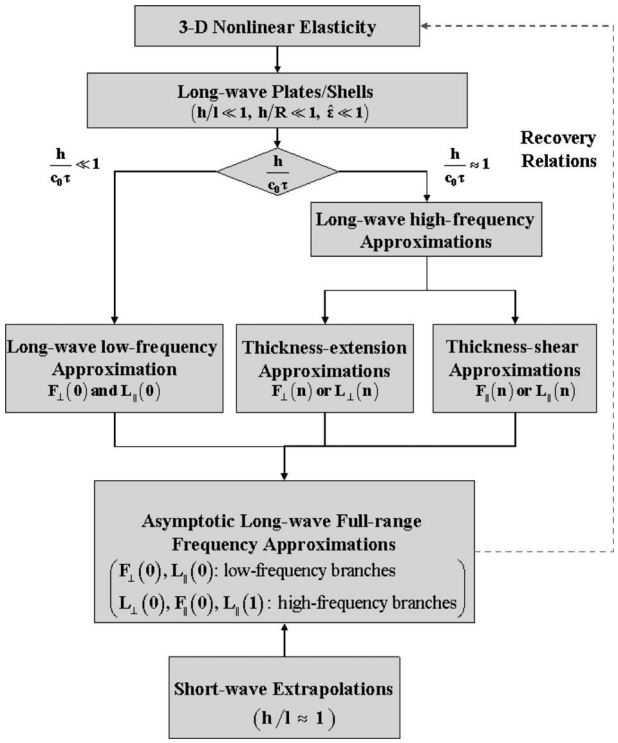

Fig. 1 Overview of the dynamic shell analysis

als and were presented in a complicated analytical form. On the other hand, the present theory is based on the intrinsic formulation and is suitable for layered composite shells of which each lamina exhibits monoclinic symmetry material. The present work is provided for insight, guidance, and as a baseline case in the development of numerical models for layered shells.

Note that since here and throughout the rest of this paper the notations employed are the same as in Part I, some sentences or equations may be skipped for the purpose of avoiding duplication, but the most important ones are repeated for clarity and smoothness of presentation.

2 Primary Approximation

In the development of a shell theory for long-wavelength low-frequency vibrations, the 2D total energy functional relies only on the three functions **u**, which describe the average displacement field of the shell. Their characteristics totally depend on the kinematics of the deformed shell reference surface, just as in statics. However, as the frequency increases, it is obvious to assume that some new degrees of freedom associated with branches of the shell high-frequency vibrations will come into play and have more and more influence over a total energy functional. Thus, it becomes imperative that we develop a general and systematic way to obtain those fields corresponding to the new degrees of freedom and then how to include those as variables in the 2D kinetic and potential energy densities without relying on mysticism. To do so the variational-asymptotic procedure will be used to analyze the vibrations of composite shells under the high-frequency long-wavelength approximation.

Before proceeding to the primary step of high-frequency vibration analysis, it is convenient to define a total energy functional, such that

$$\overline{\mathcal{L}} = \overline{\mathcal{K}} - \overline{\mathcal{P}} \tag{3}$$

where $\overline{\mathcal{K}}$ and $\overline{\mathcal{P}}$ are the 3D kinetic energy and potential energy densities per unit area, respectively.

Now, we need to determine the appropriate constraints and the exact orders of the yet-to-be-determined displacement field of a shell undergoing high-frequency long-wavelength vibrations. In contrast to the case of low-frequency vibration analysis, the kinetic energy density must now be retained in the primary step of the variational-asymptotic procedure since the frequencies are no longer small because of Eq. (2). Therefore, from Eq. (3), we obtain the functional

$$2\overline{\mathcal{L}} = \rho_0\langle(\dot{P}_\parallel^T\dot{P}_\parallel + \dot{P}_3^2)\rangle - \mu_0\left\langle \frac{1}{h^2}P_{\parallel|\zeta}^T D_s^* P_{\parallel|\zeta} + \frac{1}{h^2}D_3^* P_{3|\zeta}^2 \right\rangle \tag{4}$$

where $(\bullet)_\parallel = [(\bullet)_1 (\bullet)_2]^T$, $(\bullet)_{|\zeta} = \partial(\bullet)/\partial\zeta$, $\dot{(\bullet)} = \partial(\bullet)/\partial t$, and ρ_0 and μ_0 are the characteristic values of mass density and material constants in the material under consideration (all of which are assumed to be of the same order). Therefore, $c_0 = \sqrt{\mu_0/\rho_0}$. Here if functions P_3 and P_α are assumed to be independent of in-plane coordinates x_α, one can easily determine that each of the solutions given above represents an exact solution of 3D dynamic equations of elasticity for an infinite plate and correspond to synchronized vibrations of transverse fibers along the plate (with the zero in-plane wave number).

Calculating the variation of Eq. (4), setting the variations of P_α and P_3 at t_1 and t_2 equal to zero, and then assuming P_α and P_3 are dependent arbitrarily on the in-plane coordinates x_α and harmonically on t with frequencies ω_3 and ω_α, the stationary points of the energy functional fall into two classes, which can be regarded as the result of the primary approximation: (i) The out-of-plane displacement P_3 is much greater than the in-plane displacements P_α and (ii) the in-plane displacements P_α are much greater than the out-of-plane P_3. These correspond to four series of vibrations, as will be seen presently. Following the terminology introduced by Mindlin [6], one class is the series of thickness-extension vibrations characterized by

$$P_\alpha(x_1,x_2,\zeta,t) = 0, \quad P_3(x_1,x_2,\zeta,t) = q(\zeta)\psi_3(x_1,x_2,t) \tag{5}$$

where $q(\zeta)$ corresponds to the odd and even solutions of the one-dimensional (1D) through-thickness variational problem given by

$$\langle D_3^* q_{|\zeta}\delta q_{|\zeta} - \beta_{30}^2 q\,\delta q\rangle = 0 \tag{6}$$

with

$$\beta_{30} = \frac{\omega_3 h}{c_0}$$

The series with odd solutions is denoted by $L_\perp$ (symmetric thickness-extension vibrations), and that with even solutions by $F_\perp$ (antisymmetric thickness-extension vibrations). As expected, the branch $F_\perp(0)$ corresponds to the low-frequency vibration.

Another class is the series of thickness-shear vibrations characterized by

$$P_\alpha(x_1,x_2,\zeta,t) = p_{\alpha\beta}(\zeta)v_\beta(x_1,x_2,t), \quad P_3(x_1,x_2,\zeta,t) = 0 \tag{7}$$

where $p_{\alpha\beta}(\zeta)$ correspond to the odd or even solutions of the 1D variational problems given by

$$\langle \mathbf{p}_{|\zeta}^T D_s^* \delta\mathbf{p}_{|\zeta} - \beta_{s0}^2 \mathbf{p}^T\delta\mathbf{p}\rangle = 0 \tag{8}$$

where

$$\beta_{s0} = \begin{bmatrix} \beta_{10} & 0 \\ 0 & \beta_{20} \end{bmatrix} = \begin{bmatrix} \dfrac{\omega_1 h}{c_0} & 0 \\ 0 & \dfrac{\omega_2 h}{c_0} \end{bmatrix}$$

Note that here and throughout the shell development, we express our results in terms of the compact matrix form to make our procedure simpler. As expected, $\mathbf{p}(\zeta)$ is the 2×2 matrix, the components of which are $p_{\alpha\beta}$. Similar to the thickness-extension branches, the series with the odd solutions is denoted by $F_\parallel$ (asym-

metric thickness-shear vibrations), and that with even solutions by $L_{\|}$ (symmetric thickness-shear vibrations). Analogously, the branch $L_{\|}(0)$ corresponds to the low-frequency vibration.

Here the characteristic eigenvalues β_{t0}^2 and β_{s0}^2 run through a countable set of values; however, indices are attached neither to them nor to the corresponding eigenvectors in order to avoid complicating the notation. Since $q(\zeta)$ and $p_{\alpha\beta}(\zeta)$ are determined uniquely up to a constant from Eqs. (6) and (8), the following normalization conditions can be imposed:

$$\langle q^2\rangle = 1, \quad \langle \mathbf{p}^T\mathbf{p}\rangle = \mathbf{I} \tag{9}$$

where $\mathbf{I}$ is the 2×2 identity matrix. The constants are chosen so as to simplify later the changes of variable (see Sec. 5). Furthermore, one can also determine so-called cut-off frequencies ω_α and ω_3 from the appropriate values of β_{30} and $\beta_{\alpha 0}$, respectively, according to

$$\omega_3 = \frac{\beta_{30}c_0}{h}, \quad \omega_\alpha = \frac{\beta_{\alpha 0}c_0}{h} \tag{10}$$

Here the values of ω_α and ω_3 in these estimations are obviously taken for the same branch as the corresponding function. Based on this, the branches $F_\perp(0)$ and $L_{\|}(0)$ correspond to the low-frequency vibrations in Eq. (1). On the other hand, since ω_3, $\omega_\alpha \to \infty$ as $h\to 0$, all the remaining branches correspond to high-frequency vibrations with Eq. (2). Finally, using the results of the primary step under the low-frequency vibration analysis, the position vector $\hat{\mathbf{R}}$ in the deformed configuration can be represented as

$$\hat{\mathbf{R}}(x_1,x_2,\zeta,t) = \mathbf{R}(x_1,x_2,t) + h\zeta\mathbf{B}_3(x_1,x_2,t) + P_i(x_1,x_2,\zeta,t)\mathbf{B}_i(x_1,x_2,t) \tag{11}$$

where

$$\begin{aligned}\mathbf{P}(x_1,x_2,\zeta,t) = {} & q(\zeta)\psi_3(x_1,x_2,t)\mathbf{B}_3(x_1,x_2,t) \\ & + p_{\alpha\beta}(\zeta)v_\beta(x_1,x_2,t)\mathbf{B}_\alpha(x_1,x_2,t) \\ & + w_i(x_1,x_2,\zeta,t)\mathbf{B}_i(x_1,x_2,t)\end{aligned} \tag{12}$$

Here w_i is the unknown 3D warping functions for the high-frequency vibration approximations. Unlike the three constraints used in the low-frequency vibrations, the three new constraints may be needed to calculate w_i, which will be discussed in detail in Sec. 3.

According to Berdichevsky and Le [4], the propagation time for a perturbation through the thickness for these branches of vibrations is of the same order as the period of vibrations. Therefore, contrary to the methodology of most published plate and shell theories, it is impossible to assume the displacements to be only polynomials in $h\zeta$ even in a primary approximation (see Eq. (11)). For instance, the lowest branch of the thickness-shear vibrations $F_{\|}(0)$ is associated with vibrations for which a shift of the transverse fiber into a sinusoidal half-wave occurs for homogeneous isotropic shells. Generalized Reissner–Mindlin plate/shell theories are representative of this type of theories that take this kind of vibration into account. However, the utilization of a linear displacement field over the thickness instead of the correct sinusoid in the generalized Reissner–Mindlin plate/shell theory does not lead to a satisfactory quantitative prediction of the actual behavior of homogeneous isotropic shells [1,3].

Analogously, having made the above approximations, using Eq. (11) instead of the position vector expressed as a series with respect to $h\zeta$ and eliminating the effects of the low-frequency vibrations from the 3D strain and velocity fields and the work done by applied loads, Eq. (3) can be rewritten as a nondimensional high-frequency energy functional in terms of

$$2\overline{\mathcal{K}} = \rho_0\langle(\dot{P}_{\|}^T\dot{P}_{\|} + \dot{P}_3^2)\,\eta\rangle \tag{13}$$

and

$$\begin{aligned}2\overline{\mathcal{P}} = \mu_0\Bigg\langle\Bigg\{\Bigg[& \frac{1}{h}P_{\|\zeta} + e_\alpha P_{3;\alpha} + C_R^s P_{\|} + h\zeta C_R^s(e_\alpha P_{3;\alpha} \\ & + C_R^s P_{\|})\Bigg]^T D_s^*\Bigg[\frac{1}{h}P_{\|\zeta} + e_\alpha P_{3;\alpha} + C_R^s P_{\|} + h\zeta C_R^s(e_\alpha P_{3;\alpha} \\ & + C_R^s P_{\|})\Bigg] + \frac{1}{h^2}D_3^*(p_{3|\zeta})^2 + \frac{2}{h}[I_\alpha P_{\|;\alpha} + C_R^e P_3 + h\zeta(H_\alpha P_{\|;\alpha} \\ & + \tilde{C}_R^e P_3)]^T D_{e3}^* P_{3|\zeta} + [I_\alpha P_{\|;\alpha} + C_R^e P_3 + h\zeta(H_\alpha P_{\|;\alpha} \\ & + \tilde{C}_R^e P_3)]^T D_e^*[I_\alpha P_{\|;\alpha} + C_R^e P_3 + h\zeta(H_\alpha P_{\|;\alpha} + \tilde{C}_R^e P_3)]\Bigg\}\eta\Bigg\rangle \\ & - \alpha_{\|}^T P_{\|}^+ - \alpha_3 P_3^+ - \beta_{\|}^T P_{\|}^- - \beta_3 P_3^- - \langle\phi_{\|}^T P_{\|}\rangle - \langle\phi_3 P_3\rangle\end{aligned} \tag{14}$$

with

$$H_1 = \begin{bmatrix} -k_{11} & 0 & 0 \\ 0 & -k_{11} & 0 \end{bmatrix}^T, \quad H_2 = \begin{bmatrix} 0 & -k_{22} & 0 \\ 0 & 0 & -k_{22} \end{bmatrix}^T \tag{15}$$

$$\tilde{C}_R^e = \lfloor k_{11}^2 \quad 0 \quad k_{22}^2 \rfloor^T \tag{16}$$

and $(\bullet)_{;\alpha} = (1/A_\alpha)\,\partial(\bullet)/\partial x_\alpha$ and

$$\eta = 1 + 2h\zeta H + (h\zeta)^2 K \tag{17}$$

where $H=(k_{11}+k_{22})/2$ and $K=k_{11}k_{22}$ are called the mean and the Gaussian curvatures of the surface, respectively.

Now one is ready to use the variational-asymptotic method (VAM) to solve the unknown warping field for high-frequency vibrations asymptotically.

3 First Approximation (First-Order Warping Field)

Each branch is characterized by some specific frequency ω. According to Berdichevsky [2], it turns out that the branches possess a remarkable property: They are orthogonal in the kinetic and strain energy densities in the first approximation. This means that in the first approximation, vibrations of one type do not interact with those of other types; the possibility appears for investigating the vibrations of one branch independently of the vibrations of the others (except for the classical branches describing low-frequency vibrations). As before, the variations of v_α and ψ_3 should vanish at t_1 and t_2, just as in the case of low-frequency vibration analysis. Concerning the boundary conditions at the shell edge, we first consider the clamped edge, for which

$$p_{\alpha\beta}v_\beta = 0, \quad q\psi_3 = 0 \quad \text{at} \quad \partial S\times(-1/2\ \ 1/2) \tag{18}$$

Based on the above fact, we can find the next refinement for the warping fields in the branches associated with the thickness-extension vibrations (the series $L_\perp$ or $F_\perp$). At this step in a certain asymptotic expansion we seek the stationary w_i of Eq. (3) in the form

$$P_\alpha = w_\alpha(x_1,x_2,\zeta,t), \quad P_3 = P_{30} + w_3(x_1,x_2,\zeta,t) \tag{19}$$

with

$$P_{30} = q(\zeta)\psi_3(x_1,x_2,t)$$

where ψ_3 is regarded as one branch of this series as a given function of x_α and t satisfying the condition due to Eq. (18), namely,

$$\psi_3 = 0 \quad \text{at} \quad \partial S \tag{20}$$

while w_α and w_3 are unknown functions that should be determined by the variational-asymptotic procedure. Without any loss of generality, the following constraint can be imposed on w_3:

$$\langle q(\zeta)w_3\rangle = 0 \tag{21}$$

which corresponds to the assumption that $\psi_3=\langle q(\zeta)P_3\rangle$. Let us substitute Eq. (19) into the nondimensional kinetic and potential energies per unit area as Eqs. (13) and (14), and then the total energy functional Eq. (3). With the help of VAM and keeping the

leading terms that depend on w_i and the leading cross terms in Eq. (3), we obtain the functional

$$2\overline{\mathcal{L}} = \rho_0\langle[\dot{w}_\parallel^T\dot{w}_\parallel + \dot{w}_3^2 + \underline{2\dot{P}_{30}\dot{w}_3} + 4H\zeta w_3\dot{w}_3]\rangle - \mu_0\left\langle \frac{1}{h^2}[w_{\parallel|\zeta}^T D_s^* w_{\parallel|\zeta} + D_3^* w_{3|\zeta}^2 + \underline{2D_3^* P_{30|\zeta} w_{3|\zeta}}] + \frac{2}{h}[w_{\parallel|\zeta}^T D_s^* e_\alpha P_{30;\alpha} - \underline{\underline{w_\parallel^T I_\alpha^T D_{e3}^* P_{30|\zeta;\alpha}}} + 2HD_3^*\zeta P_{30} w_{3|\zeta} + w_{3|\zeta}^T D_{e3}^{*T} C_R^e P_{30} + w_3 C_R^{eT} D_{e3}^* P_{30|\zeta}]\right\rangle \quad (22)$$

Here the underlined terms will cancel out each other because of Eq. (6). The double-underlined term was obtained using integration by parts, and the terms evaluated at the boundary vanish due to Eq. (20). Thus, the above 3D problem can be reduced to a 1D through-the-thickness problem that does not depend on partial derivatives of w_α and w_3 with respect to x_α and t, and the last ζ enters only as a parameter. First, the stationary points w_α of Eq. (22) are easily found to be

$$w_\alpha = hs_{\beta\alpha}(\zeta)\psi_{3;\alpha} \quad (23)$$

where $s_{\beta\alpha}(\zeta)$ are solutions of the variational problems

$$\langle \mathbf{s}_{\alpha|\zeta}^T D_s^* \delta\mathbf{s}_{\beta|\zeta} + qe_\alpha^T D_s^* \delta\mathbf{s}_{\beta|\zeta} - q_{|\zeta} D_{e3}^{*T} I_\alpha \delta\mathbf{s}_\beta - \beta_{30}^2 \mathbf{s}_\alpha^T \delta\mathbf{s}_\beta\rangle = 0 \quad (24)$$

and where $\mathbf{s}_\alpha$ are the 2×1 column matrices, components of which are $s_{\beta\alpha}$. Next, let us seek the correction w_3 to P_3, which has the form

$$w_3 = h\tau_R(\zeta)\psi_3 \quad (25)$$

where $\tau_R(\zeta)$ is the solution of the variational problem

$$\langle D_3^*\tau_{R|\zeta}\delta\tau_{R|\zeta} + 2H\zeta D_3^* q_{|\zeta}\delta\tau_{R|\zeta} + qC_R^{eT} D_{e3}^*\delta\tau_{R|\zeta} + q_{|\zeta} D_{e3}^{*T} C_R^e \delta\tau_R - \beta_{30}^2[\tau_R\delta\tau_R + 2H\zeta q\,\delta\tau_R]\rangle = 0 \quad (26)$$

subject to the constraint

$$\langle q\tau_R\rangle = 0 \quad (27)$$

As expected, the in-plane warping functions turn out to be much smaller than the out-of-plane displacement in the long-wavelength regime and are $O(h\hat{q}/l)$, and the refinement w_3 to the original out-of-plane displacement $O(\hat{q})$ is of the order $O(h\hat{q}/R)$. Summarizing, we have the following distribution of the warping fields over the thickness in the series of thickness-extension vibrations (in the first approximation):

$$P_\alpha = hs_{\beta\alpha}(\zeta)\psi_{3;\alpha}, \quad P_3 = q(\zeta)\psi_3 + h\tau_R(\zeta)\psi_3 \quad (28)$$

Analogously, we also find the next refinement for the warping fields in the branches associated with the thickness-shear vibrations (the series $L_\parallel$ or $F_\parallel$). Given v_α, we seek w_α and w_3 in the first approximation for one branch of the following series:

$$P_\alpha(x_1,x_2,\zeta,t) = P_{\alpha 0} + w_\alpha(x_1,x_2,\zeta,t), \quad P_3(x_1,x_2,\zeta,t) = w_3(x_1,x_2,\zeta,t) \quad (29)$$

with

$$P_{\alpha 0} = p_{\alpha\beta}(\zeta)v_\beta(x_1,x_2,t)$$

in which, without any loss of generality, v_α are regarded as one branch of this series as given functions of x_α and t, satisfying the following condition due to Eq. (18):

$$v_\alpha = 0 \quad \text{at} \quad \partial S \quad (30)$$

Here w_α and w_3 should be determined by the variational-asymptotic procedure and satisfy the constraints

$$\langle p_{\alpha\beta}(\zeta)w_\beta\rangle = 0 \quad (31)$$

Using the same procedure as in the previous step, the stationary point w_3 is easily found to have the form

$$w_3 = hr_{\alpha\beta}(\zeta)v_{\beta;\alpha} \quad (32)$$

where $r_{\alpha\beta}(\zeta)$ are the solutions of the variational problems given by

$$\langle \mathbf{r}_{\alpha|\zeta}^T D_3^*\delta\mathbf{r}_{\beta|\zeta} + \mathbf{p}^T I_\alpha^T D_{e3}^*\delta\mathbf{r}_{\beta|\zeta} - \mathbf{p}_{|\zeta}^T D_s^* e_\alpha\delta\mathbf{r}_\beta - \beta_{s0}^2\mathbf{r}_\alpha^T\delta\mathbf{r}_\beta\rangle = 0 \quad (33)$$

Here $\mathbf{r}_\alpha$ are the 1×2 row matrices, components of which are $r_{\alpha\beta}$. As before, for the thickness-shear vibrations, the out-of-plane warping function is much smaller than the in-plane displacements and is of the order $O(h\hat{q}/l)$. Again, the stationary point w_α is of the order $O(h\hat{q}/R)$ and should have the form

$$w_\alpha = h\varphi_{R\alpha\beta}v_\beta \quad (34)$$

where $\varphi_{R\alpha\beta}(\zeta)$ are solutions of the variational problems

$$\langle \varphi_{R|\zeta}^T D_s^*\delta\varphi_{R|\zeta} + 2H\zeta\mathbf{p}_{|\zeta}^T D_s^*\delta\varphi_{R|\zeta} + \mathbf{p}_{|\zeta}^T D_s^*\delta\varphi_R + \mathbf{p}^T C_R^{sT} D_s^*\delta\varphi_{R|\zeta} - \beta_{s0}^2[\varphi_R^T\delta\varphi_R + 2H\zeta\mathbf{p}^T\delta\varphi_R]\rangle = 0 \quad (35)$$

where φ_R is the 2×2 matrix, elements of which are $\varphi_{R\alpha\beta}$. Thus, for the series of thickness-shear vibrations (within the first approximation), we have

$$P_\alpha = p_{\alpha\beta}(\zeta)v_\beta + h\varphi_{R\alpha\beta}(\zeta)v_\beta, \quad P_3 = hr_{\alpha\beta}(\zeta)v_{\beta;\alpha} \quad (36)$$

4 Total Energy Functional for Long-Wavelength High-Frequency Vibration Analysis

Before proceeding to hyperbolic short-wavelength extrapolation in Sec. 5, it is convenient to find the total Lagrangian of each branch in the long-wavelength regime. Let the 3D displacements P_α and P_3 be expressed by the infinite series of branches given above, where ψ_3 and v_α are arbitrary functions in terms of x_α and t.

We first examine a branch in the series of thickness-extension vibrations, displacements of which are given by the asymptotic formulas in Eq. (28). Substituting Eq. (28) into Eqs. (13) and (14), keeping the leading quadratic terms and the leading cross terms, and using Eqs. (6), (24), and (26), we obtain the total energy functional $\overline{\mathcal{L}}_3$ defined as in Eq. (3) for thickness-extension vibrations within the first approximation

$$\overline{\mathcal{L}}_3 = \frac{1}{2}\rho_0[\dot{\psi}_3^2] - \frac{1}{2}\mu_0\left[\left(\frac{1}{h^2}\beta_{30}^2 + \overline{\mathbf{I}}^t\right)\psi_3^2 + \overline{\mathbf{K}}_{\alpha\beta}^t\psi_{3;\alpha}\psi_{3;\beta}\right] + \overline{\mathbf{F}}^t\psi_3 \quad (37)$$

where the coefficients are of the form

$$\overline{\mathbf{I}}^t = \langle C_R^{eT} D_e^* C_R^e q^2 + KD_3^*(\zeta q_{|\zeta})^2 + 4HC_R^{eT} D_{e3}^*(\zeta q q_{|\zeta}) + 2\widetilde{C}_R^{eT} D_{e3}^*(\zeta q q_{|\zeta}) - D_3^*\tau_{R|\zeta}^2 + \beta_{30}^2[\tau_R^2 - K(\zeta q)^2]\rangle$$

$$\overline{\mathbf{K}}_{\alpha\beta}^t = \langle e_\alpha^T D_s^* e_\beta q^2 + \mathbf{s}_{\alpha|\zeta}^T D_s^* e_\beta q - \mathbf{s}_\beta^T I_\alpha^T D_{e3}^* q_{|\zeta}\rangle$$

$$\overline{\mathbf{F}}^t = \alpha_3 q^+ + \beta_3 q^- + \langle\phi_3 q\rangle \quad (38)$$

Analogously, we turn to a branch in the series of thickness-shear vibrations, displacements of which are given by the asymptotic formulas in Eq. (36). Again substituting Eq. (36) into Eq. (3), discarding the small quadratic terms and the small cross terms (i.e., of order h/R and h/l compared with unity), and using Eqs. (8), (33), and (35), we get the total energy functional $\overline{\mathcal{L}}_s$ defined as in Eq. (3) for thickness-shear vibrations

$$\overline{\mathcal{L}}_s = \frac{1}{2}\rho_0[\dot{v}_\parallel^T\dot{v}_\parallel] - \frac{1}{2}\mu_0\left[v_\parallel^T\left(\frac{1}{h^2}\beta_{s0}^2 + \overline{\mathbf{I}}^s\right)v_\parallel + v_{\parallel;\alpha}^T\overline{\mathbf{K}}v_{\parallel;\beta}\right] + \overline{\mathbf{F}}^{sT}v_\parallel \quad (39)$$

where the coefficients are given by

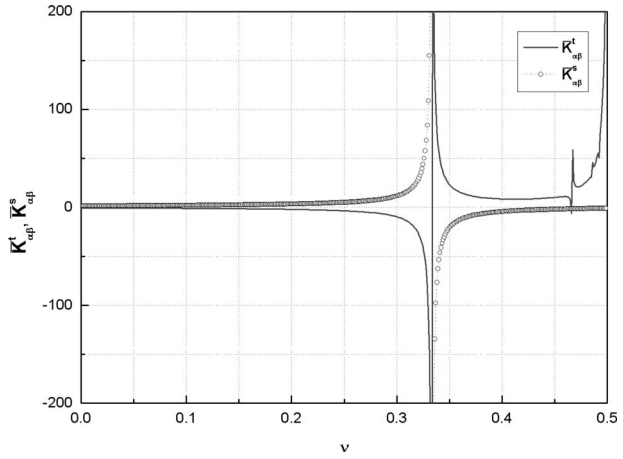

Fig. 2 Graph of $\bar{K}^t_{\alpha\beta}$ and $\bar{K}^s_{\alpha\beta}$ as functions of ν

$$\bar{\mathbf{I}}^s = \langle \mathbf{p}^T C_R^{sT} D_s^* C_R^s \mathbf{p} + K\zeta^2 \mathbf{p}_{|\zeta}^T D_s^* \mathbf{p}_{|\zeta} + 4H\zeta \mathbf{p}_{|\zeta}^T D_s^* C_R^s \mathbf{p} + 2\zeta \mathbf{p}_{|\zeta}^T D_s^* C_R^s C_R^s \mathbf{p} - \varphi_{R|\zeta}^T D_s^* \varphi_{R|\zeta} + \beta_{s0}^2 [\varphi_R^T \varphi_R - K\zeta^2 \mathbf{p}^T \mathbf{p}] \rangle$$

$$\bar{\mathbf{K}}^s_{\alpha\beta} = \langle \mathbf{p}^T I_\alpha^T D_e^* I_\beta \mathbf{p} + \mathbf{p}^T I_\alpha^T D_{e3}^* \mathbf{r}_{\beta|\zeta} - \mathbf{p}_{|\zeta}^T D_s^* e_\alpha \mathbf{r}_\beta \rangle$$

$$\bar{\mathbf{F}}^s = \alpha_\parallel^T \mathbf{p}_\parallel^+ + \beta_\parallel^T \mathbf{p}_\parallel^- + \langle \phi_\parallel^T \mathbf{p}_\parallel \rangle \tag{40}$$

Finally, we obtain the asymptotically correct, 2D dynamical equations for the long-wavelength high-frequency regime up to the first approximation, Eqs. (37) and (39). Unlike published shell theories of Kaplunov [7] derived by the asymptotic method of Goldenveizer, and of Le [5] derived by the VAM, those equations are applicable to shells in which each layer is made of monoclinic material. However, for the case of homogeneous and isotropic materials, Eqs. (37) and (39) coincide with those of Le [5].

It is interesting to note, following Refs. [8,9], that although Eqs. (37) and (39) are the correct equations in an asymptotic analysis, this is not sufficient to guarantee the positive definiteness of derived stiffness coefficients. Figure 2 shows graphs of $\bar{\mathbf{K}}^t_{\alpha\beta}$ and $\bar{\mathbf{K}}^s_{\alpha\beta}$ as functions of Poisson's ratio ν for the branches $L_\perp(0)$ and $L_\parallel(1)$ for homogeneous and isotropic materials. For example, as $\nu \to 0.33$ from below, the coefficient $\bar{\mathbf{K}}^t_{\alpha\beta} \to -\infty$. To address this anomaly we need an additional independent logical process. The so-called hyperbolic short-wavelength extrapolation is chosen for this step.

5 Hyperbolic Short-Wavelength Extrapolation

Generally speaking, the question of how to implement short-wavelength extrapolation in the general case is still open to investigation. However, it is natural to demand asymptotic equivalence in the long-wave regime for various possible short-wave extrapolations.

Let us now consider vibrations of the composite laminated shell with either clamped or free boundary conditions at its edge. Following Ref. [8], we assume that the vibrations we are going to describe can be regarded with sufficient accuracy as the superposition of the branches $F_\perp(0)$, $F_\parallel(0)$, $L_\parallel(0)$, $L_\perp(0)$, and $L_\parallel(1)$. The branches $F_\perp(0)$ and $L_\parallel(0)$ correspond to low-frequency vibrations, but the others correspond to thickness (high-frequency) vibrations with the first branches. There are two main reasons to choose those branches. First, these branches possess the lowest cut-off frequencies, so that the dominant vibrational energy is concentrated in them. Second, the necessity of also including $L_\parallel(1)$ into the present theory is dictated by its strong interaction with the branch $L_\perp(0)$, and obviously $F_\parallel(0)$ is also strongly coupled with the branch $F_\perp(0)$ [6,10]. Therefore, the dynamic equations contain eight unknown functions of the in-plane coordinates and time: $\bar{u}_\alpha$, $\bar{u}_3$, $\bar{\psi}_\alpha$, $\bar{\psi}_3$, and $\bar{v}_\alpha$ (the symbols without the bar are reserved for the functions in the final equations). Thus, we can write an asymptotically exact first approximation of the deformed position vector $\hat{\mathbf{R}}$ as

$$\begin{aligned}\hat{\mathbf{R}} = \mathbf{R} &+ h\zeta \mathbf{B}_3 + h[\bar{D}_1(\zeta)\bar{\varepsilon} + h\bar{D}_2(\zeta)(h\bar{\kappa})]\mathbf{B}_3 + g_{\alpha\beta}(\zeta)\bar{\psi}_\beta \mathbf{B}_\alpha \\ &+ hn_{\alpha\beta}(\zeta)\bar{\psi}_{\beta;\alpha}\mathbf{B}_3 + h\vartheta_{R\alpha\beta}(\zeta)\bar{\psi}_\beta \mathbf{B}_\alpha + p_{\alpha\beta}(\zeta)\bar{v}_\beta \mathbf{B}_\alpha \\ &+ hr_{\alpha\beta}(\zeta)\bar{v}_{\beta;\alpha}\mathbf{B}_3 + h\varphi_{R\alpha\beta}(\zeta)\bar{v}_\beta \mathbf{B}_\alpha + q(\zeta)\bar{\psi}_3 \mathbf{B}_3 + hs_{\beta\alpha}(\zeta)\bar{\psi}_{3;\alpha}\mathbf{B}_\alpha \\ &+ h\tau_R(\zeta)\bar{\psi}_3 \mathbf{B}_3 \end{aligned} \tag{41}$$

where

$$\mathbf{R} = \mathbf{r} + \bar{\mathbf{u}} \tag{42}$$

From Eq. (42), the functions $\bar{u}_\alpha$ and $\bar{u}_3$ describe average shell displacements in the long-wavelength, low-frequency branches, which have been studied in detail in Part I. According to Ref. [11], the 2D generalized strain and velocity fields are expressed in terms of $\bar{u}_\alpha$ and $\bar{u}_3$. The functions $\bar{D}_1$ and $\bar{D}_2$ can be calculated as the results of the first approximation step under the low-frequency vibration analysis. According to Ref. [6], the functions $\bar{\psi}_\alpha$ describe the thickness-shear branch $F_\parallel(0)$. The associated functions $g_{\alpha\beta}(\zeta)$ are the first odd solutions of the variational equations

$$\langle \mathbf{g}_{|\zeta}^T D_s^* \delta \mathbf{g}_{|\zeta} - \beta_{s1}^2 \mathbf{g}^T \delta \mathbf{g} \rangle = 0 \tag{43}$$

while $n_{\alpha\beta}$ and $\vartheta_{R\alpha\beta}$ are the solutions of Eqs. (33) and (35), respectively, in which $\mathbf{p}$ should be replaced with $\mathbf{g}$. Moreover, we choose for $g_{\alpha\beta}(\zeta)$ another normalization condition to simplify the subsequent changes of variables as follows:

$$\frac{\langle \zeta g_{\alpha\beta} \rangle}{\langle \zeta^2 \rangle} = \mathbf{I} \tag{44}$$

Finally, the functions $\bar{\psi}_3$ and $\bar{v}_\alpha$ describe the thickness branches $L_\perp(0)$ and $L_\parallel(1)$, respectively, while the functions $q(\zeta)$ and $p_{\alpha\beta}(\zeta)$ are the solutions of Eqs. (6) and (8) derived for these branches previously. We substitute Eq. (41) into Eq. (3), discarding small terms in the asymptotic sense. Using the results of Secs. 3 and 4, after lengthy but otherwise straightforward calculations, one obtains Eq. (3) with

$$\begin{aligned} 2\bar{\mathcal{K}} = \rho_0 \{ &\bar{V}_\parallel^T \bar{V}_\parallel + \bar{V}_3^2 + \dot{\bar{\psi}}_\parallel^T \langle \mathbf{g}^T \mathbf{g} \rangle \dot{\bar{\psi}}_\parallel + \dot{\bar{\psi}}_3^2 + \dot{\bar{v}}_\parallel^T \dot{\bar{v}}_\parallel + 2(h\bar{\Omega}_\parallel)^T [\langle \xi^T \mathbf{g} \rangle \dot{\bar{\psi}}_\parallel \\ &+ \langle \xi^T \mathbf{p} \rangle \dot{\bar{v}}_\parallel] + 2h[\bar{V}_\parallel^T \langle \mathbf{s}_\alpha \rangle \dot{\bar{\psi}}_{3;\alpha} + \bar{V}_3 \langle \mathbf{n}_\alpha \rangle \dot{\bar{\psi}}_{\parallel;\alpha} + \bar{V}_3 \langle \mathbf{r}_\alpha \rangle \dot{\bar{v}}_{\parallel;\alpha} \\ &+ \dot{\bar{\psi}}_3 \langle qD_1 \rangle \dot{\bar{\varepsilon}} + \dot{\bar{\psi}}_3 \langle qD_2 \rangle (h\dot{\bar{\kappa}}) + \dot{\bar{\psi}}_3 \langle q\mathbf{n}_a \rangle \dot{\bar{\psi}}_{\parallel;\alpha} + \dot{\bar{\psi}}_3 \langle q\mathbf{r}_\alpha \rangle \dot{\bar{v}}_{\parallel;\alpha} \\ &+ \dot{\bar{\psi}}_\parallel^T \langle \mathbf{g}^T \mathbf{s}_\alpha \rangle \dot{\bar{\psi}}_{3;\alpha} + \dot{\bar{v}}_\parallel^T \langle \mathbf{p}^T \mathbf{s}_\alpha \rangle \dot{\bar{\psi}}_{3;\alpha}] \} \end{aligned} \tag{45}$$

and

$$\begin{aligned} 2\bar{\mathcal{P}} = \mu_0 \Bigg\{ &\left(\frac{1}{h}\right)^2 [\bar{\psi}_\parallel^T (\beta_1^2 \langle \mathbf{g}^T \mathbf{g} \rangle) \bar{\psi}_\parallel + \beta_2^2 \bar{\psi}_3^2 + \bar{v}_\parallel^T (\beta_3^2) \bar{v}_\parallel] + \bar{\psi}_{\parallel;\alpha}^T \bar{\mathbf{K}}^1_{\alpha\beta} \bar{\psi}_{\parallel;\beta} \\ &+ \bar{\mathbf{K}}^2_{\alpha\beta} \bar{\psi}_{3;\alpha} \bar{\psi}_{3;\beta} + \bar{v}_{\parallel;\alpha}^T \bar{\mathbf{K}}^3_{\alpha\beta} \bar{v}_{\parallel;\beta} + \bar{\psi}_\parallel^T \bar{\mathbf{I}}^1 \bar{\psi}_\parallel + \bar{\mathbf{I}}^2 \bar{\psi}_3^2 + \bar{v}_\parallel^T \bar{\mathbf{I}}^3 \bar{v}_\parallel \\ &+ \bar{\varepsilon}^T \langle D_c^* \rangle \bar{\varepsilon} + 2\bar{\varepsilon}^T \langle \zeta D_c^* \rangle (h\bar{\kappa}) + (h\bar{\kappa})^T \langle \zeta^2 D_c^* \rangle (h\bar{\kappa}) + 2\left(\frac{1}{h}\right) \\ &\times [\bar{\psi}_\parallel^T \langle \mathbf{g}_{|\zeta}^T D_s^* \mathbf{s}_{\alpha|\zeta} \rangle \bar{\psi}_{3;\alpha} + \bar{v}_\parallel^T \langle \mathbf{p}_{|\zeta}^T D_s^* \mathbf{s}_{\alpha|\zeta} \rangle \bar{\psi}_{3;\alpha} + \bar{\psi}_3 \langle q_{|\zeta} D_3^* D_{1|\zeta} \rangle \bar{\varepsilon} \\ &+ \bar{\psi}_3 \langle q_{|\zeta} D_3^* D_{2|\zeta} \rangle (h\bar{\kappa}) + \bar{\psi}_3 \langle q_{|\zeta} D_3^* \mathbf{n}_{\alpha|\zeta} \rangle \bar{\psi}_{\parallel;\alpha} + \bar{\psi}_3 \langle q_{|\zeta} D_3^* \mathbf{r}_{\alpha|\zeta} \rangle \bar{v}_{\parallel;\alpha} \\ &+ \bar{\varepsilon}^T \langle D_{e3}^* q_{|\zeta} \rangle \bar{\psi}_3 + (h\bar{\kappa})^T \langle \zeta D_{e3}^* q_{|\zeta} \rangle \bar{\psi}_3 + \bar{\psi}_3 \langle q_{|\zeta} D_{e3}^{*T} I_\alpha \mathbf{g} \rangle \bar{\psi}_{\parallel;\alpha} \\ &+ \bar{\psi}_\parallel^T \langle \mathbf{g}_{|\zeta}^T D_s^* e_\alpha q \rangle \bar{\psi}_{3;\alpha} + \bar{\psi}_3 \langle q_{|\zeta} D_{e3}^{*T} I_\alpha \mathbf{p} \rangle \bar{v}_{\parallel;\alpha} + \bar{v}_\parallel^T \langle \mathbf{p}_\zeta^T D_s^* e_\alpha q \rangle \bar{\psi}_{3;\alpha}] \end{aligned}$$

$$+ 2[\bar{\varepsilon}^T\langle D_{1|\zeta}^T D_{e3}^{*T} I_\alpha \mathbf{g} + D_e^* I_\alpha \mathbf{g}\rangle \bar{\psi}_{\|;\alpha} + (\bar{\varepsilon})^T\langle D_{1|\zeta}^T D_3^* \mathbf{n}_{\alpha|\zeta}$$

$$+ D_{e3}^* \mathbf{n}_{\alpha|\zeta}\rangle \bar{\psi}_{\|;\alpha} + \bar{\varepsilon}^T\langle D_{1|\zeta}^T D_{e3}^{*T} I_\alpha \mathbf{p} + D_e^* I_\alpha \mathbf{p}\rangle \bar{\upsilon}_{\|;\alpha}$$

$$+ (\bar{\varepsilon})^T\langle D_{1|\zeta}^T D_3^* \mathbf{r}_{\alpha|\zeta} + D_{e3}^* \mathbf{r}_{\alpha|\zeta}\rangle \bar{\upsilon}_{\|;\alpha} + (h\bar{\kappa})^T\langle D_{2|\zeta}^T D_{e3}^{*T} I_\alpha \mathbf{g}$$

$$+ \zeta D_e^* I_\alpha \mathbf{g}\rangle \bar{\psi}_{\|;\alpha} + (h\bar{\kappa})^T\langle D_{2|\zeta}^T D_3^* \mathbf{n}_{\alpha|\zeta} + \zeta D_{e3}^* \mathbf{n}_{\alpha|\zeta}\rangle \bar{\psi}_{\|;\alpha}$$

$$+ (h\bar{\kappa})^T\langle D_{2|\zeta}^T D_{e3}^{*T} I_\alpha \mathbf{p} + \zeta D_e^* I_\alpha \mathbf{p}\rangle \bar{\upsilon}_{\|;\alpha} + (h\bar{\kappa})^T\langle D_{2|\zeta}^T D_3^* \mathbf{r}_{\alpha|\zeta}$$

$$+ \zeta D_{e3}^* \mathbf{r}_{\alpha|\zeta}\rangle \bar{\upsilon}_{\|;\alpha} + \bar{\psi}_\|^T\langle \mathbf{g}_{|\zeta}^T D_s^* e_\alpha D_1\rangle \bar{\varepsilon}_{;\alpha} + \bar{\psi}_\|^T\langle \mathbf{g}_{|\zeta}^T D_s^* e_\alpha D_2\rangle (h\bar{\kappa}_{;\alpha})$$

$$+ \bar{\upsilon}_\|^T\langle \mathbf{p}_{|\zeta}^T D_s^* e_\alpha D_1\rangle \bar{\varepsilon}_{;\alpha} + \bar{\upsilon}_\|^T\langle \mathbf{p}_{|\zeta}^T D_s^* e_\alpha D_2\rangle (h\bar{\kappa}_{;\alpha})]\Big\} - \bar{\mathbf{F}}^{1T}\bar{\psi}_\|$$

$$- \bar{\mathbf{F}}^2\bar{\psi}_3 - \bar{\mathbf{F}}^{3T}\bar{\upsilon}_\| \tag{46}$$

In Eqs. (45) and (46), the coefficients β_1^2, β_2^2, and β_3^2 are the eigenvalues of the variational problems for g, q, and p, respectively; while $\bar{\mathbf{K}}_{\alpha\beta}^1$, $\bar{\mathbf{K}}_{\alpha\beta}^2$, $\bar{\mathbf{K}}_{\alpha\beta}^3$, $\bar{\mathbf{I}}^1$, $\bar{\mathbf{I}}^2$, $\bar{\mathbf{I}}^3$, $\bar{\mathbf{F}}^1$, $\bar{\mathbf{F}}^2$, and $\bar{\mathbf{F}}^3$ are calculated from the corresponding coefficients according to Eqs. (38) and (40). Here the superscripts 1, 2, and 3 are not exponents, but rather are symbols referring to the associated coefficients for g, q, and **p**, respectively.

By using the normalization from Eqs. (9) and (44), one can derive the changes of variable in the following way. At first, the changes of variable for V_α, V_3, ψ_3, and υ_α can be established for Eq. (45). On the other hand, based on Eq. (46) one can make the changes of variable for $\kappa_{\alpha\beta}$ and ψ_α. See Ref. [9] for the entire procedure in detail of how to derive the changes of variable for V_α, V_3, ψ_3, υ_α, $\kappa_{\alpha\beta}$, and ψ_α.

Finally, the changes of variable are defined as

$$V_\| = \bar{V}_\| + h\mathbf{a}_\alpha^1\dot{\bar{\psi}}_{3;\alpha}$$

$$V_3 = \bar{V}_3 + h[\mathbf{a}_\alpha^5\dot{\bar{\psi}}_{\|;\alpha} + \mathbf{b}_\alpha^1\dot{\bar{\upsilon}}_{\|;\alpha}]$$

$$\varepsilon = \bar{\varepsilon} + h\bar{a}_{\alpha\beta}^1\bar{\psi}_{3;\alpha\beta}$$

$$h\kappa = h\bar{\kappa} + \bar{d}_\alpha^4\bar{\psi}_{\|;\alpha} + \bar{e}_\alpha^6\bar{\upsilon}_{\|;\alpha}$$

$$\psi_3 = \bar{\psi}_3 + h[\mathbf{a}^2\bar{\varepsilon} + \mathbf{b}^2(h\bar{\kappa}) + \mathbf{b}_\alpha^3\bar{\psi}_{\|;\alpha} + \mathbf{a}_\alpha^3\bar{\upsilon}_{\|;\alpha}]$$

$$\psi_\| = \frac{1}{h}\{\bar{\psi}_\| + h(\bar{b}_\alpha^4\bar{\psi}_{3;\alpha}) + h^2[\bar{d}_\alpha^5(h\bar{\kappa}_{;\alpha})]\}$$

$$\upsilon_\| = \bar{\upsilon}_\| + h\bar{a}_\alpha^4\bar{\psi}_{3;\alpha} \tag{47}$$

where

$$\mathbf{a}_\alpha^1 = \langle \mathbf{s}_\alpha\rangle, \quad \mathbf{a}_\alpha^5 = \langle \mathbf{n}_\alpha\rangle, \quad \mathbf{b}_\alpha^1 = \langle \mathbf{r}_\alpha\rangle$$

$$\bar{\mathrm{a}}_{\alpha\beta}^1 = I_\beta \mathbf{a}_\alpha^1, \quad \bar{\mathbf{d}}_\alpha^4 = (\bar{\mathbf{C}}^{-T})\mathbf{d}_\alpha^4, \quad \bar{\mathrm{e}}_\alpha^6 = (\bar{\mathbf{C}}^{-T})\mathbf{e}_\alpha^6$$

$$\bar{\mathbf{C}} = \langle \zeta^2 D_c^*\rangle, \quad \mathbf{d}_\alpha^4 = \langle \zeta D_c^* I_\alpha \mathbf{g}\rangle, \quad \mathbf{e}_\alpha^6 = \langle \zeta D_c^* I_\alpha \mathbf{p}\rangle$$

$$\mathbf{a}^2 = \langle qD_1\rangle, \quad \mathbf{b}^2 = \langle qD_2\rangle, \quad \mathbf{b}_\alpha^3 = \langle q\mathbf{n}_\alpha\rangle$$

$$\mathbf{a}_\alpha^3 = \langle q\mathbf{r}_\alpha\rangle, \quad \bar{\mathbf{b}}_\alpha^4 = (\mathbf{c}_1^{-T})\mathbf{b}_\alpha^4, \quad \bar{\mathbf{d}}_\alpha^5 = (\beta_1\mathbf{c}_1)^{-T}\mathbf{d}_\alpha^5$$

$$\mathbf{c}_1 = \langle \mathbf{g}^T\mathbf{g}\rangle, \quad \mathbf{b}_\alpha^4 = \langle \mathbf{g}^T\mathbf{s}_\alpha\rangle, \quad \mathbf{d}_\alpha^5 = \langle \mathbf{g}_{|\zeta}^T D_s^* e_\alpha D_2\rangle$$

$$\bar{\mathrm{a}}_\alpha^4 = \langle \mathbf{p}^T\mathbf{s}_\alpha\rangle \tag{48}$$

Retaining the leading terms in V_α, V_3, $\varepsilon_{\alpha\beta}$, $\kappa_{\alpha\beta}$, ψ_α, ψ_3, and υ_α and extrapolating the total energy functional to the short-wavelength regime, we arrive finally at the 2D refined energy functional with kinetic and strain energies per unit area, valid for a wide range of frequencies for a composite laminated shell with monoclinic symmetry layers

$$\mathcal{J} = h\int_{t_1}^{t_2}\int_s (\mathcal{K} - \mathcal{P})dSdt \tag{49}$$

where

$$\mathcal{K} = \tfrac{1}{2}\rho_0\{V_\|^T V_\| + V_3^2 + (h\dot{\psi}_\|)^T\mathbf{c}_1(h\dot{\psi}_\|) + \dot{\psi}_3^2 + \dot{\upsilon}_\|^T\dot{\upsilon}_\|\} \tag{50}$$

and

$$\mathcal{P} = \frac{1}{2}\mu_0\Bigg\{\varepsilon^T\mathbf{A}\varepsilon + 2\varepsilon^T\mathbf{B}(h\kappa) + (h\kappa)^T\mathbf{C}(h\kappa) + \left(\frac{1}{h}\right)^2[(h\psi_\|)^T\mathbf{I}^1(h\psi_\|)$$

$$+ \mathbf{I}^2\psi_3^2 + \upsilon_\|^T\mathbf{I}^3\upsilon_\|] + 2\left(\frac{1}{h}\right)[(\varepsilon^T\mathbf{S}^{e2} + (h\kappa)^T\mathbf{S}^{c2} + (h\psi_{\|;\alpha})^T\mathbf{S}_\alpha^{12}$$

$$+ \upsilon_{\|;\alpha}^T\mathbf{S}_\alpha^{32})\psi_3 + ((h\psi_\|)^T\mathbf{S}_\alpha^{21} + \upsilon^T\mathbf{S}_\alpha^{23})\psi_{3;\alpha}] + (h\psi_{\|;\alpha})^T\mathbf{K}_{\alpha\beta}^1(h\psi_{\|;\beta})$$

$$+ \mathbf{K}_{\alpha\beta}^2\psi_{3;\alpha}\psi_{3;\beta} + \upsilon_{\|;\alpha}^T\mathbf{K}_{\alpha\beta}^3\upsilon_{\|;\beta}\Bigg\} - \mathbf{F}^{1T}(h\psi_\|) - \mathbf{F}^2\psi_3 - \mathbf{F}^{3T}\upsilon_\| \tag{51}$$

For simplicity of the derivation we use the following notation:

$$\mathbf{d}^1 = \langle D_{e3}^* q_{|\zeta}\rangle, \quad \mathbf{e}^1 = \langle \zeta D_{e3}^* q_{|\zeta}\rangle, \quad \mathbf{e}_\alpha^2 = \langle q_{|\zeta} D_{e3}^{*T} I_\alpha \mathbf{g}\rangle$$

$$\mathbf{e}_\alpha^8 = \langle \mathbf{g}_{|\zeta}^T D_s^* \mathrm{e}_\alpha q\rangle, \quad \mathbf{d}_\alpha^2 = \langle q_{|\zeta} D_{e3}^{*T} I_\alpha \mathbf{p}\rangle, \quad \mathbf{d}_\alpha^3 = \langle \mathbf{p}_{|\zeta}^T D_s^* e_\alpha q\rangle$$

$$\mathbf{e}_\alpha^7 = \langle \mathbf{p}_{|\zeta}^T D_s^* e_\alpha D_2\rangle \tag{52}$$

Using Eqs. (48) and (52), all the coefficients are defined as

$$\mathbf{A} = \bar{\mathbf{A}} - \beta_2^2(\mathbf{a}^{2T}\mathbf{a}^2) - 2(\mathbf{d}^1\mathbf{a}^2)$$

$$\mathbf{B} = \bar{\mathbf{B}} - \beta_2^2(\mathbf{a}^{2T}\mathbf{b}^2) - (\mathbf{d}^1\mathbf{b}^2) - (\mathbf{a}^2\mathbf{e}^1)$$

$$\mathbf{C} = \bar{\mathbf{C}} - \beta_2^2(\mathbf{b}^{2T}\mathbf{b}^2) - 2(\mathbf{e}^1\mathbf{b}^2)$$

$$\mathbf{I}^1 = \beta_1^2\mathbf{c}_1 + (h)^2\bar{\mathbf{I}}^1, \quad \mathbf{I}^2 = \beta_2^2 + (h)^2\bar{\mathbf{I}}^2, \quad \mathbf{I}^3 = \beta_3^2 + (h)^2\bar{\mathbf{I}}^3$$

$$\mathbf{S}^{e2} = \mathbf{d}^1, \quad \mathbf{S}^{c2} = \mathbf{e}^1, \quad \mathbf{S}_\alpha^{12} = \mathbf{e}_\alpha^{2T} - (\bar{\mathbf{d}}_\alpha^{4T}\mathbf{e}^1), \quad \mathbf{S}_\alpha^{32} = \mathbf{d}_\alpha^{2T} - (\bar{\mathbf{e}}_\alpha^{6T}\mathbf{e}^1)$$

$$\mathbf{S}_\alpha^{12} = \mathbf{e}_\alpha^8, \quad \mathbf{S}_\alpha^{23} = \mathbf{d}_\alpha^3, \quad \mathbf{F}^1 = \bar{\mathbf{F}}^1, \quad \mathbf{F}^2 = \bar{\mathbf{F}}^2, \quad \mathbf{F}^3 = \bar{\mathbf{F}}^3$$

$$\mathbf{K}_{\alpha\beta}^1 = \bar{\mathbf{K}}_{\alpha\beta}^1 + (\mathbf{a}_\alpha^{5T}\beta_1^2\mathbf{a}_\beta^5) + (\mathbf{b}_\alpha^{3T}\beta_1^2\mathbf{b}_\beta^3) + 2[\beta_2^2(\mathbf{b}^2\bar{\mathbf{d}}_\alpha^4)^T\mathbf{b}_\beta^3 + (\bar{\mathbf{d}}_\alpha^4\mathrm{e}^1\mathbf{b}_\beta^3)$$
$$+ (\mathbf{b}^2\bar{\mathbf{d}}_\alpha^4)^T(\mathbf{e}_\beta^2 - \mathbf{e}_\beta^{8T})] - [(\bar{\mathbf{d}}_\alpha^4\overline{\mathbf{C}}\mathbf{d}_\beta^4) + \beta_2^2(\mathbf{b}_\alpha^{3T}\mathbf{b}_\beta^3)$$
$$+ \beta_2^2(\mathbf{b}^2\bar{\mathbf{d}}_\alpha^4)^T\mathbf{b}^2\bar{\mathbf{d}}_\alpha^4] - 2[(\bar{\mathbf{d}}_\alpha^{4T}\mathbf{e}^1\mathbf{b}^2\bar{\mathbf{d}}_\beta^4) + \mathbf{b}_\alpha^{3T}(\mathbf{e}_\beta^2 - \mathbf{e}_\beta^{8T})]$$

$$\mathbf{K}_{\alpha\beta}^2 = \bar{\mathbf{K}}_{\alpha\beta}^2 + \beta_2^2[(\mathbf{a}_\alpha^{1T}\mathbf{a}_\beta^1) + (\bar{\mathbf{b}}_\alpha^{4T}\bar{\mathbf{b}}_\alpha^4) + (\bar{\mathbf{a}}_\alpha^{4T}\bar{\mathbf{a}}_\alpha^4)] + 2[(\bar{\mathbf{a}}_{\alpha\beta}^{1T}\mathbf{d}^1) + (\mathbf{e}_\alpha^2$$
$$- \mathbf{e}_\alpha^{8T})\bar{\mathbf{b}}_\beta^4 + (\mathbf{d}_\alpha^2 - \mathbf{d}_\alpha^{3T})\bar{\mathbf{a}}_\beta^4] - [(\bar{\mathbf{b}}_\alpha^{4T}\beta_1^2\mathbf{c}_1\bar{\mathbf{b}}_\beta^4) + (\bar{\mathbf{a}}_\alpha^{4T}\beta_3^2\bar{\mathbf{a}}_\alpha^{4T})]$$
$$- 2[(\bar{\mathbf{d}}_\alpha^4\bar{\mathbf{b}}_\beta^4)^T\mathbf{e}^1 + (\bar{\mathbf{e}}_\alpha^6\bar{\mathbf{a}}_\beta^4)^T\mathbf{e}^1]$$

$$\mathbf{K}_{\alpha\beta}^3 = \bar{\mathbf{K}}_{\alpha\beta}^3 + (\mathbf{b}_\alpha^{1T}\beta_3^2\mathbf{b}_\beta^1) + (\mathbf{a}_\alpha^{3T}\beta_3^2\mathbf{a}_\beta^3) + 2[\beta_2^2(\mathbf{b}^2\bar{\mathbf{e}}_\alpha^6)^T\mathbf{a}_\beta^3 + (\bar{\mathbf{e}}_\alpha^{6T}\mathbf{e}^1\mathbf{a}_\beta^3)$$
$$+ (\mathbf{b}^2\bar{\mathbf{e}}_\alpha^6)^T(\mathbf{d}_\beta^2 - \mathbf{d}_\beta^{3T}) + (\mathbf{e}_\alpha^7\bar{\mathbf{e}}_\beta^6)] - [(\bar{\mathbf{e}}_\alpha^{6T}\overline{\mathbf{C}}\bar{\mathbf{e}}_\beta^6) + \beta_2^2(\mathbf{a}_\alpha^{3T}\mathbf{a}_\beta^3)$$
$$+ \beta_2^2(\mathbf{b}^2\bar{\mathbf{e}}_\alpha^6)^T\mathbf{b}^2\bar{\mathbf{e}}_\beta^6] - 2[(\bar{\mathbf{e}}_\alpha^{6T}\mathbf{e}^1\mathbf{b}^2\bar{\mathbf{e}}_\beta^6) + \mathbf{a}_\alpha^{3T}(\mathbf{d}_\beta^2 - \mathbf{d}_\beta^{3T})] \tag{53}$$

While transforming Eqs. (45) and (46) to Eqs. (50) and (51) terms of the type, $(h\bar{\Omega}_\|)^T\mathbf{C}_1(h\dot{\psi}_\|)$ and $(h\bar{\Omega}_\|)^T\mathbf{C}_2\dot{\upsilon}_\|$, $\varepsilon^T\mathbf{C}_3(h\psi_{\|;\alpha})$, $\varepsilon^T\mathbf{C}_4\upsilon_{\|;\alpha}$, $(h\kappa)^T\mathbf{C}_5(h\psi_{\|;\alpha})$, and $(h\kappa)^T\mathbf{C}_6\upsilon_{\|;\alpha}$ in Eqs. (50) and (51) are neglected as small compared with the remaining terms in the long-wavelength regime [8], where C_i with $i=1,2,\ldots,6$ are the coefficients corresponding to those cross term functions.

Despite the fact that the theory involves more unknown functions than in the classical theory of shells, it provides much more predictive capability: The theory is no longer a zeroth-order approximation theory, but is instead a refined theory. Indeed, it describes in an asymptotically exact manner the vibrations of a shell for both low-and high-frequencies in the long-wavelength regime,

and it can represent qualitatively the 3D stress states in the short-wavelength regime. Note that the coefficients of the present 2D theory can be determined by solving the 1D through-thickness problems, viz., Eqs. (6), (8), (24), (26), (33), (35), and (43).

Now we digress here to point out that the present theory is different from the Berdichevsky–Le theory mainly in the following two aspects. First, as mentioned before, the Berdichevsky–Le theory is restricted to geometrically linear theory with a homogenous and isotropic material, while the present theory is the intrinsic formulation for a monoclinic laminated composite material. The latter is good for both geometrically linear and nonlinear shell analyses. In particular, the nonlinearities generally appear in the velocity and strain measures, in terms of which the kinetic and strain energies are quadratic. Second, in the Berdichevsky–Le theory, all terms of the type containing $(h\psi_{\|;\alpha})$ are neglected due to additional analysis, which shows that a hyperbolic short-wavelength extrapolation describing exactly the curvature of the dispersion curve near the cut-off frequency of the branch $F_{\|}(0)$ does not exist [8]. However, those terms are proved to be important in reconstructing the 3D stresses on the basis of 2D results [12]. Therefore, we retain this term in the present theory.

As the primary type of validation procedure, if one considers an elastic shell made of a homogeneous isotropic material, all the formulas derived here can be reproduce to those in Refs. [5,8], which indirectly verifies that derivation.

6 Conclusions

The present development represents a new contribution, as there is no published work on variational-asymptotic modeling of composite shells for a wide range of frequencies and expressed in analytical form. The main contributions of the present work toward developing geometrically nonlinear dynamic composite shell models valid over a wide range of frequencies with sufficient accuracy are the following.

1. The combination of (a) the compact and elegant representation of the dynamic intrinsic formulation, including nonlinear generalized strain and velocity measures [13], (b) the rigorous dimensional reduction procedure of the variational-asymptotic method [1], and (c) the hyperbolic short-wave procedure of the nontrivial extrapolation [4,5] is itself a contribution.
2. An asymptotically correct shell model was constructed that enables one to analyze shell dynamic response for vibrations in the low-frequency long-wavelength area, including the high-frequency regime, and to achieve accurate and positive definite strain and kinetic energy functionals for all wavelengths in relatively simple form.
3. To provide insight and guidance for developing the finite-element-based shell model, an analytical procedure for one-dimensional through-thickness analysis for laminated composite materials was presented. A practical finite-element-based procedure for the through-thickness analysis will be presented in a later paper.

References

[1] Berdichevsky, V. L., 1983, *Variational Principles of Continuum Mechanics*, Nauka, Moscow.
[2] Berdichevsky, V. L., 1977, "High-Frequency Long-Wave Vibrations of Plates," Sov. Phys. Dokl., **22**(4), pp. 604–606.
[3] Berdichevsky, V. L., and Le, K. C., 1980, "High-Frequency Long-Wave Shell Vibrations," Prikl. Mat. Mekh., **44**(4), pp. 520–525.
[4] Berdichevsky, V. L., and Le, K. C., 1982, "High-Frequency Vibrations of Shells," Sov. Phys. Dokl., **27**(11), pp. 988–990.
[5] Le, K. C., 1997, "High Frequency Vibrations and Wave Propagation in Elastic Shells: Variational-Asymptotic Approach," Int. J. Solids Struct., **34**(30), pp. 3923–3939.
[6] Mindlin, R. D., 1955, *An Introduction to the Mathematical Theory of Vibrations of Elastic Plates*, Signal Corps Engineering Laboratories, Fort Monmouth, NJ.
[7] Kaplunov, J. D., 1990, "High-Frequency Stress-Strain States," Mech. Solids, **25**, pp. 147–157.
[8] Le, K. C., 1999, *Vibrations of Shells and Rods*, 1st ed., Springer, Germany.
[9] Lee, C. Y., 2007. "Dynamic Variational Asymptotic Procedure for Laminated Composite Shells," Ph.D. thesis, Aerospace Engineering, Georgia Institute of Technology, Atlanta, GA.
[10] Mindlin, R. D., 1951, "Influence of Rotary Inertia and Shear on Flexural Vibrations of Isotropic, Elastic Plates," ASME J. Appl. Mech., **18**, pp. 31–38.
[11] Hodges, D. H., Yu, W., and Patil, M. J., 2006. "Geometrically-Exact, Intrinsic Theory for Dynamics of Moving Composite Plates and Shells," *Proceedings of the 47th Structures, Structural Dynamics, and Materials Conference*.
[12] Ryazantseva, M. Y., 1985, "Flexural Vibrations of Symmetrical Sandwich Plates," Mech. Solids, **20**, pp. 153–159.
[13] Hodges, D. H., 2006, *Nonlinear Composite Beam Theory*, AIAA, Washington, DC.

M-Integral for Calculating Intensity Factors of Cracked Piezoelectric Materials Using the Exact Boundary Conditions

Yael Motola
e-mail: ymotola@eng.tau.ac.il

Leslie Banks-Sills
Mem. ASME

The Dreszer Fracture Mechanics Laboratory,
School of Mechanical Engineering,
Faculty of Engineering,
Tel Aviv University,
69978 Ramat Aviv, Israel

In this paper, the M-integral is extended for calculating intensity factors for cracked piezoelectric ceramics using the exact boundary conditions on the crack faces. The poling direction is taken at an angle to the crack faces within the plane. Since an analytical solution exists, the problem of a finite length crack in an infinite body subjected to crack face traction and electric flux density is examined. In this case, poling is taken parallel to the crack faces. Numerical difficulties resulting from multiplication of large and small numbers were treated by normalizing the variables. This problem was solved with the M-integral and displacement-potential extrapolation methods. With this example, the superiority of the conservative integral is observed. The values for the intensity factor obtained with the M-integral are found to be more accurate than those found by means of the extrapolation method. In addition, a crack parallel to the poling direction in a four-point bend specimen subjected to both an applied load and an electric field was analyzed and different electric permittivity values in the crack gap were assumed. It is seen that the electric permittivity greatly influences the stress intensity factor K_{II} and the electric flux density intensity factor K_{IV}. The absolute value of these intensity factors increases with an increase in the value of the electric permittivity in the crack. The influence of the permittivity on K_I is rather small. [DOI: 10.1115/1.2998485]

Keywords: intensity factors, piezoelectric material, boundary conditions, finite element method, M-integral, electric permittivity

1 Introduction

Piezoelectric ceramics are widely used as sensors and actuators in smart structures, despite the absence of fundamental understanding of their fracture behavior. Piezoceramics are brittle and susceptible to cracking. Because the reliability of these devices is important, there has been tremendous interest in studying their fracture and failure behavior. Electrically induced mechanical cracking is a serious degradation phenomenon, which is not yet fully understood. To this end, accurate methods are required for calculating stress and electric flux density intensity factors in these materials, using the exact boundary conditions on the crack faces.

One of the key problems in properly analyzing the fracture behavior of piezoelectric ceramics is the selection of the correct boundary conditions on the crack faces. The mechanical boundary conditions are usually formulated as in classical elasticity theory. However, the assumption of a traction free crack was recently contradicted by Landis [1]. There were four possible sets of boundary conditions presented in the literature, i.e., impermeable, permeable, semipermeable, and exact boundary conditions.

Parton [2] first attempted to define the electric boundary conditions on the crack faces. He assumed that the crack was permeable, so that the electric flux density component D_n and the electric potential ϕ are continuous across the crack faces, where n denotes the normal to the crack faces. Traction free crack conditions were taken, leading to the boundary conditions

$$\phi^+ = \phi^-, \quad D_n^+ = D_n^-, \quad \sigma_{ij} n_j = 0 \tag{1}$$

where the superscripts + and − denote the upper and lower crack faces, σ_{ij} is the stress tensor, and n_i is the unit normal vector.

A second possibility is that of an impermeable crack. Here, the fact that the permittivity of piezoelectric ceramics is 10^3 times higher than that of the environment (air or vacuum) within the crack is considered. Deeg [3] used this condition in his analyses of dislocations and cracks in piezoelectric materials. The normal component of the electric flux density was set to zero on the upper and lower crack faces and there is no traction on the crack surfaces, hence

$$D_n^+ = D_n^- = 0, \quad \sigma_{ij} n_j = 0 \tag{2}$$

In this case, the crack is impermeable to electric fields, i.e., the crack faces are charge free and thus the electric flux density vanishes inside the crack. These assumptions were examined using an antiplane crack as an example [4].

The above assumptions were improved by considering the electric permeability of air in the crack gap [5]. The boundary conditions on the crack faces were taken to be

$$D_n^+ = D_n^-, \quad D_n^+(u_n^+ - u_n^-) = -\kappa_a(\phi^+ - \phi^-), \quad \sigma_{ij} n_j = 0 \tag{3}$$

where u_n^+ and u_n^- are the normal displacements of the upper and lower crack faces, respectively, and κ_a is the dielectric permittivity of the air within the crack gap. These boundary conditions characterize a semipermeable crack [6].

The energy release rate for a Griffith crack was considered by McMeeking [7]. Both impermeable and semipermeable boundary conditions were analyzed. It was shown for semipermeable conditions that the energy release rates calculated far from and in the neighborhood of the crack tip differed. As may be expected, the energy release rate for impermeable conditions differed from the

Contributed by the Applied Mechanics Division of ASME for publication in the JOURNAL OF APPLIED MECHANICS. Manuscript received August 21, 2007; final manuscript received May 11, 2008; published online October 31, 2008. Review conducted by Robert M. McMeeking.

other two results. It was suggested that both experimental and further theoretical work are required to explore this paradox.

To solve this conundrum, Landis [1] proposed a new set of boundary conditions. These conditions consist of closing tractions on the crack surfaces, in contrast with the three former sets of boundary conditions. This traction is the Maxwell stress arising from the electric field within the crack gap. These boundary conditions are called the exact boundary conditions. The electric boundary conditions are the same as for the semipermeable conditions in Eq. (3), namely,

$$D_n^+ = D_n^- = -\kappa_a \left(\frac{\phi^+ - \phi^-}{u_n^+ - u_n^-} \right) \tag{4}$$

Instead of the traction free conditions

$$\sigma_{nn}^+ = \sigma_{nn}^- = \frac{1}{2}\kappa_a \left(\frac{\phi^+ - \phi^-}{u_n^+ - u_n^-} \right)^2 \tag{5}$$

where σ_{nn} is the normal component of the stress on the crack faces closing the crack.

Several techniques for extracting intensity factors for piezoelectric ceramics were presented in the literature. These methods include the displacement-potential correlation [8–12], displacement-potential extrapolation [8–11], stress, electric flux density and electric field extrapolation [13,14], crack closure [9–11], two- and three-dimensional J-integral [15,16], and M-integral [17,18]. Impermeable, permeable, and semipermeable crack face boundary conditions were employed. A more detailed description of these studies may be found in Ref. [18].

The M-integral for calculating intensity factors in dynamic problems with permeable and impermeable cracks was presented by Enderlein et al. [17]. It should be noted that the need for normalization was not examined, since K_{II} was not calculated. Recently, several benchmark problems for impermeable crack face conditions were examined to demonstrate the accuracy of the M-integral and the displacement-potential extrapolation methods by Banks-Sills et al. [18]. Numerical difficulties from the multiplication of large and small numbers were treated by normalizing the variables. The values of the intensity factors obtained with the M-integral were observed to be more accurate than those found by means of the extrapolation method [18].

Although the studies mentioned above deal with the calculation of intensity factors for piezoelectric ceramics, none of them used the exact boundary conditions in obtaining intensity factors. The main objective of this study was to develop an iterative framework for analyzing a realistic case of a crack with the exact boundary conditions applied and to obtain intensity factors for it. The accuracy of the M-integral is investigated for cracks that are parallel to the poling direction through a problem of a finite length crack in an infinite plate. Given traction and electric flux density are applied to the crack faces. In addition, a four-point bend specimen is analyzed with the poling parallel to the crack faces, with different values of the electric permittivity examined. In this investigation, the M-integral is extended for two-dimensional problems of a piezoelectric material using the exact boundary conditions on the crack faces, as given in Eqs. (4) and (5). This method is known to be rather accurate for mechanical loads applied to linear elastic materials and was also shown to be accurate for piezoelectric materials with impermeable crack conditions [18].

In Sec. 2, the governing equations are presented. The M-integral for calculating intensity factors using the exact boundary conditions on the crack faces is described in Sec. 3. In Sec. 4, numerical calculations are presented, which were carried out on some example problems to demonstrate the accuracy of the method and necessary mesh refinement. In addition, a four-point bend specimen was analyzed with poling parallel to the crack faces.

2 Governing Equations

The governing equations for analyzing elasto-electric problems in piezoelectric materials are presented in this section. The piezoelectric effect can be expressed in terms of constitutive relations, that may be derived from basic thermodynamic principles [19,20]. The constitutive equations presented here are for linear behavior. Under high electrical or mechanical fields, a piezoelectric material behaves nonlinearly. The latter subject is not treated in this investigation. There are four equivalent constitutive representations commonly used in the theory of linear piezoelectricity to describe a coupled interaction between the mechanical and electric variables. Each type has its own different set of independent variables and corresponds to a different thermodynamic function. One way of writing these equations is

$$\sigma_{ij} = C_{ijkl}^E \epsilon_{kl} - e_{sij} E_s \tag{6}$$

$$D_i = e_{ikl} \epsilon_{kl} + \kappa_{is}^{\epsilon} E_s \tag{7}$$

where σ_{ij} is the stress tensor, C_{ijkl}^E is the elastic stiffness tensor at a constant electric field, ϵ_{kl} is the strain tensor, e_{sij} is the piezoelectric coupling tensor, E_s is the electric field vector, D_i is the electric flux density vector, and κ_{is}^{ϵ} is the permittivity tensor at a constant strain. Note that Eqs. (6) and (7) are written in the e-form. It may be observed that C_{ijkl} is a fourth order tensor with the symmetries

$$C_{ijkl} = C_{klij} = C_{jikl} = C_{ijlk} \tag{8}$$

e_{ijs} is a third order tensor with the symmetry

$$e_{ijs} = e_{isj} \tag{9}$$

κ_{is} is a second order symmetric tensor and $i,j,k,l,s = 1,2,3$. It should be pointed out that the derivation of Eqs. (6) and (7) is based on the electric enthalpy density function

$$h = \tfrac{1}{2} C_{ijkl}^E \epsilon_{ij} \epsilon_{kl} - \tfrac{1}{2} \kappa_{ij}^{\epsilon} E_i E_j - e_{sij} E_s \epsilon_{ij} \tag{10}$$

In the absence of body forces and surface charges, the equilibrium equations and Gauss' equation are given by

$$\sigma_{ji,j} = 0 \tag{11}$$

$$D_{i,i} = 0 \tag{12}$$

The strain-displacement and electric field-potential equations are given by

$$2\epsilon_{ij} = u_{i,j} + u_{j,i} \tag{13}$$

$$E_i = -u_{4,i} \tag{14}$$

where $i,j = 1,2,3$.

In order to employ the M-integral, the first term of the asymptotic expressions for the stress, displacement, and electric fields, as well as the electric potential, is required. A complete set of these expressions was presented in Appendix A of Ref. [18].

3 M-Integral

The M-integral is employed here for calculating intensity factors subjected to the exact boundary conditions on the crack faces, as given in Eqs. (4) and (5). Quarter-point elements are used near the crack tip to model the square-root singularity of the stress, electric flux density, and electric fields. The conservative M-integral was first presented by Yau et al. [21] for mixed mode problems in isotropic materials and by Wang et al. [22] for anisotropic materials in which $x_3 = z = 0$ is a symmetry plane, as shown in Fig. 1.

The energy release rate is given by [23]

$$\mathcal{G} = \tfrac{1}{2} \mathbf{k}^T \mathbf{L}^{-1} \mathbf{k} \tag{15}$$

where $\mathbf{k}$ is the intensity factor vector, namely,

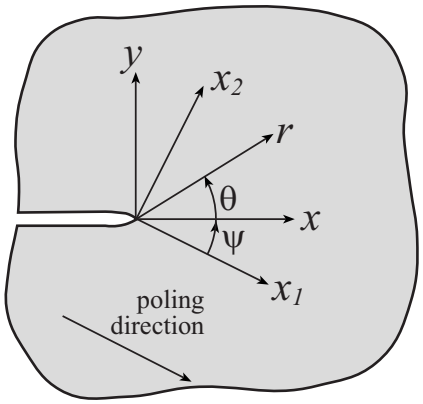

Fig. 1 Crack tip and material coordinates

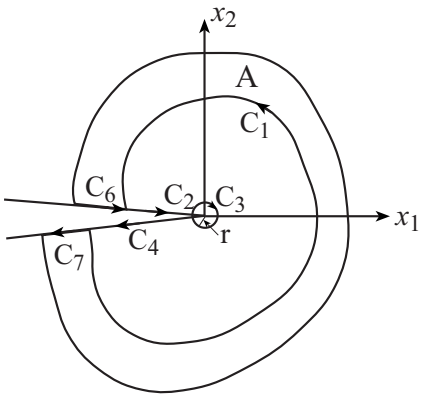

Fig. 2 Integration paths for *J*-integral calculation

$$\mathbf{k}^T = [K_{\mathrm{II}}, K_{\mathrm{I}}, K_{\mathrm{III}}, K_{\mathrm{IV}}] \tag{16}$$

and the superscript T represents transpose. The electric flux density intensity factor is denoted by K_{IV}. In Eq. (15), $\mathbf{L}$ is one of the Barnett–Lothe tensors, namely,

$$\mathbf{L}^{-1} = \Re(i\mathbf{A}\mathbf{B}^{-1}) \tag{17}$$

where $\Re$ represents the real part of the quantity in parentheses and $i=\sqrt{-1}$. The components of matrix $\mathbf{A}$ are given in Eqs. (A10)–(A14) in Ref. [18] and matrix $\mathbf{B}$ is given in Eq. (A26) of that reference.

It has been shown that the energy release rate coincides with the path independent J-integral [23], which is given by [4]

$$J = \int_{\Gamma} (hn_1 - T_i u_{i,1} + D_i n_i E_1) ds \tag{18}$$

where Γ is a path beginning at the lower crack face and ending at the upper crack face, h is the electric enthalpy density given in Eq. (10), n_i is the unit outward normal vector to Γ, $T_i = \sigma_{ij} n_j$ is the traction, u_i and D_i are the displacement and energy flux density fields, and E_1 is the electric field in the x_1-direction. Indicial notation is used in Eq. (18). By path independence, the J-integral may be redefined in the plane as

$$\begin{aligned} J &\equiv \lim_{r\to 0} \oint_{C_3} (hn_1 - T_\beta u_{\beta,1} + D_\beta n_\beta E_1)\ ds \\ &= \oint_{C_1} (hn_1 - T_\beta u_{\beta,1} + D_\beta n_\beta E_1)\ ds + \oint_{C_2} (\sigma_{\beta 2} u_{\beta,1} - D_2 E_1)\ dx_1 \\ &+ \oint_{C_4} (\sigma_{\beta 2} u_{\beta,1} - D_2 E_1)\ dx_1. \end{aligned} \tag{19}$$

where C_i, $i=1,\ldots,4$ is illustrated in Fig. 2, C_3 is an infinitesimal path with r approaching zero, and $\beta=1,2$. It may be noted again that indicial notation has been used for convenience in all of the equations. However, all calculations are made with reference to the crack tip coordinates x,y with the material properties rotated to this coordinate system (see Ref. [18] for details).

Using Green's theorem, Eq. (19) may be rewritten as

$$\begin{aligned} J &= \int_A [(\sigma_{\beta\gamma} u_{\gamma,1} - D_\beta E_1 - h\delta_{1\beta}) q_{1,\beta}]\ dA \\ &+ \oint_{C_2} (\sigma_{\beta 2} u_{\beta,1} - D_2 E_1)\ dx_1 + \oint_{C_4} (\sigma_{\beta 2} u_{\beta,1} - D_2 E_1)\ dx_1 \\ &+ \oint_{C_6} (\sigma_{\beta 2} u_{\beta,1} - D_2 E_1)\ q_1 dx_1 + \oint_{C_7} (\sigma_{\beta 2} u_{\beta,1} - D_2 E_1)\ q_1 dx_1 \end{aligned} \tag{20}$$

where δ is the Kronecker delta, C_2, C_4, C_6, and C_7 are paths along the crack faces (see Fig. 2), $\gamma=1,2$, and the function q_1 is defined for finite element analysis as

$$q_1 = \sum_{m=1}^{8} N_m(\xi,\eta) q_{1m} \tag{21}$$

where N_m are the finite element shape functions of an eight noded isoparametric element and ξ and η are the coordinates in the parent element (for further details, see Ref. [24]). The calculation of the J-integral is carried out in a ring of elements surrounding the crack tip (the area A in Eq. (20)) and along the crack faces inside and outside the ring (see Fig. 2). The elements within the ring move as a rigid body. For each of these elements q_1 is unity, so that the derivative of q_1 with respect to x_j is zero. For all elements outside the ring, q_1 is zero and again the derivative of q_1 is zero. For elements belonging to the ring, the vector q_{1m} in Eq. (21) was chosen so that the virtual crack extension does not disturb the relative nodal point positions in their new locations; for example, a regular element with nodes at the midsides contains only midside nodes after distortion.

To obtain the M-integral, two equilibrium solutions are assumed and superposed; this is possible for a material that behaves linearly. Thus, define

$$\sigma_{\beta\gamma} = \sigma^{(1)}_{\beta\gamma} + \sigma^{(2)}_{\beta\gamma} \tag{22}$$

$$\epsilon_{\beta\gamma} = \epsilon^{(1)}_{\beta\gamma} + \epsilon^{(2)}_{\beta\gamma} \tag{23}$$

$$u_\beta = u^{(1)}_\beta + u^{(2)}_\beta \tag{24}$$

$$E_\beta = E^{(1)}_\beta + E^{(2)}_\beta \tag{25}$$

$$D_\beta = D^{(1)}_\beta + D^{(2)}_\beta \tag{26}$$

The intensity factors associated with the superposed solutions are

$$K_{\mathrm{I}} = K^{(1)}_{\mathrm{I}} + K^{(2)}_{\mathrm{I}} \tag{27}$$

$$K_{\mathrm{II}} = K^{(1)}_{\mathrm{II}} + K^{(2)}_{\mathrm{II}} \tag{28}$$

$$K_{\mathrm{IV}} = K^{(1)}_{\mathrm{IV}} + K^{(2)}_{\mathrm{IV}} \tag{29}$$

Note that mode III deformation is omitted here, since only in-plane deformation is assumed.

Solution (1) is the sought after solution; the fields are obtained by means of a finite element calculation. Solution (2) consists of three auxiliary solutions, which are obtained from the first term of the asymptotic solution in Eqs. (A27) and (A29) in Ref. [18]. The intensity factors of solutions (2a), (2b), and (2c) are given, respectively, by

$$K^{(2a)}_{\mathrm{I}} = 1, \quad K^{(2a)}_{\mathrm{II}} = 0, \quad K^{(2a)}_{\mathrm{IV}} = 0 \tag{30}$$

$$K^{(2b)}_{\mathrm{I}} = 0, \quad K^{(2b)}_{\mathrm{II}} = 1, \quad K^{(2b)}_{\mathrm{IV}} = 0 \tag{31}$$

$$K_{\mathrm{I}}^{(2c)} = 0, \quad K_{\mathrm{II}}^{(2c)} = 0, \quad K_{\mathrm{IV}}^{(2c)} = 1 \tag{32}$$

As described in Ref. [18], some of the elements of the matrix $\mathbf{L}$, given in Eq. (17), differ by 19 orders of magnitude, which may lead to large errors in the results. Following Ref. [18], the variables are normalized as

$$\hat{r} = \frac{r}{L}, \quad u_1 = \frac{\hat{u}_1}{L}, \quad u_2 = \frac{\hat{u}_2}{L}, \quad u_4 = \frac{\kappa_{22}\hat{u}_4}{e_{26}L} \tag{33}$$

$$\hat{\sigma}_{ij} = \frac{\sigma_{ij}}{E_A}, \quad \hat{\epsilon}_{ij} = \epsilon_{ij}, \quad \hat{E}_i = \frac{\kappa_{22}}{e_{26}}E_i, \quad \hat{D}_i = \frac{D_i}{e_{26}} \tag{34}$$

$$\hat{K}_{\mathrm{I}} = \frac{K_I}{E_A\sqrt{L}}, \quad \hat{K}_{\mathrm{II}} = \frac{K_{\mathrm{II}}}{E_A\sqrt{L}}, \quad \hat{K}_{\mathrm{IV}} = \frac{K_{\mathrm{IV}}}{e_{26}\sqrt{L}} \tag{35}$$

where L is a characteristic length of the problem, e_{26} is a contracted piezoelectric constant, κ_{22} is a permittivity, and E_A is Young's modulus in the poling direction.

By the usual manipulation, it is possible to show that [18]

$$M^{(1,2\alpha)} = \frac{1}{2}[(\hat{\mathbf{k}}^{(1)})^T\hat{\mathbf{L}}^{-1}\hat{\mathbf{k}}^{(2\alpha)} + (\hat{\mathbf{k}}^{(2\alpha)})^T\hat{\mathbf{L}}^{-1}\hat{\mathbf{k}}^{(1)}] \tag{36}$$

where

$$\hat{\mathbf{k}} = \mathbf{V}^{-1}\mathbf{k} \tag{37}$$

$\mathbf{k}$ is given in Eq. (16). In Eq. (37),

$$\mathbf{V} = \begin{bmatrix} E_A\sqrt{L} & 0 & 0 & 0 \\ 0 & E_A\sqrt{L} & 0 & 0 \\ 0 & 0 & G_T\sqrt{L} & 0 \\ 0 & 0 & 0 & e_{26}\sqrt{L} \end{bmatrix} \tag{38}$$

and G_T is the shear modulus perpendicular to the poling direction, the superscripts (1) and (2α) represent the unknown solution and the auxiliary solutions, respectively, and $\alpha = a,b,c$. The matrix $\mathbf{L}^{-1}$ is normalized as

$$\hat{\mathbf{L}}^{-1} = \mathbf{V}\mathbf{L}^{-1}\mathbf{V} \tag{39}$$

In this way, the diagonal and off-diagonal elements are the same order of magnitude.

On the other hand, based on Eq. (20), the M-integral is derived as

$$\begin{aligned} M^{(1,2\alpha)} &= \int_A \left[\hat{C}_1^{(1,2\alpha)} - \hat{C}_2^{(1,2\alpha)} - \hat{h}^{(1,2\alpha)}\delta_{1\beta}\right]\frac{\partial q_1}{\partial \hat{x}_\beta}d\hat{A} \\ &+ \oint_{C_2}\left(\hat{\sigma}_{\beta 2}^{(1)}\hat{u}_{\beta,1}^{(2\alpha)} - c_3\hat{D}_2^{(1)}\hat{E}_1^{(2\alpha)}\right)d\hat{x}_1 \\ &+ \oint_{C_4}\left(\hat{\sigma}_{\beta 2}^{(1)}\hat{u}_{\beta,1}^{(2\alpha)} - c_3\hat{D}_2^{(1)}\hat{E}_1^{(2\alpha)}\right)d\hat{x}_1 \\ &+ \oint_{C_6}\left(\hat{\sigma}_{\beta 2}^{(1)}\hat{u}_{\beta,1}^{(2\alpha)} - c_3\hat{D}_2^{(1)}\hat{E}_1^{(2\alpha)}\right)q_1 d\hat{x}_1 \\ &+ \oint_{C_7}\left(\hat{\sigma}_{\beta 2}^{(1)}\hat{u}_{\beta,1}^{(2\alpha)} - c_3\hat{D}_2^{(1)}\hat{E}_1^{(2\alpha)}\right)q_1 d\hat{x}_1 \end{aligned} \tag{40}$$

where $\hat{C}_1^{(1,2\alpha)}$, $\hat{C}_2^{(1,2\alpha)}$, c_3, and $\hat{h}^{(1,2\alpha)}$ are given by

$$\hat{C}_1^{(1,2\alpha)} = \hat{\sigma}_{\beta\gamma}^{(1)}\hat{u}_{\gamma,1}^{(2\alpha)} + \hat{\sigma}_{\beta\gamma}^{(2\alpha)}\hat{u}_{\gamma,1}^{(1)} \tag{41}$$

$$\hat{C}_2^{(1,2\alpha)} = c_3(\hat{D}_\beta^{(1)}\hat{E}_1^{(2\alpha)} + \hat{D}_\beta^{(2\alpha)}\hat{E}_1^{(1)}) \tag{42}$$

$$c_3 = \frac{e_{26}^2}{\kappa_{22}E_A} \tag{43}$$

$$\hat{h}^{(1,2\alpha)} = \hat{\sigma}_{\beta\gamma}^{(1)}\hat{\epsilon}_{\beta\gamma}^{(2\alpha)} - c_3\hat{D}_\beta^{(1)}\hat{E}_\beta^{(2\alpha)} \tag{44}$$

and $\hat{A} = A/L^2$. It may be observed that Eq. (40) differs from the expression of the M-integral, given by Banks-Sills et al. [18], in that it has four additional terms arising from the traction and electric flux density on the crack faces. Furthermore, the first term of the asymptotic solution for $\sigma_{\beta 2}$ and D_2 on the crack faces is zero. Hence, since $\sigma_{\beta 2}^{(2\alpha)} = D_2^{(2\alpha)} = 0$, additional expressions do not appear in Eq. (40). Note that Eqs. (41) and (42) are given incorrectly in Ref. [18].

The two expressions for $M^{(1,2\alpha)}$ in Eqs. (36) and (40) are equated. The expressions in Eqs. (30)–(32) are sequentially substituted into these equations to obtain three expressions for the three unknown intensity factors $\hat{K}_{\mathrm{I}}^{(1)}$, $\hat{K}_{\mathrm{II}}^{(1)}$, and $\hat{K}_{\mathrm{IV}}^{(1)}$. The integral in Eq. (40) is calculated numerically in various rings about the crack front. The field quantities of solution (1) are obtained from a finite element analysis of the problem at hand.

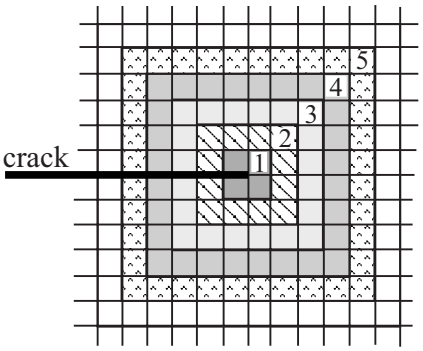

Fig. 3 Mesh and integration paths about the crack tip

4 Numerical Results

In this section, the M-integral is employed to calculate intensity factors for cracks in piezoelectric material, using the exact boundary conditions on the crack faces. The finite element program ANSYS [25] is used to obtain the displacement field and the electric potential. The elements exploited here are isoparametric, containing eight nodal points. Singular, quarter-point square elements are used at the crack tip.

The M-integral is evaluated in rings surrounding the crack tip. The five rings used in this study are shown in Fig. 3. The numbers designate the rings. In the calculations, it was observed that the results in path 1 were not as accurate as the rest of the paths. In addition, sometimes there were small differences in path 2. Consequently, the results shown in the sequel are an average of paths 3–5.

The material used in this study is PZT-5H from Morgan Electro Ceramics. Material properties were given by Berlincourt and Krueger [26] and are presented in Table 1. The poling direction is the x_1-axis.

Although the presentation here has been general, in Secs. 4.1 and 4.2, several in-plane problems are solved with the poling direction taken parallel to the crack faces; that is, in the x-direction (see Fig. 1). Other poling directions may be easily considered.

Table 1 Material properties for PZT-5H [26]

Property	C_{11}^E (GPa)	C_{22}^E (GPa)	C_{55}^E (GPa)
Value	117	126	23.0
Property	C_{12}^E (GPa)	C_{23}^E (GPa)	
Value	84.1	79.5	
Property	e_{11} (C/m^2)	e_{12} (C/m^2)	e_{26} (C/m^2)
Value	23.0	−6.55	17.0
Property	κ_{11}^ϵ (F/m)	κ_{22}^ϵ (F/m)	
Value	1.30095×10^{-8}	1.5045×10^{-8}	

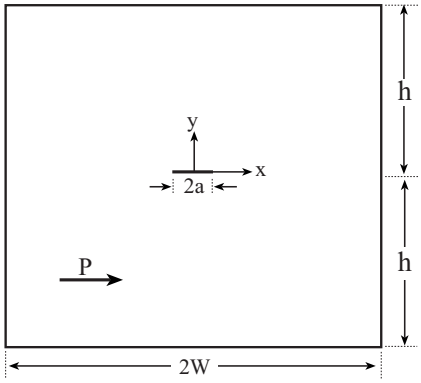

Fig. 4 Griffith crack problem

Two problems are solved: a finite length crack in an infinite body (Griffith crack) and a four-point bend specimen. For the first problem, given traction and electric flux density are prescribed on the crack faces. For the second problem, the exact boundary conditions are imposed on the crack faces.

4.1 Griffith Crack. In this section, poling is within the xy-plane and parallel to the crack faces with $\psi=0$, as shown in Fig. 1. In this problem, the intensity factors for a finite length crack in an infinite body (see Fig. 4) subjected to boundary conditions on the crack faces are determined. The results are compared with analytic solutions. This problem was chosen in order to examine the effect of prescribing boundary conditions on the crack faces, as must be done when the exact boundary conditions are used. Accuracy of the solutions and mesh refinement requirements are considered.

To model an infinite body, the normalized height and crack length are taken as $h/W=1$ and $a/W=0.05$, respectively. For $a/W=0.1$, the body is not sufficiently infinite. The applied boundary conditions on the crack faces include $\sigma_{yy}=-\sigma^*=-1$ MPa and $D_y=-D^*=-0.01$ C/m^2, applied simultaneously. The analytical solution for a finite length crack in an infinite body, subjected to the far field tensile stress $\sigma_{yy}=\sigma^\infty$ and electric flux density $D_y=D^\infty$, is [27]

$$K_{\mathrm{I}}=\sigma^\infty\sqrt{\pi a},\quad K_{\mathrm{IV}}=D^\infty\sqrt{\pi a} \tag{45}$$

Based on Eq. (45), the solution for the applied boundary conditions on the crack faces is given by

$$K_{\mathrm{I}}=\sigma^*\sqrt{\pi a},\quad K_{\mathrm{IV}}=D^*\sqrt{\pi a} \tag{46}$$

Two meshes were employed here. The coarse and fine meshes are illustrated in Figs. 5(a) and 5(b), respectively, with details surrounding the crack tips shown in Fig. 6. It may be noted that an enlargement of the area near the crack tip in Fig. 6(b) resembles the mesh in Fig. 6(a). The coarse mesh contains 4400 eight noded isoparametric elements and 13,420 nodal points, whereas the fine mesh contains 14,000 eight noded isoparametric elements and 42,400 nodal points. The ratio of the crack tip element length to crack length is $\ell/a=10^{-2}$ for the coarse mesh and 10^{-4} for the fine mesh.

With the M-integral, the intensity factors normalized in Eq. (35) are computed. These are normalized again to yield

$$\tilde{K}_{\mathrm{I}}=\frac{K_{\mathrm{I}}}{\sigma^*\sqrt{\pi a}},\quad \tilde{K}_{\mathrm{IV}}=\frac{K_{\mathrm{IV}}}{D^*\sqrt{\pi a}} \tag{47}$$

First, the path independence of the M-integral is examined. To this end, the results for this problem are presented in Tables 2 and 3. It may be observed in Table 2, that the normalized stress intensity factor $\tilde{K}_{\mathrm{I}}$ is path independent to five significant figures along paths 2–5 (see Fig. 3) for both the coarse and fine meshes. For the normalized intensity factor $\tilde{K}_{\mathrm{IV}}$, it may be seen in Table 3 that path independence is not as good as that for $\tilde{K}_{\mathrm{I}}$. For the fine mesh there is improvement to four significant figures along paths 3–5.

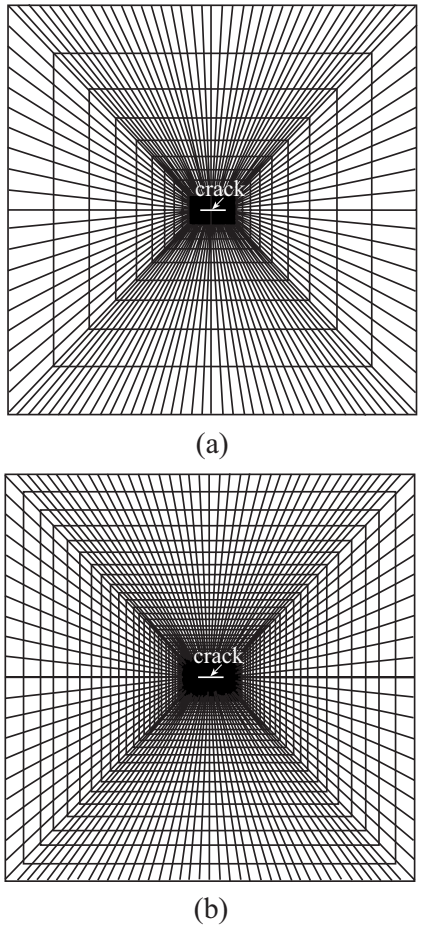

Fig. 5 Meshes for the plate in Fig. 4: (*a*) coarse and (*b*) fine meshes

In Table 4, normalized intensity factors are presented for the mixed mode problem. Values calculated by means of the M-integral are averaged from paths 3–5. In addition, values obtained using the displacement-potential extrapolation (DPE) method are presented for comparison (for details of this method see Ref. [18]). The stress intensity factor $\tilde{K}_{\mathrm{I}}$ is the same for the coarse and fine meshes and differs from the analytic value of unity by 0.4% when calculated by means of the conservative integral. With extrapolation, an error of 0.9% occurred for the coarse mesh

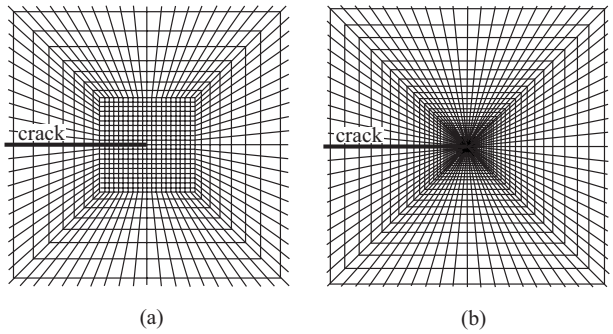

Fig. 6 Meshes in the neighborhood of the crack tip for the infinite plate: (*a*) coarse and (*b*) fine meshes

Table 2 The stress intensity factor $\tilde{K}_I$ along various paths for the infinite body problem in Fig. 4

Path	Coarse mesh	Fine mesh
1	0.9912	0.9780
2	1.0042	1.0042
3	1.0042	1.0042
4	1.0042	1.0042
5	1.0042	1.0042

Table 3 The electric flux density intensity factor $\tilde{K}_{IV}$ along various paths for the infinite body problem in Fig. 4

Path	Coarse mesh	Fine mesh
1	1.0088	0.9955
2	1.0071	1.0015
3	1.0057	1.0014
4	1.0049	1.0013
5	1.0044	1.0012

and 0.7% for the fine mesh. For the value of the normalized intensity factor $\tilde{K}_{IV}$, better results are obtained from the fine mesh and the M-integral. For the coarse mesh, an error of 0.5% occurred, while an error of 0.1% occurred for the fine mesh. With DPE, errors of 1.2% and 0.7% occurred for the coarse and fine meshes, respectively. With this example, the superiority of the conservative integral is observed. The values of the intensity factor obtained with the M-integral are found to be more accurate than those found by means of the extrapolation method. In addition, the intensity factor $\hat{K}_{II}$, which should be equal to zero, is also presented. Its values are $O(10^{-8})$ for the fine and coarse meshes for both methods.

4.2 Four-Point Bend Specimen. The methodology in this study was developed to enable the calibration of specimens that will be used in testing. To this end, a four-point bend specimen was analyzed. The poling (P) direction is parallel to the specimen width and a crack is situated parallel to this direction, as shown in Fig. 7. Following the ESIS procedure [28], the dimensions of the specimen are chosen as $L=45$ mm, $S_1=40$ mm, $S_2=20$ mm, and the width $W=4$ mm. In the finite element analyses, the thickness is $B=1$ m, whereas its actual dimension is 3 mm. The force applied to the 3 mm specimen is $F=850$ N. The applied electric field along the length of the specimen is taken to be $E_L=0.1$ MV/m and -0.1 MV/m. It should be noted that the coercive field for this material is $E_C \approx 0.8$ MV/m. In the analyses, the variables are normalized, as in Eqs. (33)–(35). Tests were reported by Jelitto et al. [29] for a four-point bend specimen shown in Fig. 7 with dimensions different from those used for the calculations here. Poling perpendicular to the crack faces was considered. In that study, stress/electric flux density extrapolation was employed to determine the relevant intensity factors with both impermeable

Table 4 Calculated intensity factors for the Griffith crack (see Fig. 4)

	$\tilde{K}_I$	$\hat{K}_{II}$	$\tilde{K}_{IV}$
M-integral			
Coarse mesh	1.004	$O(10^{-8})$	1.005
Fine mesh	1.004	$O(10^{-8})$	1.001
DPE			
Coarse mesh	1.009	$O(10^{-8})$	1.012
Fine mesh	1.007	$O(10^{-8})$	1.007

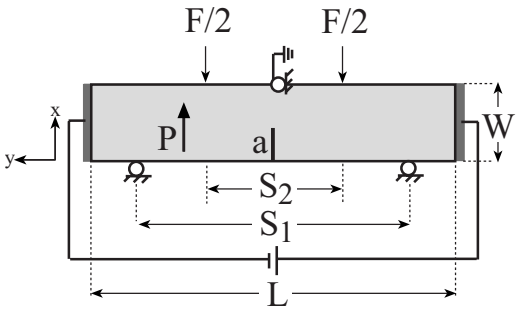

Fig. 7 Four-point bend specimen

and permeable crack face conditions.

Finite element analyses were carried out for normalized crack lengths $0.2 \le a/W \le 0.3$. These crack lengths were chosen to correspond to those prescribed in the ESIS procedure [28]. Plane strain conditions were assumed, meaning that not only is the strain component $\epsilon_3=0$ but also the electric field component $E_3=0$. Two types of meshes were employed to check for convergence. The coarse meshes contained between 7392 and 8040 eight noded isoparametric elements and 22,581 and 24,537 nodal points depending on the crack length; whereas, the fine mesh contained 141,800 elements and 436,683 nodal points. Analyses were carried out with the fine mesh for $a/W=0.2$. The mesh in the vicinity of the crack for $a/W=0.2$ for both meshes is shown in Fig. 8. The fine mesh contains many more elements outside this region especially along the crack faces. For both refinement levels, the normalized element length is $\ell/a=2.5\times10^{-4}$. The elements in the region of the crack tip are square. Meshes for other crack lengths are similar. Mesh refinement about the crack tip with a normalized element length of $\ell/a=2.5\times10^{-5}$ was also examined.

The intensity factors are normalized as

$$\tilde{K}_{I/II}=\frac{K_{I/II}}{\sigma_b\sqrt{\pi a}},\quad \tilde{K}_{IV}=\frac{K_{IV}}{D_L\sqrt{\pi a}} \tag{48}$$

where

$$\sigma_b \equiv \frac{3FS_2}{BW^2},\quad D_L \equiv \kappa_{22}E_L \tag{49}$$

F and E_L are the applied force (850 N) and electric field in the longitudinal direction of the specimen (0.1 MV/m), respectively, B and W are the thickness and width of the specimen, respectively, S_2 is the inner span length (see Fig. 7), and κ_{22} is the permittivity in the y-direction.

Different values of the permittivity within the crack gap κ_a were considered. These values were between 0 and $40\kappa_0$, where κ_0 is the permittivity of a vacuum (8.85×10^{-12} F/m). Note that when $\kappa_a=0$, impermeable boundary conditions are obtained. Schneider et al. [30] measured the electrical potential difference

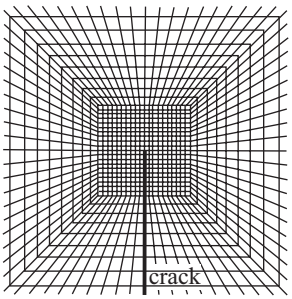

Fig. 8 Mesh in the vicinity of the crack for both meshes of the four-point bend specimen shown in Fig. 7 with $a/W=0.2$

across cracks formed by indentation in piezoelectric transducer (PZT) specimens. It was found for this particular problem that the permittivity of the medium within the cavity was $40\kappa_0$.

The analyses were conducted by means of an iterative procedure, for which the normal electric flux density D_y and stress σ_{yy} were calculated at each step from the normal displacement and electric potential values, which were obtained on the crack faces during the previous step, as

$$D^+_{y(k+1)} = D^-_{y(k+1)} = -\kappa_a \left(\frac{\phi^+ - \phi^-}{u^+_y - u^-_y} \right)_{(k)} \tag{50}$$

$$\sigma^+_{yy(k+1)} = \sigma^-_{yy(k+1)} = \frac{1}{2}\kappa_a \left(\frac{\phi^+ - \phi^-}{u^+_y - u^-_y} \right)^2_{(k)} \tag{51}$$

where k is the iteration number. For the first iteration, impermeable crack boundary conditions were enforced, so that the values of the normal electric flux density and stress on the crack surfaces were zero. Fifty to one hundred iterations were carried out for each analysis, with a maximum tolerance of 0.02% obtained for both normal electric flux density and stress. It may be noted that the convergence of the problems depends on the value of κ_a; the lower the value of κ_a, the faster the convergence. The Maxwell stresses in the piezoelectric body were neglected, since the Maxwell stress in the media inside the crack gap is three orders of magnitude larger than that in the piezoelectric body.

For $a/W=0.2$, the differences between all normalized intensity factors for the coarse and fine meshes were negligible. Hence, convergence was achieved. Good convergence was also achieved with refinement about the crack tip. Path independence was examined, as well. It was observed that the $\tilde{K}_{\mathrm{I}}$ values agree from three to five significant figures, depending on the permittivity values, for paths 3–5 for coarse and fine meshes. The differences in path 2 are slight if at all. The values of $\tilde{K}_{\mathrm{IV}}$ agree from two to four significant figures for paths 3–5. Results from the first path agree to one significant figure with those from the remainder of the paths for both $\tilde{K}_{\mathrm{I}}$ and $\tilde{K}_{\mathrm{IV}}$. Hence, the first path should be excluded in the analysis. The stress intensity factor $\tilde{K}_{\mathrm{II}}$ is $O(10^{-3})$-$O(10^{-5})$; therefore, path independence was not considered.

Results obtained by means of the coarse mesh and an average of paths 3–5 are presented in Fig. 9. It may be observed that the permittivity strongly influences the behavior of K_{II} and K_{IV} for the exact boundary conditions. Moreover, an increase in permittivity is followed by an increase in the absolute value of these intensity factors. On the other hand, the influence of the permittivity on K_{I} is rather small. For the normalized stress intensity factor $\tilde{K}_{\mathrm{I}}$, the direction of the electric field does not affect the results, whereas, for $\tilde{K}_{\mathrm{II}}$ and $\tilde{K}_{\mathrm{IV}}$ the behavior is symmetric with respect to the electric field direction. The differences between $\tilde{K}_{\mathrm{II}}$ and $\tilde{K}_{\mathrm{IV}}$ values obtained with the application of $\kappa_a=0$, $\kappa_a=\kappa_0$, and $\kappa_a=5\kappa_0$ cannot be seen in Fig. 9. However, these differences exist and they are more than 2% between the impermeable assumption and $\kappa_a=\kappa_0$ and around 10% between $\kappa_a=\kappa_0$ and $\kappa_a=5\kappa_0$.

The contribution of each intensity factor to the crack sliding and opening displacements Δu_x and Δu_y, respectively, may be calculated. Expressions for these displacements are obtained by substituting values of $\theta=\pm\pi$ into Eq. (A27) in Ref. [18] to obtain

$$\Delta u_x = 4\sqrt{\frac{r}{2\pi}}(L^{-1}_{11}K_{\mathrm{II}} + L^{-1}_{12}K_{\mathrm{I}} + L^{-1}_{14}K_{\mathrm{IV}}) \tag{52}$$

$$\Delta u_y = 4\sqrt{\frac{r}{2\pi}}(L^{-1}_{21}K_{\mathrm{II}} + L^{-1}_{22}K_{\mathrm{I}} + L^{-1}_{24}K_{\mathrm{IV}}) \tag{53}$$

where L^{-1}_{ij} are the components of the matrix $\mathbf{L}^{-1}$, given in Eq. (17). According to Eqs. (52) and (53), the contribution of each of the intensity factors to the displacements may be found. For example, the contribution of K_{I} to the crack sliding displacement is $L^{-1}_{12}K_{\mathrm{I}}$ multiplied by the factor outside the parentheses in Eqs. (52) and (53), etc. The contribution of each intensity factor to the crack sliding and opening displacement with respect to the permittivity for $a/W=0.25$ with the application of a positive electric field of $E_L=0.1$ MV/m and an applied force of $F=850$ N (for the actual specimen thickness) is presented in Tables 5 and 6, respectively. The calculations were carried out for $r=0.1$ mm and the units of the values in Tables 5 and 6 are in millimeters. It may be observed that only K_{I} affects the crack opening displacement, whereas both K_{II} and K_{IV} affect the crack sliding displacement for all permittivities. It is seen that the greater the permittivity, the greater the value of the contribution to the crack sliding displacement. It may also be pointed out that K_{IV} contributes more to the crack sliding displacement than K_{II}. This is a result of the anisotropy of the material.

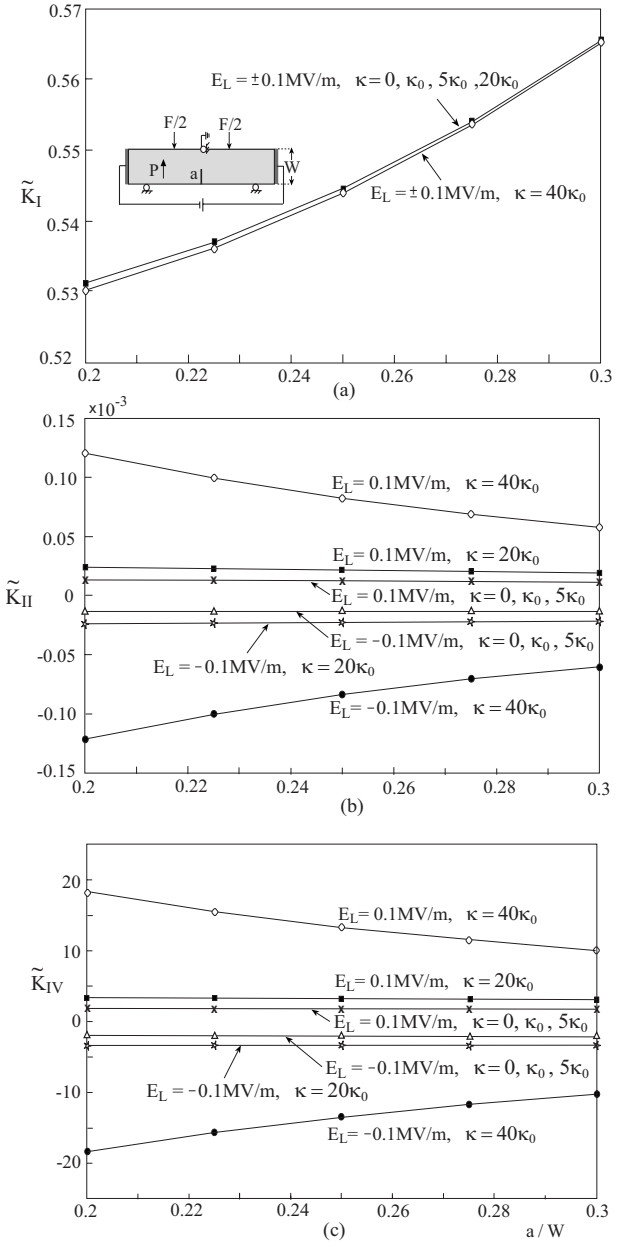

Fig. 9 Normalized intensity factors as a function of normalized crack length *a/W* as obtained from the fine mesh for the specimen in Fig. 7: (*a*) $\tilde{K}_{\mathrm{I}}$, (*b*) $\tilde{K}_{\mathrm{II}}$, and (*c*) $\tilde{K}_{\mathrm{IV}}$

Table 5 Contribution of the intensity factors to the crack sliding displacement Δu_x in millimeters for $a/W=0.25$, $E_L=0.1$ MV/m, and $F=850$ N in the four-point bend problem

κ_a/κ_0	Mode I	Mode II	Mode IV
0	0	2.51×10^{-7}	4.03×10^{-5}
1	0	2.56×10^{-7}	4.12×10^{-5}
5	0	2.79×10^{-7}	4.53×10^{-5}
20	0	4.27×10^{-7}	7.17×10^{-5}
40	0	1.60×10^{-6}	2.89×10^{-4}

Table 6 Contribution of the intensity factors to the crack opening displacement Δu_y in millimeters for $a/W=0.25$, $E_L=0.1$ MV/m, and $F=850$ N in the four-point bend problem

κ_a/κ_0	Mode I	Mode II	Mode IV
0	1.12×10^{-2}	0	0
1	1.12×10^{-2}	0	0
5	1.12×10^{-2}	0	0
20	1.12×10^{-2}	0	0
40	1.12×10^{-2}	0	0

5 Summary and Conclusions

In this study, a conservative M-integral was extended for calculating intensity factors when the exact boundary conditions are applied to the crack faces in piezoelectric materials. A Griffith crack was considered in which the crack is parallel to the poling direction and given tractions and electric flux density were prescribed on the crack faces. Results were obtained by means of the displacement-potential extrapolation method and the conservative M-integral, which enable mode separation. Accurate results were found. With this example, the superiority of the M-integral with respect to the displacement-potential extrapolation method was shown.

Intensity factors for a four-point bend specimen were calculated for applied load and electric field. This problem was analyzed in order to illustrate the calibration of specimens for carrying out fracture tests in piezoelectric materials. An iterative finite element analysis was carried out to apply the exact boundary conditions on the crack faces. The crack was taken parallel to the poling direction. Different values of the permittivity within the crack gap were considered. It was shown that the permittivity strongly affects K_{II} and K_{IV}, which are coupled. The higher the permittivity, the higher the absolute value of these intensity factors. On the other hand, the permittivity hardly affects K_{I}.

The conservative M-integral may be used to properly calibrate specimens when carrying out tests for measuring failure parameters of piezoelectric materials.

Acknowledgment

We are grateful to Robert McMeeking and Hans Jelitto for fruitful conversations. We would also like to thank the Belfer family for their ongoing support.

Nomenclature

a = crack length
c_3 = material constant combination in Eq. (43)
e_{ijk} = components of the piezoelectric coupling coefficient
$e_{i\alpha}$ = contracted piezoelectric coupling coefficient
h = electric enthalpy density
$\mathbf{k}$ = vector of intensity factors
k = iteration number
ℓ = element length at the crack tip
n_i = unit outward normal to the path Γ
q_i = normalized virtual crack extension
r = distance from the crack tip
u_i, $i=1,2,3$ = displacement components
u_n^+ and u_n^- = normal displacement of the upper and lower crack faces
u_4 = electric potential
x_i, $i=1,2,3$ = material coordinate system
x,y,z = local crack tip coordinate system
$\mathbf{A}$ and $\mathbf{B}$ = matrices dependent on material properties
B = specimen thickness
C_{ijkl} = components of the stiffness tensor
$\hat{C}_1^{(1,2\alpha)}$ and $\hat{C}_2^{(1,2\alpha)}$ = expressions in Eqs. (41) and (42)
D^* = electric flux density applied to the crack faces
D^∞ = far field electric flux density
D_i = components of the electric flux density
D_L = longitudinal electric flux density
D_n^+ and D_n^- = normal electric flux density of the upper and lower crack faces
E_A = Young's modulus in the poling direction
E_i = components of the electric field
E_L = longitudinally applied electric field
F = applied force
G_T = shear modulus perpendicular to the poling direction
$\mathcal{G}$ = energy release rate
J = J-integral
K_j, $j=\mathrm{I},\mathrm{II},\mathrm{III}$ = stress intensity factors
K_{IV} = electric flux density intensity factor
L = characteristic length, specimen length
$\mathbf{L}$ = one of the Barnett–Lotte tensors
$M^{(1,2\alpha)}$ = M-integral with 1 as the desired solution and 2α $\alpha=a,b,c$ as the auxiliary solution
N_i = finite element shape functions
P = poling
$\Re$ = real part of a complex quantity
S_1, S_2 = specimen span lengths
T_i = traction components
W = width of the four-point bend specimen
δ_{ij} = Kronecker delta
ϵ_{ij} = strain components
κ_{ij} = permittivity components
κ_a = permittivity within the crack gap
κ_0 = permittivity of a vacuum
ξ,η = coordinates in the parent element
σ^* = stress applied on the crack faces
σ^∞ = far field stress
σ_b = bending stress
σ_{ij} = stress components
σ_{nn}^+ and σ_{nn}^- = normal closing stress at the upper and lower crack faces
ϕ^+ and ϕ^- = electric potential at the upper and lower crack faces
ψ = poling angle relative to the x-direction
Γ = J-integral path (line)

References

[1] Landis, C. M., 2004, "Energetically Consistent Boundary Conditions for Electromechanical Fracture," Int. J. Solids Struct., **41**(22–23), pp. 6291–6315.
[2] Parton, V. Z., 1976, "Fracture Mechanics of Piezoelectric Materials," Acta Astronaut., **3**(9–10), pp. 671–683.
[3] Deeg, W. F. J., 1980, "The Analysis of Dislocation, Crack, and Inclusion

Problems in Piezoelectric Solids," Ph.D. thesis, Stanford University, Palo Alto, CA.
[4] Pak, Y. E., 1990, "Crack Extension Force in a Piezoelectric Material," ASME J. Appl. Mech., **57**(3), pp. 647–653.
[5] Hao, T.-H., and Shen, Z.-Y., 1994, "A New Electric Boundary Condition of Electric Fracture Mechanics and Its Applications," Eng. Fract. Mech., **47**(6), pp. 793–802.
[6] Zhang, T. Y., and Gao, C. F., 2004, "Fracture Behaviors of Piezoelectric Materials," Theor. Appl. Fract. Mech., **41**(1–3), pp. 339–379.
[7] McMeeking, R. M., 2004, "The Energy Release Rate for a Griffith Crack in a Piezoelectric Material," Eng. Fract. Mech., **71**(7–8), pp. 1149–1163.
[8] Ding, H., Wang, G., and Chen, W., 1998, "A Boundary Integral Formulation and 2D Fundamental Solutions for Piezoelectric Media," Comput. Methods Appl. Mech. Eng., **158**(1–2), pp. 65–80.
[9] Kuna, M., 1998, "Finite Element Analyses of Crack Problems in Piezoelectric Structures," Comput. Mater. Sci., **13**(1–3), pp. 67–80.
[10] Shang, F., Kuna, M., and Scherzer, M., 2002, "Analytical Solutions for Two Penny-Shaped Crack Problems in Thermo-Piezoelectric Materials and Their Finite Element Comparisons," Int. J. Fract., **117**(2), pp. 113–128.
[11] Shang, F., Kuna, M. and Abendroth, M., 2003, "Finite Element Analyses of Three-Dimensional Crack Problems in Piezoelectric Structures," Eng. Fract. Mech., **70**(2), pp. 143–160.
[12] Wippler, K., Ricoeur, A., and Kuna, M., 2004, "Towards the Computation of Electrically Permeable Cracks in Piezoelectrics," Eng. Fract. Mech., **71**(18), pp. 2567–2587.
[13] Heyer, V., Schneider, G. A., Balke, H., Drescher, J., and Bahr, H.-A., 1998, "A Fracture Criterion for Conducting Cracks in Homogeneously Poled Piezoelectric PZT-PIC 151 Ceramics," Acta Mater., **46**(18), pp. 6615–6622.
[14] Gruebner, O., Kamlah, M., and Munz, D., 2003, "Finite Element Analysis of Cracks in Piezoelectric Materials Taking Into Account the Permittivity of the Crack Medium," Eng. Fract. Mech., **70**(11), pp. 1399–1413.
[15] Abendroth, M., Groh, U., Kuna, M., and Ricoeur, A., 2002, "Finite Element-Computation of the Electromechanical J-Integral for 2-D and 3-D Crack Analysis," Int. J. Fract., **114**(4), pp. 359–378.
[16] Ricoeur, A., and Kuna, M., 2003, "Influence of Electric Fields on the Fracture of Ferroelectric Ceramics," J. Eur. Ceram. Soc., **23**(8), pp. 1313–1328.
[17] Enderlein, M., Ricoeur, A., and Kuna, M., 2005, "Finite Element Techniques for Dynamic Crack Analysis in Piezoelectrics," Int. J. Fract., **134**(3–4), pp. 191–208.
[18] Banks-Sills, L., Motola, Y., and Shemesh, L., 2008, "The M-Integral for Calculating Intensity Factors of an Impermeable Crack in a Piezoelectric Material," Eng. Fract. Mech., **75**(5), pp. 901–925.
[19] Ikeda, T., 1990, *Fundamentals of Piezoelectricity*, Oxford University Press, Oxford, UK.
[20] Qin, Q. H., 2001, *Fracture Mechanics of Piezoelectric Materials*, WIT, Southampton, UK.
[21] Yau, J. F., Wang, S. S., and Corten, H. T., 1980, "A Mixed-Mode Crack Analysis of Isotropic Solids Using Conservation Laws of Elasticity," ASME J. Appl. Mech., **47**(2), pp. 335–341.
[22] Wang, S. S., Yau, J. F., and Corten, H. T., 1980, "A Mixed-Mode Crack Analysis of Rectilinear Anisotropic Solids Using Conservation Laws of Elasticity," Int. J. Fract., **16**(3), pp. 247–259.
[23] Suo, Z., Kuo, C.-M., Barnett, D. M., and Willis, J. R., 1992, "Fracture Mechanics for Piezoelectric Ceramics," J. Mech. Phys. Solids, **40**(4), pp. 739–765.
[24] Banks-Sills, L., and Sherman, D., 1992, "On the Computation of Stress Intensity Factors for Three-Dimensional Geometries by Means of the Stiffness Derivative and J-Integral Methods," Int. J. Fract., **53**(1), pp. 1–20.
[25] 2004, ANSYS, Release 9, Ansys, Inc., Canonsburg, PA.
[26] Berlincourt, D., and Krueger, H. A., 1959, "Properties of Morgan Electro Ceramic Ceramics," Morgan Electro Ceramics, Report No. TP-226.
[27] Pak, Y. E., 1992, "Linear Electro-Elastic Fracture Mechanics of Piezoelectric Materials," Int. J. Fract., **54**(1), pp. 79–100.
[28] ESIS Procedures and Documentations, 2000, *ESIS P5-00/VAMAS: Procedure for Determining the Fracture Toughness of Ceramics Using the Single-Edge-V-Notched Beam (SEVNB) Method*, European Structural Integrity Society, Dubendorf, Switzerland.
[29] Jelitto, H., Keßler, H., Schneider, G. A., and Balke, H., 2005, "Fracture Behavior of Poled Piezoelectric PZT Under Mechanical and Electrical Loads," J. Eur. Ceram. Soc., **25**(5), pp. 749–757.
[30] Schneider, G. A., Felten, F., and McMeeking, R. M., 2003, "The Electrical Potential Difference Across Cracks in PZT Measured by Kelvin Probe Microscopy and the Implications for Fracture," Acta Mater., **51**(8), pp. 2235–2241.

Asif Israr
e-mail: asifisrar@yahoo.com

Matthew P. Cartmell
e-mail: matthewc@mech.gla.ac.uk

Department of Mechanical Engineering,
University of Glasgow,
James Watt South Building,
Glasgow, G12 8QQ, Scotland, UK

Emil Manoach
Institute of Mechanics,
Bulgarian Academy of Sciences,
Acad. G. Bontchev Strasse,
Block 4, 1113 Sofia, Bulgaria
e-mail: e.manoach@imbm.bas.bg

Irina Trendafilova
Department of Mechanical Engineering,
University of Strathclyde,
75 Montrose Strasse,
Glasgow, G1 1XJ, Scotland, UK
e-mail: irina.trendafilva@strath.ac.uk

Wiesław Ostachowicz
Institute of Fluid Flow Machinery,
Polish Academy of Sciences,
ul. Gen Fiszera 14,
80-952, Gdańsk, Poland;
Gdynia Maritime University,
Faculty of Navigation,
Al. Jana Pawla II, 81-345 Gdynia, Poland
e-mail: wieslaw@imp.gda.pl

Marek Krawczuk
Institute of Fluid Flow Machinery,
Polish Academy of Sciences,
ul. Gen Fiszera 14,
80-952, Gdańsk,Poland;
Department of Electric and Control Engineering,
Technical University of Gdańsk,
Narutowicza 11/12,
80-952 Gdańsk, Poland
e-mail: mk@imp.gda.pl

Arkadiusz Żak
Institute of Fluid Flow Machinery,
Polish Academy of Sciences,
ul. Gen Fiszera 14,
80-952, Gdańsk, Poland
e-mail: arek@imp.gda.pl

Analytical Modeling and Vibration Analysis of Partially Cracked Rectangular Plates With Different Boundary Conditions and Loading

This study proposes an analytical model for vibrations in a cracked rectangular plate as one of the results from a program of research on vibration based damage detection in aircraft panel structures. This particular work considers an isotropic plate, typically made of aluminum, and containing a crack in the form of a continuous line with its center located at the center of the plate and parallel to one edge of the plate. The plate is subjected to a point load on its surface for three different possible boundary conditions, and one examined in detail. Galerkin's method is applied to reformulate the governing equation of the cracked plate into time dependent modal coordinates. Nonlinearity is introduced by appropriate formulations introduced by applying Berger's method. An approximate solution technique—the method of multiple scales—is applied to solve the nonlinear equation of the cracked plate. The results are presented in terms of natural frequency versus crack length and plate thickness, and the nonlinear amplitude response of the plate is calculated for one set of boundary conditions and three different load locations, over a practical range of external excitation frequencies.
[DOI: 10.1115/1.2998755]

1 Overview

Thin plate structures have gained special importance and notably increased application in recent years. Complex structures such as aircraft, ships, steel bridges, sea platforms, etc., all use metal plates. For example, it has been observed that plate panels on the tips of aircraft wings are mainly under transverse pressure and are often subjected to normal and shear forces, which act in the plane of the plate. The plate may not behave as intended if it contains even a small crack or form of damage, and such small disturbances can then create a complete loss of equilibrium and cause failure.

The literature has been reviewed for research on cracked plates under tension and bending. Khadem and Rezaee [1] introduced a new technique for vibration analysis of cracked plates and considered the effect of compliance due to bending only. Okamura et al. [2] obtained the lateral deflection, the load carrying capacity, and

Contributed by the Applied Mechanics Division of ASME for publication in the JOURNAL OF APPLIED MECHANICS. Manuscript received November 2, 2007; final manuscript received August 27, 2008; published online October 31, 2008. Review conducted by Edmundo Corona.

the stress intensity factor of a rectangular cross section single-edge-cracked column with hinged ends under compression. They compared an uncracked column with a cracked column and examined the effect of a crack on the load carrying capacity. Lateral deflection decreased with the ratio of crack length to column width and the ratio of column width to column length. The effect was generally small, if the crack was short and the column was long. In particular, these authors considered the effect of compliance due to bending and ignored the effect of compliance due to rotation induced by the axial load. Khadem and Rezaee [3] established an analytical approach for damage in the form of a crack in a rectangular plate by the application of external loading for different boundary conditions. They concluded from their results that the presence of a crack at a specific depth—and depending upon its location—would affect each of the natural frequencies differently. Krawczuk et al. [4] applied a versatile numerical approach for the analysis of wave propagation and damage detection within cracked plates. Wu and Shih [5] theoretically analyzed the dynamic instability and nonlinear response of cracked plates subjected to periodic in-plane load. The results indicated that the stability behavior and the response of the system are governed by the crack location of the plate, the aspect ratio of the plate, the conditions of in-plane loading, and the amplitude of vibration. Moreover, increasing the crack ratio, i.e., the ratio of the crack length to the length of the edge parallel to the crack, and/or the static component of the in-plane load decreases the natural frequency of the system. Irwin [6] examined a part-through crack in a plate subjected to tension and derived a relation for the crack stress-field parameter and the crack extension force at the boundaries of a flat elliptical crack. Rice and Levy [7] employed two-dimensional generalized plane stresses and used Kirchhoff's plate bending theories with a continuously distributed line-spring to represent a part-through crack, and chose compliance coefficients to match those of an edge-cracked strip in-plane strain. The line of discontinuity was of length $2a$, and the plate was subjected to remote uniform stretching and bending loads along the far sides of the plate. These authors computed the force and moment across the cracked section to determine the stress intensity factor, and the solution to the problem was characterized in terms of the Airy stress function. Their results showed that $K_{rs}/\bar{K}_{rs}$ (where K_{rs} is the stress intensity factor for an all-over crack, and $\bar{K}_{rs}$ is the stress intensity factor of an edge crack in-plane strain for the same relative depth l_o/h, and for remote tensile or bending load) approaches unity with an increase in the ratio of crack length to plate thickness $2a/h$. Furthermore, at small values of relative depth l_o/h, the relative changes in stress intensity factors approaches unity for small values of $2a/h$.

The solutions obtained based on linear models are considered adequate for many practical and engineering purposes although it is recognized that linearized equations usually provide no more than a first approximation. Linearized models of vibrating systems are inadequate in cases where displacements are not small. In addition, problems treated by nonlinear theory exhibit new phenomena, for example, the dependence of frequency of vibration on amplitude that cannot be predicted by means of linear theories. Moreover, an example of such a source of nonlinearity is a crack within a plate, which can lead to profound changes in the vibrational response of the system. In this study, much previous work has been considered together, leading to a proposal for a new analytical model for the vibration analysis of a cracked plate. In Ref. [8] the authors developed an approximate analytical solution for damage detection in an aircraft panel structure modeled as a cracked isotropic plate without the application of a load, essentially for free vibration. The literature does not appear to contain any substantial references to analytical models for cracked plates undergoing forced vibration. The work presented here considers classical plate theory and includes an arbitrarily located crack within a rectangular plate. The crack consists of a continuous line and certain simplifying assumptions are made in order to get an initial tractable solution to the vibration problem. Principally, the effects of rotary inertia and through-thickness shear stress effects are neglected. Berger's formulation is used to generate the nonlinear term within the model differential equation of motion. An approximate analytical solution of the equation for the vibration in the cracked plate for given boundary conditions is found by the method of multiple scales, followed by the presentation of some numerical results and conclusions.

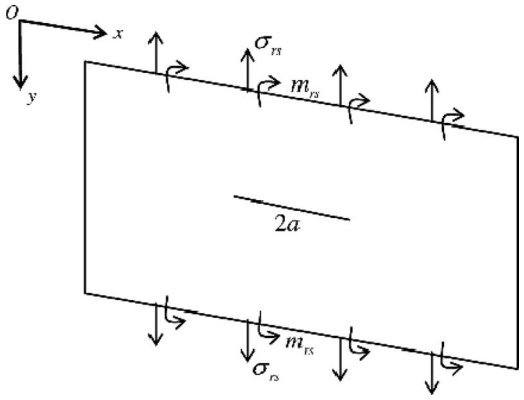

Fig. 1 Line spring model representing the bending and tensile stresses for a part-through crack of length 2*a* after Ref. [7]

2 Governing Equation of the Rectangular Plate and Crack Term

The classical form of the governing equation of the rectangular plate is rigorously treated in Refs. [9–11]. Here, the equilibrium principle is followed for the derivation of the governing equation of the cracked rectangular plate, in which a crack is present at the center and parallel to the x-direction of the plate, as depicted in Fig. 1, and consists of a continuous line of length $2a$. The following basic assumptions are summarized.

1. The plate is made of a perfectly elastic, homogeneous, isotropic material and has a uniform thickness h, which is considered small in comparison with its other dimensions.
2. All strain components are small enough to allow Hooke's law to hold.
3. The normal stress component in the direction transverse to the plate surface is small compared with other stress components and is neglected in the stress-strain relationship.
4. Shear deformation is neglected in this case, and it is assumed that sections taken normal to the middle surface before deformation remain plane and normal to the deflected middle surface of the plate.
5. The effect of the rotary inertia, shear forces, and in-plane force in the y-direction, i.e., n_y and n_{xy} are neglected to make the problem more tractable.

Based on these assumptions, the final version of the governing equation of the cracked plate takes the following form:

$$D\left(\frac{\partial^4 w}{\partial x^4} + 2\frac{\partial^4 w}{\partial x^2 \partial y^2} + \frac{\partial^4 w}{\partial y^4}\right) = -\rho h\frac{\partial^2 w}{\partial t^2} + n_x\frac{\partial^2 w}{\partial x^2} + \frac{\partial^2 \bar{M}_y}{\partial y^2} + \bar{n}_y\frac{\partial^2 w}{\partial y^2} + P_z \tag{1}$$

where $D=Eh^3/12(1-\nu^2)$, P_z is the load per unit area acting at the surface, ρ is the density of the plate, n_x is the in-plane or membrane force $\bar{M}_y$, and $\bar{n}_y$ represents the moment and in-plane force per unit length due to the inclusion of crack at the center of the plate, respectively.

In Eq. (1), two new terms $\bar{M}_y$ and $\bar{n}_y$—and caused by the crack—are introduced by the application of the equilibrium prin-

ciple based on classical plate theory. The formulation of these crack terms is obtained from the model of Rice and Levy [7] (in Eqs. (10) and (11)). The approach of Rice and Levy [7] is based on Kirchoff's bending theory for thin plates, and the assumptions involved in this theory lead to important simplifications in the governing equations. Actually, the results are presented for the stress intensity factors in part-through cracked plates, provided that the crack is not too deep. These stress relationship are used and then by making use of Eqs. (8) and (9), a new relationship for the force and moment caused by the crack was developed, which is dealt in the following section.

Later, P_z in Eq. (1) is replaced by a point load $\bar{P}_z$ based on the application of the appropriate delta function in Eq. (24) to make it compatible with the experimental configuration. Furthermore, in practice, it is straightforward to implement this type of loading.

3 Crack Terms Formulation

Rice and Levy [7] obtained an approximate relation for nominal tensile and bending stresses at the location of the crack. These two relations are taken after some rearrangement, and make use of the relationships within Eqs. (8) and (9) from which it can be deduced that $m_{rs}=6\sigma_{rs}$. A representation of these stresses is given in Fig. 1.

$$\bar{\sigma}_{rs}=\frac{2a}{(6\alpha_{tb}^{o}+\alpha_{tt}^{o})(1-\nu^2)h+2a}\sigma_{rs} \tag{2}$$

and

$$\bar{m}_{rs}=\frac{2a}{3\left(\frac{\alpha_{bt}^{o}}{6}+\alpha_{bb}^{o}\right)(3+\nu)(1-\nu)h+2a}m_{rs} \tag{3}$$

We define $\bar{\sigma}_{rs}$ and $\bar{m}_{rs}$ as the nominal tensile and bending stresses, respectively, at the crack location and on the surface of the plate, σ_{rs} and m_{rs} are the nominal tensile and bending stresses at the far sides of the plate, h is the thickness of the plate, a is the half-crack length, and α_{bb}^{o}, α_{tt}^{o}, $\alpha_{bt}^{o}=\alpha_{tb}^{o}$ are the nondimensional bending compliance, stretching compliance, and stretching-bending compliance coefficients at the crack center, respectively.

This shows that the nominal tensile and bending stresses at the crack location can be regarded as a function of the nominal tensile and bending stresses at the far side of the plate. It is worth noting that Okamura et al. [2] and Khadem and Rezaee [3] also restricted their analysis to the effects of bending compliance. These three compliance coefficients depend on the crack depth d to plate thickness h and vanish when $d=0$. It is shown in Ref. [7] that, in general, the compliance coefficient is a function of the ratio of crack depth to plate thickness. After suitable nondimensionalization, the compliance coefficients at the center of the crack take this form.

$$\alpha_{\lambda\mu}^{o}=1.1547\alpha_{\lambda\mu} \tag{4}$$

where $\lambda,\mu=b,t$ are intermediate variables used in Ref. [7] for algebraic simplification. The appropriate compliance coefficients $\alpha_{\lambda\mu}$ may then be calculated from the following relation, noting that they are valid only for $\zeta=d/h$ values within the range 0.1–0.7. In the present analysis, we take $\zeta=0.6$, leading to calculation of the compliance coefficients [1,2,7] as follows:

$$\alpha_{tt}=\zeta^2[1.98-0.54\zeta^1+18.65\zeta^2-33.70\zeta^3+99.26\zeta^4-211.90\zeta^5+436.84\zeta^6-460.48\zeta^7+289.98\zeta^8] \tag{5}$$

$$\alpha_{bb}=\zeta^2[1.98-3.28\zeta^1+14.43\zeta^2-31.26\zeta^3+63.56\zeta^4-103.36\zeta^5+147.52\zeta^6-127.69\zeta^7+61.50\zeta^8] \tag{6}$$

$$\alpha_{bt}=\alpha_{tb}=\zeta^2[1.98-1.91\zeta^1+16.01\zeta^2-34.84\zeta^3+83.93\zeta^4-153.65\zeta^5+256.72\zeta^6-244.67\zeta^7+133.55\zeta^8] \tag{7}$$

This means that uniformly distributed tensile and bending stresses are at the two sides of the crack location, and these tensile and bending stresses can be expressed in terms of tensile and bending force effects. Therefore, we can write the tensile and bending stresses at the far sides as [7]

$$\sigma_{rs}=\frac{n_{rs}}{h}=\frac{1}{h}\int_{-h/2}^{+h/2}\tau_{rs}(x,y,z)dz \tag{8}$$

$$m_{rs}=\frac{6}{h^2}M_{rs}=\frac{6}{h^2}\int_{-h/2}^{+h/2}z\tau_{rs}(x,y,z)dz \tag{9}$$

where $r,s=1,2$ are intermediate variables required for algebraic simplification. n_{rs} and M_{rs} are the force and moment per unit length in the y-direction at the far sides of the plate, respectively, and $\tau_{rs}(x,y,z)$ is the stress state.

The force and moment were calculated from two-dimensional plane stress-plate bending theory, with the cracked section represented as a continuous line-spring having its compliance matched to that of the edge-cracked strip in-plane strain. Accordingly, we can write Eqs. (2) and (3) in the form of force and moment as

$$\bar{n}_{rs}=\frac{2a}{(6\alpha_{tb}^{o}+\alpha_{tt}^{o})(1-\nu^2)h+2a}n_{rs} \tag{10}$$

and

$$\bar{M}_{rs}=\frac{2a}{3\left(\frac{\alpha_{bt}^{o}}{6}+\alpha_{bb}^{o}\right)(3+\nu)(1-\nu)h+2a}M_{rs} \tag{11}$$

where $\bar{n}_{rs}$ and $\bar{M}_{rs}$ are the force and moment per unit length in the y-direction at the crack location of the plate, respectively.

It is evident from the work of Rice and Levy [7] that when two forces are acting on the plate element to stretch and bend it, the results of their work show that the Airy stress function satisfies the compatibility condition in a region where the body force field is zero. Here, it is very useful to mention that the present theory and the model of the Rice and Levy are based on classical plate theory, therefore the force and moment obtained from Eqs. (10) and (11) are the required terms and are added into the cracked plate model with a negative sign because damage causes a reduction in the overall stiffness of the plate structure, a phenomenon that can also be seen in the literature, such as the work of Khadem and Razaee [1,3] and Wu and Shih [5]. Therefore, we can write

$$\bar{n}_y\equiv-\bar{n}_{rs}=-\frac{2a}{(6\alpha_{tb}^{o}+\alpha_{tt}^{o})(1-\nu^2)h+2a}n_{rs} \tag{12}$$

and

$$\bar{M}_y\equiv-\bar{M}_{rs}=-\frac{2a}{3\left(\frac{\alpha_{bt}^{o}}{6}+\alpha_{bb}^{o}\right)(3+\nu)(1-\nu)h+2a}M_{rs} \tag{13}$$

Substituting the values of $\bar{n}_y$ and $\bar{M}_y$ from Eqs. (12) and (13) into Eq. (1), the governing equation of the plate with crack extends to the following form:

$$\begin{aligned}D\left(\frac{\partial^4 w}{\partial x^4}+2\frac{\partial^4 w}{\partial x^2\partial y^2}+\frac{\partial^4 w}{\partial y^4}\right)&=-\rho h\frac{\partial^2 w}{\partial t^2}+n_x\frac{\partial^2 w}{\partial x^2}+P_z\\&\quad-\frac{2a}{3\left(\frac{\alpha_{bt}^{o}}{6}+\alpha_{bb}^{o}\right)(3+\nu)(1-\nu)h+2a}\frac{\partial^2 M_{rs}}{\partial y^2}\\&\quad-\frac{2a}{(6\alpha_{tb}^{o}+\alpha_{tt}^{o})(1-\nu^2)h+2a}n_{rs}\frac{\partial^2 w}{\partial y^2}\end{aligned} \tag{14}$$

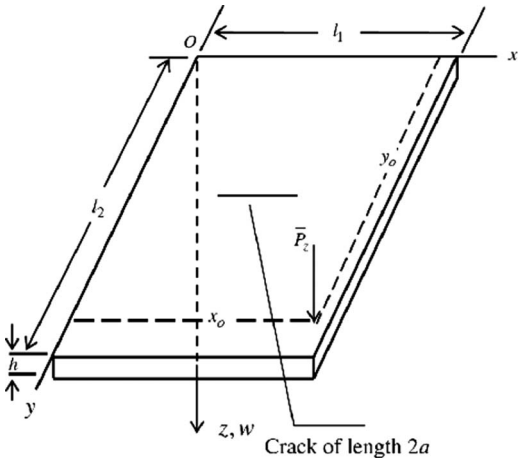

Fig. 2 Isotropic plate loaded by concentrated force and small crack of length 2*a* at the center and parallel to the *x*-axis

As the bending stresses at the far sides of the plate are defined by

$$M_{rs} = -D\left(\frac{\partial^2 w}{\partial y^2} + \upsilon\frac{\partial^2 w}{\partial x^2}\right) \tag{15}$$

then Eq. (15) can be substituted into Eq. (14) to get the final form.

$$D\left(\frac{\partial^4 w}{\partial x^4} + 2\frac{\partial^4 w}{\partial x^2\,\partial y^2} + \frac{\partial^4 w}{\partial y^4}\right) = -\rho h\frac{\partial^2 w}{\partial t^2} + n_x\frac{\partial^2 w}{\partial x^2} + P_z + \frac{2a}{3\left(\frac{\alpha^o_{bt}}{6} + \alpha^o_{bb}\right)(3+\upsilon)(1-\upsilon)h + 2a}D\left(\frac{\partial^4 w}{\partial y^4} + \upsilon\frac{\partial^4 w}{\partial y^2\,\partial x^2}\right) - \frac{2a}{(6\alpha^o_{tb} + \alpha^o_{tt})(1-\upsilon^2)h + 2a}n_{rs}\frac{\partial^2 w}{\partial y^2} \tag{16}$$

4 General Solution for a Vibrating Cracked Plate

Now we consider the rectangular plate in Fig. 2 of length l_1 in the x-direction and l_2 in the y-direction containing a crack, which consists of a continuous line of length $2a$ located at the center and parallel to the x-direction of the plate. A point load $\bar{P}_z$ based on the application of the appropriate delta function (in Eq. (24)) is introduced at the location of (x_o, y_o).

Leissa [9] studied a wide range of rectangular plates with different boundary conditions, producing seminal data on natural frequencies and mode shapes. Many approaches have been adopted from time to time to form the general solution for vibrating plate. Yagiz and Sakman [12] observed the dynamic response of a bridge modeled as an isotropic plate under the effect of a moving load with all sides simply supported. They considered a vehicle in the form of a seven degree of freedom system as the moving load. A mathematical model was obtained by the use of Lagrange's formulation and was used to investigate the dynamic response of the bridge and vehicle. Au and Wang [13] studied the dynamic responses in terms of sound radiation from forced vibration of an orthotropic plate with the effects of moving mass, damping coefficient, and boundary conditions. Fan [14] analyzed the transient vibration and the sound radiation of a rectangular plate with viscoelastic boundary supports subjected to impact loading and obtained the sound radiation pressure in the time and frequency domain by the Rayleigh integral. Mukhopadhyay [15] presented a numerical method for the solution of rectangular plates having different edge conditions and loadings. Young [16] investigated and calculated the set of functions, which define the normal modes of vibration of a uniform beam and obtained the solution for the plate problem with different boundary conditions by the use of Ritz method. Stanišić [17] and Nagaraja and Rao [18] obtained an approximate solution to find the dynamical behavior of rectangular plates for different boundary conditions.

The solution for the governing differential equation of the plate subjected to transverse loading is obtained by defining the characteristic functions depending on the boundary conditions of the plate. The basic model for the solution is the one in which all edges are simply supported, while for other boundary conditions the principle of superposition holds [11,19]. The most general form of the transverse deflection of the plate is

$$w(x,y,t) = \sum_{n=1}^{\infty}\sum_{m=1}^{\infty} A_{mn}X_mY_n\psi_{mn}(t) \tag{17}$$

where X_m and Y_n are the characteristic or modal functions of the cracked rectangular plate, A_{mn} is an, as yet, arbitrary amplitude, and $\psi_{mn}(t)$ is the time dependent modal coordinate.

The appropriate expressions for the characteristic or modal functions are given below and satisfy the stated boundary conditions of the plate. For all cases, l_1 and l_2 are the lengths of the sides of the plate along the x and y directions, respectively. Three boundary condition cases are given next.

Boundary condition 1. Two adjacent edges are clamped while the other two edges are free—CCFF [9,16,18,19].

$$X_m = \cos\left(\frac{\lambda_m x}{l_1}\right) - \cosh\left(\frac{\lambda_m x}{l_1}\right) - \gamma_m\left[\sin\left(\frac{\lambda_m x}{l_1}\right) - \sinh\left(\frac{\lambda_m x}{l_1}\right)\right] \tag{18}$$

$$Y_n = \cos\left(\frac{\lambda_n y}{l_2}\right) - \cosh\left(\frac{\lambda_n y}{l_2}\right) - \gamma_n\left[\sin\left(\frac{\lambda_n y}{l_2}\right) - \sinh\left(\frac{\lambda_n y}{l_2}\right)\right] \tag{19}$$

The $\lambda_{m,n}$ and the $\gamma_{m,n}$ are mode shape constants and can be found in standard reference text such as Refs. [9,19].

Boundary condition 2. Two adjacent edges are clamped while the other two edges are freely supported—CCSS [20].

$$X_m = \sum_{m=1}^{\infty}\sin\frac{m\pi x}{l_1}\sin\frac{m\pi x}{2l_1} = \frac{1}{2}\sum_{m=1}^{\infty}\left(\cos\frac{m\pi x}{2l_1} - \cos\frac{3m\pi x}{2l_1}\right) \tag{20}$$

$$Y_n = \sum_{n=1}^{\infty}\sin\frac{n\pi y}{l_2}\sin\frac{n\pi y}{2l_2} = \frac{1}{2}\sum_{n=1}^{\infty}\left(\cos\frac{n\pi y}{2l_2} - \cos\frac{3n\pi y}{2l_2}\right) \tag{21}$$

Boundary condition 3. All sides are simply supported—SSSS [9,10,12].

$$X_m = \sum_{m=1}^{\infty}\sin\left(\frac{m\pi x}{l_1}\right) \tag{22}$$

$$Y_n = \sum_{n=1}^{\infty}\sin\left(\frac{n\pi y}{l_2}\right) \tag{23}$$

The lateral load $\bar{P}_z$ at position (x_o, y_o) can be readily expressed as follows [14]:

$$\bar{P}_z = P_o(t)\,\delta(x - x_o)\,\delta(y - y_o) \tag{24}$$

Substituting the definition of $w(x,y,t)$ from Eq. (17) and $\bar{P}_z$ from Eq. (24) into Eq. (16), we get

$$D\left(\frac{\partial^4 X_m}{\partial x^4}Y_n + 2\frac{\partial^4 X_m Y_n}{\partial x^2\,\partial y^2} + \frac{\partial^4 Y_n}{\partial y^4}X_m\right)A_{mn}\psi(t)$$
$$= -\rho h\frac{\partial^2\psi(t)}{\partial t^2}A_{mn}X_mY_n + n_x\frac{\partial^2 X_m}{\partial x^2}Y_nA_{mn}\psi(t)$$
$$-\frac{2a}{(6\alpha_{tb}^o + \alpha_{tt}^o)(1-\upsilon^2)h + 2a}n_{rs}\frac{\partial^2 Y_n}{\partial y^2}X_mA_{mn}\psi(t)$$
$$+\frac{2a}{3\left(\frac{\alpha_{bt}^o}{6} + \alpha_{bb}^o\right)(3+\upsilon)(1-\upsilon)h + 2a}$$
$$\times D\left(\frac{\partial^4 Y_n}{\partial y^4}X_m + \upsilon\frac{\partial^4 X_mY_n}{\partial y^2\,\partial x^2}\right)A_{mn}\psi(t)$$
$$+P_o(t)\,\delta(x-x_0)\,\delta(y-y_o) \tag{25}$$

Berger [21] determined the deflection of a plate by neglecting the strain energy due to the second invariant of the middle surface strains and when the deflection is of the order of magnitude of the thickness of the plate. This can be used to obtain forms for the in-plane forces n_x and n_{rs} per unit length in the x and y direction, respectively, and to apply theory predominantly based on aspect ratios equal to 1, 1.5, 2, and infinity. Berger showed that this approach works well for combinations of simply supported and clamped boundary conditions, as shown previously. We note, in passing, that Wah [22] and Ramachandran and Reddy [23] also applied Berger's formulation efficiently for analyzing the nonlinear vibrations of undamped rectangular plates.

To make the form of the in-plane forces, the middle surface strains in the x and y directions can be given by [11]

$$\varepsilon_x = \frac{\partial u}{\partial x} + \frac{1}{2}\left(\frac{\partial w}{\partial x}\right)^2 \tag{26}$$

$$\varepsilon_y = \frac{\partial v}{\partial y} + \frac{1}{2}\left(\frac{\partial w}{\partial y}\right)^2 \tag{27}$$

where u and v are the displacements in the x and y directions, respectively.

Accordingly, we can write the in-plane forces as [11]

$$n_x = \frac{Eh}{1-\upsilon^2}(\varepsilon_x + \upsilon\varepsilon_y) \tag{28}$$

$$n_{rs} = \frac{Eh}{1-\upsilon^2}(\varepsilon_y + \upsilon\varepsilon_x) \tag{29}$$

Substituting Eqs. (26) and (27) into Eqs. (28) and (29), we get

$$\frac{n_x h^2}{12D} = \frac{\partial u}{\partial x} + \upsilon\frac{\partial v}{\partial y} + \frac{1}{2}\left(\frac{\partial w}{\partial x}\right)^2 + \frac{1}{2}\upsilon\left(\frac{\partial w}{\partial y}\right)^2 \tag{30}$$

and therefore for y

$$\frac{n_{rs} h^2}{12D} = \frac{\partial v}{\partial y} + \upsilon\frac{\partial u}{\partial x} + \frac{1}{2}\left(\frac{\partial w}{\partial y}\right)^2 + \frac{1}{2}\upsilon\left(\frac{\partial w}{\partial x}\right)^2 \tag{31}$$

We multiply Eqs. (30) and (31) by $dxdy$ and integrate over the plate area and then impose the conditions that u and v vanish at the external boundaries and around the crack due to symmetry, leading to

$$\frac{n_x h^2 l_1 l_2}{12D} = \frac{1}{2}\int_0^{l_1}\int_0^{l_2}\left[\left(\frac{\partial w}{\partial x}\right)^2 + \upsilon\left(\frac{\partial w}{\partial y}\right)^2\right]dxdy \tag{32}$$

and

$$\frac{n_{rs} h^2 l_1 l_2}{12D} = \frac{1}{2}\int_0^{l_1}\int_0^{l_2}\left[\left(\frac{\partial w}{\partial y}\right)^2 + \upsilon\left(\frac{\partial w}{\partial x}\right)^2\right]dxdy \tag{33}$$

Applying the definition of $w(x,y,t)$ from Eq. (17), we get

$$n_x = DF_{1mn}A_{mn}^2\psi_{mn}^2(t) \tag{34}$$

where

$$F_{1mn} = \frac{6}{h^2 l_1 l_2}\sum_{n=1}^{\infty}\sum_{m=1}^{\infty}\int_0^{l_1}\int_0^{l_2}\left[\left(\frac{\partial X_m}{\partial x}\right)^2 Y_n^2 + \upsilon\left(\frac{\partial Y_n}{\partial y}\right)^2 X_m^2\right]dxdy \tag{35}$$

and

$$n_{rs} = DF_{2mn}A_{mn}^2\psi_{mn}^2(t) \tag{36}$$

where

$$F_{2mn} = \frac{6}{h^2 l_1 l_2}\sum_{n=1}^{\infty}\sum_{m=1}^{\infty}\int_0^{l_1}\int_0^{l_2}\left[\left(\frac{\partial Y_n}{\partial y}\right)^2 X_m^2 + \upsilon\left(\frac{\partial X_m}{\partial x}\right)^2 Y_n^2\right]dxdy \tag{37}$$

Substituting the in-plane forces n_x and n_{rs} from Eqs. (34) and (36) into Eq. (25), multiplying each part of Eq. (25) by the modal function X_m and Y_n for one of the three example boundary conditions mentioned above, and then integrating over the plate area, we find that

$$M_{mn}\ddot{\psi}(t) + K_{mn}\psi(t) + G_{mn}\psi^3(t) = P_{mn} \tag{38}$$

where

$$M_{mn} = \frac{\rho h}{D}\sum_{n=1}^{\infty}\sum_{m=1}^{\infty}A_{mn}\int_0^{l_1}\int_0^{l_2}X_m^2Y_n^2dxdy \tag{39}$$

$$K_{mn} = \sum_{n=1}^{\infty}\sum_{m=1}^{\infty}A_{mn}\int_0^{l_1}\int_0^{l_2}\left(X_m^{iv}Y_n + 2X_m''Y_n'' + Y_n^{iv}X_m - \frac{2a(\upsilon X_m''Y_n'' + Y_n^{iv}X_m)}{3\left(\frac{\alpha_{bt}^o}{6} + \alpha_{bb}^o\right)(3+\upsilon)(1-\upsilon)h + 2a}\right)X_mY_n\,dxdy \tag{40}$$

$$G_{mn} = \sum_{n=1}^{\infty}\sum_{m=1}^{\infty}A_{mn}^3\int_0^{l_1}\int_0^{l_2}\left(-F_{1mn}X_mX_m''Y_n^2 + \frac{2aF_{2mn}X_m^2Y_nY_n''}{(6\alpha_{tb}^o + \alpha_{tt}^o)(1-\upsilon^2)h + 2a}\right)dxdy \tag{41}$$

The integral of the delta function is given by $\int_{-\infty}^{\infty}X_m(x)\,\delta(x-x_0)dx = X_m(x_o)$. Therefore, the force term in Eq. (38) can be expressed as

$$P_{mn} = \frac{P_o(t)}{D}Q_{mn} \tag{42}$$

where

$$Q_{mn} = X_m(x_0)Y_n(y_0) \tag{43}$$

Equation (38) is in the form of the well-known Duffing equation containing a cubic nonlinear term and can be restated as

$$\ddot{\psi}(t) + \omega_{mn}^2\psi(t) + \beta_{mn}\psi^3(t) = \frac{\lambda_{mn}}{D}P_o(t) \tag{44}$$

where

$$\omega_{mn}^2 = \frac{K_{mn}}{M_{mn}} \tag{45}$$

$$\beta_{mn} = \frac{G_{mn}}{M_{mn}} \tag{46}$$

$$\lambda_{mn} = \frac{Q_{mn}}{M_{mn}} \tag{47}$$

and ω_{mn} is the natural frequency of the cracked rectangular plate.

Now if it is assumed that the system is under the influence of weak classical linear viscous damping μ, then the equation of the model of the rectangular cracked plate becomes

$$\ddot{\psi}(t) + 2\mu\dot{\psi}(t) + \omega_{mn}^2\psi(t) + \beta_{mn}\psi^3(t) = \frac{\lambda_{mn}}{D}P_o(t) \tag{48}$$

Letting the load be harmonic, such that

$$P_o(t) = p\cos\Omega_{mn}t \tag{49}$$

which leads to

$$\ddot{\psi}(t) + 2\mu\dot{\psi}(t) + \omega_{mn}^2\psi(t) + \beta_{mn}\psi^3(t) = \frac{\lambda_{mn}}{D}p\cos\Omega_{mn}t \tag{50}$$

Instead of using the excitation frequency Ω_{mn} as a parameter, we introduce a detuning parameter σ_{mn}, which quantitatively describes the nearness of Ω_{mn} to ω_{mn}, and this is a case of primary resonance. This has the advantage of clarifying the identification of the terms in the governing equation at first order perturbation that lead to secular terms. Accordingly we write [24]

$$\Omega_{mn} = \omega_{mn} + \varepsilon\sigma_{mn} \tag{51}$$

where ε is an arbitrarily small perturbation parameter.

To obtain a uniformly valid approximate solution to this problem, it is necessary to order the cubic term, the damping, and the excitation. To accomplish this, we choose to set the following to $O(\varepsilon)^1$.

$$\mu = \varepsilon\mu, \quad \beta_{mn} = \varepsilon\beta_{mn}, \quad p = \varepsilon p \tag{52}$$

After substituting Eqs. (51) and (52) into Eq. (50), it becomes as follows:

$$\ddot{\psi}(t) + 2\varepsilon\mu\dot{\psi}(t) + \omega_{mn}^2\psi(t) + \varepsilon\beta_{mn}\psi^3(t) = \varepsilon\frac{\lambda_{mn}}{D}p\cos(\omega_{mn} + \varepsilon\sigma_{mn})t \tag{53}$$

This introduces damping, the cubic nonlinearity, and the excitation to first order perturbation, which is considered to be in line with the appropriate experimental configuration and other works on weakly nonlinear vibrating systems [24–27]. It is important to note here that for Duffing equations the coefficient of the cubic term, in this case $\varepsilon\beta_{mn}$, can be numerically positive or negative, leading to overhangs of the response curve in the frequency domain to the right or left, respectively.

5 The Method of Multiple Scales

The method of multiple scales is well discussed in the seminal work of Nayfeh and Mook [24] and also in the well known books of Kevorkian and Cole [25] and Murdock [26]. Cartmell et al. [27] reviewed the multiple scales method as applied to weakly nonlinear dynamics of mechanical systems. For the method of multiple scales, the solution of the equation is approximated by a uniformly valid expansion of the form

$$\psi_{mn}(t,\varepsilon) = \psi_{o\,mn}(T_o,T_1) + \varepsilon\psi_{1\,mn}(T_o,T_1) + o(\varepsilon^2) \tag{54}$$

where $\psi_{o\,mn}(T_o,T_1)$ and $\psi_{1\,mn}(T_o,T_1)$ are functions yet to be determined. Independent time scales are introduced where T_o is nominally considered as *fast time* and T_1 as *slow time*, such that, $T_o = t$ and $T_1 = \varepsilon t$. We can express the excitation in term of T_o and T_1 as

$$P_o(t) = \varepsilon p\cos(\omega_{mn}T_o + \sigma_{mn}T_1) \tag{55}$$

Substituting the expansion of Eq. (54) and the excitation term from Eq. (55) into Eq. (53), we get

$$\begin{aligned}[D_o^2 + 2\varepsilon D_oD_1 + \varepsilon^2D_1^2]\psi_{o\,mn} + \varepsilon[D_o^2 + 2\varepsilon D_oD_1 + \varepsilon^2D_1^2]\psi_{1\,mn} \\ + o(\varepsilon^2) + 2\varepsilon\mu[D_o + \varepsilon D_1]\psi_{o\,mn} + 2\varepsilon^2\mu[D_o + \varepsilon D_1]\psi_{1\,mn} \\ + 2\varepsilon\mu\, o(\varepsilon^2) + \omega_{mn}^2\psi_{o\,mn} + \varepsilon\omega_{mn}^2\psi_{1\,mn} + \omega_{mn}^2 o(\varepsilon^2) \\ + \varepsilon\beta_{mn}\{\psi_{o\,mn}^3 + \varepsilon\psi_{1\,mn}^3 + o(\varepsilon^2)\} = \varepsilon\frac{\lambda_{mn}}{D}p\cos(\omega_{mn}T_o + \sigma_{mn}T_1)\end{aligned} \tag{56}$$

Separating terms of like order ε yields, to order ε^o:

$$D_o^2\psi_{o\,mn} + \omega_{mn}^2\psi_{o\,mn} = 0 \tag{57}$$

and to order ε^1:

$$\begin{aligned}D_o^2\psi_{1\,mn} + \omega_{mn}^2\psi_{1\,mn} = &-2D_oD_1\psi_{o\,mn} - 2\mu D_o\psi_{o\,mn} - \beta_{mn}\psi_{o\,mn}^3 \\ &+ \frac{\lambda_{mn}}{D}p\cos(\omega_{mn}T_o + \sigma_{mn}T_1)\end{aligned} \tag{58}$$

The higher orders of ε^2, ε^3, and so on may be neglected because higher order perturbation equations will yield negligible corrections for the problem, as set up here. The general solution of Eq. (57) can be written as

$$\psi_{o\,mn} = B(T_1)e^{i\omega_{mn}T_o} + \bar{B}(T_1)e^{-i\omega_{mn}T_o} \tag{59}$$

where B is an unknown complex amplitude, and $\bar{B}$ is the complex conjugate of B. This amplitude will be determined by eliminating the secular terms from $\psi_{1\,mn}$. Substituting the solution from Eq. (59) into Eq. (58), we get

$$\begin{aligned}D_o^2\psi_{1\,mn} + \omega_{mn}^2\psi_{1\,mn} = &-2D_oD_1\{B(T_1)e^{i\omega_{mn}T_o} + \bar{B}(T_1)e^{-i\omega_{mn}T_o}\} \\ &- 2\mu D_o\{B(T_1)e^{i\omega_{mn}T_o} + \bar{B}(T_1)e^{-i\omega_{mn}T_o}\} \\ &- \beta_{mn}\{B(T_1)e^{i\omega_{mn}T_o} + \bar{B}(T_1)e^{-i\omega_{mn}T_o}\}^3 \\ &+ \frac{\lambda_{mn}}{D}p\cos(\omega_{mn}T_o + \sigma_{mn}T_1)\end{aligned} \tag{60}$$

which, after dropping the argument T_1 in the complex amplitudes leads to the following:

$$\begin{aligned}D_o^2\psi_{1\,mn} + \omega_{mn}^2\psi_{1\,mn} = &-2iD_1\{\omega_{mn}Be^{i\omega_{mn}T_o} - \omega_{mn}\bar{B}e^{-i\omega_{mn}T_o}\} \\ &- 2i\mu\{\omega_{mn}Be^{i\omega_{mn}T_o} - \omega_{mn}\bar{A}e^{-i\omega_{mn}T_o}\} \\ &- \beta_{mn}[B^3e^{3i\omega_{mn}T_o} + \bar{B}^3e^{-3i\omega_{mn}T_o} \\ &+ 3B\bar{B}\{Be^{i\omega_{mn}T_o} + \bar{B}e^{-i\omega_{mn}T_o}\}] \\ &+ \frac{\lambda_{mn}}{D}p\cos(\omega_{mn}T_o + \sigma_{mn}T_1)\end{aligned} \tag{61}$$

Expressing $\cos(\omega_{mn}T_o + \sigma_{mn}T_1)$ in complex form, we get

$$\begin{aligned}D_o^2\psi_{1\,mn} + \omega_{mn}^2\psi_{1\,mn} = &\Bigg[-2i\omega_{mn}D_1B - 2i\mu\omega_{mn}B - 3\beta_{mn}B^2\bar{B} \\ &+ \frac{\lambda_{mn}}{2D}pe^{i\sigma_{mn}T_1}\Bigg]e^{i\omega_{mn}T_o} - \beta_{mn}B^3e^{3i\omega_{mn}T_o} + cc\end{aligned} \tag{62}$$

where cc denotes the complex conjugate of the preceding terms. Any particular solution of Eq. (62) can have secular terms containing the factor $T_oe^{i\omega_{mn}T_o}$ unless $D_1B = 0$. To eliminate the secular terms from Eq. (62), we must put

$$-2i\omega_{mn}D_1B-2i\mu\omega_{mn}B-3\beta_{mn}B^2\bar{B}+\frac{\lambda_{mn}}{2D}pe^{i\sigma_{mn}T_1}=0 \quad (63)$$

In solving Eq. (63), it is convenient to write the complex amplitude B in the polar form

$$B=\frac{1}{2}be^{i\alpha} \quad (64)$$

where b and α are real amplitude and phase functions of T_1, respectively. Substituting Eq. (64) into Eq. (63), we get

$$\omega_{mn}b\alpha'-i\omega_{mn}b'-i\omega_{mn}\mu b-\frac{3\beta_{mn}}{8}b^3+\frac{\lambda_{mn}}{2D}p[\cos(\sigma_{mn}T_1-\alpha)+i\sin(\sigma_{mn}T_1-\alpha)]=0 \quad (65)$$

where the prime denotes the derivative with respect to T_1. Now, separating the result into real and imaginary parts, we obtain

$$b'=-\mu b+\frac{\lambda_{mn}}{2\omega_{mn}D}p\sin(\sigma_{mn}T_1-\alpha) \quad (66)$$

$$b\alpha'=\frac{3\beta_{mn}b^3}{8\omega_{mn}}-\frac{\lambda_{mn}}{2\omega_{mn}D}p\cos(\sigma_{mn}T_1-\alpha) \quad (67)$$

Equations (66) and (67) can be transformed into an autonomous system, i.e., one in which T_1 does not appear explicitly, by letting

$$\kappa=\sigma_{mn}T_1-\alpha \quad (68)$$

Substituting Eq. (68) into Eqs. (66) and (67), we get

$$b'=-\mu b+\frac{\lambda_{mn}}{2\omega_{mn}D}p\sin\kappa \quad (69)$$

$$b\kappa'=\sigma_{mn}b-\frac{3\beta_{mn}b^3}{8\omega_{mn}}+\frac{\lambda_{mn}}{2\omega_{mn}D}p\cos\kappa \quad (70)$$

In the case of steady-state motion $b'=\kappa'\approx 0$—and this corresponds to the singular points of Eqs. (69) and (70)—that is,

$$\mu b=\frac{\lambda_{mn}}{2\omega_{mn}D}p\sin\kappa \quad (71)$$

$$-\frac{3\beta_{mn}b^3}{8\omega_{mn}}+\sigma_{mn}b=-\frac{\lambda_{mn}}{2\omega_{mn}D}p\cos\kappa \quad (72)$$

Squaring and adding these equations, we obtain,

$$\left[\mu^2+\left(\sigma_{mn}-\frac{3\beta_{mn}b^2}{8\omega_{mn}}\right)^2\right]b^2=\frac{\lambda_{mn}^2}{4\omega_{mn}^2D^2}p^2 \quad (73)$$

It is then possible to rearrange Eq. (73) to give the amplitude of the response b as a function of the detuning parameter σ_{mn} and the amplitude of the excitation p_o, and this is the frequency-response equation, as follows:

$$\sigma_{mn}=\frac{3\beta_{mn}b^2}{8\omega_{mn}}\pm\sqrt{\frac{\lambda_{mn}^2}{4\omega_{mn}^2b^2D^2}p^2-\mu^2} \quad (74)$$

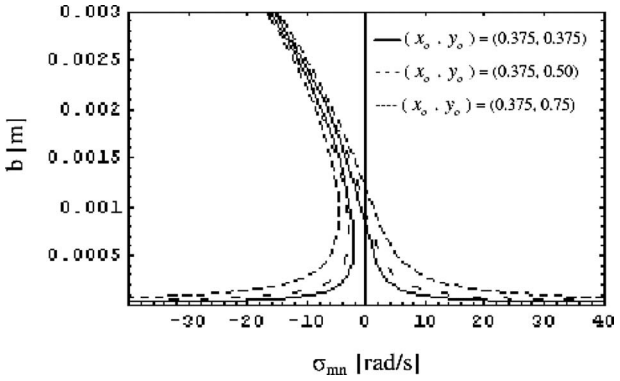

Fig. 3 The amplitude of the response as a function of the detuning parameter (rad/s) and the point load at different locations (m) of the plate element

6 Numerical Results and Discussion

In this section, the results are presented as functions of frequency, half-crack length, and plate thickness. Figure 3 shows the plot of amplitude b as a function of σ_{mn} for a given μ and p in the form of a frequency-response curve. Each point on this curve corresponds to a singular point. To draw such a curve, one solves for σ_{mn} in terms of b. The material properties of aluminum have been considered for different cases of half-crack length, i.e., $E=7.03\times10^{10}$ N/m^2, $\rho=2660$ kg/m^3, $\nu=0.33$, and damping factor $\mu=0.08$, while the geometric values of the plate are $l_1=0.5$ m, $l_2=1$ m, $h=0.01$ m, and $p=10$ N is the load acting on the surface of the plate at different points. The effect of changing the position of the load is shown in Fig. 3. The natural frequencies without and with the crack for different boundary conditions and aspect ratios are tabulated in Table 1.

It may be seen from Table 1 that the presence of the crack (shown here as a deliberately large) at the center of the plate significantly influences the natural frequency of the first mode of the plate, in all three cases. In the subsequent section, attention will be focused on the case for which two adjacent edges are clamped while the other two edges are free (CCFF), and the results are shown for the first mode only. Although it cannot be easily shown in Fig. 3 due to the necessary scaling of the plot, increasing the half-crack length from 0.05 m to 0.125 m introduces small changes to the degree of nonlinear overhang in the softening direction, with some attendant change in the modal natural frequency. It has also been observed that changing the location of the load on the plate slightly affects the global nonlinearity of the system, as shown in Fig. 3 and evidenced by the increasingly wide nonlinear region as the excitation location moves closer to the unsupported corner.

Figure 4 shows the decrease in the natural frequency as we go on to increase the half-crack length for the same parameters, as considered earlier. These changes are very small for small half-

Table 1 Natural frequencies of cracked plate model for different boundary conditions and aspect ratios

Lengths of the sides of the plate		Two adjacent edges clamped, the other two free (CCFF)		Two adjacent edges clamped, the other two simply supported (CCSS)		All edges simply supported (SSSS)	
		First mode natural frequency, ω_{mn} (rad/s) for a half-crack length, $a=0.05$ (m)					
l_1 (m)	l_2 (m)	Uncracked	Cracked	Uncracked	Cracked	Uncracked	Cracked
1	1	80.462	70.559	445.666	403.779	77.580	71.119
0.5	1	231.061	227.611	1161.770	1138.530	193.951	189.581
0.5	0.5	321.849	282.237	1782.660	1615.120	310.322	284.475

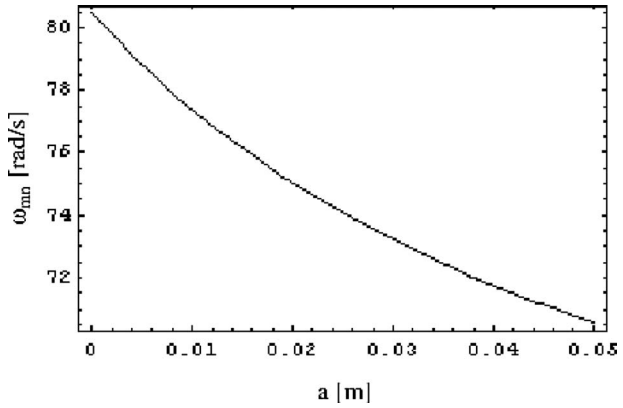

Fig. 4 Plate first mode natural frequency as a function of half-crack length

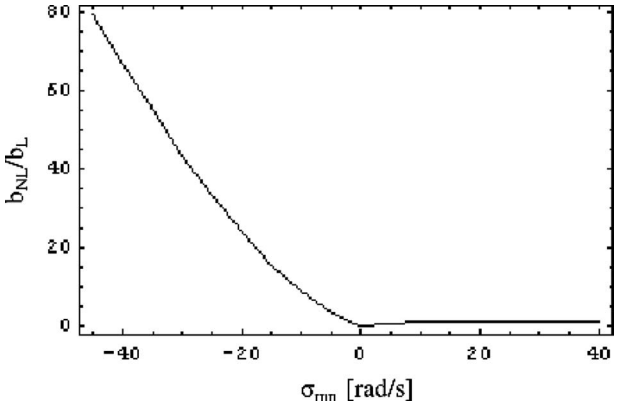

Fig. 6 Comparison between linear and nonlinear models of the cracked rectangular plate

crack lengths, as one would expect. Moreover, the natural frequency is also influenced if the geometry of the plate is changed, in particular, its length and thickness, in addition to the effect of the half-crack length. Similarly, it may be seen from Fig. 5 that by increasing the thickness of the plate the natural frequency of the first mode also increases for different values of half-crack length. This means that this natural frequency is directly related to the thickness of the plate. The theory presented in this paper currently holds only for a plate with a crack at the center and defined by a continuous line model. The results of this sort could equally be obtained for the cases of CCSS and SSSS, but space limitations currently preclude that.

It is also instructive to note that if the cubic nonlinearity β_{mn} is set to zero, then the problem is linearized. However. in the case of the nonlinear problem the significant effect of including this term is apparent from the numerical results depicted in Fig. 6. It can be seen in Fig. 6 that the ratio of the nonlinear solution amplitude (where β_{mn} is set to zero) is very large for negative detuning. This exactly emulates the softening nonlinear characteristic shown in Fig. 4. It can be seen that this ratio reduces close to unity for zero and positive detuning, again fully in line with the softening characteristic observable in Fig. 3. In the figure, b_{NL} is the nonlinear amplitude and b_{L} is the corresponding linear amplitude.

Orientation of the crack at some angle will change the model because there will be more than two components of the crack geometry: one for tensile loading and one for bending along the plate element. Here, it is assumed that the crack is parallel to the x-direction of the plate.

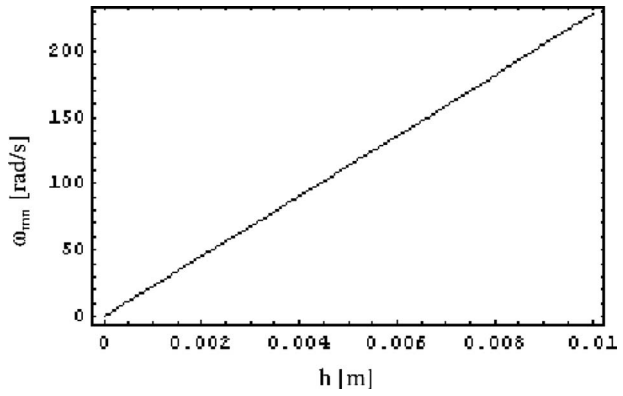

Fig. 5 Plate first mode natural frequency as a function of the thickness of the plate for the half-crack length 0.05 m

7 Conclusions

This research presents a new analytical model for the vibration analysis of cracked plates subjected to transverse loading at some specified position with different sets of boundary conditions. Berger's formulation is effectively applied to make the governing equation for vibration of a cracked plate nonlinear and in the form of a Duffing equation. It has been found that for a square plate with the CCFF boundary conditions there is an approximately 12% reduction in natural frequency in the presence of a large centrally located crack of length 0.1 m. However, the reduction in the value of natural frequency is lower for other plate aspect ratios, and linear and nonlinear results tend to coalesce for very low amplitude ratios.

Finally, it is concluded that the decrease in the natural frequency when there is a crack present may substantiate the use of the model in constructing a vibration based analysis methodology for plate structures and for further development of vibration based health monitoring. Further work is under way to extend the theory of this paper to cracks in arbitrary locations and orientations.

Acknowledgment

This work is part of a larger program of work that has been carried out under NATO Grant No. CBP.EAP.CLG.981517, and A. Israr's studentship was kindly provided by the Institute of Space Technology, Pakistan, and the Goudie Bequest of the University of Glasgow, U.K.

References

[1] Khadem, S. E., and Rezaee, M., 2000, "Introduction of Modified Comparison Functions for Vibration Analysis of a Rectangular Cracked Plate," J. Sound Vib., **236**(2), pp. 245–258.
[2] Okamura, H., Liu, H. W., Chu, C., and Liebowitz, H., 1969, "A Cracked Column Under Compression," Eng. Fract. Mech., **1**, pp. 547–563.
[3] Khadem, S. E., and Rezaee, M., 2000, "An Analytical Approach for Obtaining the Location and Depth of an All-Over Part-Through Crack On Externally In-Plane Loaded Rectangular Plate Using Vibration Analysis," J. Sound Vib., **230**(2), pp. 291–308.
[4] Krawczuk, M., Palacz, M., and Ostachowicz, W., 2004, "Wave Propagation in Plate Structures for Crack Detection," Finite Elem. Anal. Design, **40**, pp. 991–1004.
[5] Wu, G. Y., and Shih, Y. S., 2005, "Dynamic Instability of Rectangular Plate With an Edge Crack," Comput. Struct., **84**, pp. 1–10.
[6] Irwin, G. R., 1962, "Crack Extension Force for a Part Through Crack in a Plate," ASME J. Appl. Mech., **29**, pp. 651–654.
[7] Rice, J. R., and Levy, N., 1972, "The Part Through Surface Crack in an Elastic Plate," ASME J. Appl. Mech., **3**, pp. 185–194.
[8] Israr, A., Cartmell, M. P., Krawczuk, M., Ostachowicz, W. M., Manoach, E., Trendafilova, I., Shiskina, E. V., and Palacz, M., 2006, "On Approximate Analytical Solutions for Vibrations in Cracked Plates," *Modern Practice in Stress and Vibration Analysis VI*, Vols. 5–6, P. Keogh, ed., Trans Tech, Switzerland, pp. 315–322.
[9] Leissa, A., 1993, "Vibration of Plates," National Acoustical and Space Administration, Report No. NASA SP-160.

[10] Szilard, R., 2004, *Theories and Applications of Plate Analysis*, Wiley, New York, p. 89.
[11] Timoshenko, S., 1940, *Theory of Plates and Shells*, McGraw-Hill, New York.
[12] Yagiz, N., and Sakman, L. E., 2006, "Vibrations of a Rectangular Bridge as an Isotropic Plate Under a Traveling Full Vehicle Model," J. Vib. Control, **12**(1), pp. 83–98.
[13] Au, F. T. K., and Wang, M. F., 2005, "Sound Radiation From Forced Vibration of Rectangular Orthotropic Plates Under Moving Loads," J. Sound Vib., **281**, pp. 1057–1075.
[14] Fan, Z., 2001, "Transient Vibration and Sound Radiation of a Rectangular Plate With Viscoelastic Boundary Supports," Int. J. Numer. Methods Eng., **51**, pp. 619–630.
[15] Mukhopadhyay, M., 1979, "A General Solution for Rectangular Plate Bending," Forsch. Ingenieurwes., **45**(4), pp. 111–118.
[16] Young, D., 1950, "Vibration of Rectangular Plates by the Ritz Method," ASME J. Appl. Mech., **17**(4), pp. 448–453.
[17] Stanišić, M. M., 1957, "An Approximate Method Applied to the Solution of the Problem of Vibrating Rectangular Plates," J. Aeronaut. Sci., **24**, pp. 159–160.
[18] Nagaraja, J. V., and Rao, S. S., 1953, "Vibration of Rectangular Plates," J. Aeronaut. Sci., **20**, pp. 855–856.
[19] Berthelot, J. M., 1999, *Dynamics of Composite Materials and Structures*, Institute for Advanced Materials and Mechanics, Springer, New York.
[20] Iwato, S., 1951, "Approximate Calculation for the Frequency of Natural Vibration of a Thin Rectangular Plate the Two Adjacent Edges of Which are Clamped While the Other Two Edges are Freely Supported," Trans. Jpn. Soc. Mech. Eng., **17**(57), pp. 30–33 (in Japanese).
[21] Berger, H. M., 1955, "A New Approach to the Analysis of Large Deflections of Plates," ASME J. Appl. Mech., **22**, pp. 465–472.
[22] Wah, T., 1964, "The Normal Modes of Vibration of Certain Nonlinear Continuous Systems," ASME J. Appl. Mech., **31**, pp. 139–140.
[23] Ramachandran, J., and Reddy, D. V., 1972, "Nonlinear Vibrations of Rectangular Plates With Cut-Outs," AIAA J., **10**, pp. 1709–1710.
[24] Nayfeh, A. H., and Mook, D. T., 1979, *Nonlinear Oscillations*, Wiley, Germany.
[25] Kevorkian, J., and Cole, J. D., 1981, *Perturbation Methods in Applied Mathematics*, Vol. 34, Springer-Verlag, Berlin.
[26] Murdock, J. A., 1999, *Perturbations Theory and Methods*, SIAM, Philadelphia.
[27] Cartmell, M. P., Ziegler, S. W., Khanin, R., and Forehand, D. I. M., 2003, "Multiple Scales Analysis of the Dynamics of Weakly Nonlinear Mechanical Systems," Appl. Mech. Rev., **56**(5), pp. 455–492.

N. Ali[1]
e-mail: nasirali_qau@yahoo.com

Y. Wang

Chair of Fluid Dynamics,
Department of Mechanical Engineering,
Darmstadt University of Technology,
Hochschulstrasse 1, 64289 Darmstadt, Germany

T. Hayat
Department of Mathematics,
Quaid-i-Azam University,
Islamabad, 45320, Pakistan

M. Oberlack
Chair of Fluid Dynamics,
Department of Mechanical Engineering,
Darmstadt University of Technology,
Hochschulstrasse 1, 64289 Darmstadt, Germany

Slip Effects on the Peristaltic Flow of a Third Grade Fluid in a Circular Cylindrical Tube

Peristaltic flow of a third grade fluid in a circular cylindrical tube is undertaken when the no-slip condition at the tube wall is no longer valid. The governing nonlinear equation together with nonlinear boundary conditions is solved analytically by means of the perturbation method for small values of the non-Newtonian parameter, the Debroah number. A numerical solution is also obtained for which no restriction is imposed on the non-Newtonian parameter involved in the governing equation and the boundary conditions. A comparison of the series solution and the numerical solution is presented. Furthermore, the effects of slip and non-Newtonian parameters on the axial velocity and stream function are discussed in detail. The salient features of pumping and trapping are discussed with particular focus on the effects of slip and non-Newtonian parameters. It is observed that an increase in the slip parameter decreases the peristaltic pumping rate for a given pressure rise. On the contrary, the peristaltic pumping rate increases with an increase in the slip parameter for a given pressure drop (copumping). The size of the trapped bolus decreases and finally vanishes for large values of the slip parameter.
[DOI: 10.1115/1.2998761]

Keywords: slip condition, peristaltic flow, third grade fluid, trapping

1 Introduction

In recent years, there has been a growing interest in peristaltic transport. This is perhaps due to the fact that fluid transport through tube by peristaltic motion as a fundamental physiological process has key importance in biomechanical and engineering sciences. To be more specific it encounters in urine transport from the kidney to the bladder, chyme transport in the gastrointestinal tract, the movement of spermatozoa in the ductus efferents of the male reproductive tract, the movement of the ovum in the fallopian tube, and the vasomotion of small blood vessels. Roller and finger pumps also operate under this principle. Although peristaltic motion has been found in living systems for many centuries, the mathematical modeling on the topic began with pioneering works by Shapiro et al. [1] using a wave frame of reference and Fung and Yih [2] employing a laboratory frame of reference. Later several investigations were carried out using these frames, which classify them according to the geometries, wave shapes, fluids, and assumptions of the Reynolds number, wavelength parameter, and wave amplitude parameter.

Literature survey indicates that most of the contributions on peristaltic motion deal with the blood and other physiological fluids as Newtonian fluids. This approach is satisfactory for peristalsis in the ureter but it is not adequate when the peristaltic mechanism involved in small blood vessels, lymphatic vessels, intestine, ductus afferents of the male reproductive tract, and transport of spermatozoa in the cervical canal is considered. It is now readily acknowledged that majority of the physiological fluids behave like a non-Newtonian fluid. Some recent investigations, which were contributed to the study of peristaltic action, were mentioned in the references [3–17].

Although the no-slip condition is known as the central tents of the Navier–Stokes theory, there are problems where it does not hold. Such problems are then described by defining a partial slip between the fluid and boundary, e.g., the fluid may be particulate or it could be a rarefied gas with a suitable Knudsen number value. Beavers and Joseph [18] proposed the slip condition in terms of the tangential components of the velocity and the stress at the boundary. The slip condition is important in the polishing of artificial heart valves and internal cavities in a variety of manufactured parts, microchannels, or nanochannels and in applications where a thin film of light oil is attached to the moving plates or when the surface is coated with a special coating such as a thick monolayer of hydrophobic octadecyltrichlorosilane [19]. There is always a certain amount of slip, which is very hard to detect experimentally because of the required space resolution. Kwang-Hua Chu and Fang [20] analyzed the peristalsis in a slip flow in a two dimensional channel with small amplitude sinusoidal waves. The compressible viscous flow in slits with the wall slip is discussed by Georgiou and Crochet [21]. In view of modeling the oscillations observed in constant piston speed rheometers and other extruding devices, they also performed computations for the viscous flow of a compressible fluid in a channel with slip at the wall. The effects of slip on the flow of a viscous fluid in a channel were investigated by Rao and Rajagopal [22]. They used the slip condition in terms of both the shear and normal stresses. Kwang-Hua Chu[23] and Chu [24] analyzed the slip effects within static, rigid, and corrugated-wall microchannels or microtubes, which are common in micro-electro-mechanical system (MEMS) applications. Moreover it is interesting and realistic to note that microdomains, such as arteries and capillaries, are prone to constrictions for various pathological reasons. Such microdomain flow problems may be studied as flows through axially corrugated pipes using the continuum theory, with the slip condition prescribed on the pipe surface. Very recently, El-Shehawy et al. [25] examined the slip effects on the peristaltic mechanism of a Maxwell fluid. Despite the overwhelming importance and frequent occurrence of the complex rheology of biological fluids, no work has been reported yet regarding the slip effects on the peristaltic flows of third grade fluids. In the present work we put forward the peristaltic flow analysis of the third grade fluid in the presence of a slip condition. The slip condition is taken in terms of the shear

[1]Corresponding author. Permanent address: Department of Mathematics, Faculty of Basic and Applied Sciences, International Islamic University Islamabad, Pakistan.

Contributed by the Applied Mechanics Division of ASME for publication in the JOURNAL OF APPLIED MECHANICS. Manuscript received December 12, 2007; final manuscript received August 29, 2008; published online October 31, 2008. Review conducted by Nesreen Ghaddar.

stress. Peristaltic flow in a circular cylindrical tube is studied under long wavelength and small Deborah number considerations. This paper runs as follows. In Sec. 2 we present the basic equations. Problem formulation is given in Sec. 3. Section 4 includes the series solution. The numerical method used here is presented in Sec. 5. Section 6 highlights the influence of various interesting parameters on the flow. Comparison of the series and numerical solutions is also made in the same section. Section 7 provides the concluding remarks.

2 Field Equations

In the absence of body forces, the balances of mass and linear momentum lead to

$$\operatorname{div} \overline{\mathbf{V}} = 0 \tag{1}$$

$$\rho \frac{d\overline{\mathbf{V}}}{d\bar{t}} = \operatorname{div} \overline{\mathbf{T}} \tag{2}$$

where ρ is the density, $\overline{\mathbf{V}}$ is the velocity vector, $\bar{p}$ is the pressure, $\overline{\mathbf{T}}$ is the Cauchy stress tensor, and d/dt denotes the material time derivative. The constitutive relation for the stress tensor of an incompressible third grade homogenous fluid, as proposed by Fosdick and Rajagopal [26], has the form

$$\overline{\mathbf{T}} = -p\overline{\mathbf{I}} + \overline{\mathbf{S}} \tag{3}$$

$$\overline{\mathbf{S}} = \mu\overline{\mathbf{A}}_1 + \alpha_1\overline{\mathbf{A}}_2\alpha_2\overline{\mathbf{A}}_1^2 + \beta(tr\overline{\mathbf{A}}_1^2)\overline{\mathbf{A}}_1 \tag{4}$$

Here, $-p\overline{\mathbf{I}}$ is the indeterminate part of the stress due to the constraint of incompressibility, μ is the coefficient of shear viscosity, and α_1, α_2, and β are the material constants. The Rivlin–Ericksen tensors $\mathbf{A}_n$ are defined by

$$\overline{\mathbf{A}}_1 = (\operatorname{grad} \overline{\mathbf{V}}) + (\operatorname{grad} \overline{\mathbf{V}})^T$$

$$\overline{\mathbf{A}}_n = \frac{d\overline{\mathbf{A}}_{n-1}}{d\bar{t}} + \overline{\mathbf{A}}_{n-1}(\operatorname{grad} \overline{\mathbf{V}}) + (\operatorname{grad} \overline{\mathbf{V}})^T\overline{\mathbf{A}}_{n-1}, \quad n > 1 \tag{5}$$

The Clausius–Duhem inequality and the requirement that the Helmholtz free energy be a minimum in equilibrium impose the following constraints on the dynamic viscosity μ, the normal stress coefficients α_1 and α_2, and the coefficient β

$$\mu \geq 0, \quad \alpha_1 \geq 0, \quad \beta \geq 0, \quad |\alpha_1 + \alpha_2| \leq \sqrt{24\mu\beta} \tag{6}$$

It is noted that this constitutive relation is able to predict not only the normal stress differences, but also the shear thickening phenomenon (since $\beta > 0$), which indicates the increase in the viscosity by the increasing shear rate.

3 Mathematical Model

Let us consider a circular cylindrical tube of radius a filled with a homogenous incompressible third grade fluid. The flow is induced by an infinite wave train traveling with velocity c along the walls of the tube. We choose a cylindrical coordinate system with $\bar{R}$ along the radial direction and $\bar{Z}$ along the axis of the tube. The geometry of the wall surface is

$$\bar{h}(\bar{Z},\bar{t}) = a + b\cos\left[\frac{2\pi}{\lambda}(\bar{Z} - c\bar{t})\right] \tag{7}$$

in which a is the radius of the undisturbed tube, b is the wave amplitude, λ is the wavelength, c is the wave speed, and $\bar{t}$ is the time.

In the fixed frame of reference the flow phenomenon is unsteady. To carry out the steady analysis we change the coordinate system from the fixed frame to a wave frame. The two frames are related through the following transformations:

$$\bar{r} = \bar{R}, \quad \bar{z} = \bar{Z} - c\bar{t}$$

$$\bar{u} = \bar{U}, \quad \bar{w} = \bar{W} - c \tag{8}$$

where $(\bar{U},\bar{W})$ and $(\bar{u},\bar{w})$ are the radial and axial velocity components in the fixed and wave frames, respectively.

For the subsequent calculations it is convenient to introduce the following dimensionless quantities:

$$r = \frac{\bar{r}}{a}, \quad z = \frac{2\pi\bar{z}}{\lambda}, \quad u = \frac{\bar{u}}{c}, \quad w = \frac{\bar{w}}{c}$$

$$h = \frac{\bar{h}}{a}, \quad p = \frac{a^2\bar{p}}{\lambda\mu c}, \quad \mathbf{S} = \frac{a\overline{\mathbf{S}}}{\mu c}, \quad t = \frac{2\pi c}{\lambda}\bar{t} \tag{9}$$

Utilizing the relations (8) and (9) and introducing the stream function $\psi(r,z)$ by

$$u = \frac{-\delta}{r}\frac{\partial\psi}{\partial z}, \quad w = \frac{1}{r}\frac{\partial\psi}{\partial r} \tag{10}$$

with $\delta = 2\pi a/\lambda$, the continuity equation (1) is satisfied identically and the resulting equation of Eq. (2) under a long wavelength yields

$$\frac{\partial p}{\partial r} = 0 \tag{11}$$

$$\frac{\partial p}{\partial z} = \frac{1}{r}\frac{\partial(rS_{rz})}{\partial r} \tag{12}$$

where by Eq. (4)

$$S_{rz} = \frac{\partial}{\partial r}\left(\frac{1}{r}\frac{\partial\psi}{\partial r}\right) + 2\Gamma\left(\frac{\partial}{\partial r}\left(\frac{1}{r}\frac{\partial\psi}{\partial r}\right)\right)^3 \tag{13}$$

and $\Gamma = \beta c^2/\mu a^2$ is the Debroah number. It is noted that for the Newtonian fluid $\Gamma = 0$ and for all nonzero positive values of Γ, the viscosity increases by increasing the shear rate.

The appropriate boundary conditions in the fixed frame are

$$\frac{\partial\bar{W}}{\partial\bar{R}} = 0 \quad \text{at} \quad \bar{R} = 0$$

$$\bar{U} = 0 \quad \text{and} \quad \bar{W} = -\frac{\xi}{\mu}\bar{S}_{\bar{R}\bar{Z}} \quad \text{at} \quad \bar{R} = \bar{h} \tag{14}$$

Upon making use of Eq. (8) into the above equation and then using the variables defined in Eq. (9) one can write

$$\frac{\partial w}{\partial r} = 0 \quad \text{at} \quad r = 0$$

$$u = 0 \quad \text{and} \quad w = -1 - \gamma S_{rz} \quad \text{at} \quad r = h = 1 + \phi\cos z \tag{15}$$

where

$$S_{rz} = \frac{\partial w}{\partial r} + 2\Gamma\left(\frac{\partial w}{\partial r}\right)^3 \tag{16}$$

and γ $(=\xi/a, \xi$ is the dimensional slip parameter) is the dimensionless slip parameter. Furthermore we note that $\gamma = 0$ yields the no-slip case and $\gamma \to \infty$ corresponds to the free-slip condition.

The instantaneous volume rate of flow in the fixed $\bar{R}$ and $\bar{Z}$ coordinate system is given as

$$\bar{Q} = 2\pi\int_0^{\bar{h}} \bar{W}\bar{R}\,d\bar{R} \tag{17}$$

where $\bar{h}$ is a function of $\bar{Z}$ and $\bar{t}$. By substituting Eq. (8) into Eq. (17), and then integrating, one obtains

$$\bar{Q} = \bar{q} + \pi c\bar{h}^2$$

where

$$\bar{q} = 2\pi \int_0^{\bar{h}} \bar{w}\bar{r}d\bar{r} \tag{18}$$

is the volume flow rate in the moving coordinate system and is independent of time. Here $\bar{h}$ is a function of $\bar{z}$ alone and is defined through Eq. (8). Using dimensionless variables, we find

$$F = \frac{\bar{q}}{2\pi a^2 c} = \int_0^h \frac{\partial \psi}{\partial r} dr = \psi(h) - \psi(0) \tag{19}$$

From Eqs. (10), (15), (16), and (19) we can write

$$\psi = 0, \quad \frac{\partial}{\partial r}\left(\frac{1}{r}\frac{\partial \psi}{\partial r}\right) = 0 \quad \text{at} \quad r = 0$$

$$\psi = F, \quad \frac{1}{r}\frac{\partial \psi}{\partial r} = -\gamma S_{rz} - 1 \quad \text{at} \quad r = h = 1 + \phi \cos z \tag{20}$$

where $\phi = b/a$ is the amplitude ratio.

Elimination of pressure from Eqs. (11) and (12) leads to the following compatibility equation:

$$\frac{\partial}{\partial r}\left[\frac{1}{r}\frac{\partial (rS_{rz})}{\partial r}\right] = 0 \tag{21}$$

The dimensionless mean flow rates Θ in the fixed frame and F in the wave frame are related through the following expression:

$$\Theta = F + \frac{1}{2}\left(1 + \frac{\phi^2}{2}\right) \tag{22}$$

4 Series Solution

Here we attempt to find the approximate solution to the boundary-value problem consisting of Eqs. (20) and (21) by employing the perturbation method for small Debroah numbers. For this purpose we expand the flow quantities in powers of the Debroah number Γ as follows:

$$\psi = \psi_0 + \Gamma\psi_1 + \cdots$$

$$p = p_0 + \Gamma p_1 + \cdots$$

$$F = F_0 + \Gamma F_1 + \cdots \tag{23}$$

Invoking above equations into Eqs. (12), (20), and (21) and then equating the coefficients of like powers of Γ on both sides we have the following systems.

For the system of order zero,

$$\frac{\partial}{\partial r}\left[\frac{1}{r}\frac{\partial}{\partial r}\left\{r\frac{\partial}{\partial r}\left(\frac{1}{r}\frac{\partial \psi_0}{\partial r}\right)\right\}\right] = 0$$

$$-\frac{dp_0}{dz} + \frac{1}{r}\frac{\partial}{\partial r}\left\{r\frac{\partial}{\partial r}\left(\frac{1}{r}\frac{\partial \psi_0}{\partial r}\right)\right\} = 0 \tag{24}$$

$$\psi_0 = 0, \quad \frac{\partial}{\partial r}\left(\frac{1}{r}\frac{\partial \psi_0}{\partial r}\right) = 0 \quad \text{at} \quad r = 0$$

$$\psi = F_0, \quad \frac{1}{r}\frac{\partial \psi_0}{\partial r} = -\gamma\frac{\partial}{\partial r}\left(\frac{1}{r}\frac{\partial \psi_0}{\partial r}\right) - 1 \quad \text{at} \quad r = h \tag{25}$$

For the system of order one,

$$\frac{\partial}{\partial r}\left[\frac{1}{r}\frac{\partial}{\partial r}\left\{r\left(\frac{\partial}{\partial r}\left(\frac{1}{r}\frac{\partial \psi_1}{\partial r}\right) + 2\left(\frac{\partial}{\partial r}\left(\frac{1}{r}\frac{\partial \psi_0}{\partial r}\right)\right)^3\right)\right\}\right] = 0$$

$$-\frac{dp_1}{dz} + \frac{1}{r}\frac{\partial}{\partial r}\left\{r\left(\frac{\partial}{\partial r}\left(\frac{1}{r}\frac{\partial \psi_1}{\partial r}\right) + 2\left(\frac{\partial}{\partial r}\left(\frac{1}{r}\frac{\partial \psi_0}{\partial r}\right)\right)^3\right)\right\} = 0 \tag{26}$$

$$\psi_1 = 0, \quad \frac{\partial}{\partial r}\left(\frac{1}{r}\frac{\partial \psi_1}{\partial r}\right) = 0 \quad \text{at} \quad r = 0$$

$$\psi = F_1, \quad \frac{1}{r}\frac{\partial \psi_1}{\partial r} = -\gamma\left\{\frac{\partial}{\partial r}\left(\frac{1}{r}\frac{\partial \psi_1}{\partial r}\right) + 2\left(\frac{\partial}{\partial r}\left(\frac{1}{r}\frac{\partial \psi_0}{\partial r}\right)\right)^3\right\}$$

$$\text{at} \quad r = h \tag{27}$$

4.1 Zeroth-Order Solution. The stream function, axial velocity, and axial pressure gradient at this order are, respectively, given by

$$\psi_0 = \frac{h^2(h^2 + 2F_0)}{2(h^2 + 4\gamma h)}(L^2 - L^4) + F_0 L^2 \tag{28}$$

$$w_0 = \left(\frac{h^2 + 2F_0}{h^2 + 4\gamma h}\right)(1 - 2L^2) + 2\frac{F_0}{h^2} \tag{29}$$

$$\frac{dp_0}{dz} = -\frac{8(h^2 + 2F_0)}{h^4 + 4\gamma h^3} \tag{30}$$

where $L = r/h$. For $\gamma = 0$ the above results correspond to a Newtonian fluid [1,9,10].

At this order, the pressure rise per wavelength in dimensionless form is given as

$$\Delta P_0 = \int_0^{2\pi} \frac{dp_0}{dz} dz \tag{31}$$

4.2 First-Order Solution. Substituting Eq. (28) into Eq. (26) and solving the resulting equation subject to the boundary conditions (27) we obtain

$$\psi_1 = \left(\frac{dp_0}{dz}\right)^3 \frac{r^2 h^4}{96}\left[1 - L^4 + \frac{2L^2 h}{4\gamma + h} - \frac{2h}{4\gamma + h}\right] + F_1 L^2\left[-\frac{L^2 h}{4\gamma + h} + \frac{h}{4\gamma + h} + 1\right] \tag{32}$$

$$w_1 = \left(\frac{dp_0}{dz}\right)^3 \frac{h^4}{96}\left[-6L^4 + \frac{8L^2 h}{4\gamma + h} - \frac{4h}{4\gamma + h} + 2\right] + \frac{F_1}{h^2}\left[-\frac{4L^2 h}{4\gamma + h} + \frac{2h}{4\gamma + h} + 2\right] \tag{33}$$

$$\frac{dp_1}{dz} = -\frac{16F_1}{h^3(4\gamma + h)} + \left(\frac{dp_0}{dz}\right)^3 \frac{h^3}{3(4\gamma + h)} \tag{34}$$

The pressure rise over a wavelength is

$$\Delta P_1 = \int_0^{2\pi} \frac{dp_1}{dz} dz \tag{35}$$

The expressions of stream function and axial pressure gradient up to the first order may be written as

$$\psi = \frac{h^2(h^2 + 2F_0)}{2(h^2 + 4\gamma h)}(L^2 - L^4) + F_0 L^2 + \Gamma\left(\left(\frac{dp_0}{dz}\right)^3 \frac{r^2 h^4}{96} \times \left[1 - L^4 + \frac{2L^2 h}{4\gamma + h} - \frac{2h}{4\gamma + h}\right] + F_1 L^2\left[-\frac{L^2 h}{4\gamma + h} + \frac{h}{4\gamma + h} + 1\right]\right) \tag{36}$$

$$\frac{dp}{dz} = -\frac{8(h^2 + 2F_0)}{h^4 - 4\gamma h^3} + \Gamma\left(-\frac{16F_1}{h^3(4\gamma + h)} + \left(\frac{dp_0}{dz}\right)^3 \frac{h^3}{3(4\gamma + h)}\right) \tag{37}$$

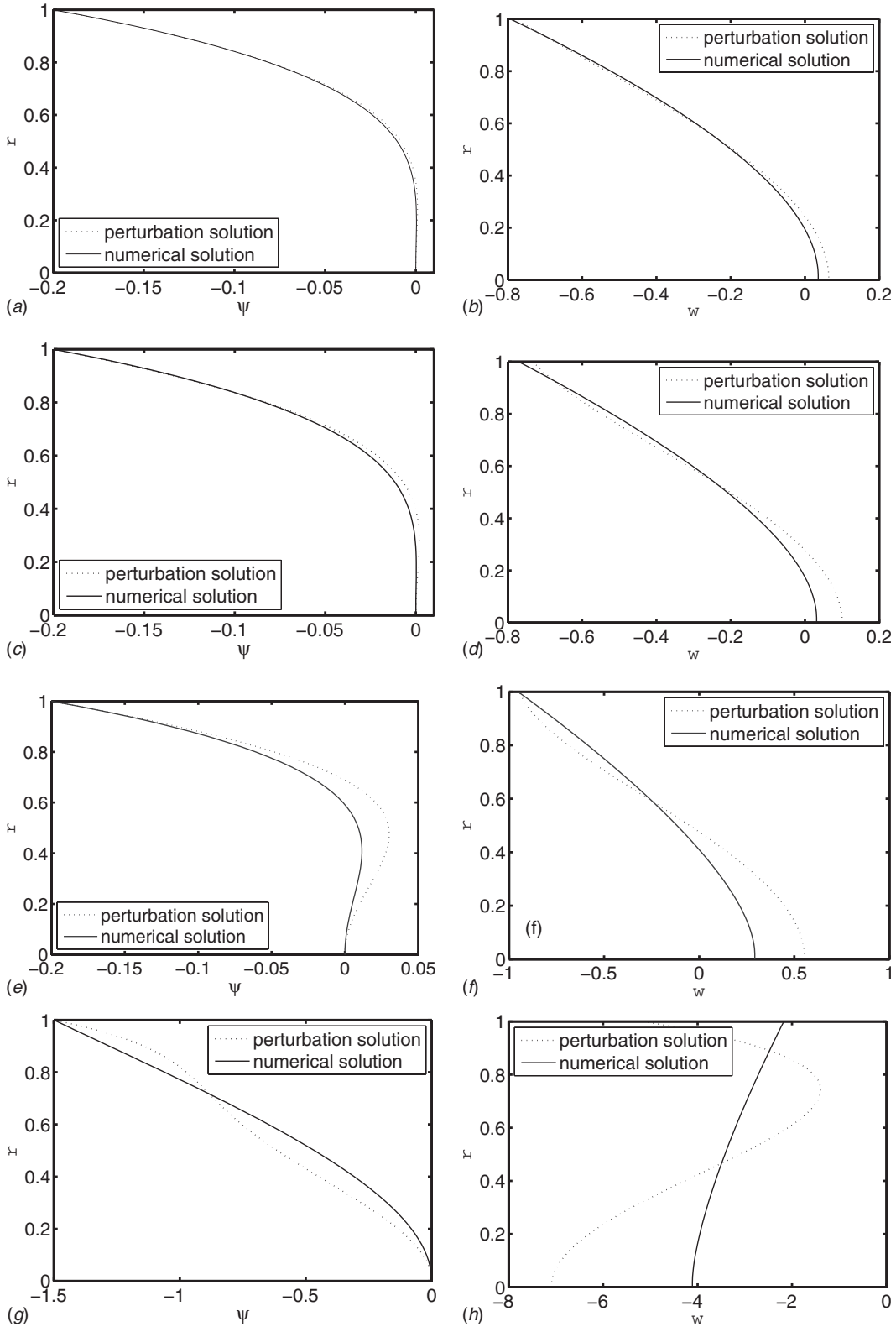

Fig. 1 Plot showing profiles for the stream function $\psi(r)$ (left panels) and axial velocity $w(r)$ (right panels) for different values of F and γ and Γ. Solid lines indicate the numerical solution while dotted lines indicate the perturbation solution of the problem. (*a*) and (*b*) correspond to $F=-0.2$, $\gamma=0.1$, and $\Gamma=0.1$; (*c*) and (*d*) correspond to $F=-0.2$, $\gamma=0.1$, and $\Gamma=0.2$; (*e*) and (*f*) correspond to $F=-0.2$, $\gamma=0.01$, and $\Gamma=0.2$; (*g*) and (*h*) correspond to $F=-1.5$, $\gamma=0.1$, and $\Gamma=0.2$. The other parameters chosen are $z=\pi/2$ and $a=0.2$.

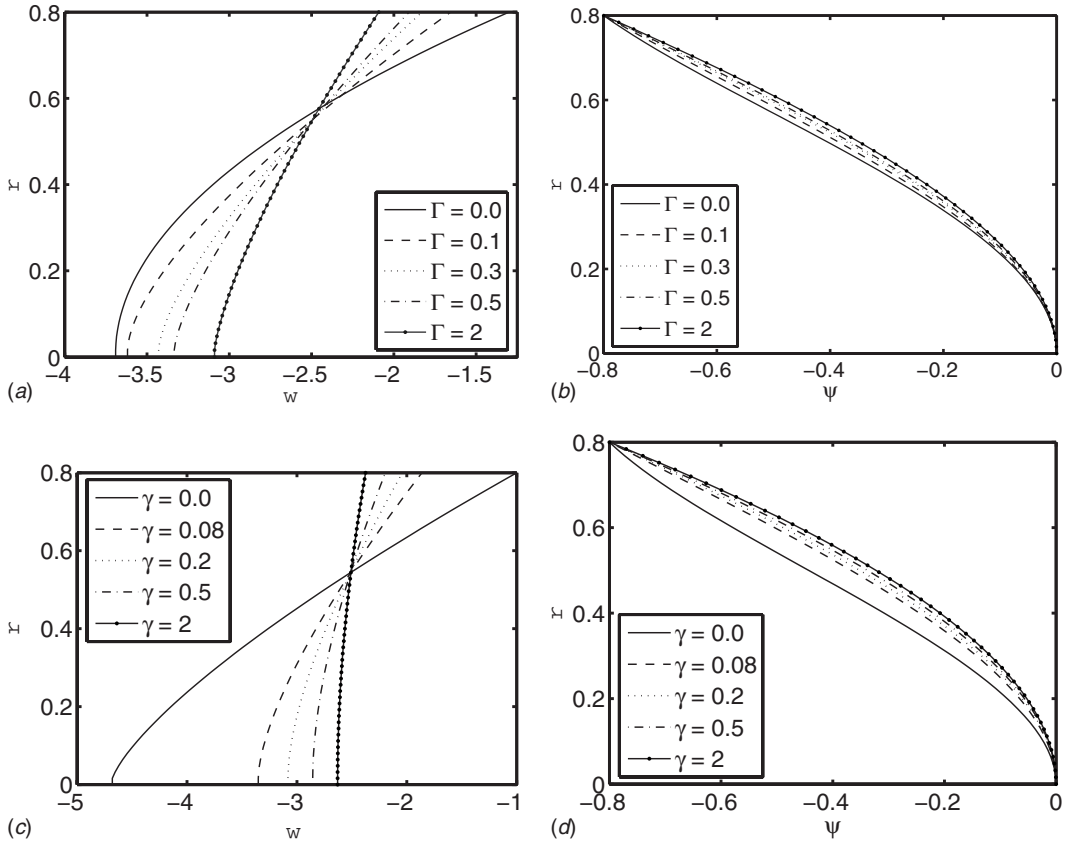

Fig. 2 Transverse profiles of axial velocity $w(r)$ (left panels) and stream function $\psi(r)$ (right panels) for different values of Γ (γ=0.05) ((*a*) and (*b*)) and γ (Γ=0.2) ((*c*) and (*d*)). The other parameters chosen are $z=-\pi$, $F=-0.8$, and $a=0.2$.

Defining $F=F_0+\Gamma F_1$ the expressions of stream function and axial pressure gradient can be expressed as

$$\psi=\frac{h^2(h^2+2F)}{2(h^2+4\gamma h)}(L^2-L^4)+FL^2+\Gamma\left(\frac{r^2h^4}{96}\left(-\frac{8(h^2+2F)}{h^4+4\gamma h^3}\right)^3\times\left[1-L^4+\frac{2L^2h}{4\gamma+h}-\frac{2h}{4\gamma+h}\right]\right) \tag{38}$$

$$\frac{dp}{dz}=-\frac{8(h^2+2F)}{h^4+4\gamma h^3}+\Gamma\left(-\frac{8(h^2+2F)}{h^4+4\gamma h^3}\right)^3\frac{h^3}{3(4\gamma+h)} \tag{39}$$

5 Numerical Method

In this section we intend to find the direct numerical solution of the differential equation (21) and the boundary conditions (20) by means of a suitable numerical technique. Because the differential equation (21) is nonlinear in ψ, we cannot solve this boundary-value problem by the direct finite-difference method. In solving such nonlinear equations, iterative methods are commonly used. We can now construct an iterative procedure in the form

$$\frac{\partial}{\partial r}\left[\frac{1}{r}\frac{\partial}{\partial r}\left\{r\left(\frac{\partial}{\partial r}\left(\frac{1}{r}\frac{\partial\psi^{(n+1)}}{\partial r}\right)+2\Gamma\left(\frac{\partial}{\partial r}\left(\frac{1}{r}\frac{\partial\psi^{(n)}}{\partial r}\right)\right)^3\right)\right\}\right]=0 \tag{40}$$

$$\psi^{(n+1)}=0,\quad \frac{\partial}{\partial r}\left(\frac{1}{r}\frac{\partial\psi^{(n+1)}}{\partial r}\right)=0,\quad \text{at}\quad r=0$$

$$\psi^{(n+1)}=F,\quad \frac{1}{r}\frac{\partial\psi^{(n+1)}}{\partial r}=-\gamma\left[\frac{\partial}{\partial r}\left(\frac{1}{r}\frac{\partial\psi^{(n+1)}}{\partial r}\right)+2\Gamma\left(\frac{\partial}{\partial r}\left(\frac{1}{r}\frac{\partial\psi^{(n)}}{\partial r}\right)\right)^3\right]-1,\quad \text{at}\quad r=h \tag{41}$$

where the index (n) indicates the iterative step. It is easy to confirm that if the indices (n) and $(n+1)$ are withdrawn, Eqs. (40) and (41) are consistent with the original differential equation (21) and the boundary conditions (20). Equation (40) and the boundary conditions (41) define a linear differential boundary-value problem for $\psi^{(n+1)}$. By means of the finite-difference method a linear algebraic system can be deduced and solved for each iterative step $(n+1)$. Therefore, a sequence of functions $\psi^{(0)}(r,z)$, $\psi^{(1)}(r,z)$, and $\psi^{(2)}(r,z),\ldots$ is determined in the following manner: if an initial estimated $\psi^{(0)}(r,z)$ is given, then $\psi^{(1)}(r,z)$ and $\psi^{(2)}(r,z),\ldots$ are calculated successively as the solutions of the boundary-value problem consisting of Eqs. (20) and (21). Unfortunately, such an iteration is often divergent, especially when the initial estimated $\psi^{(0)}(r,z)$ is not given carefully and suitably. Usually, in order to achieve a better convergence, the so-called method of successive under-relaxation is used. We solve the boundary-value problem (40) and (41) for the iterative step $(n+1)$ to obtain an estimated value of $\psi^{(n+1)}$: $\tilde{\psi}^{(n+1)}$, then $\psi^{(n+1)}$ is defined by the formula

$$\psi^{(n+1)}=\psi^{(n)}+\tau(\tilde{\psi}^{(n+1)}-\psi^{(n)}),\quad \tau\in(0,1] \tag{42}$$

where τ is an under-relaxation parameter. We should choose a small τ so that convergent iteration is reached. In our simulations we choose an initial guess of $\psi^{(0)}(r,z)=\psi_0$, i.e., the zeroth order perturbation solution in Eq. (28), which fulfills the first, second,

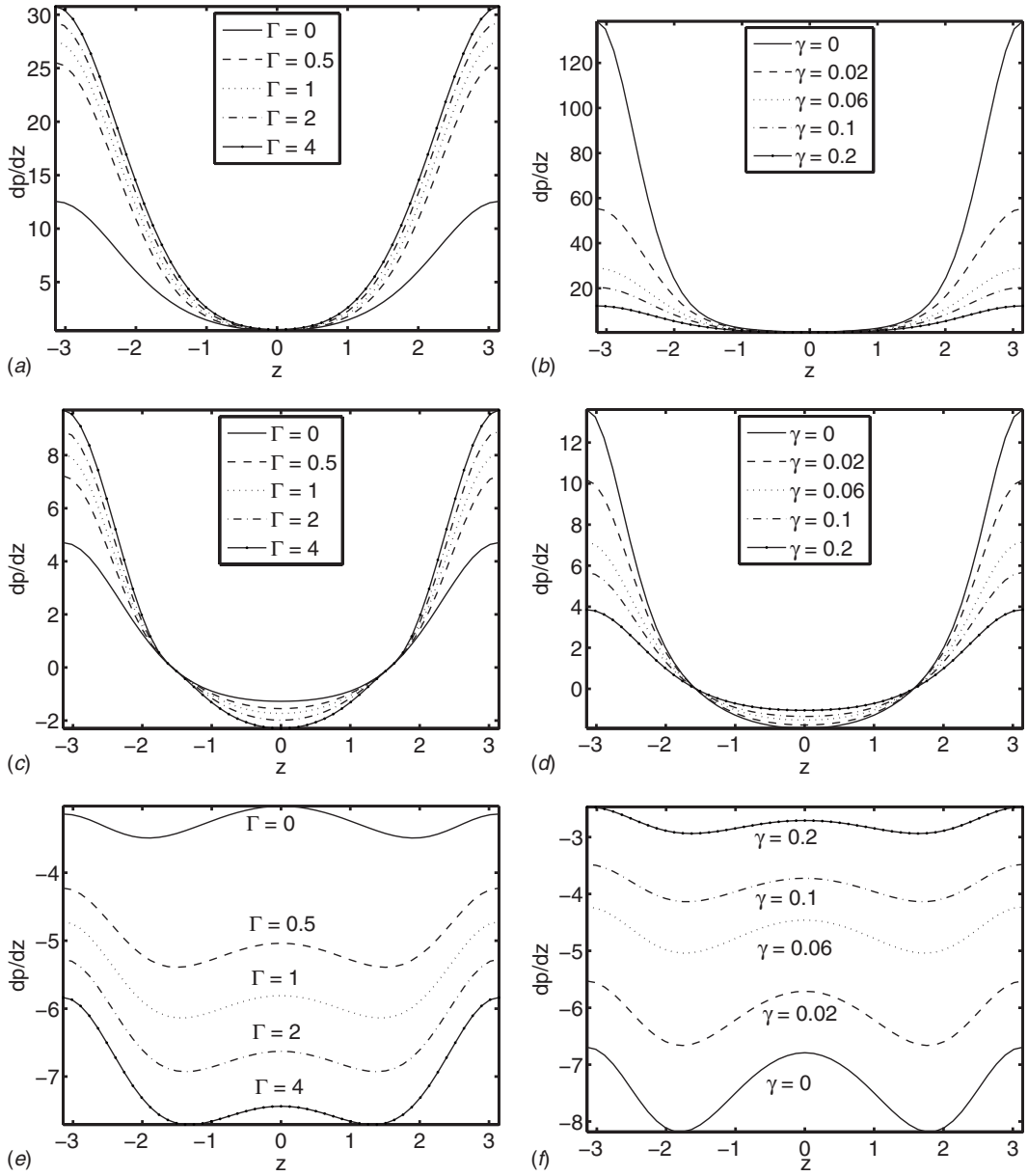

Fig. 3 Axial distribution of axial pressure gradient dp/dz within a wavelength $z \in [-\pi, \pi]$ for various values of Γ (γ=0.1) (left panels) and γ (Γ=0.1) (right panels) for three flow rates F=−0.8(Θ=−0.29) ((*a*) and (*b*)), F=−0.5(Θ=0.01) ((*c*) and (*d*)), and F=−0.2(Θ=0.31) ((*e*) and (*f*)). The value of ϕ is chosen to be equal to 0.2.

and third boundary conditions in Eq. (41). Of course, some other choices are also possible. The iteration should be carried out until the relative differences of the computed $\psi^{(n+1)}$ and $\psi^{(n)}$ between two iterative steps are smaller than a given error chosen to be 10^{-8}.

6 Results and Discussion

This section is divided into four subsections. In Sec. 6.1, we give the comparison of perturbation and numerical solutions. The flow characteristics are discussed in the Sec. 6.2. In Sec. 6.3 the effects of various parameters on the pumping characteristics are investigated. The trapping phenomenon is illustrated in Sec. 6.4.

6.1 Comparison of Numerical and Perturbation Solutions. A comparison of the perturbation and numerical solutions is presented in Fig. 1. It is observed from this figure that a good agreement between both solutions is highly dependent on the parameters Γ, γ, and F. Comparison of Figs. 1(*a*) and 1(*b*) with Figs. 1(*c*) and 1(*d*) shows that with an increase in Γ, the deviation of the perturbation solution from the numerical solution increases. As anticipated for large values of Γ the perturbation solution is no longer valid. Even for same values of Γ the validity of the perturbation solution is also dependent on the values of F and γ. With the decrease in the slip parameter γ, the deviation of the perturbation solution from the numerical solution increases, which is obvious by comparing Figs. 1(*c*) and 1(*d*) with Figs. 1(*e*) and 1(*f*). Similarly by increasing the magnitude of flux F the perturbation solution diverges from the numerical solution (Figs. 1(*e*) and 1(*f*)). That is because in the perturbation solution, the magnitude of the neglected high-order terms is dependent on these parameters. However, when γ is small or F is large, the perturbation solution can be made closer to the numerical solution by suitably choosing

the value of Γ. Test computations show that for $F \in [-1.5, 1.5]$ and $\gamma \in [0, 0.5]$, an acceptable perturbation solution can be obtained by taking $\Gamma \in [0.0001, 0.2]$.

6.2 Flow Characteristics. In this subsection the effects of non-Newtonian and slip parameters on the velocity and stream functions are discussed. For this purpose only the solutions obtained by the iterative method are illustrated. The results for various values of the non-Newtonian and slip parameters on the transverse profiles of the axial velocity and stream function for the cross section $z=-\pi$ are presented in Fig. 2 for a fixed value of the flux F. Note that for $z=-\pi$ the tube radius, in fact, becomes 0.8. From Fig. 2(*a*) we can observe that an increase in the non-Newtonian parameter Γ causes an increase in the magnitude of the velocity at the tube wall and a decrease near the center of the tube, i.e., with the increase in Γ, the radial distribution of the axial velocity becomes much flatter. It means that the transverse profile of the velocity for a third grade fluid is much flatter than that for a Newtonian fluid. This effect indicates that for large values of Γ the shear thickening effects of the third grade fluid are pronounced and the velocity profile tends to linear over a fixed cross section. The effects of varying slip parameters γ on the velocity profile can be seen in Fig. 2(*c*). By increasing the slip parameter γ the velocity increases near the wall of the tube and decreases near the center of the channel; the velocity distribution becomes flatter. It is also interesting to note that for large values of the slip parameter the flow velocity is almost uniform across the cross section. For this case, the flow caused by the peristaltic wall is negligibly small due to the near free-slip condition and the flow is driven mainly by the pressure gradient. To get an impression on the distribution of the stream function the corresponding profiles of the stream function are displayed in Figs. 2(*b*) and 2(*d*).

6.3 Pumping Characteristics. The variations of the axial pressure gradient dp/dz over one wavelength for different values of Γ and γ with three different flux rates F are shown in Fig. 3. It is revealed that for $F=-0.8(\Theta=-0.29)$ in Figs. 3(*a*) and 3(*b*), dp/dz is positive over the whole wavelength, i.e., the pressure gradient is a resistance to the flow driven by the peristalsis. For $\Theta=0.01$ Figs. 3(*c*) and 3(*d*), dp/dz resists the flow in the narrow part of the tube (near $z=\pm\pi$) while it assists the flow in the wider part (near $z=0$). Furthermore, it is observed that for larger values of the mean flow rate $\Theta=0.31$ (Figs. 3(*e*) and 3(*f*)), dp/dz is negative over the whole wavelength, i.e., it assists the flow in both the wide and narrow parts of the tube. From Figs. 3(*a*), 3(*c*), and 3(*e*) it is noted that with the increase in Γ, the pressure gradient increases. This is due to an increase in the fluid viscosity. From Figs. 3(*b*), 3(*d*), and 3(*f*) we note that an increase in the slip parameter decreases the magnitude of dp/dz for all three values of the mean flow rate Θ. The reason is that increasing the slip near the walls will decrease the wall resistance to the flow, hence a smaller pressure gradient is needed to maintain a given flux rate.

A characteristic feature of peristalsis is pumping against the pressure rise. To discuss this feature we have plotted the pressure rise per wavelength Δp with respect to the mean flow rate Θ for different values of Γ (Fig. 4(*a*)) and γ (Fig. 4(*b*)) in Fig. 4. The maximum pressure rise against, which the peristalsis works as a pump, i.e., Δp for $\Theta=0$, is denoted by P_0. When $\Delta p > P_0$, then the flux is negative, i.e., against the peristaltic direction. The value of Θ corresponding to $\Delta p=0$ (which is known as free pumping) is denoted by Θ_0. When $\Delta p<0$, the pressure assists the flow and this is known as copumping. Figure 4(*a*) indicates that P_0 increases by increasing Γ. This means that peristalsis has to work against a greater pressure rise for the third grade fluid when compared with the Newtonian fluid. For a fixed $\Delta p>0$, the peristaltic pumping rate increases for the third grade fluid in comparison with the Newtonian fluid. Furthermore, in the case of free pumping there is no obvious difference between the Newtonian and the third grade fluids. However, in the case of copumping ($\Delta p<0$) a larger pressure propulsion is needed to maintain a given flux rate for a third grade fluid when compared with the Newtonian fluid. From Fig. 4(*b*) we observe that P_0 decreases by increasing γ. This means that the fluid slippage at the wall reduces the maximum pressure against which the peristalsis works as a pump. The peristaltic pumping rate (for the fixed $\Delta p>0$) decreases by increasing γ. However, the flow rate in copumping (for the fixed $\Delta p<0$) increases by increasing γ.

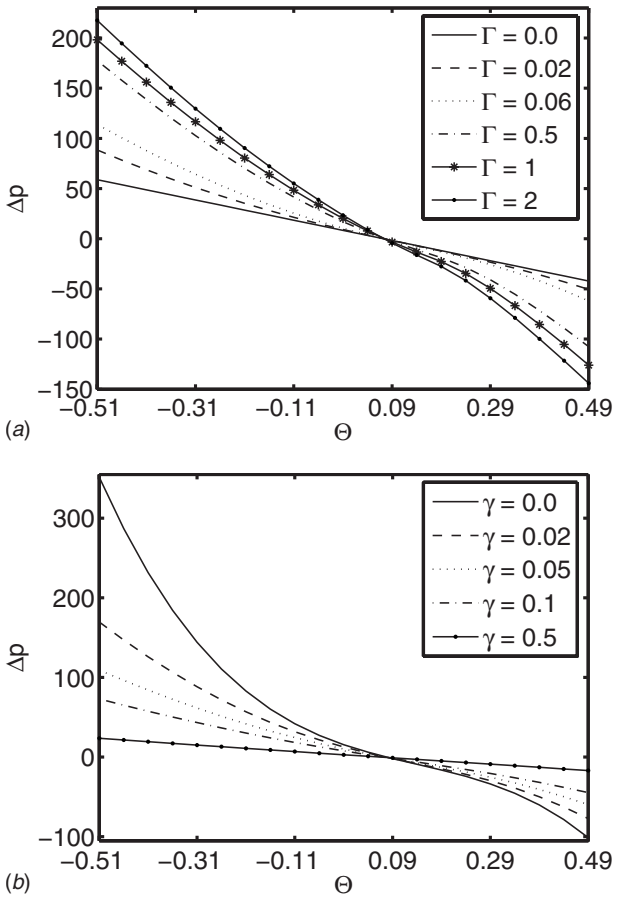

Fig. 4 Pressure rise per wavelength Δp versus flow rate Θ for various values of Γ ($\gamma=0.05$) (*a*) and γ ($\Gamma=0.05$) (*b*). Here ϕ is chosen to be equal to 0.2.

6.4 Trapping. In general the shape of streamlines is similar to that of the boundary wall in the wave frame. However under certain conditions some of the streamlines split and enclose a bolus, which moves as a whole with the wave. This phenomenon is known as trapping. We note that the trapping phenomenon is largely dependent on Θ [27]. For various values of Θ one may decide that either the trapping occurs or not. Moreover, one can easily find such values of Θ for which trapping occurs near the boundary, centerline, or nowhere. We have chosen a value of Θ in which the fluid near the center is trapped. To discuss the effects of Γ and γ on the trapping, we have plotted Figs. 5 and 6, respectively. In both figures the streamline with value $\psi=0$ is identified by a dotted line. The streamlines below or inside this streamline have positive values. The topmost streamline corresponds to $\psi=F=-0.2$. All the rest of the streamlines correspond to values of stream function between 0 and −0.2. Figure 5 shows that increasing Γ, on one hand, increases the size of the bolus, and on the other hand, also increases the circulation of the bolus. For large values of Γ, the change in the bolus size and circulation is almost no longer visible. The effects of γ on trapping can be seen in Fig. 6. It is interesting to note that the trapping exists for only small

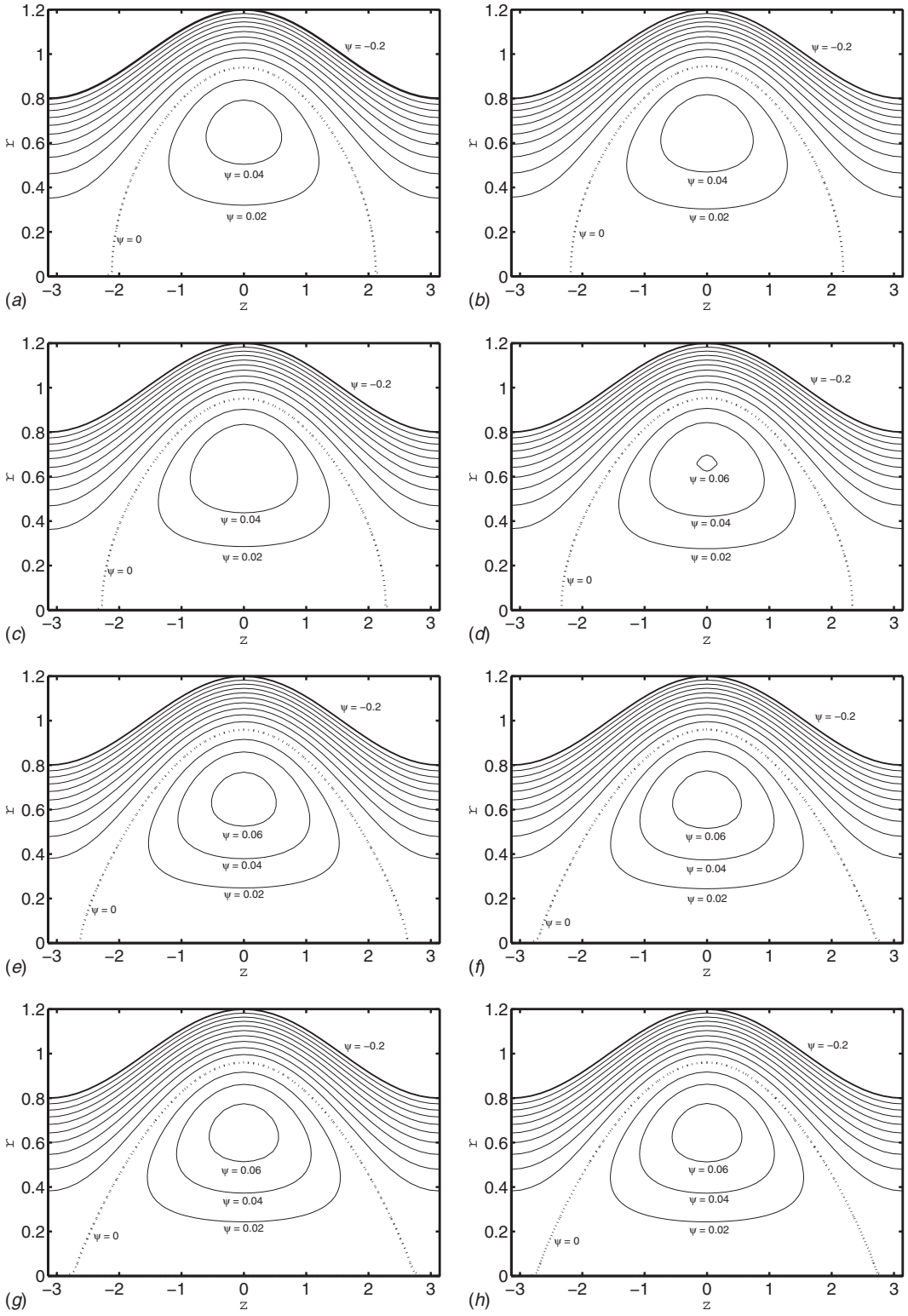

Fig. 5 Streamlines for different values of Γ. (*a*)–(*h*) correspond to the values of Γ =(0,0.02,0.06,0.1,1,5,10,20), respectively. The other parameters chosen are γ=0.0, ϕ=0.2, and Θ =0.31.

values of the slip parameter [27]. The size of the trapped bolus decreases with an increase in γ and finally the bolus vanishes for large values of γ.

7 Concluding Remarks

We have analyzed the problem of peristaltic transport of a third grade fluid in a circular cylindrical tube under the influence of a slip condition near the tube wall. Both the perturbation and numerical solutions were developed. The validity of the perturbation analytic solution is explicitly highlighted and a comparison is made with the numerical solution. It is seen that the perturbation solution can provide a good approximation for small perturbation parameters. In this investigation, the flow features, pumping characteristics, and trapping phenomenon are studied for various val-

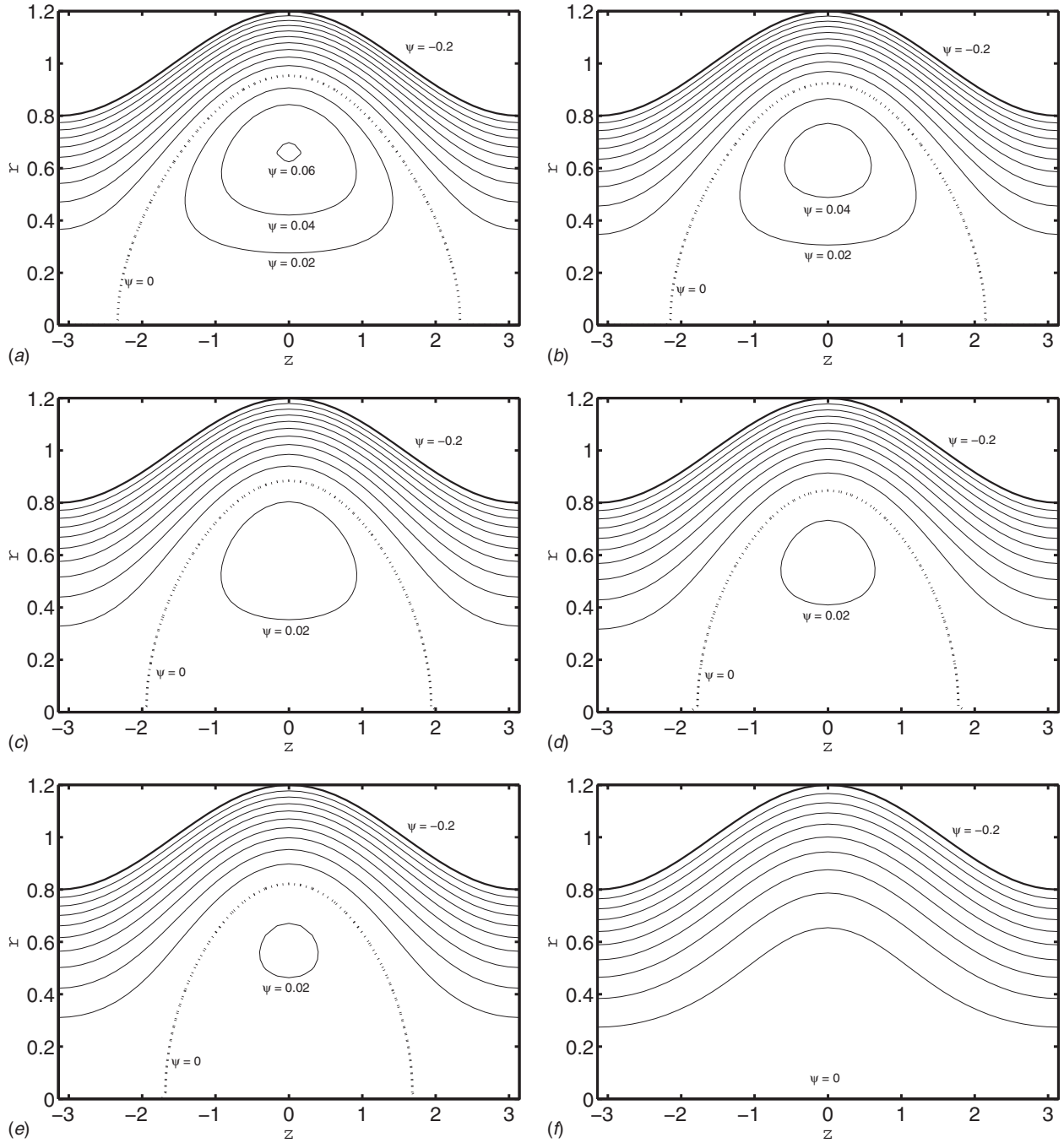

Fig. 6 Streamlines for different values of γ. (*a*)–(*f*) correspond to the values of $\gamma=(0,0.02,0.05,0.08,0.1,0.5)$, respectively. The other parameter chosen are $\Gamma=0.1$, $\phi=0.2$, and $\Theta=0.31$.

ues of non-Newtonian and slip parameters. From the presented analysis it is concluded that a third grade fluid peristalsis has to work against a greater pressure rise as compared with a Newtonian fluid. However, the slip at the wall considerably reduces the pressure rise per wavelength in the pumping region. The size and circulation of the trapped bolus increase when going from a Newtonian to a third grade fluid. Furthermore an increase in the slip parameter reduces the size of trapped bolus, and the bolus may vanish when the slip at the peristaltic wall is especially large. The corresponding results in absence of slip can be deduced by choosing $\gamma=0$. The presented analysis has importance in applications of the MEMS. Microchannels built in the MEMS, however, are easily subjected to environment noises, such as oscillations or vibrations and externally excited traveling waves. For flexible walls the last one normally corresponds to the peristaltic transport [28]. In bio-MEMS applications the investigators found interesting behavior due to nonlinear coupling between the surface wave and slip velocity when the Knudsen number K_n in the slip flow regime is $0.001 \leq K_n \leq 0.1$.

Acknowledgment

The first author is grateful to the Higher Education Commission of Pakistan for the financial support to conduct this research under the international research support initiative program. We are further grateful to the reviewers for their constructive comments and invaluable suggestions regarding an earlier version of this paper.

Nomenclature

$\overline{\mathbf{V}}$ = velocity vector
$\overline{\mathbf{T}}$ = Cauchy stress tensor
$\overline{\mathbf{S}}$ = extra stress tensor
$\overline{\mathbf{I}}$ = identity tensor
$\overline{\mathbf{A}}_1$ = first Rivilin–Ericksen tensor
$\mathbf{A}_n$ = Rivilin–Ericksen tensors for $n>1$
ρ = density
$\bar{p}$ = dimensional pressure
μ = dynamic viscosity
$\alpha_1, \alpha_2, \beta$ = material constants of the third grade fluid
$\bar{t}$ = dimensional time
$\bar{R}, \bar{Z}$ = radial and axial coordinates in fixed frame
$\bar{U}, \bar{W}$ = radial and axial velocities in fixed frame
$\bar{h}$ = radius of the tube in fixed frame
a = radius of the undisturbed tube
λ = wavelength of the wave
c = speed of the wave
b = amplitude of the wave
$\bar{r}, \bar{z}$ = radial and axial coordinates in wave frame
$\bar{u}, \bar{w}$ = radial and axial velocities in wave frame
r, z = dimensionless radial and axial coordinates in wave frame
u, w = dimensionless radial and axial velocities in wave frame
ψ = dimensionless stream function
p = dimensionless pressure
$\mathbf{S}$ = dimensionless extra stress tensor
t = dimensionless time
h = dimensionless radius of the tube in wave frame
Γ = Debroah number
ξ = dimensional slip parameter
γ = dimensionless slip parameter
ϕ = amplitude ratio
δ = wave number
$\bar{Q}$ = dimensional volume flow rate in fixed frame
$\bar{q}$ = dimensional volume flow rate in wave frame
Θ = dimensionless mean flow rate in fixed frame
F = dimensionless mean flow rate in wave frame
dp/dz = axial pressure gradient
ΔP = pressure rise per wavelength
τ = under-relaxation parameter

References

[1] Shapiro, A. H., Jaffrin, M. Y., and Weinberg, S. L., 1969, "Peristaltic Pumping With Long Wavelength at Low Reynolds Number," J. Fluid Mech., **37**, pp. 799–825.
[2] Fung, Y. C., and Yih, C. S., 1968, "Peristaltic Transport," ASME J. Appl. Mech., **33**, pp. 669–675.
[3] Mekheimer, Kh. S., 2002, "Peristaltic Transport of a Couple-Stress Fluid in Uniform and Non-Uniform Channels," Biorheology, **39**, pp. 755–765.
[4] El Shehawey, E. F., and Mekheimer, Kh. S., 1994, "Couple-Stresses in Peristaltic Transport of Fluids," J. Phys. D, **27**, pp. 1163–1170.
[5] Mekheimer, Kh. S., El-Shehawey, E. F., and Alaw, A. M., 1998, "Peristaltic Motion of a Particle Fluid Suspension in a Planar Channel," Int. J. Theor. Phys., **37**, pp. 2895–2920.
[6] Haroun, M. H., 2007, "Non-Linear Peristaltic Flow of a Fourth Grade Fluid in an Inclined Asymmetric Channel," Comput. Mater. Sci., **39**, pp. 324–333.
[7] Haroun, M. H., 2007, "Effect of Deborah Number and Phase Difference on Peristaltic Transport of a Third-Order Fluid in an Asymmetric Channel," Commun. Nonlinear Sci. Numer. Simul., **12**(8), pp. 1464–1480.
[8] El-Shahed, M., and Haroun, M. H., 2003, "Peristaltic Transport of Johnson–Segalman Fluid Under Effect of a Magnetic Field," Math. Probl. Eng., **6**, pp. 663–677.
[9] Siddiqui, A. M., and Schwarz, W. H., 1994, "Peristaltic Flow of a Second Order Fluid in Tubes," J. Non-Newtonian Fluid Mech., **53**, pp. 257–284.
[10] Hayat, T., Wang, Y., Siddiqui, A. M., Hutter, K., and Asghar, S., 2002, "Peristaltic Transport of a Third Order Fluid in a Circular Cylindrical Tube," Math. Models Meth. Appl. Sci., **12**, pp. 1691–1706.
[11] Hayat, T., Wang, Y., Hutter, K., Asghar, S., and Siddiqui, A. M., 2004, "Peristaltic Transport of an Oldroyd-B Fluid in a Planar Channel," Math. Probl. Eng., **2004**, pp. 347–376.
[12] Hayat, T., Mahomed, F. M., and Asghar, S., 2005, "Peristaltic Flow of Magnetohydrodynamic Johnson–Segalman Fluid," Nonlinear Dyn., **40**, pp. 375–385.
[13] Hayat, T., and Ali, N., 2006, "On Mechanism of Peristaltic Flows for Power-Law Fluids," Physica A, **371**, pp. 188–194.
[14] Hayat, T., and Ali, N., 2006, "Peristaltically Induced Motion of a MHD Third Grade Fluid in a Deformable Tube," Physica A, **370**, pp. 225–239.
[15] Hayat, T., Khan, M., Asghar, S., and Siddiqui, A. M., 2006, "A Mathematical Model of Peristalsis in Tubes Through a Porous Medium," J. Porous Media, **9**, pp. 55–67.
[16] Hayat, T., and Ali, N., 2007, "A Mathematical Description of Peristaltic Hydromagnetic Flow in a Tube," Appl. Math. Comput., **188**, pp. 1491–1502.
[17] Wang, Y., Hayat, T., and Hutter, K., 2007, "Peristaltic Flow of a Johnson–Segalman Fluid Through a Deformable Tube," Theor. Comput. Fluid Dyn., **21**, pp. 369–380.
[18] Beavers, G. S., and Joseph, D. D., 1967, "Boundary Condition at a Naturally Permeable Wall," J. Fluid Mech., **30**, pp. 197–207.
[19] Tretheway, D. C., and Meinhart, C. D., 2002, "Apparent Fluid Slip at Hydrophobic Microchannel Walls," Phys. Fluids, **14**, pp. L9–L12.
[20] Kwang-Hua Chu, W., and Fang, J., 2000, "Peristaltic Transport in a Slip Flow," Eur. Phys. J. B, **16**, pp. 543–547.
[21] Georgiou, G. C., and Crochet, M. J., 1994, "Compressible Viscous Flow in Slits With Slip at the Wall," J. Rheol., **38**, pp. 639–654.
[22] Rao, I. J., and Rajagopal, K. R., 1999, "The Effect of Slip Boundary Conditions on the Flow of Fluids in a Channel," Acta Mech., **135**, pp. 113–126.
[23] Kwang-Hua Chu, W., 1996, "Stokes Slip Flow Between Corrugated Walls," ZAMP, **47**, pp. 591–598.
[24] Chu, K.-H. W., 1999, "Small Knudsen Number Flow in a Corrugated Tube," Meccanica, **34**, pp. 133–137.
[25] El-Shehawy, E. F., El-Dabe, N. T., and El-Desoky, I. M., 2006, "Slip Effects on the Peristaltic Flow of a Non-Newtonian Maxwellian Fluid," Acta Mech., **186**, pp. 141–159.
[26] Fosdick, R. L., and Rajagopal, K. R., 1980, "Thermodynamics and Stability of Fluids of Third Grade," Proc. R. Soc. London, Ser. A, **339**, pp. 351–377.
[27] Wang, Y., Hayat, T., Ali, N., and Oberlack, M., 2008, "Magnetohydrodynamic Peristaltic Motion of a Sisko Fluid in a Symmetric or Asymmetric Channel," Physica A, **387**, pp. 347–362.
[28] Kwang-Hua Chu, W., and Fang, J., 2000, "On Peristaltic Transport in Small-Knudsen-Number Flow," Meccanica, **35**, pp. 69–74.

Comparisons of Probabilistic and Two Nonprobabilistic Methods for Uncertain Imperfection Sensitivity of a Column on a Nonlinear Mixed Quadratic-Cubic Foundation

Xiaojun Wang
Institute of Solid Mechanics,
Beijing University of Aeronautics and Astronautics,
Beijing 100083, P.R.C.
e-mail: xjwang@buaa.edu.cn

Isaac Elishakoff
Department of Mechanical Engineering,
Florida Atlantic University,
Boca Raton, FL 33431-0991
e-mail: elishako@fau.edu

Zhiping Qiu
e-mail: zpqiu@buaa.edu.cn

Lihong Ma
e-mail: lhma@ase.buaa.edu.cn

Institute of Solid Mechanics,
Beijing University of Aeronautics and Astronautics,
Beijing 100083, P.R.C.

Two nonprobabilistic set-theoretical treatments of the initial imperfection sensitive structure—a finite column on a nonlinear mixed quadratic-cubic elastic foundation—are presented. The minimum buckling load is determined as a function of the parameters, which describe the range of possible initial imperfection profiles of the column. The two set-theoretical models are "interval analysis" and "convex modeling." The first model represents the range of variation of the most significant N Fourier coefficients by a hypercuboid set. In the second model, the uncertainty in the initial imperfection profile is expressed by an ellipsoidal set in N-dimensional Euclidean space. The minimum buckling load is then evaluated in both the hypercuboid and the ellipsoid. A comparison between these methods and the probabilistic method are performed, where the probabilistic results at different reliability levels are taken as the benchmarks of accuracy for judgment. It is demonstrated that a nonprobabilistic model of uncertainty may be an alternative method for buckling analysis of a column on a nonlinear mixed quadratic-cubic elastic foundation under limited information on initial imperfection. [DOI: 10.1115/1.2998763]

Keywords: uncertain initial imperfection, nonlinear buckling, interval analysis, convex modeling, probabilistic method

1 Introduction

A central difficulty in most deterministic buckling analyses of imperfection sensitive structures is the choice of an appropriate imperfection form, as it is conditional on prior knowledge of both the shape and magnitude of the initial deviation—both of which vary widely from case to case—seeing that they derive from an arbitrary manufacturing process, itself subject (by its very nature) to a large number of uncertain variables. Moreover, the state of perfection (or imperfection) of the structure is governed during its useful lifetime by a variety of external influences, which are more or less uncertain. It is thus obvious that to be practicable, the analysis of the buckling theories should be combined with uncertainty analysis of the imperfection.

A probabilistic approach was first suggested in a study of imperfect-sensitive structures by Bolotin [1], who recognized that the initial geometric imperfections were uncertain quantities that a rigorous solution could be obtained in statistical terms. His work was followed by a number of analyses [2–5]. On the other hand, it was recognized in the recent decades that the probabilistic model is not the only one that can be used to describe the uncertainty and that uncertainty is not tantamount to randomness.

Nonprobabilistic set-theoretic models consist mostly of interval analysis and convex modeling, where only the bounds on the uncertain initial imperfection are needed. Ben-Haim and Elishakoff [6] employed two classes of nonprobabilistic convex models to determine the minimum buckling load of shells with general imperfection and gave a theoretical estimate of the knockdown factor. Lindberg [7,8] obtained the convex and probabilistic solutions for the multimode dynamic buckling of cylindrical shells with uncertain imperfections under symmetric radial impulsive loads. Elseifi et al. [9] adopted a convex modeling of uncertainties in the imperfection to predict the buckling load of a thin-walled stiffened composite. Qiu and Wang [10] compared convex modeling and interval analysis for the buckling failure measures of bars with uncertain-but-bounded initial imperfection from mathematical proof and numerical calculation.

This study is a generalization of earlier works of Elishakoff et al. [11] and Qui et al. [12], where buckling of a column on a purely cubic foundation was considered. Here, the buckling load of a finite column on a nonlinear mixed quadratic-cubic elastic foundation for the worst possible imperfection shape within hypercuboid bounds and ellipsoidal bounds are calculated first; then they are compared with the probabilistic buckling load from random imperfection of comparable measure.

2 Deterministic Buckling Analysis of a Column on a Nonlinear Mixed Quadratic-Cubic Foundation

Consider the system, as shown in Fig. 1, and the governing equation is

$$EI\frac{d^4w}{dx^4} + P\frac{d^2(w+\bar{w})}{dx^2} + k_1w - k_2w^2 - k_3w^3 = 0 \tag{1}$$

where EI is the bending rigidity; $\bar{w}$ is the initial imperfection function; w is the additional deflection due to the axial load P; k_1, k_2, and k_3 are positive constants, representing the linear and non-

Contributed by the Applied Mechanics Division of ASME for publication in the JOURNAL OF APPLIED MECHANICS. Manuscript received January 10, 2008; final manuscript received June 20, 2008; published online October 31, 2008. Review conducted by Edmundo Corona.

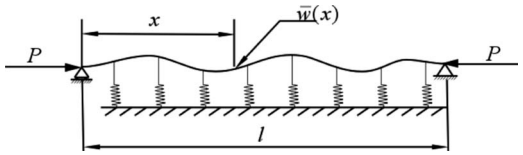

Fig. 1 A column on a nonlinear mixed quadratic-cubic elastic foundation

linear spring constants of the foundation, respectively; and x is the axial coordinate.

The column is simply supported, so that the boundary conditions are

$$w = \frac{d^2w}{dx^2} = 0 \quad \text{at} \quad x = 0 \quad \text{and} \quad x = l \tag{2}$$

where l is the length of the column.

Equation (1) can be modified by introducing dimensionless independent and dependent variables in the form

$$\eta = \frac{x}{l}, \quad u = \frac{w}{\Delta}, \quad \bar{u} = \frac{\bar{w}}{\Delta}, \quad \alpha = \frac{P}{P_{\text{cl}}}, \quad P_{\text{cl}} = \frac{EI}{l^2}\left(\pi^2 m_*^2 + \frac{k_1 l^4}{EI\pi^2 m_*^2}\right)$$

$$\chi_1 = \frac{k_1 l^4}{EI}, \quad \chi_2 = \frac{k_2 \Delta l^4}{EI}, \quad \chi_3 = \frac{k_3 \Delta^2 l^4}{EI}, \quad \gamma(\chi_1) = m_*^2\pi^2 + \frac{\chi_1}{m_*^2\pi^2} \tag{3}$$

where Δ is the radius of gyration of the cross section, and P_{cl} is the classical buckling load of a column on a linear elastic foundation. Equations (1) and (2) then become

$$\frac{d^4u}{d\eta^4} + \alpha\gamma(\chi_1)\frac{d^2u}{d\eta^2} + \chi_1 u - \chi_2 u^2 - \chi_3 u^3 = -\alpha\gamma(\chi_1)\frac{d^2\bar{u}}{d\eta^2} \tag{4}$$

$$u = \frac{d^2u}{d\eta^2} = 0 \quad \text{at} \quad \eta = 0 \quad \text{and} \quad \eta = 1 \tag{5}$$

Resorting to Galerkin's method, we expand $\bar{u}(\eta)$ and $u(\eta)$ in series in terms of the modes of stability loss of associated linear structure

$$\bar{u}(\eta) = \sum_{k=1}^{\infty} \bar{\xi}_k \sin k\pi\eta \tag{6}$$

and

$$u(\eta) = \sum_{k=1}^{\infty} \xi_k \sin k\pi\eta \tag{7}$$

Substituting them in Eq. (4), multiplying the resulting equation by $\sin(m\pi\eta)$, and integrating, we arrive at the following infinite set of coupled nonlinear algebraic equations for ξ_m:

$$\alpha_m\xi_m - \alpha(\xi_m + \bar{\xi}_m) - s_1\left(\frac{m_*}{m}\right)^2 J_m - \left(\frac{s_2}{8}\right)\left(\frac{m_*}{m}\right)^2 I_m = 0,$$

$$m = 1,2,\ldots \tag{8}$$

where

$$J_m = \sum_{p=1}^{\infty}\sum_{q=1}^{\infty} B_{pqm}\xi_p\xi_q, \quad I_m = 8\sum_{p=1}^{\infty}\sum_{q=1}^{\infty}\sum_{r=1}^{\infty} A_{pqrm}\xi_p\xi_q\xi_r \tag{9}$$

$$B_{pqm} = \int_0^1 \sin(p\pi\eta)\sin(q\pi\eta)\sin(m\pi\eta)d\eta$$

$$= B(p+q,m) + B(m+q,p) + B(m+p,q) - B(p+q,-m) \tag{10}$$

$$B(p+q,m) = \begin{cases} 0 & m = p+q \\ \dfrac{1}{4\pi}\dfrac{1-(-1)^{(p+q-m)}}{p+q-m} & m \neq p+q \end{cases}$$

$$A_{pqrm} = \int_0^1 \sin(p\pi\eta)\sin(q\pi\eta)\sin(r\pi\eta)\sin(m\pi\eta)d\eta$$

$$= \frac{1}{8}[\delta_{p+q,r+m} - \delta_{|p-q|,r+m} - \delta_{p+q,|r-m|} + \delta_{|p-q|,|r-m|} + \delta_{p,q}\delta_{r,m}] \tag{11}$$

$$\alpha_m = \frac{(m\pi)^2 + \chi_1(m\pi)^{-2}}{(m_*\pi)^2 + \chi_1(m_*\pi)^{-2}}, \quad s_1 = \frac{2\chi_2}{\chi_1 + (m_*\pi)^4}, \quad s_2 = \frac{2\chi_3}{\chi_1 + (m_*\pi)^4} \tag{12}$$

and δ_{ij} is the Kronecker delta.

Although a closed solution of the infinite set of nonlinear equations in Eq. (8) seems to be unfeasible, these equations have to be truncated and solved numerically.

Retaining only the m_*-th term in the series in Eqs. (6) and (7), Eqs. (8) and (9) are reduced to a single equation, namely,

$$\alpha(\xi_m + \bar{\xi}_m) = \alpha_m\xi_m - s_1\xi_m^2 - \frac{3m_*^2 s_2}{8m^2}\xi_m^3 \tag{13}$$

where

$$s_1 = \frac{4\chi_2[1-(-1)^m]}{3m^3\pi^3\gamma(\chi_1)}, \quad s_2 = \frac{2\chi_3}{(m_*\pi)^2\gamma(\chi_1)} \tag{14}$$

When $\chi_2 = 0$ and/or m is even, Eq. (13) is associated with a column on a cubic foundation. It has been discussed in Refs. [11,12]. In this study, the case that $\chi_2 \neq 0$ and m is odd to be considered, namely, a column on a nonlinear mixed quadratic-cubic foundation is studied. It is also worth noting that according to Eq. (13), ξ_m and $\bar{\xi}_m$ have the same sign. This is seen from the fact that the assumption $\bar{\xi}_m\xi_m < 0$ may imply $\alpha < 0$ for $0 < |\xi_m| < \bar{\xi}_m$ (a tensile force), which contradicts the terms of the problem.

Let us first consider a specific case where $m = m_* = 1$, $\chi_1 = \pi^4$, $\chi_2 = 0.4\chi_1$, and $\chi_3 = 0.1\chi_1$. The initial deflection $\bar{\xi}_m$ is deterministic in Eq. (13), and if one arbitrary value is given for ξ_{m_*}, the external axial load α can be calculated. By changing the value of ξ_{m_*}, we can obtain the varying curve of α versus ξ_{m_*}, as shown in Figs. 2(*a*) and 2(*b*) for $\bar{\xi}_m > 0$ and $\bar{\xi}_m < 0$, respectively.

It can be seen from Figs. 2(*a*) and 2(*b*) that the external axial load α experiences a course of "low-high-low," where the maximum value is taken as the buckling load α_*. It is worth noting that the buckling load can exceed that of a perfect structure in Fig. 2(*b*) for $\bar{\xi}_m < 0$. Hence, only the branch associated with $\bar{\xi}_m > 0$ has a physical sense.

The buckling load α_* versus the initial deflection is shown in Fig. 3 for $m = m_* = 1$, $\chi_1 = \pi^4$, $\chi_2 = 0.4\chi_1$, and $\chi_3 = 0.1\chi_1$. The dashed lines represent the meaningless branches of Eq. (13).

We truncate Eqs. (8) and (9) and retain "the most important modes." Thus, Eqs. (8) and (9) can be rewritten as

$$F(\xi_1, \xi_2, \ldots, \xi_N, \alpha) = \alpha_m\xi_m - \alpha(\xi_m + \bar{\xi}_m) - s_1\left(\frac{m_*}{m}\right)^2 J_m^{(N)}$$

$$-\left(\frac{s_2}{8}\right)\left(\frac{m_*}{m}\right)^2 I_m^{(N)} = 0, \quad m = 1,2,\ldots,N \tag{15}$$

where

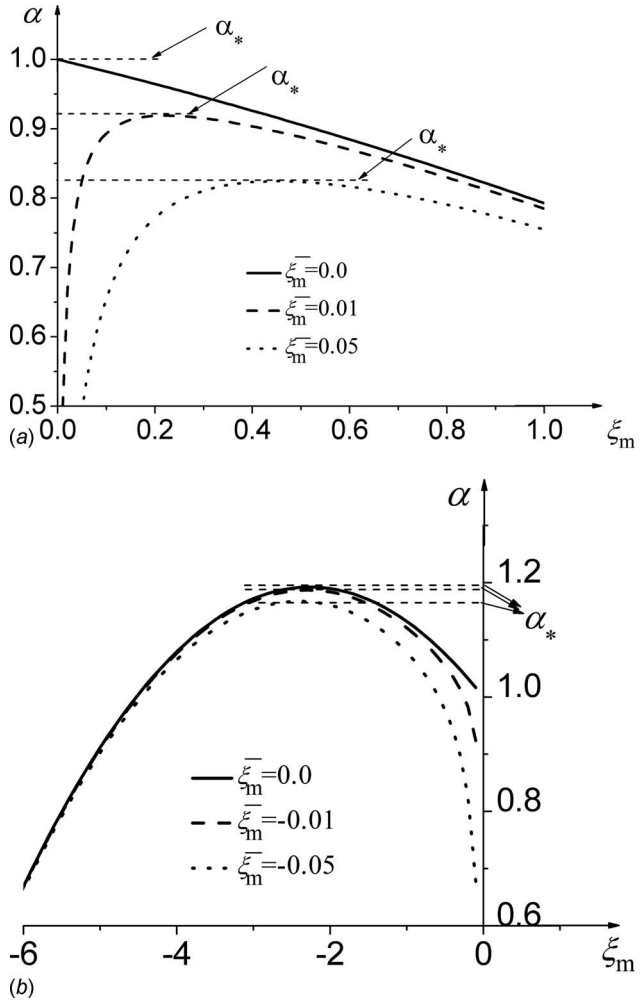

Fig. 2 External axial load α versus the additional deflection ξ_{m_*}

$$J_m^{(N)} = \sum_{p=1}^{N}\sum_{q=1}^{N} B_{pqm}\xi_p\xi_q, \quad I_m^{(N)} = 8\sum_{p=1}^{N}\sum_{q=1}^{N}\sum_{r=1}^{N} A_{pqrm}\xi_p\xi_q\xi_r \quad (16)$$

in which N is the remained mode number.

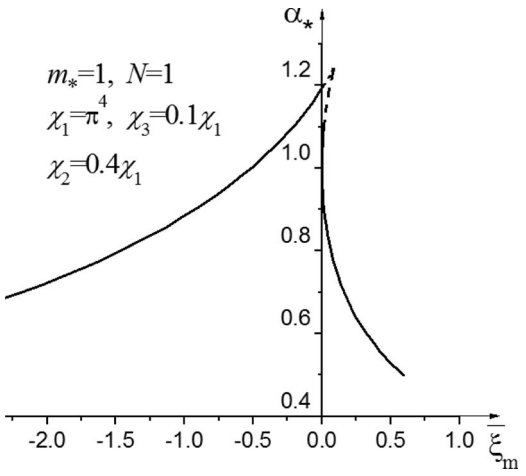

Fig. 3 Buckling load α_* versus the initial imperfection amplitude

As a result, Eq. (15) becomes the nonlinear algebraic equations containing N equations and $N+1$ unknown quantities ($\xi_m(m=1,2,\ldots,N)$ and α). For convenience in solving Eq. (15), they can be rewritten as

$$\alpha = \frac{\alpha_m\xi_m - s_1\left(\frac{m_*}{m}\right)^2 J_m^{(N)} - \left(\frac{s_2}{8}\right)\left(\frac{m_*}{m}\right)^2 I_m^{(N)}}{\xi_m + \bar{\xi}_m}, \quad m = 1,2,\ldots,N \quad (17)$$

Subtracting the two adjacent equations in Eqs. (17) yields

$$(\xi_{m+1}+\bar{\xi}_{m+1})\left(\alpha_m\xi_m - s_1\left(\frac{m_*}{m}\right)^2 J_m^{(N)} - \left(\frac{s_2}{8}\right)\left(\frac{m_*}{m}\right)^2 I_m^{(N)}\right) - (\xi_m+\bar{\xi}_m)\left(\alpha_{m+1}\xi_{m+1} - s_1\left(\frac{m_*}{m+1}\right)^2 J_{m+1}^{(N)} - \left(\frac{s_2}{8}\right)\left(\frac{m_*}{m+1}\right)^2 I_{m+1}^{(N)}\right) = 0, \quad m = 1,2,\ldots,N-1 \quad (18)$$

Equation (18) defines a relationship curve between $\xi_m(m=1,2,\ldots,N)$ and α in $N+1$ dimensional Euclidean space. Since Eq. (18) is comprised of nonlinear equations containing $N-1$ equations and N unknown quantities, we can use the same solution procedure similar to the single equation Eq. (13); namely, given one arbitrary value for the additional deflection ξ_{m_*}, the other $N-1$ unknown ξ_m ($m \neq m_*$) can be solved from Eq. (18) by the Newton–Raphson method. Thereby, the external axial load α can be calculated from Eq. (17). By changing the value of ξ_{m_*}, we can obtain the curve of α versus ξ_{m_*}.

If the coefficients of the Fourier series are assigned to be constants, it represents a deterministic initial deflection, and the buckling load can be solved by the abovementioned method. However, the initial geometrical imperfection usually exhibit uncertainties due to the manufacture errors, measurement inaccuracies, and other factors. In these cases, new approaches must be developed to evaluate the buckling load according to the different descriptive ways of uncertain initial imperfection.

3 Interval Analysis for Buckling Load

The first nonprobabilistic model for the initial imperfection is that its Fourier expansion coefficient vector $\bar{\xi}=(\bar{\xi}_1,\bar{\xi}_2,\ldots,\bar{\xi}_N)^T$ varies in the following hypercuboid set:

$$W(\bar{\xi}^c,\Delta A): |\bar{\xi}_m - \bar{\xi}_m^c| \le \Delta A_m \quad (\Delta A_m \ge 0,\ m = 1,2,\ldots,N) \quad (19)$$

where $\bar{\xi}_m^c$ and $\Delta A=(\Delta A_1,\Delta A_2,\ldots,\Delta A_N)^T$ are, respectively, the central vector and bound vector of the Fourier series coefficient interval.

As discussed before, the buckling load is a function of $\bar{\xi}$ and can be expressed formally as

$$\alpha_* = \varphi(\bar{\xi}) \quad (20)$$

Now the objective is to find the minimum buckling load for all possible initial deflection $\bar{\xi}=(\bar{\xi}_1,\bar{\xi}_2,\ldots,\bar{\xi}_N)^T$ that is subject to the constraint set in Eq. (20). Then the problem becomes an extreme value problem

$$\min_{\bar{\xi}\in W(\bar{\xi}^c,\Delta A)} \alpha_* = \min_{\bar{\xi}\in W(\bar{\xi}^c,\Delta A)} \varphi(\bar{\xi}) \quad (21)$$

By virtue of the method of Lagrange multipliers, the Lagrangian function is defined as

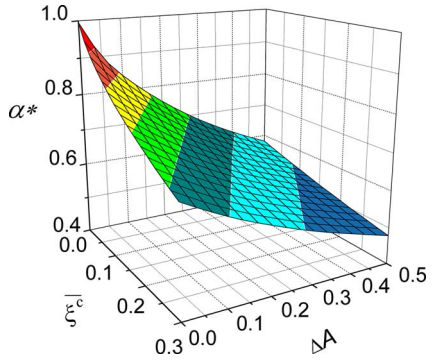

Fig. 4 Buckling load α_* from interval analysis

$$L(\bar{\xi},\lambda,x)=\varphi(\bar{\xi})+\sum_{m=1}^{N}\lambda_m[(\bar{\xi}_m-\bar{\xi}_m^c)^2-\Delta A_m^2+z_m^2] \tag{22}$$

where N is the number of the most significant modes involved in computations, $z=(z_1,z_2,\ldots,z_N)^T$ is an auxiliary variable vector, and λ_m $(m=1,2,\ldots,N)$ are Lagrange multipliers. According to the extreme condition, we can obtain

$$\frac{\partial L}{\partial \bar{\xi}_m}=\frac{\partial \varphi}{\partial \bar{\xi}_m}+2\lambda_m(\bar{\xi}_m-\bar{\xi}_m^c)=0,\quad m=1,2,\ldots,N \tag{23}$$

$$\frac{\partial L}{\partial x_m}=\lambda_m z_m=0,\quad m=1,2,\ldots,N \tag{24}$$

$$(\bar{\xi}_m-\bar{\xi}_m^c)^2-\Delta A_m^2+z_m^2=0,\quad m=1,2,\ldots,N \tag{25}$$

By solving the nonlinear algebraic equations Eqs. (23)–(25), the extreme points can be obtained. For example, if $N=3$, the solutions for the set of equations (23)–(25) are

$$\bar{\xi}_i=\bar{\xi}_i^c\pm\Delta A_i,\quad \bar{\xi}_j=\bar{\xi}_j^c\pm\Delta A_j,\quad \bar{\xi}_k=\bar{\xi}_k^c\pm\Delta A_k \tag{26}$$

$$\bar{\xi}_i=\bar{\xi}_i^c\pm\Delta A_i,\quad \bar{\xi}_j=\bar{\xi}_j^c\pm\Delta A_j,\quad \bar{\xi}_k=0 \tag{27}$$

$$\bar{\xi}_i=\bar{\xi}_i^c\pm\Delta A_i,\quad \bar{\xi}_j=0,\quad \bar{\xi}_k=0 \tag{28}$$

$$\bar{\xi}_i=0,\quad \bar{\xi}_j=0,\quad \bar{\xi}_k=0 \tag{29}$$

From Eqs. (26)–(29), 3^N combinations must be solved. The minimum value among the 3^N solutions is taken as the minimum buckling load.

Figure 4 gives a surface of the minimum buckling load obtained by interval analysis with the variation in the center value of the initial imperfections and their bounds. The parameters used for the calculation in Fig. 4 are $\chi_1=\pi^4$, $\chi_2=\chi_3=0.1\chi_1$, $m^*=2$, and $N=3$. The minimum buckling load surface will decrease with the center value and their bounds of initial imperfections increasing.

4 Convex Modeling for Buckling Load

Following the method developed by Ben-Haim and Elishakoff [13], uncertainty in the initial imperfection profile is represented by allowing the initial imperfection to vary in a convex set of values bounded by an ellipsoid.

$$Z(\bar{\xi}^c,e)=\left\{\bar{\xi}_m:\sum_{m=1}^{N}\frac{(\bar{\xi}_m-\bar{\xi}_m^c)^2}{e_m^2}\le 1\right\} \tag{30}$$

The semiaxes of the ellipsoid can be determined from an interval vector

$$e_m=\Delta A_m,\quad m=1,2,\ldots,N \tag{31}$$

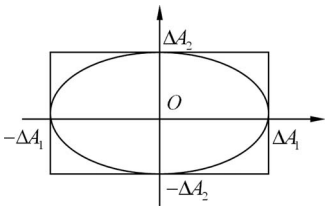

Fig. 5 The ellipse enclosed by a rectangle

For example, in two dimensional circumstances their relationship can be represented, as shown Fig. 5.

To seek the minimum or least-favorable buckling load, the problem can be transformed to a nonlinear optimization problem in Eq. (20), which is subject to constraint condition (Eq. (30)) as follows:

$$\min_{\bar{\xi}\in Z(\bar{\xi}^c,e)}\alpha_*=\min_{\bar{\xi}\in Z(\bar{\xi}^c,e)}\varphi(\bar{\xi}) \tag{32}$$

We still utilize the method of Lagrange multipliers and construct a Lagrangian function as follows:

$$L(\bar{\xi},\lambda)=\varphi(\bar{\xi})+\lambda\left(\sum_{m=1}^{N}\frac{(\bar{\xi}_m-\bar{\xi}_m^c)^2}{e_m^2}-1\right) \tag{33}$$

where λ is Lagrange multiplier.

Due to the necessary conditions for a minimum of φ, the derivative of the Lagrangian function vanishes

$$\frac{\partial L}{\partial \bar{\xi}_m}=\frac{\partial \varphi(\bar{\xi})}{\partial \bar{\xi}_m}+2\lambda\frac{(\bar{\xi}_m-\bar{\xi}_m^c)}{e_m^2}=0,\quad m=1,2,\ldots,N \tag{34}$$

and the constraint condition is satisfied.

$$\sum_{m=1}^{N}\frac{(\bar{\xi}_m-\bar{\xi}_m^c)^2}{e_m^2}\le 1 \tag{35}$$

Equation (35) is an inequality, so the Lagrange multiplier must satisfy one of the following relations:

$$\lambda=0\quad \text{if}\quad \sum_{m=1}^{N}\frac{(\bar{\xi}_m-\bar{\xi}_m^c)^2}{e_m^2}<1 \tag{36}$$

and

$$\lambda\ge 0\quad \text{if}\quad \sum_{m=1}^{N}\frac{(\bar{\xi}_m-\bar{\xi}_m^c)^2}{e_m^2}=1 \tag{37}$$

Under the condition of Eq. (36), it implies that the possible minimum value point occurs in the interior. If the derivatives of $\partial\varphi(\bar{\xi})/\partial\bar{\xi}_m$ exist, then the combination of Eqs. (34) and (36) yields

$$\frac{\partial \varphi(\bar{\xi})}{\partial \bar{\xi}_m}=0,\quad m=1,2,\ldots,N \tag{38}$$

Under the condition of Eq. (37), it is implied that the possible minimum value point occurs on the boundary. Then, the following nonlinear simultaneous algebraic equations need to be solved:

$$\frac{\partial \varphi(\bar{\xi})}{\partial \bar{\xi}_m}+2\lambda\frac{(\bar{\xi}_m-\bar{\xi}_m^c)}{e_m^2}=0,\quad m=1,2,\ldots,N$$

$$\sum_{m=1}^{N}\frac{(\bar{\xi}_m-\bar{\xi}_m^c)^2}{e_m^2}-1=0 \tag{39}$$

The differences of Eq. (39) from the general formula of convex modeling are that it is implicit and that it contains the derivative

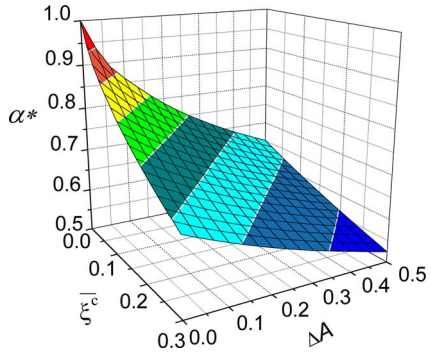

Fig. 6 Buckling load α computed from convex modeling

terms. We can obtain the nonlinear solutions of Eq. (39) by using Newton–Raphson method, where the derivatives $\partial\varphi(\bar{\xi})/\partial\bar{\xi}_m$ will be replaced with difference approximation.

However, at some points, $\partial\varphi(\bar{\xi})/\partial\bar{\xi}_m$ may not exist. Thus, the points at which the derivatives $\partial\varphi(\bar{\xi})/\partial\bar{\xi}_m$ do not exist and the solution points in Eqs. (34)–(39) are all the candidate extreme points.

Substituting all candidate extreme points into Eq. (20) yields all candidate extreme values, and the smallest one among them will be the minimum or least-favorable buckling load by convex modeling.

Figure 6 depicts the surface of the buckling load computed by convex modeling with the variation in the center value of the initial imperfections and their bounds. The parameters used for the calculation in Fig. 6 are $\chi_1=\pi^4$, $\chi_2=\chi_3=0.1\chi_1$, $m^*=2$, and $N=3$. The minimum buckling load surface will decrease with the center value and their bounds increasing.

5 Monte Carlo Method for Buckling Load

In some cases, if we can obtain statistical properties of an initial deflection by measurements or past experience, the initial deflection should be treated as the random variable. The normal distribution is a popular choice, but it may not be appropriate for realistic cases since the initial deflection can be visualized as limited in a certain range. To proceed with the reliability analysis, a truncated normal distribution model for the Fourier series coefficients of uncertain initial imperfection can be applied as follows [11]:

$$p(\bar{\xi}_m)=\begin{cases} c_m \exp\left(-\dfrac{\bar{\xi}_m^2}{b_m^2}\right), & |\bar{\xi}_m-\bar{\xi}_m^c|\le \Delta A_m \\ 0, & |\bar{\xi}_m-\bar{\xi}_m^c|>\Delta A_m \end{cases} \tag{40}$$

where $p(\bar{\xi}_m)$ is the probability density function of $\bar{\xi}_m$, each ΔA_m is the maximum possible value for the random variable $\bar{\xi}_m$, b_m represents various parameters, and c_m represents the normalization constants, which can be derived from

$$c_m=\left[2b_m \operatorname{erf}\left(\frac{\Delta A_m}{b_m}\right)\right]^{-1} \tag{41}$$

in which erf(·) is the error function and is defined as [14]

$$\operatorname{erf}(x)=\int_0^x e^{-t^2}dt \tag{42}$$

Figure 7 shows the probability density functions of the random coefficients at different parameters b_m and ΔA_m. If ΔA_m is given, then the probability density depends exclusively on b_m. The deviation in $\bar{\xi}_m$ increases with the growth in b_m, namely, a large b_m

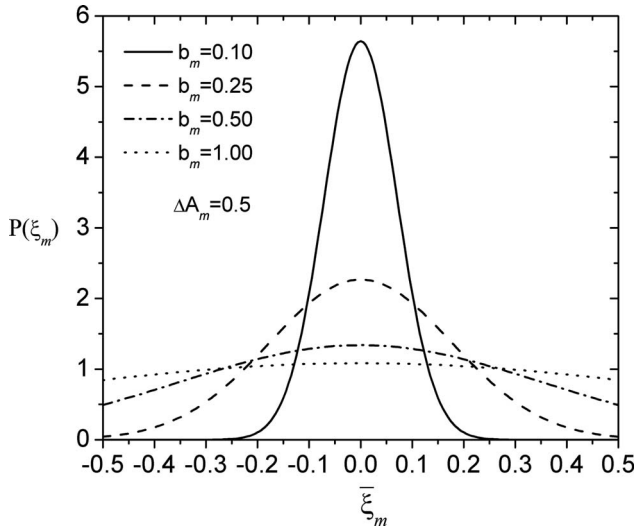

Fig. 7 Probability density function for a truncated normally distributed random variable

corresponds to a large deviation in $\bar{\xi}_m$. When $b_m^2 \gg \Delta A_m^2$, $\bar{\xi}_m$ is nearly uniformly distributed, as shown by the case of $b_m=1$ in Fig. 7.

The realization of $\bar{\xi}_m$, denoted by $(\bar{\Sigma}_m)_k$, $k=1,2,\ldots$, can be generated by

$$(\bar{\Sigma}_m)_k=b_m \operatorname{erf}^{-1}\left[(2\delta_k-1)\operatorname{erf}\left(\frac{\Delta A_m}{b_m}\right)\right] \tag{43}$$

where δ_k, $k=1,2,\ldots$ are independent random numbers uniformly distributed in [0,1].

With the given parameters ΔA_m and b_m in the probability density functions $p(\bar{\xi}_m)$ for the initial deflection, Monte Carlo simulations can be carried out to obtain the probability density for the buckling load. Consequently, at different reliability levels the buckling loads can be obtained by the following reliability function definition:

$$R(\alpha)=\text{Prob}[\alpha_* \ge \alpha] \tag{44}$$

where α_* is the admissible value for the axial load.

6 Numerical Examples

6.1 Single-Mode Imperfection Model. First, for $m=m_*=1$ the single-mode approximation suffices for the buckling load approximation [5]. The linear and nonlinear spring constants are taken as $\chi_1=\pi^4$, and $\chi_2=\chi_3=0.1\chi_1$, respectively. The initial deflection is uncertain and the Fourier coefficients are given by the inequality $\bar{\xi}_m \in \{\bar{\xi}_m: |\bar{\xi}_m-\bar{\xi}_m^c| \le \Delta A\}$ for the interval bound and $\bar{\xi}_m \in \left\{\bar{\xi}_m: (\bar{\xi}_m-\bar{\xi}_m^c)^2/\Delta A^2 \le 1\right\}$ for the ellipsoidal bound. For $m=1$—noting that the constrained conditions of the initial deflection are identical for interval bound and ellipsoidal bound—the buckling loads yielded by interval analysis and convex modeling are also identical.

From the methodology in Secs. 3–5, we can calculate the buckling load with the single-mode initial imperfection. Figures 8 and 9 depict the curves of the buckling load α_* of two nonprobabilistic methods versus the uncertain radius ΔA with different center values $\bar{\xi}^c$ in comparison with the Monte Carlo method at different cases of $b=0.1$ and $b=1$.

One case, namely, for $b=0.1$ for the truncated normal distribution of the initial deflection, is shown in Fig. 8(*a*) ($\bar{\xi}^c=0.0$) and Fig. 8(*b*) ($\bar{\xi}^c=0.01$). The following conclusions hold.

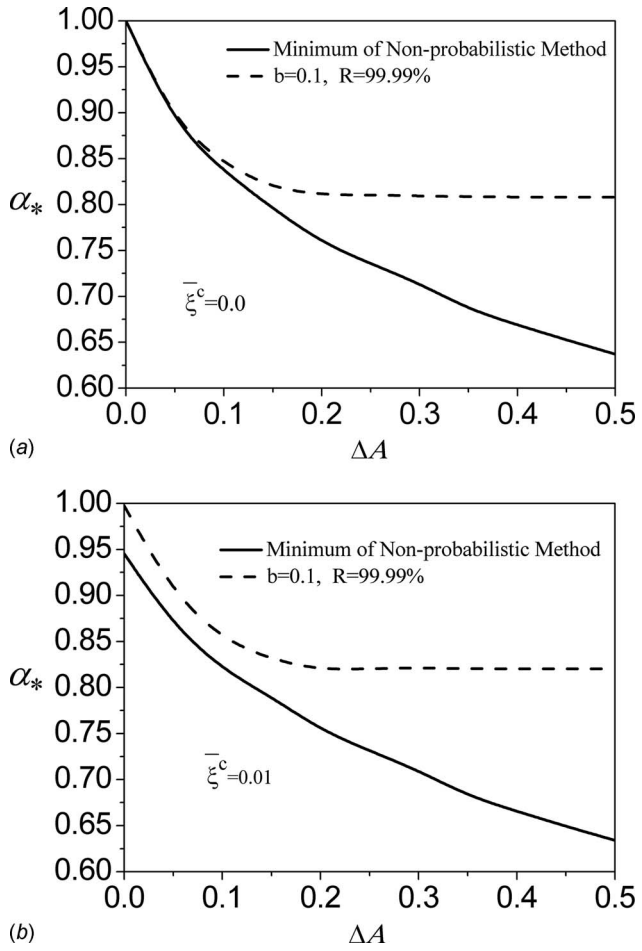

Fig. 8 Comparison of the buckling load computed from probabilistic and nonprobabilistic methods for cases of $b=0.1$: (*a*) $\bar{\xi}^c=0.0$, and (*b*) $\bar{\xi}^c=0.01$

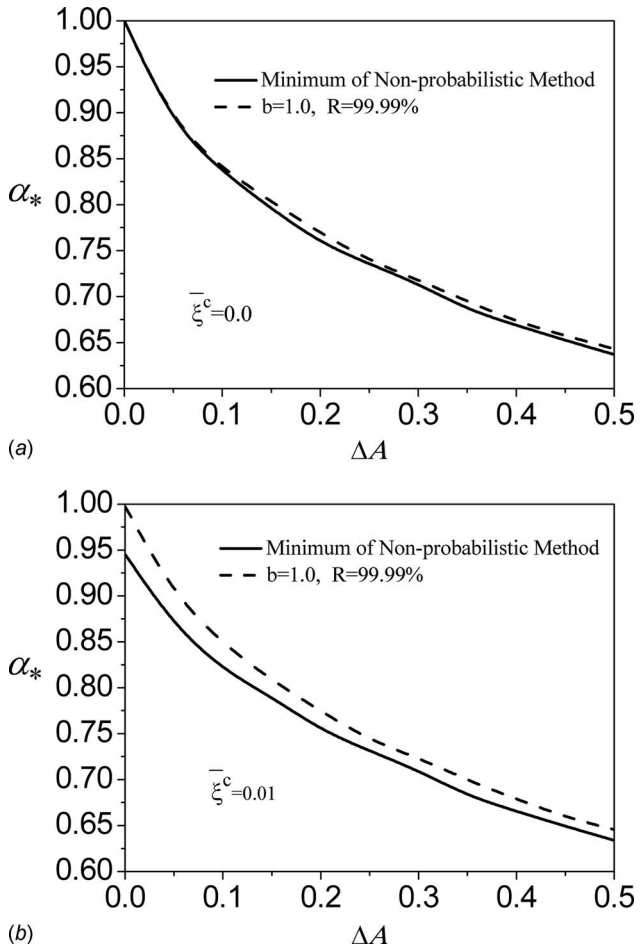

Fig. 9 Comparison of the buckling loads computed from probabilistic and nonprobabilistic methods for case of $b=1.0$: (*a*) $\bar{\xi}^c=0.0$, and (*b*) $\bar{\xi}^c=0.01$

(a) The influence of the uncertainty radius ΔA on the buckling load α_* decreases as ΔA increases (with the given center value $\bar{\xi}^c$).

(b) The buckling load α_* decreases with an increase in the center value $\bar{\xi}^c$. For example, when $\bar{\xi}^c=0.0$ and $\Delta A=0.0$, the probabilistic and nonprobabilistic solutions are 1.0. At $\bar{\xi}^c=0.01$ and $\Delta A=0.0$, they are 0.99748 and 0.94528, respectively.

(c) The minimum buckling load obtained from the probabilistic approach may be well above that calculated by nonprobabilistic methods for large ΔA ($\Delta A>0.1$ in the present case). This implies that the use of the nonprobabilistic methods may lead to a conservative design. However, if the deviation in the initial deflection is small ($\Delta A<0.1$ in the present case), a design can be made based on the nonprobabilistic methods since it is much simpler than the probabilistic one.

Another case, namely, for $b=1$ for approximately uniform distribution of the initial deflection, is shown in Fig. 9(*a*) ($\bar{\xi}^c=0.0$) and Fig. 9(*b*) ($\bar{\xi}^c=0.01$). We observed from Figs. 9(*a*) and 9(*b*) that the minimum buckling load α_* decreases with an increase in $\bar{\xi}^c$ and ΔA. Moreover, the minimum buckling loads yielded by the nonprobabilistic methods and the probabilistic approach do not exhibit much difference. Therefore, a design can be made based on the nonprobabilistic methods when the sufficient knowledge about the initial imperfection is absent and cannot be substantiated for substantiation of the probabilistic analysis.

6.2 Multimode Imperfection Model. Consider the multimode imperfection model. The linear and nonlinear spring constants are taken as $\chi_1=16\pi^4$ and $\chi_2=\chi_3=0.1\chi_1$, respectively. Three modes are retained in the computations, and every Fourier coefficient $\bar{\xi}_m$ $(m=1,2,3)$ is assumed to have the same bound ΔA_m, the same center value $\bar{\xi}_m^c$, and the same parameters b_m, namely, $\Delta A_1=\Delta A_2=\Delta A_3=\Delta A$, $\bar{\xi}_1^c=\bar{\xi}_2^c=\bar{\xi}_1^c=\bar{\xi}^c$, and $b_1=b_2=b_3=b$. For $m_*=2$, the variations in the minimum buckling load with ΔA in the cases of $b=0.1$ and $b=1$ will be investigated.

Figure 10(*a*) ($\bar{\xi}^c=0.0$) and Fig. 10(*b*) ($\bar{\xi}^c=0.02$), for the case of $b=0.1$, present a comparison of the minimum buckling load with the increasing ΔA computed from the interval analysis and convex modeling. The admissible loads corresponding to the given reliability levels ($R=0.90,0.99,0.999$) are calculated from the Monte Carlo method and are depicted in the same figures.

For small ΔA (namely, $\Delta A<0.2$ in the present case), Figs. 10(*a*) and 10(*b*) demonstrate that the minimum buckling load and the admissible load corresponding to different reliability levels ($R=0.90,0.99,0.999$) do not show much difference. However, if the bound for the initial deflection is large ($\Delta A>0.2$ in the present case shown in Fig. 10), the admissible value for the axial load obtained from the Monte Carlo method may be well above the

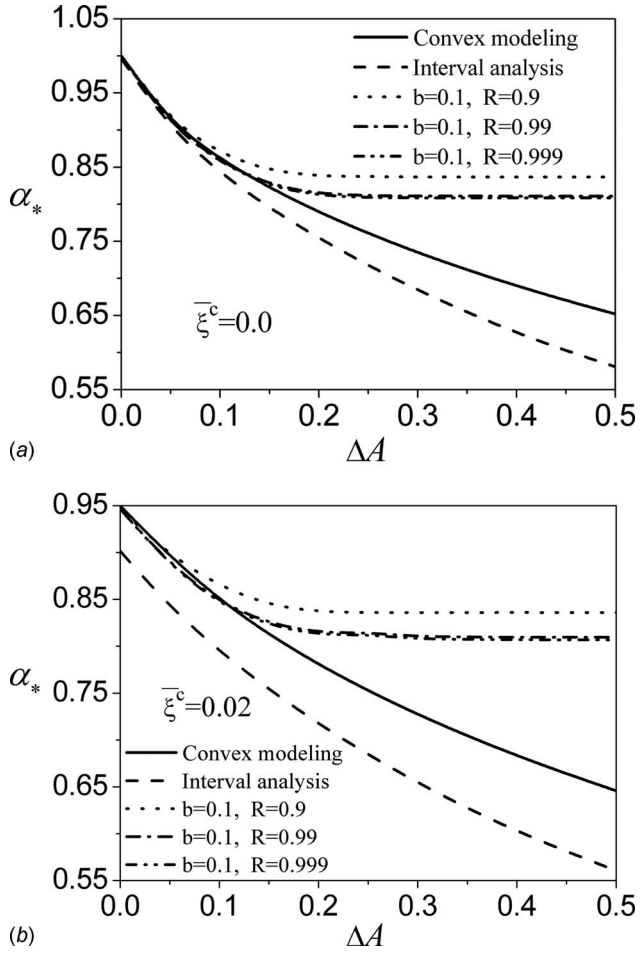

Fig. 10 Comparison of the buckling loads computed from probabilistic and nonprobabilistic methods for case of b=0.1: (*a*) $\bar{\xi}^c$=0.0, and (*b*) $\bar{\xi}^c$=0.02

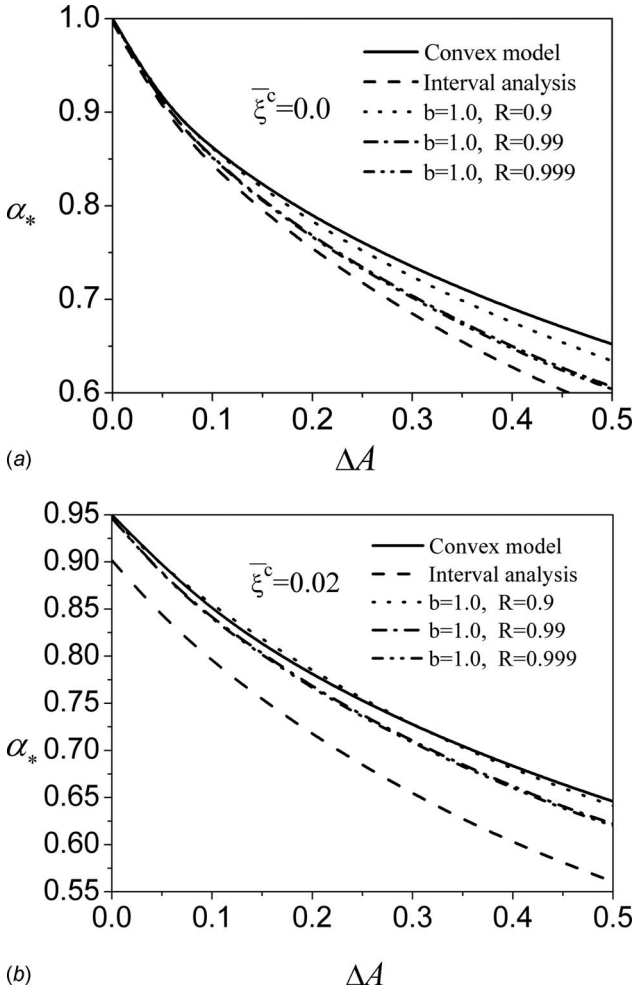

Fig. 11 Comparison of the buckling loads computed from probabilistic and nonprobabilistic methods for case of b=1.0: (*a*) $\bar{\xi}^c$=0.0, and (*b*) $\bar{\xi}^c$=0.02

minimum buckling load calculated by either convex modeling or interval analysis. This implies that the use of the nonprobabilistic methods may lead to a conservative design.

It also can be seen from Figs. 10(*a*) and 10(*b*) that the center value $\bar{\xi}^c$ has significant influence on the buckling load α_*. It decreases with an increase in $\bar{\xi}^c$.

Figures 11(*a*) ($\bar{\xi}^c$=0.0) and 11(*b*) ($\bar{\xi}^c$=0.02) give the results for the case of b=1.0. The buckling loads obtained by convex modeling are above the results of the reliability at different reliability levels (R=0.90,0.99,0.999). However, the buckling loads obtained by interval analysis are below those obtained by the probabilistic approach.

7 Conclusion

In this paper, two classes of set-theoretical models, interval analysis, and convex modeling are employed for the initial imperfection sensitive structure—a finite column on nonlinear mixed quadratic-cubic elastic foundation. The minimum buckling load is determined as a function of the parameters, which describe the range of possible initial imperfection profiles of the column, where the nonzero central values for them are studied. The comparison of the results obtained from nonprobabilistic methods and probabilistic approach indicates that the design based on the nonprobabilistic methods is acceptable for a large deviation in the initial deflection but may be conservative for that with a small deviation.

It is remarkable that although being of cardinally different nature, the nonprobabilistic and probabilistic methods may yield close values for the design axial loads. If probabilistic information is unavailable, one should not propose the probabilistic method based on an arbitrary assumption on the distribution of the Fourier coefficients. One should use the nonprobabilistic method to uncertainty. The difference between interval analysis and convex modeling is the description of the uncertain variable, a hypercuboid for the former and a hyperellipsoid set for the latter. The selection for the two nonprobabilistic models is decided by the descriptive form of the prior information.

Acknowledgment

X.W., Z.Q., and L.M. would like to thank the National Outstanding Youth Science Foundation of the P. R. China (Project No. 10425208), 111 Project (No. B07009), and FanZhou Science and Research Foundation for Young Scholars (Project No. 20080503) for the support. I.E. expresses his grateful thanks to Beihang University, for their kind and warm hospitality during his stay as a Visiting Professor during the months of April and May, 2007. He also appreciates the J. M. Rubin Foundation of the Florida Atlantic University, Florida-Israel Institute, and the University Center of Ariel in Israel, where he served as a Visiting Professor of Civil Engineering during May–August 2007.

References

[1] Bolotin, V. V., 1958, "Statistical Methods in the Nonlinear Theory of Elastic Shells," English Translation, NASA TTF-85 of a paper presented at a seminar in the Institute of Mechanics of Academy of Sciences, USSR, 1957.

[2] Boyce, W. E., 1962, "Buckling of a Column With Random Initial Displacements," J. Aerosp. Sci., **28**, pp. 308–320.

[3] Elishakoff, I., 1985, "Reliability Approach to the Random Imperfection Sensitivity of Columns," Acta Mech., **55**, pp. 151–170.

[4] Elishakoff, I., 1978, "Axial Impact Buckling of a Column With Random Initial Imperfections," ASME J. Appl. Mech., **45**, pp. 361–365.

[5] Elishakoff, I., 1979, "Buckling of a Stochastically Imperfect Finite Column on a Nonlinear Elastic Foundation: A Reliability Study," ASME J. Appl. Mech., **46**, pp. 411–416.

[6] Ben-Haim, Y., and Elishakoff, I., 1989, "Non-Probabilistic Models of Uncertainty in the Nonlinear Buckling of Shells With General Imperfections: Theoretical Estimates of the Knockdown Factor," ASME J. Appl. Mech., **56**, pp. 403–410.

[7] Lindberg, H. E., 1992, "Evaluation of Convex Modeling for Multimode Dynamic Buckling," ASME J. Appl. Mech., **59**(4), pp. 929–936.

[8] Lindberg, H. E., 1992, "Convex Models for Uncertain Imperfection Control in Multimode Dynamic Buckling," ASME J. Appl. Mech., **59**(4), pp. 937–945.

[9] Elseifi, M. A., Gürdal, Z., and Nikolaidis, E., 1999, "Convex/Probabilistic Models of Uncertainties in Geometric Imperfections of Stiffened Composite Panels," AIAA J., **37**(4), pp. 468–474.

[10] Qiu, Z. P., and Wang, X. J., 2005, "Two Non-Probabilistic Set-Theoretical Models for Dynamic Response and Buckling Failure Measures of Bars With Unknown-But-Bounded Initial Imperfections," Int. J. Solids Struct., **42**, pp. 1039–1054.

[11] Elishakoff, I., Cai, G. Q., and Starnes, Jr., J. H., 1994, "Non-Linear Buckling of a Column With Initial Imperfection Via Stochastic and Non-Stochastic Convex Models," Int. J. Non-Linear Mech., **29**(1), pp. 71–82.

[12] Qiu, Z. P., Ma, L. H., and Wang, X. J., 2006, "Ellipsoidal-Bound Convex Model for the Non-Linear Buckling of a Column With Uncertain Initial Imperfection," Int. J. Non-Linear Mech., **41**, pp. 919–925.

[13] Ben-Haim, Y., and Elishakoff, I., 1989, "Dynamics and Failure of Structures Based on the Unknown-But-Bounded Imperfection Model," Recent Advances in Impact Dynamics of Engineering Structures, **105**(17), pp. 89–95.

[14] Lebedev, N. N., 1972, *Special Functions and Their Applications*, Dover, New York.

Light Activated Shape Memory Polymer Characterization

Richard V. Beblo
e-mail: rvb2@pitt.edu

Lisa Mauck Weiland[1]
e-mail: lweiland@engr.pitt.edu

Department of Mechanical Engineering and
Materials Science,
University of Pittsburgh,
Pittsburgh, PA 15261

Since their development, shape memory polymers (SMPs) have been of increasing interest in active materials and structures design. In particular, there has been a growing interest in SMPs for use in adaptive structures because of their ability to switch between low and high stiffness moduli in a relatively short temperature range. However, because a thermal stimulus is inappropriate for many morphing applications, a new light activated shape memory polymer (LASMP) is under development. Among the challenges associated with the development of a new class of material is establishing viable characterization methods. For the case of LASMP both the sample response to light stimulus and the stimulus itself vary in both space and time. Typical laser light is both periodic and Gaussian in nature. Furthermore, LASMP response to the light stimulus is dependent on the intensity of the incident light and the time varying through the thickness penetration of the light as the transition progresses. Therefore both in-plane and through-thickness stimulation of the LASMP are nonuniform and time dependent. Thus, the development of a standardized method that accommodates spatial and temporal variations associated with mechanical property transition under a light stimulus is required. First generation thick film formulations are found to have a transition time on the order of 60 min. The characterization method proposed addresses optical stimulus irregularities. A chemical kinetic model is also presented capable of predicting the through-thickness evolution of Young's modulus of the polymer. This work discusses in situ characterization strategies currently being implemented as well as the current and projected performance of LASMPs. [DOI: 10.1115/1.2999447]

Keywords: light activated shape memory polymer (LASMP), material characterization, morphing materials

1 Introduction

Recently, shape memory polymers (SMPs) have been the subject of increasing attention among materials with promising characteristics for adaptive structures. Their ability to switch between high and low moduli while retaining a "memorized" shape make them desirable for ambitious designs requiring deformable components capable of carrying complex loads. For instance, biodegradable formulations have been designed [1] and are being implemented in the biomedical field as stents for treatment of cardiovascular disease and aneurysms [2,3]. They are being utilized in the aeronautical and astronautical fields in morphing aircraft structures [4,5] and in the automotive industry as active air dams and actuators for improved fuel economy and performance [6].

By far the most researched class of SMP is the heat activated type. Extensive experimental studies have been performed characterizing their thermomechanical properties [7–10], their resistance to humidity [11–13], strain induced anisotropic characteristics [14], thin film characteristics [15,16], and shape recovery characteristics [17,18].

While there may be advantages to applying a heat activated SMP in some designs, effective delivery and control of the thermal stimulus often requires sophisticated heating and cooling schemes such as the use of magnetic nanoparticles [19,20]. Furthermore, all of the proposed schemes still suffer from one fundamental disadvantage. Heat activated SMP requires continuous energy input to maintain the polymer in its low modulus state, resulting in large energy requirements over time.

One alternative is to replace heat activated SMPs with optically stimulated SMPs [21–24]. Light activated shape memory polymers (LASMPs) benefit from lower energy requirements to switch between moduli. The LASMP virgin state is soft; additional cross-links form upon the application of a particular wavelength of light thereby increasing the stiffness. When the light stimulus is removed, the polymer remains in this stiff state. Imposing a different wavelength of light reverses the cross-linking, returning the sample to a soft state [21,23]. Lee et al. [25] report the heat of crystallization of a *thermally* stimulated polyurethane block copolymers as being between 16.4 J/g and 324.2 J/g, depending on the composition. Conversely, as reported below, current formulations of LASMP require only ~ 1.4 J/g for transition, representing at least an order of magnitude reduction in power consumption and offering clear motivation for further developments of LASMPs.

While there have been several successful research initiatives formulating and characterizing various LASMPs [21–24,26–30], few formulations have been designed and characterized based on their ability to reversibly switch between two unique stiffness states. Polymers labeled as LASMP fall under two main categories: those requiring external forces to undergo shape change and those that do not. The former, such as that developed by Lendlein et al. [24] are mechanically similar to heat activated SMPs, in that the light supplied to the polymer is utilized solely for material property changes. Such a polymer is the object of the presented work. The latter subcategory of LASMP is most often presented as an artificial muscle [28–30]. These LASMPs are capable of length changes [30] and/or bending [28,29] initiated by light stimulus. However, all of the aforementioned studies focus on thin film samples where the transmission of light through the sample is not a significant concern. As an example, Ikeda et al. [28] report using 10 μm thick samples with only the material within 1 μm of the surface of the sample significantly altered by optical stimu-

[1]Corresponding author.

Contributed by the Applied Mechanics Division of ASME for publication in the JOURNAL OF APPLIED MECHANICS. Manuscript received February 1, 2008; final manuscript received July 10, 2008; published online October 31, 2008. Review conducted by Krishna Garikipati. Paper presented at the SAMPE Cincinnati 2007.

lus. While in comparison to thermally stimulated SMPs, LASMP transition power requirements motivate its development as a viable alternative, this development also comes with the challenge of establishing that LASMP could be meaningfully employed in similar load bearing applications such as morphing aircraft structures.

In the current effort the emphasis is enabling the development and application of LASMP in load bearing structures inappropriate for thin films; in this scenario through-thickness delivery and transmission of light become important parameters. Because the characterization process will necessarily face temporal and spatial variations in stimulus and material property transition, application of a well defined and standardized approach will be imperative to the successful development and evolution of LASMPs. Material properties of immediate importance include Young's modulus and Poisson's ratio in both the hard and soft states, and the time and power required for the transitions between the states. In addition, an appropriate understanding of how the transition manifests itself in the light activated material is required. Thus this effort seeks foremost to define a characterization methodology appropriate to the physical phenomena inherent to the optical stimulus as well as the class of material itself; experimental results and analysis are provided for an example case.

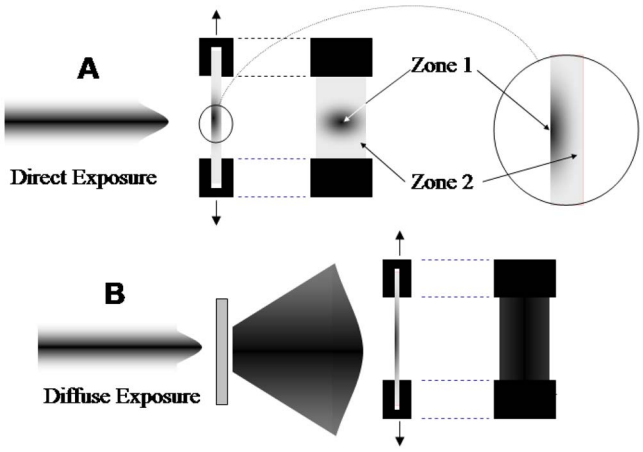

Fig. 1 A (top)—sample exposed to direct laser light: Zone 1 is the high optical stimulus in the laser beam center and Zone 2 is the little optical stimulation away from the beam; B (bottom)—laser diffused with convex cylindrical lens

2 Experimental Considerations

LASMPs employ the use of lasers at different wavelengths to switch between modulus states. The virgin state for the samples considered in this study is soft; imposing a 325–385 nm laser light activates photomonomer cross-linking, resulting in increased stiffness. Reverse stimulus is achieved by imposing a 248–280 nm laser light.

2.1 Laser Considerations and Sample Positioning. Nonuniform distribution of laser light at the sample and fluctuations in the intensity of the laser result in a complex pattern of polymer stimulation. With the intention of standardizing the practices used to describe this new class of polymers, these fluctuations in stimulation by the laser must be accounted for. The following discusses typical variations and corresponding proposed LASMP characterization procedures.

2.1.1 Laser Intensity Fluctuations With Time. It is not uncommon for laser output intensity to vary periodically in time. By placing an optical power meter in the path of the laser beam and measuring the intensity of the light over a length of time, fluctuations in the power output of the laser can be measured. For instance, the laser utilized for this particular study is a 150 mW class IIIb He-Cd Omnichrome laser manufactured by Melles Groit Laser Group, has an optical power output of 19.0 mW at 325 mW and 55.0 mW at 442 nm, and is allowed an ample warm-up time of 20 min or more before testing. The resulting steady state sinusoidal output displays a period of 1200 s ($\sim$20 min) with a 0.015 nW peak-to-trough amplitude with 9.2 μW incident at the sample. The LASMP characterization must accommodate for the time variation of the imposed stimulus.

The LASMP proof-of-concept samples investigated in this effort require $\sim$60 ($\pm$20) minutes to fully transition. For this case it is adequate to place an optical power meter behind the sample to monitor the extent and rate of fluctuation. Ultimately however, LASMP development efforts are expected to yield formulations that transition in about 1 s [31]. Simply monitoring the exiting light will not be adequate for establishing the position of the laser output on its intensity curve. This will have to be established immediately prior to sample stimulation in order to properly compute the polymer's power requirements.

2.1.2 Laser Intensity Distribution. In addition to fluctuating over time, the laser's power output is also nonuniform in space. While it is generally accepted that most lasers will exhibit beams that are Gaussian in nature [32], this is not desirable for establishing a repeatable LASMP characterization method, rather, imposing a stimulus that is as uniform as possible is sought. Figure 1 illustrates the significance of this point. The rate of state change of an infinitesimal unit element of LASMP is dependent on the intensity of light imposed. Furthermore, and as will be discussed in more detail below, the through-thickness penetration of the light intensity is nonuniform in space and time. In the worst case scenario (Fig. 1(*a*)) the region of material at the center of the incident light will fully transition to the stiff state in a short time, while regions removed from this location will transition at progressively slower rates. Some regions of the sample will transition so slowly that experimental identification of complete transition will be premature. While the through-thickness penetration effect is unavoidable, the effects of in-plane variation in incident light may be minimized by diffusing the light (Fig. 1(*b*)). However, the optics required to position and diffuse the beam making it viable for transitioning the polymer over a large area also cause the resulting beam, as seen by the sample, to be somewhat irregular. Therefore, it is appropriate to characterize the spatial light distribution prior to investigating the stimulus response.

A contour map of the optical power delivered to the sample considered in this work is created by (1) covering the power meter with an opaque material (in this case, a 1.2 mm thick posterboard) with a 0.58 mm diameter pinhole, (2) attaching the meter to a sliding 90 deg optical mounting bracket that is fixed to the crosshead of the load frame, and (3) mapping the laser power incident on the sample over 1 mm square grid increments, with the area of the sample being centered on the grid and encompassing 4 $\times$25 mm^2. Since the optical power meter sensor is 20 mm in diameter and thus unsuitable for characterizing a beam 10 mm in width, an opaque material is used to cover it with a centrally located pinhole. A pinhole size of 0.58 mm was chosen to allow the precision needed for a 1 mm square grid of data while still allowing enough light to penetrate through to the sensor for an accurate reading. The load frame utilized throughout the study is an MTI 1-K tabletop load frame with a 2.5 lb (11 N) ell, accurate to 7.5×10^{-4} lb (3.3 mN). The data are then conditioned in MATLAB® using the griddata(cubic) function to produce contour and surface plots of the optical power seen by the sample, pictured as Figs. 2 and 3, respectively. Figure 2 also illustrates how this information is to be used to properly place the sample within the diffused light in order to impose a stimulus that is as uniform as possible.

To determine where within the contour the sample lies during testing, a strip of 35 mm film is positioned behind the sample in the load frame and is exposed to the laser. By examining the

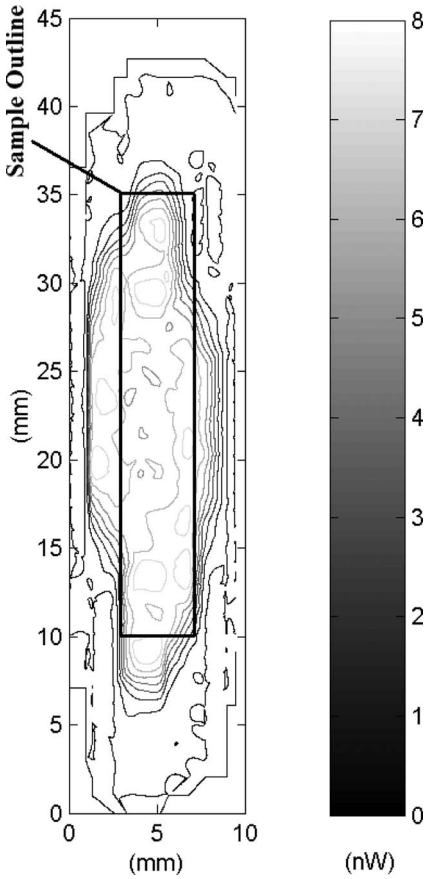

Fig. 2 Contour plot of optical power, sample location outlined by black rectangle

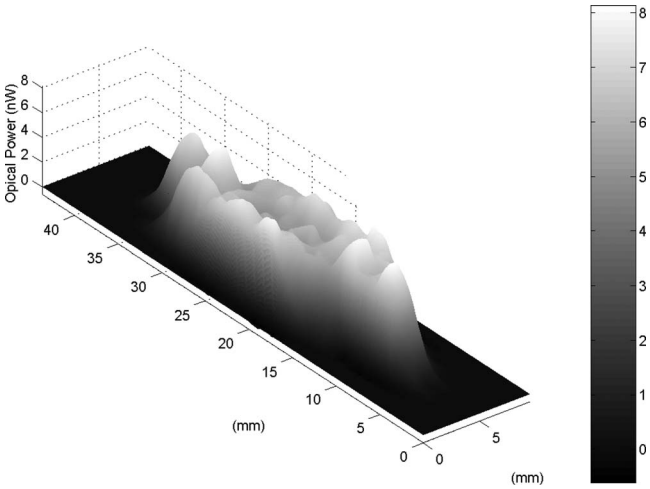

Fig. 3 Surface plot of optical power as seen in the sample

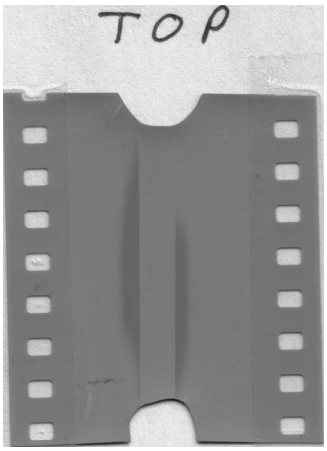

Fig. 4 Film depicting the laser shadow of a sample during testing

resulting shadow of the sample on the film, pictured in Fig. 4, one can locate the position of the sample within the laser light. For the LASMP sample considered here, this comparison leads to the sample encompassing the space outlined from 3.0 mm to 6.9 mm horizontally and from 7.5 mm to 37.5 mm vertically in the contour plot in Fig. 2.

Once the sample has been appropriately placed within the light stimulus, the portion of the sample experimentally monitored is further refined via the application of a video extensometer. Only the material between the marked lines tracked by the system is responsible for the material's measured properties. Accounting for the gauge length measured by the video extensometer, the area of the sample utilized for material characterization is reduced to the vertical space contained from 10 mm to 35 mm in Fig. 2, indicated by the rectangular box. Dividing the sample into five vertical strips, the extent of irregularity in incident light intensity delivered to the surface is summarized in Table 1. Utilization of these data is addressed below in the discussion of results and data analysis.

2.2 In Situ Measurements. Because it is desirable to establish property changes of LASMP as a function of time, in situ characterization is required. In addition, the fundamental concepts underlying dynamic material analysis (DMA) characterization are particularly favorable for characterizing the soft-to-hard transition. Dynamic material analyzers allow the creation of a modulus versus the time curve to be created for each test specimen. However, it is infeasible to optically stimulate and subsequently monitor LASMP response within a traditional DMA or similar available devices. The strategy proposed below mimics DMA testing while employing a video extensometer to monitor response.

2.2.1 Experimental Control. Custom DMA-mimicking load frame control software was created. This control strategy effectively converts a small tabletop load frame into a DMA that waits for user input before completing each cycle. The software is easily interfaced with other experimental control software, such as laser-to-load-frame synchronization. This experimental setup effectively allows the laser to be turned off or shuttered during inter-

Table 1 Average and median optical power for five bins spaced horizontally across the sample

		3.0	3.80	4.59	5.38	6.17
Bin	(mm)	3.79	4.58	5.37	6.16	6.90
Ave.	(nW)	5.19	5.85	6.18	5.98	4.89
Med.	(nW)	5.56	5.77	6.10	6.11	6.17

mittent cycles of testing. A brief tensile test (approximately 2 min in duration) restricted to below the yield stress of the polymer is periodically performed, with the grips returning to their pretest position after the completion of each cycle. Testing continues until steady state loading response is achieved. The result is a measurement of overall sample stiffness and Poisson's ratio with respect to laser exposure during transition, allowing small time spans between data points.

2.2.2 Sample Type and Grip Interface. An important area of interest when mechanically testing any polymer is the choice of sample type and the interface between the grips and the sample. Dogbone samples are generally preferred; the thinnest segment, or gauge length, of the sample dominates the strain response, thereby minimizing grip effects. However, LASMP synthesis constraints result in sample sizes too small to justify the material loss associated with the creation of dogbone samples. The proposed strategy subsequently adheres to ASTM Standard 882 for thin films, where the typical sample thickness is 0.10 mm. Furthermore, this approach better enables comparison between early LASMP thin film reports and the comparatively thick films considered here. (While the ASTM standard is entitled "for thin films," 0.10 mm is considered thick for LASMP, and appropriately allows consideration of the evolution of through-thickness property transition.)

It should be noted that when transitioning from the soft to hard states, only the sample is exposed to light transitions. The result is that the portion of the sample covered by the grips remains in the virgin soft state. When testing a sample in this circumstance, the sample tends to undergo slight necking in the region of the grips (but does not slip, as seen in the video feed from the extensometer). In order to prevent this phenomenon from skewing the data, a video extensometer accurate to 0.3 μm (1×10^{-6}% strain) is employed to monitor only a region far from the grips where the assumption of uniform load distribution is appropriate. From Saint-Venant's principle we know that the stress field "sufficiently far" from the application of forces can be considered uniform; "sufficiently far" is generally considered to be one characteristic length of the test specimen [33]. The video extensometer accomplishes this by tracking appropriately placed lines painted on the back of the sample. Furthermore, a filter is placed between the video extensometer lens and the specimen to reduce glare caused by the laser.

2.2.3 Effects of Cyclic Loading. When testing any one sample multiple times, as described above, it is necessary to consider sample cyclic effects such as low cycle fatigue. As an example, a test to determine the evolution of Young's modulus as a function of exposure time may be subject to a total of 25 cycles. Therefore, low cycle fatigue tests, without the lasers, must be conducted to establish the extent of change that may be attributed to the light stimulation alone versus that attributed to cyclic loading. (While cyclic degradation of response is not expected to be an issue in future LASMP formulations, this characterization is currently necessary to ensure the elimination, via a synthesis feedback loop, of this undesirable property [31].)

As an example, one of the early LASMP formulations demonstrated 7% and 10% strain softening after 25 cycles in the fully hard and fully soft states, respectively. This fatigue style test also revealed that the degradation in stiffness with each cycle, for this particular formulation, is nearly linear. So in this example case, knowing the number of cycles completed, an adjusted light stimulated Young's modulus may also be reported.

3 Results and Data Analysis

3.1 Stiffness Versus Nonuniform Incident Light. As discussed in Sec. 2.1.2, even after centering the sample the incident light is nonuniform. At this point there are several acceptable approaches to relating the experimentally determined volume averaged modulus to the in-plane variations in sample modulus given the distribution of optical intensity. The first, and easiest, approach is to treat the areas of low intensity as small compared to the size of the test specimen.

In the sample in Fig. 2, 8.8 mm^2 of the sample (9% of the total area) is exposed to intensities below 5.0 nW. As noted in Table 1, the median value of the optical power across the sample horizontally is relatively constant. The difference between the maximum and minimum median values is 0.61 nW, which corresponds to a difference of about 11% with respect to the minimum median. In some instances it may be adequate to simply assume a uniform sample when calculating Young's modulus, as well as other properties, using the average or median optical power intensity over the sample, in this case 5.62 nW and 5.83 nW, respectively. (It is noteworthy that these values are based on the "pinhole" method described earlier and thus are numerically accurate for investigating the spatial variations in optical intensity. To calculate the actual power hitting the sample, the percentage of power hitting the sample based on the pinhole method is multiplied by the total power reaching the sample. Such a calculation results in the sample receiving 0.066 W/m^2 of optical power.)

In cases where incident light variation is significant, or higher degrees of accuracy are sought, it may be acceptable to adapt the rule of mixtures [34] to fit this specific test

$$E_s = \sum_{i=1}^{j} \varphi_i E_i \tag{1}$$

where E_i is Young's modulus of one bin, φ_i is the volume fraction of that bin, and E_s is the volume averaged Young's modulus of the LASMP sample. In application, E_i would then be dependent on position, optical intensity, and time. Such an approach lends itself well to the method described above of dividing the sample into bins of relatively constant intensities. The accuracy could easily be manipulated through varying the resolution of the bin sizes.

3.2 An Example of Experimentally Observed Stiffness Evolution. The method described above was applied to several recent LASMP formulations. For the current state of the art LASMP experimental emphasis is on enabling a synthesis feedback loop in the identification of especially promising LASMP chemical formulations. At present it is prohibitively expensive to create more than one to a few samples per formulation in this evolutionary process. However, once select formulations have demonstrated promise synthesis costs will become justifiable and the application of the procedures detailed here will transition to characterization concerns such as repeatability of material response.

The transition time of all of the thick samples considered here ranged from ~40 min to ~80 min while the increase in stiffness ranged from ~3*X* to ~8*X* when exposed to 325–385 nm light. The formulation presented for illustration was selected because of its relative lack of cyclic property degradation and strength of property change (~7*X*).

Because the total transition time of the example formulation is ~80 min, the lasers are not shuttered during these tests. The resulting error is assumed to be small; this assumption is supported by inspection of the linear nature of the loading portion of the sequentially nested stress-strain curves illustrated in Fig. 5. The data collected from the test are then divided into individual stress-strain curves and evaluated for material parameters. Volume averaged Young's modulus of the sample E_s is then calculated to be the slope of the linear portion of each cycle, a time dependent graph of which is pictured in Fig. 6.

The region of the curve pictured in Fig. 5 depicting negative stress is a result of the experimental procedure. After each strain cycle is completed, the grips of the load frame are instructed to return to their prestrain location more rapidly than the polymer recovers from the strain. This ensures that the sample recovers from the applied strain as quickly as possible before beginning the subsequent cycle. This viscous behavior is not observed in all

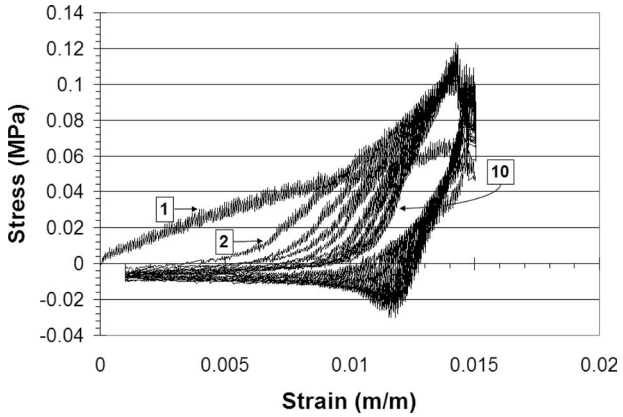

Fig. 5 Example in situ experimental results. Shown are the results of the ten 2 min tests spaced 5 min apart with the loading portion of select curves labeled.

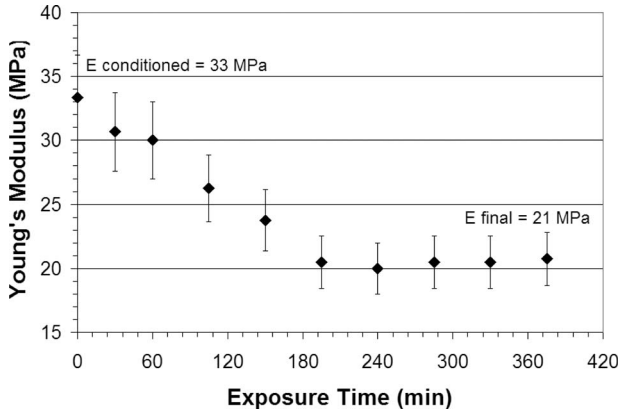

Fig. 7 Time evolution of Young's modulus for sample exposed to 248–280 nm light

LASMPs and is not expected to be prevalent in the evolution of LASMP formulations. Detailed consideration of this response is therefore neglected at this time.

The formulation presented in Fig. 5 has an initial Young's modulus of 4 MPa and stiffens through cross-linking to a steady state value 30 MPa in approximately 80 min. This represents a sevenfold increase in Young's modulus of the material.

Cleaving of the light stimulated cross-links is achieved through reverse stimulation via exposure to 248–280 nm light. A similar procedure to that outlined above for the time evolution of the hardening of the sample is then employed for the time evolution of the softening of the sample. The resulting data similar to Fig. 5 are then evaluated for Young's modulus yielding Fig. 7. The formulation shown reaches a steady state Young's modulus of 21 MPa after just over 3 h. The extended time period needed for cleaving is expected in this effort because the reverse-stimulus light source is a pulsed UV laser emitting 40 μs pulses at 20 Hz versus the continuously emitting laser used for cross-linking.

The total time for transition of the sample may at first appear large compared with thin film studies. For instance, Ikeda et al. [28] report transition times of 20 s and 30 s. However, the current investigation focuses on the property evolution of a polymer with dimensions suitable for load bearing applications. This necessitates the application of thick polymer samples and the corresponding consideration of light transmittance and property evolution through the sample thickness. Earlier studies of thin films neglect these issues via study of sample thickness one to two orders of magnitude smaller.

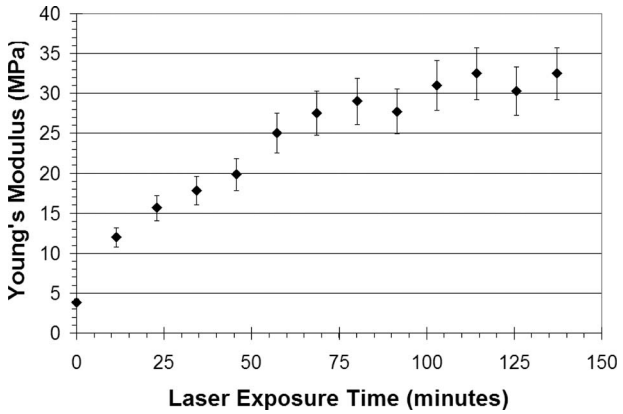

Fig. 6 Time evolution of Young's modulus for sample exposed to 325–385 nm light

3.3 Through Thickness Optical Properties. LASMPs are unique in that the absorption of light enables transition, while the transmission of light is required for through-thickness property transition. It is therefore desirable to quantify the evolution of both absorption and transmission in LASMP. In inactive materials the Beer–Lambert–Bouguer law (Eqs. (2)–(4) [35]) predicts an exponential decay in the transmitted optical power through the thickness of the material [35]. Thus, the intensity of light transmitted through the material quickly diminishes.

$$A = \log_{10}\left(\frac{I_o}{I_i}\right) \tag{2}$$

$$\alpha = \frac{4\pi k}{\lambda} \tag{3}$$

$$A = \alpha l S \tag{4}$$

Here, A is the absorbance of the polymer, I_o and I_i are the incident and transmitted optical intensities, respectively, α is the absorption coefficient, k is the extinction coefficient, λ is the wavelength of incident light, l is the sample thickness, and S is the concentration of absorbing species of the material.

To measure the absorption of the LASMP and to validate the use of Beer–Lambert–Bouguer's law, the optical power meter is positioned behind a sample and measurements are taken at incremental sample strains. The laser is shuttered between measurements; the total amount of time the sample is exposed to the laser is negligible compared with the time required for transition. The thickness of the sample at each measurement is calculated from the measured strain and Poisson's ratio. Equations (2)–(4) are then used to calculate the absorbance of the polymer. Figure 8 illustrates that the absorbance of the polymer is nearly linear with respect to sample thickness, as required by Eq. (4), supporting the use of Beer–Lambert–Bouguer's law to model LASMP.

Not illustrated, but of potential significance in the development of LASMP is that the absorbance of the polymer changes with transition. Absorbance of light results in photomonomer cross-linking and a corresponding decrease in the concentration of that absorbing species. Two experimental procedures are required to assess the impact of the evolution of light absorption: (1) analogous to the procedure accompanying Fig. 8, measurement of the light transmitted through a sample must be taken at several different exposure times and strains, and (2) measurement of the light transmitted through the sample throughout the transition process (Fig. 9).

For the current state of the art LASMP it is found that at any given point in time the polymer follows Beer–Lambert–Bouguer's law, while the total change in transmitted light is only 9%. Furthermore, when the magnitude of this exiting light intensity I_i is

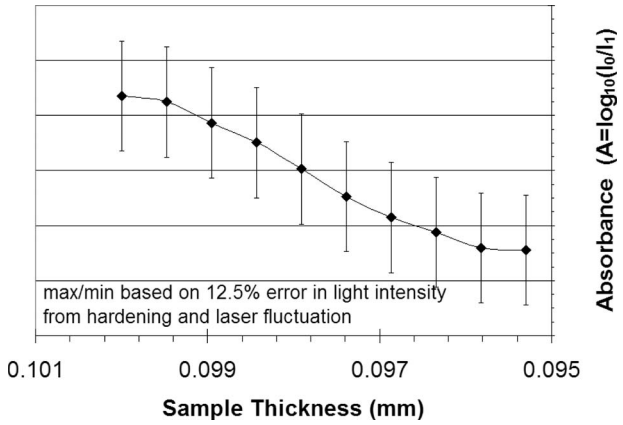

Fig. 8 First generation LASMP absorbance

compared with the magnitude of incident intensity I_o (0.354 μW), a change of only 0.005% is observed. Thus for the current state of the art in LASMP the Beer–Lambert–Bouguer law may be applied directly, without modification. (Also evident in Fig. 9 are the fluctuations of laser intensity discussed in Sec. 2.1.1.)

While for the current state of the art in LASMP development the experimental procedures described for assessing the evolution of absorbance prove only to be precautionary, discarding these procedures as LASMP formulations evolve is discouraged. LASMP performance will improve as synthesis procedures progress toward enabling higher concentrations of photomonomer coupled with improved optical transparency. The paradox is that the Beer–Lambert–Bouguer law is known to become less accurate at high species concentrations, as well as in materials with high scattering [35]; in future LASMP formulations it may become inappropriate to directly impose the Beer–Lambert–Bouguer law. A possible solution is to phenomenologically treat the absorption coefficient as dependent on material thickness as well as laser exposure time.

4 Modeling Through-Thickness Stiffness Evolution

In this section a model appropriate for the through-thickness evolution of stiffness for a current state of the art LASMP is presented. Based on the Beer–Lambert–Bouguer law; the optical intensity of light through the thickness of a sample decays exponentially. From data collected to generate Fig. 8, this decay is found to be

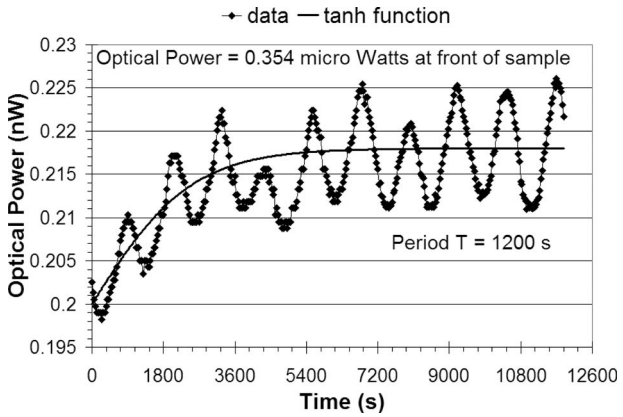

Fig. 9 Time dependence of absorbance

$$I(x) = e^{-82x} \tag{5}$$

where x is the through-thickness position. The chemical kinetics of the system are assumed to be bimolecular in nature, making the reaction causing cross-linking second order (Eq. (6)) [36].

$$\frac{\partial P}{\partial t} = k_1 S(S - P) \tag{6}$$

Here, P is the concentration of the cross-linked product, t is time, k_1 is a constant, and S is the concentration of optically activated species. The degree of cross-linking is assumed to be proportional to the intensity of the light and the concentration of photo-active species at any given point and time, thus,

$$S = k_2 IU \tag{7}$$

Here, k_2 is a constant, U is the concentration of uncross-linked photo-active species, and I is the light intensity at the given location, expressed by Eq. (5). It is important to note the distinction between S, the concentration of optically activated species, and U, the concentration of optically active species. U is the amount of material in the sample that, given enough time and optical energy, has the ability to cross-link. S is the amount of material in the sample that, at the current time, has sufficient optical energy to cross-link.

The local modulus of the polymer at any given point in the material is assumed to be proportional to the degree of cross-linking. Thus, having an expression for the change in concentration of cross-linked product P with respect to time and the change in concentration of optically activated species S, Young's modulus of the polymer at any point through the thickness of the sample may be expressed as

$$E = k_3 P + E_0 \tag{8}$$

where k_3 is a constant and E_0 is the experimentally determined initial Young's modulus of the sample before laser exposure, which in the presented example is 4.5 MPa. Equation (8) predicts the modulus at any given point and time where the quantities I, P, S, and E are dependent on position, x. Finally, the maximum attainable value of Young's modulus at any given location, x, within the sample is fixed at $E_{\max}$ while Young's modulus for the entire sample is found by integrating Eq. (8) over the depth of the sample.

From Eq. (6), we assume that before exposure to the laser, P, the concentration of the cross-linked product, is equal to 0. If we then assume that the polymer used for the current study has a time constant similar to that reported by Ikeda et al. [28] of 0.5 min, then over 0.5 min dP should equal the initial concentration of photo-active species U_0. We then solve for k_1 as

$$k_1 = \frac{1}{0.5 * U_0} \tag{9}$$

From Eq. (7), if we again assume sample conditions before light exposure, I at $x=0$, the front face of the sample, is equal to I_0 and U is equal to U_0. We then assume that the amount of optical energy incident on the front surface of the sample is sufficient to activate all of the available uncross-linked photo-active material, thus S is also equal to U_0. Then,

$$k_2 = 1/I_0 \tag{10}$$

Finally, from Eq. (8) we assume that as time approaches infinity, the Young's modulus of the total sample, and at every position x within the sample, should approach $E_{\max}$. Also, all of the photo-active species in the material should have undergone cross-linking, resulting in P approaching U_0. Then,

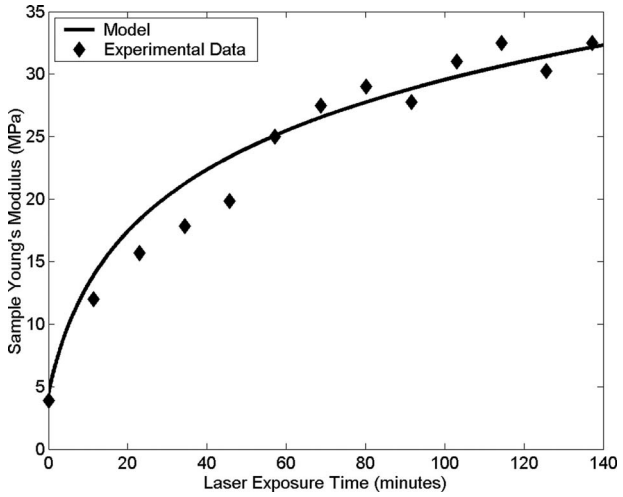

Fig. 10 Model prediction as compared with experimental data

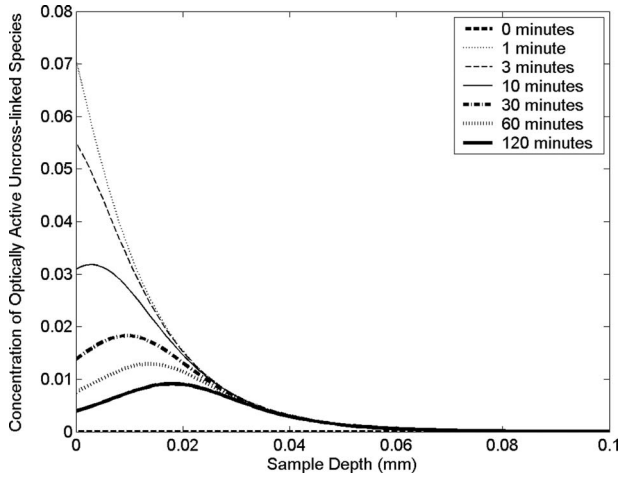

Fig. 11 Predicted through-thickness evolution of photo activated uncross-linked species

$$k_3 = \frac{E_{\max} - E_0}{U_0} \tag{11}$$

As can be inferred from Eqs. (6)–(8), k_1 is related to the efficiency at which the polymer mechanically cross-links given an acceptable environment. An acceptable environment is associated with the amount of optical energy available, the spatial location of cross-linking polymer chains within the sample, as well as other factors. k_2 is representative of the polymer's optical efficiency and the degree to which available light is utilized for cross-linking versus those transmitted, reflected, or absorbed as heat. The constant k_3 is then a measure of the effect cross-linking has on the magnitude of the sample's stiffness.

Finally, the value of $E_{\max}$ is varied until the resulting curve of the total sample Young's modulus versus time coincides with experimental data. Figure 10 illustrates the predicted time evolution of the volume averaged stiffness as compared with the experiment; corresponding to a theoretical value of $E_{\max}$ of 147 MPa. Hence if cross-linking of *every* polymer chain within the sample occurs, the resulting volume averaged Young's modulus would be 147 MPa. As is displayed in the figure, the model prediction corresponds well with the experimental data.

Having an experimentally calibrated model, it is instructive to analyze the through-thickness time evolution of other parameters, such as the concentration of optically activated uncross-linked species, S, and the through-thickness evolution of Young's modulus, E. Pictured in Fig. 11, before exposure to light, S is equal to 0 throughout the sample. After 1 min of exposure, the amount of photo activated material forms a shape similar to that of the exponentially decaying transmitted optical power predicted by the Beer–Lambert law, which is consistent with our assumptions in deriving the equation governing k_1 and k_2. As time progresses, the amount of photo activated species decreases as cross-linking occurs.

Figure 12 illustrates the through-thickness evolution of Young's modulus for various laser exposure times, as predicted by the presented model. The effect of the polymer's ability to transmit light, as expressed through the Beer–Lambert law, is clearly evident in the through-thickness distribution of Young's modulus. Such an observation leads to the realization that while the cross-linking kinetic characteristics play a significant role in the transition time of LASMP, equally important is the ability of the polymer to transmit sufficient amounts of light to enable through-thickness cross-linking. Thus, goals of LASMP synthesis will necessarily include optimization of both of these properties. Application of an empirical modeling strategy, such as this one, enables the assessment of the interplay between these important properties in any given formulation. This information is critical in mapping viable synthesis strategies leading to formulations with increased penetration of property change, and also an increased rate of this change. For instance an inspection of Figs. 11 and 12 together illustrates that even in the absence of an increased rate of chemical kinetics (a conservative assumption), increased transmittance alone will result in deeper penetration of light at any given moment in time, and therefore a larger increase in the volume averaged stiffness at that moment in time; the result is an increased rate of property change at the macroscopic level. Once the interplay between chemical kinetics and transmittance has been optimized for a given formulation family, creative light delivery strategies, such as optical fiber or particle doping, may be employed to further enhance the rate and depth of property transition in LASMP structural components.

5 Conclusions

LASMPs have the potential to rapidly and reversibly transition between hard and soft modulus states separated by an order of magnitude. Furthermore, application of a light stimulus offers significant reduction in power requirements as compared with thermally stimulated SMPs. These qualities make LASMPs attractive for use in multifunction, load bearing adaptive structures. However, LASMP characterization to date has focused on thin films,

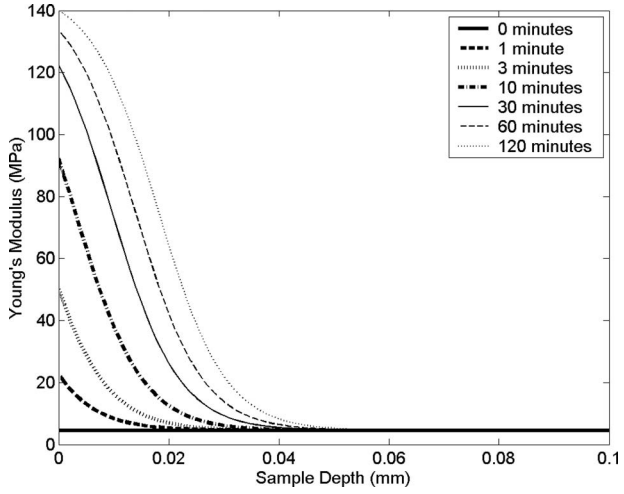

Fig. 12 Predicted evolution of Young's modulus through sample thickness

thereby neglecting the role of through-thickness property evolution. Consideration of through-thickness property evolution is essential for meaningfully assessing and subsequently optimizing the effectiveness of new LASMP formulations in terms of the extent of property change, rate of property change, and power requirements. This work proposes a standardized in situ method for characterizing the temporal and spatial variations inherent in both the stimulus and material transition. Furthermore, the proposed methods enable a detailed consideration of the importance of both the absorbance of the active photomonomer and the through-thickness material transmittance. Application of such a standardized characterization technique will ensure accurate and comparable results across the field as well as aid in the development of this new class of active polymers.

Acknowledgment

The authors would like to acknowledge the assistance and guidance of Ernie Havens, Robert Schueler, Emily Snyder, and Tat Tong of Cornerstone Research Group, Inc. and the financial support of DARPA; Army Contract No. W31P4Q-06-C-0408.

Nomenclature

E_s = Young's modulus of the entire sample
φ_i = volume fraction of the individual bins
E_i = Young's modulus of the individual bins
j = number of bins
A = absorbance
I_o = intensity of the incident light
I_i = light intensity exiting the material
α = absorption coefficient
k = extinction coefficient
λ = wavelength of the light
S = concentration of photo activated species
l = distance light travels through the material
x = position through sample thickness
$E(x)$ = Young's modulus at x position
t = time
$I(x)$ = intensity of light at position x
P = concentration of the cross-linked product
U = concentration of photo-active species
k_1, k_2, k_3 = constants
E_0 = Young's modulus in the soft state
$E_{\max}$ = Young's modulus in the hard state
U_0 = initial concentration of photo-active species before transition

References

[1] Lendlein, A., and Langer, R., 2002, "Biodegradable, Elastic Shape-Memory Polymers for Potential Biomedical Applications," Science, **296**, pp. 1673–1676.
[2] Wache, H. M., Tartakowska, D. J., Hentrich, A., and Wagner, M. H., 2003, "Development of a Polymer Stent With Shape Memory Effect as a Drug Delivery System," J. Mater. Sci.: Mater. Med., **14**, pp. 109–112.
[3] Small, W., IV, Buckley, P. R., Wilson, T. S., Benett, W. J., Hartman, J., Saloner, D., and Maitland, D. J. 2007, "Shape Memory Polymer Stent With Expandable Foam: A New Concept for Endovascular Embolization of Fusiform Aneurysms," IEEE Trans. Biomed. Eng., **54**(6), pp. 1157–1160.
[4] Pastor, C., Sanders, B., Joo, J. J., and McCarty, R., 2006, "Kinematically Designed Flexible Skins for Morphing Aircraft," ASME Paper No. IMECE2006-69674.
[5] Reed, J. L., Jr., Hemmelgarn, C. D., Pelley, B. M., and Havens, E., 2005, "Adaptive Wing Structures," Proc. SPIE, **5762**, pp. 132–142.
[6] Merx, K., 2007, *GM's Grand Experiment: Miracle Materials*, Detroit Free Press, Detroit, MI.
[7] Lendlein, A., and Kelch, S., 2002, "Shape-Memory Effect," Angew. Chem., Int. Ed., **41**, pp. 2036–2057.
[8] Lee, B. S., Chun, B. C., Chung, Y.-C., Sul, K., II, and Cho, J. W., 2001, "Structure and Thermomechanical Properties of Polyurethane Block Copolymers With Shape Memory Effect," Macromolecules, **34**, pp. 6431–6437.
[9] Gall, K., Dunn, M. L., Liu, Y., Stefanic, G., and Balzar, D., 2004, "Internal Stress Storage in Shape Memory Polymer Nanocomposites," Appl. Phys. Lett., **85**(2), pp. 290–292.
[10] Chernous, D. A., Shil'ko, S. V., and Pleskachevskii, Y. M., 2004, "Description of the Shape Memory Effect of Radiation-Modified Polymers Under Thermomechanical Action," J. Eng. Phys. Thermophys., **77**(1), pp. 6–10.
[11] Yang, B., Huang, W., Li, C., Lee, C. M., and Lee, L., 2004, "On the Effects of Moisture in a Polyurethane Shape Memory Polymer," Smart Mater. Struct., **13**, pp. 191–195.
[12] Yang, B., Huang, W. M., Li, C., and Li, L., 2006, "Effects of Moisture on the Thermomechanical Properties of a Polyurethane Shape Memory Polymer," Polymer, **47**, pp. 1348–1356.
[13] Huang, W. M., Yang, B., An, L., Li, C., and Chan, Y. S., 2005, "Water-Driven Programmable Polyurethane Shape Memory Polymer: Demonstration and Mechanism," Appl. Phys. Lett., **86**, p. 114105.
[14] Beblo, R., and Weiland, L. M., 2006, "Polymer Chain Alignment in Shape Memory Polymer," ASME Paper No. IMECE2006-13703.
[15] Poilane, C., Delobelle, P., Lexcellent, C., Hayashi, S., and Tobushi, H., 2000, "Analysis of the Mechanical Behavior of Shape Memory Polymer Membranes by Nanoindentation, Bulging and Point Membrane Deflection Tests," Thin Solid Films, **379**, pp. 156–165.
[16] Tobushi, H., Hara, H., Yamada, E., and Hayashi, S., 1996, "Thermomechanical Properties in a Thin Film of Shape Memory Polymer of Polyurethane Series," Smart Mater. Struct., **5**, pp. 483–491.
[17] Tobushi, H., Matsui, R., Takada, T., and Hayashi, S., 2004, "Shape Fixity and Shape Recovery of Shape Memory Polymer and Their Applications," *Proceedings of the XXI ICTAM*, Warsaw, Poland, Aug. 15–21.
[18] Tobushi, H., Matsui, R., Hayashi, S., and Shimada, D., 2004, "The Influence of Shape-Holding Conditions on Shape Recovery of Polyurethane-Shape Memory Polymer Foams," Smart Mater. Struct., **13**, pp. 881–887.
[19] Wei, Z. G., Sandstrom, R., and Miyazaki, S., 1998, "Shape-Memory Materials and Hybrid Composites for Smart Systems," J. Mater. Sci., **33**, pp. 3743–3762.
[20] Schmidt, A. M., 2006, "Electromagnetic Activation of Shape Memory Polymer Networks Containing Magnetic Nanoparticles," Macromol. Rapid Commun., **27**, pp. 1168–1172.
[21] Snyder, E. A., and Tong, T. H., 2005, "Towards Novel Light-Activated Shape Memory Polymer: Thermomechanical Properties of Photo-Responsive Polymers," Mater. Res. Soc. Symp. Proc., **872**, pp. 353–358.
[22] Havens, E., Snyder, E. A., and Tong, T. H., 2005, "Light-Activated Shape Memory Polymers and Associated Applications," Proc. SPIE, **5762**, pp. 48–55.
[23] Tong, T., and Snyder, E., "Light Activated Shape Memory Co-Polymers," World Intellectual Property Organization, Publication No. WO/2007/001407.
[24] Lendlein, A., Jiang, H., Jünger, O., and Langer, R., 2005, "Light-Induced Shape Memory Polymers," Nature (London), **434**, pp. 879–882.
[25] Lee, B. S., Chun, B. C., Chung, Y.-C., Sul, K. I, and Cho, J. W., 2001, "Structure and Thermomechanical Properties of Polyurethane Block Copolymers With Shape Memory Effect," Macromolecules, **34**, pp. 6431–6437.
[26] Racz, L. M., Li, L., and Abedian, B., 1998, "Cure Kinetics of Light-Activated Polymers," J. Polym. Sci., Part B: Polym. Phys., **36**, pp. 2887–2894.
[27] Finkelmann, H., Nishikawa, E., Pereira, G. G., and Warner, M., 2001, "A New Opto-Mechanical Effect in Solids," Phys. Rev. Lett., **87**(1), p. 015501.
[28] Ikeda, T., Nakano, M., Yu, Y., Tsutsumi, O., and Kanazawa, A., 2003, "Anisotropic Bending and Unbending Behavior of Azobenzene Liquid-Crystalline Gels by Light Exposure," Adv. Mater. (Weinheim, Ger.), **15**(3), pp. 201–205.
[29] Yu, Y., Nakano, M., and Ikeda, T., 2003, "Directed Bending of a Polymer Film by Light," Nature (London), **425**, p. 145.
[30] Li, M.-H., Keller, P., Li, B., Wang, X., and Brunet, M., 2003, "Light-Driven Side-on Nematic Elastomer," Adv. Mater. (Weinheim, Ger.), **15**(7–8), pp. 569–572.
[31] Personal correspondence with Tat Tong of Cornerstone Research Group, Dayton, OH.
[32] Figger, H., Meschede, D., and Zimmermann, C., 2002, *Laser Physics at the Limits*, Springer-Verlag, Berlin, Germany.
[33] Slaughter, W. S., 2002, *The Linearized Theory of Elasticity*, Birkhauser, Boston, pp. 226–232.
[34] Hodgkinson, J. M., 2000, *Mechanical Testing of Advanced Fibre Composites*, Woodhead, Cambridge, UK, pp. 15–16.
[35] Akhmanov, S. A., and Nikitin, S. Y., 1997, *Physical Optics*, Oxford University Press, New York, pp. 93–100.
[36] Pannetier, G., and Souchay, P., 1967, *Chemical Kinetics*, Elsevier, New York, pp. 133–137.

A Nonlinear Rubber Material Model Combining Fractional Order Viscoelasticity and Amplitude Dependent Effects

N. Gil-Negrete[1]
e-mail: ngil@ceit.es

J. Vinolas

Department of Applied Mechanics,
CEIT and Tecnun (University of Navarra),
Paseo Manuel Lardizabal 15,
20018 San Sebastian, Spain

L. Kari
Department Aeronautical and Vehicle
Engineering, MWL,
KTH,
SE-10044 Stockholm, Sweden

A nonlinear rubber material model is presented, where influences of frequency and dynamic amplitude are taken into account through fractional order viscoelasticity and plasticity, respectively. The problem of simultaneously modeling elastic, viscoelastic, and friction contributions is removed by additively splitting them. Due to the fractional order representation mainly, the number of parameters of the model remains low, rendering an easy fitting of the values from tests on material samples. The proposed model is implemented in a general-purpose finite element (FE) code. Since commercial FE codes do not contain any suitable constitutive model that represents the full dynamic behavior of rubber compounds (including frequency and amplitude dependent effects), a simple approach is used based on the idea of adding stress contributions from simple constitutive models: a mesh overlay technique, whose basic idea is to create a different FE model for each material definition (fractional derivative viscoelastic and elastoplastic), all with identical meshes but with different material definition, and sharing the same nodes. Fractional-derivative viscoelasticity is implemented through user routines and the algorithm for that purpose is described, while available von Mises' elastoplastic models are adopted to take rate-independent effects into account. Satisfactory results are obtained when comparing the model results with tests carried out in two rubber bushings at a frequency range up to 500 Hz, showing the ability of the material model to accurately describe the complex dynamic behavior of carbon-black filled rubber compounds.
[DOI: 10.1115/1.2999454]

Keywords: rubber, dynamic stiffness, viscoelasticity, Fletcher–Gent effect, FE code, vibration isolator

1 Introduction

Since in 1839 Charles Goodyear discovered that a material with unique mechanical properties was produced by heating a mixture of rubber, lead, and sulfur, rubber has played an important role in many applications in the field of vibration isolation and noise abatement. Its properties of viscoelasticity have resulted in a variety of applications, ranging from bearings, springs, or seals to shock absorbing bushings. When a source has to be connected to a receiving structure, mounting it upon vibration isolators attains a simple vibration transmission reduction. Rubber elements play here an important role as they are designed to reduce transmissibility while providing adequate dynamic behavior and stability.

Despite rubber being so common, deep knowledge of material properties is quite often poor among design engineers. Insufficient knowledge of transmission and damping properties of rubber mounts requires industry to carry out costly experimental work for optimizing the shape, location, and volume of these units. Without the appropriate material knowledge, modeling of mounts is usually simplified by considering a single linear spring. Values used in the design stage are estimated from quasistatic elastic characteristics, and damping, if considered, is most of the times represented by a unique dashpot of arbitrary parameter. When vibration isolation becomes an important issue in a specific design, a deeper understanding of the dynamic behavior of rubber and of the modeling techniques that help producing the final component is needed.

Rubber compound frequently has carbon-black filler added, consisting of very small carbon particles forming agglomerates within the rubber material. Inclusion of filler increases the hardness and damping of the material while resulting in nonlinear characteristics. Dynamic properties of rubber, dependent on frequency and temperature, develop amplitude dependent characteristics, an effect known as Fletcher–Gent effect [1]. Jurado et al. [2], Medalia [3], Sjöberg [4], Dean et al. [5], and Wang [6], for example, have conducted good reviews of the influence of strain amplitude, frequency, and temperature on the mechanical rubber characteristics based on experimental measurements. The work by Wang also presents theories and observations about why the inclusion of filler alters the linear dynamic stress-strain response of unfilled rubber compounds. Because of its nonlinear characteristics, the prediction of the response of a rubber bushing to excitation becomes a complex issue.

Nonlinear elasticity has been the characteristic receiving special attention over the years, since the early 20th century [7–10] up to present [11–14]. A convenient technique to include preload dependence is to assume hyperelastic material behavior using strain energy functions. Numerous variations of strain energy functions are reported in literature (see Refs. [7–17], for example), where Mooney–Rivlin, Arruda–Boyce, Ogden, and Yeoh forms are the most popular ones.

The frequency dependence of the material is usually represented by viscoelastic models. The most popular model is the Kelvin–Voigt model, where a viscous dashpot is coupled in par-

[1]Corresponding author.

Contributed by the Applied Mechanics Division of ASME for publication in the JOURNAL OF APPLIED MECHANICS. Manuscript received February 18, 2008; final manuscript received July 16, 2008; published online November 5, 2008. Review conducted by Krishna Garikipati.

allel to an elastic frequency independent spring. Nevertheless, this model cannot be tuned except for a very small frequency range, as it either overestimates at higher frequencies or underestimates at the lowest frequencies the loss factor of the dynamic stiffness [18]. Better description of material behavior can be obtained by adding a spring in series with the dashpot (known as a Maxwell chain) and increasing the number of Maxwell chains in the model [18–21]. For a full multiaxial case, linear viscoelastic constitutive equations are usually formulated in terms of hereditary or convolution integrals. The most interesting such models have been proposed by Lubliner [22], Johnson et al. [23,24], Yang et al. [25], and Simo [26], whose model is also focused on the inclusion of Mullins' effect [27].

As the models include more elements (springs and dashpots), the complexity and the number of parameters needed to accurately describe material properties are highly increased (see discussion in Ref. [18]), complicating the fitting of material constant values. An alternative method to obtain good description of viscoelastic material's frequency dependence while reducing drastically the required number of parameters is by using constitutive relations that include derivatives of noninteger order, known as fractional order derivatives. Although the mathematical history of fractional order derivatives goes back to the 17th century [28], its use in the field of linear viscoelasticty became known with Bagley and Torvik in the 1980s [29]. Since then numerous authors conducted research on fractional order derivative viscoelasticity and successfully included it in their applications connected to rubber mounts, e.g., Refs. [30–38].

Fractional-derivative viscoelastic models are suitable to be used in a structural dynamic analysis and may be implemented in a general-purpose finite element (FE) code. Time domain formulations are given by, e.g., Padovan [39], Enelund et al. [40], Zhang and Shimizu [41], and Schmidt and Gaul [42]. Equations of motion are usually solved using Grünwald's algorithm [40,41].

Viscoelastic models are all linear, meaning that they do not account for amplitude dependence. While interesting due to their reduced number of material parameters, the main drawback of the above mentioned material models [39–42] is that they are only suitable for lightly filled rubbers with negligible amplitude dependent characteristics. However, as the amount of carbon-black filler increases in the mixture, a good model for the amplitude dependence might be equally important as a proper frequency description. One approach involves working with nonlinear viscous damping forces [43–46]. Nevertheless, the Fletcher–Gent effect is usually denoted as plastic effect [47]. It can be attributed to irreversible slip processes between the filler particles and their plastic deformations [48]. This has motivated the characterization of amplitude dependent effects through friction elements, which is the idea behind Gregory [49] or Austrell [50] models, where several friction chains involving Coulomb friction elements are connected in parallel to obtain good results. In the latter work, implementation in a general-purpose finite element code is done making use of the von Mises elastoplasticity already available in the FE codes.

In this paper, we develop a rubber material model that considers both frequency and friction characteristics and that can be implemented in a commercial FE code. The model is an extension of Enelund's one [40] incorporating the amplitude dependent behavior of carbon-black filled rubber, ignored there. Friction effects are implemented through Coulomb friction elements.

The inclusion of friction effects in the material model makes it suitable to predict the dynamic behavior of bushings under working conditions, where applied displacements do not have to be known in advance. The development of a model that includes frequency and amplitude dependencies allows predicting an accurate response of a system in the moderate frequency range where various amplitudes are often found. Furthermore, its implementation in a finite element code provides a powerful tool for the design of isolators: The dynamic frequency and amplitude dependent dynamic stiffness can be estimated without having to physically produce the mount, avoiding the "trial and error" method so common in the rubber industry. Finally, due to the implementation of fractional order viscoelasticity, the number of parameters remains lower than in other models adopting classical viscoelasticity [50] and rendering an easier fitting of their values from tests conducted on material samples. This is another clear advantage that speeds the process of predicting the dynamic stiffness of rubber elements in a desired frequency and amplitude range.

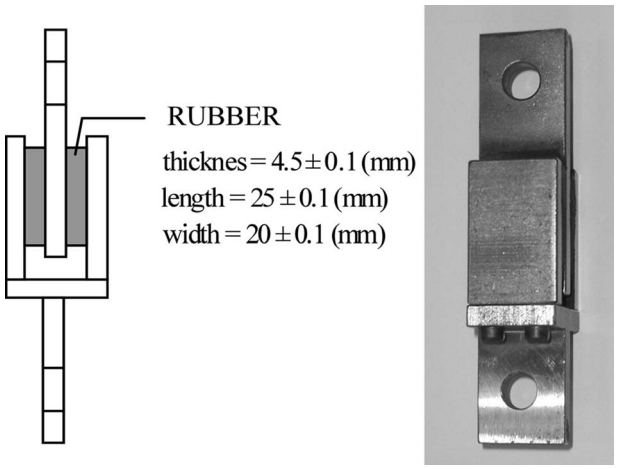

Fig. 1 Simple shear specimen

2 Material Testing

Because rubbers are not perfectly elastic, the strain during cyclic (harmonic) deformation always lags slightly behind the stress. Therefore, the application of a sinusoidal strain will result in a stress of the same frequency but shifted an amount termed loss angle. It is very convenient to consider both the elastic in phase response and the out of phase response, in terms of two moduli. The overall response can then be expressed as a complex modulus (Eq. (1)):

$$G^* = G_{\text{stor}} + iG_{\text{loss}} = G_{\text{stor}}(1 + i \tan \delta) \tag{1}$$

G_{stor} represents the in phase storage modulus, G_{loss} represents the out of phase loss modulus, and $i = \sqrt{-1}$. The phase or loss angle δ is given by $\tan \delta = G_{\text{loss}}/G_{\text{stor}}$. The ratio $G_{\text{loss}}/G_{\text{stor}}$ is usually denoted as the loss factor η. The loss angle provides a measure of the damping or hysteretical energy losses within the rubber subjected to cyclic deformation.

Both the magnitude ($|G^*| = \sqrt{G_{\text{stor}}^2 + G_{\text{loss}}^2}$) and the loss angle of natural rubber compounds generally depend on temperature, frequency, and dynamic strain amplitude. To accurately characterize the dynamic behavior of a mixture, its shear modulus and its dependencies of the above parameters have to be measured.

Following the guide edited by the ASTM [51], which is focused on describing various procedures for determining the dynamic properties of vulcanized rubber materials, a forced nonresonant simple shear test has been conducted using the specimen shown in Fig. 1. Measurement results will be used to fit the material model described in this paper.

Four different natural rubber mixtures have been investigated, with various amounts and types of carbon-black and thus showing different hardness. The mixtures are named after their hardness, from Shore A 40 to Shore A 70 (approximately). Four specimens of each compound are measured, to ensure the repeatability of the results. Furthermore, the samples have been mechanically conditioned to account for Mullins' effect [27], meaning that three or four previous cycles have been applied before recording the measurement to avoid further stress softening due to cyclic loading.

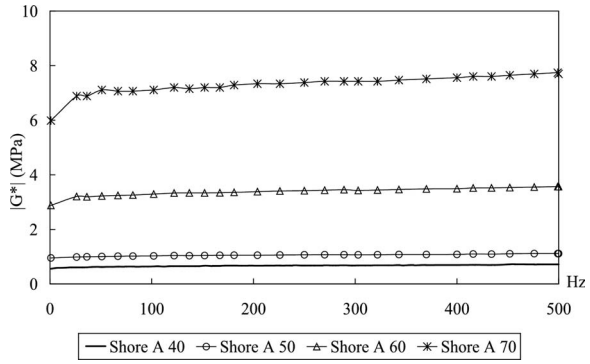

Fig. 2 Magnitude of shear modulus (MPa) as a function of frequency. Dynamic strain amplitude of 0.02 mm. Room temperature (23°C).

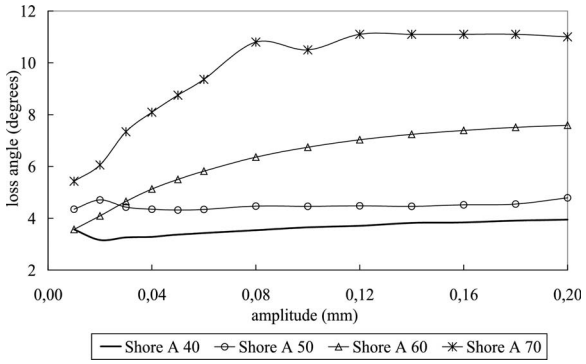

Fig. 4 Loss angle of shear modulus (deg) as a function of dynamic strain amplitude. Frequency of 102 Hz. Room temperature (23°C).

Experimental tests have been carried out at Seat Centro Técnico in a Schenck, hydropulse High-Frequency Testing Machine VHF 7. In the test with simple shear specimens, the frequency range covers 0–500 Hz and the peak amplitude range varies between 0.01 mm and 0.2 mm. Applied maximum strain level is sufficiently small to ensure a simple shear deformation. In what follows, the influence of frequency and dynamic strain amplitude on the complex shear modulus are presented briefly.

The magnitude of shear modulus as a function of frequency is shown in Fig. 2. In the region of interest, the influence of frequency is slight, although an increase of the value is observed as the mixture is more heavily filled. Similar pattern might be observed for the loss angle, with heavily filled mixtures exhibiting higher loss angles than unfilled ones.

The dependence of the magnitude and loss angle of shear modulus with the dynamic strain amplitude might be seen in Figs. 3 and 4. Natural rubber compounds display larger dynamic modulus at small amplitudes than at larger dynamic strain amplitudes. The effect is more pronounced as the amount of fillers is increased in the compound, so that unfilled rubbers could be considered not dependent on amplitude at all. The main reason of this effect is believed to be the breakdown of interactions within the filler and between the filler and the rubber matrix [52].

3 Description of the Material Model Proposed

The mechanical analogy to the material model adopted is presented in Fig. 5. It combines a fractional order Zener model, described later in Sec. 3.1, with a number of N friction chains in parallel, yielding a model that sums elastic, viscous, and friction stresses:

$$\tau_{\text{total}} = \tau_{\text{elastic}} + \tau_{\text{FD}} + \sum_{k=1}^{N} \tau_{\text{friction},k} \tag{2}$$

In Eq. (2), $\tau_{\text{elastic}} + \tau_{\text{FD}}$ represents the stress on the fractional-derivative Zener model and $\tau_{\text{friction},k}$ represents the stress over the kth friction chain.

The model in Fig. 5 is an extension of that proposed by Enelund et al. [40] by incorporating the amplitude dependent characteristics of the material. Friction Maxwell chains are selected to represent the rate-independent part of the model. Note that several friction chains are needed to get smooth hysteretic loops, similar to the measured ones. Note also that linear elasticity is defined in the model due to the constant parameter for the elastic spring. Therefore, the S-shaped hysteresis loops that appear at very high excitation amplitudes are not considered by the model. It is suggested that the model includes nonlinear elasticity to be completely general, which means that the spring should follow a hyperelastic law [21,36,50].

The material model proposed herein and described in more details below makes the most of Enelund's [40] proposal, that is, its ability to provide an accurate description of frequency dependent characteristics of vulcanized rubbers with a low number of parameters, while the inclusion of friction chains extends its use to characterize carbon-black filled rubbers where amplitude dependent behavior is not negligible. The result is an easy to fit nonlinear material model that accounts for both frequency and amplitude effects of rubber, making it extremely straightforward to predict the dynamic stiffness of rubber isolators in working conditions, where various amplitudes may be found in a frequency range.

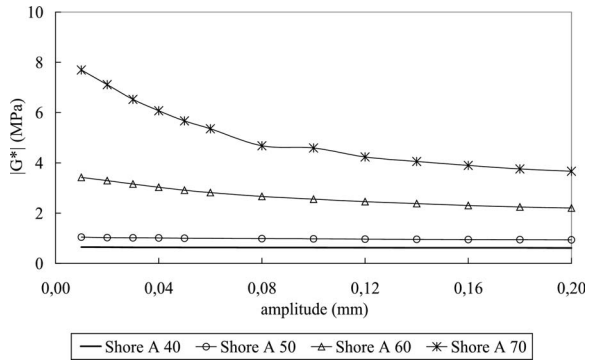

Fig. 3 Magnitude of shear modulus (MPa) as a function of dynamic strain amplitude. Frequency of 102 Hz. Room temperature (23°C).

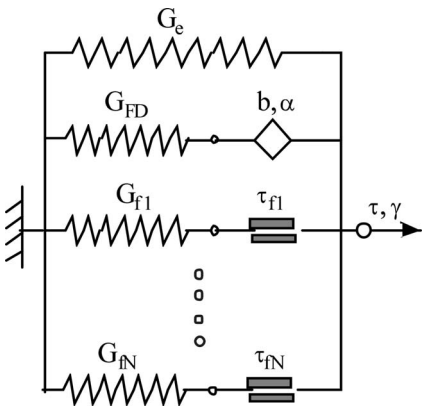

Fig. 5 Mechanical analogy of the non-linear material model adopted

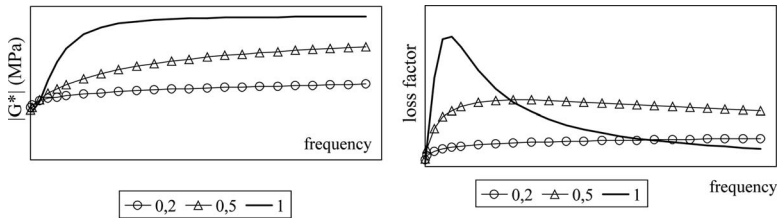

Fig. 6 Frequency dependent complex shear modulus provided by fractional order Zener modulus for different values of α

A short description of the different parts of this mechanical model is given below.

3.1 Fractional-Derivative Zener Model. The basis of fractional-derivative technique for linear viscoelasticity is to use constitutive equations (similar to those given by the simple viscoelastic models) including time derivatives of noninteger order, known as fractional derivatives. Dashpot elements on classical viscoelastic models are replaced by pot elements (see Fig. 5), rendering a stress that is proportional to the time derivative of fractional order of the strain.

Elastic and viscous stresses in the nonlinear model adopted are represented through the fractional-derivative Zener model, which combines a linear spring of constant G_e in parallel with another spring of constant G_{FD} and a pot of constants b and α (the order of derivatives). Modeling of viscoelasticity normally results in the order of the time derivative $\alpha \in (0,1]$. When the model in Fig. 5 is subjected to a shear strain γ, the stress over the elastic and viscous chains lead to a value:

$$\tau_{\mathrm{FD\ Zener}} = \tau_{\mathrm{elastic}} + \tau_{\mathrm{FD}} = G_e\gamma + G_{\mathrm{FD}}(\gamma - \gamma^v_{\mathrm{FD}}) \tag{3}$$

where γ^v_{FD} in Eq. (3) represents the strain over the pot element in the fractional-derivative chain. Its value is obtained through the resolution of the following equation:

$$D^\alpha(\gamma^v_{\mathrm{FD}}) = \frac{G_{\mathrm{FD}}}{b}(\gamma - \gamma^v_{\mathrm{FD}}) \tag{4}$$

where $D^\alpha(\cdot)$ operator stands for the α-order fractional derivative.

Probably the most common definition of a fractional derivative is through the Riemann–Liouville convolution integral [28]. For $\alpha \in (0,1]$, it reads

$$D^\alpha(f(t)) = \frac{1}{\Gamma(1-\alpha)}\frac{d}{dt}\int_0^t \frac{f(\tau)}{(t-\tau)^\alpha}d\tau, \quad \alpha \in (0,1] \tag{5}$$

Equation (5), in general, cannot be solved analytically for γ^v_{FD} in Eq. (4) and the fractional derivative has to be numerically evaluated. A suitable truncation of Grünwalds algorithm of differential-integration allows evaluating fractional derivatives in time domain [28]:

$$D^\alpha(f(t)) = \lim_{n\to\infty}\frac{(t/n)^{-\alpha}}{\Gamma(-\alpha)}\sum_{j=0}^{n-1}\frac{\Gamma(j-\alpha)}{\Gamma(j+1)}f\left(t - \frac{jt}{n}\right) \tag{6}$$

By simply omitting the $n\to\infty$ operation and letting $t=n\Delta t$, Δt being the time increment, Eq. (6) provides the value of the fractional derivative of function $f(t)$ at time $n\Delta t$. At time $t=(n+1)\Delta t$,

$$D^\alpha({}^{n+1}f) = \frac{1}{(\Delta t)^\alpha}\sum_{j=0}^{n} c_j(\alpha)^{n+1-j}f \tag{7}$$

where ${}^nf$ represents the value of fractional derivative of function $f(t)$ at time $n\Delta t$. Coefficients $c_j(\alpha)$ are given by Eq. (8), by the recursion formula for the gamma function:

$$c_0(\alpha) = 1, \quad c_1(\alpha) = 1,$$

$$c_j(\alpha) = \frac{\Gamma(j-\alpha)}{\Gamma(-\alpha)\Gamma(j+1)} = \frac{j-1-\alpha}{j}c_{j-1}(\alpha) \tag{8}$$

The definition of fractional derivative (Eq. (5)) is greatly simplified when applying the Fourier transform to it. The Fourier transform of the fractional derivative of order α of $f(t)$ results in $(i\omega)^\alpha$ times the Fourier transform of $f(t)$ [21]:

$$\int_{-\infty}^{\infty}[D^\alpha(f(t))]e^{-i\omega t}dt = (i\omega)^\alpha\int_{-\infty}^{\infty}f(t)e^{-i\omega t}dt = (i\omega)^\alpha\hat{f} \tag{9}$$

In Eq. (9), $\hat{f}$ represents the Fourier transform of $f(t)$.

Applying Fourier transforms to Eqs. (3) and (4) leads to

$$\hat{\tau}_{\mathrm{FD\ Zener}} = \hat{\gamma}\left(G_e + \frac{G_{\mathrm{FD}}b(i\omega)^\alpha}{G_{\mathrm{FD}} + b(i\omega)^\alpha}\right) \rightarrow G^* = G_e + \frac{G_{\mathrm{FD}}b(i\omega)^\alpha}{G_{\mathrm{FD}} + b(i\omega)^\alpha} \tag{10}$$

The magnitude and loss factor of the complex shear modulus according to Eq. (10) are represented in Fig. 6. Variation of the order of the time derivative α in the $(0,1]$ range leads to different responses of the model in the frequency domain, making it very promising to represent frequency dependent characteristics with a low number of parameters. The classical viscoelastic Zener model ($\alpha=1$ in the previous definitions) is not able to reproduce accurately measured characteristics of the material, especially the loss factor (see experimental results for natural rubber compounds in Sec. 2).

3.2 Friction Chains. The presence of filler in rubber compounds distorts the hysteresis loop: filled rubbers develop parallelogram-shaped hysteresis loops, instead of elliptical ones characteristic of lightly filled rubber compounds. This rate-independent response of the material is modeled through chains composed of a Coulomb friction element connected in series to a spring, a model known as a friction Maxwell model.

When the model in Fig. 5 is subjected to a shear strain γ, the stress over a friction chain is given by

$$\tau_{\mathrm{friction},k} = G_{fk}\gamma \quad \text{while} \quad \tau_{\mathrm{friction},k} < T_{fk}$$

$$\tau_{\mathrm{friction},k} = T_{fk} \quad \text{while} \quad \tau_{\mathrm{friction},k} \geq T_{fk} \tag{11}$$

The rate-independent damping in a friction chain is fully developed when the stress in the component reaches T_{fk}. While the stress in the chain is less than T_{fk}, the two blocks in the Coulomb element are fixed together and a linear response is given by the spring (see Fig. 7). Once the maximum stress level T_{fk} is achieved sliding in the Coulomb element occurs. Equation (11) might be rewritten as Eq. (12), where $\gamma_{fk}=T_{fk}/G_{fk}$ denotes the strain level at which sliding occurs.

$$\tau_{\mathrm{friction},k} = G_{fk}\gamma \quad \text{while} \quad \gamma < \gamma_{fk} = T_{fk}/G_{fk}$$

$$\tau_{\mathrm{friction},k} = T_{fk} \quad \text{while} \quad \gamma \geq \gamma_{fk} = T_{fk}/G_{fk} \tag{12}$$

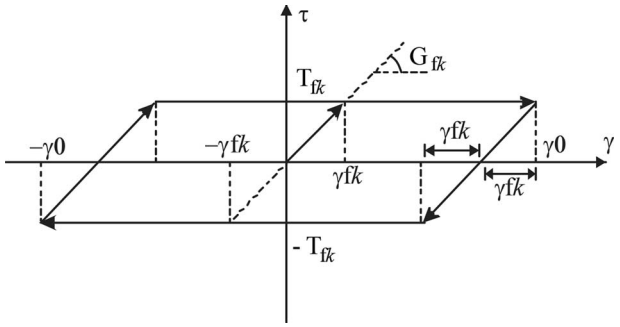

Fig. 7 Rate-independent behavior of a unique Maxwell friction chain

The addition of several friction Maxwell chains in parallel results in a smoother stress/strain curve or hysteresis loop than that shown in Fig. 7, which is closer to measured characteristics of rubber mixtures.

4 Implementation of the Model in a FE Code

4.1 The Overlay Technique. Since the commercial FE codes do not contain any suitable constitutive model that represents the full dynamic behavior of rubber compounds (including frequency and amplitude dependent effects), a simple approach is used based on the idea of adding stress contributions from simple constitutive models: An overlay technique. This fraction model was originally proposed by Besseling [53] and has successfully been used by Austrell et al. [50]. Its basic idea is to create a different FE model for each material definition (fractional derivative viscoelastic and friction), all with identical meshes but with different material definitions, and sharing the same nodes. The results obtained would be the equivalent to those of the mechanical model in Fig. 5 with elastic, viscoelastic, and friction models in parallel, as displacements (or strains) are maintained the same, and forces (or stresses) are summed up.

A generalization of the one-dimensional constitutive model represented in Eq. (2) to the multiaxial state would be to add the stress tensors:

$$\boldsymbol{\sigma}_{\text{total}} = \boldsymbol{\sigma}_{\text{elastic}} + \boldsymbol{\sigma}_{\text{FD}} + \boldsymbol{\sigma}_{\text{friction}} \tag{13}$$

4.2 Implementation of Fractional-Derivative Viscoelasticity. In a multiaxial stress/strain system and decomposing stress and strain tensors in their volumetric and deviatoric parts (σ_{vol} and $\boldsymbol{\sigma}_{\text{dev}}$ for the stress and ε_{vol} and $\boldsymbol{\varepsilon}_{\text{dev}}$ for the strain), Eqs. (3) and (4) become

$$\sigma_{\text{vol}} = \sigma_{e,\text{vol}} + \sigma_{\text{FD,vol}} = 3K_e\varepsilon_{\text{vol}} + 3K_{\text{FD}}(\varepsilon_{\text{vol}} - \varepsilon^v_{\text{FD,vol}})$$

$$\boldsymbol{\sigma}_{\text{dev}} = \boldsymbol{\sigma}_{e,\text{dev}} + \boldsymbol{\sigma}_{\text{FD,dev}} = 2G_e\boldsymbol{\varepsilon}_{\text{dev}} + 2G_{\text{FD}}(\boldsymbol{\varepsilon}_{\text{dev}} - \boldsymbol{\varepsilon}^v_{\text{FD,dev}}) \tag{14}$$

where $\sigma_{e,\text{vol}}$ and $\sigma_{\text{FD,vol}}$ represent the contributions of the elastic and fractional order chains to the total volumetric stress, whereas $\boldsymbol{\sigma}_{e,\text{dev}}$ and $\boldsymbol{\sigma}_{\text{FD,dev}}$ represent the contributions of the elastic and fractional order chains to the total deviatoric stress. Similarly, $\varepsilon^v_{\text{FD,vol}}$ and $\boldsymbol{\varepsilon}^v_{\text{FD,dev}}$ stand for the volumetric and deviatoric strains over the pot element.

$$D^{\alpha_{\text{vol}}}(\varepsilon^v_{\text{FD,vol}}) = \frac{G_{\text{FD}}}{b_{\text{vol}}}(\varepsilon_{\text{vol}} - \varepsilon^v_{\text{FD,vol}})$$

$$D^{\alpha_{\text{dev}}}(\boldsymbol{\varepsilon}^v_{\text{FD,dev}}) = \frac{G_{\text{FD}}}{b_{\text{dev}}}(\boldsymbol{\varepsilon}_{\text{dev}} - \boldsymbol{\varepsilon}^v_{\text{FD,dev}}) \tag{15}$$

Note that the generalization of the uniaxial model in Fig. 5 to the multiaxial stress/strain state results in eight parameters: K_e and G_e (elastic chain); K_{FD}, G_{FD}, α_{vol}, α_{dev}, b_{vol}, and b_{dev} (fractional-derivative chain).

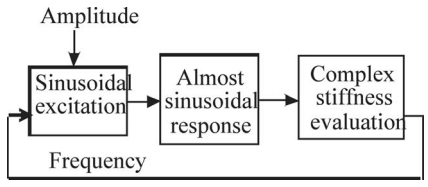

Fig. 8 Practical procedure to obtain the dynamic stiffness of components

Implementation in a commercial FE code requires Eq. (15) to be numerically evaluated, both for the volumetric and deviatoric parts. The algorithm created for the integration of the response is based on the work by Enelund et al. [40], applying the suitable truncation of differ-integration in Eq. (6). Therefore, considering only the fractional derivative and volumetric part of the response in Eqs. (14) and (15):

$$D^{\alpha_{\text{vol}}}(\varepsilon^v_{\text{FD,vol}}) = \frac{G_{\text{FD}}}{b_{\text{vol}}}\left(\frac{\sigma_{\text{FD,vol}}}{3K_{\text{FD}}}\right) \tag{16}$$

Applying the general midpoint rule to Eq. (16),

$$D^{\alpha_{\text{vol}}}({}^{n+1}\varepsilon^v_{\text{FD,vol}}) = \frac{G_{\text{FD}}}{b_{\text{vol}}}\frac{1}{3K_{\text{FD}}}(\theta^{n+1}\sigma_{\text{FD,vol}} + (1-\theta)^n\sigma_{\text{FD,vol}}) \tag{17}$$

where ${}^{n+1}(\ )$ denotes the value of the function at time $(n+1)\Delta t$ and $\theta \in (0,1]$ shows the implicitness of the integration in standard fashion, e.g., the classical midpoint rule is defined by $\theta=\frac{1}{2}$, whereas the backward Euler rule is defined by $\theta=1$. As for the fractional derivative in Eq. (17), Eq. (7) is recalled, giving

$$D^{\alpha_{\text{vol}}}(\varepsilon^v_{\text{FD,vol}}) = \frac{1}{(\Delta t)^{\alpha_{\text{vol}}}}(c_0{}^{n+1}\varepsilon^v_{\text{FD,vol}} - {}^n\bar{\varepsilon}^v_{\text{FD,vol}}) \tag{18}$$

where

$${}^n\bar{\varepsilon}^v_{\text{FD,vol}} = -\sum_{j=1}^{n} c_j(\alpha_{\text{vol}})^{n+1-j}\varepsilon^v_{\text{FD,vol}} \tag{19}$$

The term ${}^n\bar{\varepsilon}^v_{\text{FD,vol}}$ in Eq. (19) stores the complete history of the viscous strain (see Sec. 3.1 and Eq. (8) for evaluation of the coefficients c_j).

Operating with Eqs. (17)–(19) leads to the numerical solution for the updated dissipative stress:

$${}^{n+1}\sigma_{\text{FD,vol}} = {}^{n+1}\sigma^{vv}_{\text{FD,vol}} + c_0A\Delta\sigma^{ve}_{\text{FD,vol}} \tag{20}$$

where

$${}^{n+1}\sigma^{vv}_{\text{FD,vol}} = A\left[\frac{G_{\text{FD}}(\Delta t)^{\alpha_{\text{vol}}}}{b_{\text{vol}}}(\theta-1) + c_0\right]{}^n\sigma_{\text{FD,vol}} + 3K_{\text{FD}}A[c_0{}^n\varepsilon^v_{\text{FD,vol}} - {}^n\bar{\varepsilon}^v_{\text{FD,vol}}] \tag{21}$$

and

$$\Delta\sigma^{ve}_{\text{FD,vol}} = 3K_{\text{FD}}\Delta\varepsilon_{\text{vol}} = 3K_{\text{FD}}({}^{n+1}\varepsilon_{\text{vol}} - {}^n\varepsilon_{\text{vol}}) \tag{22}$$

The term A in Eqs. (20) and (21) is provided below:

$$A = \left[\frac{G_{\text{FD}}(\Delta t)^{\alpha_{\text{vol}}}}{b_{\text{vol}}}\theta + c_0\right]^{-1} \tag{23}$$

The updated strains can now be calculated:

$${}^{n+1}\varepsilon^v_{\text{FD,vol}} = \frac{1}{c_0}\left[{}^n\bar{\varepsilon}^v_{\text{FD,vol}} + \frac{G_{\text{FD}}(\Delta t)^{\alpha_{\text{vol}}}}{b_{\text{vol}}}\frac{1}{K_{\text{FD}}}(\theta^{n+1}\sigma_{\text{FD,vol}} + (1-\theta)^n\sigma_{\text{FD,vol}})\right] \tag{24}$$

Fig. 9 Bushing 1: cylindrical rubber bushing with two holes. Shore A 50.

A similar procedure might be applied for the deviatoric part in expressions (14) and (15), which would provide the final numerical solution for the deviatoric updated dissipative stress and strain.

$$^{n+1}\boldsymbol{\sigma}_{\mathrm{FD,dev}} = {}^{n+1}\boldsymbol{\sigma}^{vv}_{\mathrm{FD,dev}} + c_0 B \Delta \boldsymbol{\sigma}^{ve}_{\mathrm{FD,dev}} \tag{25}$$

where

$$^{n+1}\boldsymbol{\sigma}^{vv}_{\mathrm{FD,dev}} = B\left[\frac{G_{\mathrm{FD}}(\Delta t)^{\alpha_{\mathrm{dev}}}}{b_{\mathrm{dev}}}(\theta - 1) + c_0\right]{}^{n}\boldsymbol{\sigma}_{\mathrm{FD,dev}} + 2G_{\mathrm{FD}}B[c_0{}^{n}\boldsymbol{\varepsilon}^{v}_{\mathrm{FD,dev}} - {}^{n}\overline{\boldsymbol{\varepsilon}}^{v}_{\mathrm{FD,dev}}] \tag{26}$$

and

$$\Delta \boldsymbol{\sigma}^{ve}_{\mathrm{FD,dev}} = 2G_{\mathrm{FD}}\Delta \boldsymbol{\varepsilon}_{\mathrm{dev}} \tag{27}$$

The term B in Eqs. (25) and (26) is defined by

$$B = \left[\frac{G_{\mathrm{FD}}(\Delta t)^{\alpha_{\mathrm{dev}}}}{b_{\mathrm{dev}}}\theta + c_0\right]^{-1} \tag{28}$$

Finally, the updated deviatoric strain is provided by

$$^{n+1}\boldsymbol{\varepsilon}^{v}_{\mathrm{FD,dev}} = \frac{1}{c_0}\left[{}^{n}\overline{\boldsymbol{\varepsilon}}^{v}_{\mathrm{FD,dev}} + \frac{G_{\mathrm{FD}}(\Delta t)^{\alpha_{\mathrm{dev}}}}{b_{\mathrm{dev}}}\frac{1}{2G_{\mathrm{FD}}}(\theta^{n+1}\boldsymbol{\sigma}_{\mathrm{FD,dev}} + (1-\theta)^{n}\boldsymbol{\sigma}_{\mathrm{FD,dev}})\right] \tag{29}$$

The above proposed algorithms might be incorporated to commercial FE codes through user routines. $\theta=1$ in the algorithm is described for implicit calculation, whereas $\theta=0$ is imposed for explicit resolution. Note that numerical evaluation of fractional derivatives requires a large portion of the strain history to be stored and used in each increment of the calculation when updating the values of stress and strain. Material constants needed (K_e, G_e, K_{FD}, G_{FD}, α_{vol}, α_{dev}, b_{vol}, and b_{dev}) must be provided to the code. Sec. 5 summarizes the fitting procedure that leads to their values.

4.3 Implementation of the Friction Part. Friction effects are introduced in the model by using appropriate plasticity models already implemented in the commercial FE codes. Although originally thought for metal plasticity, von Mises' elastoplasticity model shows good resemblance to the multiaxial behavior of the models based on the Coulomb friction (described in Sec. 3.2).

4.4 Practical Procedure to Determine the Dynamic Stiffness. Due to the nonlinearities associated to the model, calculations must be carried out in time domain and some postprocessing is needed to evaluate the complex dynamic stiffness of a component (see procedure in Fig. 8).

At each frequency, a sinusoidal displacement of the required amplitude is provided and force response is calculated. Dynamic stiffness is evaluated at each frequency through the frequency domain transfer function. A transfer function H_{xy} between an input signal x (displacement) and an output signal y (force) is defined by Eq. (30), where P_{xy} and P_{xx} are the cross and autospectral density functions, respectively.

Fig. 10 Bushing 2: cylindrical rubber bushing. Shore A 70.

$$H_{xy} = \frac{P_{xy}}{P_{xx}} \tag{30}$$

Letting x be the displacement and y the force signals, the transfer function in Eq. (30) represents the complex stiffness K^* at the given frequency. The modulus of the complex stiffness $|K^*|$ is defined as the absolute value of the complex transfer function H_{xy}. Loss angle is defined through the complex transfer function phase, according to

$$|K^*| = |H_{xy}(f)| \quad (\mathrm{N/m})$$

$$\text{Loss angle } (K^*) = \frac{180}{\pi}(H_{xy}(f)) \quad (\mathrm{deg}) \tag{31}$$

Although nonlinear effects are present in the behavior of the material, the above-mentioned effective linear representation is used for the dynamic stiffness evaluation with very satisfactory results, as shown in Sec. 5.

5 Prediction of the Dynamic Stiffness of Two Rubber Bushings

5.1 Description of the Cases. The material model described here and implemented in the FE code ABAQUS has been used to predict the dynamic stiffness of the two rubber bushings shown in Figs. 9 and 10. Simulations in ABAQUS have been compared to experimental results in order to validate the accuracy of the model.

Both silent-blocks are relatively small: 18 mm height, with an inner radius of 7 mm and an outer one of 15 mm in the case of bushing 1, and 24 mm height, with an inner radius of 7.5 mm and an outer radius of 13.55 mm, for bushing 2. Bushing 1 is compounded of Shore A 50 natural rubber, whereas bushing 2 is made of Shore A 70 natural rubber. The bushings are compounded together with the outer and inner walls, thus guaranteeing that no preload and residual stresses exist in the isolators prior to the

Table 1 Values of the material parameters for the Shore A 50 NR compound

Shore A 50 NR	Parameters	Values
Linear elasticity	G_e	$G_e = 6.926\times10^5$ Pa
Fractional derivative viscoelasticity	G_{FD}, α, b	$G_{\mathrm{FD}} = 5.79\times10^5$ Pa; $\alpha = 0.479$; $b = 560\times10^3$ N s$^{\alpha}$/m^2
Friction (von Mises' elastoplasticity)	G_{f1}, T_{f1}	$G_{f1} = 2.28\times10^5$ Pa; $T_{f1} = 6.84\times10^3$ Pa

Table 2 Values of the parameters of the nonlinear model for the Shore A 70 NR compound

Shore A 70 NR	Parameters	Values
Linear elasticity	G_e	$G_e = 1.665 \times 10^6$ Pa
Fractional derivative viscoelasticity	G_{FD}, α, b	$G_{FD} = 7.99 \times 10^6$ Pa; $\alpha = 0.382$; $b = 8.25 \times 10^4$ N s^α/m^2
	G_{f1}, T_{f1}	$G_{f1} = 2.08 \times 10^6$ Pa; $T_{f1} = 5.06 \times 10^4$ Pa
Friction (von Mises' elastoplasticity)	G_{f2}, T_{f2}	$G_{f2} = 1.54 \times 10^6$ Pa; $T_{f2} = 1.23 \times 10^4$ Pa
	G_{f3}, T_{f3}	$G_{f3} = 1.01 \times 10^6$ Pa; $T_{f3} = 2.12 \times 10^3$ Pa

dynamic excitation.

In both cases, the outer steel cylinder is fixed and a sinusoidal displacement of 0.025 mm is imposed in the inner one in the axial and radial directions.

As for the FE model, the number of elements is limited to around 350 due to the available memory resources, as the calculation of fractional derivatives requires that the whole strain history of the material is stored at each element and increment during the calculation. In all directions, existing symmetry conditions have been applied in order to reduce as much as possible the number of elements of the FE meshes.

5.2 Parameter Fitting Procedure. The values of the material parameters of the model for Shore A 50 and Shore A 70 rubber compounds tested in Sec. 2 are displayed in Tables 1 and 2. Rubber has been considered incompressible, implying Poisson's ratio of almost 0,5. It has also been assumed that α and b take the same value in the deviatoric and volumetric decompositions. The previous assumptions reduce the number of parameters of the model to only 4 if no friction effects are introduced in it. Two more parameters are added for each elastoplastic mesh added to the material definition (according to the overlay technique in Sec.4.1). In order to maintain the number of parameters as low as possible, which is one of the main advantages of the model proposed, the number of friction meshes should be reduced to a minimum.

Shore A 50 NR mixture is not highly filled and the amplitude dependence is small, as shown in Figs. 2 and 3, unlike Shore A 70 NR compound. A single elastoplastic mesh provides a very good fitting of observed characteristics in the case of the softest rubber.

Nevertheless, three elastoplastic meshes have been necessary to obtain a good fit to experimental results in the case of Shore A 70 NR mixture, increasing the number of parameters of the model up to 10.

The fitting procedure can be seen as a minimization of the error of the material model compared with experimental data. Its aim is, thus, a material model with the same stiffness and damping (loss angle) properties as tested rubber material for a given range of frequencies and strain amplitudes. For this purpose, the relative error function in Eq. (32) is proposed.

$$\text{error} = \sum \frac{|G^*_{\text{test}} - G^*_{\text{num}}|^2}{|G^*_{\text{test}}|^2} \tag{32}$$

where G^*_{test} represents the measured complex shear modulus of the material and G^*_{num} represents the evaluated complex dynamic shear modulus.

When the error is minimized with regard to the model parameters, a best fit of the simulated complex stiffness to the measured complex stiffness is obtained in a least squares sense. The error function has to be evaluated repeatedly for all amplitudes and frequencies where measurements have been made.

Note that the model does not include any damage effects associated with Mullin's effect [27]. This assumption is introduced by the fact that the parameters of the model are fitted from tests conducted on mechanically conditioned material samples (as stated in Sec. 2). Nevertheless, for many applications, such as shock absorbers and vibration isolators, there is no limitation since those mounts are normally conditioned in one way or another.

5.3 Results and Discussion. Predicted dynamic stiffness of bushings show good agreement to measured characteristics in radial and axial directions (see Figs. 11–14). The radial direction considered in Fig. 12 for bushing 1 corresponds to the softest direction (in the direction of the holes according to Fig. 9). The perpendicular radial direction for bushing 1 is not shown here, although the conclusions are similar to the rest of the results.

In all the cases, errors are below the limits usually accepted by rubber manufacturers, which involve differences under 10% in the modulus of the stiffness and 2.5 deg in loss angle. One of the most important factors affecting the accuracy of the calculations might be the number of elements of the meshes, which have been reduced so that the models could be solved in the finite element code with the available memory. It is expected that mesh refinements would produce better fit to experimental test results.

6 Concluding Remarks

Commercial FE codes provide designers with a tool that helps predicting at a design stage, which is the effect in the final response of changes carried out in the geometry of a bushing or the type of rubber compound. Nevertheless, the accuracy of finite element methods depends on the accuracy to which the elastic and

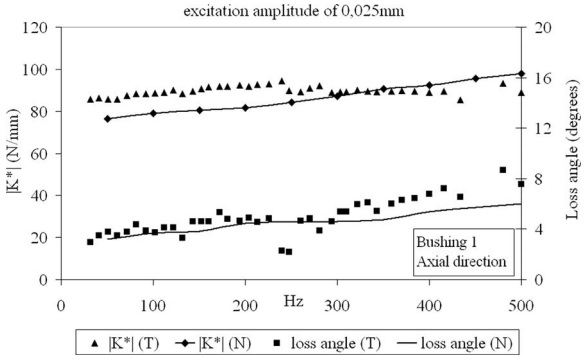

Fig. 11 Axial stiffness of bushing 1. *T*: experimental test; *N*: simulation in the FE code.

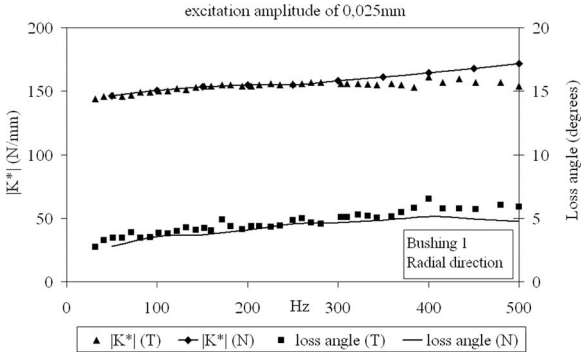

Fig. 12 Complex dynamic stiffness of bushing 1 in the softest radial direction. *T*: experimental test; *N*: simulation in the FE code.

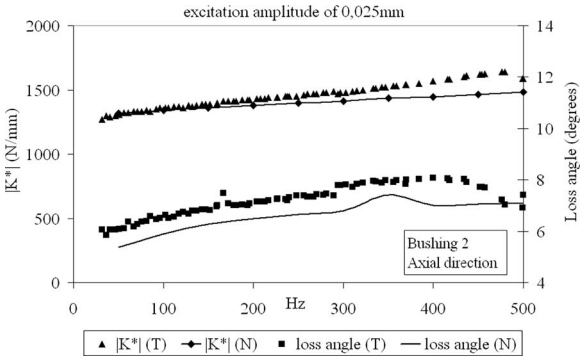

Fig. 13 Axial stiffness of bushing 2. *T*: Experimental test; *N*: Simulation in the FE code.

dynamic natures of the design material can be defined. Nowadays, there are no material models in commercial FE codes that fully represent the observed dynamic characteristics of rubber compounds, including both frequency and amplitude dependent effects.

The work carried out here proposes a material model that combines elastoplasticity and fractional order viscoelasticity to represent the complex behavior of natural rubber mixtures. A fractional-derivative viscoelastic model reproduces the frequency dependent behavior of rubber while maintaining the number of parameters low and, thus, simplifying the parameter fitting procedure. The way to implement fractional order viscoelasticity in a finite element code is summarized, making it easy to the user to program its own user routine where necessary. A von Mises' elastoplastic material model shows good resemblance to the rate-independent behavior of rubber mixtures, when subjected to harmonic excitation. Both material models are combined through an overlay technique.

Two are the main advantages of the model proposed. The first one, inherent to its definition, is its capability to simulate the complex dynamic behavior of carbon-black filled rubber elements using a FE code, when the units are subjected to different excitation amplitudes in a frequency range. The nonlinear model accounts for both frequency and amplitude dependent effects of rubber and directly provides accurate estimation of the dynamic stiffness of isolators. The second advantage is related to the lower number of parameters needed to define the material behavior, compared with those models where classical viscoelasticity is adopted. Dynamic simple shear tests, conducted at different amplitude values in a frequency range, provide enough data to fit the values of the material parameters.

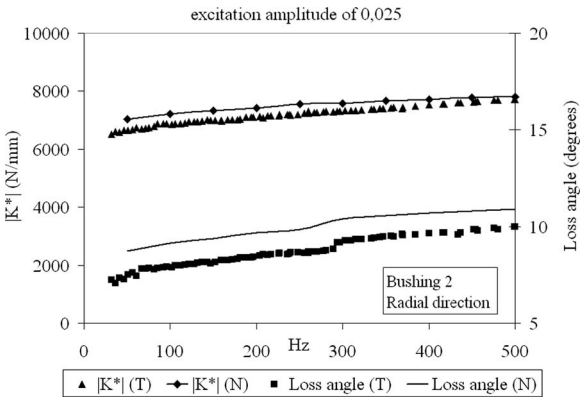

Fig. 14 Radial stiffness of bushing 2. *T*: Experimental test; *N*: Simulation in the FE code.

Two rubber bushings have been investigated and simulation results have been compared with experiments. The nonlinear model presented provides an accurate description of the dynamic behavior of a rubber isolator in time domain. Estimated dynamic stiffness is also satisfactory, obtained mean error falling within the dispersion in the manufacturing process itself, which exists normally between the two components having the same geometry and identical material composition.

Acknowledgment

M.E., from Chalmers Institute of Technology, is acknowledged for the help he provided in the implementation of fractional-derivative viscoelastic models.

References

[1] Fletcher, W. P., and Gent, A. N., 1953, "Non-Linearity in the Dynamic Properties of Vulcanised Rubber Compounds," Trans. Inst. Rubber Ind., **29**, pp. 266–280.
[2] Jurado, F. J., Mateo, A., Gil-Negrete, N., Viñolas, J., and Kari, L., 1999, "Testing and FE Modelling of the Dynamic Properties of Carbon Black Filled Rubbers," *Proceedings of the EAEC*, Barcelona, pp. 119–126.
[3] Medalia, A. I., 1978, "Effects of Carbon Black on Dynamic Properties of Rubber," Rubber Chem. Technol., **51**, pp. 437–523.
[4] Sjöberg, M., 2000, "Dynamic Behaviour of a Rubber Component in the Low Frequency Range: Measurements and Modelling," *Proceedings of the Seventh International Conference of Sound and Vibration*, Garmisch-Partenkirchen, pp. 2955–2962.
[5] Dean, G. D., Duncan, J. C., and Johnson, A. F., 1984, "Determination of Nonlinear Dynamic Properties of Carbon-Black Filled Rubbers," Polym. Test., **4**, pp. 225–249.
[6] Wang, M. J., 1998, "Effect of Polymer-Filler and Filler-Filler Interactions on Dynamic Properties of Filled Vulcanizates," Rubber Chem. Technol., **71**, pp. 520–589.
[7] Mooney, M., 1940, "A Theory of Large Elastic Deformation," J. Appl. Phys., **11**, pp. 582–592.
[8] Valanis, K. C., and Landel, R. F., 1967, "The Strain-Energy Function of a Hyperelastic Material in Terms of Extension Ratios," J. Appl. Phys., **38**, pp. 2997–3002.
[9] Treloar, L. R. G., 1975, *The Physics of Rubber*, Clarendon, Oxford.
[10] Rivlin, R. S., 1992, "The Elasticity of Rubber," Rubber Chem. Technol., **65**, pp. G51–G66.
[11] Yeoh, O. H., 1990, "Characterization of Elastic Properties of Carbon-Black Filled Rubber Vulcanizates," Rubber Chem. Technol., **69**, pp. 792–805.
[12] Arruda, E. M., and Boyce, M. C., 1993, "A Three-Dimensional Constitutive Model for Large Stretch Behaviour of Rubber Elastic Materials," J. Mech. Phys. Solids, **41**, pp. 389–412.
[13] Yeoh, O. H., 1997, "On the Ogden Strain-Energy Function," Rubber Chem. Technol., **70**, pp. 175–182.
[14] Lambert-Diani, J., and Rey, C., 1999, "New Phenomenological Behaviour Laws for Rubbers and Thermoplastic Elastomers," Eur. J. Mech. A/Solids, **18**, pp. 1027–1043.
[15] James, A. G., Green, A., and Simpson, G. M., 1975, "Strain Energy Functions of Rubber: I. Characterization of Gum Vulcanizates," J. Appl. Polym. Sci., **19**, pp. 2033–2055.
[16] Charlton, D. J., Yang, J., and The, K. K., 1994, "A Review of Methods to Characterize Rubber Elastic Behaviour for Use in Finite Element Analysis," Rubber Chem. Technol., **67**, pp. 481–503.
[17] Yeoh, O. H., 1993, "Some Forms of the Strain-Energy Function for Rubber," Rubber Chem. Technol., **66**, pp. 754–771.
[18] Gil-Negrete, N., García-Tárrago, M. J., and Viñolas, J., 2006, "Influence of the Number of Parameters of a Rubber Isolator Viscoelastic Model on the Predicted Dynamic Behaviour of a Suspended Mass," *Proceedings of the ISMA 2006*, Leuven, pp. 1039–1050.
[19] Betz, E., 1968, *Spring and Dashpot Models and Their Applications in the Study of the Dynamic Properties of Rubber*, "Engineering Bulletin Series," University of Newcastle, Faculty of Engineering, Department of Mechanical Engineering.
[20] Flügge, W., 1975, *Viscoelasticity*, Springer-Verlag, Berlin.
[21] Gil-Negrete, N., 2004, "On the Modelling and Dynamic Stiffness Prediction of Rubber Isolators," Ph.D. thesis, University of Navarra, San Sebastián, Spain.
[22] Lubliner, J., 1985, "A Model of Rubber Viscoelasticity," Mech. Res. Commun., **12**, pp. 93–99.
[23] Johnson, A. R., Quigley, C. J., and Mead, J. L., 1994, "Large Strain Viscoelastic Constitutive Models for Rubber," Rubber Chem. Technol., **67**, pp. 904–917.
[24] Johnson, A. R., Quigley, C. J., and Freese, C. E., 1995, "A Viscohyperelastic Finite Element Model for Rubber," Comput. Methods Appl. Mech. Eng., **127**, pp. 163–180.
[25] Yang, L. M., Shim, V. P. W., and Lim, C. T., 2000, "A Visco-Hyperelastic Approach to Modeling the Constitutive Behaviour of Rubber," Int. J. Impact Eng., **42**, pp. 339–362.
[26] Simo, J. C., 1987, "On a Fully Three-Dimensional Finite-Strain Viscoelastic

Damage Model: Formulation and Computational Aspects," Comput. Methods Appl. Mech. Eng., **60**, pp. 153–173.
[27] Mullins, L., 1969, "Softening of Rubber by Deformation," Rubber Chem. Technol., **42**, pp. 339–362.
[28] Oldham, K. B., and Spanier, J., 1974, *The Fractional Calculus*, Academic, New York.
[29] Bagley, R., and Torvik, P., 1983, "Fractional Calculus: A Different Approach to the Analysis of Viscoelastically Damped Structures," AIAA J., **21**, pp. 741–748.
[30] Koeller, R. C., 1984, "Applications of Fractional Calculus to the Theory of Viscoelasticity," ASME J. Appl. Mech., **51**, pp. 299–307.
[31] Eldred, L. B., Baker, W. B., and Palazotto, A. N., 1996, "Numerical Application of Fractional Derivative Model Constitutive Relations for Viscoelastic Materials," Comput. Struct., **60**, pp. 875–882.
[32] Shimizu, N., and Zhang, W., 1999, "Fractional Calculus Approach to Dynamic Problems of Viscoelastic Materials," JSME Int. J., Ser. C, **42**(4), pp. 825–837.
[33] Enelund, M., and Olsson, P., 1999, "Damping Described by Fading Memory: Analysis and Applications to Fractional Derivative Models," Int. J. Solids Struct., **36**, pp. 939–970.
[34] Park, S. W., 2001, "Analytical Modelling of Viscoelastic Dampers for Structural and Vibration Control," Int. J. Solids Struct., **38**, pp. 8065–8092.
[35] Sjöberg, M., and Kari, L., 2002, "Non-Linear Behavior of a Rubber Isolator System Using Fractional Derivatives," Veh. Syst. Dyn., **37**(3), pp. 217–236.
[36] Sjöberg, M., and Kari, L., 2003, "Nonlinear Isolator Dynamics at Finite Deformations: An Effective Hyperelastic, Fractional Derivative, Generalized Friction Model," Nonlinear Dyn., **33**(3), pp. 323–336.
[37] García-Tárrago, M. J., Kari, L., Viñolas, J., and Gil-Negrete, N., 2007, "Torsion Stiffness of a Rubber Bushing: A Simple Effective Engineering Formula Including Amplitude Dependence," J. Strain Anal. Eng. Des., **42**(1), pp. 13–21.
[38] García-Tárrago, M. J., Kari, L., Viñolas, J., and Gil-Negrete, N., 2007, "Frequency and Amplitude Dependence of the Radial and Axial Stiffness of the Carbon Black Filled Rubber Bushings," Polym. Test., **26**, pp. 629–638.
[39] Padovan, J., 1987, "Computational Algorithms for FE Formulations Involving Fractional Operators," Comput. Mech., **2**, pp. 271–287.
[40] Enelund, M., Mähler, L., Runesson, K., and Josefson, B. L., 1999, "Formulation and Integration of the Standard Linear Viscoelastic Solid With Fractional Order Rate Laws," Int. J. Solids Struct., **36**, pp. 2417–2442.
[41] Zhang, W., and Shimizu, N., 2001, "FE Formulation for the Viscoelastic Body Modeled by Fractional Constitutive Law," Acta Mech. Sin., **17**(4), pp. 354–365.
[42] Schmidt, A., and Gaul, L., 2002, "Finite Element Formulation of Viscoelastic Constitutive Equations Using Fractional Time Derivatives," Nonlinear Dyn., **29**, pp. 37–55.
[43] Ravindra, B., and Mallik, A. K., 1994, "Performance of Non-Linear Vibration Isolators Under Harmonic Excitation," J. Sound Vib., **170**, pp. 325–337.
[44] Ulmer, J. D., 1995, "Strain Dependence of Dynamic Mechanical Properties of Carbon-Black Filled Rubber Compounds," Rubber Chem. Technol., **69**, pp. 15–47.
[45] Wineman, A., Van Dyke, T., and Shi, S., 1998, "A Nonlinear Viscoelastic Model for One-Dimensional Response of Elastomeric Bushings," Int. J. Mech. Sci., **40**, pp. 1295–1305.
[46] Lion, A., 1999, "Strain-Dependent Properties of Filled Rubber: A Non-Linear Viscoelastic Approach Based on Structural Variables," Rubber Chem. Technol., **72**, pp. 410–429.
[47] Miehe, C., and Keck, J., 2000, "Superimposed Finite Elastic-Viscoelastic-Plastoelastic Stress Response With Damage in Filled Rubbery Polymers. Experiments, Modelling and Algorithmic Implementation," J. Mech. Phys. Solids, **48**, pp. 323–365.
[48] Kaliske, M., and Rothert, H., 1998, "Constitutive Approach to Rate-Independent Properties of Filled Elastomers," Int. J. Solids Struct., **35**, pp. 2057–2071.
[49] Gregory, M. J., 1985, "Dynamic Properties of Rubber in Automotive Engineering," Elastomerics, **117**, pp. 17–24.
[50] Austrell, E., Olsson, A. K., and Jönsson, M., 2001, "A Method to Analyse the Non-Linear Dynamic Behaviour of Carbon-Black Filled Rubber Components Using Standard FE Codes," *Proceedings of the Second Conference on Constitutive Models for Rubbers*, pp. 231–235.
[51] ASTM, 1996, "Standard Guide for Dynamic Testing of Vulcanized Rubber and Rubber-Like Materials Using Vibratory Methods," ASTM D5992-96, revised 2001.
[52] Payne, A. R., and Whittaker, R. E., 1971, "Low Strain Dynamic Properties of Filled Rubbers," Rubber Chem. Technol., **44**, pp. 440–478.
[53] Besseling, J. F., 1958, "A Theory of Elastic, Plastic and Creep Deformation of an Initially Isotropic Material," ASME J. Appl. Mech., **25**, pp. 529–536.

Modeling and Analysis of Cylindrical Nanoindentation of Graphite

B. Yang

R. M. Rethinam

Department of Mechanical and Aerospace Engineering,
Florida Institute of Technology,
Melbourne, FL 32901

S. Mall

Department of Aeronautics and Astronautics,
Air Force Institute of Technology,
Wright-Patterson AFB, OH 45433

Graphite at the nanoscale is modeled as a material system consisting of a stack of parallel plates buffered by an elastic material. While the plates represent individual graphene sheets, the buffer material models the Van der Waals interaction between the graphene sheets. As such, the loading on graphite at the nanoscale is characterized by the membrane force, the bending moment, and the shear force in the graphene sheets. Cylindrical nanoindentation of graphite is analyzed by applying a special boundary element method that employs Green's function for multilayers with platelike interfaces. Because Green's function satisfies the traction-free surface, the interfacial displacement continuity and the interfacial traction discontinuity conditions, only the indentation surface area where the boundary condition is altered, are numerically discretized. Numerical results of cylindrical nanoindentation are presented. It is shown that the bending moment and the shear force in the graphene sheets are concentrated around the edge of contact, consistent with the singularities existing in the second and the third derivatives of the surface displacement in the reduced case of a semi-infinite homogeneous solid under cylindrical contact. Kinks of single, double, and triple joints are related to the bending moment, the shear force, and the concentrated force, respectively.
[DOI: 10.1115/1.2999412]

Keywords: boundary elements, contact mechanics, graphene, graphite, kink banding, Kirchhoff plate, membrane, multilayers, nanoindentation, singularity

1 Introduction

Graphite has long been applied to develop nuclear shields and composite materials among many other applications due to its excellent thermal, electrical, and mechanical properties [1]. Most recently, its building element, i.e., graphene sheet, in the form of single or a few stacked layers, has been realized in laboratories that have renewed and heightened great interest in the material at the nanoscale [2–4]. Their unique 2D electronic and magnetic properties may be utilized to develop novel nanodevices. Understanding of the mechanical behavior of graphene sheets and graphite at the nanoscale is important.

Nanoindentation test was used to investigate the mechanical behavior of graphite at small scales [5]. It was shown that a highly oriented pyrolytic graphite (HOPG) sample may undergo significant nonlinear elastic behavior. This elastic behavior was explained by the reversible incipient kink banding underneath the indentation site [6]. The classical dislocation theory [7] was applied to quantitatively explain this phenomenon.

At the microscale and beyond, graphite can be adequately modeled as a homogeneous continuum solid [1]. In contrast, at the lattice level, it is a stack of graphene sheets of carbon atoms covalently bonded within a basal plane but weakly bonded by Van der Waals forces between the planes [1]. Thus, it displays itself at the nanometer scale as a stack of plates buffered by a relatively "soft" material. The plates represent the graphene sheets, while the buffer material represents the Van der Waals bonding effect. In this work, we develop such a continuum model to take into account the discrete-plate nanostructure of graphite and study the loading conditions on individual graphene sheets in graphite under nanoindentation. The two-phase continuum model stands between the existing atomistic and homogeneous continuum models. It is more efficient than the atomistic model and more accurate than the homogeneous continuum model for simulation of the mechanical behavior of graphite at the nanoscale.

The rest of the paper is organized as follows. In Sec. 2, the discrete-plate model of graphite at the nanoscale is described. In Sec. 3, a special boundary element method is developed to solve the problem of cylindrical nanoindentation of graphite. Because the special Green's function for multilayers with platelike interfaces [8] is employed that satisfies the surface and interfacial conditions, only the surface contact area needs to be numerically discretized. The loading fields in the plates modeling the graphene sheets are acquired in the postprocess. In Sec. 4, numerical results are presented and analyzed. In Sec. 5, kink banding in graphite under nanoindentation is discussed. Finally, conclusions are drawn in Sec. 6.

2 Discrete-Plate Model for Graphite at the Nanoscale

Graphite at the nanoscale is modeled as a stack of Kirchhoff plates buffered by an elastic material, as schematically shown in Fig. 1. While the plates represent the covalent interaction of carbon atoms within individual graphene sheets, the buffer material does the relatively weak Van der Waals interaction between adjacent graphene sheets. The plates are assumed to be isotropic and of the Kirchhoff type. The buffer material is transversely isotropic.

The graphite modeled as a two-phase continuum requires two sets of equilibrium equations: one for the plates and the other for the buffer material. The set of equilibrium equations for stretching and bending of a graphene sheet is given by [9]

Contributed by the Applied Mechanics Division of ASME for publication in the JOURNAL OF APPLIED MECHANICS. Manuscript received March 24, 2008; final manuscript received June 24, 2008; published online November 5, 2008. Review conducted by Yonggang Huang.

$$\begin{bmatrix} E_{11}\dfrac{\partial^2}{\partial x_1^2}+E_{66}\dfrac{\partial^2}{\partial x_2^2} & (E_{12}+E_{66})\dfrac{\partial^2}{\partial x_1\,\partial x_2} & 0 \\ (E_{21}+E_{66})\dfrac{\partial^2}{\partial x_1\,\partial x_2} & E_{66}\dfrac{\partial^2}{\partial x_1^2}+E_{22}\dfrac{\partial^2}{\partial x_2^2} & 0 \\ 0 & 0 & -D\left(\dfrac{\partial^4}{\partial x_1^4}+2\dfrac{\partial^4}{\partial x_1^2\,\partial x_2^2}+\dfrac{\partial^4}{\partial x_2^4}\right) \end{bmatrix} \begin{Bmatrix} u_1 \\ u_2 \\ u_3 \end{Bmatrix} + \begin{Bmatrix} [p_1] \\ [p_2] \\ [p_3] \end{Bmatrix} = 0 \tag{1}$$

where $\boldsymbol{u}$ is the displacement, $[\boldsymbol{p}]$ is the traction discontinuity across a graphene sheet, $\boldsymbol{E}$ denotes the membrane elastic constants, and D is the flexural rigidity. The Cartesian reference frame is attached with the x_3-axis being normal to the basal plane.

The equilibrium equations for the 3D buffer material are given by [10]

$$C_{ijkl}u_{k,lj}+f_i=0 \tag{2}$$

where C_{ijkl} is the elastic stiffness matrix, f_i is the body force component, the prime in the subscript denotes the partial differentiation with respect to the index that follows, and the repeated indices indicate the Einstein convention of summation.

Very recently, Yang and Tewary [11] analytically showed that the fundamental deflection behavior of a graphene lattice at the long-wavelength limit is the same as that of a continuum Kirchhoff plate under a concentrated force. This correspondence establishes a rigorous linkage of the continuum parameter of a plate with the discrete lattice parameters of graphene. They consequently determined the flexural rigidity D of graphene lattice to be

$$D=0.797\ \text{eV} \tag{3}$$

based on the Born von Karman model [12] and the Tersoff–Brenner potential [13].

The membrane elastic constants of graphene are defined by

$$E_{11}=\frac{\partial^2 V}{\partial\varepsilon_{11}\,\partial\varepsilon_{11}},\quad E_{22}=\frac{\partial^2 V}{\partial\varepsilon_{22}\,\partial\varepsilon_{22}}$$
$$E_{12}=E_{21}=\frac{\partial^2 V}{\partial\varepsilon_{11}\,\partial\varepsilon_{22}},\quad E_{66}=\frac{\partial^2 V}{\partial\varepsilon_{12}\,\partial\varepsilon_{12}} \tag{4}$$

where V is the interatomic potential and ε_{11}, ε_{22}, and ε_{12} are the in-plane strain components. By taking the Tersoff–Brenner potential [13], the constants are given by [14]

$$E_{11}=E_{22}=1.7731\ \text{keV/nm}^2$$
$$E_{12}=E_{21}=0.73084\ \text{keV/nm}^2,\quad E_{66}=0.52116\ \text{keV/nm}^2 \tag{5}$$

In contrast, little has been known about the elastic constants of the buffer material representing the Van der Waals interaction. It is partially due to the inadequate understanding of the Van der Waals interaction that is much weaker than the covalent interaction in graphite. In the present study, the out-of-plane elastic constants of graphite are used for the buffer material. This is reasonable because the atom-thin graphene sheets should contribute very little to these components of overall stiffness, C_{13}, C_{33}, and C_{44}. These out-of-plane components were found in Ref. [1]. Meanwhile, the in-plane components C_{11} and C_{12} are derived from them by assuming that the buffer material is fully isotropic (rather than transversely isotropic). There is no way for us to estimate the error caused by this assumption at the time being. It is hoped to affect the present study insignificantly by considering the fact that the contribution of the buffer layer to the in-plane elastic rigidity is small compared to that of the graphene sheets. The former is only about 4% of the latter. In summary, the elastic constants of the buffer material are taken as

$$C_{11}=0.2278\ \text{keV/nm}^3,\quad C_{12}=0.0936\ \text{keV/nm}^3$$
$$C_{13}=0.0936\ \text{keV/nm}^3,\quad C_{33}=0.2278\ \text{keV/nm}^3 \tag{6}$$
$$C_{44}=0.0281\ \text{keV/nm}^3$$

Note that the second moment of inertia of one buffer layer with elastic constants given above is about 0.7–0.8 eV, roughly the same as that of a single graphene sheet.

The continuity conditions of displacement and traction are enforced at the interfaces between the plates and the buffer material. Therefore, the graphite may be alternatively viewed as a material system consisting of multiple buffer layers bonded through platelike interfaces, i.e., interfaces exhibiting finite membrane and flexural rigidities. Equation (2) is the governing equation of the buffer layers. Equation (1) is the interfacial traction jump condition. In addition, the interfacial displacement continuity condition is enforced.

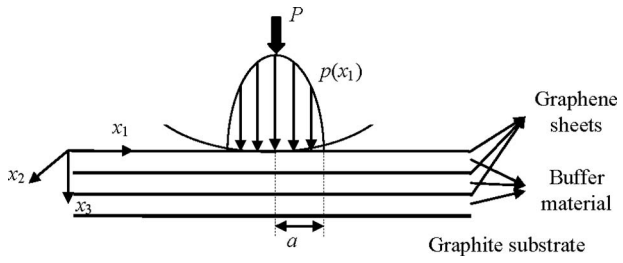

Fig. 1 Cylindrical nanoindentation of a graphite sample specimen modeled as a stack of buffered plates on top of a homogeneous graphite substrate

3 Boundary Element Method for Graphite Under Nanoindentation

In order to predict the loading on individual graphene sheets in a semi-infinite graphite sample under cylindrical nanoindentation, as shown in Fig. 1, a novel boundary element method is developed. Green's function for multilayers with platelike interfaces is employed as the kernel. Green's function that can analytically account for the discrete-plate nanostructure of graphite was recently derived in 3D [8]. Its 2D reduction, which is used in the present study, is summarized in the Appendix. Since the special Green's function satisfies the interfacial displacement continuity condition, the interfacial traction jump condition, and the free surface condition, only the contact area on the surface where the boundary condition is altered needs for numerical discretization. The loading parameters in graphene sheets are calculated after the indentation pressure is solved by using the boundary element method.

Employing the special Green's function for multilayers with platelike interfaces [8], the displacement at a point $\boldsymbol{y}$ in the graphite (including the surface) can be expressed as

$$u_p(\mathbf{X}) = \int_{S_I} G_{pi}(\mathbf{X},\mathbf{x}) t_i(\mathbf{x}) dS(\mathbf{x}) \tag{7}$$

where $G_{pi}(\mathbf{X},\mathbf{x})$ is Green's function, representing the ith component of displacement at $\boldsymbol{x}$ due to a unit point force applied in the pth direction at $\mathbf{X}$, and $\mathbf{t}$ and S_I are the pressure and contact area on the surface, respectively. Note that the boundary integral equation of a regular solid, i.e., Somigliana's identity [15], consists of two integral terms including the one given in Eq. (7). The other term, which is given by Green's function of traction times displacement, vanishes in the present case where the integral kernel is identically equal to zero on the surface satisfying the traction-free boundary condition [8]. Furthermore, since Green's function in Eq. (7) is derived with the point force directly applied on the surface, no usual limiting process is necessary to take $\mathbf{X}$ from the interior to the surface that would have led to a coefficient equal to one-half in front of the displacement on the left-hand side of the equation [15].

Because the out-of-plane elastic constants of graphite are over ten times smaller in magnitude than those of a common indentation tip material, which is either silicon or diamond, the indenter is assumed to be rigid. In addition, the nonconformal contact angle between the opposite contact surfaces is assumed to be small. The contact is frictionless. The rigid indenter initially in touch with the graphite surface is pressed with depth δ. The indenter tip profile is described by a function $h(x_1)$, which sets up a rigid normal confinement to the sample surface deformation. The tangential traction component is always equal to zero.

Based on the above integral-equation formulation, one can devise an efficient numerical scheme to solve the problem of graphite under nanoindentation. The (potential) contact area is discretized into constant elements each with a single node placed at the middle point. The displacement and traction are uniform in each element. The approximate fields are plugged into Eq. (7), which results in the following system of algebraic equations:

$$u_p^m = \sum_n g_{pi}^{mn} t_i^n \tag{8}$$

where the superscripts m and n indicate nodes, and $\boldsymbol{g}^{mn}$ is the integral of Green's function $\boldsymbol{G}^{mn}(\mathbf{y}^m,\boldsymbol{x})$ in terms of $\boldsymbol{x}$ over the element of node n.

Since the contact problem is nonlinear, an iterative scheme is necessary to solve the system of equations (8). The iterative scheme of successive over-relaxation [16,17] is adopted, which is summarized below. Let us define a residual function for each component of a node

$$r_p^m = u_p^m - \sum_n g_{pi}^{mn} t_i^n \tag{9}$$

The initial nodal displacement is set to be $\delta - h(x_1)$. Recall that δ is the indentation depth. It can be incrementally increased from zero to simulate a continuous indentation test. During the iteration process, the displacement components are updated by

$$(u_p^m)^{\text{iterat}+1} = (u_p^m)^{\text{iterat}} - \alpha r_p^m \tag{10}$$

where iterat indicates the iteration step, and α is a numerical parameter that one can adjust to obtain the best convergence rate of the iteration process. If it happens that the normal component $(u_3^m)^{\text{iterat}+1}$ exceeds the confining gap, i.e., $\delta - h(x_1)$, this node comes in contact with the rigid tip. In this case, the normal displacement component is set to be

$$(u_3^m)^{\text{iterat}+1} = \delta - h(x_1^m) \tag{11}$$

The corresponding normal traction component is calculated by

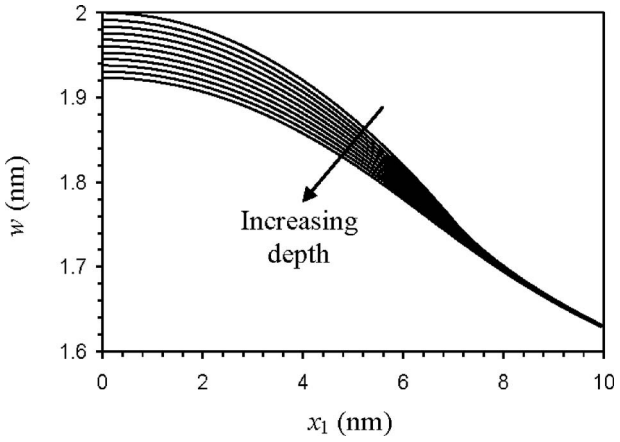

Fig. 2 Variation of transverse displacement on the surface and along the graphene sheets under cylindrical nanoindentation

$$(t_3^m)^{\text{iterat}+1} = (t_3^m)^{\text{iterat}} + \alpha \frac{r_3^m}{g_{33}^{mm}} \tag{12}$$

Meanwhile, the tangential displacement components are calculated by

$$(u_\tau^m)^{\text{iterat}+1} = (u_\tau^m)^{\text{iterat}} - \alpha r_\tau^m \tag{13}$$

where τ is equal to 1 or 2. It is found that this scheme is efficient in solving the present contact problem. In later simulations, the numerical parameter α is set to 0.7.

4 Numerical Results

In this section, numerical results are presented with a cylindrical indentation tip of radius 100 nm and a contact half width within 10 nm. The graphite specimen is modeled as a material system consisting of 50 units of alternating buffer layers and graphene sheets bonded on top of a bulk graphite substrate. There is no graphene sheet placed on the top surface. The first graphene sheet is at a depth of 0.335 nm. The number of discrete units was found to be adequate for a smooth transition of fields across the interface. Otherwise, more discrete units would have been used. The elastic constants of the bulk graphite used are

$$C_{11} = 5.2928 \text{ keV/nm}^3, \quad C_{12} = 2.1816 \text{ keV/nm}^3$$

$$C_{13} = 0.0936 \text{ keV/nm}^3, \quad C_{33} = 0.2278 \text{ keV/nm}^3 \tag{14}$$

$$C_{44} = 0.0281 \text{ keV/nm}^3$$

The out-of-plane components, C_{13}, C_{33}, and C_{44} are found in Ref. [1]. The in-plane components, C_{11} and C_{12}, are derived by dividing the membrane elastic constants of a graphene sheet given in Eq. (5) by the graphene-sheet spacing, 0.335 nm. A total of 200 elements were used to discretize the potential contact area of width 20 nm on the top surface.

Before presenting the results, it may be worth mentioning that the above formulation is applicable to general 3D cases. For the present case of cylindrical nanoindentation, the deformation is uniform along the cylindrical axis, which is taken to be the x_2-axis. Thus, all the field quantities are effectively functions of variables x_1 and x_3, as shown in Fig. 1. The Green functions used are correspondent to those described in the Appendix.

Results of a typical simulation with $\delta = 2$ nm are first presented. The contact half width a is about 7 nm. The total indentation force is about 62 eV/nm^2. Figure 2 shows the variation of the transverse displacement component w (i.e., the deflection) along the interfaces modeling the graphene sheets. Figures 3 and 4 show variations of the second and the third derivatives of w with respect to x_1 along the interfaces, respectively. These derivatives are pro-

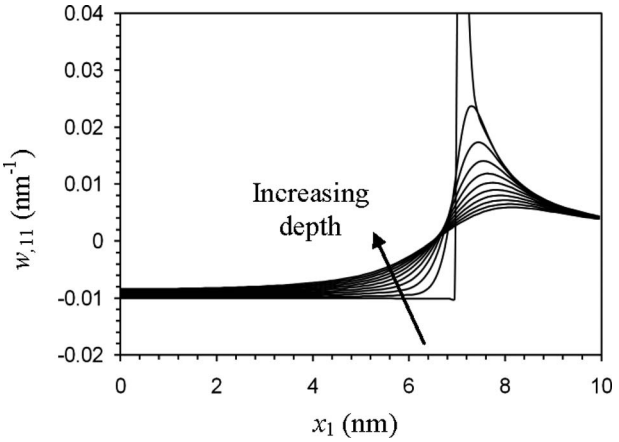

Fig. 3 Variation of the second derivative of transverse displacement on the surface and along the graphene sheets

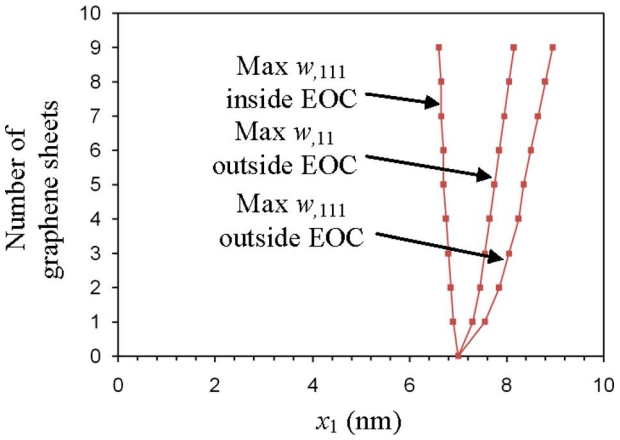

Fig. 5 Traces of maximum $w_{,11}$ and $w_{,111}$ in individual graphene sheets across the stack of graphene sheets. The number of graphene sheets is counted from the top surface (0).

portional to the bending moment M and the shear force Q by $M=-Dw_{,11}$ and $Q=-Dw_{,111}$, respectively. The corresponding fields on the surface are also included for comparison.

From Figs. 3 and 4, it can be seen that both the second and the third derivatives of deflection, $w_{,11}$ and $w_{,111}$, exhibit singularities at the edge of contact (EOC). This is consistent with the analytical solution of the surface displacement field in the case of a homogeneous substrate under cylindrical indentation [18]. The second derivative $w_{,11}$ is singular by the order of $\log(\rho)$ outside the EOC, where ρ is the distance from the EOC. The third derivative $w_{,111}$ is singular by the order of $1/\rho$ on both sides of the EOC. Correspondingly, both of the bending moment and the shear force in the graphene sheets exhibit a high concentration of magnitude around the EOC. The bending moment proportional to $w_{,11}$ is concentrated outside of the EOC. The shear force proportional to $w_{,111}$ is concentrated on both sides of the EOC.

The maximum values of the (absolute) bending moment and shear force, equivalently, $w_{,11}$ and $w_{,111}$, and their locations in individual graphene sheets near the surface are estimated from Figs. 3 and 4. The results are plotted in Figs. 5–7. The $w_{,111}$ maxima are estimated on both sides of the EOC. The $w_{,11}$ maximum is estimated outside the EOC as well as at the contact center. The traces of $w_{,11}$ and $w_{,111}$ maxima across the stack of graphene sheets are shown in Fig. 5. Variations of the $w_{,11}$ and $w_{,111}$ maxima with number of graphene sheets counted from the top surface are shown in Figs. 6 and 7. It can be seen that the $w_{,11}$ and $w_{,111}$ maxima both decay rapidly with depth from the surface. Meanwhile, $w_{,11}$ maximum underneath the center of contact (COC) decreases slowly with depth. $w_{,111}$ is concentrated in greater magnitude inside than outside the contact zone. The trace of absolute $w_{,111}$ maximum is at an average angle roughly equal to 81 deg from the surface inside the contact zone. Meanwhile, the

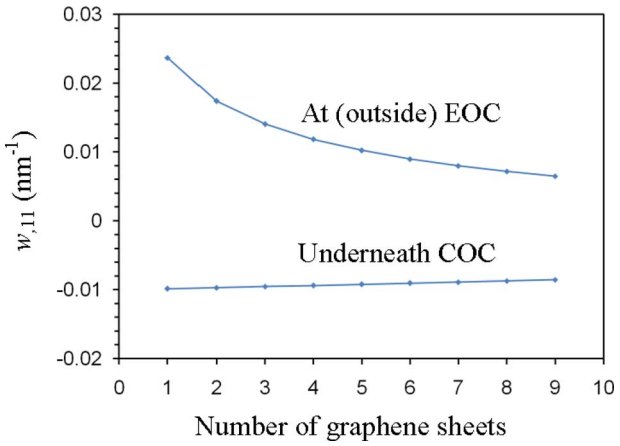

Fig. 6 Variation of maximum $w_{,11}$ in individual graphene sheets across the stack of graphene sheets

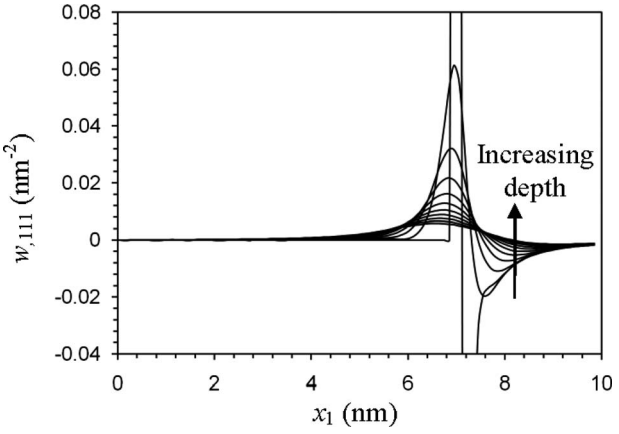

Fig. 4 Variation of the third derivative of transverse displacement on the surface and along the graphene sheets

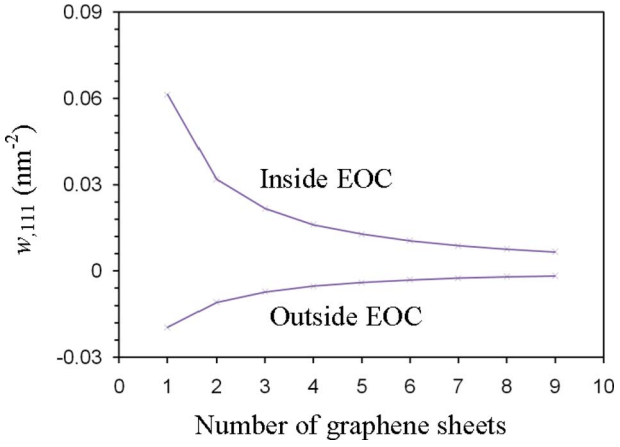

Fig. 7 Variation of maximum $w_{,111}$ in individual graphene sheets across the stack of graphene sheets

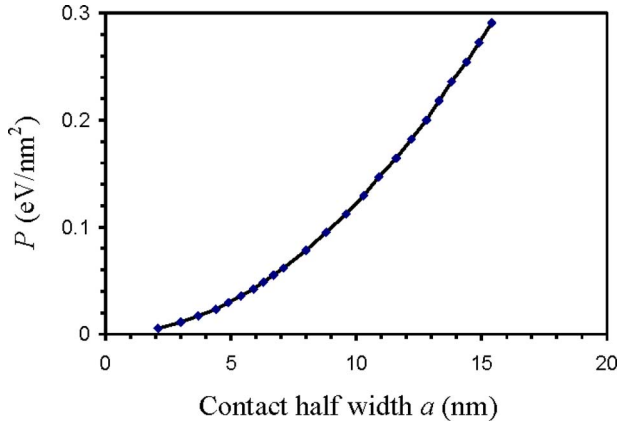

Fig. 8 Variation of total indentation force *P* with contact half width *a*

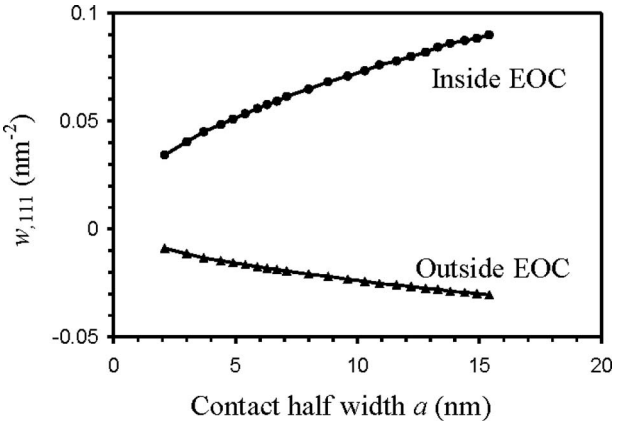

Fig. 10 Variation of maximum $w_{,111}$ at the EOC with contact half width *a*

trace of the $w_{,11}$ maximum is at an average angle roughly equal to 73 deg from the surface outside the contact zone.

A series of simulations with various loading magnitudes were carried out. They show the same characteristic behavior of the graphene sheets. From the series of simulations, the contact half width a and total indentation force P are recorded. The maximum absolute values of $w_{,11}$ and $w_{,111}$ in the first graphene sheet are also recorded. Variation of P with a is plotted in Fig. 8. Variations of $w_{,11}$ and $w_{,111}$ maxima in the first graphene sheet with P are plotted in Figs. 9 and 10. A power-law curve fitted to the data points in Fig. 8 shows an exponent of 2, the same as the case of a homogeneous substrate under cylindrical contact [18].

5 Discussions

One of the failure mechanisms in ductile plates is kinking [7,19]. The kinks may initiate in one plate and propagate in a narrow band across a stack of plates held together by high pressure. This theory of kink banding has been adopted to explain the nonlinear elastic behavior observed in graphite under nanoindentation [5,6]. The classical dislocation theory [7] was applied. In the following, we characterize the phenomenon within the discrete plate theory.

Three types of kink may occur in the case of a stack of buffered plates under indentation, depending on the number of joints involved, as schematically shown in Figs. 11(*a*)–11(*c*). Figure 11(*a*) shows a single-joint kink. It is characterized by an abrupt change of slope, and thus operated by excessive bending moment. Figure 11(*b*) shows a double-joint kink. It consists of a couple of opposite single-joint kinks close to each other. Overall it is characterized by an abrupt change in deflection, and thus operated by excessive shear force. Figure 11(*c*) shows a triple-joint kink. This may be the case when treating all the kinks underneath an indenter as a single event. Thus, it is operated by a concentrated force applied on the surface. The three types of a kink are discontinuities at various orders, characterized by $w_{,11}$, $w_{,111}$, and $w_{,1111}$, and driven by the bending moment, the shear force and the concentrated body force, respectively.

Based on the previous simulations, it can be seen that all of the three aforementioned types of a kink may occur in graphite under nanoindentation. Near the contact edge, single- and the double-joint kinks may occur since the bending moment and the shear force are both highly concentrated. Underneath the center of contact, a single-joint kink may occur if the indenter tip radius is sufficiently small. It would add to the kinks at the EOC forming a triple-joint kink. Upon initiation, the near-singular fields at the EOC may drive the single- and double-joint kinks to propagate across the stack of graphene sheets in a narrow band, i.e., kink banding. The angle of the kink band would be roughly 81 deg from the surface inside the contact zone if it is a double-joint kink and is operated by the shear force. If it is a single-joint kink and is operated by the bending moment, it would be roughly 73 deg from the surface outside the contact zone, as suggested by the simulations presented in Sec. 4.

The exponent of 2 in the power-law curve fitted to the total indentation force P versus contact half width a as shown in Fig. 8 indicates that the overall behavior of graphite under nanoindentation at a contact width of several nanometers can be well described within a homogeneous elasticity model. However, in order to predict the detailed deformation field in the vicinity of EOC at the nanometer scale, as shown in Figs. 9 and 10, an advanced model like the present one that can resolve the discrete-plate nanostructure is needed. This detailed deformation field is neces-

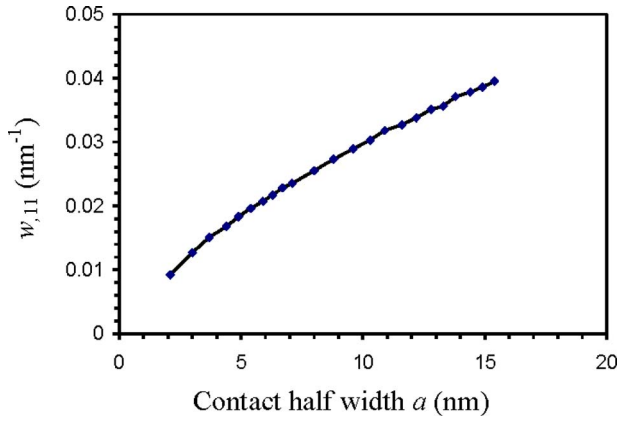

Fig. 9 Variation of maximum $w_{,11}$ at the EOC with contact half width *a*

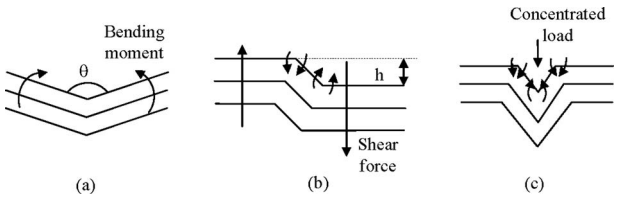

Fig. 11 (a) Bending moment-controlled single-joint kink, (b) shear force-controlled double-joint kink, and (c) concentrated load-controlled triple-joint kink

sary in order to explain the nanoscale damage processes. The model must be capable of accurately predicting the responsible loading parameters.

In order to fully understand the damage mechanisms in graphite and materials alike [20], a combined experimental and computational study is indispensable. The present study with quantitative prediction of loading parameters on individual graphene sheets may provide insights and guidance to future experimentation. Further studies are needed to understand the effects of various parameters, such as indenter tip geometry including wedge, spherical and Berkovich tips, etc., finite plate deformation, and progressive damage in various forms.

6 Conclusions

A novel two-phase continuum model has been developed for graphite at the nanoscale. It is modeled as a stack of buffered plates. While the plates represent the graphene sheets of strong covalent bonding, the buffer material models the relatively weak Van der Waals interaction between the graphene sheets. Furthermore, an efficient and accurate boundary element method has been developed to analyze the discrete-plate nanostructure under cylindrical indentation. Because the special Green's function for multilayers with platelike interfaces is employed, only the contact area on the surface where the boundary condition is altered needs to be numerically discretized. The long-range behavior of an infinite plate, which is normally troublesome to a numerical method, is analytically taken into account. The fields of bending moment and shear force in the graphene sheets have been examined. They exhibit high concentrations at the EOC. These concentrated fields are suggested to predict the initiation and the subsequent banding of single-and double-joint kinks at the EOC, whichever to occur in the reality remains unclear. The discrete-plate theory of graphite is suggested to better explain the kinking phenomenon observed in graphite than the conventional homogeneous elasticity theory.

Acknowledgment

B.Y. and R.M.R. acknowledge the financial support from the National Science Foundation (CMMI-0723486). The discussions with Vinod Tewary and Dave Read of the National Institute of Standards and Technology are greatly appreciated.

Appendix

The Green's function for multilayers with platelike interfaces has been derived in 3D [8]. The generalized Stroh formalism and 2D Fourier transformation were applied. In the following, the derivation is summarized, and the 2D reduction is described.

1 3D Green's Function for Multilayers With Platelike Interfaces. The following 2D Fourier transformation is applied to a field quantity, e.g., the displacement (i.e., the 3D Green's function),

$$\tilde{\boldsymbol{u}}(y_1,y_2;\boldsymbol{X},x_3)=\int_{-\infty}^{\infty}\int_{-\infty}^{\infty}\boldsymbol{G}^{(3D)}(\boldsymbol{X},\boldsymbol{x})e^{ix_\alpha y_\alpha}dx_1dx_2 \tag{A1}$$

where e stands for the exponential function, and i in the exponent denotes $\sqrt{-1}$. This transformation turns the 3D governing Eq. (2) (with the body force being a unit point force applied at $\mathbf{X}$) into a 1D ordinary differential equation, given by

$$C_{i3k3}\tilde{u}_{k,33}-i(C_{i\alpha k3}+C_{i3k\alpha})y_\alpha\tilde{u}_{k,3}-C_{i\alpha k\beta}y_\alpha y_\beta\tilde{u}_k=-f_i e^{iX_\alpha y_\alpha}\delta(x_3-X_3), \tag{A2}$$

where δ is the Dirac delta.

Solving the above Eq. (A2) and applying the solution to each layer result in

$$\tilde{\boldsymbol{u}}_m(y_1,y_2;\boldsymbol{X},x_3)=e^{iy_\alpha X_\alpha}[\tilde{\boldsymbol{u}}_m^{(\infty)}(y_1,y_2;x_3-X_3)+i\eta^{-1}(\overline{\boldsymbol{A}}_m\langle e^{-i\overline{\boldsymbol{p}}_m\eta(x_3-h_{m-1})}\rangle\boldsymbol{V}_m+\boldsymbol{A}_m\langle e^{-i\boldsymbol{p}_m\eta(x_3-h_m)}\rangle\boldsymbol{W}_m)] \tag{A3}$$

The subscript m indicates the quantities are associated to the mth layer where the field point $\boldsymbol{x}$ resides. $\tilde{\boldsymbol{u}}_m^{(\infty)}$, a seed solution, is taken to be the infinite-space Green's function. $\boldsymbol{V}_m$ and $\boldsymbol{W}_m$ are a pair of unknown functions to be determined by the boundary and interfacial conditions. In addition, the overbar denotes the complex conjugate, (η,θ) are the polar coordinates corresponding to (y_1,y_2) by $y_1=\eta\cos\theta$ and $y_2=\eta\sin\theta$. $\boldsymbol{p}$ and $\boldsymbol{A}$ as functions of θ and C_{ijkl} are the eigenvalues and eigenvectors of the generalized Stroh eigenproblem [10], and

$$\langle e^{-i\boldsymbol{p}\eta x_3}\rangle\equiv\mathrm{diag}[e^{-ip_1\eta x_3},e^{-ip_2\eta x_3},e^{-ip_3\eta x_3}]. \tag{A4}$$

By applying the constitutive law of the elastic layer material, the transform-domain in-plane and out-of-plane stress components, $\tilde{\boldsymbol{s}}\equiv(\tilde{\sigma}_{I11},\tilde{\sigma}_{I12},\tilde{\sigma}_{I22})$ and $\tilde{\boldsymbol{t}}\equiv(\tilde{\sigma}_{I13},\tilde{\sigma}_{I23},\tilde{\sigma}_{I33})$, respectively, can be derived from the Green's function in Eq. (A3) as

$$\tilde{\boldsymbol{t}}_m(y_1,y_2;\boldsymbol{X},x_3)=e^{iy_\alpha X_\alpha}[\tilde{\boldsymbol{t}}_m^{(\infty)}(y_1,y_2;x_3-X_3)+(\overline{\boldsymbol{B}}_m\langle e^{-i\overline{\boldsymbol{p}}_m\eta(x_3-h_{m-1})}\rangle\boldsymbol{V}_m+\boldsymbol{B}_m\langle e^{-i\boldsymbol{p}_m\eta(x_3-h_m)}\rangle\boldsymbol{W}_m)] \tag{A5}$$

$$\tilde{\boldsymbol{s}}_m(y_1,y_2;\boldsymbol{X},x_3)=e^{iy_\alpha X_\alpha}[\tilde{\boldsymbol{s}}_m^{(\infty)}(y_1,y_2;x_3-X_3)+(\overline{\boldsymbol{C}}_m\langle e^{-i\overline{\boldsymbol{p}}_m\eta(x_3-h_{m-1})}\rangle\boldsymbol{V}_m+\boldsymbol{C}_m\langle e^{-i\boldsymbol{p}_m\eta(x_3-h_m)}\rangle\boldsymbol{W}_m)] \tag{A6}$$

where $\tilde{\boldsymbol{t}}_m^{(\infty)}$ and $\tilde{\boldsymbol{s}}_m^{(\infty)}$ are derived from $\tilde{\boldsymbol{u}}_m^{(\infty)}$ in the same way as $\tilde{\boldsymbol{t}}_m$ and $\tilde{\boldsymbol{s}}_m$ from $\tilde{\boldsymbol{u}}_m$, and matrix $\boldsymbol{B}$ and $\boldsymbol{C}$ are derived from $\boldsymbol{A}$ and $\boldsymbol{p}$. Note that the matrix $\boldsymbol{C}$ here is different from the fourth-rank elastic stiffness tensor C_{ijkl} as well as its reduced matrix form.

The infinite-space Green's functions of displacement and stress are given by

$$\tilde{\boldsymbol{u}}^{(\infty)}(y_1,y_2;x_3-X_3)=\begin{cases}i\eta^{-1}\boldsymbol{A}\langle e^{-i\boldsymbol{p}\eta(x_3-X_3)}\rangle\boldsymbol{A}^{-1}(\boldsymbol{M}-\overline{\boldsymbol{M}})^{-1}, & x_3<X_3\\ i\eta^{-1}\overline{\boldsymbol{A}}\langle e^{-i\overline{\boldsymbol{p}}\eta(x_3-X_3)}\rangle\overline{\boldsymbol{A}}^{-1}(\boldsymbol{M}-\overline{\boldsymbol{M}})^{-1}, & x_3>X_3\end{cases} \tag{A7a}$$

$$\tilde{\boldsymbol{t}}^{(\infty)}(y_1,y_2;x_3-X_3)=\begin{cases}\boldsymbol{B}\langle e^{-i\boldsymbol{p}\eta(x_3-X_3)}\rangle\boldsymbol{A}^{-1}(\boldsymbol{M}-\overline{\boldsymbol{M}})^{-1}, & x_3<X_3\\ \overline{\boldsymbol{B}}\langle e^{-i\overline{\boldsymbol{p}}\eta(x_3-X_3)}\rangle\overline{\boldsymbol{A}}^{-1}(\boldsymbol{M}-\overline{\boldsymbol{M}})^{-1}, & x_3>X_3\end{cases} \tag{A7b}$$

$$\tilde{\boldsymbol{s}}^{(\infty)}(y_1,y_2;x_3-X_3)=\begin{cases}\boldsymbol{C}\langle e^{-i\boldsymbol{p}\eta(x_3-X_3)}\rangle\boldsymbol{A}^{-1}(\boldsymbol{M}-\overline{\boldsymbol{M}})^{-1}, & x_3<X_3\\ \overline{\boldsymbol{C}}\langle e^{-i\overline{\boldsymbol{p}}\eta(x_3-X_3)}\rangle\overline{\boldsymbol{A}}^{-1}(\boldsymbol{M}-\overline{\boldsymbol{M}})^{-1}, & x_3>X_3\end{cases} \tag{A7c}$$

where $\boldsymbol{M}=\boldsymbol{B}\boldsymbol{A}^{-1}$

The traction-free boundary condition on the top surface, the interfacial displacement continuity condition and the interfacial traction discontinuity condition in the transform domain are given by

$$\tilde{\boldsymbol{t}}_1=0 \quad \text{at } x_3=0 \tag{A8a}$$

$$\tilde{\boldsymbol{u}}_m=\tilde{\boldsymbol{u}}_{m+1} \quad \text{at } x_3=h_m \tag{A8b}$$

$$(\tilde{\boldsymbol{\sigma}}_{m+1}-\tilde{\boldsymbol{\sigma}}_m)\boldsymbol{n}=\tilde{\boldsymbol{A}}_m\tilde{\boldsymbol{u}}_m \quad \text{at } x_3=h_m \tag{A8c}$$

with

$$\tilde{\boldsymbol{A}}=\begin{bmatrix}E_{11}y_1^2+E_{66}y_2^2 & (E_{12}+E_{66})y_1y_2 & 0\\ (E_{21}+E_{66})y_1y_2 & E_{66}y_1^2+E_{22}y_2^2 & 0\\ 0 & 0 & D(y_1^4+2y_1^2y_2^2+y_2^4)\end{bmatrix} \tag{A9}$$

Imposition of the above conditions would result in a linear system of algebraic equations. Solving it, one may obtain the unknown

quantities $\boldsymbol{V}_m$ and $\boldsymbol{W}_m$ for all layers. This completes the solution of the Green's function for multilayers with platelike interfaces in the transform domain.

The physical-domain Green's function is obtained by applying the Fourier inverse transformation

$$\boldsymbol{G}^{(3D)}(\boldsymbol{X},\boldsymbol{x}) = \frac{1}{(2\pi)^2}\int_{-\infty}^{\infty}\int_{-\infty}^{\infty}\tilde{\boldsymbol{u}}(y_1,y_2;\boldsymbol{X},x_3)e^{-iy_\alpha x_\alpha}dy_1dy_2 \tag{A10}$$

2 2D Green's Function Due to a Line Force. The above Green's function is derived with a point force in the 3D space. In the case of a line force distributed along the x_2 axis in parallel to the interfaces, the corresponding 2D Green's function is given by

$$\mathbf{G}^{(2D)}(\mathbf{X},\mathbf{x}) = \int_{-\infty}^{\infty}\mathbf{G}^{(3D)}(\mathbf{X},\mathbf{x})dX_2 \tag{A11}$$

where the 3D Green's function is derived above. Substituting Eq. (A10) in Eq. (A11) results in

$$\boldsymbol{G}^{(2D)}(\boldsymbol{X},\boldsymbol{x}) = \frac{1}{(2\pi)^2}\int_{-\infty}^{\infty}\int_{-\infty}^{\infty}\tilde{\boldsymbol{u}}^{*}(y_1,y_2;X_3,x_3)e^{-iy_1(x_1-X_1)} \times\int_{-\infty}^{\infty}e^{-iy_2(x_2-X_2)}dX_2dy_1dy_2 \tag{A12}$$

where $\tilde{\boldsymbol{u}}^{*}$ is the function $\tilde{\boldsymbol{u}}$ divided by $e^{iy_\alpha X_\alpha}$ in Eq. (A3), and both $\mathbf{X}$ and $\mathbf{x}$ on the left-hand side effectively take components in 1 and 3 in this 2D case.

The following identity is applied to the inner integration over X_2 in Eq. (A12),

$$\int_{-\infty}^{\infty}e^{-is\eta}ds = 2\pi\delta(s). \tag{A13}$$

Further carrying out the integration involving the Dirac delta function δ results in

$$\boldsymbol{G}^{(2D)}(\boldsymbol{X},\boldsymbol{x}) = \frac{1}{2\pi}\int_{-\infty}^{\infty}\tilde{\boldsymbol{u}}^{*}(y_1,y_2=0;X_3,x_3)e^{-iy_1(x_1-X_1)}dy_1 \tag{A14}$$

Therefore, the 2D Green's function due to a line force is given in a 1D integral, while the 3D Green's function due to a point force is given in a 2D integral.

For the boundary element application, a line integral of the Green's function over an element is needed; see Eq. (8). Examining Eqs. (A3) and (A14), one may realize that the line integral over the physical element can be analytically carried out before the numerical integration over y_1. For detail of this technique, one may refer to Ref. [21].

References

[1] Kelly, B. T., 1981, *Physics of Graphite*, Applied Science, London.
[2] Novoselov, K. S., Geim, A. K., Morozov, S. V., Jiang, D., Zhang, Y., Dubonos, S. V., Grigorieva, I. V., and Firsov, A. A., 2004, "Electrical Field Effect in Atomically Thin Carbon Films," Science, **306**, pp. 666–669.
[3] Geim, A. K., and Novoselov, K. S., 2007, "The Rise of Graphene," Nat. Mater., **6**, pp. 183–191.
[4] Katsnelson, M. I., 2007, "Graphene: Carbon in Two Dimensions," Mater. Today, **10**, pp. 20–27.
[5] Barsoum, M. W., Murugaiah, A., Kalidindi, S. R., Zhen, T., and Gogotsi, Y., 2004, "Kink Band, Nonlinear Elasticity and Nanoindentations in Graphite," Carbon, **42**, pp. 1435–1445.
[6] Barsoum, M. W., Zhen, T., Zhou, A., Basu, S., and Kalidindi, S. R., 2005, "Microscale Modeling of Kinking Nonlinear Elastic Solids," Phys. Rev. B, **71**, p. 134101.
[7] Frank, F. C., and Stroh, A. N., 1952, "On the Theory of Kinking," Proc. Phys. Soc. London, **65**, pp. 811–821.
[8] Yang, B., and Tewary, V. K., 2008, "Green's Function for Multilayers With Interfacial Membrane and Flexural Rigidities," Comput., Mater., Continua, **8**, pp. 23–31.
[9] Timoshenko, S., and Woinowsky-Krieger, S., 1959, *Theory of Plates and Shells*, McGraw-Hill, New York.
[10] Ting, T. C. T., 1996, *Anisotropic Elasticity*, Oxford University Press, Oxford.
[11] Yang, B., and Tewary, V. K., 2008, "Multiscale Green's Function of Deflection in Graphene Lattice," Phys. Rev. B, **77**, p. 245442.
[12] Maradudin, A. A., Montroll, E. W., Weiss, G. H., and Ipatova, I. P., 1971, *Theory of Lattice Dynamics in the Harmonic Approximation* (Solid State Physics Suppl. 3), 2nd ed., H. Ehrenreich, F. Seitz, and D. Turnbull, eds., Academic, New York.
[13] Brenner, D. W., 1990, "Empirical Potential for Hydrocarbons for Use in Simulating the Chemical Vapor Deposition of Diamond Films," Phys. Rev. B, **42**, pp. 9458–9471.
[14] Zhou, J., and Huang, R., 2008, "Internal Lattice Relaxation of Single-Layer Graphene Under in-Plane Deformation," J. Mech. Phys. Solids, **56**, pp. 1609–1623.
[15] Brebbia, C. A., Telles, J. C. F., and Wrobel, L. C., 1984, *Boundary Elements Techniques: Theory and Applications in Engineering*, Springer-Verlag, New York.
[16] Yang, B., and Ravi-Chandar, K., 1998, "A Single-Domain Dual-Boundary-Element Formulation Incorporating a Cohesive Zone Model for Elastostatic Cracks," Int. J. Fract., **93**, pp. 115–144.
[17] Yang, B., Pan, E., and Yuan, F. G., 2003, "Three-Dimensional Stress Analysis of Composite Laminates With an Elastically Fastened Hole," Int. J. Solids Struct., **40**, pp. 2017–2035.
[18] Johnson, K. L., 1985, *Contact Mechanics*, Cambridge University Press, Cambridge, England.
[19] Wadee, M. A., Hunt, G. W., and Peletier, M. A., 2004, "Kink Band Instability in Layered Structures," J. Mech. Phys. Solids, **52**, pp. 1071–1091.
[20] Barsoum, M. W., 2004, "Mechanical Properties of the MAX Phases," *Encyclopedia of Materials: Science and Technology*, K. H. J. Buschow, R. W. Cahn, M. C. Flemings, E. J. Kramer, S. Mahajan, and P. Veyssiere, eds., Elsevier Science, New York, pp. 1–16.
[21] Yang, B., and Tewary, V. K., 2006, "Efficient Green's Function Method of Line and Surface Defects in Multilayered Elastic and Piezoelectric Materials," Comput. Model. Eng. Sci., **15**, pp. 165–178.

Wrinkling of a Fiber-Reinforced Membrane

E. Shmoylova

A. Dorfmann[1]
e-mail: luis.dorfmann@tufts.edu

Department of Civil and Environmental Engineering,
Tufts University,
Medford, MA 02155

In this paper we investigate the response of fiber-reinforced cylindrical membranes subject to axisymmetric deformations. The membrane is considered as an incompressible material, and the phenomenon of wrinkling is taken into account by means of the relaxed energy function. Two cases are considered: transversely isotropic membranes, characterized by one family of fibers oriented in one direction, and orthotropic membranes, characterized by two family of fibers oriented in orthogonal directions. The strain-energy function is considered as the sum of two terms: The first term is associated with the isotropic properties of the base material, and the second term is used to introduce transverse isotropy or orthotropy in the mechanical response. We determine the mechanical response of the membrane as a function of fiber orientations for given boundary conditions. The objective is to find possible fiber orientations that make the membrane as stiff as possible for the given boundary conditions. Specifically, it is shown that for transversely isotropic membranes a unique fiber orientation exists, which does not affect the mechanical response, i.e., the overall behavior is identical to a nonreinforced membrane.
[DOI: 10.1115/1.2967888]

1 Introduction

The importance of mechanical properties of elastic membranes is nowhere more evident than in nature where the study of morphology identifies cylindrically shaped membranes as the predominant structural configuration in plants and animals [1]. In biological organisms, examples of cylindrically shaped soft membranes are found in snakes, worms, caterpillars, guts, arteries, and seaweeds. Arbitrary shaped elastic membranes enclose, for example, living cells and the human body [2,3]. Thin-walled cylindrically shaped tubes are ideal to support internal pressure, since they have high flexural and torsional stiffnesses and represent the most economical use of available material. In engineering applications, membranes were first used as sails to harvest the force of wind and as tents to protect against the environment. More recently, due to their low weight, high stiffness-to-weight ratio, and ease of stowing and deploying, membranes have seen many applications in the space program. Unfortunately, unlike other structures such as plates or shells, membranes cannot withstand compression, so they respond by folding and wrinkling. Because wrinkling affects both the static and dynamic characteristics of membranes, the phenomenon of wrinkling needs to be accounted for in any analysis of membranes. For example, Burton and Taylor [4] and Harris et al. [5] showed how the mechanics of wrinkling provides insight into living cell locomotion. Stafford et al. [6] developed an effective technique for measuring the elastic moduli of polymeric thin films based on the critical wavelength of wrinkles.

A detailed review of wrinkling theories up to 1996 is given in the review paper by Jenkins [7]. In 1929, Wagner [8] introduced the ideas of wrinkling and the tension-field theory in connection with flexible shear panels used in airplane construction. When a thin panel is under shear in post-buckling state, the load is transmitted primarily along one of the principal axes of stress, while bending effects remain secondary. The panel deforms into a wavy or wrinkly surface, where the wrinkles align with the direction of the tensile stress. Wagner [8] developed the tension-field theory that neglects bending stiffness entirely and assumes stress to be uniaxial. Reissner [9] generalized Wagner's results and put the theory into a useful mathematical form. Early studies lacked a general theoretical framework and were limited to case-by-case analyses. Only in 1990 did Steigmann [10] develop the general tension-field theory for isotropic membranes based on the concept of the relaxed energy function introduced by Pipkin [11]. More recently, general theories have been developed that include bending stiffness [12–15].

There have also been studies on anisotropic membranes. Pipkin [16,17] modified the tension-field theory developed by Steigmann [10] to include the response of anisotropic membranes. Epstein [18] and Epstein and Forcinito [19] developed an effective algorithm to determine the relaxed energy function for anisotropic membranes that can be implemented into a finite element code.

The purpose of this paper is to examine a particular problem arising in membrane theory, which is wrinkling of a cylindrical fiber-reinforced membrane with a wire tightened around its middle. This problem is derived from the example that was first considered by Steigmann and Pipkin [20] for isotropic membranes without reinforcements. Since most biological tissues have a complex anisotropic structure and often contain naturally formed fibers, fiber-reinforced membranes deserve special attention. Therefore, to further develop the analysis of incompressible fiber-reinforced membranes, two cases are investigated: A material with one set of oriented fibers—*transversely isotropic material*, and a material reinforced by two mutually orthogonal sets of fibers—*orthotropic material*. We change the orientation of the fibers to determine the direction that requires the maximum force to squeeze the membrane by a constant amount. This direction makes the membrane as stiff as possible under the given boundary conditions and is called the *optimal direction*.

2 Preliminaries

Greek and Latin indices take values of {1,2} and {1,2,3}, respectively. We denote the transpose of $\mathbf{A}$ by $\mathbf{A}^T$, the identity tensor by $\mathbf{I}$, and the partial derivative with respect to x_α by $(\cdots)_{,\alpha} \equiv \partial(\cdots)/\partial x_\alpha$. We apply the standard summation convention over repeated indices and the dyadic notation, in which, for any two vectors $\mathbf{f}$ and $\mathbf{g}$, $\mathbf{f} \otimes \mathbf{g}$ is the tensor whose ij-component is $f_i g_j$. If $\mathbf{A}$ is a positive semidefinite, we write $\mathbf{A} \geqslant 0$.

We consider deformations of a nonlinear elastic membrane endowed with preferred directions due to embedded oriented fibers. The membrane in the reference configuration occupies a bounded

[1]Corresponding author.

Contributed by the Applied Mechanics Division of ASME for publication in the JOURNAL OF APPLIED MECHANICS. Manuscript received April 20, 2007; final manuscript received June 22, 2008; published online November 5, 2008. Review conducted by Ellen M. Arruda.

region Ω in the (x_1,x_2)-plane with a piecewise-smooth boundary $\partial\Omega$. A generic point of the region Ω is identified by the position vector $\mathbf{x}=x_\alpha\mathbf{e}_\alpha$ with respect to an arbitrary chosen origin. The coordinates of $\mathbf{x}$ are (x_1,x_2) and $\mathbf{e}_1$ and $\mathbf{e}_2$ indicate a fixed orthonormal system of base vectors.

Suppose the membrane is subjected to a three-dimensional deformation so that the material particle at $\mathbf{x}\in\Omega$ is displaced to the new position $\mathbf{r}(\mathbf{x})=r_i(\mathbf{x})\mathbf{e}_i$, where $\mathbf{e}_3=\mathbf{e}_1\times\mathbf{e}_2$ is the unit normal to the plane containing Ω. The deformation gradient tensor, denoted $\mathbf{F}(\mathbf{x})$, is given by

$$\mathbf{F}=F_{i\alpha}\mathbf{e}_i\otimes\mathbf{e}_\alpha \tag{1}$$

with components $F_{i\alpha}=\partial r_i/\partial x_\alpha$. The gradient tensor $\mathbf{F}$ describes the deformation of an infinitesimal material line element $d\mathbf{x}$ at $\mathbf{x}$ into a spatial line element $d\mathbf{r}$ at $\mathbf{r}$ given by $d\mathbf{r}=\mathbf{F}d\mathbf{x}$. The corresponding right Cauchy–Green strain tensor $\mathbf{C}(\mathbf{x})$ is given by

$$\mathbf{C}=\mathbf{F}^T\mathbf{F}=C_{\alpha\beta}\mathbf{e}_\alpha\otimes\mathbf{e}_\beta \tag{2}$$

$\mathbf{C}$ being a symmetric 2×2 tensor with components $C_{\alpha\beta}=F_{i\alpha}F_{i\beta}$.

The elastic stored strain energy, called the *strain-energy function*, is denoted by $\bar{W}(\mathbf{F})$. It is equivalent to the work done per unit initial area at $\mathbf{x}$ in changing the deformation gradient from $\mathbf{I}$ to $\mathbf{F}$. The strain energy is a scalar valued function and is therefore indifferent to a superposed rigid-body rotation after deformation, i.e., it is objective. Objectivity implies that the strain-energy function can equivalently be expressed as a function of the Cauchy–Green strain tensor $\mathbf{C}$ as follows:

$$\bar{W}(\mathbf{F})=W(\mathbf{C}) \tag{3}$$

For full details of the relevant theory on objectivity of strain-energy functions, the reader is referred to Ref. [21].

The nonsymmetric first Piola–Kirchhoff stress tensor of an unconstrained hyperelastic material, also known as the transpose of the nominal stress, is defined as

$$\boldsymbol{\sigma}=\frac{\partial\bar{W}}{\partial\mathbf{F}}=2\mathbf{F}\frac{\partial W}{\partial\mathbf{C}} \tag{4}$$

with components $\sigma_{i\alpha}=\partial\bar{W}/\partial F_{i\alpha}=2F_{i\beta}\partial W/\partial C_{\alpha\beta}$. The symmetric second Piola–Kirchhoff stress tensor is given by

$$\mathbf{S}=\mathbf{S}^T=\mathbf{F}^{-1}\frac{\partial\bar{W}}{\partial\mathbf{F}}=2\frac{\partial W}{\partial\mathbf{C}} \tag{5}$$

with components $S_{\alpha\beta}=F^{-1}_{\alpha i}\partial\bar{W}/\partial F_{i\beta}=2\partial W/\partial C_{\alpha\beta}$. The key relationship between the first Piola–Kirchhoff stress tensor $\boldsymbol{\sigma}$ and second Piola–Kirchhoff stress tensor $\mathbf{S}$ is

$$\boldsymbol{\sigma}=\mathbf{FS} \tag{6}$$

3 Relaxed Energy Function for Anisotropic Membranes

Pipkin [17] showed that for an equilibrium state to be stable, the deformation of a membrane must be noncompressive everywhere. Following the definition proposed by Pipkin, $\mathbf{F}$ is a tensile state if the normal stress on all arcs through a material particle $\mathbf{x}$ is noncompressive. This is true only if $\mathbf{S}\geqslant0$.

In actual wrinkling of membranes, the mathematical formulation may not always have a stable solution. Pipkin [17] showed that this situation can be rectified by replacing the strain-energy function, W, with a relaxed energy density, W_r, defined by

$$W_r(\mathbf{C})=\inf_{\boldsymbol{\phi}\geqslant0}W(\mathbf{C}+\boldsymbol{\phi}) \tag{7}$$

W_r represents the *lowest* strain-energy density that can be associated with the deformation $\mathbf{C}$ by allowing for the possibility that $\mathbf{C}$ accounts for fine-scale wrinkling. The minimum in Eq. (7) is achieved at a unique value, $\boldsymbol{\phi}^*(\mathbf{C})$, where $\boldsymbol{\phi}^*$ is the wrinkling strain. The associated elastic strain is then defined by the quantity

$$\mathbf{C}^*(\mathbf{C})=\mathbf{C}+\boldsymbol{\phi}^*(\mathbf{C}) \tag{8}$$

The relaxed strain-energy functions in terms of $\mathbf{F}$ and $\mathbf{C}$ are given by

$$\bar{W}_r(\mathbf{F})=W_r(\mathbf{C})=W(\mathbf{C}^*(\mathbf{C})) \tag{9}$$

The associated relaxed second Piola–Kirchhoff stress has the simple form

$$\mathbf{S}_r(\mathbf{C})=\mathbf{S}(\mathbf{C}^*(\mathbf{C}))=2\frac{\partial W_r}{\partial\mathbf{C}} \tag{10}$$

Equation (6) becomes

$$\boldsymbol{\sigma}_r=\frac{\partial\overline{W_r}}{\partial\mathbf{F}}=\mathbf{FS}_r(\mathbf{C})=\mathbf{FS}(\mathbf{C}^*(\mathbf{C})) \tag{11}$$

There are three different situations possible in practice. Membrane can be slack, tense, or neither completely slack nor completely tense, which we call wrinkled. These situations are represented by the subsets of the right Cauchy–Green deformation tensor, S, T, and U defined as

$$S=\{\mathbf{C}|\mathbf{C}\leqslant\mathbf{I}\},\quad T=\{\mathbf{C}|\mathbf{S}(\mathbf{C})\geqslant0\},\quad U=\{\mathbf{C}|\mathbf{C}\quad\text{not in } S \text{ or } T\} \tag{12}$$

Within the slack set, S, the strain can be attributed entirely to wrinkling of the undeformed state $\mathbf{C}^*(\mathbf{C})=\mathbf{I}$, and the energy and stresses are

$$W_r=0,\quad \mathbf{S}_r=\mathbf{0}\quad\text{in } S \tag{13}$$

Within the tense set, T, the calculated stress, $\mathbf{S}$, is positive. No wrinkling occurs; therefore, $\mathbf{C}^*(\mathbf{C})=\mathbf{C}$ and the energy and stresses are given by

$$W_r(\mathbf{C})=W(\mathbf{C}),\quad \mathbf{S}_r(\mathbf{C})=\mathbf{S}(\mathbf{C})\quad\text{in } T \tag{14}$$

Within the wrinkled set, U, the associated elastic strain, $\mathbf{C}^*$, produces a uniaxial tension

$$\mathbf{S}(\mathbf{C}^*)=\sigma\mathbf{t}\otimes\mathbf{t}\quad(\sigma>0,\quad|\mathbf{t}|=1) \tag{15}$$

and the wrinkling is in the direction orthogonal to $\mathbf{t}$. If $\mathbf{n}$ is a unit vector orthogonal to $\mathbf{t}$ then

$$\mathbf{C}=\mathbf{C}^*(\mathbf{C})-a^2\mathbf{n}\otimes\mathbf{n}\quad(a\neq0) \tag{16}$$

$\mathbf{C}$ is in U if and only if Eqs. (15) and (16) can be satisfied, and $\mathbf{C}$ determines the parameters in these relations uniquely, apart from sign changes of $\mathbf{t}$, $\mathbf{n}$, and a. In subset U we have

$$W_r(\mathbf{C})=W(\mathbf{C}+a^2\mathbf{n}\otimes\mathbf{n})\quad\text{and}\quad\mathbf{S}_r(\mathbf{C})=\sigma\mathbf{t}\otimes\mathbf{t} \tag{17}$$

We see that, for all $\mathbf{C}$, $\mathbf{C}^*(\mathbf{C})$ is in T; therefore, $\mathbf{S}_r(\mathbf{C})\geqslant0$. Therefore, when W_r is used as the strain-energy function, every $\mathbf{F}$ is tensile. If $\mathbf{F}$ is not tensile for W, the membrane relaxes by wrinkling, and $W_r<W$.

Stress distribution in a wrinkled region is called a tension field. In U, $\boldsymbol{\sigma}$ has rank 1, $\boldsymbol{\sigma}=\mathbf{p}\otimes\mathbf{t}$, where $|\mathbf{t}|=1$ and we say that $\boldsymbol{\sigma}$ is uniaxial. For consistency with Eq. (15), $\mathbf{p}=\sigma\mathbf{F}_0\mathbf{t}$, where $\mathbf{F}_0$ is such that $\mathbf{C}^*=\mathbf{F}_0^T\mathbf{F}_0$.

Stress trajectories are curves in the initial plane defined by the direction $\mathbf{t}$. The images of these stress trajectories are the curves with tangents $\mathbf{F}_0\mathbf{t}$ known as tension lines [10].

The relaxed energy function is obtained by assuming that the stress in the wrinkled domain is uniaxial. To solve for the wrinkling state in a membrane using tension-field theory, we first determine the direction of the stress trajectories, $\mathbf{t}$.

4 Energy Function for a Reinforced Neo-Hookean Material

In the present work we investigate wrinkling of fiber-reinforced membranes subjected to axisymmetric deformations. The mem-

brane is comprised of an incompressible neo-Hookean base material and embedded oriented fibers. Two cases are considered: transversely isotropic membranes characterized by one family of oriented fibers and orthotropic membranes with two preferred directions. In three-dimensional theory, the strain energy of an incompressible isotropic neo-Hookean material is

$$W_{\text{neo}} = \tfrac{1}{2}G(\lambda_1^2+\lambda_2^2+\lambda_3^2-3), \quad \lambda_3=(\lambda_1\lambda_2)^{-1} \tag{18}$$

where λ_i are the principal stretches, G is the shear modulus of a neo-Hookean material, and the incompressibility constraint is given by $\lambda_1\lambda_2\lambda_3=1$. For each set of fibers, we add the quadratic standard reinforcement model [22]

$$W_{\text{fib}} = \tfrac{1}{2}G\nu(\mathbf{M}\cdot(\tilde{\mathbf{C}}\mathbf{M})-1)^2 \tag{19}$$

where ν is a material constant that provides a measure of the stiffness of reinforcement in the fiber direction, i.e., the ratio between the shear moduli of the fibers and the matrix material, $\mathbf{M}$ is a vector that defines the direction of fibers, and $\tilde{\mathbf{C}}$ is the three-dimensional right Cauchy–Green strain tensor. Therefore, the total strain energy of a transversely isotropic material is

$$W = W_{\text{neo}} + W_{\text{fib}} \tag{20}$$

The associated membrane energy may be approximated by setting $\lambda_1^2=\mu_1$, $\lambda_2^2=\mu_2$, where μ_1 and μ_2 are eigenvalues of the right Cauchy–Green tensor $\mathbf{C}$ of a membrane defined by Eq. (2), and λ_3 is the stretch through the thickness. Expressing μ_1 and μ_2 in terms of components of $\mathbf{C}$, the strain-energy function of a transversely isotropic membrane is obtained as follows:

$$W = \frac{1}{2}G^*\left(C_{11}+C_{22}+\frac{1}{C_{11}C_{22}-C_{12}C_{21}}-3\right)+\frac{1}{2}G^*\nu(C_{11}\cos^2\eta + (C_{12}+C_{21})\cos\eta\sin\eta + C_{22}\sin^2\eta-1)^2 \tag{21}$$

where $G^*=Gh$, h is the initial thickness of the membrane, and η is the angle between vectors $\mathbf{M}$ and $\mathbf{e}_1$.

The strain-energy function of an isotropic membrane endowed with two sets of orthogonal fibers with the same stiffness characteristics (ν) has the form

$$W = \frac{1}{2}G^*\left(C_{11}+C_{22}+\frac{1}{C_{11}C_{22}-C_{12}C_{21}}-3\right)+\frac{1}{2}G^*\nu(C_{11}\cos^2\eta + (C_{12}+C_{21})\cos\eta\sin\eta + C_{22}\sin^2\eta-1)^2+\frac{1}{2}G^*\nu(C_{11}\sin^2\eta - (C_{12}+C_{21})\cos\eta\sin\eta + C_{22}\cos^2\eta-1)^2 \tag{22}$$

5 Geometry of Deformation

We consider axisymmetric deformations of a membrane that has the form of a circular cylindrical tube with radius R and with top and bottom ends located at $z=\pm L$. We assume these ends to be fixed and use cylindrical coordinates (r,θ,z). The results of the preceding section can be applied to the deformation considered here because the circular cylinder degenerates into a plane. If we take $x_1=R\theta$ and $x_2=z$, we can regard any deformation of the cylinder as a mapping from the (x_1,x_2)-plane.

The radial, azimuthal, and axial unit vectors are denominated by $\mathbf{i}(\theta)$, $\mathbf{j}(\theta)$, and $\mathbf{k}$, respectively, with the first two being defined in terms of $\mathbf{i}=\mathbf{i}(0)$ and $\mathbf{j}=\mathbf{j}(0)$ by

$$\mathbf{i}(\theta)=\mathbf{i}\cos\theta+\mathbf{j}\sin\theta, \quad \mathbf{j}(\theta)=-\mathbf{i}\sin\theta+\mathbf{j}\cos\theta \tag{23}$$

A wire is tightened around the cylinder in the plane $z=0$, reducing the radius to $r_0<R$. The constriction induces wrinkling of the cylinder along the generators, which implies that $\mathbf{t}=\mathbf{k}$. The deformation is axisymmetric; consequently, the displacement function $\mathbf{r}$ is independent of θ, and thus independent of x_1 in the reference plane.

An approximate solution is first constructed by assuming that the cylinder is wrinkled over its entire length, so the deformation is of class U. This solution indicates that there are taut regions near the ends $z=\pm L$; therefore, the application of the boundary conditions to the fully wrinkled solution yields only an approximation.

With regard to the upper half of the cylinder, $z\geqslant 0$, the wrinkled region of the deformed membrane is conical. A particle originally at the place (R,θ,z) is displaced to the new location

$$\mathbf{r}=r(z)\mathbf{i}(\theta)+z\mathbf{k} \tag{24}$$

where $r(z)=r_0+z\tan\gamma$ and γ is the angle between the wrinkled meridian and the axial direction. The condition $r(L)=R$ gives

$$\tan\gamma=\frac{R-r_0}{L} \tag{25}$$

The deformation gradient is $\mathbf{F}=r_{i,\alpha}\mathbf{e}_i\otimes\mathbf{e}_\alpha$, with $\mathbf{e}_1=\mathbf{j}$, $\mathbf{e}_2=\mathbf{k}$, and $\mathbf{e}_3=\mathbf{i}$ (in the initial plane $\mathbf{e}_1=\mathbf{j}(\theta)$ because $x_1=R\theta$). It follows that the components of $\mathbf{r}$ have the form

$$r_1=(r_0+z\tan\gamma)\sin\theta, \quad r_2=z, \quad r_3=(r_0+z\tan\gamma)\cos\theta \tag{26}$$

We note that $(\cdot)_{,1}=(\cdot)_{,\theta}(\mathrm{d}\theta/\mathrm{d}x_1)=(\cdot)_{,\theta}/R$; thus, we obtain

$$r_{1,1}=\frac{r\cos\theta}{R}, \quad r_{2,1}=0, \quad r_{3,1}=-\frac{r\sin\theta}{R}$$

$$r_{1,2}=\tan\gamma\sin\theta, \quad r_{2,2}=1, \quad r_{3,2}=\tan\gamma\cos\theta \tag{27}$$

Finally, the deformation gradient is

$$\mathbf{F}=\left(\frac{r}{R}\right)\mathbf{j}(\theta)\otimes\mathbf{j}(\theta)+\sec\gamma\mathbf{u}\otimes\mathbf{k} \tag{28}$$

where $\mathbf{u}$ is given by

$$\mathbf{u}=\sin\gamma\mathbf{i}(\theta)+\cos\gamma\mathbf{k} \tag{29}$$

The corresponding expression of the right Cauchy–Green strain tensor is

$$\mathbf{C}=\mathbf{F}^T\mathbf{F}=\left(\frac{r}{R}\right)^2\mathbf{j}(\theta)\otimes\mathbf{j}(\theta)+\sec^2\gamma\mathbf{k}\otimes\mathbf{k} \tag{30}$$

and the associated principal stretches are

$$\lambda_1=\frac{r(z)}{R}, \quad \lambda_2=\sec\gamma \tag{31}$$

6 Determination of the Relaxed Energy Function

As outlined in Sec. 3, the initial step consists of characterizing the stress trajectories in the membrane. For a deformation given by $\mathbf{C}=C_{11}\mathbf{j}(\theta)\otimes\mathbf{j}(\theta)+C_{22}\mathbf{k}\otimes\mathbf{k}$, expressions of the stress deformation are

$$\mathbf{S}(\mathbf{C})=2\frac{\partial W}{\partial\mathbf{C}}=2\frac{\partial W}{\partial C_{11}}\mathbf{j}(\theta)\otimes\mathbf{j}(\theta)+2\frac{\partial W}{\partial C_{22}}\mathbf{k}\otimes\mathbf{k}$$

$$\sigma=\mathbf{F}\mathbf{S}(\mathbf{C})=2\frac{\partial W}{\partial C_{11}}(\mathbf{F}\mathbf{j}(\theta))\otimes\mathbf{j}(\theta)+2\frac{\partial W}{\partial C_{22}}(\mathbf{F}\mathbf{k})\otimes\mathbf{k} \tag{32}$$

where

$$\mathbf{F}\mathbf{k}=\sec\gamma\mathbf{u} \tag{33}$$

The tension-field theory dictates that $\boldsymbol{\sigma}=\sigma\mathbf{F}_0\mathbf{t}\otimes\mathbf{t}$. Given the geometry and the axisymmetric deformation described in Sec. 5, we have $\mathbf{t}=\mathbf{k}$ and therefore for a fully wrinkled domain the stress deformation relation simplifies to

$$\boldsymbol{\sigma} = 2\frac{\partial W}{\partial C_{22}}(\mathbf{Fk}) \otimes \mathbf{k} = 2 \sec \gamma \frac{\partial W}{\partial C_{22}} \mathbf{u} \otimes \mathbf{k} \tag{34}$$

Then, the relaxed strain-energy function must satisfy the conditions

$$\frac{\partial W_r}{\partial C_{11}} = 0, \quad \frac{\partial W_r}{\partial C_{12}} \left(= \frac{\partial W_r}{\partial C_{21}} \right) = 0 \tag{35}$$

A method proposed by Epstein and Forcinito [19] is used to prove that these conditions specify the formulation of the relaxed energy function. The fact that the membrane is unable to withstand any in-plane compressive stresses can be written as $\mathbf{S}(\mathbf{C}) \geqslant 0$ or

$$S_{11}S_{22} - S_{12}S_{21} \geqslant 0 \tag{36}$$

The following is defined in Ref. [19] as the condition for an impending wrinkling of an anisotropic membrane at a given point

$$\frac{\partial W}{\partial C_{11}}\frac{\partial W}{\partial C_{22}} - \frac{\partial W}{\partial C_{12}}\frac{\partial W}{\partial C_{21}} = 0 \tag{37}$$

which can be interpreted as an equation for a surface Σ' in three-dimensional space C_{11}, C_{22}, $\sqrt{2}C_{12} = \sqrt{2}C_{21}$ (**C**-space). The characteristic lines corresponding to Eq. (37) can be determined from the conditions

$$\overline{C_{11}} = \left.\frac{\partial W}{\partial C_{22}}\right|_{\mathbf{C}^0} s + C_{11}^0 \tag{38}$$

$$\overline{C_{22}} = \left.\frac{\partial W}{\partial C_{11}}\right|_{\mathbf{C}^0} s + C_{22}^0 \tag{39}$$

$$\overline{C_{12}} = -\left.\frac{\partial W}{\partial C_{22}}\right|_{\mathbf{C}^0} s + C_{12}^0 \tag{40}$$

where $\bar{\mathbf{C}} \in \mathbf{C}$-space and $\mathbf{C^0} \in \Sigma'$ [23]. Epstein [18] also showed that the relaxed energy function has a constant value along the characteristic lines that corresponds to the value on the impending wrinkling surface, $W_r(\bar{\mathbf{C}}) = W(\mathbf{C}^0) \forall s \geqslant 0$. Therefore, to find the value of the relaxed energy function corresponding to a given strain $\bar{\mathbf{C}}$, we need to find $\mathbf{C}^0 \in \Sigma'$, which lies on the same characteristic line and evaluate $W(\mathbf{C}^0)$. The following nonlinear system of equations must be solved to find corresponding $\mathbf{C}^0 \in \Sigma'$ as follows:

$$\overline{C_{11}} = \left.\frac{\partial W}{\partial C_{22}}\right|_{\mathbf{C}^0} s + C_{11}^0 \tag{41}$$

$$\overline{C_{22}} = \left.\frac{\partial W}{\partial C_{11}}\right|_{\mathbf{C}^0} s + C_{22}^0 \tag{42}$$

$$\overline{C_{12}} = -\left.\frac{\partial W}{\partial C_{22}}\right|_{\mathbf{C}^0} s + C_{12}^0 \tag{43}$$

$$\left.\frac{\partial W}{\partial C_{11}}\right|_{\mathbf{C}^0} \left.\frac{\partial W}{\partial C_{22}}\right|_{\mathbf{C}^0} - \left.\frac{\partial W}{\partial C_{12}}\right|_{\mathbf{C}^0} \left.\frac{\partial W}{\partial C_{21}}\right|_{\mathbf{C}^0} = 0 \tag{44}$$

From Eq. (30) $\overline{C_{11}} = (r/R)^2, \overline{C_{22}} = \sec^2 \gamma$, and $\overline{C_{12}} = 0$. Taking into account the conditions given by Eq. (35), from Eq. (43) it is concluded that

$$C_{12}^0 = 0 \tag{45}$$

Then Eq. (44) simplifies to

$$\left.\frac{\partial W}{\partial C_{11}}\right|_{\mathbf{C}^0} \left.\frac{\partial W}{\partial C_{22}}\right|_{\mathbf{C}^0} = 0 \tag{46}$$

If $\partial W/\partial C_{22}|_{\mathbf{C}^0} = 0$, $\sigma = 0$, which is not the case. It follows that C_{11}^0 is such that

$$\left.\frac{\partial W}{\partial C_{11}}\right|_{\mathbf{C}^0} = 0 \tag{47}$$

and

$$C_{22}^0 = \sec^2 \gamma \tag{48}$$

Thus, we have shown that condition (35) defines the relaxed energy function that for $\bar{\mathbf{C}}$, given by Eq. (30), has the value $W_r(\bar{\mathbf{C}}) = W(\mathbf{C}_0)$, with $\mathbf{C}_0$ determined from Eqs. (45)–(48).

Using Eq. (47) with the strain-energy function given by Eq. (21), we obtain a cubic equation with respect to C_{11}^0 as follows:

$$a(C_{11}^0)^3 + b(C_{11}^0)^2 - 1 = 0 \tag{49}$$

where

$$a = 2\nu \sec^2 \gamma \cos^4 \eta$$

$$b = \sec^2 \gamma + 2\nu \sec^4 \gamma \sin^2 \eta \cos^2 \eta - 2\nu \sec^2 \gamma \cos^2 \eta \tag{50}$$

For the strain-energy function given by Eq. (22), we also get a cubic equation of the form of Eq. (49) with coefficients

$$a = 2\nu \sec^2 \gamma (\cos^4 \eta + \sin^4 \eta)$$

$$b = (1 - 2\nu)\sec^2 \gamma + 4\nu \sec^4 \gamma \sin^2 \eta \cos^2 \eta \tag{51}$$

For all possible values of ν, γ, and η in Eqs. (50) and (51), Eq. (49) has three roots, only one of which is a real positive number, which gives C_{11}^0 as a function of C_{22}^0 denoted by

$$C_{11}^0 = w(C_{22}^0) \tag{52}$$

Remark 1. A numerical analysis of the function $w(C_{22}^0)$ shows that $w(C_{22}^0) \leqslant 1$, $w(C_{22}^0) = 1$ when $C_{22}^0 = 1$, and $w(C_{22}^0)$ decreases as C_{22}^0 increases.

7 Tension Field

The force per unit initial length exerted across a parallel plane located at $z = \text{const}$ is

$$\boldsymbol{\sigma}\mathbf{k} = 2 \sec \gamma \left.\frac{\partial W}{\partial C_{22}}\right|_{\mathbf{C}^0} \mathbf{u} \tag{53}$$

Then, using Eq. (29), the resultant axial force applied to the membrane is

$$F = 2\pi R \left(2 \sec \gamma \left.\frac{\partial W}{\partial C_{22}}\right|_{\mathbf{C}^0} \right) \cos \gamma = 4\pi R \left.\frac{\partial W}{\partial C_{22}}\right|_{\mathbf{C}^0} \tag{54}$$

The magnitude of the force in the constricting wire H is given by summing the radial forces around a semicircle and imposing equilibrium. Using Eqs. (29) and (53) we have

$$H = 2R \left(2 \sec \gamma \left.\frac{\partial W}{\partial C_{22}}\right|_{\mathbf{C}^0} \right) \sin \gamma = 4R \tan \gamma \left.\frac{\partial W}{\partial C_{22}}\right|_{\mathbf{C}^0} \tag{55}$$

The assumption that the cylinder is wrinkled along its entire length has been used in the construction of the previous solution, but, in fact, $\partial W/\partial C_{11}|_{\mathbf{C}^0} = 0$ only where $C_{11} \leqslant w(C_{22}^0)$. From Eq. (30), C_{22}^0 is constant, but C_{11} increases with z. According to this solution, the value $z = z_t$ at which $C_{11} = w(C_{22}^0)$ is given by

$$\frac{L - z_t}{R} = (1 - \sqrt{w(\sec^2 \gamma)})\cot \gamma \tag{56}$$

At the maximum deformation corresponding to $r_0 = 0$ we have

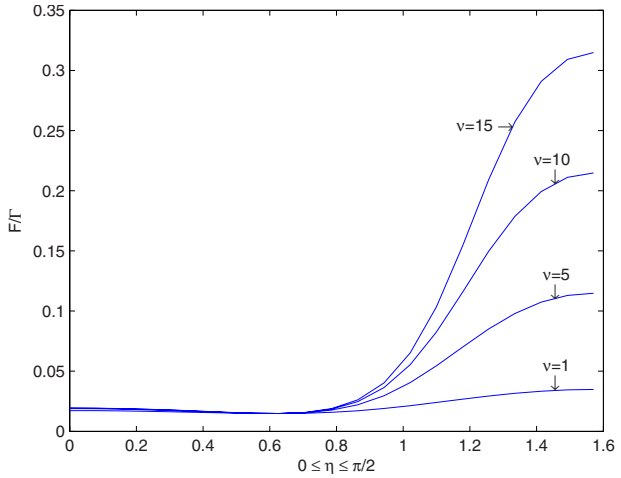

Fig. 1 The nondimensional ratios of the resultant axial force *F* to the parameter Γ versus fiber orientation η for a transversely isotropic membrane. Geometric characteristics of the cylinder: *L*=5 cm, *R*=0.5 cm, and r_0=0 cm.

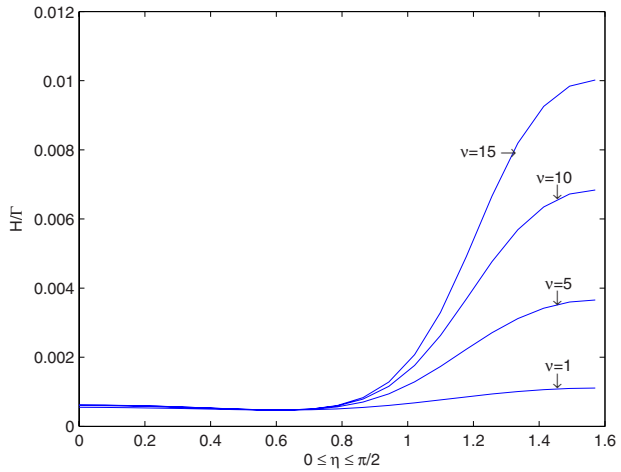

Fig. 2 The nondimensional ratios of the force in the constricting wire *H* to the parameter Γ versus fiber orientation η for a transversely isotropic membrane. Geometric characteristics of the cylinder: *L*=5 cm, *R*=0.5 cm, and r_0=0 cm.

$$\tan \gamma_m = R/L \quad \text{and} \quad (C_{22}^0)_m = 1 + (R/L)^2 \tag{57}$$

and Eq. (56) yields

$$z_t = L\sqrt{w\left(1 + \frac{R^2}{L^2}\right)} \tag{58}$$

From Remark 1, we conclude that there is a band $z_t < z \leqslant L$ that is not wrinkled. However, if R/L is small this taut zone is a relatively small fraction of the total length of the cylinder. Since the boundary conditions were applied to the fully wrinkled solution at $z=L$, where that solution is not valid, the values of C_{22}^0 and γ for the wrinkled region are in error by terms of the order of $(R/L)^2$. Thus the solution given here is only an approximation, valid to the lowest order on the parameter $(R/L)^2$.

Remark 2. A numerical analysis of the function z_t in Eq. (58) with w given by, Eq. (52) for different angles η shows that if the ratio $R/L=0.1$ the taut band $(z_t < z \leqslant L)$ is less than 0.5 of the total length L. We note that under this restriction the deformations are small, and the neo-Hookean strain-energy formulation gives the same result as infinitesimal deformation theory.

8 Numerical Example

As a numerical illustration of the theory outlined above the forces given by Eqs. (54) and (55) are determined as a function of the angle of reinforcement η for different values of nondimensional reinforcing parameter ν. In view of Remark 2, the following geometrical parameters are selected: $L=5$ cm, $R=0.5$ cm, and $r_0=0$ cm. We note that the material modulus G^* in expression (54) for the axial forces F and in the formulation (55) for H appears only as a factor. The parameter $\Gamma=2\pi RG^*$ is introduced and the nondimensional ratios F/Γ and H/Γ are defined, which depend only on fiber orientation η and on the stiffness parameter ν. For a membrane reinforced with one set of oriented fibers, the ratios of the resultant axial force F to Γ versus η for values of $\nu=1$, 5, 10, and 15 are shown in Fig. 1. The ratios of the force in the constricting wire H to Γ versus η, for the same values of ν, are shown in Fig. 2. For the value $\eta=0$ the fibers form horizontal circles around the cylinder. When $\eta=\pi/2$ the fibers are aligned with the generators of the cylinder, and for any value $0<\eta<\pi/2$ the fibers form a family of helices on the cylinder. For a membrane reinforced by two sets of fibers, Fig. 3 shows the ratios of the resultant axial force F to Γ versus η for $\nu=1$, 5, 10, and 15, and Fig. 4 show the ratios of the force in the constricting wire H to Γ versus η for the corresponding values of ν.

If the membrane is not reinforced $(\nu=0)$, the results coincide with the results given in Ref. [20]. For $\nu \neq 0$, it is shown that the forces increase linearly with the magnitude of ν, i.e., if the ratio of the shear moduli of fibers and matrix material increases, the forces required to squeeze the cylinder by the same amount increase proportionally.

For a membrane characterized by a single family of oriented fibers, a change in the direction from horizontal to vertical induces first a gradual decrease in the magnitude of the forces until a minimum value is reached, then the magnitude starts to increase rapidly. The minimum values of the forces are $F_m/\Gamma=0.0148$ and $H_m/\Gamma=0.00047156$. These are equal to the magnitude of the forces in the cylinder when no fibers are present $(\nu=0)$. The corresponding fiber orientation is given by $\eta=0.612846$ and depends on the geometric dimensions of the cylinder. It can be found numerically, but it does not have an obvious physical interpretation. The maximum values, as expected, are reached, when $\eta=\pi/2$. Thus, this is the *optimal fiber* orientation for the given boundary conditions. For two sets of fibers oriented along orthogonal directions, the forces have maxima at $\eta=0$ and $\eta=\pi/2$ and minima at $\eta=\pi/4$. The corresponding maximum values coincide approxi-

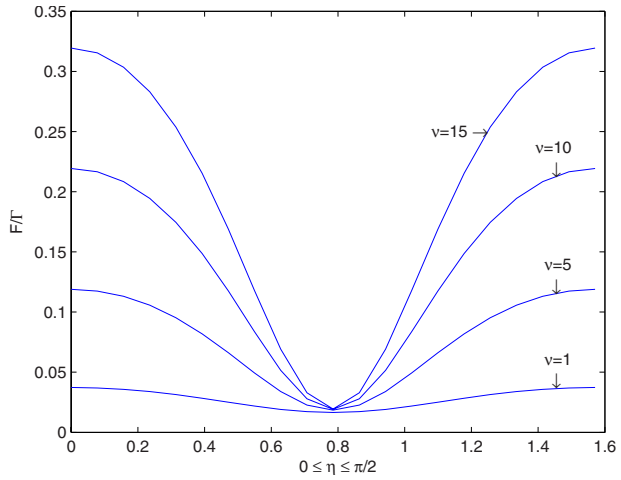

Fig. 3 The nondimensional ratios of the resultant axial force *F* to the parameter Γ versus fiber orientation η for a membrane with two families of oriented fibers. Geometric characteristics of the cylinder: *L*=5 cm, *R*=0.5 cm, and r_0=0 cm.

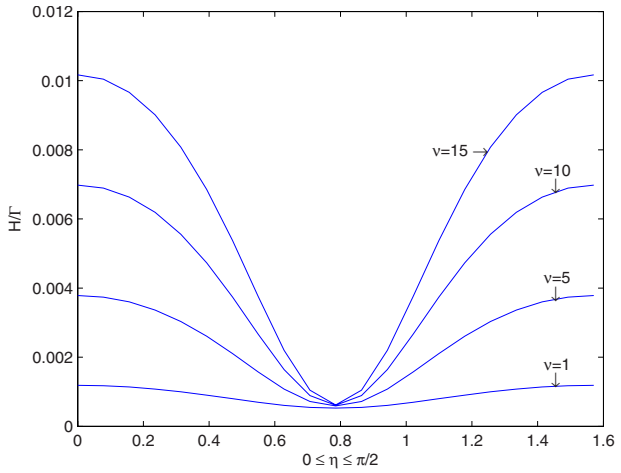

Fig. 4 The nondimensional ratios of the force in the constricting wire H to the parameter Γ versus fiber orientation η for a membrane with two families of oriented fibers. Geometric characteristics of the cylinder: $L=5$ cm, $R=0.5$ cm, and $r_0=0$ cm.

mately with the maximum values found for unidirectional reinforcement, and the minimum values are larger.

Therefore, for the given boundary conditions, one set of fibers oriented in the direction of the tensile stress, which in this case coincides with the axis of the cylinder, is sufficient to achieve the maximum stiffness of the membrane. The second set of fibers is not needed. However, if other boundary conditions are considered that generate tensile stresses oriented in different directions, two sets of fibers make the membrane stiffer compared to one set only.

References

[1] Wainwright, S. A., 1988, *Axis and Circumference, The Cylindrical Shape of Plants and Animals*, Harvard University Press, London.

[2] Danielson, D. A., 1973, "Human Skin as an Elastic Membrane," J. Biomech., **6**, pp. 539–546.

[3] Danielson, D. A., and Natarajan, S., 1975, "Tension Field Theory and the Stress in Stretched Skin," J. Biomech., **8**, pp. 135–142.

[4] Burton, K., and Taylor, D. L., 1997, "Traction Forces of Cytokinesis Measured Using Optically Modified Elastic Substrata," Nature (London), **385**, pp. 450–454.

[5] Harris, A. K., Wild, P., and Stopak, D., 1980, "Silicone Rubber Substrata: A New Wrinkle in Cell Locomotion," Science, **208**, pp. 177–179.

[6] Stafford, C. M., Harrison, C., Beers, K. L., Karim, A., Amis, E. J., Vanlandingham, M. R., Kim, H.-C., Volksen, W., Miller, R. D., and Simonyi, E., 2004, "A Buckling-Based Metrology for Measuring the Elastic Moduli of Polymeric Thin Films," Nature Mater., **3**(8), pp. 545–550.

[7] Jenkins, C. H., 1996, "Nonlinear Dynamic Response of Membranes: State of the Art—Update," Appl. Mech. Rev., **49**(10), pp. S41–S48.

[8] Wagner, H., 1929, "Flat Sheet Metal Girders With Very Thin Metal Web," Z. Flugtechnik Motorluftshiffahrt, **20**, pp. 200–207.

[9] Reissner, E., 1938, "On Tension Field Theory," *Proceedings of the 5th International Congress for Applied Mechanics*, Wiley, New York, pp. 88–92.

[10] Steigmann, D. J., 1990, "Tension-Field Theory," Proc. R. Soc. London, Ser. A, **429**, pp. 141–173.

[11] Pipkin, A. C., 1986, "The Relaxed Energy Density for Isotropic Elastic Membranes," IMA J. Appl. Math., **36**, pp. 85–99.

[12] Cerda, E., and Mahadevan, L., 2003, "Geometry and Physics of Wrinkling," Phys. Rev. Lett., **90**(7), p. 074302.

[13] Coman, C. D., 2007, "Edge-Buckling in Stretched Thin Films Under In-Plane Bending," ZAMP, **58**, pp. 510–525.

[14] Coman, C. D., and Haughton, D. M., 2006, "Localized Wrinkling Instabilities in Radially Stretched Annular Thin Films," Acta Mech., **185**, pp. 179–200.

[15] Wong, Y. W., and Pellegrino, S., 2006, "Wrinkled Membranes II: Analitical Models," J. Mech. Mater. Struct., **1**, pp. 25–59.

[16] Pipkin, A. C., 1993, "Relaxed Energy Densities for Small Deformations of Membranes," IMA J. Appl. Math., **50**, pp. 225–237.

[17] Pipkin, A. C., 1994, "Relaxed Energy Densities for Large Deformations of Membranes," IMA J. Appl. Math., **52**, pp. 297–308.

[18] Epstein, M., 1999, "On the Wrinkling of Anisotropic Elastic Membranes," J. Elast., **55**, pp. 99–109.

[19] Epstein, M., and Forcinito, M. A., 2001, "Anisotropic Membrane Wrinkling: Theory and Analysis," Int. J. Solids Struct., **38**, pp. 5253–5272.

[20] Steigmann, D. J., and Pipkin, A. C., 1989, "Finite Deformations of Wrinkled Membranes," Q. J. Mech. Appl. Math., **42**, pp. 427–440.

[21] Ogden, R. W., 1997, *Non-Linear Elastic Deformations*, Dover, New York.

[22] Merodio, J., and Ogden, R. W., 2005, "Mechanical Response of Fiber-Reinforced Incompressible Non-Linearly Elastic Solids," Int. J. Non-Linear Mech., **40**, pp. 213–227.

[23] Courant, R., and Hilbert, D., 1962, *Methods of Mathematical Physics*, Vol. 2, Wiley, New York.

On Partially Debonded Circular Inclusions in Finite Plane Elastostatics of Harmonic Materials

X. Wang[1]
e-mail: xuwang_sun@hotmail.com

E. Pan

Department of Civil Engineering,
and Department of Applied Mathematics,
University of Akron,
Akron, OH 44325-3905

*We investigate a partially debonded circular elastic inclusion embedded in a particular class of harmonic materials by using the complex variable method under finite plane-strain deformations. A complete (or full-field) solution is derived. It is observed that the stresses in general exhibit oscillatory singularities near the two tips of the arc shaped interface crack. Particularly the traditional inverse square root singularity for stresses is observed when the asymptotic behavior of the harmonic materials obeys a constitutive restriction proposed by Knowles and Sternberg (1975, "On the Singularity Induced by Certain Mixed Boundary Conditions in Linearized and Nonlinear Elastostatics," Int. J. Solids Struct., **11**, pp. 1173–1201). It is also found that the number of admissible states under finite plane deformations for given external loads can be two, one, or even zero.*
[DOI: 10.1115/1.3000023]

Keywords: finite deformation, circular inclusion, arc shaped crack

1 Introduction

The problem of a circular arc shaped crack lying along the interface of an elastic inclusion is a classical one and has received considerable amount of attention [1–4]. In these studies, the mixed-boundary value problem was formulated on the basis of the complex variable approach and was finally reduced to an inhomogeneous Riemann–Hilbert problem whose exact solution can be easily derived. These studies show that the stresses near the tips of an interface arc crack still exhibit the same oscillatory singularities as those obtained for a straight crack between dissimilar media [5,6]. In previous investigations [1,4], the problem of an arc shaped interfacial crack was solved within the framework of linear elastostatics. In contrast, an exact solution to the analogous problem in *finite* elasticity is still absent.

An elegant complex variable formulation of a class of problems involving the finite plane-strain deformations of a set of compressible hyperelastic materials of harmonic type was recently developed [7]. The complex variable formulation [7] has also been applied to (i) get a complete solution for a planar interface crack between two half-planes occupied by two dissimilar harmonic materials [7], (ii) obtain a complete solution for an elliptical inclusion with uniform interior stress field perfectly bonded to a matrix of harmonic materials under any uniform remote stress distribution [8], (iii) identify the harmonic shapes for harmonic materials [9], and (iv) analyze the surface instability of a harmonic solid attracted by a rigid body through the influence of van der Waals forces [10].

The objective of the present work is to investigate in detail a two-dimensional crack along the interface of a circular elastic inclusion embedded in an unbounded matrix of harmonic materials loaded by remote uniform Piola stresses. By using the complex variable method, the original mixed-boundary value problem is finally reduced to an inhomogeneous Riemann–Hilbert problem. It is found that the Piola stresses near the tips of the arc interface crack still exhibit the oscillatory singularities as those obtained for a straight crack [7]. Particularly the conventional inverse square root singularity for stresses near the tips of the interface arc crack is still observed when the asymptotic behavior of the harmonic materials obeys a constitutive restriction proposed by Knowles and Sternberg [11].

2 Basic Formulations

Let the complex variable $z=x_1+ix_2$ be the initial coordinates of a material particle in the undeformed configuration and $w(z)=y_1(z)+iy_2(z)$ be the corresponding spatial coordinates in the deformed configuration. The deformation gradient tensor is defined as

$$F_{ij}=\frac{\partial y_i}{\partial x_j} \tag{1}$$

For a particular class of harmonic materials, the strain energy density W defined with respect to the undeformed unit area can be expressed by

$$W=2\mu[F(I)-J],\quad F'(I)=\frac{1}{4\alpha}[I+\sqrt{I^2-16\alpha\beta}] \tag{2}$$

Here I and J are the scalar invariants of FF^T given by

$$I=\lambda_1+\lambda_2=\sqrt{F_{ij}F_{ij}+2J},\quad J=\lambda_1\lambda_2=\det[F] \tag{3}$$

where λ_1 and λ_2 are the principal stretches, μ is the shear modulus, and $1/2\leq\alpha<1$, $\beta>0$ are two material constants. This special class of harmonic materials has attracted considerable attention [12,13].

According to the formulation developed by Ru [7], the deformation $w(z)$ can be written in terms of two analytic functions $\varphi(z)$ and $\psi(z)$ as

$$iw(z)=\alpha\varphi(z)+i\overline{\psi(z)}+\frac{\beta z}{\varphi'(z)} \tag{4}$$

and the complex Piola stress function $\chi(z)$ is given by

[1]Corresponding author.

Contributed by the Applied Mechanic Division of ASME for publication in the JOURNAL OF APPLIED MECHANICS. Manuscript received April 14, 2008; final manuscript received June 19, 2008; published online November 5, 2008. Review conducted by Martin Ostoja-Starzewski.

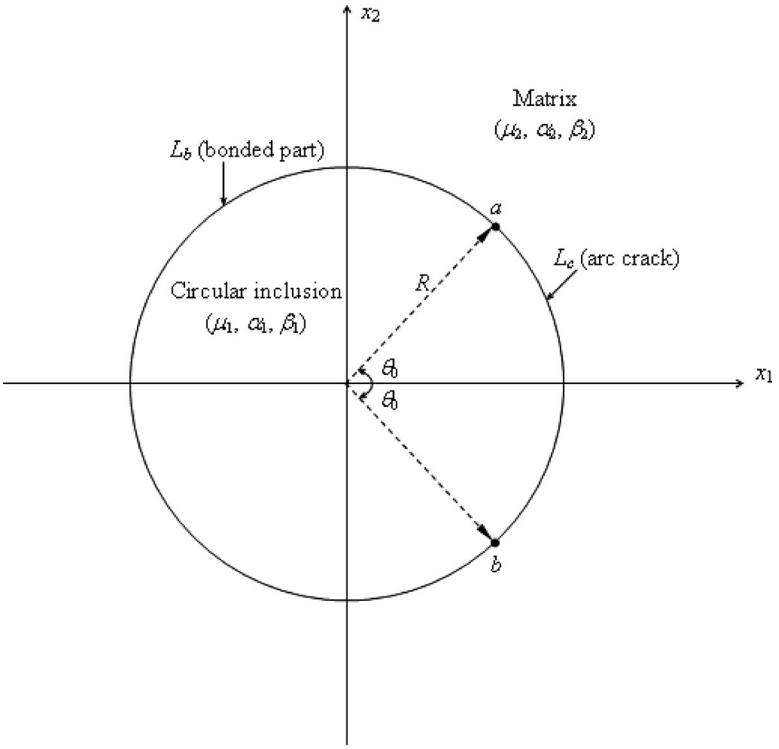

Fig. 1 An arc crack along the interface between a circular inclusion and the matrix

$$\chi(z) = 2i\mu\left[(\alpha-1)\varphi(z) + i\overline{\psi(z)} + \frac{\beta z}{\varphi'(z)}\right] \tag{5}$$

In addition, the Piola stress components can be written in terms of the Piola stress function χ as

$$-\sigma_{21} + i\sigma_{11} = \chi_{,2}, \quad \sigma_{22} - i\sigma_{12} = \chi_{,1} \tag{6}$$

3 Complete Solution for a Partially Debonded Circular Inclusion

As shown in Fig. 1, we consider a circular inclusion of radius R partially bonded to an infinite matrix. We take the origin at the center of the inclusion and assume that an interfacial arc crack, whose surface is traction-free, is made along the arc L_c of the interface while along the remaining arc L_b the inclusion is still perfectly bonded to the matrix. Furthermore, let the center of the arc L_c lie on the positive x_1-axis and the central angle subtended by the arc L_c is $2\theta_0$. $a=Re^{i\theta_0}$ and $b=Re^{-i\theta_0}$ are two crack tips. The elastic materials occupying the inclusion and the matrix belong to the special class of harmonic materials characterized by Eq. (2) with the associated elastic constants μ_1, α_1, and β_1 and μ_2, α_2, and β_2, respectively. The composite system is assumed to be under the remote uniform Piola stresses σ_{11}^{∞}, σ_{22}^{∞}, σ_{12}^{∞}, and σ_{21}^{∞}. Throughout this paper, all physical quantities associated with the circular inclusion and unbounded matrix are identified by the subscripts 1 and 2, respectively.

The continuity condition of tractions across the total interface $|z|=R$ can be expressed as

$$\Gamma(\alpha_1-1)\varphi_1^+(z) + i\Gamma\overline{\psi}_1^-(R^2/z) + \frac{\Gamma\beta_1 z}{\overline{\varphi}_1'^-(R^2/z)} = (\alpha_2-1)\varphi_2^-(z) + i\overline{\psi}_2^+(R^2/z) + \frac{\beta_2 z}{\overline{\varphi}_2'^+(R^2/z)}, \quad (|z|=R) \tag{7}$$

where $\Gamma=\mu_1/\mu_2$, and the superscripts "+" and "−" denote the limit values from the inner and outer sides of the interface $|z|=R$, respectively.

It follows from Eq. (7) that

$$\Gamma(\alpha_1-1)\varphi_1^+(z) - i\overline{\psi}_2^+(R^2/z) - \frac{\beta_2 z}{\overline{\varphi}_2'^+(R^2/z)} = (\alpha_2-1)\varphi_2^-(z) - i\Gamma\overline{\psi}_1^-(R^2/z) - \frac{\Gamma\beta_1 z}{\overline{\varphi}_1'^-(R^2/z)}, \quad (|z|=R) \tag{8}$$

At infinity, it is assumed that the remote Piola stresses are uniform. Then $\varphi_2(z)$ and $\psi_2(z)$ exhibit the following asymptotic behavior:

$$\varphi_2(z) = Az + o(1), \quad \psi_2(z) = Bz + o(1), \quad |z| \to \infty \tag{9}$$

where the two complex constants A and B are related to the remote Piola stresses $\sigma_{11}^{\infty}, \sigma_{22}^{\infty}, \sigma_{12}^{\infty}$, and σ_{21}^{∞} through the following relations:

$$-\sigma_{21}^{\infty} + i\sigma_{11}^{\infty} = 2\mu_2\left[(1-\alpha_2)A + i\overline{B} - \frac{\beta_2}{\overline{A}}\right]$$

$$i\sigma_{22}^{\infty} + \sigma_{12}^{\infty} = 2\mu_2\left[(1-\alpha_2)A - i\overline{B} - \frac{\beta_2}{\overline{A}}\right] \tag{10}$$

In view of Eqs. (8) and (9), we now define the following new function $\Omega(z)$ as

$$\Omega(z)=\begin{cases}\Gamma(\alpha_1-1)\varphi_1(z)-i\bar{\psi}_2(R^2/z)-\dfrac{\beta_2 z}{\bar{\varphi}_2'(R^2/z)}+\left[\dfrac{\Gamma\beta_1}{\overline{\varphi_1'(0)}}-(\alpha_2-1)A\right]z+i\bar{B}R^2z^{-1}, & |z|<R\\ (\alpha_2-1)\varphi_2(z)-i\Gamma\bar{\psi}_1(R^2/z)-\dfrac{\Gamma\beta_1 z}{\bar{\varphi}_1'(R^2/z)}+\left[\dfrac{\Gamma\beta_1}{\overline{\varphi_1'(0)}}-(\alpha_2-1)A\right]z+i\bar{B}R^2z^{-1}, & |z|>R\end{cases} \tag{11}$$

It is apparent that $\Omega(z)$ is continuous across the interface $|z|=R$ and then analytic in the whole plane including the points at zero and at infinity. Consequently, $\Omega(z)=0$. As a result we arrive at the following relationships:

$$i\bar{\psi}_2(R^2/z)+\frac{\beta_2 z}{\bar{\varphi}_2'(R^2/z)}=\Gamma(\alpha_1-1)\varphi_1(z)+\left[\frac{\Gamma\beta_1}{\overline{\varphi_1'(0)}}-(\alpha_2-1)A\right]z+i\bar{B}R^2z^{-1} \tag{12a}$$

$$i\bar{\psi}_1(R^2/z)+\frac{\beta_1 z}{\bar{\varphi}_1'(R^2/z)}=\Gamma^{-1}(\alpha_2-1)\varphi_2(z)+\left[\frac{\beta_1}{\overline{\varphi_1'(0)}}-\Gamma^{-1}(\alpha_2-1)A\right]z+i\Gamma^{-1}\bar{B}R^2z^{-1} \tag{12b}$$

The traction-free condition of the cracked part L_c of the interface can be expressed as

$$(\alpha_1-1)\varphi_1^+(z)+i\bar{\psi}_1^-(R^2/z)+\frac{\beta_1 z}{\bar{\varphi}_1'^-(R^2/z)}=0,\quad z\in L_c \tag{13}$$

Substituting the result of Eq. (12*b*) into Eq. (13) yields

$$(\alpha_1-1)\varphi_1^+(z)+\Gamma^{-1}(\alpha_2-1)\varphi_2^-(z)+\left[\frac{\beta_1}{\overline{\varphi_1'(0)}}-\Gamma^{-1}(\alpha_2-1)A\right]z+i\Gamma^{-1}\bar{B}R^2z^{-1}=0,\quad z\in L_c \tag{14}$$

In view of Eq. (14), we introduce an auxiliary function $h(z)$ defined by

$$h(z)=\begin{cases}(\alpha_1-1)\varphi_1(z)+\dfrac{\beta_1}{\overline{\varphi_1'(0)}}z, & |z|<R\\ \Gamma^{-1}(1-\alpha_2)\varphi_2(z)+\Gamma^{-1}(\alpha_2-1)Az-i\Gamma^{-1}\bar{B}R^2z^{-1}, & |z|>R\end{cases} \tag{15}$$

Apparently $h(z)$ is holomorphic in $|z|<R$ and $|z|>R$, respectively. $h(z)=o(1)$ as $|z|\to\infty$. Furthermore,

$$h^+(z)-h^-(z)=0,\quad z\in L_c \tag{16}$$

The continuity condition of displacements across the bonded part L_b of the interface can be expressed as

$$\alpha_1\varphi_1^+(z)+i\bar{\psi}_1^-(R^2/z)+\frac{\beta_1 z}{\bar{\varphi}_1'^-(R^2/z)}=\alpha_2\varphi_2^-(z)+i\bar{\psi}_2^+(R^2/z)+\frac{\beta_2 z}{\bar{\varphi}_2'^+(R^2/z)},\quad z\in L_b \tag{17}$$

Utilizing Eqs. (12) and (15), the above expression can be equivalently expressed in terms of $h(z)$ as

$$h^+(z)+kh^-(z)=\frac{\alpha_1-1}{\alpha_1-\Gamma(\alpha_1-1)}\left[\frac{\beta_1}{(\alpha_1-1)\overline{\varphi_1'(0)}}+A\right]z-\frac{i\bar{B}R^2(\alpha_1-1)}{(\alpha_2-1)[\alpha_1-\Gamma(\alpha_1-1)]}z^{-1},\quad z\in L_b \tag{18}$$

where

$$k=\frac{(1-\alpha_1)[\Gamma\alpha_2+(1-\alpha_2)]}{(1-\alpha_2)[\alpha_1+\Gamma(1-\alpha_1)]}>0 \tag{19}$$

Therefore, it is observed that the stresses near the two crack tips $a=Re^{i\theta_0}$ and $b=Re^{-i\theta_0}$ exhibit oscillatory singularities, a phenomenon in agreement with that observed for a planar interface crack [7].

If we choose $\alpha_1=\alpha_2=1/2$ for the situation in which $F'(I)/I$ approaches unity as I tends to infinity [7,11], then Eq. (18) simplifies to

$$h^+(z)+h^-(z)=\frac{1}{1+\Gamma}\left(\frac{2\beta_1}{\overline{\varphi_1'(0)}}-A\right)z-\frac{2i\bar{B}R^2}{1+\Gamma}z^{-1},\quad z\in L_b \tag{20}$$

The solution to the inhomogeneous Riemann–Hilbert problem (i.e., Eqs. (16) and (20)) can be expediently given by

$$h(z)=\frac{1}{1+\Gamma}\left(\frac{\beta_1}{\overline{\varphi_1'(0)}}-\frac{A}{2}\right)[z-X(z)]-\frac{i\bar{B}R^2}{1+\Gamma}[z^{-1}-z^{-1}X^{-1}(0)X(z)] \tag{21}$$

where the multivalued function $X(z)=\sqrt{(z-a)(z-b)}$ is discontinuous across the bonded part L_b of the interface, and $X(z)=z+o(1)$ as $|z|\to\infty$. It follows from the above result and Eq. (15) that

$$\begin{aligned}\varphi_1(z)&=-\frac{2}{1+\Gamma}\left(\frac{\beta_1}{\overline{\varphi_1'(0)}}-\frac{A}{2}\right)[z-X(z)]+\frac{2i\bar{B}R^2}{1+\Gamma}[z^{-1}-z^{-1}X^{-1}(0)X(z)]+\frac{2\beta_1}{\overline{\varphi_1'(0)}}z, && (|z|<R)\\ \varphi_2(z)&=\frac{2\Gamma}{1+\Gamma}\left(\frac{\beta_1}{\overline{\varphi_1'(0)}}-\frac{A}{2}\right)[z-X(z)]-\frac{2i\Gamma\bar{B}R^2}{1+\Gamma}[z^{-1}-z^{-1}X^{-1}(0)X(z)]+2i\bar{B}R^2z^{-1}+Az, && (|z|>R)\end{aligned} \tag{22}$$

Once $\varphi_1(z)$ and $\varphi_2(z)$ are determined, the other two analytic functions $\psi_1(z)$ and $\psi_2(z)$ can be determined from Eq. (12) as

$$\psi_1(z) = i\Gamma^{-1}(\alpha_2 - 1)\bar{\varphi}_2(R^2/z) - \frac{i\beta_1 R^2}{z\varphi_1'(z)} + i\left[\frac{\beta_1}{\varphi_1'(0)} - \Gamma^{-1}(\alpha_2 - 1)\bar{A}\right]R^2 z^{-1} + \Gamma^{-1}Bz, \quad (|z| < R)$$
$$\psi_2(z) = i\Gamma(\alpha_1 - 1)\bar{\varphi}_1(R^2/z) - \frac{i\beta_2 R^2}{z\varphi_2'(z)} + i\left[\frac{\Gamma\beta_1}{\varphi_1'(0)} - (\alpha_2 - 1)\bar{A}\right]R^2 z^{-1} + Bz, \quad (|z| > R) \tag{23}$$

Now the unknown $\varphi_1'(0)$ has to be determined by the following equation:

$$\varphi_1'(0) - \frac{2\beta_1(X'(0)+\Gamma)}{1+\Gamma}\frac{1}{\overline{\varphi_1'(0)}} = \frac{A[1-X'(0)]}{1+\Gamma} - \frac{i\bar{B}R^2}{1+\Gamma}\frac{X''(0)}{X(0)} \tag{24}$$

where

$$X(0) = R, \quad X'(0) = -\cos\theta_0, \quad X''(0) = \frac{\sin^2\theta_0}{R} \tag{25}$$

Next we discuss the roots to Eq. (24) according to the three cases: $\Gamma > \cos\theta_0$, $\Gamma = \cos\theta_0$, and $\Gamma < \cos\theta_0$.

- $X'(0)+\Gamma > 0$ (or $\Gamma > \cos\theta_0$)

  In this case there exist two distinct roots for $\varphi_1'(0)$.

$$|\varphi_1'(0)| = \frac{|A(1+\cos\theta_0) - i\bar{B}\sin^2\theta_0| + \sqrt{|A(1+\cos\theta_0) - i\bar{B}\sin^2\theta_0|^2 + 8\beta_1(1+\Gamma)(\Gamma - \cos\theta_0)}}{2(1+\Gamma)}$$
$$\arg\{\varphi_1'(0)\} = \arg\{A(1+\cos\theta_0) - i\bar{B}\sin^2\theta_0\} \tag{26a}$$

or

$$|\varphi_1'(0)| = \frac{-|A(1+\cos\theta_0) - i\bar{B}\sin^2\theta_0| + \sqrt{|A(1+\cos\theta_0) - i\bar{B}\sin^2\theta_0|^2 + 8\beta_1(1+\Gamma)(\Gamma - \cos\theta_0)}}{2(1+\Gamma)}$$
$$\arg\{\varphi_1'(0)\} = \arg\{A(1+\cos\theta_0) - i\bar{B}\sin^2\theta_0\} - \pi \tag{26b}$$

- $X'(0)+\Gamma = 0$ (or $\Gamma = \cos\theta_0$)

  In this case there exists only one single root for $\varphi_1'(0)$.

$$\varphi_1'(0) = A - \frac{i\bar{B}\sin^2\theta_0}{1+\cos\theta_0} \tag{27}$$

- $X'(0)+\Gamma < 0$ (or $\Gamma < \cos\theta_0$)

  This case includes three subcases.

- If $|A(1+\cos\theta_0) - i\bar{B}\sin^2\theta_0| > 2\sqrt{2\beta_1(1+\Gamma)(\cos\theta_0 - \Gamma)}$, then there also exist two roots for $\varphi_1'(0)$.

$$|\varphi_1'(0)| = \frac{|A(1+\cos\theta_0) - i\bar{B}\sin^2\theta_0| \pm \sqrt{|A(1+\cos\theta_0) - i\bar{B}\sin^2\theta_0|^2 + 8\beta_1(1+\Gamma)(\Gamma - \cos\theta_0)}}{2(1+\Gamma)}$$
$$\arg\{\varphi_1'(0)\} = \arg\{A(1+\cos\theta_0) - i\bar{B}\sin^2\theta_0\} \tag{28}$$

- If $|A(1+\cos\theta_0) - i\bar{B}\sin^2\theta_0| = 2\sqrt{2\beta_1(1+\Gamma)(\cos\theta_0 - \Gamma)}$, then there exists only one root for $\varphi_1'(0)$.

$$\varphi_1'(0) = \frac{A(1+\cos\theta_0) - i\bar{B}\sin^2\theta_0}{2(1+\Gamma)} \tag{29}$$

- If $|A(1+\cos\theta_0) - i\bar{B}\sin^2\theta_0| < 2\sqrt{2\beta_1(1+\Gamma)(\cos\theta_0 - \Gamma)}$, then there is no possible root for $\varphi_1'(0)$.

  Due to the fact that the mean Piola stress within the circular inclusion is given by [9]

$$\sigma_{11} + \sigma_{22} = 4\mu_1 \,\mathrm{Im}\left\{(1-\alpha_1)\varphi_1'(z) + \frac{\beta_1}{\varphi_1'(z)}\right\}, \quad (|z| < R) \tag{30}$$

  Then the average mean Piola stress within the circular inclusion is

$$[\sigma_{11} + \sigma_{22}]_{\text{average}} = 4\mu_1 \,\mathrm{Im}\left\{(1-\alpha_1)\varphi_1'(0) + \frac{\beta_1}{\varphi_1'(0)}\right\} \tag{31}$$

It is observed from the above expression that the average mean Piola stress within the circular inclusion is closely related with $\varphi_1'(0)$.

4 Complete Solution for a Perfectly Bonded Circular Inclusion

If the circular inclusion is perfectly bonded to the matrix, then the two pairs of analytic functions $\varphi_1(z), \psi_1(z)$ and $\varphi_2(z), \psi_2(z)$ can be easily determined to be

$$\varphi_1(z) = \frac{A - \dfrac{(1-\Gamma)\beta_1}{\overline{\varphi_1'(0)}}}{\alpha_1 + \Gamma(1-\alpha_1)} z, \quad \psi_1(z) = \frac{B}{\Gamma\alpha_2 + (1-\alpha_2)} z, \quad (|z| < R) \tag{32}$$

$$\varphi_2(z) = Az - \frac{i(\Gamma-1)\bar{B}R^2}{\Gamma\alpha_2 + (1-\alpha_2)} z^{-1}, \quad \psi_2(z) = Bz + i\left[\left(\frac{\alpha_1}{\alpha_1 + \Gamma(1-\alpha_1)} - \alpha_2\right)\bar{A} + \frac{\Gamma\beta_1}{\alpha_1 + \Gamma(1-\alpha_1)} \frac{1}{\varphi_1'(0)}\right] R^2 z^{-1} - \frac{i\beta_2 R^2 z}{Az^2 + \dfrac{i(\Gamma-1)\bar{B}R^2}{\Gamma\alpha_2 + (1-\alpha_2)}}, \quad (|z| > R) \tag{33}$$

It then follows from Eq. (32) that stresses are uniform within the perfectly bonded circular inclusion. The uniformity of stresses within a more general elliptical inclusion has been observed by Ru et al. [8]. The unknown $\varphi_1'(0)$ in Eqs. (32) and (33) can be determined by the following equation.

$$\varphi_1'(0) + \frac{(1-\Gamma)\beta_1}{\alpha_1 + \Gamma(1-\alpha_1)} \frac{1}{\overline{\varphi_1'(0)}} = \frac{A}{\alpha_1 + \Gamma(1-\alpha_1)} \tag{34}$$

In the following, we discuss the roots to Eq. (34) for the three cases: $\Gamma > 1$ (the inclusion is stiffer than the matrix), $\Gamma = 1$ (the inclusion and the matrix have the same shear modulus), and $\Gamma < 1$ (the inclusion is softer than the matrix).

- $\Gamma > 1$ (the inclusion is stiffer than the matrix)
  In this case there are two roots for $\varphi_1'(0)$.

$$|\varphi_1'(0)| = \frac{|A| + \sqrt{|A|^2 + 4[\alpha_1 + \Gamma(1-\alpha_1)](\Gamma-1)\beta_1}}{2[\alpha_1 + \Gamma(1-\alpha_1)]}$$

$$\arg\{\varphi_1'(0)\} = \arg\{A\} \tag{35a}$$

  or

$$|\varphi_1'(0)| = \frac{-|A| + \sqrt{|A|^2 + 4[\alpha_1 + \Gamma(1-\alpha_1)](\Gamma-1)\beta_1}}{2[\alpha_1 + \Gamma(1-\alpha_1)]}$$

$$\arg\{\varphi_1'(0)\} = \arg\{A\} - \pi \tag{35b}$$

- $\Gamma = 1$ (the inclusion and matrix have the same shear modulus)
  In this case there is only one root for $\varphi_1'(0)$.

$$\varphi_1'(0) = A \tag{36}$$

- $\Gamma < 1$ (the inclusion is softer than the matrix)
  This case includes three subcases.

- If $|A| > 2\sqrt{[\alpha_1 + \Gamma(1-\alpha_1)](1-\Gamma)\beta_1}$, then there also exist two roots for $\varphi_1'(0)$.

$$|\varphi_1'(0)| = \frac{|A| \pm \sqrt{|A|^2 - 4[\alpha_1 + \Gamma(1-\alpha_1)](1-\Gamma)\beta_1}}{2[\alpha_1 + \Gamma(1-\alpha_1)]}$$

$$\arg\{\varphi_1'(0)\} = \arg\{A\} \tag{37}$$

- If $|A| = 2\sqrt{[\alpha_1 + \Gamma(1-\alpha_1)](1-\Gamma)\beta_1}$, then there exists only one root for $\varphi_1'(0)$.

$$\varphi_1'(0) = \frac{A}{2[\alpha_1 + \Gamma(1-\alpha_1)]} \tag{38}$$

- If $|A| < 2\sqrt{[\alpha_1 + \Gamma(1-\alpha_1)](1-\Gamma)\beta_1}$, then there is no possible root for $\varphi_1'(0)$.

  Finally if we let $\theta_0 = 0$ (there is no crack on the interface) in Eq. (24), and let $\alpha_1 = \alpha_2 = 1/2$ in Eq. (34), then Eqs. (24) and (34) will both reduce to the following equation.

$$\varphi_1'(0) + \frac{2\beta_1(1-\Gamma)}{1+\Gamma} \frac{1}{\overline{\varphi_1'(0)}} = \frac{2A}{1+\Gamma} \tag{39}$$

which partially verifies the correctness of both Eqs. (24) and (34).

5 Conclusions

We have investigated the finite plane-strain deformation of a circular elastic inclusion bonded partially to an unbounded matrix. The elastic materials occupying the inclusion and the matrix belong to the class of harmonic materials. A complete solution to the arc interface crack problem is derived by means of the complex variable method. During the derivation, we focus on the case $\alpha_1 = \alpha_2 = 1/2$ in which the oscillatory singularity will disappear. We also present the complete solution for a circular inclusion perfectly bonded to the matrix. The results show that:

- When one of the two conditions (i) $\Gamma > \cos\theta_0$ or (ii) $\Gamma < \cos\theta_0$ and $|A(1+\cos\theta_0) - i\bar{B}\sin^2\theta_0| > 2\sqrt{2\beta_1(1+\Gamma)(\cos\theta_0 - \Gamma)}$ is satisfied, it is possible to find two different states under finite plane deformations for the given remote uniform Piola stresses.
- When one of the two conditions (i) $\Gamma = \cos\theta_0$ or (ii) $\Gamma < \cos\theta_0$ and $|A(1+\cos\theta_0) - i\bar{B}\sin^2\theta_0| = 2\sqrt{2\beta_1(1+\Gamma)(\cos\theta_0 - \Gamma)}$ is satisfied, there exists only one possible state under finite plane deformations for the given remote uniform Piola stresses.
- Otherwise when the condition $\Gamma < \cos\theta_0$ and $|A(1+\cos\theta_0) - i\bar{B}\sin^2\theta_0| < 2\sqrt{2\beta_1(1+\Gamma)(\cos\theta_0 - \Gamma)}$ is met, there exists no possible state under finite plane deformations for the given remote uniform Piola stresses.

Acknowledgment

This work was supported in part by AFRL/ARL. The authors would like to thank the reviewers for their constructive comments.

References

[1] England, A. H., 1966, "An Arc Crack Around a Circular Elastic Inclusion," ASME J. Appl. Mech., **33**, pp. 637–640.
[2] Perlman, A. B., and Sih, G. C., 1967, "Elastostatic Problems of Curvilinear Cracks in Bonded Dissimilar Materials," Int. J. Eng. Sci., **5**, pp. 845–867.
[3] Toya, M., 1974, "Crack Along Interface of a Circular Inclusion Embedded in an Infinite Solid," J. Mech. Phys. Solids, **22**, pp. 325–348.
[4] Luo, H. A., and Chen, Y., 1991, "Interface Crack in a 3-Phase Composite Constitutive Model," ASME J. Appl. Mech., **58**, pp. 428–434.
[5] Rice, J. R., and Sih, G. C., 1965, "Plane Problems of Cracks in Dissimilar Media," ASME J. Appl. Mech., **32**, pp. 418–423.
[6] Rice, J. R., 1988, "Elastic Fracture-Mechanics Concepts for Interface Cracks," ASME J. Appl. Mech., **55**, pp. 98–103.
[7] Ru, C. Q., 2002, "On Complex-Variable Formulation for Finite Plane Elastostatics of Harmonic Materials," Acta Mech., **156**, pp. 219–234.
[8] Ru, C. Q., Schiavone, P., Sudak, L. J., and Mioduchowski, A., 2005, "Uniformity of Stresses Inside an Elliptical Inclusion in Finite Elastostatics," Int. J. Non-Linear Mech., **40**, pp. 281–287.
[9] Wang, G. F., Schiavone, P., and Ru, C. Q., 2005, "Harmonic Shapes in Finite Elasticity Under Nonuniform Loading," ASME J. Appl. Mech., **72**, pp. 691–694.
[10] Wang, G. F., Schiavone, P., and Ru, C. Q., 2005, "Surface Instability of a Semi-Infinite Harmonic Solid Under Van Der Waals Attraction," Acta Mech., **180**, pp. 1–10.
[11] Knowles, J. K., and Sternberg, E., 1975, "On the Singularity Induced by Certain Mixed Boundary Conditions in Linearized and Nonlinear Elastostatics," Int. J. Solids Struct., **11**, pp. 1173–1201.
[12] Varley, E., and Cumberbatch, E., 1980, "Finite Deformation of Elastic Materials Surrounding Cylindrical Hole," J. Elast., **10**, pp. 341–405.
[13] Abeyaratne, R., 1983, "Some Finite Elasticity Problems Involving Crack Tips," *Modelling Problems in Crack Tip Mechanics*, J. T. Pindera, ed., University Waterloo, Waterloo, CA, pp. 3–24.

Quadrilateral Subcell Based Finite Volume Micromechanics Theory for Multiscale Analysis of Elastic Periodic Materials

Xiguang Gao
e-mail: gaoxiguang@gmail.com

Yingdong Song

Zhigang Sun

College of Energy and Power Engineering,
Nanjing University of Aeronautics and Astronautics,
29 Yudao Street,
Nanjing, 210016, P.R.C

In this paper, we extend the finite volume direct average micromechanics to enable the use of quadrilateral subcells. To do this work, the quadrilateral subcells are used to discretize the repeating unit cells first. Then the average displacement and traction defined on the boundary of the subcell are evaluated by direct integral method. This contrasts with the original formulation in which all of the subcells are rectangular. Following the discretization, the cell problem is defined by combining the directly volume-average of the subcell stress equilibrium equations with the displacement and traction continuity in a surface-average sense across the adjacent subcell faces. In order to assemble the above equations and conditions into a global equation system, the global and local number systems, which index the boundary of subcell in different manners, are employed by the extended method. Finally, the global equation system is solved and the solutions give the formulations of the microstress field and the global elastic moduli of material. The introduction of quadrilateral subcells increases the efficiency of modeling the material's microstructure and eliminates the stress concentrations at the curvilinear bimaterial corners. Herein, the advantage of the extension is presented by comparing the global moduli and local stress fields predicted by the present method with the corresponding results obtained from the original version. [DOI: 10.1115/1.2966176]

Keywords: FVDAM, computational mechanics, multiscale modeling, elastic properties

1 Introduction

Multiscale mechanics method that evaluates the effective mechanical properties of heterogeneous materials is becoming a very important method in present day engineering. The finite volume direct average micromechanics (FVDAM) for periodic multiphase materials is a recently developed micromechanics model for the response of multiphase materials with an arbitrary periodic microstructure [1–4]. The analytical framework of FVDAM is based on the homogenization theory for periodic materials (cf. Kalamkarov and Kolpakov [5]), but the solution of the local displacement and stress fields within the repeating unit cell utilizes the concept of local/global stiffness matrix approach. This approach discards the two-level unit cell discretization, which is used by high-fidelity generalized method of cells (HFGMC) [6–8] and constructs the cell problems by a standard elasticity approach involving the direct volume-averaging of the local field equations and the satisfaction of the local continuity conditions in a surface-average sense. This simplifies the derivation of the global system of equations governing the unit cell response, whose size is substantially reduced through the elimination of redundant continuity equations employed in HFGMC [1].

Even though the FVDAM increases the efficiency of HFGMC, the subcells used by FVDAM to discretize the repeating unit cell are limited to rectangles (Fig. 1). The approximation of curvilinear inclusions through rectangular discretization increases the required number of subcells, which makes the analysis more expensive and also results in stress concentration at the curvilinear bimaterial corners [4]. In order to mitigate the negative impact of rectangular subcell mentioned above, the quadrilateral subcell discretization capability was incorporated into the finite-volume theory for functional graded materials by Cavalcante et al. [9–11] and into FVDAM by Gattu [12] recently. In contrast with the parametric mapping used by Cavalcante et al., in this paper, we present another approach, which directly extends the FVDAM to enable the use of quadrilateral subcells. This is accomplished by first improving the unit cell volume discretization using quadrilateral subcells as the fundamental building blocks of a periodic material's microstructure (Fig. 2). Then the cell problem is defined within the theoretical framework of FVDAM. The average quantities defined on the subcell's boundaries and the stress equilibrium equations in average sense are evaluated by direct integral method. Finally, these equations are solved and the solution gives the microstress field and the global elastic moduli directly. According to the character of quadrilateral subcell discretization and theoretical framework of FVDAM, the method presented in this paper is named quadrilateral finite volume direct average micromechanics (QFVDAM). The accuracy and efficiency of the QFVDAM are demonstrated by comparing the global properties and the local stress fields of a boron/aluminum composite with the corresponding results obtained from the FVDAM.

2 Theoretical Framework

The multiscale theory [13,14] is employed to derive the formulations of QFVDAM. Within the domain of repeating unit cell, the construction of the displacement field is based on the two scale expansion of the form

$$u_i(\mathbf{x},\mathbf{y}) = u_{0i}(\mathbf{x},\mathbf{y}) + \delta \cdot u_{1i}(\mathbf{x},\mathbf{y}) + \delta^2 \cdot u_{2i}(\mathbf{x},\mathbf{y}) + \cdots \quad (1)$$

where $\mathbf{x}=(x_1,x_2,x_3)$ are the global or macroscopic coordinates, $\mathbf{y}=(y_1,y_2,y_3)$ are the local or microscopic coordinates defined with respect to the repeating unit cell, and $u_{ji}(\mathbf{x},\mathbf{y})$ are y-periodic. The small parameter δ characterizes the size of the repeating unit

Contributed by the Applied Mechanics Division of ASME for publication in the JOURNAL OF APPLIED MECHANICS. Manuscript received December 5, 2007; final manuscript received May 21, 2008; published online November 6, 2008. Review conducted by Anthony Waas. Paper presented at the 2007 ASME Applied Mechanics and Materials Conference (McMat2007), Austin, TX, June 3–7, 2007.

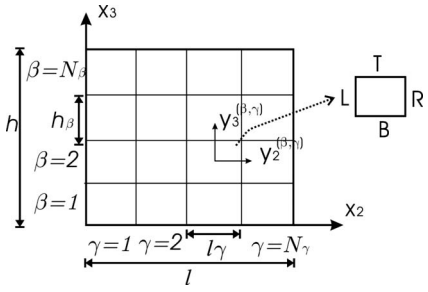

Fig. 1 Subcell of FVDAM is strictly limited to a rectangle

cell and relates the microscale to macroscale by $\mathbf{y}=\mathbf{x}/\delta$. Combining the above displacement field representation with the relation $\mathbf{y}=\mathbf{x}/\delta$ between the two scales, the strain field is separated into the average stains $\bar{\varepsilon}_{ij}(\mathbf{x})$ and local strains $\tilde{\varepsilon}_{ij}(\mathbf{x})$, respectively

$$\varepsilon_{ij} = \bar{\varepsilon}_{ij}(\mathbf{x}) + \tilde{\varepsilon}_{ij}(\mathbf{x},\mathbf{y}) + \mathbf{O}(\delta) \tag{2}$$

The average and local strains are derived by the corresponding displacement components $\bar{u}_i$ and $\tilde{u}_i$, as

$$\bar{\varepsilon}_{ij}(\mathbf{x}) = \frac{1}{2}\left(\frac{\partial \bar{u}_i}{\partial x_j} + \frac{\partial \bar{u}_j}{\partial x_i}\right), \quad \tilde{\varepsilon}_{ij}(\mathbf{x},\mathbf{y}) = \frac{1}{2}\left(\frac{\partial \tilde{u}_i}{\partial y_j} + \frac{\partial \tilde{u}_j}{\partial y_i}\right) \tag{3}$$

Using the decomposition of the strains mentioned above, the displacement field representation is expressed in the form

$$u_i(\mathbf{x},\mathbf{y}) = \bar{\varepsilon}_{ij}x_j + \tilde{u}_i + \mathbf{O}(\delta^2) \tag{4}$$

where $\bar{\varepsilon}_{ij}$ are the known or applied macroscopic strains. This form is employed in constructing an approximate displacement field for the solution of the cell problem.

In the analysis framework of QFVDAM, the fluctuating displacements $\tilde{u}_i$ are the fundamental variables. In order to obtain the solution of $\tilde{u}_i$, some equations and conditions are employed, i.e., the local stress equilibrium equations within the individual subcells, the traction and displacement continuity conditions between the individual subcells, and the periodic boundary conditions prescribed at the boundary of repeating unit cell. The above concepts, which are also employed in FVDAM, are quite different from FVDAM in detail due to the imposition of the quadrangular subcell. Herein, the details of QFVDAM are presented next.

3 Definition of the Cell Problem

The local analysis is performed on the repeating unit cell representative of a periodic material's microstructure in the x_2-x_3 plane, see Fig. 2(*a*), with continuous reinforcement along the x_1 axis. In order to perform the analysis the repeating unit cell highlighted in Fig. 2(*a*) is discretized into subcells designated by an integer (q). In the case of Fig. 2, just 400 quadrangular subcells were used to capture the two reinforcement shapes with sufficient fidelity. In order to impose the periodic conditions, the discretization along the unit cell's boundary at one side must identify with the other side.

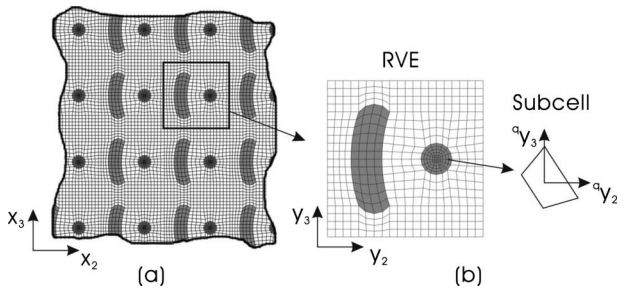

Fig. 2 (*a*) A continuously reinforced multiphase composite with a periodic microstructure in the x_2-x_3 plane constructed with repeating unit cells. (*b*) RVE is discretized by a quadrangular subcell, which is employed by QFVDAM.

Following the displacement field representation within the unit cell given by Eq. (4), the displacement field in each (q) subcell is written as follows:

$$^{q}u_i = \bar{\varepsilon}_{ij}x_j + {}^{q}\tilde{u}_i \tag{5}$$

Since the reinforcement is continuous along the x_1 axis the fluctuating displacement field that arises due to the heterogeneity of the material is a function of the local coordinates $({}^{q}y_2, {}^{q}y_3)$, which is located at the center of the subcell. The fluctuating displacement field is approximated in each (q) subcell by the second-order polynomial

$$^{q}\tilde{u}_i = {}^{q}W_{i1} + {}^{q}W_{i2}{}^{q}y_2 + {}^{q}W_{i3}{}^{q}y_3 + {}^{q}W_{i4}({}^{q}y_2)^2 + {}^{q}W_{i5}({}^{q}y_3)^2$$

$$i = 1,2,3, \quad q = 1, \ldots, N_q \tag{6}$$

where N_q is the total number of subcells and ${}^{q}W_{ij}$ are the unknown microvariables associated with each subcell. Using the above fluctuating displacement field representation in the strain-displacement relations

$$^{q}\varepsilon_{ij} = \bar{\varepsilon}_{ij} + \frac{1}{2}\left(\frac{\partial^q \tilde{u}_i}{\partial^q y_j} + \frac{\partial^q \tilde{u}_j}{\partial^q y_i}\right) \tag{7}$$

The strain components in each (q) subcell are obtained in the form

$$^{q}\varepsilon_{11} = \bar{\varepsilon}_{11} \tag{8a}$$

$$^{q}\varepsilon_{22} = \bar{\varepsilon}_{22} + {}^{q}W_{22} + 2{}^{q}W_{24}{}^{q}y_2 \tag{8b}$$

$$^{q}\varepsilon_{33} = \bar{\varepsilon}_{33} + {}^{q}W_{33} + 2{}^{q}W_{35}{}^{q}y_3 \tag{8c}$$

$$^{q}\varepsilon_{23} = \bar{\varepsilon}_{23} + ({}^{q}W_{23} + {}^{q}W_{32})/2 + {}^{q}W_{34}{}^{q}y_2 + {}^{q}W_{25}{}^{q}y_3 \tag{8d}$$

$$^{q}\varepsilon_{13} = \bar{\varepsilon}_{13} + {}^{q}W_{13}/2 + {}^{q}W_{15}{}^{q}y_3 \tag{8e}$$

$$^{q}\varepsilon_{12} = \bar{\varepsilon}_{12} + {}^{q}W_{12}/2 + {}^{q}W_{14}{}^{q}y_2 \tag{8f}$$

For orthotropic subcells considered herein, the stiffness matrix is characterized by nine independent elements, and Hooke's law has the form

$$\begin{bmatrix} {}^{q}\sigma_{11} \\ {}^{q}\sigma_{22} \\ {}^{q}\sigma_{33} \\ {}^{q}\sigma_{23} \\ {}^{q}\sigma_{13} \\ {}^{q}\sigma_{12} \end{bmatrix} = \begin{bmatrix} {}^{q}C_{11} & {}^{q}C_{12} & {}^{q}C_{13} & 0 & 0 & 0 \\ {}^{q}C_{21} & {}^{q}C_{22} & {}^{q}C_{23} & 0 & 0 & 0 \\ {}^{q}C_{31} & {}^{q}C_{32} & {}^{q}C_{33} & 0 & 0 & 0 \\ 0 & 0 & 0 & 2{}^{q}C_{44} & 0 & 0 \\ 0 & 0 & 0 & 0 & 2{}^{q}C_{55} & 0 \\ 0 & 0 & 0 & 0 & 0 & 2{}^{q}C_{66} \end{bmatrix} \cdot \begin{bmatrix} {}^{q}\varepsilon_{11} \\ {}^{q}\varepsilon_{22} \\ {}^{q}\varepsilon_{33} \\ {}^{q}\varepsilon_{23} \\ {}^{q}\varepsilon_{13} \\ {}^{q}\varepsilon_{12} \end{bmatrix} \tag{9}$$

Using the approximated expression of fluctuating displacement field in each (q) subcell in Hooke's law, the stresses are expressed in terms of the unknown microvariables ${}^{q}W_{ij}$ and applied average strains $\bar{\varepsilon}_{ij}$

$$^{q}\boldsymbol{\sigma} = {}^{q}\mathbf{N}_s \cdot {}^{q}\tilde{\mathbf{W}} + {}^{q}\mathbf{C}_s \cdot \bar{\boldsymbol{\varepsilon}} \tag{10}$$

where

$$^{q}\boldsymbol{\sigma} = [{}^{q}\sigma_{11} \quad {}^{q}\sigma_{22} \quad {}^{q}\sigma_{33} \quad {}^{q}\sigma_{23} \quad {}^{q}\sigma_{13} \quad {}^{q}\sigma_{12}]^T,$$

$$\bar{\boldsymbol{\varepsilon}} = [\bar{\varepsilon}_{11} \quad \bar{\varepsilon}_{22} \quad \bar{\varepsilon}_{33} \quad \bar{\varepsilon}_{23} \quad \bar{\varepsilon}_{13} \quad \bar{\varepsilon}_{12}]^T$$

${}^{q}\tilde{\mathbf{W}} = [{}^{q}\tilde{\mathbf{W}}_1 \; {}^{q}\tilde{\mathbf{W}}_2 \; {}^{q}\tilde{\mathbf{W}}_3]^{\mathrm{T}}$, ${}^{q}\tilde{\mathbf{W}}_i = [{}^{q}W_{i2} \; {}^{q}W_{i3} \; {}^{q}W_{i4} \; {}^{q}W_{i5}]$, the superscript T denotes the transpose. The matrix ${}^{q}\mathbf{N}_s$ contains 6×12 elements while ${}^{q}C_s$ contains 6×6 elements.

In the formulation of FVDAM, the surface-average fluctuating displacements and surface-average tractions are defined at the

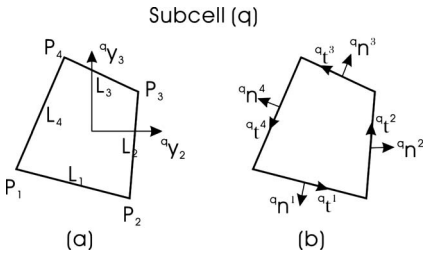

Fig. 3 (*a*) Illustration of boundaries and corner points of subcell and the (*b*) definition of the direction vector and the normal vector of the subcell's boundary

boundary of the subcell, which is limited to a rectangle. In order to impose the quadrangular subcell in the analysis framework, the surface-average fluctuating displacements and surface-average tractions are redefined at the quadrangular subcell's boundary, which is not vertical or horizontal anymore. The presentation of the local stiffness matrix for the quadrangular subcell constructed in such manner is described below.

3.1 Reformulation of Local Stiffness Matrix. The quadrangular subcell is composed of four points and linear boundaries (Fig. 3). They are counterclockwise arranged about the subcell's center at which the local coordinates locate. At each (q) subcell, the vector ${}^q\mathbf{t}^\eta=[{}^qt_2^\eta\ {}^qt_3^\eta]$ points out in the direction of the ηth boundary. The components of ${}^q\mathbf{t}^\eta$ are expressed in terms of local coordinates of the subcell's corner points

$$ {}^qt_2^\eta=\frac{{}^qy_2^{\eta+1}-{}^qy_2^\eta}{\mathfrak{L}_\eta},\quad {}^qt_3^\eta=\frac{{}^qy_3^{\eta+1}-{}^qy_3^\eta}{\mathfrak{L}_\eta} \tag{11}$$

where $\mathfrak{L}_\eta$ is the length of ηth boundary. The normal vector ${}^q\mathbf{n}^\eta=[{}^qn_2^\eta\ {}^qn_3^\eta]$ of the ηth boundary is obtained by rotating the direction vector deasil through 90 deg. The components of ${}^q\mathbf{n}^\eta$ are determined from

$$ {}^qn_2^\eta={}^qt_3^\eta,\quad {}^qn_3^\eta=-{}^qt_2^\eta \tag{12}$$

In order to derive the presentation of the local stiffness matrix, two sets of surface-average quantities are defined at the subcell's boundary. First, the tractions are expressed in the terms of stresses through Cauchy's relations

$$ {}^qP_i^\eta=\sigma_{ij}{}^qn_j^\eta \tag{13}$$

The corresponding surface-average traction components are defined in the standard manner

$$ {}^q\bar{P}_i^\eta=\frac{1}{{}^q\mathfrak{L}_\eta}\int_{{}^qL_\eta}{}^qP_i^\eta dl=\frac{1}{{}^q\mathfrak{L}_\eta}\int_{{}^qL_\eta}{}^q\sigma_{ij}n_j dl,\quad \eta=1,2,3,4 \tag{14}$$

Similarly, the surface-average fluctuating displacement components are determined from

$$ {}^q\bar{u}_i^\eta=\frac{1}{{}^q\mathfrak{L}_\eta}\int_{{}^qL_\eta}{}^q\tilde{u}_i dl \tag{15}$$

In order to carry out the integration along the subcell's boundary, the local coordinates in each (q) subcell are expressed in the form

$$ {}^qy_i={}^qy_i^\eta+l\cdot{}^qt_i^\eta,\quad i=2,3,\quad \eta=1,\ldots,4 \tag{16}$$

where ${}^qy_i^\eta$ is the local coordinate of point ${}^qP^\eta$, l is the distance between any point at ${}^qL_\eta$ and ${}^qP^\eta$. By carrying out the above integration, the surface-average displacements and surface-average tractions become linear functions of the local variables ${}^qW_{ij}$ in each (q) subcell and the applied average strain $\bar{\boldsymbol{\varepsilon}}$.

$$ {}^q\bar{\mathbf{P}}={}^q\mathbf{N}_p\cdot{}^q\tilde{\mathbf{W}}+{}^q\mathbf{C}_p\cdot\bar{\boldsymbol{\varepsilon}} \tag{17}$$

$$ {}^q\bar{\mathbf{u}}={}^q\mathbf{N}_u\cdot{}^q\mathbf{W} \tag{18}$$

where

$${}^q\bar{\mathbf{P}}=[{}^q\bar{\mathbf{P}}_1\quad {}^q\bar{\mathbf{P}}_2\quad {}^q\bar{\mathbf{P}}_3]^T,\quad {}^q\bar{\mathbf{P}}_i=[{}^q\bar{P}_i^1\quad {}^q\bar{P}_i^2\quad {}^q\bar{P}_i^3\quad {}^q\bar{P}_i^4]$$

$${}^q\bar{\mathbf{u}}=[{}^q\bar{\mathbf{u}}_1\quad {}^q\bar{\mathbf{u}}_2\quad {}^q\bar{\mathbf{u}}_3]^T,\quad {}^q\bar{\mathbf{u}}_i=[{}^q\bar{u}_i^1\quad {}^q\bar{u}_i^2\quad {}^q\bar{u}_i^3\quad {}^q\bar{u}_i^4]$$

$${}^q\mathbf{W}=[{}^q\mathbf{W}_1\quad {}^q\mathbf{W}_2\quad {}^q\mathbf{W}_3]^T$$

$${}^q\mathbf{W}_i=[{}^qW_{i1}\quad {}^qW_{i2}\quad {}^qW_{i3}\quad {}^qW_{i4}\quad {}^qW_{i5}]^T,\quad i=1,2,3$$

The matrixes ${}^qN_P$ and ${}^qC_P$ are the functions of ${}^qn_i^\eta$, ${}^qy_i^\eta$, ${}^q\mathfrak{L}_\eta$, and ${}^qC_{ij}$, while ${}^qN_u$ is the function of ${}^qn_i^n$ and ${}^qC_{ij}$.

The expression of surface-average displacements in Eq. (18) contains a total of 15 unknown ${}^qW_{ij}$ variables in each subcell. In order to express these unknown variables in terms of the 12 surface-average displacements in each subcell, three additional equations are required. These three equations are obtained by satisfying the stress equilibrium equations in each subcell in an average sense.

$$ \frac{1}{{}^qS}\int_{{}^q\Omega}\sigma_{ij,j}ds=0 \tag{19}$$

Then, substituting Eq. (10) into Eq. (19), performing the required integration, we obtain the three additional equations about the microvariables ${}^qW_{ij}$ in each (q) subcell.

$$ {}^qC_{66}{}^qW_{14}+{}^qC_{55}{}^qW_{15}=0 \tag{20a}$$

$$ {}^qC_{22}{}^qW_{24}+{}^qC_{44}{}^qW_{25}=0 \tag{20b}$$

$$ {}^qC_{44}{}^qW_{34}+{}^qC_{33}{}^qW_{35}=0 \tag{20c}$$

Using Eqs. (18) and (20), the microvariables ${}^qW_{ij}$ are expressed in terms of the surface-average displacement.

$$ {}^q\tilde{\mathbf{W}}={}^q\tilde{\mathbf{N}}_{wu}\cdot{}^q\bar{\mathbf{u}},\quad {}^q\mathbf{W}={}^q\mathbf{N}_{wu}\cdot{}^q\bar{\mathbf{u}} \tag{21}$$

Substitution of Eq. (21) into Eq. (17) gives the formulation of the surface-average tractions expressed in terms of surface-average displacements and the given global strain

$$ {}^q\bar{\mathbf{P}}={}^q\mathbf{K}_p\cdot{}^q\bar{\mathbf{u}}+{}^q\mathbf{C}_p\cdot\bar{\boldsymbol{\varepsilon}} \tag{22}$$

where ${}^q\mathbf{K}_p$ is the local subcell stiffness, which is obtained by the multiplication of ${}^q\mathbf{N}_p$ and ${}^q\tilde{\mathbf{N}}_{wu}$.

$$ {}^q\mathbf{K}_p={}^q\mathbf{N}_p\cdot{}^q\tilde{\mathbf{N}}_{wu} \tag{23}$$

Equation (22) describes the mechanical behavior of each (q) subcell as a Hooke's law. The approach of constructing the global stiffness matrix in conjunction with the interfacial traction and displacement continuity conditions and periodic conditions is presented next.

3.2 Global Stiffness Matrix. Due to the imposition of the quadrangular subcell, the manner of constructing the global stiffness matrix in QFVDAM is quite different from that in FVDAM. In the analysis framework of FVDAM, each subcell is indexed by a pair of integers (β,γ), see Fig. 1. Between the subcells (β,γ) and $(\beta+1,\gamma)$ or (β,γ) and $(\beta,\gamma+1)$ there always exists an interface. So the surface-average traction continuity conditions are ensured by [1]

$$ \bar{p}_i^{2+(\beta,\gamma)}+\bar{p}_i^{2-(\beta+1,\gamma)}=0,\quad \bar{p}_i^{3+(\beta,\gamma)}+\bar{p}_i^{3-(\beta,\gamma+1)}=0,\quad i=1,2,3 \tag{24}$$

The surface-average displacement continuity conditions are enforced by setting the corresponding displacement component to

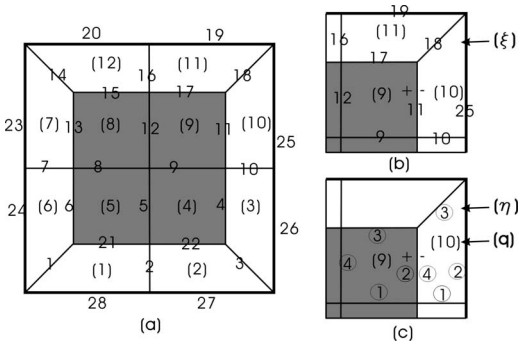

Fig. 4 Number system of QFVDAM: (*a*) relation between the global number system and the subcell number system, (*b*) definition of the global number system, and (*c*) definition of the subcell number system

common unknown quantities as shown below [1]

$$\bar{u}_i^{2+(\beta,\gamma)} = \bar{u}_i^{2-(\beta+1,\gamma)} = \bar{u}_i^{2(\beta+1,\gamma)}, \quad \bar{u}_i^{3+(\beta,\gamma)} = \bar{u}_i^{3-(\beta,\gamma+1)} = \bar{u}_i^{3(\beta,\gamma+1)}$$
$$i = 1,2,3 \tag{25}$$

In the case of QFVDAM, the above methodology is not appropriate anymore because the distribution of the subcell is not ordered. To construct the global stiffness matrix for QFVDAM, two types of number systems are imposed to index the subcell's boundary. The first type is the subcell number system (SNS), which is composed of a pair of integers (q,η). The variable q denotes the index of the subcell while η denotes the local index of the subcell's boundary (Fig. 4). This number system was used to construct the local stiffness matrix previously. The other number system is the global number system (GNS), in which the subcell's boundary (involving the interface between adjacent subcells and that attached to the boundary of the repeating unit cell), is designated by an exclusive integer (ξ) (Fig. 4).

Then, the boundaries of the subcell are divided into two classes: (1) the interface of adjacent subcells and (2) the boundary of the repeating unit cell. If the subcell's boundary (ξ) belongs to Class (1), the surface-average displacement continuity conditions are enforced by setting the corresponding displacement component to common unknown quantities as shown below

$$\bar{u}_i^{\xi+} = \bar{u}_i^{\xi-} = \bar{u}_i^{\xi}, \quad i = 1,2,3, \quad \xi = 1, \ldots, N_c \tag{26}$$

where N_c is the total number of interfaces between two adjacent subcells. The superscript $\xi+$ and $\xi-$, respectively, denote each side of ξth interface. The surface-average traction continuity conditions are ensured by

$$\bar{P}_i^{\xi+} + \bar{P}_i^{\xi-} = 0, \quad i = 1,2,3, \quad \xi = 1, \ldots, N_c \tag{27}$$

If the subcell's boundary (ξ) belongs to Class (2), the periodic boundary conditions are ensured by

$$\bar{u}_i^{\xi(k)+} = \bar{u}_i^{\xi(k)-}, \quad i = 1,2,3, \quad k = 1, \ldots, N_k \tag{28}$$

and

$$\bar{P}_i^{\xi(k)+} + \bar{P}_i^{\xi(k)-} = 0, \quad i = 1,2,3, \quad k = 1, \ldots, N_k \tag{29}$$

where N_k is equal to half of the total number of the subcell's boundaries that attach to the boundary of repeating unit cell. The integer k indexes the kth periodic boundary condition. The superscripts $\xi(k)+$ and $\xi(k)-$ denote the indices of corresponding subcell's boundaries that belong to the kth periodic boundary condition.

Equation (27) is written in terms of the surface-average displacement using Eq. (23)

$$q^{\xi+}K_{\mathrm{p}(3\cdot(i-1)+\eta^{\xi+},3\cdot(j-1)+l)} \cdot {}^{q^{\xi+}}\bar{u}_j^l + {}^{q^{\xi-}}K_{\mathrm{p}(3\cdot(i-1)+\eta^{\xi-},3\cdot(j-1)+l)} \cdot {}^{q^{\xi-}}\bar{u}_j^l + ({}^{q^{\xi+}}C_{\mathrm{p}(3\cdot(i-1)+\eta^{\xi+},m)} + {}^{q^{\xi-}}C_{\mathrm{p}(3\cdot(i-1)+\eta^{\xi-},m)}) \cdot \bar{\varepsilon}_m = 0$$
$$i,j = 1,2,3, \quad l = 1, \ldots, 4, \quad m = 1, \ldots, 6, \quad \xi = 1, \ldots, N_c \tag{30}$$

where $(q^{\xi+},\eta^{\xi+})$ is the SNS's index of subcell's boundary (ξ) in the $q^{\xi+}$ subcell. $(q^{\xi-},\eta^{-})$ is the SNS's index of subcell's boundary (ξ) in q^{-} subcell. $\bar{\varepsilon}_m$ are the components of applied global strain.

Similarly, Eq. (29) is written in terms of the surface-average displacement using Eq. (23)

$$q^{k+}K_{\mathrm{p}(3\cdot(i-1)+\eta^{k+},3\cdot(j-1)+l)} \cdot {}^{q^{k+}}\bar{u}_j^l + {}^{q^{k-}}K_{\mathrm{p}(3\cdot(i-1)+\eta^{k-},3\cdot(j-1)+l)} \cdot {}^{q^{k-}}\bar{u}_j^l + ({}^{q^{k+}}C_{\mathrm{p}(3\cdot(i-1)+\eta^{k+},m)} + {}^{q^{k-}}C_{\mathrm{p}(3\cdot(i-1)+\eta^{k-},m)}) \cdot \bar{\varepsilon}_m = 0$$
$$i,j = 1,2,3, \quad l = 1, \ldots, 4, \quad m = 1, \ldots, 6, \quad k = 1, \ldots, N_k \tag{31}$$

where the hyposuperscripts $k+$ and $k-$ denote the two corresponding items, which belong to kth periodic boundary condition.

Changing the number system of the surface-average displacement to GNS in Eqs. (30) and (31) gives

$$q^{\xi+}K_{\mathrm{p}(3\cdot(i-1)+\eta^{\xi+},3\cdot(j-1)+l)} \cdot \bar{u}_j^{\gamma(q^{\xi+},l)} + q^{\xi+}K_{\mathrm{p}(3\cdot(i-1)+\eta^{\xi-},3\cdot(j-1)+l)} \cdot \bar{u}_j^{\gamma(q^{\xi-},l)} + ({}^{q^{\xi+}}C_{\mathrm{p}(3\cdot(i-1)+\eta^{\xi+},m)} + {}^{q^{\xi-}}C_{\mathrm{p}(3\cdot(i-1)+\eta^{\xi-},m)}) \cdot \bar{\varepsilon}_m = 0$$
$$i,j = 1,2,3, \quad l = 1, \ldots, 4, \quad m = 1, \ldots, 6, \quad \xi = 1, \ldots, N_c \tag{32}$$

$$q^{k+}K_{\mathrm{p}(3\cdot(i-1)+\eta^{k+},3\cdot(j-1)+l)} \cdot \bar{u}_j^{\gamma(q^{k+},l)} + q^{k-}K_{\mathrm{p}(3\cdot(i-1)+\eta^{k-},3\cdot(j-1)+l)} \cdot \bar{u}_j^{\gamma(q^{k+},l)} + ({}^{q^{k+}}C_{\mathrm{p}(3\cdot(i-1)+\eta^{k+},m)} + {}^{q^{k-}}C_{\mathrm{p}(3\cdot(i-1)+\eta^{k-},m)}) \cdot \bar{\varepsilon}_m = 0$$
$$i,j = 1,2,3, \quad l = 1, \ldots, 4, \quad m = 1, \ldots, 6, \quad k = 1, \ldots, N_k \tag{33}$$

where γ is the corresponding index of the subcell's boundary (q,l) in GNS.

Equations (28), (32), and (33) provide us with a total of $3N_c + 3N_k + 3N_k$ equations in terms of the surface-average displacement $\bar{u}_i^{\xi}$ indexed by GNS. The total number of $\bar{u}_i^{\xi}$ is equal to $3N_c + 3N_k + 3N_k$. Hence, the solutions of fundamental unknown variables $\bar{u}_i^{\xi}$ can be derived from Eqs. (28), (32), and (33). This is accomplished by assembling Eqs. (28), (32), and (33) into a final system of equations, which is presented by the form of matrix

$$\mathbf{K} \cdot \bar{\mathbf{u}} = \mathbf{\Delta C} \cdot \bar{\boldsymbol{\varepsilon}} \tag{34}$$

where $\bar{\mathbf{u}} = [\bar{\mathbf{u}}^1, \ldots, \bar{\mathbf{u}}^{\xi}, \ldots, \bar{\mathbf{u}}^{\mathrm{N_b}}]^{\mathrm{T}}$ and $\bar{\mathbf{u}}^{\xi} = [\bar{u}_1^{\xi}, \bar{u}_2^{\xi}, \bar{u}_3^{\xi}]$. $\mathbf{N}_b$ is the total number of subcell boundaries and it is equal to $N_c + 2N_k$. The size of the global stiffness matrix $\mathbf{K}$ is $3\mathbf{N}_b \times 3\mathbf{N}_b$. While the size of the global load matrix $\mathbf{\Delta}C$ is $3\mathbf{N}_b \times 6$.

The above equation relates the unknown surface-average interfacial and boundary displacement to the applied macroscopic strains. In fact, the global stiffness matrix in Eq. (34) is singular due to the rigid body motion. Based on the periodic condition presented in Refs. [15–20], eight corner subcell faces are constrained to eliminate the singularity (Fig. 5). Then Eq. (34) is reduced by combining and deleting appropriate rows and columns of $\mathbf{K}$, $\bar{\mathbf{u}}$, and $\mathbf{\Delta C}$. The resulting reduced equation is written as

$$\mathbf{K}^* \cdot \bar{\mathbf{u}}^* = \cdot \mathbf{\Delta C}^* \cdot \bar{\boldsymbol{\varepsilon}} \tag{35}$$

The presentation of the surface-average displacement has the form

$$\bar{\mathbf{u}}^* = \mathbf{K}^{*-1} \cdot \mathbf{\Delta C}^* \cdot \bar{\boldsymbol{\varepsilon}} \tag{36}$$

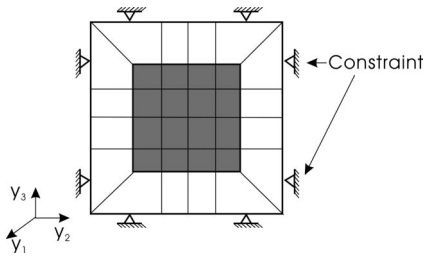

Fig. 5 The corners of the repeating unit cell are constrained

3.3 Homogenized Constitutive Equations. Through Hill's strain concentration tensor [19], the average strains in each subcell are related to the applied average strain as

$$^{q}\bar{\boldsymbol{\varepsilon}} = {}^{q}\mathbf{A} \cdot \bar{\boldsymbol{\varepsilon}} \tag{37}$$

where the components of $^{q}\bar{\boldsymbol{\varepsilon}}$ are defined by averaging the microstrains over the subcell volume as

$$^{q}\bar{\varepsilon}_{ij} = \int_{^{q}V} \varepsilon_{ij} \mathrm{d}v \tag{38}$$

Substitution of Eq. (8) into Eq. (38) gives the expression of $^{q}\bar{\boldsymbol{\varepsilon}}$ in terms of microscopic variables $^{q}\mathbf{W}_{ij}$ and the applied average strain $\bar{\boldsymbol{\varepsilon}}$. These microvariables are then expressed in terms of the interfacial surface-average displacements using Eq. (21). Equation (36) yields the interfacial and boundary-averaged displacements as a function of the macroscopic strains. Using this function, the average strain components in each subcell are obtained in terms of the applied average strain as presented in Eq. (37).

The average stress in each subcell is given by Eq. (9). Substitution of Eq. (37) into Eq. (9) gives the expression of the average stress in each (q) subcell in terms of the applied average strain.

$$^{q}\bar{\boldsymbol{\sigma}} = {}^{q}\mathbf{C}^{q}\mathbf{A} \cdot \bar{\boldsymbol{\varepsilon}} \tag{39}$$

The macrostress is obtained by averaging the subcell stress over the entire repeating unit cell.

$$\bar{\boldsymbol{\sigma}} = \frac{1}{V}\sum_{q=1}^{N_q} {}^{q}\mathbf{C}^{q}\mathbf{A} \cdot \bar{\boldsymbol{\varepsilon}} \tag{40}$$

where V is the volume of the repeating unit cell and N_q is the total number of subcells. Equation (40) can be written in the form of a macroscopic constitutive equation for the unit cell response as follows:

Table 1 Material properties of the fiber and matrix constituents

	Young's moduli (GPa)	Poisson's ratio
Boron fiber	379.3	0.1
Aluminum matrix	68.3	0.3

$$\bar{\boldsymbol{\sigma}} = \mathbf{C}^{*} \cdot \bar{\boldsymbol{\varepsilon}} \tag{41}$$

where $\mathbf{C}^{*}$ represents the effective elastic stiffness matrix for the repeating unit cell and is given by

$$\mathbf{C}^{*} = \frac{1}{V}\sum_{q=1}^{N_q} {}^{q}\mathbf{C}^{q}\mathbf{A} \tag{42}$$

4 Numerical Results

The use of quadrilateral subcells makes QFVDAM convenient in modeling the microstructure of material. Herein, we test QFVDAM's efficiency by determining the effective moduli and the local stress field of a unidirectional composite, with a square array of fibers in the x_2-x_3 plane. To highlight the advantage of QFVDAM, the moduli, as well as the local stress fields predicted by QFVDAM are compared with the corresponding FVDAM, results.

Figure 6 shows the mesh of a boron/aluminum composite with a fiber volume fraction of 0.47 for both FVDAM and QFVDAM. Both of the fiber and the matrix phases are isotropic. The values of actual constituent moduli are given in Table 1. Figures 6(*a*)–6(*c*) are the meshes for FVDAM with unit cells discretized into 10 $\times$ 10, 20 $\times$ 20, and 40 $\times$ 40 subcells. Figure 6(*d*) shows the unit cell discretization for QFVDAM with 441 subcells. The applied transverse global strain $\bar{\varepsilon}_{22}$ is 0.1.

Table 2 gives the macroproperties of boron/aluminum predicted by QFVDAM and FVDAM. These results are compared with the corresponding FEM prediction [20] and the experimental results [21]. In order to mimic the fiber shape exactly, 1600 subcells are employed by FVDAM (Fig. 6(*c*)) while QFVDAM used only 112 subcells, which is similar to Fig. 6(*d*). The properties predicted by QFVDAM are close to the experiment for the 112 subcell discretization, while FVDAM achieves the same results for the 1600 subcell discretization. The reduction of the total number of subcells increases the efficiency of QFVDAM because the time for calculation is the exponential function of the total number of subcells (see Fig. 7). The results predicted by a classical microme-

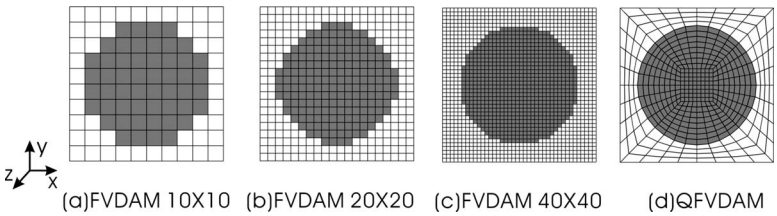

Fig. 6 Unit cell discretization for FVDAM and QFVDAM

Table 2 Global properties obtained by numerical method and experiment

	FVDAM						
	10 $\times$ 10	20 $\times$ 20	40 $\times$ 40	QFVDAM	Micromechanics method	FEM	Experiment
E_z/GPa	230.9	215.4	213.0	215.1	215.5	215	21610 $\times$ 10
E_x/GPa	158.5	144.7	142.6	142.7	122.9	144	140
E_{xz}/GPa	59.79	55.0	53.7	52.17	54.3	57.2	52
μ_{xz}/GPa	0.2319	0.2538	0.2548	0.252	0.194	0.29	0.29

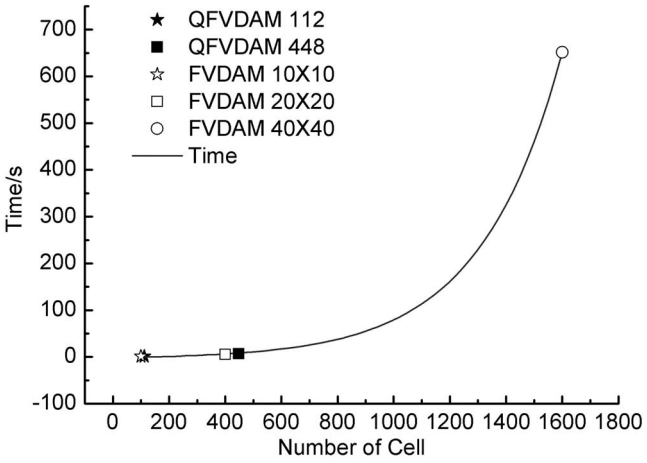

Fig. 7 Time for calculation

chanics method [22] are also listed in Table 2. Since the fiber radius is close to the distance between fibers, the cylinder repeating element is not appropriate to mimic the microstructure. This results in the deviation of E_x and μ_{xz} predicted by the classic micromechanics method from the experiment.

The local effective stress predicted by QFVDAM is compared with the corresponding FVDAM results as presented in Fig. 8. The approximation of circular fibers through rectangular discretization results in stress concentrations at the corners of the subcell, as shown in Figs. 8(*a*)–8(*c*), while the concentration is eliminated in the case of QFVDAM. Figure 8 indicates that the distribution of the local effective stress predicted by FVDAM with 40×40 subcells is similar to the corresponding result predicted by QFVDAM with 441 subcells. Based on Fig. 7, we conclude that the use of quadrangular subcells reduces the unnecessary subcells to mimic the microstructure of materials and makes QFVDAM more efficient in calculating the microscopic stress fields.

5 Discussion

Beginning with the previous work of Aboudi et al. a series multiscale mechanics method, such as GMC [23–27], HFGMC [6–8], and FVDAM [1–4], is proposed to predict the macroscopic behavior and microscopic stress field. All of these methods are based on the average stress equilibrium equations within the subcell and the surface-average displacement and traction continuity conditions at the boundaries of subcells. In order to simplify the derivation of the equations system, rectangular subcells are employed into those methods because the boundaries of the subcell are either vertical or horizontal. On the other hand, this simplification increases the required number of subcells, which makes the analysis more expensive and also results in stress concentrations at the curvilinear bimaterial corners. In this paper, within the theoretical framework of FVDAM, the local stiffness matrices for quadrangular subcells are developed to decrease the required mesh refinement for modeling curvilinear shapes and to eliminate the undesired stress concentrations. This advantage of QFVDAM is significant for nonlinear analysis and for topological optimization of the material's microstructure because these types of analysis may contain thousands of iterations.

There are many differences and similarities between FVDAM and QFVDAM. First, both methods are based on the average stress equilibrium equations in conjunction with the surface-average displacement continuity conditions and the surface-average traction continuity conditions. Second, both FVDAM and QFVDAM employ the concept of the local/global stiffness matrix to solve the cell problem. Third, the subcell of FVDAM is strictly limited to rectangles while the QFVDAM's subcell is extended to quadrangles. This character of QFVDAM results in the different manner of constructing the stiffness matrix of the subcell in contrast with FVDAM. Fourth, the distribution of subcells for FVDAM is regular and we can index the boundary of subcell by a pair of integers (β, γ). However, the subcells of QFVDAM can be distributed arbitrarily. In order to assemble and construct the global stiffness matrix, the local and global number systems are employed.

Although the parametric formulation developed by Gattu [12] and Cavalcante et al. [10,11] and QFVDAM incorporate quadrilateral subcell discretization capability into the FVDAM theory, they differ in the manner of constructing the stiffness matrix of a subcell. In fact, the key problems in extending FVDAM include (1) how to perform the integration within the quadrilateral subcell and (2) how to assemble the stiffness matrix of each subcell into the global equation system. In the parametric formulation, the integration is performed by a parametric mapping of coordinates from a reference square subcell onto a quadrilateral subcell. However, in QFVDAM, the integral is performed by a direct approach, which is described in this paper. Except this difference, both methods employ global/local number systems to assemble the global equation system.

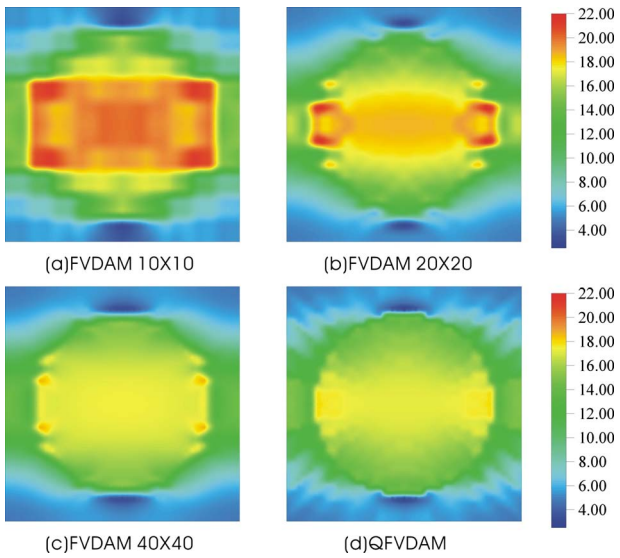

Fig. 8 Local effective stress predicted by QFVDAM and FVDAM, comparison of the QFVDAM prediction with the corresponding result predicted by FVDAM

6 Conclusions

Combining the theoretical framework of FVDAM and the quadrilateral subcell discretization, an extension of FVDAM is developed in this paper. The present method employs quadrilateral subcells to model the microstructure of multiphase materials. In the numerical example presented here, QFVDAM and FVDAM are used to determine the global elastic moduli and local effective stress field of the B/Al composite. A series of repeating unit cells with an increasing total number of subcells were used for FVDAM to generate a convergent result. These results were compared with the corresponding QFVDAM's results. The comparison indicated that the extension presented in this paper is important for FVDAM since the quadrilateral subcell discretization not only substantially reduces the size of the equation system governing the unit cell response but also eliminates the stress concentration at the microscopic level observed in the FVDAM results.

Acknowledgment

The work presented in this paper is supported by the National Natural Science Foundation of China. The authors also acknowledge the referees' useful revision.

References

[1] Bansal, Y., and Pindera, M.-J., 2005, "A Second Look at the Higher-Order Theory for Periodic Multiphase Materials," ASME J. Appl. Mech., **72**, pp. 177–195.

[2] Pinderal, M.-J., and Bansal, Y., 2007, "On the Micromechanics-Based Simulation of Metal Matrix Composite Response," ASME J. Eng. Mater. Technol., **129**, pp. 468–482.

[3] Bansal, Y., and Pindera, M.-J., 2006, "Finite-Volume Direct Averaging Micromechanics of Heterogeneous Materials With Elastic-Plastic Phases," Int. J. Plast., **22**(5), pp. 775–825.

[4] Bansal, Y., 2005, "Finite Volume Direct Averaging Micromechanics of Heterogeneous Media," Ph.D., thesis, Engineering and Applied Science University of Virginia, VA.

[5] Kalamkarov, A. L., and Kolpakov, A. G., 1997, *Analysis, Design and Optimization of Composite Structures*, Wiley, New York.

[6] Aboudi, J., Pindera, M.-J., and Arnold, S. M., 1999, "Higher-Order Theory for Functionally Graded Materials," Composites, Part B, **33**(8), pp. 777–832.

[7] Aboudi, J., Pindera, M.-J., and Arnold, S. M., 2002, "High-Fidelity Generalization Method of Cells for Inelastic Periodic Multiphase Materials," Paper No. NASA-TM-2002-211469.

[8] Bansal, Y., and Pindera, M.-J., 2003, "Efficient Reformulation of the Thermo-Elastic Higher-Order Theory for Functionally Graded Materials," J. Therm. Stresses, **26**(11–12), pp. 1055–1092.

[9] Cavalcante, M. A. A., 2006, "Modeling of the Transient Thermo-Mechanical Behavior of Composite Material Structures by the Finite-Volume Theory," MS thesis, Civil Engineering Department, Federal University of Alagoas, Maceio, Alagoas, Brazil.

[10] Cavalcante, M. A. A., Marques, S. P. C., and Pindera, M.-J., 2007, "Parametric Formulation of the Finite-Volume Theory for Functionally Graded Materials. Part I: Analysis," ASME J. Appl. Mech., **74**(5), pp. 935–945.

[11] Cavalcante, M. A. A., Marques, S. P. C., and Pindera, M.-J., 2007, "Parametric Formulation of the Finite-Volume Theory for Functionally Graded Materials. Part II: Numerical Results," ASME J. Appl. Mech., **74**(5), pp. 946–957.

[12] Gattu, M., 2007, "Parametric Finite Volume Theory for Periodic Heterogeneous Materials," MS thesis, Civil Engineering Department, University of Virginia, VA.

[13] Benssousan, A., Lions, J.-L., and Papanicolaou, G., 1978, *Asymptotic Analysis for Periodic Structures*, North-Holland, Amsterdam.

[14] Sanchez-Palencia, E., 1980, *Non-Homogeneous Media and Vibration Theory* (Lecture Notes in Physics Vol. 127) Springer-Verlag, Berlin.

[15] Kouznetsova, V., Brekelemans, W. A. M., and Baaijens, F. P. T., 2001, "An Approach to Micro-Macro Modeling of Heterogeneous Materials," Comput. Mech., **27**, pp. 37–48.

[16] Kouznetsova, V., Greers, M. G. D., and Brekelmans, W. A. M., 2002, "Multi-Scale Constitutive Modeling of Heterogeneous Materials With a Gradient-Enhanced Computational Homogenization Scheme," Int. J. Numer. Methods Eng., **54**, pp. 1235–1260.

[17] Van der Sluis, O., Schreurs, P. J. G., Brekelmans, W. A. M., and Meijer, H. E. H., 2000, "Overall Behaviour of Heterogeneous Elastoviscoplastic Materials: Effect of Microstructural Modeling," Mech. Mater., **32**, pp. 449–462.

[18] Terada, K., Hori, M., Kyoya, T., and Kikuchi, N., 2000, "Simulation of the Multi-Scale Convergence in Computational Homogenization Approach," Int. J. Solids Struct., **37**, pp. 2285–2311.

[19] Hill, R., 1963, "Elastic Properties of Reinforced Solids: Some Theoretical Principles," J. Mech. Phys. Solids, **11**, pp. 357–372.

[20] Sun, C. T., Vaidya, R. S., 1996, "Prediction of Composite Properties From a Representative Volume Element," Compos. Sci. Technol., **56**(2), pp. 171–179.

[21] Kenaga, D., Doyle, J. F., and Sun, C. T., 1987, "The Characterization of Boron/Aluminum Composite in the Nonlinear Range as an Orthotropic Elastic-Plastic Material," J. Compos. Mater., **21**(6), pp. 516–531.

[22] Whitney, J. M., and Riley, M. B., 1966, "Elastic Properties of Fiber Reinforced Composite Materials," AIAA J., **4**(9), pp. 1537–1542.

[23] Paley, M., and Aboudi, J., 1992, "Micromechanical Analysis of Composites by the Generalized Method of Cells," Mech. Mater., **14**, pp. 127–139.

[24] Gao, X. G., Song, Y. D., and Sun, Z. G., 2005, "Research on Variation of Effective Performances of Composites Induced by the Stochastic Fiber Size," J. Materials Science Engineering, **23**(95), pp. 335–340.

[25] Gao, X. G., Song, Y. D., and Sun, Z. G., 2005, "Research on the Discrepancy of Composite Effective Properties Induced by the Stochastic Fiber Location," J. Aerospace Power, **20**(4), pp. 584–589.

[26] Sun, Z. G., Song, Y. D., Gao, X. G., and Gao, D. P., 2004, "Influence of Micro-Structural Geometry on Thermal Expansion Coefficient of Composites," Chinese Journal of Applied Mechanics, **21**, pp. 146–150.

[27] Song, Y. D., Sun, Z. G., and Gao, X. G., 2005, "Research on Discrepancy of Fiber Reinforced Composite Effective Performance," J. Aerospace Power, **20**, pp. 230–235.

Structure of Near-Tip Stress Field and Variation of Stress Intensity Factor for a Crack in a Transversely Graded Material

Sarveshwar C. Wadgaonkar

Venkitanarayanan Parameswaran[1]
e-mail: venkit@iitk.ac.in

Department of Mechanical Engineering,
Indian Institute of Technology Kanpur,
Kanpur, 208 016, India

*The existing studies on the behavior of cracks in continuously graded materials assume the elastic properties to vary in the plane of the crack. In the case of a plate graded along the thickness and having a crack in its plane, the elastic properties will vary along the crack front. The present study aims at investigating the effect of elastic gradients along the crack front on the structure of the near-tip stress fields in such transversely graded materials. The first four terms in the expansion of the stress field are obtained by the eigenfunction expansion approach (Hartranft and Sih, 1969, "The Use of Eigen Function Expansion in the General Solution of Three Dimensional Crack Problems," J. Math. Mech., **19**(2), pp. 123–138) assuming an exponential variation of the elastic modulus. The results of this part of the study indicated that for an opening mode crack, the angular structure of the first three terms in the stress field expansion corresponding to $r^{(-1/2)}$, r^0, and $r^{1/2}$ are identical to that given by Williams's solution for homogeneous material (Williams, 1957, "On the Stress Distribution at the Base of a Stationary Crack," ASME J. Appl. Mech., **24**, pp. 109–114). Transversely graded plates having exponential gradation of elastic modulus were prepared, and the stress intensity factor (SIF) on the compliant and stiffer face of the material was determined using strain gauges for an edge crack subjected to pure bending. The experimental results indicated that the SIF can vary as much as two times across the thickness for the gradation and loading considered in this study.* [DOI: 10.1115/1.2966177]

Keywords: stress intensity factor, transversely graded materials, opening mode crack, elastic gradient

1 Introduction

There exists a large body of literature dealing with the analysis of cracks in graded materials [1–10]. In these studies, the geometry of the problem is such that the elastic properties remain constant along the crack front, and hence the problem can be analyzed as a plane problem. In other words, the elastic properties vary in the plane of the problem and the crack may be oriented at an angle, in the range 0–180 deg, to the direction of the property variation. For these crack configurations, the existence of the classical inverse square root singularity in the stress field has been unanimously established, and hence the stress intensity factor (SIF) completely characterizes the near-tip stress field [1,2]. There are also studies, which addressed the influence of the elastic gradient on the structure of the stress field [6,7], crack kinking [3,8], size of the singularity dominant zone [5,9], etc., for cracks in graded materials.

One problem, which has received less attention, is the case of a crack oriented such that there is elastic gradation along the crack front. This case cannot be considered as a plane problem and has to be treated in the three-dimensional framework. Walters et al. have studied semielliptical surface cracks in plates having gradation through the thickness using finite element method [11]. In their study the elastic properties vary along the crack front, and they have developed a general domain integral method to calculate the variation of J along the crack front. Subsequently, Yildirim et al. have carried out a three-dimensional finite element analysis of semielliptic surface cracks in a graded coating bonded to a homogeneous substrate and subjected to thermomechanical loading [12]. Recently, Ayhan used enriched finite elements to determine the SIF variation along the crack front for semielliptical cracks in graded plates [13]. To the best of our knowledge, the asymptotic structure of the stress field for a through thickness crack in a plate having elastic properties varying along the plate thickness (crack front) has not received attention so far. To distinguish this problem from those discussed in Refs. [1–10], we refer to this case as a crack in a transversely graded material, implying that the gradation is transverse to the crack.

Hartranft and Sih [14] were the first to provide the asymptotic three-dimensional stress fields for cracks in homogeneous materials. They used eigenfunction expansion to determine the near-tip structure of the displacement and stress components and established that, within the material, all stress components exhibit the inverse square root singularity. Using integral transform method, Hartranft and Sih [15] also determined the variation of SIF through the thickness of a cracked plate made of homogeneous material. Subsequently, Badaliance and Sih [16] have provided an approximate three-dimensional theory for cracks in a layered plate having layer properties and configuration distributed symmetrically with respect to the middle plane of the assembly. In their work, the elastic properties have jumps across the crack front. From the context of graded materials, this plate configuration can be viewed as a transversely graded plate, which is discretely graded along the thickness. However, the material is homogeneous within each layer, and hence the governing equations will still retain the classical form given in Ref. [14].

Sih [17] has given an extensive review of the issues and com-

[1]Corresponding author.

Contributed by the Applied Mechanics Division of ASME for publication in the JOURNAL OF APPLIED MECHANICS. Manuscript received December 5, 2007; final manuscript received June 5, 2008; published online November 6, 2008. Review conducted by Martin Ostoja-Starzewski.

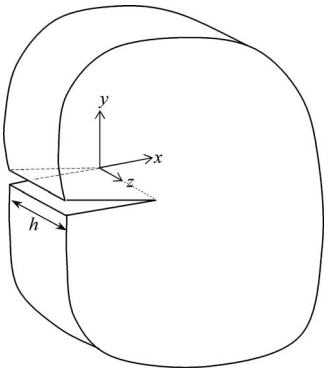

Fig. 1 Transversely graded plate with an edge crack

plexities associated with three-dimensional problem of a cracked plate, and concluded that the problem in its entirety is not amenable to an exact solution. Approximate solutions obtained using variational principle [15] also have some limitations; nevertheless, given the complexity of such problems, the results provide considerable insight into the nature of the stress field. Subsequently there are several investigations [18–22] attempting to explain/remedy some of the inconsistencies mentioned in Ref. [17].

In this paper, the three-dimensional problem of a cracked plate is revisited in the context of a transversely graded material where the elastic modulus varies continuously along the crack front (plate thickness). The eigenfunction expansion technique [14] is used to develop the structure of the crack-tip stress field. For mathematical tractability, an exponential variation of the elastic modulus is assumed. Subsequently, the effect the elastic gradient on the SIF is studied through experimental measurements. To this extent, a transversely graded plate with exponential variation of elastic modulus was prepared in the form of a particulate composite with varying particle volume fraction along the thickness. An edge cracked plate of this material was loaded in pure bending in the plane of the plate, and the SIF on the compliant side and stiff side of the pate was determined using strain gauges. The mathematical derivation, preparation, and characterization of the transversely graded plate and the determination of the SIF are presented sequentially in the following sections.

2 Expansion of the Displacement and Stress Fields

The geometric configuration of the problem at hand is depicted in Fig. 1. In this figure, the straight crack front is along the z axis. The plate is bounded in the thickness (z) direction and the crack faces are traction free. The elastic modulus variation is assumed, as given in Eq. (1), whereas the Poisson's ratio ν is assumed to be constant. The problem is formulated in cylindrical coordinates with the origin located at the crack tip.

$$E(z) = E_0 e^{\alpha z} \tag{1}$$

where E_0 is the elastic modulus at $z=0$ and α, referred to as the nonhomogeneity parameter, is a constant having dimension L^{-1}. The Navier equations of equilibrium in cylindrical coordinates can be written for this material as

$$\frac{\partial \vartheta}{\partial r} + (1-2\nu)\left\{\left[\nabla^2 - \frac{1}{r^2}\right]u_r - \frac{2}{r^2}\frac{\partial u_\theta}{\partial \theta} + \alpha\left[\frac{\partial u_r}{\partial z} + \frac{\partial u_z}{\partial r}\right]\right\} = 0$$

$$\frac{1}{r}\frac{\partial \vartheta}{\partial \theta} + (1-2\nu)\left\{\left[\nabla^2 - \frac{1}{r^2}\right]u_\theta + \frac{2}{r^2}\frac{\partial u_r}{\partial \theta} + \alpha\left[\frac{1}{r}\frac{\partial u_z}{\partial \theta} + \frac{\partial u_\theta}{\partial z}\right]\right\} = 0$$

$$\frac{\partial \vartheta}{\partial z} + (1-2\nu)\nabla^2 u_z + 2(1-\nu)\alpha\frac{\partial u_z}{\partial z} + 2\nu\alpha\left[\frac{\partial u_r}{\partial r} + \frac{u_r}{r} + \frac{1}{r}\frac{\partial u_\theta}{\partial \theta}\right] = 0 \tag{2}$$

where $\vartheta = (\partial u_r/\partial r) + (1/r)(\partial u_\theta/\partial \theta) + (u_r/r) + (\partial u_z/\partial z)$ and $\nabla^2 = (\partial^2/\partial r^2) + (1/r)(\partial/\partial r) + (1/r^2)(\partial^2/\partial \theta^2) + (\partial^2/\partial z^2)$ and u_r, u_θ, and u_z are the components of the displacements in the r, θ, and z directions, respectively.

Note that by letting α be zero, Eq. (2) will reduce to the classical form given in Ref. [14] for a homogeneous material. Following the approach of Hartranft and Sih [14], the displacement components are expanded as a double series, as given in

$$u_r = \sum_{m=0}^{\infty}\sum_{n=0}^{\infty} r^{\lambda_m+n} U_n^{(m)}(\theta,z)$$

$$u_\theta = \sum_{m=0}^{\infty}\sum_{n=0}^{\infty} r^{\lambda_m+n} V_n^{(m)}(\theta,z)$$

$$u_z = \sum_{m=0}^{\infty}\sum_{n=0}^{\infty} r^{\lambda_m+n} W_n^{(m)}(\theta,z) \tag{3}$$

where the powers of r, λ_m ($m=0,1,2\ldots$), and the functions $U_n^{(m)}$, $V_n^{(m)}$, and $W_n^{(m)}$ are yet to be determined. Substitution of Eq. (3) in Eq. (2) and collecting the terms associated with identical powers of r, we can construct a set of partial differential equations as follows:

$$\begin{aligned}
&2(1-\nu)[(\lambda_m+n)^2-1]U_n^{(m)} + [(\lambda_m+n)-3+4\nu]\frac{\partial V_n^{(m)}}{\partial \theta} + (1-2\nu)\frac{\partial^2 U_n^{(m)}}{\partial \theta^2} \\
&\quad = -(\lambda_m+n-1)\frac{\partial W_{n-1}^{(m)}}{\partial z} - \alpha(1-2\nu)(\lambda_m+n-1)W_{n-1}^{(m)} \\
&\qquad - (1-2\nu)\frac{\partial^2 U_{n-2}^{(m)}}{\partial z^2} - \alpha(1-2\nu)\frac{\partial U_{n-2}^{(m)}}{\partial z} \\
&2(1-\nu)\frac{\partial^2 V_n^{(m)}}{\partial \theta^2} + (1-2\nu)[(\lambda_m+n)^2-1]V_n^{(m)} + [(\lambda_m+n)+3-4\nu]\frac{\partial U_n^{(m)}}{\partial \theta} \\
&\quad = -(1-2\nu)\frac{\partial^2 V_{n-2}^{(m)}}{\partial z^2} - \frac{\partial^2 W_{n-1}^{(m)}}{\partial \theta \partial z} \\
&\qquad - \alpha(1-2\nu)\frac{\partial W_{n-1}^{(m)}}{\partial \theta} - \alpha(1-2\nu)\frac{\partial V_{n-2}^{(m)}}{\partial z} \\
&(1-2\nu)\frac{\partial^2 W_n^{(m)}}{\partial \theta^2} + (1-2\nu)(\lambda_m+n)^2 W_n^{(m)} \\
&\quad = -(\lambda_m+n)\frac{\partial U_{n-1}^{(m)}}{\partial z} - \frac{\partial^2 V_{n-1}^{(m)}}{\partial \theta \partial z} - 2(1-\nu)\frac{\partial^2 W_{n-2}^{(m)}}{\partial z^2} \\
&\qquad - 2\alpha(1-\nu)\frac{\partial W_{n-2}^{(m)}}{\partial z} - 2\nu\alpha(\lambda_m+n)U_{n-1}^{(m)} - 2\nu\alpha\frac{\partial V_{n-1}^{(m)}}{\partial \theta}
\end{aligned} \tag{4}$$

It should be noted that the functions $U_{-1}^{(m)}, U_{-2}^{(m)}, V_{-1}^{(m)}, V_{-2}^{(m)}, W_{-1}^{(m)}, W_{-2}^{(m)}$, etc., in Eq. (4) are zero. Now the solutions to $U_n^{(m)}$, $V_n^{(m)}$, and $W_n^{(m)}$ can be obtained for each value of n. For $n=0$, the right-hand side of the equations in Eq. (4) will be zero and Eq. (4) will reduce to the form given in Ref. [14], even though the Navier equations (Eq. (2)) in the present study are

different. The solution for $n=0$ is therefore the same as that given in Ref. [14]; however, they are provided here for the sake of completeness. For $n=0$ we can obtain $U_0^{(m)}$, $V_0^{(m)}$, and $W_0^{(m)}$ as

$$U_0^{(m)} = B_1^{(m)}(z)\cos(\lambda_m+1)\theta + B_2^{(m)}(z)\sin(\lambda_m+1)\theta + C_1^{(m)}(z)\cos(\lambda_m - 1)\theta + C_2^{(m)}(z)\sin(\lambda_m-1)\theta$$

$$V_0^{(m)} = -B_1^{(m)}(z)\sin(\lambda_m+1)\theta + B_2^{(m)}(z)\cos(\lambda_m+1)\theta + \frac{(\lambda_m+3-4\nu)}{(\lambda_m-3+4\nu)}[-C_1^{(m)}(z)\sin(\lambda_m-1)\theta + C_2^{(m)}(z)\cos(\lambda_m - 1)\theta]$$

$$W_0^{(m)} = A_1^{(m)}(z)\cos(\lambda_m\theta) + A_2^{(m)}(z)\sin(\lambda_m\theta) \tag{5}$$

in which $A_j^{(m)}$, $B_j^{(m)}$, and $C_j^{(m)}$ $(j=1,2)$ are functions of z.

Using the strain displacement relations and Hooke's law, the stress components are evaluated and on imposing the traction free condition on the crack face, $\sigma_{\theta\theta}=\sigma_{r\theta}=\sigma_{\theta z}=0$, $\theta=\pm\pi$, we get the following equations:

$$B_1^{(m)}(z)\cos(\lambda_m+1)\pi \pm B_2^{(m)}(z)\sin(\lambda_m+1)\pi + \frac{(\lambda_m+1)}{(\lambda_m-3+4\nu)}[C_1^{(m)} \times(z)\cos(\lambda_m-1)\pi \pm C_2^{(m)}(z)\sin(\lambda_m-1)\pi] = 0$$

$$B_1^{(m)}(z)\sin(\lambda_m+1)\pi \pm B_2^{(m)}(z)\cos(\lambda_m+1)\pi + \frac{(\lambda_m-1)}{(\lambda_m-3+4\nu)}[C_1^{(m)} \times(z)\sin(\lambda_m-1)\pi \pm C_2^{(m)}(z)\cos(\lambda_m-1)\pi] = 0$$

$$A_1^{(m)}(z)\sin(\lambda_m)\pi \pm A_2^{(m)}(z)\cos(\lambda_m)\pi = 0 \tag{6}$$

For a nontrivial solution of the above set of equations, the determinant of the coefficients of functions of z must vanish, and this condition is achieved for the following values of λ_m:

$$\lambda_m = \frac{m}{2}, \quad m = 0,1,2,\ldots \tag{7}$$

The negative values of m have been excluded in Eq. (7) so that the displacements are bounded as $r\to 0$. At this stage, the dependence of the displacements on r is established and hence Eq. (3) can be written as a single series, as follows:

$$u_r = \sum_{n=0}^{\infty} r^{n/2} f_n(\theta,z), \quad u_\theta = \sum_{n=0}^{\infty} r^{n/2} g_n(\theta,z), \quad u_z = \sum_{n=0}^{\infty} r^{n/2} h_n(\theta,z) \tag{8}$$

where f_n, g_n, and h_n are yet to be determined. Using the strain displacement relations and Hooke's law, the stress components corresponding to the displacements in Eq. (8) can be written in terms of the functions f_n, g_n, and h_n as

$$\frac{(1+\nu)(1-2\nu)}{E_0 e^{\alpha z}}\sigma_{rr} = \sum_{n=0}^{\infty} r^{(n/2-1)}\left\{\left[\frac{n}{2} - \left(\frac{n}{2}-1\right)\nu\right]f_n + \nu\left[\frac{\partial g_n}{\partial\theta} + \frac{\partial h_{n-2}}{\partial z}\right]\right\}$$

$$\frac{(1+\nu)(1-2\nu)}{E_0 e^{\alpha z}}\sigma_{\theta\theta} = \sum_{n=0}^{\infty} r^{(n/2-1)}\left\{\left[1+\left(\frac{n}{2}-1\right)\nu\right]f_n + (1-\nu)\frac{\partial g_n}{\partial\theta} + \nu\frac{\partial h_{n-2}}{\partial z}\right\}$$

$$\frac{(1+\nu)(1-2\nu)}{E_0 e^{\alpha z}}\sigma_{zz} = \sum_{n=0}^{\infty} r^{(n/2-1)}\left\{\nu\left[\left(\frac{n}{2}+1\right)f_n + \frac{\partial g_n}{\partial\theta}\right] + (1-\nu)\frac{\partial h_{n-2}}{\partial z}\right\}$$

$$\frac{2(1+\nu)}{E_0 e^{\alpha z}}\sigma_{r\theta} = \sum_{n=0}^{\infty} r^{(n/2-1)}\left\{\frac{\partial f_n}{\partial\theta} + \left(\frac{n}{2}-1\right)g_n\right\}$$

$$\frac{2(1+\nu)}{E_0 e^{\alpha z}}\sigma_{\theta z} = \sum_{n=0}^{\infty} r^{(n/2-1)}\left\{\frac{\partial h_n}{\partial\theta} + \frac{\partial g_{n-2}}{\partial z}\right\}$$

$$\frac{2(1+\nu)}{E_0 e^{\alpha z}}\sigma_{rz} = \sum_{n=0}^{\infty} r^{(n/2-1)}\left\{\frac{n}{2}h_n + \frac{\partial f_{n-2}}{\partial z}\right\} \tag{9}$$

The new series representation of the displacement field given in Eq. (8) is substituted in Eq. (2) resulting in the following set of partial differential equations:

$$(1-2\nu)\frac{\partial^2 f_n}{\partial\theta^2} + \left[\frac{n}{2} - 3 + 4\nu\right]\frac{\partial g_n}{\partial\theta} + 2(1-\nu)\left[\frac{n^2}{4}-1\right]f_n = -\left(\frac{n}{2}-1\right)\frac{\partial h_{n-2}}{\partial z} - \alpha(1-2\nu)\left(\frac{n}{2}-1\right)h_{n-2} - (1-2\nu)\frac{\partial^2 f_{n-4}}{\partial z^2} - \alpha(1-2\nu)\frac{\partial f_{n-4}}{\partial z}$$

$$2(1-\nu)\frac{\partial^2 g_n}{\partial\theta^2} + \left[\frac{n}{2} + 3 - 4\nu\right]\frac{\partial f_n}{\partial\theta} + (1-2\nu)\left[\frac{n^2}{4}-1\right]g_n = -\frac{\partial^2 h_{n-2}}{\partial\theta\partial z} - \alpha(1-2\nu)\frac{\partial h_{n-2}}{\partial\theta} - (1-2\nu)\frac{\partial^2 g_{n-4}}{\partial z^2} - \alpha(1-2\nu)\frac{\partial g_{n-4}}{\partial z}$$

$$(1-2\nu)\left[\frac{\partial^2 h_n}{\partial\theta^2} + \frac{n^2}{4}h_n\right] = -\frac{n}{2}\frac{\partial f_{n-2}}{\partial z} - \frac{\partial^2 g_{n-2}}{\partial\theta\partial z} - 2(1-\nu)\frac{\partial^2 h_{n-4}}{\partial z^2} - 2\alpha(1-\nu)\frac{\partial h_{n-4}}{\partial z} - n\nu\alpha f_{n-2} - 2\nu\alpha\frac{\partial g_{n-2}}{\partial\theta} \tag{10}$$

Equation (10) is solved for each value of n starting with $n=0$ to determine the functions f_n, g_n, and h_n. For $n=0$ and 1, the right hand side of Eq. (10) will be zero and we will get the following solution:

$$f_0 = {}^{(1)}B_0(z)\cos\theta + {}^{(2)}B_0(z)\sin\theta + (3-4\nu)[{}^{(1)}C_0(z)\theta\sin\theta - {}^{(2)}C_0(z)\theta\cos\theta]$$

$$g_0 = -[{}^{(1)}B_0(z) + {}^{(1)}C_0(z)]\sin\theta + [{}^{(2)}B_0(z) + {}^{(2)}C_0(z)]\cos\theta + (3-4\nu)[{}^{(1)}C_0(z)\theta\cos\theta + {}^{(2)}C_0(z)\theta\sin\theta]$$

$$h_0 = {}^{(1)}A_0(z) + {}^{(2)}A_0(z)\theta$$

$$f_1 = (5-8\nu)\left[{}^{(1)}B_1(z)\cos\frac{\theta}{2} + {}^{(2)}B_1(z)\sin\frac{\theta}{2}\right] - {}^{(1)}C_1(z)\cos\frac{3\theta}{2} + {}^{(2)}C_1(z)\sin\frac{3\theta}{2}$$

$$g_1 = (7-8\nu)\left[{}^{(2)}B_1(z)\cos\frac{\theta}{2} - {}^{(1)}B_1(z)\sin\frac{\theta}{2}\right] + {}^{(1)}C_1(z)\sin\frac{3\theta}{2} + {}^{(2)}C_1(z)\cos\frac{3\theta}{2}$$

$$h_1 = {}^{(1)}A_1(z)\cos\frac{\theta}{2} + {}^{(2)}A_1(z)\sin\frac{\theta}{2} \tag{11}$$

By this way the functions f_n, g_n, and h_n for each value of n can be obtained, and these are given in the Appendix up to $n=4$. It should be noticed that the solution is complete only to the extent of their dependence on r and θ at this stage and the functions ${}^{(i)}A_j(z)$, ${}^{(i)}B_j(z)$, ${}^{(i)}C_j(z)$, etc., are yet to be determined. The terms in the expansion of the stress field corresponding to each value of n, obtained using Eq. (11) in Eq. (9), are as follows. For $n=0$ after applying the traction free boundary condition on the crack face, we get ${}^{(2)}A_0(z) = {}^{(i)}C_0(z) = 0$, $i \in \{1,2\}$ and all the stress components will vanish for this case. For $n=1$, after imposing the traction free crack face boundary condition, we will get the following singular stress components:

$$\frac{(1+\nu)}{E_0 e^{\alpha z}}(\sigma_{rr})_1 = r^{-1/2}\left\{\frac{1}{2}{}^{(1)}B_1(z)\left[\cos\frac{3\theta}{2} - 5\cos\frac{\theta}{2}\right] + \frac{1}{2}{}^{(2)}B_1(z) \times \left[\sin\frac{3\theta}{2} - \frac{5}{3}\sin\frac{\theta}{2}\right]\right\}$$

$$\frac{(1+\nu)}{E_0 e^{\alpha z}}(\sigma_{\theta\theta})_1 = r^{-1/2}\left\{-\frac{1}{2}{}^{(1)}B_1(z)\left[\cos\frac{3\theta}{2} + 3\cos\frac{\theta}{2}\right] - \frac{1}{2}{}^{(2)}B_1(z) \times \left[\sin\frac{3\theta}{2} + \sin\frac{\theta}{2}\right]\right\}$$

$$\frac{(1+\nu)}{E_0 e^{\alpha z}}(\sigma_{zz})_1 = r^{-1/2}\left\{-4\nu\left[{}^{(1)}B_1(z)\cos\frac{\theta}{2} + \frac{1}{3}{}^{(2)}B_1(z)\sin\frac{\theta}{2}\right]\right\}$$

$$\frac{(1+\nu)}{E_0 e^{\alpha z}}(\sigma_{r\theta})_1 = r^{-1/2}\left\{-\frac{1}{2}{}^{(1)}B_1(z)\left[\sin\frac{3\theta}{2} + \sin\frac{\theta}{2}\right] + \frac{1}{2}{}^{(2)}B_1(z) \times \left[\cos\frac{3\theta}{2} + \frac{1}{3}\cos\frac{\theta}{2}\right]\right\}$$

$$\frac{(1+\nu)}{E_0 e^{\alpha z}}(\sigma_{\theta z})_1 = \frac{1}{4}{}^{(2)}A_1(z)r^{-1/2}\cos\frac{\theta}{2}$$

$$\frac{(1+\nu)}{E_0 e^{\alpha z}}(\sigma_{rz})_1 = \frac{1}{4}{}^{(2)}A_1(z)r^{-1/2}\sin\frac{\theta}{2} \tag{12}$$

One can notice that all the stress components in Eq. (12) have the classical inverse square root behavior. In fact, this solution is exactly the same as that given in Ref. [14]. Therefore, one can conclude that for the exponential variation of the elastic modulus, the transverse elastic gradient does not affect the inverse square root singular nature of the stress field at the crack tip. The same conclusion has been established for elastic gradients in the plane of the crack [1,2]. Furthermore, the angular structure of the stress field in Eq. (12) is also identical to that reported in Ref. [14] for homogeneous materials and it is same as that given by Williams for a plane crack [23]. Hence the effect of the nonhomogeneity has to be captured by the functions ${}^{(i)}A_j(z)$, ${}^{(i)}B_j(z)$, etc., which are to be determined. Another observation is that the function ${}^{(1)}B_1(z)$ is associated with deformation symmetric about the crack line (the classical opening mode) and ${}^{(2)}B_1(z)$ is associated with the skew-symmetric displacements (sliding mode). The function ${}^{(2)}A_1(z)$ will correspond to the antiplane mode of loading (tearing mode). The singular stress components from each mode is separable. In this context, the functions ${}^{(1)}B_1(z)$, ${}^{(2)}B_1(z)$, and ${}^{(2)}A_1(z)$ can be related to the classical Mode-I, Mode-II, and Mode-III stress intensity factors $k_1(z)$, $k_2(z)$, and $k_3(z)$, respectively, as follows:

$$k_1(z) = -\frac{2\sqrt{2\pi}}{(1+\nu)}{}^{(1)}B_1(z)E(z)$$

$$k_2(z) = \frac{2\sqrt{2\pi}}{3(1+\nu)}{}^{(2)}B_1(z)E(z)$$

$$k_3(z) = \frac{\sqrt{2\pi}}{4(1+\nu)}{}^{(2)}A_1(z)E(z) \tag{13}$$

Equation (13) indicates that the SIF will vary along the crack front and is explicitly dependent on the elastic gradient. The stress field for $n=2$ is given below:

$$\frac{(1+\nu)}{E_0 e^{\alpha z}}(\sigma_{rr})_2 = {}^{(1)}B_2(z)(1+\cos 2\theta)$$

$$\frac{(1+\nu)}{E_0 e^{\alpha z}}(\sigma_{\theta\theta})_2 = {}^{(1)}B_2(z)(1-\cos 2\theta)$$

$$\frac{(1+\nu)}{E_0 e^{\alpha z}}(\sigma_{zz})_2 = 2\nu{}^{(1)}B_2(z) + (1+\nu){}^{(1)}A_0'(z)$$

$$\frac{(1+\nu)}{E_0 e^{\alpha z}}(\sigma_{r\theta})_2 = -{}^{(1)}B_2(z)\sin 2\theta$$

$$\frac{(1+\nu)}{E_0 e^{\alpha z}}(\sigma_{\theta z})_2 = -\frac{1}{2}({}^{(1)}A_2(z) + {}^{(1)}B_0'(z))\sin\theta$$

$$\frac{(1+\nu)}{E_0 e^{\alpha z}}(\sigma_{rz})_2 = \frac{1}{2}({}^{(1)}A_2(z) + {}^{(1)}B_0'(z))\cos\theta \tag{14}$$

In Eq. (14) and subsequent equations, primes denote differentiation with respect to z. Equation (14) indicates that all the stresses are independent of r. Furthermore, it can be seen from Eqs. (13) and (14) that the in plane stress components $(\sigma_{rr}, \sigma_{\theta\theta}, \sigma_{r\theta})$ are not affected by either the three dimensionality or the elastic gradient and have the same structure as that given by William's solution [23]. The same is not true for the other three stress components $(\sigma_{zz}, \sigma_{z\theta}, \sigma_{rz})$. The effect of the three dimensionality manifests in the additional terms, which are multiplied by ${}^{(1)}A_0'(z)$ and ${}^{(1)}B_0'(z)$. For the $n=3$ and 4, the stress components are given as follows:

$$\frac{(1+\nu)}{E_0 e^{\alpha z}}(\sigma_{rr})_3 = r^{1/2}\left\{\frac{3}{2}{}^{(1)}B_3(z)\left[\cos\frac{5\theta}{2} + 3\cos\frac{\theta}{2}\right] + \frac{3}{2}{}^{(2)}B_3(z) \times \left[\sin\frac{5\theta}{2} + \frac{3}{5}\sin\frac{\theta}{2}\right] - \frac{1}{5}{}^{(2)}A_1'(z)\sin\frac{\theta}{2} - \frac{1}{5}{}^{(2)}A_1(z)\alpha\sin\frac{\theta}{2}\right\}$$

$$\frac{(1+\nu)}{E_0 e^{\alpha z}}(\sigma_{\theta\theta})_3 = r^{1/2}\left\{-\frac{3}{2}{}^{(1)}B_3(z)\left[\cos\frac{5\theta}{2} - 5\cos\frac{\theta}{2}\right] - \frac{3}{2}{}^{(2)}B_3(z) \times \left[\sin\frac{5\theta}{2} - \sin\frac{\theta}{2}\right]\right\}$$

$$\frac{(1+\nu)}{E_0 e^{\alpha z}}(\sigma_{zz})_3 = r^{1/2}\left\{12\nu\left[{}^{(1)}B_3(z)\cos\frac{\theta}{2} + \frac{1}{5}{}^{(2)}B_3(z)\sin\frac{\theta}{2}\right] + \frac{1}{5}(5 + 4\nu){}^{(2)}A_1'(z)\sin\frac{\theta}{2} - \frac{1}{5}\nu{}^{(2)}A_1(z)\alpha\sin\frac{\theta}{2}\right\}$$

$$\frac{(1+\nu)}{E_0 e^{\alpha z}}(\sigma_{r\theta})_3 = r^{1/2}\left\{-\frac{3}{2}{}^{(1)}B_3(z)\left[\sin\frac{5\theta}{2}-\sin\frac{\theta}{2}\right]+\frac{3}{2}{}^{(2)}B_3(z)\times\left[\cos\frac{5\theta}{2}-\frac{1}{5}\cos\frac{\theta}{2}\right]-\frac{1}{10}{}^{(2)}A_1'(z)\cos\frac{\theta}{2}-\frac{1}{10}{}^{(2)}A_1(z)\alpha\cos\frac{\theta}{2}\right\}$$

$$\frac{(1+\nu)}{E_0 e^{\alpha z}}(\sigma_{\theta z})_3 = r^{1/2}\left\{\frac{3}{4}{}^{(2)}A_3(z)\cos\frac{\theta}{2}+(3-4\nu)^{(1)}B_1'(z)\left[\sin\frac{3\theta}{2}+\sin\frac{\theta}{2}\right]+\frac{1}{2}{}^{(2)}B_1'(z)\left[\cos\frac{3\theta}{2}-\frac{2}{3}(3-4\nu)\cos\frac{\theta}{2}\right]-\alpha\left\{\nu^{(1)}B_1(z)\left[\sin\frac{3\theta}{2}+\sin\frac{\theta}{2}\right]+\frac{1}{3}\nu^{(2)}B_1(z)\cos\frac{\theta}{2}\right\}\right\}$$

$$\frac{(1+\nu)}{E_0 e^{\alpha z}}(\sigma_{rz})_3 = r^{1/2}\left\{-{}^{(1)}B_1'(z)\left[(3-4\nu)\cos\frac{3\theta}{2}+(1-4\nu)\cos\frac{\theta}{2}\right]+\frac{3}{4}{}^{(2)}A_3(z)\sin\frac{\theta}{2}+\frac{1}{2}{}^{(2)}B_1'(z)\left[\sin\frac{3\theta}{2}-\frac{2}{3}(1-4\nu)\sin\frac{\theta}{2}\right]+\alpha\left\{3\nu^{(1)}B_1(z)\left[\frac{1}{3}\cos\frac{3\theta}{2}+\cos\frac{\theta}{2}\right]+\nu^{(2)}B_1(z)\sin\frac{\theta}{2}+\frac{3}{4}{}^{(2)}A_3(z)\sin\frac{\theta}{2}\right\}\right\} \quad (15)$$

For $n=4$,

$$\frac{(1+\nu)}{E_0 e^{\alpha z}}(\sigma_{rr})_4 = r\left\{2^{(1)}B_4(z)\left[\cos 3\theta+\frac{1}{3}\cos\theta\right]+2^{(2)}B_4(z)[\sin 3\theta+\sin\theta]-\frac{1}{3}[{}^{(1)}A_2'(z)+{}^{(1)}B_0''(z)+\alpha^{(1)}A_2(z)+\alpha^{(1)}B_0'(z)]\cos\theta\right\}$$

$$\frac{(1+\nu)}{E_0 e^{\alpha z}}(\sigma_{\theta\theta})_4 = r\{-2^{(1)}B_4(z)[\cos 3\theta-\cos\theta]-2^{(2)}B_4(z)[\sin 3\theta-\sin\theta]\}$$

$$\frac{(1+\nu)}{E_0 e^{\alpha z}}(\sigma_{zz})_4 = r\left\{8\nu\left[\frac{1}{3}{}^{(1)}B_4(z)\cos\theta+{}^{(2)}B_4(z)\sin\theta\right]-(1+\nu)^{(2)}B_0''(z)\sin\theta+\frac{1}{3}[(3+2\nu)^{(1)}A_2'(z)-\nu^{(1)}B_0''(z)-\nu\alpha^{(1)}A_2(z)-\nu\alpha^{(1)}B_0'(z)]\cos\theta\right\}$$

$$\frac{(1+\nu)}{E_0 e^{\alpha z}}(\sigma_{r\theta})_4 = r\left\{-2^{(1)}B_4(z)\left[\sin 3\theta-\frac{1}{3}\sin\theta\right]+2^{(2)}B_4(z)[\cos 3\theta-\cos\theta]+\frac{1}{6}[{}^{(1)}A_2'(z)+{}^{(1)}B_0''(z)+\alpha^{(1)}A_2(z)+\alpha^{(1)}B_0'(z)]\sin\theta\right\}$$

$$\frac{(1+\nu)}{E_0 e^{\alpha z}}(\sigma_{\theta z})_4 = r\left\{-\left[{}^{(1)}A_4(z)+\frac{1}{2}{}^{(1)}B_2'(z)\right]\sin 2\theta+\frac{1}{2}{}^{(2)}B_2'(z)[1-\cos 2\theta]\right\}$$

$$\frac{(1+\nu)}{E_0 e^{\alpha z}}(\sigma_{rz})_4 = r\left\{\left[{}^{(1)}A_4(z)+\frac{1}{2}{}^{(1)}B_2'(z)\right]\cos 2\theta-\frac{1}{2}{}^{(2)}B_2'(z)\sin 2\theta-\nu^{(1)}B_2'(z)-\frac{(1+\nu)}{2}{}^{(1)}A_0''(z)-\alpha\frac{(1+\nu)}{2}{}^{(1)}A_0'(z)+\nu\alpha^{(1)}B_2(z)\right\} \quad (16)$$

In Eqs. (15) and (16), the stress components have three parts: one part, which is similar to that of William's plane solution [23], the second from the three-dimensional effects [14], and the third due to the elastic gradient. The additional terms arising out of the elastic gradient have the nonhomogeneity parameter α as the multiplier. Similar effects of elastic gradient on the structure of the stress field have been reported for the case of the elastic gradient in the plane of the crack [6,7]. It should be pointed out here that Eqs. (15) and (16) will reduce to that given in Ref. [14] if α is set to zero. For opening mode cracks, ${}^{(i)}A_j'(z)=0$ and ${}^{(2)}B_j'(z)=0$ and one can easily notice from Eqs. (12)–(15) that the first three terms corresponding to $r^{(-1/2)}$, r^0, and $r^{1/2}$ in the stress components $(\sigma_{rr},\sigma_{\theta\theta},\sigma_{r\theta})$ are identical to that for a homogeneous material [14,23]. Three-dimensional and nonhomogeneity effects appear only from the term corresponding to r^1. The stress components $(\sigma_{rr},\sigma_{\theta\theta},\sigma_{r\theta},\sigma_{zz})$ exhibit the inverse square root singular behavior as r tends to be zero, as pointed out in Ref. [14].

3 Discussion on the Stress Field

The expansion of the stress field obtained in the previous section was developed without considering any far-field loading. Hence the expansion only brings out the structure of the stress field in the r and θ coordinates and how the structure is influenced by the material nonhomogeneity. The only boundary condition that was enforced is the traction free condition on the crack surfaces. The two faces ($z=0$ and h) of the plate (see Fig. 1), which are perpendicular to the z axis, are essentially free surfaces, and therefore the stress components $(\sigma_{zz},\sigma_{zr},\sigma_{z\theta})$ should be zero on these surfaces. A closer look at the stress field (Eqs. (12)–(16)) will reveal that the stress components $(\sigma_{zz},\sigma_{zr},\sigma_{z\theta})$ do not vanish on these surfaces. Even in the case of homogeneous materials, the solutions provided in Ref. [14] do not satisfy the traction free condition on the faces of the plate. A detailed discussion on this fact and a possible remedy to this situation using the concept of a boundary layer is given in Ref. [15]. Accordingly, the stresses given by Eqs. (12)–(15) are perfectly valid inside the material where the singular stress components satisfy the conditions of plane strain for opening mode and shear mode loading. The stresses, however, are not valid within a small layer of material adjacent to the free surfaces.

Subsequently, for homogeneous material researchers have pointed out that, in a region very close to the intersection of the crack front and the free surface, the deformation field should be governed by the corner singularity [18–22]. Very near the intersection of the crack front and the free surface, the asymptotic nature of the stress components is as follows [18–21].

$$\sigma_{ij} = \rho^{\lambda} g_{ij}(\lambda,\theta,\phi) \quad (17)$$

where g_{ij} are dimensionless functions defined in the spherical coordinates $\rho=\sqrt{r^2+z^2}$, $\phi=\tan^{-1}(r/z)$, having the origin at the intersection of the crack front and the free surface. The value of the index λ depends on the Poisson's ratio and, in fact, deviates very little from -0.5 ($-0.5\leq\lambda\leq-0.332$ for $0\leq\nu\leq0.5$) [18,19]. The

local stress intensity factor varies along the z axis as $z^{(\lambda+1/2)}$ and will therefore become zero on the surface ($z=0$) and the stress components ($\sigma_{zz}, \sigma_{zr}, \sigma_{z\theta}$) vanish. This does not imply that the in plane stress components ($\sigma_{rr}, \sigma_{\theta\theta}, \sigma_{r\theta}$) also vanish on the surface [18,19]. Nakamura and Parks [20,21] have carried out a detailed investigation on the behavior of the stresses near the intersection of the crack front and the free surface using finite element analysis. Their study for opening mode cracks [20] indicates that the corner singularity field exists within a spherical radius of $\rho/h = 0.03$, h being the thickness of the plate. They have also defined a corner stress intensity factor and demonstrated how it is related to the classical SIF. The region of existence of the corner singular stress field being so small in homogeneous materials, we will make the assumption that the elastic gradients will not alter either the character of the corner stress field or the region of its influence in the case of graded materials. Within the region of existence of the corner singularity, the stress field satisfies the traction free conditions on the end faces. To the best of our knowledge, there are no studies that address in detail the state of the stress outside this region on the surface.

4 Experimental Determination of SIF Under Pure Bending

In general, the asymptotic expansion of the stress field is used to determine the fracture parameters from the experimental data. In the present case, this would mean determining the functions ${}^{(1)}B_n(z)$ for an opening mode problem. The use of the stress field given in Sec. 2 to determine the SIF for a cracked transversely graded plate subjected to bending is demonstrated in this section.

4.1 Preparation of Transversely Graded Plate. The transversely graded plate was prepared as a particulate composite with continuously varying volume fraction of filler particles along the thickness. Solid A-glass spheres of average diameter 60 μm were used as filler material in epoxy resin (LY556 supplied by Vantico Performance Polymers Ltd., India) matrix. LY556 is a medium viscosity resin, which can be cured by the addition of the hardener HY951 and has a relatively shorter gelation time of 40 min. Aluminum molds, having the dimension $200\times40\times25$ mm^3, were used for casting the graded plate. A mixture of epoxy resin and appropriate amount of glass bead was first prepared. The mixture was degassed in a vacuum chamber to remove any entrapped air bubbles and then 10% w/w hardener was added and gently mixed. Simultaneously epoxy resin mixed with 10% w/w of hardener was poured into the aluminum mold. After 20 min, the mixture of epoxy resin and glass beads was poured into the mold. Due to the higher density, the glass particles will settle down at the bottom of the mold. Once the particles had completely settled, the mold was sealed from the top, flipped upside down, and left in that position for 36 h.

Glass beads have a higher specific gravity of 2.2 as compared to 1.17 for the epoxy resin. When the mold is flipped upside down, the top layer of the mixture, which is rich in glass beads, starts moving down due to its higher specific gravity. Simultaneously, the resin starts gelling and offers more resistance to the settling of the glass beads. This results in a casting with a glass bead rich region, a resin rich region, and an intermediate region with continuously varying glass bead content. The sides of the mold were coated with grease to obtain smooth surface and to facilitate easy removal of the cast specimen. The specimens were postcured in an air circulating oven for 4 h at 100°C.

4.2 Characterization of the Transverse Elastic Gradient. Since the glass beads have higher specific gravity than that of the epoxy resin, the density of the plate increases in the direction of increasing glass bead content. In order to determine the variation of density along the thickness of the specimen, 1 mm thick slices were cut along the direction of the gradient. The density of these samples was measured by hydrostatic weighing, and the density profile of the specimen was determined. The spatial variation of glass bead volume fraction was calculated from the density profile using the rule of mixtures. The variation of glass bead volume fraction along the thickness of a typical sample is shown in Fig. 2. Evidently, in the middle region (3–15 mm) of the cast sample, there is a continuous variation of the glass bead volume fraction from 5% to 40%.

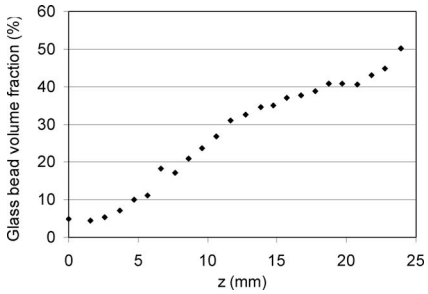

Fig. 2 Variation of glass bead volume fraction along the thickness

In order to relate the volume fraction data to the elastic modulus, homogeneous strips having glass bead volume fractions of 10%, 20%, 30%, 40%, and 50% were separately cast. The mold was rotated at 6 rpm while casting these specimens to avoid settling of the particles. The elastic modulus and Poisson's ratio for each glass bead volume fraction was determined following the ASTM standard testing procedure D638. The elastic modulus increased by three times for a glass bead content of 50% whereas Poisson's ratio changed from 0.375 to 0.34. A regression fit relating the elastic modulus to the volume fraction was derived from this data, and this relation was used to obtain the elastic gradient from the volume fraction gradient.

Subsequently, plates of the required thickness were sectioned out of the appropriate region of the casting. The elastic modulus profile of a typical specimen is shown in Fig. 3. The elastic gradient for this specimen is over two times across a thickness of 12 mm, and the variation is nearly exponential in nature. For each casting the density and volume fraction profile was characterized, as mentioned above, and it was observed that the method of preparing the graded sheet is fairly repeatable. An edge notched specimen of span 140 mm and width of 40 mm was prepared. A 0.25 mm wide notch of length 12 mm was cut using a diamond saw. A sharp crack was initiated from the notch tip by forcing a sharp razor blade into the notch. The final crack length was 14 mm resulting in an a/W ratio of 0.35.

5 Experimental Details

As there is no theoretical expression relating the far-field loading and the SIF for transversely graded material, the SIF has to be

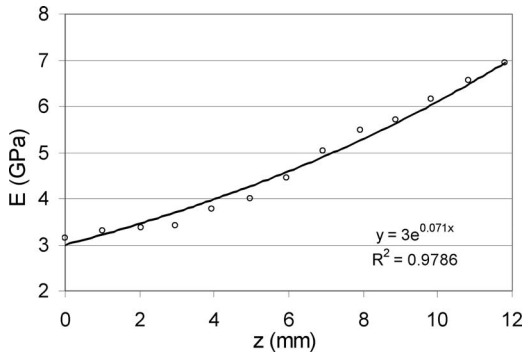

Fig. 3 Elastic modulus profile of the transversely graded plate

obtained from the measurement of the crack-tip fields. There are several techniques, which are used to measure the local crack-tip fields [24–29]. The SIF is then calculated by fitting the theoretical near-tip field to the experimental data. Photoelasticity and coherent gradient sensor (CGS) are the two full field techniques commonly used to measure the mechanical fields near the crack tip. In the transmission mode, these techniques are sensitive to the stress field, which in the case of a transversely graded material will vary along the thickness. Such transmission techniques can, therefore, capture only the integrated (through the thickness) effect and may not resolve the SIF variation through the thickness in real time. Stress frozen methods have been successfully used in the past [24] for determining the SIF variation through the thickness for homogenous materials. However in the present case, the graded specimen is not transparent and hence precludes the use of any optical technique in the transmission mode.

Measurements, therefore, are possible only from the surface and hence at most the value of the SIF at the two surfaces can be determined. Photoelasticity and CGS can be used in reflection mode as well. In the case of reflection CGS, the technique measures the in plane gradient of the out of plane deformation [25,26]. Unlike plane problems, the displacements in the present case may vary along the thickness of the plate; and therefore, relating the SIF to the in plane gradient of the out of plane displacement on the surfaces is not as straightforward as in the case of homogeneous materials. Reflection photoelasticity was not contemplated for the present material as the fracture initiation toughness at the epoxy side of the specimen is small (0.65 $\mathrm{MPa}\sqrt{\mathrm{m}}$); and hence, the level of SIF that can be applied may not be high enough to produce sufficient number of fringe orders in the photoelastic coating. Furthermore, photoelastic coatings typically have an elastic modulus comparable to epoxy and will bring in issues related to reinforcement effects.

The application of strain gauges to measure SIF has been demonstrated successfully for plane cracks in homogeneous materials [27,28]. Given the simplicity and noninvasiveness of this technique, strain gauges were used in the present study to evaluate the SIF on the two surfaces of the specimen, henceforth referred to as the epoxy rich side (lower modulus, $z=0$) and glass bead side (higher modulus, $z=h$). By applying stress transformation law, a three term expansion of the stress components (σ_{xx}, σ_{yy}, and σ_{xy}) for opening mode loading can be obtained from Eqs. (12)–(15) as follows.

$$\sigma_{xx} = C_1(z) r^{(-1/2)} \cos\frac{\theta}{2}\left\{1 - \sin\frac{\theta}{2}\sin\frac{3\theta}{2}\right\} + 2C_2(z) + C_3 r^{(1/2)} \cos\frac{\theta}{2}\left\{1 + \sin^2\frac{\theta}{2}\right\}$$

$$\sigma_{yy} = C_1(z) r^{(-1/2)} \cos\frac{\theta}{2}\left\{1 + \sin\frac{\theta}{2}\sin\frac{3\theta}{2}\right\} + C_3 r^{(1/2)} \cos\frac{\theta}{2}\left\{1 - \sin^2\frac{\theta}{2}\right\}$$

$$\sigma_{xy} = C_1(z) r^{(-1/2)} \cos\frac{\theta}{2}\sin\frac{\theta}{2}\sin\frac{3\theta}{2} + C_3 r^{(1/2)} \cos^2\frac{\theta}{2}\sin\frac{\theta}{2} \tag{18}$$

The functions $C_n(z)$ of Eq. (18) are related to the functions ${}^{(1)}B_n(z)$ as follows:

$$C_1(z) = -2\frac{{}^{(1)}B_1(z)E(z)}{(1+\nu)}, \quad C_2(z) = \frac{{}^{(1)}B_2(z)E(z)}{(1+\nu)}, \quad C_3(z) = 6\frac{{}^{(1)}B_3(z)E(z)}{(1+\nu)} \tag{19}$$

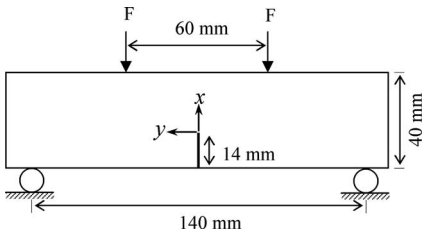

Fig. 4 Single edge notched plate subjected to four-point bending

Using Eq. (13) we will get $C_1(z)=k_1(z)/\sqrt{2\pi}$ where $k_1(z)$ is the opening mode SIF, which is a function of z. For a strain gauge oriented at an angle β with the x-axis and located at position (r,θ) on the surface ($z=0$ or h), using Eq. (18), a three term representation of the strain along the gauge can be written as

$$2\mu\varepsilon_G = C_1\left[\kappa\cos\frac{\theta}{2} - \frac{1}{2}\sin\theta\sin\frac{3\theta}{2}\cos 2\beta + \frac{1}{2}\sin\theta\cos\frac{3\theta}{2}\sin 2\beta\right] + C_2(\kappa + \cos 2\beta) + C_3 r^{1/2}\cos\frac{\theta}{2}\left[\kappa + \sin^2\frac{\theta}{2}\cos 2\beta - \frac{1}{2}\sin\theta\sin 2\beta\right] \tag{20}$$

where $\kappa=(1-\nu)/(1+\nu)$. By choosing the angles β and θ such that $\cos 2\beta=-\kappa$ and $\tan(\theta/2)=-\cot 2\beta$, we can eliminate the effects of the terms corresponding to C_2 and C_3, and the SIF can be calculated from the strain directly using the following relation [27].

$$2\mu\varepsilon_G = \frac{k_1}{\sqrt{2\pi r}}\left[\kappa\cos\frac{\theta}{2} - \frac{1}{2}\sin\theta\sin\frac{3\theta}{2}\cos 2\beta + \frac{1}{2}\sin\theta\cos\frac{3\theta}{2}\sin 2\beta\right] \tag{21}$$

In the context of the present study, C_n in Eq. (20) indicates the value of the function $C_n(z)$ on the surface ($z=0$ or h) on which the gauge is placed. It should be noted that in writing Eq. (20) we have used the condition that the stresses (σ_{zz}, σ_{xz}, and σ_{yz}) are zero on the surfaces and the in plane stresses (σ_{xx}, σ_{yy}, and σ_{xy}) have the structure given in Sec. 2. As discussed in Sec. 3, the stress field given in Sec. 2 does not satisfy the traction free condition on the surfaces, which is the case even for homogeneous materials. However, there are several studies that have successfully demonstrated that the SIF can be evaluated accurately by making measurements from the surface using optical techniques or strain gauges for homogeneous materials [25–29]. In these studies, the experimental data used to calculate the SIF are invariably taken from a region not too close to the crack tip thereby avoiding the region of the corner singular stress field and the 3D effects. These studies, however, make the tacit assumption that in the region from which the data are collected, the in plane stress components (σ_{xx}, σ_{yy}, and σ_{xy}) have the structure given by William's expansion [23]. In the present study also, we make the same assumptions with the exception that the constants in Eq. (20) have different values on the two surfaces ($z=0$ and h).

A single edge notched (SEN) specimen was subjected to four-point bending in the plane of the plate using a universal testing machine, as shown in Fig. 4. Two strain gauges were installed at a radial distance of $3h/4$ from the crack tip at the appropriate angles calculated, as mentioned earlier. The angles θ and β were 55.1 deg and 58.8 deg for the epoxy rich side and 58.3 deg and 59.6 deg for the glass bead rich side. The load was recorded using

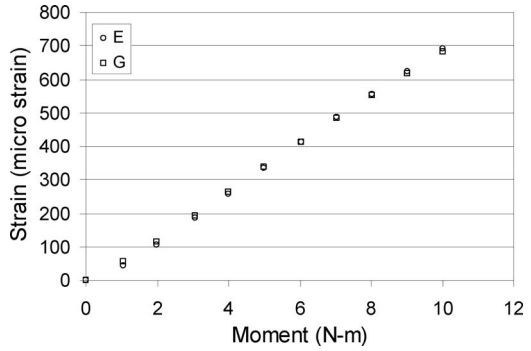

Fig. 5 Strain on the epoxy side (*E*) and glass bead side (*G*) for edge crack subjected to pure bending

a 1000 N load cell and an Ectron 530 amplifier was used to condition the strain signals. The variation of the strain on epoxy rich side (ε_E) and on the glass bead side (ε_G) as a function of the applied bending moment, shown in Fig. 5, indicates that the two strains are nearly equal and vary linearly with the applied bending moment. In the case of a transversely graded plate subjected to out of plane bending or in plane stretching, there will be coupling between these two modes of deformations, and the magnitude of the strains on the surfaces of the plate will not be equal. In the present case, the fact that the two strains are equal (see Fig. 5) indicates that the plate bends exclusively in the plane of the plate. The same behavior can be expected for a thick transversely graded plate ($h>12$ mm) when the plate is subjected, bending, as shown in Fig. 4.

The SIF calculated from the strains using Eq. (21) is shown in Fig. 6 as a function of the applied bending moment. It can be noticed that the SIF, K_{IG} on the glass bead side (stiffer side) is nearly two times that of the SIF, K_{IE} on the epoxy side. The SIF, K_{IH} for a homogeneous material, calculated using the plane solution [30], for the same bending moment is also shown in Fig. 6 for comparison. It can be noticed that K_{IE} is 25% less than K_{IH} whereas K_{IG} is 50% higher than K_{IH}.

As mentioned in Sec. 5, when the crack front intersects the free surface at an angle of 90 deg, the inverse square root singular stress field is not valid on the free surface and the SIF on the surface should be theoretically zero for an opening mode crack [11–13,18–20]. The SIF calculated using the classical crack-tip fields from the experimental data obtained from the surface does not reflect this behavior [25–29]. We believe the reason for this to be the following. The corner singularity field exists in a very small zone [13,20], and the experimental data are usually collected from a region ($r>0.5h$), which is outside this zone. In this region, the classical fields can represent the stress/displacement field reasonably well. Furthermore, when a natural crack is extended from a notch, as in the present case, the crack front will not be perpendicular to the free surface. It is reasonable to expect that the extended crack front will intersect the free surface at an angle that will preserve the inverse square root singular field on the surface [22,31]. Thus for such natural cracks, the use of the classical fields can be expected to provide good estimate of the SIF. For homogeneous materials, it has been reported in earlier studies [27,28] that the single strain gauge method of measuring SIF underestimates the SIF by as much as 12% in comparison to the theoretical SIF. We believe that the SIF reported in the present study will also have similar levels of error. However, this error will be the same for the SIF calculated on either faces of the graded plate; and therefore, the conclusion that the SIF varies by a factor of 2 across the plate thickness remains valid.

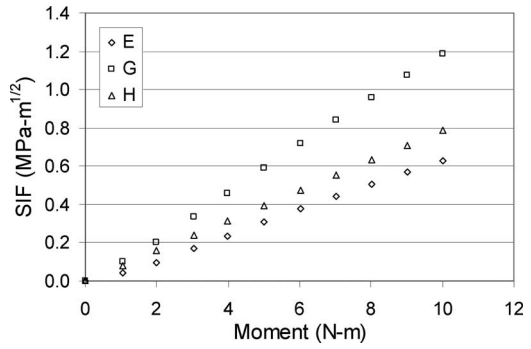

Fig. 6 SIF on the epoxy side (*E*) and on the glass bead side (*G*) for an edge crack subjected to pure bending. The SIF for a homogeneous material (*H*) is also shown for comparison.

Graded materials used in high temperature applications typically have ceramic on one face and metal on the other. The results of this investigation point out that for a through thickness crack with the crack front along the direction of the gradation and subjected to bending, the SIF on the ceramic side can be considerably higher than that on the metallic side especially when the ceramic side modulus is higher than that on the metallic side. Ceramics, in general, have low fracture toughness; and hence, this increase in the SIF due to gradation can further reduce the fracture tolerance of ceramic-metal graded materials subjected to in plane bending especially when the ceramic side modulus is higher than that on the metallic side.

6 Conclusions

The structure of the near-tip stress field for a crack in a graded material oriented such a way that the elastic properties vary along the crack front was obtained through eigenfunction expansion. The results of this part of the study indicated that for exponential gradation of elastic modulus, the structure of the first three terms ($r^{(-1/2)}$, r^0, and $r^{1/2}$) in the expansion of the stress field is not affected by the transverse elastic gradient for opening mode conditions. An edge cracked plate with near exponential variation of the elastic modulus along the thickness was prepared and was subjected to pure bending. The strains near the crack tip on the two faces of the graded plate were measured using strain gauges. The SIF on the faces of the plate was calculated from the measured strains. The results indicated that the SIF on the stiffer face of the plate can be as much as two times that on the compliant face for the gradation and loading considered in this study.

Appendix

For $n=2$,

$$f_2 = {}^{(1)}B_2(z)\cos 2\theta + (1-2\nu){}^{(1)}B_2(z) - \nu{}^{(1)}A_0'$$

$$g_2 = -{}^{(1)}B_2(z)\sin 2\theta + {}^{(2)}C_2$$

$$h_2 = {}^{(1)}A_2(z)\cos\theta - {}^{(2)}B_0'(z)\sin\theta \tag{A1}$$

For $n=3$,

$$f_3 = {}^{(1)}B_3(z)\left[\cos\frac{5\theta}{2} + (3-8\nu)\cos\frac{\theta}{2}\right] + {}^{(2)}B_3(z)\left[\sin\frac{5\theta}{2} + \frac{1}{5}(3-8\nu)\sin\frac{\theta}{2}\right] - \frac{2}{15}(1+4\nu){}^{(2)}A_1'(z)\sin\frac{\theta}{2} - \frac{2}{15}\alpha(1-\nu){}^{(2)}A_1(z)\sin\frac{\theta}{2}$$

$$g_3 = -{}^{(1)}B_3(z)\left[\sin\frac{5\theta}{2} - (9-8\nu)\sin\frac{\theta}{2}\right] + {}^{(2)}B_3(z)\left[\cos\frac{5\theta}{2} - \frac{1}{5}(9-8\nu)\cos\frac{\theta}{2}\right] - \frac{4}{15}(1-2\nu){}^{(2)}A_1'(z)\cos\frac{\theta}{2} - \frac{2}{15}\alpha(2+\nu){}^{(2)}A_1(z)\cos\frac{\theta}{2}$$

$$h_3 = 2{}^{(1)}B_1'(z)\left[\cos\frac{\theta}{2} - \frac{1}{3}(7-8\nu)\cos\frac{3\theta}{2}\right] + \frac{2}{3}{}^{(2)}B_1'(z)\sin\frac{\theta}{2} + 4\nu\alpha{}^{(1)}B_1(z)\left[\cos\frac{\theta}{2} + \frac{1}{3}\cos\frac{3\theta}{2}\right] + \frac{4}{3}\nu\alpha{}^{(2)}B_1(z)\sin\frac{\theta}{2} + {}^{(2)}A_1(z)\sin\frac{3\theta}{2} \tag{A2}$$

For $n=4$,

$$f_4 = {}^{(1)}B_4(z)\left[\cos 3\theta + \frac{1}{3}(1-4\nu)\cos\theta\right] + {}^{(2)}B_4(z)[\sin 3\theta + (1-4\nu)\sin\theta] + \frac{1}{2}[\nu^{(2)}B_0''(z)]\sin\theta - \frac{1}{6}[(1+2\nu)^{(1)}A_2'(z) + (1-\nu)^{(1)}B_0''(z) + \alpha(1-\nu)^{(1)}A_2(z) + \alpha(1-\nu)^{(1)}B_0'(z)]\cos\theta$$

$$g_4 = -{}^{(1)}B_4(z)\left[\sin 3\theta - \frac{1}{3}(5-4\nu)\sin\theta\right] + {}^{(2)}B_4(z)[\cos 3\theta - (5-4\nu)\cos\theta] - \frac{1}{2}[\nu^{(2)}B_0''(z)]\cos\theta + \frac{1}{6}[(1-2\nu)^{(1)}A_2'(z) + (1+\nu)^{(1)}B_0''(z) + \alpha(1+\nu)^{(1)}A_2(z) + \alpha(1+\nu)^{(1)}B_0'(z)]\sin\theta$$

$$h_4 = {}^{(1)}A_4(z)\cos 2\theta - \frac{1}{2}{}^{(2)}B_2'(z)\sin 2\theta - \frac{1}{2}[{}^{(1)}B_2'(z) + {}^{(1)}A_0''(z) + \alpha(1+\nu)^{(1)}A_0'(z) + 2\nu\alpha{}^{(1)}B_2(z)] \tag{A3}$$

References

[1] Erdogan, F., 1995, "Fracture Mechanics of Functionally Graded Materials," Composites Eng., **5**(7), pp. 753–770.

[2] Gu, P., and Asaro, R. J., 1997, "Cracks in Functionally Graded Materials," Int. J. Solids Struct., **34**(1), pp. 1–17.

[3] Gu, P., and Asaro, R. J., 1997, "Cracks Deflection in Functionally Graded Materials," Int. J. Solids Struct., **34**(24), pp. 3085–3098.

[4] Rousseau, C.-E., and Tippur, H. V., 2001, "Influence of Elastic Gradient Profiles on Dynamically Loaded Functionally Graded Materials: Cracks Along the Gradient," Int. J. Solids Struct., **38**, pp. 7839–7856.

[5] Anlas, G., Lambros, J., and Santare, M. H., 2002, "Dominance of Asymptotic Crack Tip Fields in Elastic Functionally Graded Materials," Int. J. Fract., **115**, pp. 193–204.

[6] Parameswaran, V., and Shukla, A., 2002, "Asymptotic Stress Fields for Stationary Cracks Along the Gradient in Functionally Graded Materials," ASME J. Appl. Mech., **69**, pp. 240–243.

[7] Chalivendra, V. B., Shukla, A., and Parameswaran, V., 2003, "Quasi-Static Stress Fields for a Crack Inclined to the Property Gradation in Functionally Graded Materials," Acta Mech., **162**, pp. 167–184.

[8] Jain, N., Shukla, A., and Rousseau, C.-E., 2004, "Crack Tip Stress Fields in Materials With Linearly Varying Properties," Theor. Appl. Fract. Mech., **42**, pp. 155–170.

[9] Shim, D. J., Paulino, G. H., and Dodds, R. H., 2006, "Effect of Material Gradation on K-Dominance of Fracture Specimens," Eng. Fract. Mech., **73**, pp. 643–648.

[10] Abanto-Bueno, J., and Lambros, J., 2006, "An Experimental Study of Mixed Mode Crack Initiation and Growth in Functionally Graded Materials," Exp. Mech., **46**(2), pp. 179–196.

[11] Walters, M. C., Paulino, G. H., and Dodds Jr., R. H., 2004, "Stress Intensity Factors for Surface Cracks in Functionally Graded Materials Under Mode-I Thermomechanical Loading," Int. J. Solids Struct., **41**, pp. 1081–1118.

[12] Yildirim, B., Dag, S., and Erdogan, F., 2005, "Three Dimensional Fracture Analysis of FGM Coatings Under Thermomechanical Loading," Int. J. Fract., **132**, pp. 369–395.

[13] Ayhan, A. O., 2007, "Stress Intensity Factors for Three-Dimensional Cracks in Functionally Graded Materials Using Enriched Finite Elements," Int. J. Solids Struct., **44**, pp. 8579–8599.

[14] Hartranft, R. J., and Sih, G. C., 1969, "The Use of Eigen Function Expansion in the General Solution of Three Dimensional Crack Problems," J. Math. Mech., **19**(2), pp. 123–138.

[15] Hartranft, R. J., and Sih, G. C., 1970, "An Approximate Three-Dimensional Theory of Plates With Application to Crack Problem," Int. J. Eng. Sci., **8**, pp. 711–729.

[16] Badaliance, R., and Sih, G. C., 1975, "An Approximate Three-Dimensional Theory of Layered Plates Containing Through Thickness Cracks," Eng. Fract. Mech., **7**, pp. 1–22.

[17] Sih, G. C., 1971, "A Review of Three-Dimensional Stress Problem for a Cracked Plate," Int. J. Fract. Mech., **7**(1), pp. 39–61.

[18] Benthem, J. P., 1977, "State of Stress at the Vertex of a Quarter-Infinite Crack in a Half Space," Int. J. Solids Struct., **13**, pp. 479–492.

[19] Benthem, J. P., 1980, "The Quarter-Infinite Crack in a Half Space; Alternative and Additional Solutions," Int. J. Solids Struct., **16**, pp. 119–130.

[20] Nakamura, T., and Parks, D. M., 1988, "Three-Dimensional Stress Field Near the Crack Front in a Thin Elastic Plate," ASME J. Appl. Mech., **55**, pp. 805–813.

[21] Nakamura, T., and Parks, D. M., 1989, "Antisymmetrical 3-D Stress Field Near the Crack Front of a Thin Elastic Plate," Int. J. Solids Struct., **25**, pp. 1411–1426.

[22] Bazant, Z. P., and Estenssoro, L. F., 1979, "Surface Singularity and Crack Propagation," Int. J. Solids Struct., **15**, pp. 405–426.

[23] Williams, M. L., 1957, "On the Stress Distribution at the Base of a Stationary Crack," ASME J. Appl. Mech., **24**, pp. 109–114.

[24] Villarreal, G., Sih, G. C., and Hartranft, R. J., 1975, "Photoelastic Investigation of Thick Plate With a Transverse Crack," ASME J. Appl. Mech., **42**, pp. 9–13.

[25] Rousseau, C.-E., and Tippur, H. V., 2000, "Compositionally Graded Materials With Cracks Normal to the Elastic Gradient," Acta Mater., **48**, pp. 4021–4033.

[26] Tippur, H. V., Krishnaswamy, S., and Rosakis, A. J., 1991, "A Coherent Gradient Sensor for Crack Tip Deformation Measurements: Analysis and Experimental Results," Int. J. Fract., **48**, pp. 193–204.

[27] Dally, J. W., and Sanford, R. J., 1987, "Strain Gage Methods for Measuring the Opening Mode Stress Intensity Factor K_I," Exp. Mech., **27**, pp. 381–388.

[28] Berger, J. R., and Dally, J. W., 1988, "An Error Analysis of Single Strain Gage Determination of the Stress Intensity Factor," Exp. Tech., **12**(8), pp. 31–33.

[29] McNeill, S. R., Peters, W. H., and Sutton, M. A., 1987, "Estimation of Stress Intensity Factor by Digital Image Correlation," Eng. Fract. Mech., **28**, pp. 101–112.

[30] Anderson, T. L., 1995, *Fracture Mechanics: Fundamentals and Applications*, 2nd ed., CRC, Boca Raton.

[31] Joseph, P. F., and Erdogan, F., 1989, "Surface Crack Problems in Plates," Int. J. Fract., **41**, pp. 105–131.

A. Milanese[1]
Graduate Student
e-mail: milanesa@clarkson.edu

P. Marzocca
Assistant Professor

Department of Mechanical and
Aeronautical Engineering,
Clarkson University,
P. O. Box. 5725,
Potsdam, NY 13699

M. Belubekyan
Professor

K. Ghazaryan
Professor

H. P. Mkrtchyan
Research Scientist

Institute of Mechanics,
National Academy of Sciences of Armenia,
24 Marshal Baghramian Avenue,
Yerevan 375019, Armenia

On the Magnetic Field Effect in Electroconductive Plates Under Nonconservative Loading

This work investigates the behavior of an electroconductive plate under the action of a nonconservative load and subjected to a transversal magnetic field. The governing equation of the bending vibrations of an electroconductive plate, subjected to a transverse magnetic field and a follower type force at one edge, is presented. The assumption of an elongated plate leads to a simplified equation, which is conveniently written in dimensionless terms. For a cantilevered configuration, the characteristic equation relative to the magnetoelastic modes of vibration of the system is derived. Approximate solutions based on Galerkin method and an adjoint formulation are also presented and compared with the semi-analytical results. Root loci plots are computed as a function of the proper dimensionless parameters. The behavior of the system is very similar to the one exhibited by other structures subjected to nonconservative loads when damping is present. A relaxed definition of stability is used to regain continuity in the instability envelope.
[DOI: 10.1115/1.3005573]

1 Introduction

The instability of elastic systems, such as columns, plates, and cylindrical curved shells, subjected to mechanical nonconservative loads has been widely studied. Since its first appearance, represented by the problem of Beck's column [1], a vast literature dealing with the argument flourished. The books by Bolotin [2], Ziegler [3], and Leipholz [4] thoroughly addressed this issue. Furthermore, several review papers have also been written on the subject; see, for example, the detailed one by Langthjem and Sugiyama [5]. For a thorough critical review of the dynamic stability of structures under the action of "follower type" forces, the reader is referred to the review by Elishakoff [6]. Such studies have found application in the design of many engineering structures and, in particular, in the dynamics of space structures (e.g., Higuchi and Dowell [7]).

It is well known that the dynamic behavior of structures subjected to nonconservative loads can be largely affected by the presence of damping terms. The destabilizing effects of mechanical damping in elastic and viscoelastic structures subjected to follower type loads have also been studied in detail. As highlighted first by Ziegler [8], paradoxical results can be found, where, for example, an infinitesimal small damping has a finite destabilizing effect. This phenomenon is still object of investigations. Much emphasis has been given to the mathematical aspects of the eigenvalues discontinuity at zero damping; see, for example, the works by Seyranian [9], Seyranian and Kirillov [10], and Kirillov and Seyranian [11]. From a more physical perspective, Semler et al. [12] analyzed the simple system of Ziegler's [8] double pendulum, while Sugiyama and Langthjem [13] considered the continuous example of Beck's [1] column. Experimental verifications of such a destabilizing effect can be found in the references listed in the review paper by Langthjem and Sugiyama [5].

On the other hand, the damping character of a magnetic field in electroconductive thin walled plates and shells has been revealed in several studies, as is reported by Ambartsumian et al. [14] and in the review paper by Ambartsumian [15]. The interaction between magnetic fields and conducting elastic solids is important in several practical applications. In the field of nondestructive testing technologies, this principle is exploited to detect defects and cracks, and it may be used in a structural health monitoring framework. It is also relevant to mention that it is possible to measure stress distribution through measurements of an electromagnetic field at a distance from an elastic body. Furthermore, in microelectromechanical systems (MEMSs), such interactions need also to be analyzed [16].

The present work takes advantage of the previous literature, investigating the behavior of an electroconductive plate subjected to a follower load and under the effect of an external transversal magnetic field.

The rest of the paper is organized as follows. Section 2 presents the mathematical modeling with the proper governing equation, along with selected solution methodologies. Section 3 presents detailed results in the form of root loci plots, with discussions. In particular, the need of a relaxed definition of stability is highlighted. Finally, pertinent conclusions are presented. The Appendix reports the coefficients of the polynomials used for the approximate solutions obtained by means of trial functions.

2 Mathematical Modeling

2.1 Magnetoelastic Governing Equations. A thin electroconductive plate is considered in this analysis. As shown in Fig. 1, the plate is clamped on one side, and subjected at the opposite edge to a follower type load, applied tangentially to the deflected surface. A constant external magnetic field acts transversally on the plate. The force is characterized by the load per unit surface Q

[1]Corresponding author.

Contributed by the Applied Mechanics Division of ASME for publication in the JOURNAL OF APPLIED MECHANICS. Manuscript received October 2, 2007; final manuscript received September 15, 2008; published online November 12, 2008. Review conducted by Arvind Raman.

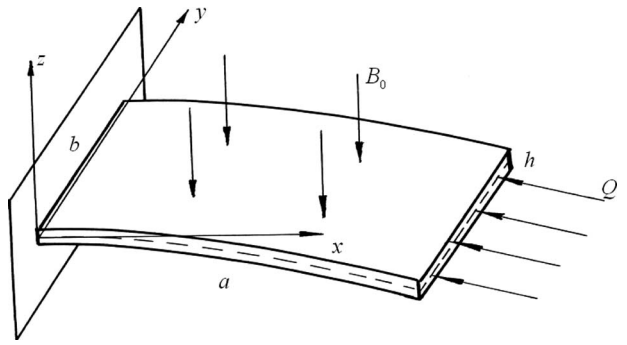

Fig. 1 Cantilevered panel under in-plane follower load and transverse magnetic field

(taken positive if compressive, as shown in Fig. 1), while the magnetic field is described by the magnetic field induction B_0. The reference system is shown in Fig. 1.

The governing dynamic equation for the plate bending vibrations, taking into account the follower type load, can be written as

$$D\nabla^4 w + 2Qh\frac{\partial^2 w}{\partial x^2} + 2\rho h\frac{\partial^2 w}{\partial t^2} = F \tag{1}$$

Herein, $w(x,y,t)$ represents the plate middle plane normal displacements, $2h$ is the thickness of the plate, $D=2Eh^3/3(1-\nu^2)$ is the plate flexural stiffness, E and ν are the Young modulus and Poisson ratio, respectively, and ρ is the bulk density of the plate material. In addition, F is the electromagnetic load due to the interaction of the external magnetic field with the electroconductive plate. Using the electrodynamic theory of deformable bodies and the hypothesis of magnetoelasticity of thin bodies, as reported, for example, by Ambartsumian et al. [14] and by Ambartsumian [15], the electromagnetic load F through the thickness can be written as

$$F = \int_{-h}^{h}\left[f_z + \left(\frac{\partial f_x}{\partial x} + \frac{\partial f_y}{\partial y}\right)z\right]dz \tag{2}$$

where

$$\boldsymbol{f} = f_x\boldsymbol{i} + f_y\boldsymbol{j} + f_z\boldsymbol{k} = \frac{1}{\gamma}\left[\left(\frac{\partial \boldsymbol{u}}{\partial t}\times\boldsymbol{B}_0\right)\times\boldsymbol{B}_0\right] \tag{3}$$

In Eq. (3), γ is the electroresistivity of the plate material and $\boldsymbol{B}_0$ is the magnetic field induction. The displacement vector of the plate points $\boldsymbol{u}=u_x\boldsymbol{i}+u_y\boldsymbol{j}+u_z\boldsymbol{k}$ can be written, according to the assumptions of Kirchhoff's plate theory, as

$$u_x(x,y,z) = -z\frac{\partial w}{\partial x} \tag{4a}$$

$$u_y(x,y,z) = -z\frac{\partial w}{\partial y} \tag{4b}$$

$$u_z(x,y,z) = w(x,y) \tag{4c}$$

By considering $\boldsymbol{B}_0=-B_0\boldsymbol{k}$, this results in

$$F = \frac{2h^3B_0^2}{3\gamma}\frac{\partial}{\partial t}\nabla^2 w \tag{5}$$

Consequently, Eq. (1) can be rewritten as

$$D\nabla^4 w + 2Qh\frac{\partial^2 w}{\partial x^2} + 2\rho h\frac{\partial^2 w}{\partial t^2} - \frac{2h^3B_0^2}{3\gamma}\frac{\partial}{\partial t}\nabla^2 w = 0 \tag{6}$$

In the absence of magnetic field, that is, when $B_0=0$, the problem reduces to the well known nonconservative stability problem of Beck's column [1], where the follower force has a destabilizing effect on the structure.

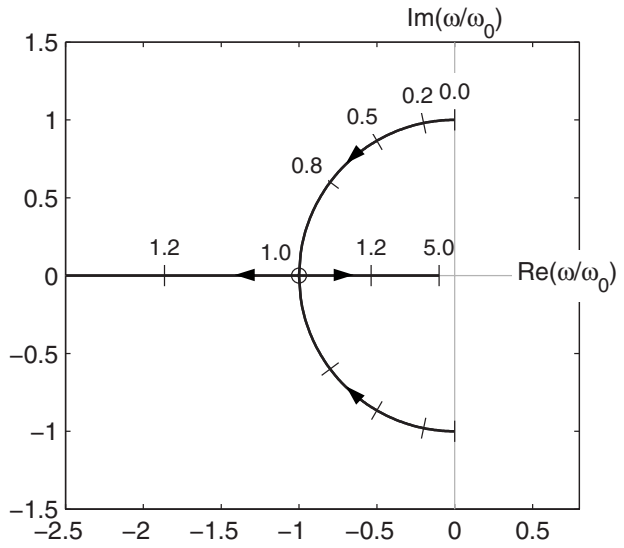

Fig. 2 Root loci plot for a simply supported electroconductive plate in a transversal magnetic field for different values of α/ω_0

On the other hand, in the absence of the pressure load, that is, $Q=0$, this problem has been studied by Ambartsumian et al. [14], where the stabilizing damping character of the magnetic field has been highlighted. In this case, and for a plate simply supported on the four edges, solutions of Eq. (6) are in the form

$$w(x,y,t) = w_0 e^{\omega t}\sin(px)\sin(qy) \tag{7}$$

with $p=(\pi n)/a$ and $q=(\pi m)/b$. Consequently, the magnetoelastic complex frequencies ω of the plate can be readily found as

$$\omega = -\alpha \pm \sqrt{\alpha^2 - \omega_0^2} \tag{8}$$

having introduced the parameters

$$\alpha = \frac{h^2B_0^2(p^2+q^2)}{6\gamma\rho}, \quad \omega_0^2 = \frac{D(p^2+q^2)^2}{2\rho h} \tag{9}$$

For $\alpha/\omega_0 < 1$, that is, for $B_0 < (12E\rho\gamma^2/[h^2(1-\nu^2)])^{1/4}$, underdamped vibrations are found, while for $\alpha/\omega_0 \geq 1$, and consequently $B_0 \geq (12E\rho\gamma^2/[h^2(1-\nu^2)])^{1/4}$, an overdamped behavior is experienced. In the latter case, the roots tend to the origin of the complex plane for increasing values of α/ω_0 (and hence B_0). This is shown in the form of a root loci plot in Fig. 2, which reports the real and imaginary parts of the dimensionless frequency ω/ω_0 as a function of the ratio α/ω_0.

For an elongated cantilevered plate, investigations accounting for both the effects of the follower force and the magnetic field on the stability of the system are presented, along with an understanding of their mutual interactions. Under this assumption, $b \gg a$, and all partial derivatives with respect to y are negligible, so that Eq. (6) becomes

$$D\frac{\partial^4 w}{\partial x^4} + 2Qh\frac{\partial^2 w}{\partial x^2} + 2\rho h\frac{\partial^2 w}{\partial t^2} - \frac{2h^3B_0^2}{3\gamma}\frac{\partial^3 w}{\partial t\partial x^2} = 0 \tag{10}$$

Equation (10) can be solved by separating the time and spatial variables as

$$w(x,t) = U(\eta)e^{\omega t} \tag{11}$$

If a dimensionless coordinate $\eta=x/a$ is introduced, the governing equation can be recast in dimensionless terms as follows:

$$\frac{d^4U}{d\eta^4} + (q-\beta\theta)\frac{d^2U}{d\eta^2} + \theta^2 U = 0 \tag{12}$$

where q, β, and θ are dimensionless parameters, defined as

$$q = \frac{3(1-\nu^2)a^2 Q}{Eh^2} \tag{13a}$$

$$\beta = \frac{hB_0^2\sqrt{1-\nu^2}}{\gamma\sqrt{3E\rho}} \tag{13b}$$

$$\theta = \frac{\omega a^2}{h}\sqrt{\frac{3\rho(1-\nu^2)}{E}} \tag{13c}$$

The parameters q and β are related to the follower force and the magnetic field, respectively, while θ is a linear function of the complex frequency ω, and thus its real part is directly related to the stability of the system.

For a cantilevered plate with a follower force, the boundary conditions that accompany Eq. (12) are

$$U(0) = 0 \quad \text{(clamped side, } \eta = 0) \tag{14a}$$

$$\frac{dU(0)}{d\eta} = 0 \quad \text{(clamped side, } \eta = 0) \tag{14b}$$

$$\frac{d^2U(1)}{d\eta^2} = 0 \quad \text{(side with follower load, } \eta = 1) \tag{14c}$$

$$\frac{d^3U(1)}{d\eta^3} - \beta\theta\frac{dU(1)}{d\eta} = 0 \quad \text{(side with follower load, } \eta = 1) \tag{14d}$$

As a remark, the follower nature of the force is such that it does not appear in the boundary conditions, especially in Eq. (14*d*). This, in fact, describes in dimensionless terms the shear at the free edge of the plate, which is not affected by the follower load, since the latter is by definition always tangential to the deflected free surface.

The general solution of the magnetoelastic governing equation, Eq. (12), can be expressed in terms of complex trigonometric functions as

$$U(\eta) = C_1\sin(p_1\eta) + C_2\cos(p_1\eta) + C_3\sin(p_2\eta) + C_4\cos(p_2\eta) \tag{15}$$

where p_1 and p_2 are functions of θ, defined as

$$p_1 = \tfrac{1}{2}\left(\sqrt{(q-\beta\theta)+2\theta} + \sqrt{(q-\beta\theta)-2\theta}\right) \tag{16a}$$

$$p_2 = \tfrac{1}{2}\left(\sqrt{(q-\beta\theta)+2\theta} - \sqrt{(q-\beta\theta)-2\theta}\right) \tag{16b}$$

The coefficients C_is in Eq. (15) can be obtained applying the boundary conditions of Eqs. (14), leading to a system of four linear homogeneous equations. The nontrivial solution is sought by imposing the determinant of the matrix of coefficients equal to zero. After some algebraic manipulations, the following characteristic equation in the dimensionless variables q, β, and θ is obtained:

$$2q\beta\theta + 4\theta^2 - 2q^2 + \theta(\beta-1)[(q-\beta\theta)-2\theta]\cos\sqrt{(q-\beta\theta)+2\theta} + \theta(\beta+1)[(q-\beta\theta)+2\theta]\cos\sqrt{(q-\beta\theta)-2\theta} = 0 \tag{17}$$

Equation (17) yields infinite solutions for θ, corresponding to the infinite magnetoelastic complex frequencies ω of the continuum structure. To assure stability, all the ωs need to be checked. From a practical viewpoint, it is enough to track the first two magnetoelastic modes and to infer the overall stability of the system from the position of the roots of these first modes. This has been mathematically proven in the case of Beck's column problem by Carr and Malhardeen [17], whose paper has appeared almost three decades after the original brief report of Beck [1]. Before proceeding with the solution of Eq. (17), it is viable to recall that its zeros in the complex plane will appear as complex conjugate pairs. This can be directly inferred from the physical meaning of the response, which in order to be real needs the counter-rotating pair $e^{\omega t}$ and $e^{\bar{\omega}t}$, for every ω.

It can be observed that two purely real solutions of Eq. (17) exist, and one of them is positive. These solutions have no physical meaning and are related to a further rank loss of the matrix of coefficients coming from the boundary conditions, as it is explained next. It can be shown (by simple substitution) that if $p_1 = p_2$, then $\theta = q/(\beta+2)$ is a solution of Eq. (17). This value of θ is real and positive, but it does not involve any instability, that is, a trivial solution is encountered. In fact, it is possible to show that the constants in Eq. (15) become $C_3 = -C_1$ and $C_4 = -C_2$, so that the corresponding eigenfunction vanishes identically, as $U(\eta) = C_1\sin(p_1\eta) + C_2\cos(p_1\eta) - C_1\sin(p_1\eta) - C_2\cos(p_1\eta) = 0$. The same is observed when $p_1 = -p_2$, which implies $\theta = q/(\beta-2)$.

2.2 Solution Using an Optimization Approach. Finding the zeros, in θ, of Eq. (17) can be reformulated as an optimization problem, so that a general minimization algorithm can be utilized. In a straightforward way this is obtained by defining the objective function F_{cost} as

$$F_{\text{cost}} = |2q\beta\theta + 4\theta^2 - 2q^2 + \theta(\beta-1)[(q-\beta\theta) - 2\theta]\cos\sqrt{(q-\beta\theta)+2\theta} + \theta(\beta+1)[(q-\beta\theta) + 2\theta]\cos\sqrt{(q-\beta\theta)-2\theta}| \tag{18}$$

Clearly, when $F_{\text{cost}}(\bar{\theta}) = 0$, the characteristic equation is also satisfied and $\tilde{\theta}$ is a local minimum of F_{cost}, and vice versa. Therefore, the problem becomes that of finding the minima of F_{cost}, having as free variable the complex $\theta = \theta_R + i\theta_I$. For convenience, this can be rewritten using two real variables, namely, the real and imaginary components θ_R and θ_I. The search of the minima can be restricted to positive θ_I, since all the roots are complex conjugate.

The minimization can be achieved using a standard optimization code handling multiple variables. In this case, the MATLAB® routine `fminsearch` [18], which implements the Nelder–Mead simplex method, is used. Since multiple minima are of interest, as well as coalescence of minima, special care needs to be utilized. The following procedure is used.

- For a given value of q and β, a contour plot of F_{cost} is obtained, with contour lines logarithmically spaced.
- In order to return the local minimum of interest, an initial guess for θ is specified.
- The minimization code is run and the solution is shown on the contour plot.
- A variation of either q or β is introduced, and a new minimum is sought using the previous value as initial guess for θ.

Although such a procedure may appear to be lengthy, it provides a continuous check on the precise and correct tracking of the magnetoelastic roots. When necessary, for example when coalescence is present, an artificial bias in the direction of interest is introduced in the starting point for the optimization.

This approach, involving recasting the problem in optimization terms and using a general purpose minimization code, has proven to work well for the problem of interest. It does not require any additional mathematical steps, and it is rather straightforward and independent of the form of the characteristic equation. Furthermore, direct control is given to the user on the tracking of the modes.

2.3 Solution Using Galerkin Method. Approximate solutions to Eq. (12), together with the boundary conditions specified in Eqs. (14), can also be sought using Galerkin method. The approach follows the one presented by Forray [19]. An approximate solution of the form

$$U_n = \sum_{k=1}^{n} a_k \phi_k(\eta) \tag{19}$$

can be found, where the trial functions $\phi_k(\eta)$ are chosen as to satisfy the boundary conditions. Then, defining the differential operator $L(\cdot)$ from Eq. (12), the unknown coefficients a_k can be obtained imposing the orthogonality of the residual to the trial functions, that is,

$$\int_0^1 L\left(\sum_{j=1}^{n} a_j \phi_j(\eta)\right)\phi_k(\eta)d\eta = 0, \quad k = 1,2,\ldots,n \tag{20}$$

A homogeneous linear system in a_k is found, and singularity of the matrix of coefficients needs to be imposed.

In this case, two polynomial trial functions are chosen:

$$\phi_1(\eta) = 3(2+\beta\theta)\eta^4 - 8(3+\beta\theta)\eta^3 + 6(6+\beta\theta)\eta^2$$

$$\phi_2(\eta) = 6(6+\beta\theta)\eta^5 - 15(8+\beta\theta)\eta^4 + 10(12+\beta\theta)\eta^3 \tag{21}$$

Carrying out the integrations and imposing the zero determinant of the matrix of coefficients, a polynomial equation of degree 8 is found in θ as

$$c_8\theta^8 + c_7\theta^7 + c_6\theta^6 + c_5\theta^5 + c_4\theta^4 + c_3\theta^3 + c_2\theta^2 + c_1\theta + c_0 = 0 \tag{22}$$

The coefficients c_0–c_8 are given in the Appendix, in Eqs. (A1*a*)–(A1*i*). When $\beta=0$, the polynomial in Eq. (22) becomes a biquadratic equation in θ, and a closed-form formula for the roots is therefore available. On the other hand, when $\beta\neq 0$, a numerical approach needs to be utilized to find the roots of Eq. (22).

Convergence issues may arise when using non-orthogonal trial functions; in this specific case, however, it is observed that the approximate eigenvalues compare very well with the exact ones, as shown in Sec. (3). A set of orthogonal functions $\varphi_k(\eta)$ can be constructed from a set of linear independent functions $f_k(\eta)$ using, for example, Gram–Schmidt technique, by taking $\varphi_1=f_1$, $\varphi_2=f_2-\varphi_1\langle\varphi_1,f_2\rangle/\langle\varphi_1,\varphi_1\rangle$, $\varphi_3=f_3-\varphi_1\langle\varphi_1,f_3\rangle/\langle\varphi_1,\varphi_1\rangle-\varphi_2\langle\varphi_2,f_3\rangle/\langle\varphi_2,\varphi_2\rangle$, and so on.

2.4 Solution Using Adjoint Problem Formulation. A more powerful method to obtain approximate solutions of the boundary value problem specified in Eqs. (12)–(14) is based on the concept of adjoint system, which enables to build an appropriate variational approach; see, for example, the notes of Pedersen [20]. Herrmann and Nemat-Nasser [21] showed how this method works for Beck's column, whose adjoint problem is Reut's column. A similar analysis was also presented by Prasad and Herrmann [22].

The boundary value problem can be cast as

$$\hat{L}[U,\theta] = 0 \tag{23}$$

where the linear differential operator $\hat{L}$ operates on the eigenfunction $U(\eta)$. This, together with the boundary conditions, constitutes a non-self-adjoint boundary value problem. The corresponding adjoint system operator $\hat{L}^*$ can be defined via a function $V(\eta)$ using the internal product as

$$\langle\hat{L}[U,\theta],V\rangle = \langle\hat{L}^*[V,\theta_*],U\rangle \tag{24}$$

The function $V(\eta)$ is a solution of the adjoint system

$$\frac{d^4V}{d\eta^4} + (q-\beta\theta_*)\frac{d^2V}{d\eta^2} + \theta_*^2 V = 0 \tag{25}$$

with boundary conditions

$$V(0) = 0 \tag{26a}$$

$$\frac{dV(0)}{d\eta} = 0 \tag{26b}$$

$$\frac{d^2V(1)}{d\eta^2} + qV(1) = 0 \tag{26c}$$

$$\frac{d^3V(1)}{d\eta^3} + (q-\beta\theta_*)\frac{dV(1)}{d\eta} = 0 \tag{26d}$$

For linear differential boundary value problems of the type $\hat{L}(U)=\lambda U$, when the eigenvalues λ are not involved in the boundary conditions, it is well known that the original and adjoint systems have the same set of eigenvalues, while the eigenvectors U_n and V_m are orthogonal for $n\neq m$. Prasad and Herrmann [22], considering the stability problem of elastic continua subjected to nonconservative forces, proved that the eigenvalues of the original and the adjoint systems are identical, based on assumptions of completeness of eigenfunctions of the original system. In our case, the eigenvalues appear in the equations and in the boundary conditions as θ and θ^2; therefore, it may be more straightforward to prove the identity of the eigenvalues by direct method. The general solution of Eq. (25) can be expressed in terms of complex trigonometric functions as

$$V(\eta) = C_{1*}\sin(p_{1*}\eta) + C_{2*}\cos(p_{1*}\eta) + C_{3*}\sin(p_{2*}\eta) + C_{4*}\cos(p_{2*}\eta) \tag{27}$$

where

$$p_{1*} = \tfrac{1}{2}\left(\sqrt{(q-\beta\theta_*)+2\theta_*} + \sqrt{(q-\beta\theta_*)-2\theta_*}\right) \tag{28a}$$

$$p_{2*} = \tfrac{1}{2}\left(\sqrt{(q-\beta\theta_*)+2\theta_*} - \sqrt{(q-\beta\theta_*)-2\theta_*}\right) \tag{28b}$$

To obtain the characteristic equation, a nontrivial solution for C_{1*}, C_{2*}, C_{3*}, and C_{4*} needs to be sought, using the boundary conditions of Eqs. (26*a*)–(26*d*). Imposing the nontrivial solution to the corresponding homogenous system yields the characteristic equation

$$2q\beta\theta_* + 4\theta_*^2 - 2q^2 + \theta_*(\beta-1)[(q-\beta\theta_*) - 2\theta_*]\cos\sqrt{(q-\beta\theta_*)+2\theta_*} + \theta_*(\beta+1)[(q-\beta\theta_*) + 2\theta_*]\cos\sqrt{(q-\beta\theta_*)-2\theta_*} = 0 \tag{29}$$

which coincides with Eq. (17) of the original boundary value problem. This concludes the proof. Generalized orthogonality conditions for the eigenvectors can also be found in this case, similar to the orthogonality property of modes in linear vibration theory.

A variational principle can be used to obtain an approximate solution. Two sets of trial functions, $U_k(\eta)$ and $V_i(\eta)$, satisfying the boundary conditions of the original and adjoint systems, respectively, can be selected, in the form

$$U(\eta) = \sum_{m=1}^{M} C_m U_m(\eta) \quad \text{and} \quad V(\eta) = \sum_{m=1}^{M} C_m V_m(\eta) \tag{30}$$

This allows writing an algebraic equation in terms of θ as

$$\det\|A_{kj}\| = 0 \quad \text{with } A_{kj} = \langle\hat{L}[U_k],V_j\rangle \tag{31}$$

This approximate method, which uses two sets of trial functions, is usually thought to be more powerful than the commonly used Galerkin approach presented in the previous section. The success of this method has been demonstrated in the analysis of many nonconservative stability systems, as shown by Herrmann and Nemat-Nasser [21] for Beck's and Reut's columns, and by Ghazaryan and Isabekyan [23] for a current carrying beam subjected to the action of a longitudinal magnetic field, only to name a few.

In the present case, $M=2$ is chosen, together with the following set of functions, satisfying the proper boundary conditions:

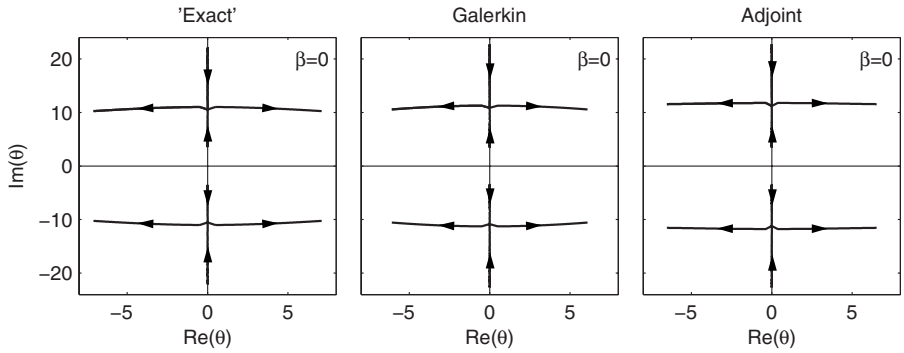

Fig. 3 Root loci plot for $\beta=0$

$$U_1(\eta) = 3(2+\beta\theta)\eta^4 - 8(3+\beta\theta)\eta^3 + 6(6+\beta\theta)\eta^2$$

$$U_2(\eta) = 6(6+\beta\theta)\eta^5 - 15(8+\beta\theta)\eta^4 + 10(12+\beta\theta)\eta^3 \tag{32a}$$

$$V_1(\eta) = (12+q^2+6\beta\theta-q\beta\theta)\eta^4 - 2(24+4q+q^2+8\beta\theta - q\beta\theta)\eta^3 + (72+6q+q^2+12\beta\theta-q\beta\theta)\eta^2$$

$$V_1(\eta) = (72+6q+q^2+12\beta\theta-q\beta\theta)\eta^5 - 2(120+12q+q^2 + 15\beta\theta-q\beta\theta)\eta^4 + (240+16q+q^2+20\beta\theta-q\beta\theta)\eta^3 \tag{32b}$$

The trial functions of Eq. (32*a*) are the same used for the Galerkin method in Eq. (21); the same considerations on convergence issues and orthogonalization apply here as well. Substituting the trial functions in Eq. (31), a polynomial in θ of degree 8 is obtained as

$$k_8\theta^8 + k_7\theta^7 + k_6\theta^6 + k_5\theta^5 + k_4\theta^4 + k_3\theta^3 + k_2\theta^2 + k_1\theta + k_0 = 0 \tag{33}$$

where the coefficients k_0–k_8 are given in the Appendix, in Eqs. (A2*a*)–(A2*i*). In this case, as for Galerkin method, a polynomial of degree 8 is obtained.

3 Results and Discussions

Since parametric analyses varying β are of interest, it is found convenient to establish first the range of variation of this dimensionless parameter. Assuming $2h=0.01$ m, $E=70$ GPa, $\rho=2700$ kg/m^3, $\nu=0.34$, $\gamma=2.7\times10^{-8}$ Ω m, and $B_0=1$ T, a value of about 7.3×10^{-3} is obtained for β. In the above, typical values for an aluminum alloy are used for density, Young's modulus, Poisson's ratio, and electrical resistivity. If typical values for copper are used instead, namely, $E=130$ GPa, $\rho=8900$ kg/m^3, $\nu=0.32$, and $\gamma=1.72\times10^{-8}$ Ω m, with the same value of magnetic field and plate thickness, a value of about 4.7×10^{-3} is obtained for β. Therefore, for the analyses, an upper bound value of 0.01 is chosen for β. However, because of the quadratic dependency on the magnetic field B_0, in some applications higher values for β may be experienced.

Three different methods have been presented in the previous section to solve the equation of motion and hence determine the stability of the system. They are the ones obtained from the numerical solution of Eqs. (17), (22), and (33), and are referred to in the following as "exact," "Galerkin," and "adjoint" solutions. This section starts analyzing the different solutions obtained with these methods. It has to be noted that also the exact solution needs a numerical approach, as described in Sec. 2.2, so it may be regarded also as semi-analytic. Although the roots of the degree 8 polynomials in Eqs. (22) and (33) can be found by carefully using standard root extraction algorithms, the same optimization-based approach is used for the Galerkin and adjoint cases as well, to exploit a common numerical framework.

Figure 3 reports the root loci plot obtained without a magnetic field, that is, for $\beta=0$ and for different values of q. All methods present the coalescence of the first and second modes, leading to instability. When a magnetic field is introduced, taking, for example, $\beta=0.01$, the root loci plot of Fig. 4 is obtained. In this case, the coalescence disappears, though the first two modes get closer and then the first one becomes unstable. The plots are again very similar for the three approaches.

The Argand diagrams shown in Figs. 3 and 4 are qualitatively very similar to the ones found for structures subjected to nonconservative loads in the presence of damping; see, for example, Ref. [24]. Zooming in around the Re(θ) axis, it is possible to see that the roots cross "gently" into the right hand part of the complex plane, before diverging sensibly. In other words, the solution stays close to the Re(θ)=0 line for a quite large range of q before actually diverging into the positive half-plane. Table 1 reports the values of q for which a root θ has a positive real part for a range

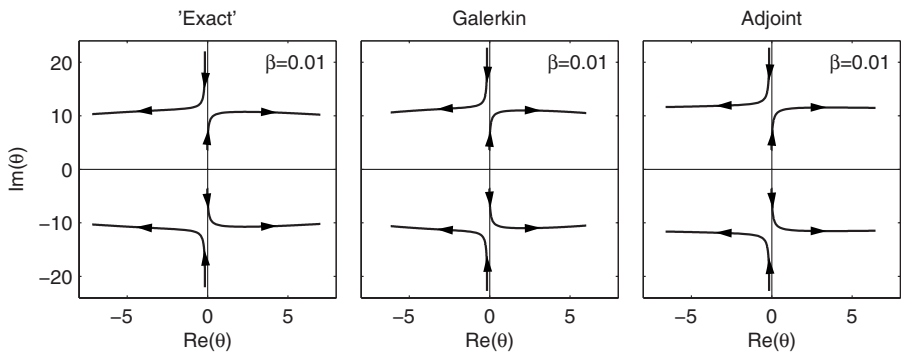

Fig. 4 Root loci plot for $\beta=0.01$

Table 1 Values of q for which $\mathrm{Re}(\theta)=0$

	Exact	Galerkin	Adjoint
$\beta=0$	$q_{\mathrm{cross}}=20.05$	$q_{\mathrm{cross}}=21.65$	$q_{\mathrm{cross}}=21.57$
$10^{-10}\leq\beta\leq10^{-2}$	$q_{\mathrm{cross}}=11.57$	$q_{\mathrm{cross}}=12.42$	$q_{\mathrm{cross}}=11.73$

of values of β. The value of 20.05 obtained with the semi-analytical solution is exactly the same found by Beck in his original paper [1]. In this case, the weighted residual methods return slightly greater estimates for q; however, this overestimation trend does not hold in general; see, for example, the work of Prasad and Herrmann [22].

It is interesting to observe that the q_{cross} value does not depend on β; if this is different from zero, that is, for the whole range $10^{-10}\leq\beta\leq10^{-2}$, the same result is obtained. This implies that a magnetic field, of arbitrary small strength, seems to have a finite effect on the load capability of the structure. Values of $\beta<10^{-10}$, but different from 0, are not reported in Table 1, since a numerical dispersion of the root loci becomes prevalent. Figure 5 shows this issue for $\beta=10^{-14}$, adopting the exact method to find the eigenvalue θ_1. The same phenomenon is observed also with the other two methods investigated in this work.

In order to present the results as a function of the parameter q, it is convenient to plot the real and imaginary parts of θ_1 and θ_2 versus q for different values of β. This approach of finding the complex frequencies—functions of several parameters—introducing one variation at the time is quite common in dynamic stability theory (see, for example, the recent book by Seyranian and Mailybaev [25]). Also the coalescence of two modes observed in this case is often encountered in the field. Figure 6 reports the real and imaginary parts of θ, obtained using the semi-analytical method, without any magnetic field, that is, $\beta=0$. A vertical line is drawn when the real part of θ_1 becomes positive. Figure 7 reports the same solution as a function of q with a magnetic field, where $\beta=0.01$ is considered. The real/imaginary plots versus q are not reported for the intermediate cases of $0<\beta<0.01$, since they are very much like Figs. 6 and 7.

Very similar results have been found in previous works that examined the damping influence (not due to a magnetic field) on the stability of structures under nonconservative forces. The results reported above can be summarized as follows. It is observed that a small value of magnetic field has a destabilizing effect, with a maximum allowable compressive load about half the one carried without a magnetic field. This is obtained consistently using a semi-analytical approach, Galerkin method, and an adjoint formulation. Furthermore, when the magnetic field tends to very small

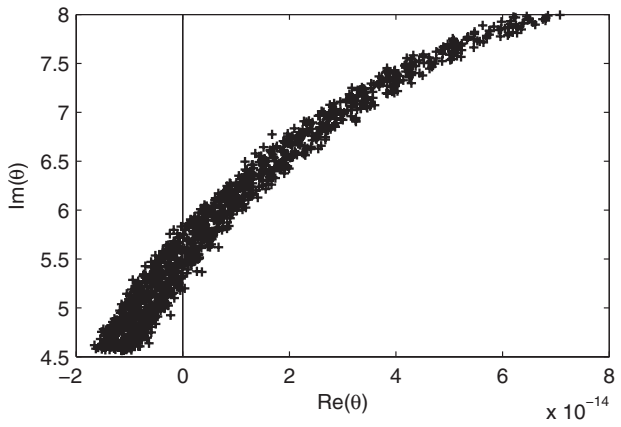

Fig. 5 Zoom of the root loci plot for $\beta=10^{-14}$, semi-analytic solution

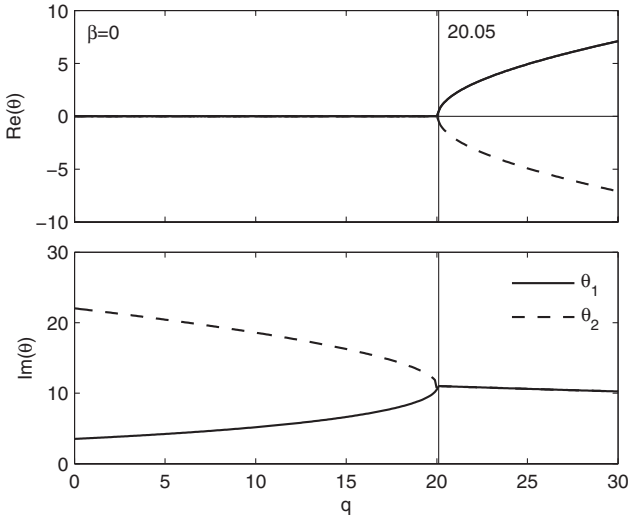

Fig. 6 Real/imaginary parts of θ for $\beta=0$

values, still there is a pair of roots of the system that exhibit a positive (although small) real part. The famous (and widely debated) paradox of the destabilizing effect of damping, first presented by Ziegler [8], is therefore encountered in this case. There have been different approaches, also supported by experimental verifications, to resolve the paradox, as reported in the review paper by Langthjem and Sugiyama [5], for example. What is needed is basically a relaxed definition of stability. Lyapunov's definition is based on stability in an infinite interval of time, and hence it requires the real part of all roots to be nonpositive. Such a requirement may be too restrictive in some cases, which may require a new terminology in dynamic stability. This has been proposed, for example, by Bolotin and Zhinzher [24], which introduced the notion of "quiet" and "violent" flutters, and by Higuchi and Dowell [7], with their "weak" flutter. The approach adopted here is similar to the one proposed by this last reference, and it is preferred for its simple and intuitive physical interpretation. With this approach, the system is considered stable as long as all the roots have a real part below a certain threshold, which can be determined considering the time scales involved in the system, and, in particular, the lapse of time during which the follower force is present. A numerical example can be useful to make the point. The free response of the system is modulated in amplitude

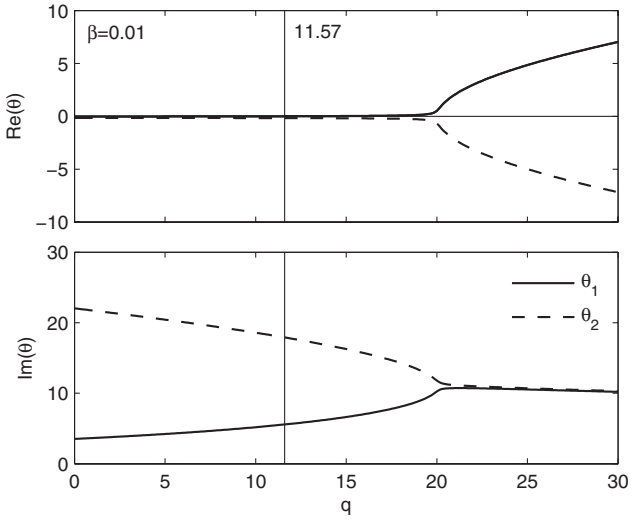

Fig. 7 Real/imaginary parts of θ for $\beta=0.01$

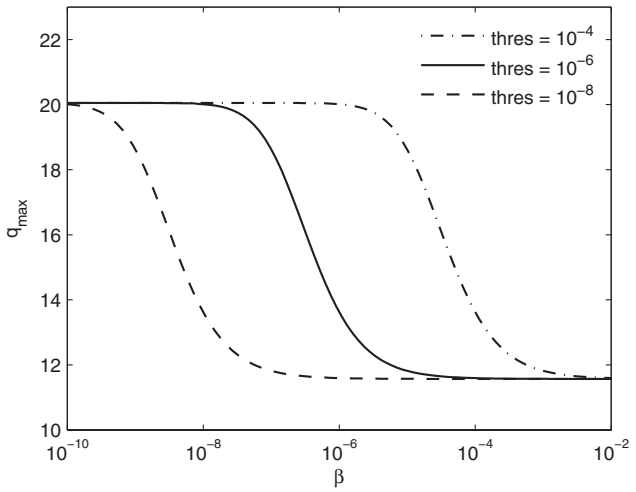

Fig. 8 Envelope q_{max} versus β for different thresholds on the real part of θ (exact approach)

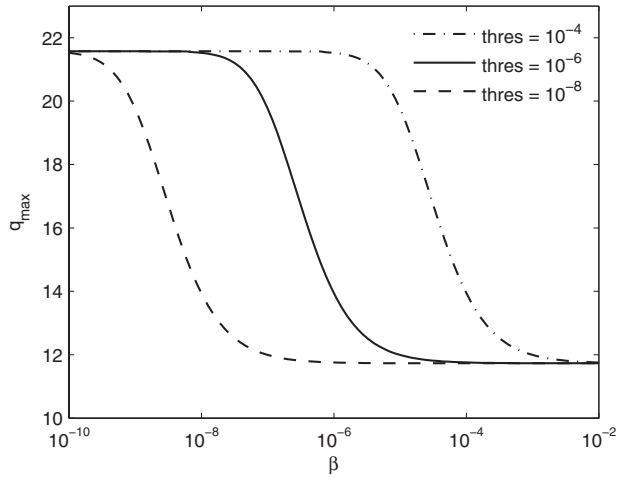

Fig. 10 Envelope q_{max} versus β for different thresholds on the real part of θ (adjoint approach)

by a factor $e^{\mathrm{Re}(\omega)t}$. Therefore, if $\mathrm{Re}(\omega)$ is 10^{-6}, then 10^6 s (that is, more than 11 days) are needed in order to have an amplification of the perturbation of about 2.7. It is clear, therefore, how a system can be considered stable in practice even when it admits roots with positive (though small) real parts.

As in this analysis the roots are in terms of the dimensionless parameter θ, and not directly in terms of the complex frequency ω, an additional step is required. Using Eq. (13*c*), it is possible to show that ω may be considered to be about two orders of magnitude greater than θ. In fact, taking $a=1$ m, $2h=0.01$ m, $\rho=2700\ \mathrm{kg/m^3}$, $\nu=0.34$, and $E=70$ GPa, it is found that $\theta \approx 0.064\omega$. If the values $\rho=8900\ \mathrm{kg/m^3}$, $\nu=0.32$, and $E=130$ GPa are used instead, then $\theta \approx 0.0086\omega$. Therefore, $\omega \approx 10^2\theta$ is a reasonable assumption. Although these computations are limited in scope, they are reported here to give a feeling of the numbers that may be actually used in practical circumstances.

With these considerations, the "relaxed" stability of the system is analyzed, imposing three different thresholds of 10^{-4}, 10^{-6}, and 10^{-8} on the maximum allowable real part of θ, as reported in Figs. 8–10, obtained using the semi-analytical approach, Galerkin method, and the adjoint formulation, respectively. The outcomes of the three methods are very much alike, predicting transitions in correspondence of the same values of β, though the actual asymptotic values on the left and right parts of the plots are different, as noted in Table 1. The continuity character of the dynamic instability is regained with such a relaxed definition of stability, and the paradox that implies a finite loss in load capability for an infinitesimal amount of magnetic field is hence eliminated. It is also observed, as expected, that the larger the threshold on the real part of θ, the larger the maximum allowable compressive load for a given magnetic field intensity.

To obtain the results reported in Figs. 8–10, instead of running a parametric analysis for a set of values of q (as in Figs. 6 and 7, for example), the algorithm shown in Fig. 11 is used. This is based on incrementing the value of q until an instability is found. Then, a refinement is added stepping back and decreasing the increment Δq, iteratively, until the given precision is obtained. At that point, the q_{max} is returned and the routine ends. The "find_θ" block at the innermost core of the loop stands for the root finding procedure, based on a minimization approach, and applies for the three methods outlined in Secs. 2.2–2.4.

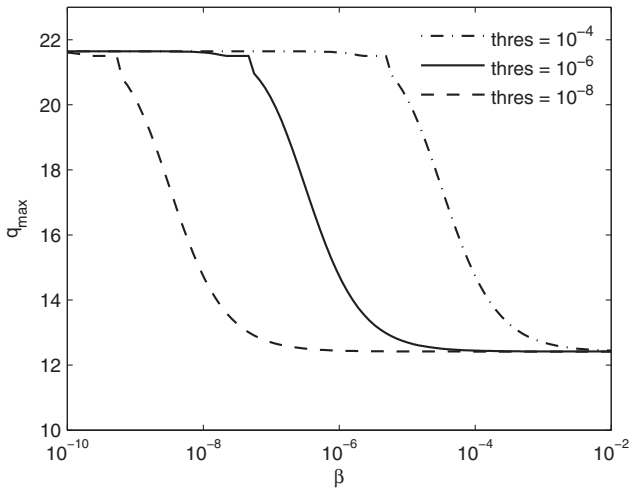

Fig. 9 Envelope q_{max} versus β for different thresholds on the real part of θ (Galerkin approach)

4 Conclusions

The effect of a transversal magnetic field on an electroconductive plate, cantilevered at one edge and subjected to a follower force at the opposite edge, has been considered. The magnetoelastic governing equation has been established, combining the formulation of Beck's column with the formulas coming from the magnetoelasticity of thin bodies. The formulation has then been simplified for the case of an elongated plate, and the corresponding equation has been rewritten in dimensionless terms. The problem has then been solved using three different approaches, a semi-

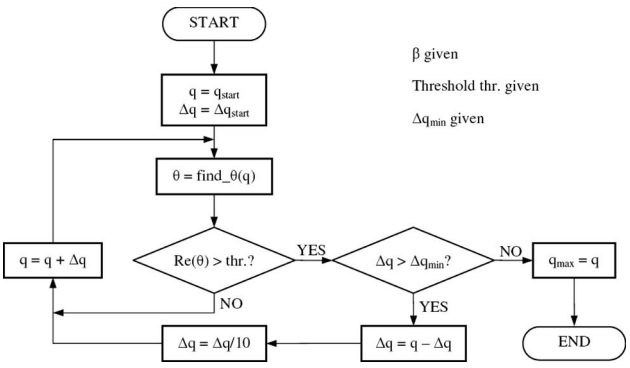

Fig. 11 Algorithm for determining the stability envelope

analytical formulation, Galerkin method, and an adjoint formulation. The results of the three methods agree very well on the character of the instability, and the marginal differences in the actual values have been highlighted. The Argand plots for selected values of the magnetic field have been computed for the first two magnetoelastic roots. It is found that the magnetic field produces effects comparable to those due to damping. Ziegler's paradox is encountered, that is, the maximum allowable compressive follower force sees a finite drop when an infinitesimal magnetic field is introduced. A modified definition of stability is used, where the roots of the system are allowed to have a positive (though small) real part. With this, the continuity of the instability envelope is regained.

Acknowledgment

A.M. would like to thank the MAE Department at Clarkson University for providing partial support for this research through a Teaching Assistantship. The partial funding support of the National Science Foundation, NSF Grant No. OISE-0532683, is also gratefully acknowledged. The authors would like to thank the anonymous reviewer for the constructive feedback provided, which helped shaping an improved revision of the paper.

Nomenclature

a, b = plate dimensions in the x and y directions, respectively (m)
B_0 = magnetic field induction (T)
D = plate flexural rigidity (N m)
E = Young's modulus of elasticity (N/m^2)
F = electromagnetic force per unit area (N/m^2)
$\boldsymbol{f}$ = specific electromagnetic force (N/m^2)
$2h$ = plate thickness (m)
Q = follower type load per unit area (N/m^2)
q = dimensionless load
$\boldsymbol{u}$ = displacement vector of the plate points (m)
w = plate middle plane normal displacements (m)
x, y, z = coordinates along the two sides and the thickness of the plate (m)
α, ω_0 = components of the magnetoelastic complex frequencies (rad/s)
β = dimensionless magnetic field
γ = electroresistivity of the plate material (Ω m)
η = dimensionless coordinate, $\eta = x/a$.
ρ = bulk density of the plate material (kg/m^3)
υ = Poisson's ratio
ω = magnetoelastic complex frequency (rad/s)
θ = magnetoelastic dimensionless complex frequency

$()' = \partial/\partial\eta$, $()'' = \partial^2/\partial\eta^2$ spatial derivatives
$\nabla^2 = \Delta = \partial^2/\partial x^2 + \partial^2/\partial y^2$ Laplace operator
$\nabla^4 = (\nabla^2)^2 = \Delta^2$ biharmonic operator

Appendix

The coefficients $c_0 - c_8$ of the polynomial in Eq. (22) are given as follows:

$$c_0 = \frac{4,478,976}{49}q + \frac{19,440}{7}q^2 + \frac{14,929,920}{7} \tag{A1a}$$

$$c_1 = \tfrac{1}{49}(71,280q^2 - 777,600q + 85,224,960)\beta \tag{A1b}$$

$$c_2 = \frac{13,602,816}{77} - \frac{11,400,192}{2695}q + \left(\frac{12,960}{49}q^2 - \frac{104,976}{7}q + \frac{23,140,080}{49}\right)\beta^2 \tag{A1c}$$

$$c_3 = \left[(900q^2 - 98,280q + 2,623,104)\frac{\beta^2}{49} - \frac{899,664}{539}q + \frac{42,542,784}{539}\right]\beta \tag{A1d}$$

$$c_4 = (15q^2 - 3204q + 121,608)\frac{\beta^4}{49} + \left(\frac{6,537,948}{539} - \frac{80,194}{385}q\right)\beta^2 + \frac{4,506,624}{13,475} \tag{A1e}$$

$$c_5 = \left[(2304 - 30q)\frac{\beta^4}{49} + (1,998,994 - 23,374q)\frac{\beta^2}{2695} + \frac{1,688,352}{13,475}\right]\beta \tag{A1f}$$

$$c_6 = \left[\frac{15}{49}\beta^4 + (89,066 - 663q)\frac{\beta^2}{5390} + \frac{757,797}{53,900}\right]\beta^2 \tag{A1g}$$

$$c_7 = \left(\frac{663}{5390}\beta^2 + \frac{307}{700}\right)\beta^3 \tag{A1h}$$

$$c_8 = \frac{181}{39,600}\beta^4 \tag{A1i}$$

The coefficients $k_0 - k_8$ of the polynomial in Eq. (33) are given as follows:

$$k_0 = \frac{6}{49}q^6 + \frac{228}{49}q^5 + \frac{9144}{49}q^4 + \frac{308,016}{49}q^3 + \frac{7,843,392}{49}q^2 + \frac{52,752,384}{49}q + \frac{59,719,680}{7} \tag{A2a}$$

$$k_1 = \left(\frac{1}{35}q^6 - \frac{4}{49}q^5 + \frac{11,292}{245}q^4 - \frac{382,464}{245}q^3 + \frac{3,267,648}{49}q^2 + \frac{13,685,760}{49}q + \frac{340,899,840}{49}\right)\beta \tag{A2b}$$

$$k_2 = \left(\frac{1}{735}q^6 - \frac{43}{245}q^5 + \frac{1236}{245}q^4 - \frac{2844}{5}q^3 + \frac{3,150,648}{245}q^2 + \frac{92,560,320}{49} - \frac{2,746,224}{49}q\right)\beta^2 - \frac{1306}{40,425}q^5 + \frac{3526}{1925}q^4 - \frac{123,484}{539}q^3 + \frac{114,897,648}{13,475}q^2 + \frac{112,338,432}{2695}q + \frac{54,411,264}{77} \tag{A2c}$$

$$k_3 = \left(-\frac{926}{121,275}q^5 + \frac{2852}{5775}q^4 - \frac{450,682}{8085}q^3 + \frac{36,571,504}{13,475}q^2 - \frac{2,770,848}{13,475}q + \frac{170,171,136}{539}\right)\beta + \left(-\frac{4}{735}q^5 + \frac{116}{245}q^4 - \frac{912}{35}q^3 + \frac{304,716}{245}q^2 - \frac{4,157,424}{245}q + \frac{10,492,416}{49}\right)\beta^3 \tag{A2d}$$

$$k_4 = \left(\frac{2}{245}q^4 - \frac{32}{49}q^3 + \frac{1858}{49}q^2 - \frac{223,872}{245}q + \frac{486,432}{49}\right)\beta^4 + \left(-\frac{13}{34,650}q^5 + \frac{21}{550}q^4 - \frac{5627}{1617}q^3 + \frac{10,576,978}{40,425}q^2 - \frac{31,594,844}{13,475}q + \frac{26,151,792}{539}\right)\beta^2 + \frac{51}{21,560}q^4 - \frac{2441}{161,700}q^3 + \frac{50,059}{2695}q^2 + \frac{1,473,792}{13,475}q + \frac{18,026,496}{13,475} \quad \text{(A2}e\text{)}$$

$$k_5 = \left(-\frac{4}{735}q^3 + \frac{109}{245}q^2 - \frac{636}{35}q + \frac{9216}{49}\right)\beta^5 + \left(\frac{13}{11,550}q^4 - \frac{381}{3850}q^3 + \frac{67,618}{8085}q^2 - \frac{9,114,794}{40,425}q + \frac{7,995,976}{2695}\right)\beta^3 + \left(\frac{907}{1,940,400}q^4 - \frac{1051}{161,700}q^3 + \frac{52,739}{13,475}q^2 + \frac{10,116}{2695}q + \frac{6,753,408}{13,475}\right)\beta \quad \text{(A2}f\text{)}$$

$$k_6 = \left(\frac{1}{735}q^2 - \frac{29}{245}q + \frac{60}{49}\right)\beta^6 + \left(-\frac{13}{11,550}q^3 + \frac{27,631}{242,550}q^2 - \frac{33,709}{5775}q + \frac{178,132}{2695}\right)\beta^4 + \left(\frac{71}{5,821,200}q^4 - \frac{4717}{5,821,200}q^3 + \frac{143,569}{970,200}q^2 - \frac{20,407}{6468}q + \frac{757,797}{13,475}\right)\beta^2 \quad \text{(A2}g\text{)}$$

$$k_7 = \left(\frac{13}{34,650}q^2 - \frac{3679}{80,850}q + \frac{1326}{2695}\right)\beta^5 + \left(-\frac{71}{2,910,600}q^3 + \frac{11,717}{5,821,200}q^2 - \frac{5408}{40,425}q + \frac{307}{175}\right)\beta^3 \quad \text{(A2}h\text{)}$$

$$k_8 = \left(\frac{71}{5,821,200}q^2 - \frac{9721}{5,821,200}q + \frac{181}{9900}\right)\beta^4 \quad \text{(A2}i\text{)}$$

As a remark, it can be easily found that, when $\beta=0$, the Galerkin and the adjoint method yield the same polynomial, since in that case $k_i=4c_i$, for $i=0,1,\ldots,8$.

References

[1] Beck, M., 1952, "Die Knicklast des einseitig eingespannten, tangential gedrückten Stabes," Z. Angew. Math. Phys., **3**, pp. 225–229.
[2] Bolotin, V., 1963, *Nonconservative Problems of the Theory of Elastic Stability*, Pergamon, New York.
[3] Ziegler, H., 1968, *Principles of Structural Stability*, Blaisdel, Waltham, MA.
[4] Leipholz, H., 1980, *Stability of Elastic Systems*, Kluwer, The Netherlands.
[5] Langthjem, M. A., and Sugiyama, Y., 2000, "Dynamic Stability of Columns Subjected to Follower Loads: A Survey," J. Sound Vib., **238**, pp. 809–851.
[6] Elishakoff, I., 2005, "Controversy Associated With the So-Called "Follower Forces:" Critical Overview," Appl. Mech. Rev., **58**, pp. 117–142.
[7] Higuchi, K., and Dowell, E. H., 1992, "Effect of Structural Damping on Flutter of Plates With a Follower Force," AIAA J., **30**, pp. 820–825.
[8] Ziegler, H., 1952, "Die Stabilitätskriterien der Elastomechanik," Ing.-Arch., **20**, pp. 49–56.
[9] Seyranian, A. P., 1990, "Destabilization Paradox in Stability Problems of Nonconservative Systems," Adv. Mech., **13**, pp. 89–124.
[10] Seyranian, A. P., and Kirillov, O. N., 2003, "Effects of Small Dissipative and Gyroscopic Forces on the Stability of Nonconservative Systems," Dokl. Phys., **48**, pp. 679–684.
[11] Kirillov, O. N., and Seyranian, A. P., 2005, "Instability of Distributed Nonconservative Systems Caused by Weak Dissipation," Dokl. Math., **71**, pp. 470–475.
[12] Semler, C., Alighanbari, H., and Païdoussis, M. P., 1998, "A Physical Explanation of the Destabilizing Effect of Damping," ASME J. Appl. Mech., **65**, pp. 642–648.
[13] Sugiyama, Y., and Langthjem, M. A., 2007, "Physical Mechanism of the Destabilizing Effect of Damping in Continuous Non-Conservative Dissipative Systems," Int. J. Non-Linear Mech., **42**, pp. 132–145.
[14] Ambartsumian, S. A., Belubekyan, M. V., and Minassyan, M. M., 1983, "On the Problem of Non-Linear Elastic Electroconductive Plates in Transverse and Longitudinal Magnetic Fields," Int. J. Non-Linear Mech., **19**, pp. 141–149.
[15] Ambartsumian, S. A., 2002, "Nontraditional Theories of Shells and Plates," Appl. Mech. Rev., **5**, pp. R35–R44.
[16] Qin, F., and Yan, D., 2008, "Analytical Solution of the Perturbed Magnetic Fields of Plates Under Tensile Stress," ASME J. Appl. Mech., **75**, p. 031004.
[17] Carr, J., and Malhardeen, M. Z. M., 1979, "Beck's Problem," SIAM J. Appl. Math., **37**, pp. 261–262.
[18] MATLAB® User's Guide, 2006, The MathWorks Inc.
[19] Forray, M. J., 1968, *Variational Calculus in Science and Engineering*, McGraw-Hill, New York.
[20] Pedersen, P., 1984, "Sensitivity Analysis for Non-Self Adjoint Problems," Lect. Notes Math., **1086**, pp. 119–130.
[21] Herrmann, G., and Nemat-Nasser, S., 1966, "Adjoint Systems in Nonconservative Problems of Elastic Stability," AIAA J., **4**, pp. 2221–2222.
[22] Prasad, S. N., Herrmann, G., 1969, "The Usefulness of Adjoint Systems in Solving Nonconservative Stability Problems of Elastic Continua," Int. J. Solids Struct., **5**, pp. 727–735.
[23] Ghazaryan, K. B., and Isabekyan, N. G., 1989, "On Some Problem of Current-Carrying Rod Stability," *Proceedings of Symposium: Theoretical Problems of Magnetoelasticity*, Yerevan State University, Yerevan, Armenia, pp. 90–95, in Russian.
[24] Bolotin, V. V., and Zhinzher, N. I., 1969, "Effects of Damping on Stability of Elastic Systems Subjected to Nonconservative Forces," Int. J. Solids Struct., **5**, pp. 965–989.
[25] Seyranian, A. P., and Mailybaev, A. A., 2003, *Multiparameter Stability Theory With Mechanical Applications*, World Scientific, Singapore.

The Characteristics of Fluid Flow Through Multilayer Porous Media

F. M. Allan

M. A. Hajji

M. N. Anwar

Department of Mathematical Sciences,
United Arab Emirates University,
P. O. Box 17551,
Al Ain, United Arab Emirates

The characteristics of fluid flow through three porous layers are investigated. The two outer porous layers are considered to be of infinite width, while the middle porous layer is assumed to be of finite width. The mathematical model of the fluid flow in the middle region can be described as laminar fully developed flow and is assumed to be governed by Brinkman equations. The flow through the upper and lower porous media is governed by Forchheimer equations. At the two interface regions between the middle finite width porous layer and the outer infinite porous layers, the continuity of the velocity and of the shear stress are imposed. Under these matching conditions, the exact solutions for the set of equations describing the flow velocity are obtained. It is found that the flow velocity is affected by two parameters, namely, Reynolds number and Darcy's number. The effects of these parameters on the flow velocity profiles through the flow regions are investigated and presented. [DOI: 10.1115/1.2998483]

1 Introduction

The problem of flow through layered porous media finds applications in various fields of science and engineering. For example, the flow of ground water, oil, and gas in the ground layers are typical problems that have been considered by many researchers such as Allan and Hamdan [1], Beavers and Joseph [2], Ford and Hamdan [3], Harr [4], Polubarinova-Kochina [5], and Vafai and Kim [6].

The mathematical model for these types of problems has been based on Darcy's law, which, as it is well known, is valid for slow flow through low permeability media. It ignores inertial effects, which arise due to the microstructure of the medium and curvilinearity of the flow path and ignores the viscous shear effects, which inevitably arise when a viscous fluid flows near a macroscopic solid boundary on which a no-slip condition must be imposed. To account for such effects, one must abandon Darcy's law in favor of another flow model. Popular among the models of flow through porous media are the Darcy–Lapwood–Brinkman (DLB) and the Darcy–Lapwood–Forchheimer–Brinkman (DFB) models. The former is applicable when viscous shear effects are important, and macroscopic inertia is sufficient to describe the flow inertia through the porous material. The latter model accounts for viscous shear effects and describes both microscopic and macroscopic inertia in the medium. The flows described by these models are encountered in various natural, physical, biological, and industrial settings, (cf. Refs. [7,8], and references therein).

The fluid mechanics of the interface region of multilayer flows has gained interest over the past three decades due to its applications in various physical settings. These applications include packed-bed heat exchangers, heat pipes, thermal insulation petroleum reservoirs nuclear waste repositories, and geothermal engineering. The problem of two layers flow was investigated by several authors. Vafai and Thiyagaja [9] studied the fluid mechanics of the interface region between a fluid layer and a porous medium. They presented an analytical solution based on matched asymptotic expansions for velocity and temperature distributions. Vafai and Kim [6] adjusted the result of Vafai and Thiyagaja [9] and used matching conditions on the interface region and obtained an exact solution for the problem, which depends on Darcy's number and Reynolds number that are based on the channel height. Lately, Allan and Hamdan [1] reviewed the extent of research in these areas. They studied the fluid mechanics of the interface region between two porous media. An exact solution to the problem was obtained. The solution obtained depends also on the Darcy's number and Reynolds number, which again depend on the channel height.

Most of the studies in porous media carried out so far have been based on the Darcy's flow model, which is an empirical law for creeping flow through an extended uniform medium. The importance of the non-Darcian effect was recognized by many authors [10–12]. Most of these studies dealt with two-channel problems. In this paper, however, we consider a three-channel problem, which, to the knowledge of the authors, is being considered for the first time. We believe that the results of this work will lay the ground for extensions to the case of more than three layers. We also investigate the non-Darcian effect on the flow.

In this work, the fluid mechanics of the interface regions between three layers will be discussed. It is an attempt to shed some light on the fluid mechanics near the interface between the porous layers. Two flow configurations will be considered. The first configuration consists of a fluid flow through a porous medium of finite width, which is sandwiched between two porous layers of infinite height. The flow in the middle region in this case is governed by the Brinkman equation (DLB model), while the flow in the upper and the lower regions are assumed to be governed by the Forchheimer model (DFB model). In the second case, the middle channel is assumed to be of infinite permeability, and the same model as in the first configuration for the outer channels. In both cases, appropriate matching conditions are imposed, namely, the continuity of the velocity and the shear stress.

The paper is organized as follows. In Sec. 2, the physical settings and the mathematical formulations of the problem are presented. In Sec. 3, we present the derivation of the exact solutions for both configurations considered. Section 4 presents the results obtained. Finally, we close by a summary and conclusion in Sec. 5.

2 Mathematical Formulation

In this section, we shall present the mathematical formulations of the model equations governing the three-channel problem depicted in Fig. 1, where the middle region (Region I) is of finite width H, and the upper and lower regions (Regions II and III, respectively) are of infinite heights. The dashed lines between the regions represent the interface between the different porous layers.

2.1 Configuration 1. In this case, we consider that the flow in Region I is governed by the BLB model, and the flows in Regions II and III are modeled by the BFB model. Let u_j, $1 \le j \le 3$, be the velocity of the assumed fully developed flow in region j. In Region I, the flow is governed by the Brinkman equation, which takes the following form for the configuration at hand:

$$-\frac{dp}{dx} + \mu\frac{d^2u_1}{dY^2} - \frac{\mu}{k_1}u_1 = 0 \tag{2.1}$$

In Regions II and III, the flow is assumed to be one where microscopic inertial effects are important, and hence is governed by

Contributed by the Applied Mechanic Division of ASME for publication in the JOURNAL OF APPLIED MECHANICS. Manuscript received March 8, 2007; final manuscript received March 25, 2008; published online October 23, 2008. Review conducted by Nesreen Ghaddar.

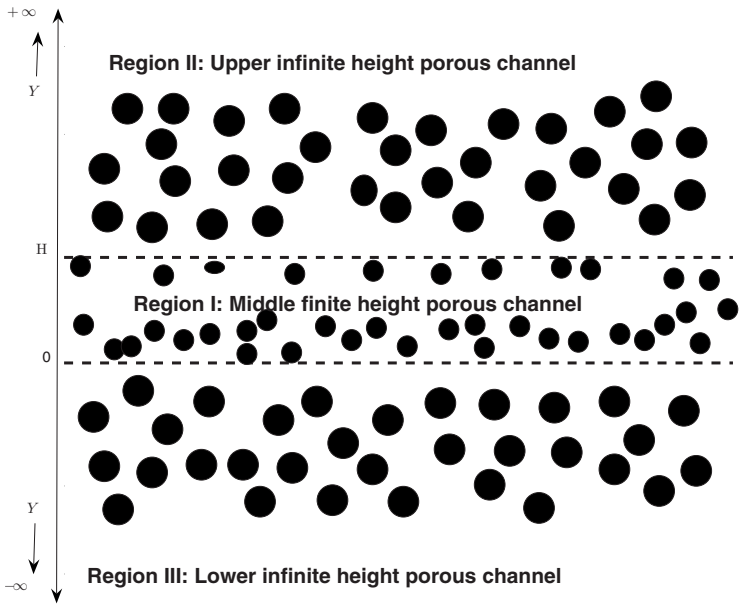

Fig. 1 A schematic of the flow configuration through three porous layers

Forchheimer-type equation, which takes the following form [10].

$$-\frac{dp}{dx}+\mu\frac{d^2u_j}{dY^2}-\frac{\mu}{k_j}u_j-\frac{\rho\delta F\mu}{\sqrt{k_j}}u_j^2=0,\quad j=2,3 \tag{2.2}$$

In Eqs. (2.1) and (2.2), u_j, $j=1,2,3$, are the horizontal velocity components in Regions I, II, and III, respectively, $p(x)$ is the pressure, δ is the medium porosity, ρ is the fluid density, k_j, $j=1,2,3$, are the permeabilities of Regions I, II and III, respectively, μ is the viscosity constant (we assumed here that $\mu_1=\mu_2=\mu_3=\mu$), and F is the drag coefficient [10].

The boundary conditions associated with the flow situation are given the following. At the interface regions ($Y=0$ and $Y=H$), we assume the continuity of the velocity as

$$\begin{aligned} u_1(0^+)&=u_3(0^-)\\ u_1(H^-)&=u_2(H^+)\end{aligned} \tag{2.3}$$

and the continuity of the shear stress as

$$\begin{aligned} \frac{du_1}{dY}(H^-)&=\frac{du_2}{dY}(H^+)\\ \frac{du_1}{dY}(0^+)&=\frac{du_3}{dY}(0^-)\end{aligned} \tag{2.4}$$

For Regions II and III, we assume that as $Y\to\pm\infty$, the flow velocity approaches the main velocity U_∞, i.e.,

$$u_2 \quad \text{and} \quad u_3\to U_\infty \quad \text{as} \quad Y\to\pm\infty \tag{2.5}$$

The problem can be rendered dimensionless with respect to the characteristic length H and the characteristic velocity U_∞. Using the definitions,

$$U_j=\frac{u_j}{U_\infty},\quad y=\frac{Y}{H},\quad \mathrm{Da}_j=\frac{k_j}{H^2},\quad \mathrm{Re}=\frac{U_\infty H\rho}{\mu},\quad \lambda_j=\frac{\mu\delta FH}{\sqrt{k_j}},\quad j=1,2,3 \tag{2.6}$$

where Da_j, $j=1,2,3$ refer to the Darcy numbers of Regions I, II, and III, respectively. Equations (2.1) and (2.2) take the following dimensionless forms:

$$\frac{-H^2}{\mu U_\infty}\frac{dp}{dx}+\frac{d^2U_1}{dy^2}-\frac{U_1}{\mathrm{Da}_1}=0 \tag{2.7}$$

$$\frac{-H^2}{\mu U_\infty}\frac{dp}{dx}+\frac{d^2U_j}{dy^2}-\frac{U_j}{\mathrm{Da}_j}-\mathrm{Re}\,\lambda_jU_j^2=0,\quad j=2,3 \tag{2.8}$$

The boundary conditions given in the system of Eqs. (2.3) and (2.4) and in Eq. (2.5) take, respectively, the following dimensionless form:

$$\begin{aligned} U_1(0^+)&=U_3(0^-)\equiv u_{i3}\\ U_1(1^-)&=U_2(1^+)\equiv u_{i2}\end{aligned} \tag{2.9}$$

$$\begin{aligned} \frac{dU_1}{dy}(1^-)&=\frac{dU_2}{dy}(1^+)\\ \frac{dU_1}{dy}(0^+)&=\frac{dU_3}{dy}(0^-)\end{aligned} \tag{2.10}$$

$$U_2 \quad \text{and} \quad U_3\to 1 \quad \text{as} \quad y\to\pm\infty \tag{2.11}$$

where u_{i2} and u_{i3} are the interface velocities at the upper (Region II) and lower (Region III) interface regions, respectively.

The pressure terms in Eqs. (2.7) and (2.8) can be eliminated by considering the fact that $U_j\to 1$ and $(dU_j/dy)\to 0$, $j=2,3$, as $y\to\pm\infty$. Following Allan and Hamdan [1], we find that outside the momentum boundary layer, Eq. (2.8) becomes

$$\frac{-H^2}{\mu U_\infty}\frac{dp}{dx}=\frac{1}{\mathrm{Da}_j}+\mathrm{Re}\,\lambda_j \tag{2.12}$$

Using Eq. (2.12) in Eqs. (2.7) and (2.8), assuming that the pressure term in the middle Region I satisfies Eq. (2.12) with $j=2$, we have the following ordinary differential equations governing the flow in the three layers. For Region I, Eq. (2.7) becomes

$$\frac{d^2U_1}{dy^2} - \frac{U_1}{\mathrm{Da}_1} = -\frac{1}{\mathrm{Da}_2} - \mathrm{Re}\,\lambda_2 \tag{2.13}$$

and for Regions II and III, Eq. (2.8) becomes

$$\frac{d^2U_j}{dy^2} = \frac{1}{\mathrm{Da}_j}(U_j - 1) + \mathrm{Re}\,\lambda_j(U_j^2 - 1), \quad j = 2,3 \tag{2.14}$$

It is thus required to solve Eqs. (2.13) and (2.14) subject to the continuity of velocities and shear stress at the interface regions at $y=0$ and at $y=1$, and subject to Eq. (2.11).

2.2 Configuration 2. In the second case, we consider the flow in the finite height layer (Region I) to be a free fully developed flow. The other two regions (II and III) are as in Configuration 1. The flow in region I is then governed by the Navier–Stokes equation

$$\mu\frac{d^2u_f}{dY^2} = \frac{dp}{dx} \tag{2.15}$$

where u_f is the fluid velocity (the subscript f stands for free). Equation (2.15) is obtained from Eq. (2.13) by considering $\mathrm{Da}_1 = \infty$ (infinite permeability). The boundary conditions at the interface regions are given by

$$u_f(0^+) = u_3(0^-)$$

$$u_f(H^-) = u_2(H^+)$$

Casting Eq. (2.15) in nondimensional form and using Eq. (2.12) will result in the following equation for the free fluid flow in the middle region (Region I).

$$\frac{d^2U_f}{dy^2} = -\frac{1}{\mathrm{Da}_2} - \mathrm{Re}\,\lambda_2 \tag{2.16}$$

which is associated with the following dimensionless boundary conditions:

$$\begin{aligned} U_f(0^+) &= U_3(0^-) \equiv u_{i3} \\ U_f(1^-) &= U_2(1^+) \equiv u_{i2} \end{aligned} \tag{2.17}$$

Note that the flow equations for Regions II and III are still given by Eq. (2.14) subject to Eq. (2.17) in addition to Eq. (2.11).

3 Derivation of the Exact Solutions

In this section we shall derive the exact solutions to the flow problems in the cases outlines in the previous section.

3.1 Case 1. Consider the configuration presented in the Sec. 2.1. First, it can be easily seen that Eq. (2.13) admits the general solution.

$$U_1(y) = c_1e^{\alpha_1 y} + c_2e^{-\alpha_1 y} + K \tag{3.1}$$

where c_1 and c_2 are arbitrary constants, $\alpha_1 = (1/\sqrt{\mathrm{Da}_1})$, and $K = (\mathrm{Da}_1/\mathrm{Da}_2) + \mathrm{Re}\,\lambda_2\mathrm{Da}_1$.

Using the fact that $U_1(0) = u_{i3}$ and $U_1(1) = u_{i2}$, the velocities at the lower and upper interface regions, respectively, we get the following system of equations for c_1 and c_2:

$$\begin{aligned} c_1 + c_2 &= u_{i3} - K \\ e^{\alpha_1}c_1 + e^{-\alpha_1}c_2 &= u_{i2} - K \end{aligned} \tag{3.2}$$

whose solution is

$$c_1 = \frac{u_{i2} - u_{i3}e^{-\alpha_1} + K(e^{-\alpha_1} - 1)}{e^{\alpha_1} - e^{-\alpha_1}} \tag{3.3}$$

$$c_2 = \frac{-u_{i2} + u_{i3}e^{\alpha_1} - K(e^{\alpha_1} - 1)}{e^{\alpha_1} - e^{-\alpha_1}} \tag{3.4}$$

Substituting Eqs. (3.3) and (3.4) into Eq. (3.1) and simplifying them, we obtain the flow velocity $U_1(y)$ in terms of the interface velocities u_{i2} and u_{i3}.

$$U_1(y) = \frac{u_{i2} - K}{\sinh(\alpha_1)}\sinh(\alpha_1 y) + \frac{u_{i3} - K}{\sinh(\alpha_1)}\sinh(\alpha_1(1-y)) + K \tag{3.5}$$

The interface velocities u_{i2} and u_{i3} will be determined by matching the flow velocities and shear stress at the interfaces $y=0$ and $y=1$.

For Region II (and III), we integrate Eq. (2.14) once we obtain

$$\frac{dU_j}{dy} = \pm (U_j - 1)\sqrt{C_j(U_j + D_j)} \tag{3.6}$$

where

$$C_j = \frac{2\,\mathrm{Re}\,\lambda_j}{3}, \quad D_j = 2 + \frac{3}{2\,\mathrm{Re}\,\lambda_j\mathrm{Da}_j}, \quad j = 2,3$$

Further integrating (3.23) and using the fact that $\lim_{y\to\pm\infty} U_j(y) = 1$, $U_3(0) = u_{i3}$, and $U_2(1) = u_{i2}$, we obtain the following solutions for the velocity in Region j ($j=2$ or 3):

$$U_j(y) = -D_j + (D_j + 1)\left[\frac{1 + z_j(y)}{1 - z_j(y)}\right]^2 \tag{3.7}$$

where

$$z_2(y) = e_2e^{\alpha_2(1-y)} \tag{3.8}$$

$$z_3(y) = e_3e^{\alpha_3 y} \tag{3.9}$$

$$e_2 = \frac{\sqrt{u_{i2} + D_2} - \sqrt{D_2 + 1}}{\sqrt{u_{i2} + D_2} + \sqrt{D_2 + 1}} \tag{3.10}$$

$$e_3 = \frac{\sqrt{u_{i3} + D_3} - \sqrt{D_3 + 1}}{\sqrt{u_{i3} + D_3} + \sqrt{D_3 + 1}} \tag{3.11}$$

$$\alpha_j = \sqrt{C_j(D_j + 1)}, \quad j = 2,3 \tag{3.12}$$

Now, matching the velocities and shear stress at $y=0$ and $y=1$ leads to the following nonlinear system for the interface velocities u_{i2} (at $y=1$) and u_{i3} (at $y=0$).

$$\begin{aligned} &\sqrt{C_3\mathrm{Da}_1}\sinh(\alpha_1)(u_{i3} - 1)\sqrt{u_{i3} + D_3} \\ &\quad = u_{i2} - \cosh(\alpha_1)u_{i3} - K(1 - \cosh(\alpha_1)) \\ &\sqrt{C_2\mathrm{Da}_1}\sinh(\alpha_1)(u_{i2} - 1)\sqrt{u_{i2} + D_2} \\ &\quad = -\cosh(\alpha_1)u_{i2} + u_{i3} - K(1 - \cosh(\alpha_1)) \end{aligned} \tag{3.13}$$

Thus by solving simultaneously the system of the two nonlinear equations given by Eq. (3.13), one can find the velocities at the interface regions. The velocity distribution in the porous regions is given by Eq. (3.5) for Region I and Eqs. (3.7)–(3.9) for Regions II and III.

3.2 Case 2. Consider the second configuration where the flow model for Region I is given by Eq. (2.16).

$$\frac{d^2U_f}{dy^2} = -\frac{1}{\mathrm{Da}_2} - \mathrm{Re}\,\lambda_2 \tag{3.14}$$

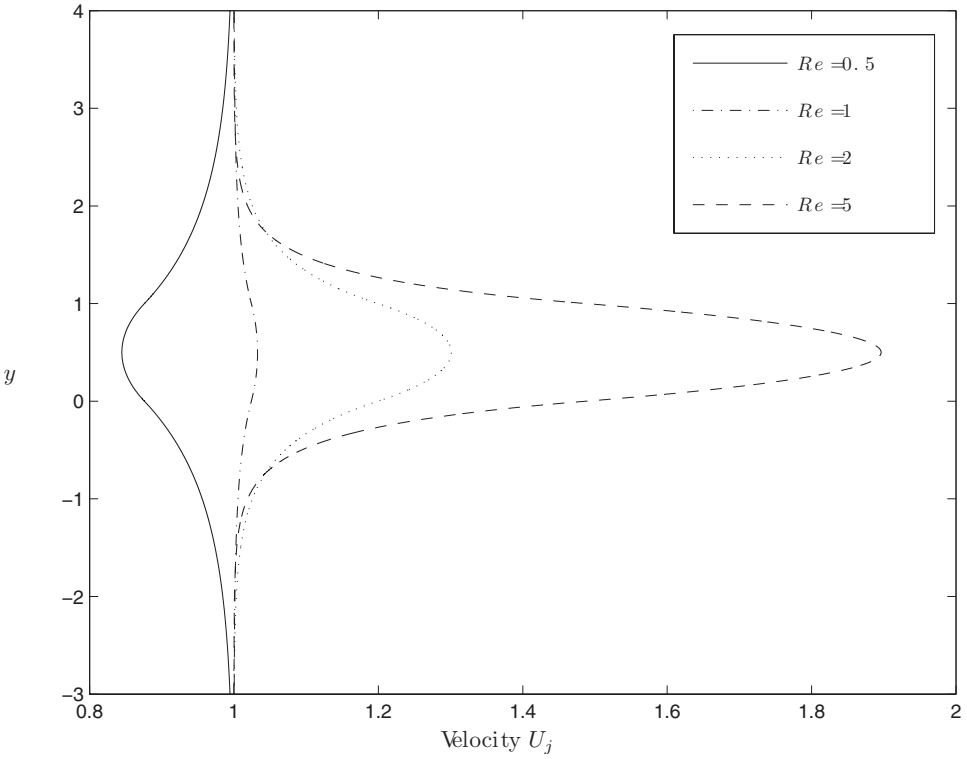

Fig. 2 Velocity profile for Configuration 1 with $Da_1=1$, $Da_2=Da_3=10$. and $Re=0.5,1,2,5$

where the subscript f stands for "free" flow, and the flow model for Regions II and III are the same as in Case 1, i.e., given by Eq. (2.14) whose exact solution is given by Eq. (3.7).

The exact solution of Eq. (3.14), in terms of $u_{i3} \equiv U_f(0)$ and $u_{i2} \equiv U_f(1)$, is given by

$$U_f(y) = -\frac{1}{2}\left(\frac{1}{\mathrm{Da}_2} + \mathrm{Re}\,\lambda_2\right)y^2 + \left[u_{i2} - u_{i3} + \frac{1}{2}\left(\frac{1}{\mathrm{Da}_2} + \mathrm{Re}\,\lambda_2\right)\right]y + u_{i3} \tag{3.15}$$

Matching the interface velocities ($U_f(0)=U_3(0)$ and $U_f(1)=U_2(1)$) and the shear stress ($U_f'(0)=U_3'(0)$ and $U_f'(1)=U_2'(1)$), we obtain the following nonlinear system of equations defining the interface velocities:

$$\sqrt{C_3}(u_{i3}-1)\sqrt{u_{i3}+D_3} = u_{i2} - u_{i3} + \frac{1}{2}\left(\frac{1}{\mathrm{Da}_2} + \mathrm{Re}\,\lambda_2\right)$$

$$\sqrt{C_2}(u_{i2}-1)\sqrt{u_{i2}+D_2} = -u_{i2} + u_{i3} + \frac{1}{2}\left(\frac{1}{\mathrm{Da}_2} + \mathrm{Re}\,\lambda_2\right) \tag{3.16}$$

where the various constants are as defined in the previous sections.

4 Results and Discussions

The velocity distribution in the three regions and at the interface is influenced by the so called inertia parameter Re λ, Reynolds number Re, and the Darcy numbers Da_j, $j=1,2,3$. The effect of these parameters on the velocities for the two cases are presented in Figs. 2–7.

In the first configuration, we first assume fix the Darcy numbers and vary the Reynolds number Re. Precisely, we set $\mathrm{Da}_1=1$ and $\mathrm{Da}_2=\mathrm{Da}_3=10$ and vary $\mathrm{Re}=0.5,1,2,5$. The results are shown on Fig. 2. It is clear from this figure that as Reλ increases, the velocity increases. However, the flow is perfectly symmetric about the middle region (this is expected as $\mathrm{Da}_2=\mathrm{Da}_3$), and as a result the velocities at both interface regions are the same.

In the second case of Configuration 1, we fix the Reynolds number $\mathrm{Re}=10$, $\mathrm{Da}_2=\mathrm{Da}_3=10$, and varied $\mathrm{Da}_1=0.001,0.01,0.5,1$. The velocity profile is shown in Fig. 3, where it is clear that the flow is still symmetric about the middle region and the velocity increases with increased Da_1, as expected. The interface region velocities still have the same values because $\mathrm{Da}_2=\mathrm{Da}_3$. Notice that as Da_1 tends to zero the flow velocity in the middle region tends to zero as well.

As a third case of Configuration 1, we fix $\mathrm{Re}=10$ and $\mathrm{Da}_1=10$ and consider $\mathrm{Da}_2 \neq \mathrm{Da}_3$. We chose $\mathrm{Da}_2=0.1\mathrm{Da}_3$. The effect of changing the values of Da_3 on the flow field and on the interface velocities, in particular, is shown in Fig. 4. The flow in this case is no longer symmetric, and therefore the values of the velocities at the interface are not the same. The nonsymmetry is more visible as the difference between Da_2 and Da_3 get larger. It can be seen that the interface velocity at the lower region is larger since the Darcy number Da_3 is larger than Da_2. It is also shown that as $y \to \pm\infty$, $U_2, U_3 \to 1$ very rapidly.

To investigate the effect of the difference between Da_3 and Da_2 on the relative values of the interface velocities, we plotted in Fig. 5 the ratio of the interface velocities u_{i3}/u_{i2} versus the ratio of the Darcy numbers $\mathrm{Da}_3/\mathrm{Da}_2$ for fixed Reynolds number $\mathrm{Re}=10$ and $\mathrm{Da}_1=10$. It can be seen that the relationship is not linear. From Fig. 5, we see that even if Da_3 is 100 times bigger than Da_2, u_{i3} is not even twice u_{i2}.

For the second configuration, two cases are investigated: the effect of the Reynolds number Re and the effect of different Darcy numbers at the lower and upper regions. For the first case, we fixed $\mathrm{Da}_2=\mathrm{Da}_3=10$ and varied $\mathrm{Re}=0.5$, 1, 2, and 5. The flow velocity profile is shown in Fig. 6. This figure shows that the flow is also symmetric as in Configuration 1, but the flow is faster (as expected) since $\mathrm{Da}_1=\infty$. In the second case, we fixed $\mathrm{Re}=10$, $\mathrm{Da}_2=10$, and varied $\mathrm{Da}_3=1,10,100,1000$. The results of this case

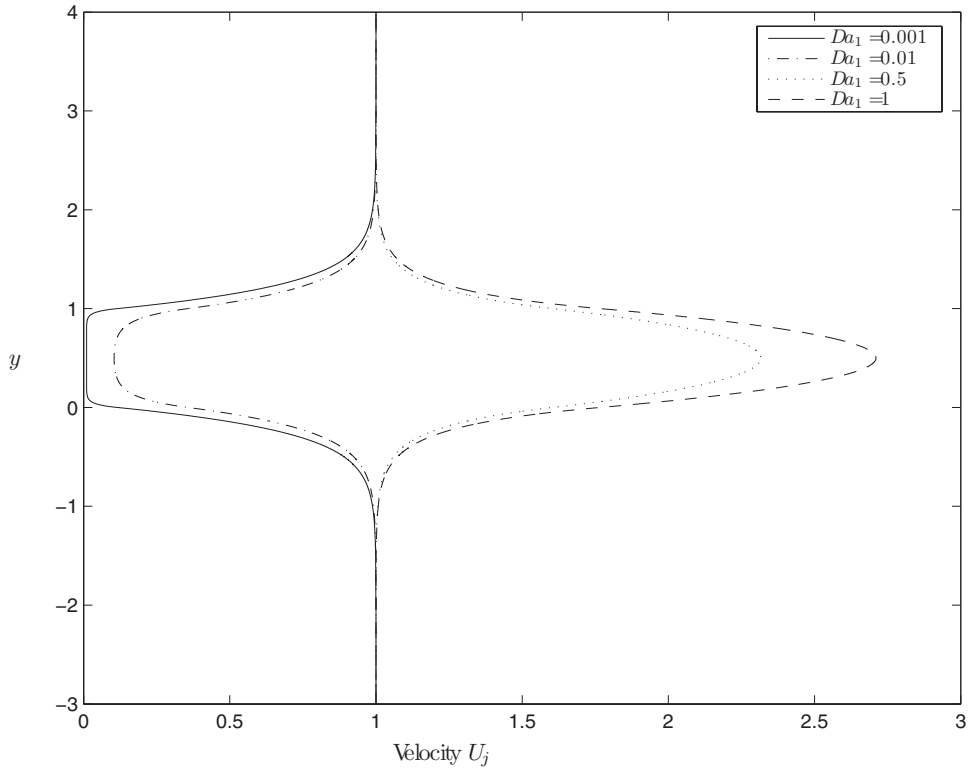

Fig. 3 Velocity profile for Configuration 1 with $Da_2=Da_3=10$, $Re=10$, and $Da_1=0.001, 0.01, 0.5, 1$

are exactly the same as in Configuration 1, as shown in Fig. 7, which again shows that the flow is not symmetric about the middle region and the interface velocities are not the same. This indicated that having a porous-free channel in the middle of the two infinite porous channels does not affect the flow in a sensible way.

5 Conclusion

In this paper we have presented a mathematical model for the fluid flow through three porous layers. Matching conditions at the interface regions, which is consistent with the physical conditions, are presented. Basically, these conditions depend on the continuity

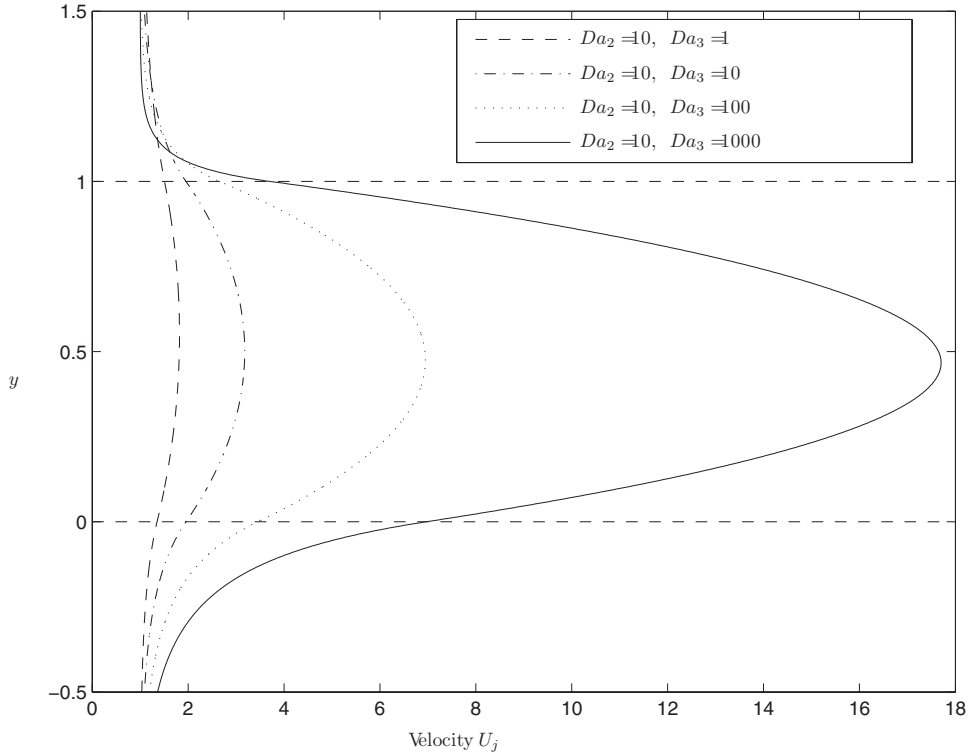

Fig. 4 Velocity profile for Configuration 1 with $Re=10$, $Da_1=10$, $Da_2=10$, and $Da_3=1, 10, 100, 1000$

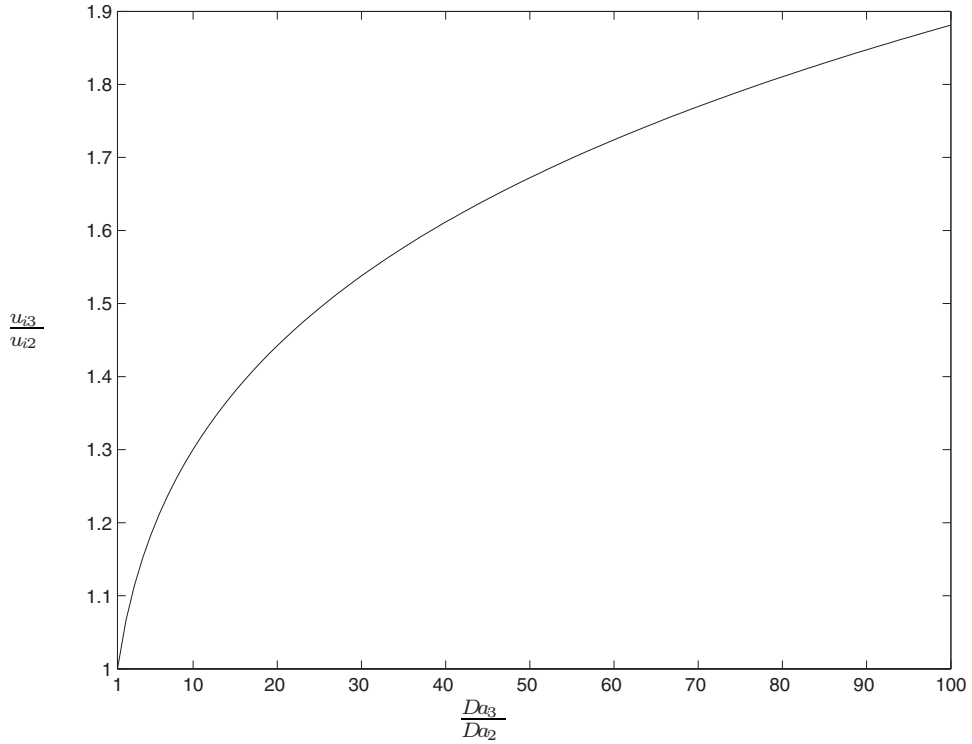

Fig. 5 A plot of (u_{i3}/u_{i2}) versus (Da_3/Da_2) for Configuration 1 with Re=10, $Da_1=10$, $Da_2=10$, and $Da_3=10i$, $i=1,2,\ldots,100$

of the velocity distribution and the continuity of the shear stress. In the two configurations considered, exact solutions were obtained. The exact solutions obtained consist of exponentials for the first configuration and exponentials and polynomials for the second configuration. It was interestingly found that the interface velocities did not differ by much as the Darcy numbers of the upper and lower regions differ greatly. The effect of the Reynolds number was observed to increase the flow velocity in the middle

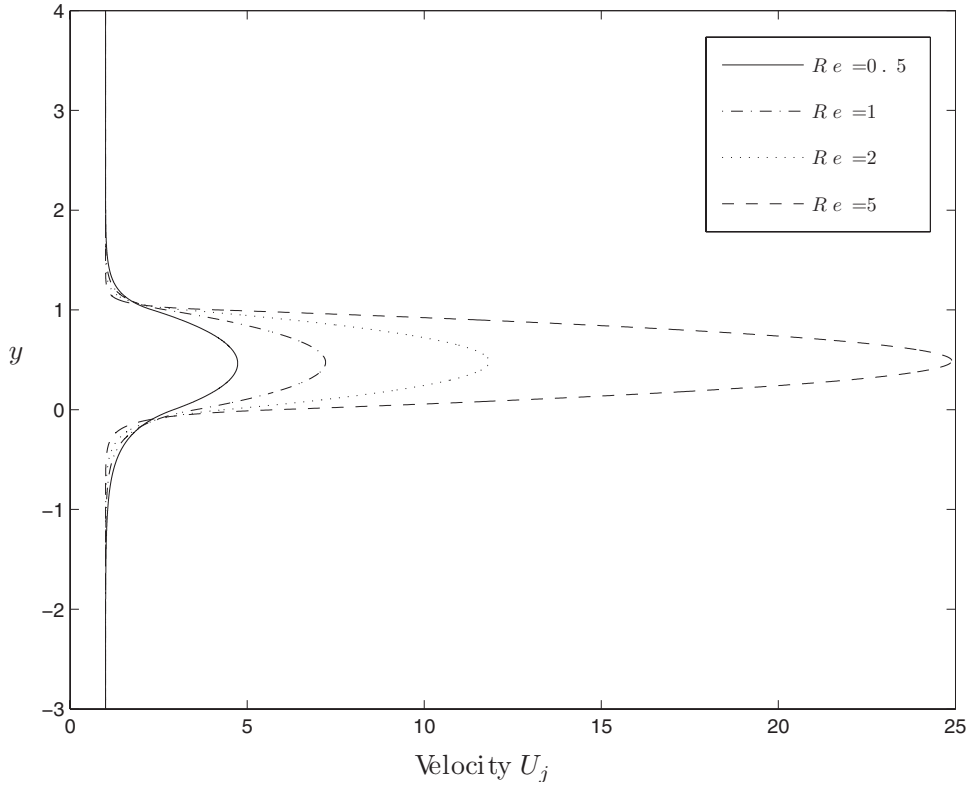

Fig. 6 Velocity profile for Configuration 2 with $Da_2=Da_3=10$, and Re=0.5,1,2,5

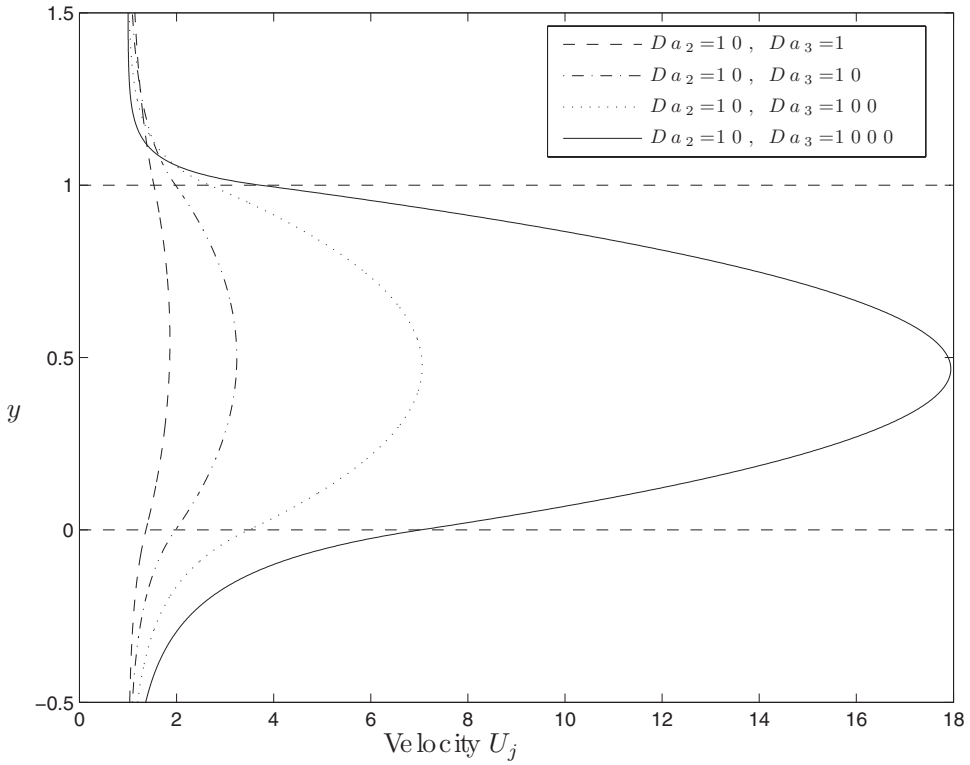

Fig. 7 Velocity profile for Configuration 2 with Re=10, Da_2=10, and Da_3=1,10,100,1000

region. It was also observed that when the middle region is assumed to be porous-free, the velocity profile did not differ from the first configuration.

References

[1] Allan, F. M., and Hamdan, M. H., 2002, "Fluid Mechanics of the Interface Region Between Two Porous Layers," Appl. Math. Comput., **128**(1), pp. 37–43.

[2] Beavers, G. S., and Joseph, D. D., 1967, "Boundary Conditions at a Naturally Permeable Wall," J. Fluid Mech., **30**(1), pp. 197–207.

[3] Ford, R. A., and Hamdan, M. H., 1998, "Coupled Parallel Flow Through Composite Porous Layers," Appl. Math. Comput., **97**, pp. 261–271.

[4] Harr, M., 1962, *Groundwater and Seepage*, McGraw-Hill, New York.

[5] Polubarinova-Kochina, P. Y., 1960, *Theory of Groundwater Movement*, Princeton University Press, Princeton, NJ.

[6] Vafai, K., and Kim, S. J., 1990, "Fluid Mechanics of the Interface Region Between a Porous Medium and a Fluid Layer: An Exact Solution," Int. J. Heat Fluid Flow, **11**(3), pp. 254–256.

[7] Chandrasekhara, B. C., Rajani, K., and Rudraiah, N., 1987, "Effect of Slip on Porous-Wall Squeeze Films in the Presence of a Magnetic Field," Appl. Sci. Res., **34**, pp. 393–411.

[8] Schlichting, H., 1979, *Boundary Layer Theory*, McGraw-Hill, New York.

[9] Vafai, K., and Thiyagaja, R., 1987, "Analysis of Flow and Heat Transfer at the Interface Region of a Porous Medium," Int. J. Heat Mass Transfer, **30**, pp. 1391–1405.

[10] Awartani, M. M., and Hamdan, M. H., 2005, "Fully Developed Flow Through a Porous Channel Bounded by Flat Plates," Appl. Math. Comput., **169**, pp. 749–757.

[11] Beavers, G. S., Sparrow, E. M., and Masha, B. A., 1974, "Experiments of Coupled Parallel Flows in a Channel and a Bounding Porous Medium," AIChE J., **20**, pp. 596–597.

[12] Rudraiah, N., 1986, "Flow Past Porous Layers and Their Stability," *Encyclopedia of Fluid Mechanics: Slurry Flow Technology*, Gulf Publishing Company, Houston, TX, Chap. 14, p. 568.

Thermodynamics of Infinitesimally Constrained Equilibrium States

Q. Yang[1]
e-mail: yangq@tsinghua.edu.cn

L. J. Xue

Y. R. Liu

State Key Laboratory of Hydroscience and Engineering,
Tsinghua University,
Beijing 100084, P. R. China

*This paper is concerned with infinitesimally constrained equilibrium states, which are nonequilibrium states and infinitesimally close to equilibrium states. The corresponding thermodynamics is established in this paper within the thermodynamic framework of Rice (1971, "Inelastic Constitutive Relations for Solids: An Internal Variable Theory and Its Application to Metal Plasticity," J. Mech. Phys. Solids, **19**, pp. 433–455). It is shown that the thermodynamics of infinitesimally constrained equilibrium states belongs to linear irreversible thermodynamics. The coefficient matrix is the Hessian matrix of the flow potential function at the equilibrium state. The process of a state change induced by an infinitesimal stress increment in time-independent plasticity can be viewed as a sequence of infinitesimally constrained equilibrium states. The thermodynamic counterpart of yield functions are flow potential functions, and their convexity is required by intrinsic dissipation inequality. Drucker and Il'yushin's inequalities are not essential thermodynamic requirements.*
[DOI: 10.1115/1.2998484]

Keywords: thermodynamics, internal variables, equilibrium states, Drucker's inequality, plasticity

1 Introduction

The concept of constrained equilibrium states is essential to irreversible thermodynamics with internal variables for solids (see, e.g., Ref. [1]). This approach views the inelastic deformation of a given material sample of the type considered under macroscopically homogeneous stress or strain and temperature as a sequence of *constrained equilibrium states*: The state of the material sample at any given time in the deformation history can be fully characterized by the corresponding values of stress or strain and temperature and a collection of internal variables that represent the extent of microstructural rearrangement within the sample. In other words, constrained equilibrium states are nonequilibrium states, which can be fully characterized by state variables including internal variables. Thus, the thermostatic equation for the variation in equilibrium states can be extended to deal with the variation in constrained equilibrium states (see, e.g., Eq. (2)). Furthermore, the thermostatic equation is generalized as the thermodynamic equation by recasting the variational equation as rate equation or by replacing δ with d/dt (see, e.g., Eq. (11)).

Thermostatics is based on the assumption that the system under study is always at or sufficiently close to an equilibrium state that the thermodynamic potential functions (internal energy, free energy, etc.) can be defined as functions of the state variables, which are independent of the time and independent of the history of the system. Thus, the generalization implies an extrapolation from infinitely slow processes to processes that proceed with arbitrary rates and for arbitrary departures from the equilibrium states. Needless to say, this process of extrapolation has been a point of considerable controversy in deciding the applicability of nonequilibrium thermodynamic results, as remarked by Edelen [2].

This paper is concerned with the thermodynamics of infinitesimally constrained equilibrium states. The constrained equilibrium states whose state variables are located in the infinitesimal neighborhood of the state variables of an equilibrium state are termed the *infinitesimally constrained equilibrium states* associated with the equilibrium state in this paper. Thermodynamic theory with internal variables in Ref. [1] are briefed in Sec. 2. Various nonlinear kinetic rate laws of internal variables including Refs. [1,3,4] are addressed in Sec. 3. The thermodynamics of infinitesimally constrained equilibrium states is established in the thermodynamic framework in Ref. [1] in Sec. 4. It is shown that *the second-order variation of the entropy production function plays a dominant role for infinitesimally constrained equilibrium states*.

Basically, the time-independent plasticity is a formalism to deal with a state change in loading induced by an infinitesimal stress or strain increment for a material sample. The initial and final states of the infinitesimal state change are two equilibrium states with the stress state on the current yield surface. Since the initial and final states are equilibrium states and the disturbance is infinitesimal, it is reasonable to assume the process of the state change to be a sequence of infinitesimally constrained equilibrium states. In Sec. 5, some classic plastic restrictions on the state change, e.g., Drucker's inequality, are addressed from the viewpoint of infinitesimally constrained equilibrium states. It should be noted that the thermodynamic basis of time-independent plasticity has been addressed by many authors (see, e.g., Refs. [1,5,4,6–14]). *It is shown that Drucker and Il'yushin's inequalities are not essential thermodynamic requirements. However, the convexity of yield surfaces is required by intrinsic dissipation inequality.*

2 Thermodynamics of Constrained Equilibrium States

The irreversible thermodynamic theory by Rice [1] is a discrete internal-variable theory for finite deformation of solids. This approach views inelastic deformation of a given material sample of the type considered under macroscopically homogeneous stress or strain and temperature as a sequence of constrained equilibrium states: The state of the material sample at any given time in the deformation history can be fully characterized by the corresponding values of stress or strain and temperature and a collection of internal variables that represent the extent of microstructural rearrangement within the sample.

Consider a material sample of size V, which is measured in an unloaded reference state and at a reference temperature ϑ_0. Thus, $\boldsymbol{\sigma}$ or $\boldsymbol{\varepsilon}$ and ϑ, together with $\boldsymbol{\xi}$, are the thermodynamic state variables. ϑ denotes temperature, $\boldsymbol{\varepsilon}$ denotes any strain tensor, objective, and symmetric, which measures deformation from an arbitrary reference state, $\boldsymbol{\sigma}$ denotes the symmetric conjugate stress such that $\boldsymbol{\sigma}:d\boldsymbol{\varepsilon}$ is the work per unit volume of the adopted reference state in any virtual deformation $d\boldsymbol{\varepsilon}$, and $\boldsymbol{\xi}$ denotes a set of scalar internal variables $\boldsymbol{\xi}=\{\xi_1,\xi_2\ldots,\xi_n\}$, which characterizes the specific local rearrangements at sites throughout the material sample. Introduce the specific free energy ϕ and its Legendre transform ψ with respect to strain.

$$\phi=\phi(\boldsymbol{\varepsilon},\vartheta,\boldsymbol{\xi}),\quad \psi=\psi(\boldsymbol{\sigma},\vartheta,\boldsymbol{\xi})=\boldsymbol{\varepsilon}:\frac{\partial\phi}{\partial\boldsymbol{\varepsilon}}-\phi \tag{1}$$

Neighboring constrained equilibrium states corresponding to different sets of internal variables are related by

[1]Corresponding author.

Contributed by the Applied Mechanics Division of ASME for publication in the JOURNAL OF APPLIED MECHANICS. Manuscript received July 2, 2007; final manuscript received September 15, 2008; published online October 23, 2008. Review conducted by Zhigang Suo.

$$\boldsymbol{\varepsilon}:\delta\boldsymbol{\sigma}+\frac{1}{V}\mathbf{f}\cdot\delta\boldsymbol{\xi}+\eta\delta\vartheta=\delta\psi \tag{2}$$

where η denotes the specific entropy, and $\mathbf{f}=\{f_1,f_2,\cdots,f_n\}$ denotes the thermodynamic forces conjugate to the internal variables $\boldsymbol{\xi}$ and[1]

$$\mathbf{f}\cdot\delta\boldsymbol{\xi}=f_\alpha\delta\xi_\alpha \tag{3}$$

Eqs. (2) and (1) lead to the following stress-strain relations.

$$\boldsymbol{\sigma}=\frac{\partial\phi(\boldsymbol{\varepsilon},\vartheta,\boldsymbol{\xi})}{\partial\boldsymbol{\varepsilon}} \tag{4a}$$

$$\boldsymbol{\varepsilon}=\frac{\partial\psi(\boldsymbol{\sigma},\vartheta,\boldsymbol{\xi})}{\partial\boldsymbol{\sigma}} \tag{4b}$$

$$\eta=\frac{\partial\psi}{\partial\vartheta} \tag{4c}$$

and the following thermodynamic conjugate forces:

$$f_\alpha=V\frac{\partial\psi}{\partial\xi_\alpha}=-V\frac{\partial\phi}{\partial\xi_\alpha},\quad \mathbf{f}=\mathbf{f}(\boldsymbol{\sigma},\vartheta,\boldsymbol{\xi})\quad\text{or}\quad\mathbf{f}=\mathbf{f}(\boldsymbol{\varepsilon},\vartheta,\boldsymbol{\xi}) \tag{5}$$

Based on Eq. (4*b*), a strain increment is

$$d\boldsymbol{\varepsilon}=\frac{\partial^2\psi}{\partial\boldsymbol{\sigma}^2}:d\boldsymbol{\sigma}+\frac{\partial^2\psi}{\partial\boldsymbol{\sigma}\,\partial\vartheta}d\vartheta+d^p\boldsymbol{\varepsilon} \tag{6}$$

where the inelastic part of the strain increment is

$$d^p\boldsymbol{\varepsilon}=d^p\boldsymbol{\varepsilon}(\boldsymbol{\sigma},\vartheta,\boldsymbol{\xi})=\frac{\partial^2\psi}{\partial\boldsymbol{\sigma}\,\partial\boldsymbol{\xi}}\cdot d\boldsymbol{\xi}=\frac{1}{V}\frac{\partial\mathbf{f}}{\partial\boldsymbol{\sigma}}\cdot d\boldsymbol{\xi}=\frac{1}{V}\frac{\partial f_\alpha}{\partial\boldsymbol{\sigma}}d\xi_\alpha \tag{7}$$

Multiplying Eq. (7) by $d\boldsymbol{\sigma}$, one obtains

$$d\boldsymbol{\sigma}:d^p\boldsymbol{\varepsilon}=\frac{1}{V}df_\alpha d\xi_\alpha \tag{8}$$

Similarly, we have

$$d^p\boldsymbol{\sigma}=d^p\boldsymbol{\sigma}(\boldsymbol{\varepsilon},\vartheta,\boldsymbol{\xi})=-\frac{\partial^2\phi}{\partial\boldsymbol{\varepsilon}\,\partial\boldsymbol{\xi}}\cdot d\boldsymbol{\xi}=\frac{1}{V}\frac{\partial\mathbf{f}}{\partial\boldsymbol{\varepsilon}}\cdot d\boldsymbol{\xi}=\frac{1}{V}\frac{\partial f_\alpha}{\partial\boldsymbol{\varepsilon}}d\xi_\alpha \tag{9}$$

and

$$d\boldsymbol{\varepsilon}:d^p\boldsymbol{\sigma}=\frac{1}{V}df_\alpha d\xi_\alpha \tag{10}$$

Note that df_α is induced by $d\varepsilon$ in Eq. (10), but df_α is induced by $d\boldsymbol{\sigma}$ in Eq. (8) (see also Ref. [15]).

Nonequilibrium thermodynamics extended the thermostatic relation (2) to dynamics processes with δ replaced by d/dt where t denotes time, i.e.,

$$\boldsymbol{\varepsilon}:\dot{\boldsymbol{\sigma}}+\frac{1}{V}\mathbf{f}\cdot\dot{\boldsymbol{\xi}}+\eta\dot{\vartheta}=\dot{\psi} \tag{11}$$

The rate equation (11) is concerned with a specific constrained equilibrium state unlike the variational equation (2) dealing with the neighboring constrained equilibrium states.

It is required by the second law of thermodynamics that the entropy production function should be always non-negative.

$$\sigma=\frac{1}{\vartheta V}f_\alpha\dot{\xi}_\alpha=\frac{1}{\vartheta V}\mathbf{f}\cdot\dot{\boldsymbol{\xi}}\geq 0 \tag{12}$$

The intrinsic dissipation inequality determines the irreversibility of the thermodynamic processes.

[1]In this paper, Einstein's summation convention is adopted for repeated indices. However, if an index range is listed like α in Eq. (15), the index is considered as a free index without the summation convention.

3 Kinetic Rate Laws of Internal Variables

The thermodynamic fluxes $\dot{\boldsymbol{\xi}}$ are state functions as their conjugate forces $\mathbf{f}$ given by Eq. (5)

$$\dot{\boldsymbol{\xi}}=\dot{\boldsymbol{\xi}}(\boldsymbol{\sigma},\vartheta,\boldsymbol{\xi}) \tag{13}$$

It is usually assumed that thermodynamic fluxes are only driven by their conjugate forces. Thus, the following kinetic rate laws of the internal variables are postulated.

$$\dot{\boldsymbol{\xi}}=\dot{\boldsymbol{\xi}}(\mathbf{f},\vartheta,\boldsymbol{\xi}) \tag{14}$$

or

$$\dot{\xi}_\alpha=\dot{\xi}_\alpha(\mathbf{f},\vartheta,\boldsymbol{\xi}),\quad(\alpha=1,2,\ldots,n) \tag{15}$$

The conjugate force $\mathbf{f}$ space is a n-dimensional Euclidean space $\mathbb{R}^n$. The gradient of the thermodynamic fluxes $\dot{\boldsymbol{\xi}}$ in $\mathbf{f}$ space is denoted by

$$\mathbf{G}(\dot{\boldsymbol{\xi}},\mathbf{f})=\nabla_{\mathbf{f}}\dot{\boldsymbol{\xi}}=\frac{\partial\dot{\xi}_\alpha}{\partial f_\beta}=G_{\alpha\beta} \tag{16}$$

The kinetic rate laws should satisfy the following conditions:

$$\mathbf{f}\cdot\dot{\boldsymbol{\xi}}(\mathbf{f},\vartheta,\boldsymbol{\xi})\geq 0,\quad\forall\,\mathbf{f}\in\mathbb{R}^n \tag{17}$$

Thermodynamic fluxes and forces vanish at equilibrium states. Thus, equilibrium states are determined by $\mathbf{f}=0$. In order to describe equilibrium states, it is required that

$$\dot{\boldsymbol{\xi}}(0,\vartheta,\boldsymbol{\xi})=0 \tag{18}$$

If the gradient matrix is symmetric, i.e., $G_{\alpha\beta}=G_{\beta\alpha}$, or

$$\frac{\partial\dot{\xi}_\alpha}{\partial f_\beta}=\frac{\partial\dot{\xi}_\beta}{\partial f_\alpha},\quad(\alpha,\beta=1,2,\ldots,n) \tag{19}$$

the symmetric condition ensures $\dot{\xi}_\alpha df_\alpha$ to be a total differential at fixed ϑ and $\boldsymbol{\xi}$. Then a flow potential function Q as a state function exists

$$Q=Q(\mathbf{f},\vartheta,\boldsymbol{\xi})=\frac{1}{V}\int_0^{\mathbf{f}}\dot{\boldsymbol{\xi}}\cdot d\mathbf{f}=\frac{1}{V}\int_0^{\mathbf{f}}\dot{\xi}_\alpha df_\alpha \tag{20}$$

where the integration is carried out at a fixed ϑ and $\boldsymbol{\xi}$. The flow potential function is a primary function. The kinetic rate laws can be derived from the following function:

$$\dot{\boldsymbol{\xi}}=V\frac{\partial Q}{\partial\mathbf{f}}\quad\text{or}\quad\dot{\xi}_\alpha=V\frac{\partial Q}{\partial f_\alpha} \tag{21}$$

The inelastic strain rate is obtained based on Eqs. (7) and (20).

$$\frac{\mathrm{d}^p\boldsymbol{\varepsilon}}{dt}=\frac{1}{V}\frac{\partial f_\alpha}{\partial\boldsymbol{\sigma}}\dot{\xi}_\alpha=\frac{\partial Q}{\partial\boldsymbol{\sigma}} \tag{22}$$

The entropy production function is

$$\sigma=\frac{1}{\vartheta}\mathbf{f}\cdot\frac{\partial Q}{\partial\mathbf{f}}=\frac{1}{\vartheta}f_\alpha\frac{\partial Q}{\partial f_\alpha}\geq 0 \tag{23}$$

It is shown in Eq. (23) that the flow potential Q is a monotonic increasing function along any ray originated from $\mathbf{f}=\mathbf{0}$. Note that $Q=0$ at $\mathbf{f}=\mathbf{0}$ due to Eq. (20). Therefore, the flow potential Q should be always non-negative. The Hessian matrix of the flow potential Q in $\mathbf{f}$ is denoted by

$$\mathbf{H}(Q,\mathbf{f})=\frac{\partial^2Q}{\partial\mathbf{f}^2}=H_{\alpha_\beta}=\frac{\partial^2Q}{\partial f_\alpha\,\partial f_\beta} \tag{24}$$

which is symmetric following its definition, i.e., $H_{\alpha\beta}=H_{\beta\alpha}$ or $\mathbf{H}=\mathbf{H}^T$. In view of Eqs. (16) and (21), the following relation is obvious:

$$\mathbf{G}(\dot{\boldsymbol{\xi}},\mathbf{f}) = \mathbf{H}(Q,\mathbf{f}) \quad \text{or} \quad G_{\alpha\beta} = H_{\alpha\beta} \tag{25}$$

The symmetric condition (19) is the so-called "nonlinear Onsager reciprocal relations" in Ref. [3]. Some equivalent expressions of the nonlinear Onsager reciprocal relations (19) are given as follows. Evidently, the nonlinear Onsager reciprocal relations (19) are equivalent to the following condition at every point in the vector field:

$$\nabla_{\mathbf{f}} \times \dot{\boldsymbol{\xi}} = \mathbf{0} \tag{26}$$

where $\nabla_{\mathbf{f}}\times$ denote the curl operator in $\mathbf{f}$ space. Therefore, from a fluid point of view, the Onsager fluxes $\dot{\boldsymbol{\xi}}$ represent an irrotational or potential flow in its affinity space. The irrotational condition (26) can be reformulated into an equivalent integral form based on Stokes' theorem.

$$\oint \dot{\boldsymbol{\xi}} \cdot d\mathbf{f} = \oint \dot{\xi}_\alpha df_\alpha = 0 \tag{27}$$

at a fixed ϑ and $\boldsymbol{\xi}$ and for any oriented simple closed curve in $\mathbf{f}$ space.

Thermodynamic fluxes $\dot{\boldsymbol{\xi}}$ satisfying the nonlinear Onsager reciprocal relations are termed the "Onsager fluxes" in Ref. [2]. If the kinetic rate laws (15) give a linear relation, i.e., $\dot{\xi}_\alpha = L_{\alpha\beta} f_\beta$, the well-established reciprocal relations of Onsager [16,17] $L_{\alpha\beta} = L_{\beta\alpha}$ is reproduced from the nonlinear Onsager reciprocal relations (19).

Rice [1] proposed the following class of kinetic rate laws: At any given temperature and pattern of internal rearrangement within the material sample, the rate at which any specific structural rearrangement occurs is fully determined by the thermodynamic force associated with that rearrangement. That is,

$$\dot{\xi}_\alpha = \dot{\xi}_\alpha(f_\alpha, \vartheta, \boldsymbol{\xi}), \quad (\alpha = 1,2,\ldots,n) \tag{28}$$

The thermodynamic fluxes satisfying Eq. (28) are termed the *Rice fluxes* in this paper. Evidently, the gradient matrix and Hessian matrix for the Rice fluxes are diagonal ones. The Onsager fluxes embody the Rice fluxes as a special case since the nonlinear Onsager reciprocal relations are fulfilled automatically for the Rice fluxes.

Ziegler [4] proposed that the entropy production function can also be used as a potential function to determine the kinetic rate laws

$$\dot{\boldsymbol{\xi}} = V\lambda \frac{\partial(\vartheta\sigma)}{\partial \mathbf{f}} \tag{29}$$

which is the well-known "orthogonality condition." Evidently, the Ziegler fluxes given by Eq. (29) also belong to the Onsager fluxes. Substituting Eq. (12) into Eq. (29), the homogeneity of the kinetic rate laws is required by the orthogonality condition.

$$\frac{\partial \dot{\xi}_\alpha}{\partial f_\beta} f_\beta = q\dot{\xi}_\alpha, \quad q = \frac{1}{\lambda} - 1 \tag{30}$$

The homogeneity (30) leads to the nonlinear phenomenological equations

$$\dot{\xi}_\alpha = L_{\alpha\beta} f_\beta, \quad L_{\alpha\beta} = \frac{1}{q} H_{\alpha\beta} \tag{31}$$

and the linear relation $\vartheta\sigma = (q+1)Q$ (see Refs. [18,19]).

4 Thermodynamics of Infinitesimally Constrained Equilibrium States

In this paper, the values of the state variables and functions at equilibrium states are denoted by the subscript "0." Consider a typical equilibrium state for a given material sample. The state variables of the equilibrium state are $(\boldsymbol{\sigma}_0, \vartheta_0, \boldsymbol{\xi}_0)$. The thermodynamic fluxes and forces vanish at the equilibrium state, i.e.,

$$\dot{\boldsymbol{\xi}}_0 = \dot{\boldsymbol{\xi}}(\boldsymbol{\sigma}_0, \vartheta_0, \boldsymbol{\xi}_0) = \mathbf{0}, \quad \mathbf{f}_0 = \mathbf{f}(\boldsymbol{\sigma}_0, \vartheta_0, \boldsymbol{\xi}_0) = \mathbf{0} \tag{32}$$

Similarly, we can define other state functions at the equilibrium state, e.g., the entropy production function σ_0, the flow potential function Q_0, the gradient matrix $\mathbf{G}_0$, the Hessian matrix $\mathbf{H}_0$, etc. The constrained equilibrium states in the infinitesimal neighborhood of the equilibrium state are termed *infinitesimally constrained equilibrium states* associated with the equilibrium state in this paper. In other words, infinitesimally constrained equilibrium states are characterized by the state variables $(\boldsymbol{\sigma}_0 + \delta\boldsymbol{\sigma}, \vartheta_0 + \delta\vartheta, \boldsymbol{\xi}_0 + \delta\boldsymbol{\xi})$. It is shown by Eqs. (5) and (32) that a thermodynamic equilibrium point $(\boldsymbol{\sigma}_0, \vartheta_0, \boldsymbol{\xi}_0)$ is the stationary point of the specific free and complementary energies ϕ and ψ with respect to the internal variables $\boldsymbol{\xi}$.

With the expansion at the equilibrium state, the thermodynamic fluxes and forces of infinitesimally constrained equilibrium states are infinitesimal.

$$\dot{\boldsymbol{\xi}} = \dot{\boldsymbol{\xi}}_0 + \delta\dot{\boldsymbol{\xi}} = \delta\dot{\boldsymbol{\xi}}, \quad \mathbf{f} = \mathbf{f}_0 + \delta\mathbf{f} = \delta\mathbf{f} \tag{33}$$

where

$$\delta\dot{\boldsymbol{\xi}} = \frac{\partial \dot{\boldsymbol{\xi}}}{\partial \boldsymbol{\sigma}} : \delta\boldsymbol{\sigma} + \frac{\partial \dot{\boldsymbol{\xi}}}{\partial \vartheta} : \delta\vartheta + \frac{\partial \dot{\boldsymbol{\xi}}}{\partial \boldsymbol{\xi}} : \delta\boldsymbol{\xi} \tag{34}$$

$$\delta\mathbf{f} = \frac{\partial \mathbf{f}}{\partial \boldsymbol{\sigma}} : \delta\boldsymbol{\sigma} + \frac{\partial \mathbf{f}}{\partial \vartheta} : \delta\vartheta + \frac{\partial \mathbf{f}}{\partial \boldsymbol{\xi}} : \delta\boldsymbol{\xi} \tag{35}$$

4.1 Entropy Production Functions. In this subsection, the entropy production function is denoted by

$$\sigma = \sigma(\mathbf{f}, \dot{\boldsymbol{\xi}}, \vartheta) = \frac{1}{\vartheta V} f_\alpha \dot{\xi}_\alpha = \frac{1}{\vartheta V} \mathbf{f} \cdot \dot{\boldsymbol{\xi}} \geq 0 \tag{36}$$

where $\mathbf{f}$, $\dot{\boldsymbol{\xi}}$, and ϑ are considered to be independent variables. The derivative of σ with respect to $\mathbf{f}$ is

$$\frac{\partial \sigma}{\partial \mathbf{f}} = \frac{1}{\vartheta V} \dot{\boldsymbol{\xi}} \tag{37}$$

The first- and second-order variations of σ are

$$\delta\sigma = \frac{1}{\vartheta V}(\delta\mathbf{f} \cdot \dot{\boldsymbol{\xi}} + \mathbf{f} \cdot \delta\dot{\boldsymbol{\xi}}), \quad \delta^2\sigma = \frac{1}{\vartheta V} \delta\mathbf{f} \cdot \delta\dot{\boldsymbol{\xi}} \tag{38}$$

at fixed ϑ. Therefore, the entropy production function has the following properties at the equilibrium state, in view of Eqs. (37), (38), and (32).

$$\sigma_0 = 0, \quad \frac{\partial \sigma}{\partial \mathbf{f}} = \mathbf{0}, \quad \delta\sigma = 0 \tag{39}$$

The entropy production function of infinitesimally constrained equilibrium states can be expanded to

$$\sigma = \sigma_0 + \delta\sigma + \delta^2\sigma = \delta^2\sigma = \frac{1}{\vartheta V} \delta\mathbf{f} \cdot \delta\dot{\boldsymbol{\xi}} = \frac{1}{\vartheta V} \delta f_\alpha \delta\dot{\xi}_\alpha \geq 0 \tag{40}$$

at fixed ϑ due to Eq. (39). The variational conditions $\delta\sigma = 0$ and $\delta^2\sigma = 0$ imply that the the entropy production function σ attains its minimum at the equilibrium state among all infinitesimally constrained equilibrium states. The condition $\delta f_\alpha \delta\dot{\xi}_\alpha \geq 0$ is first proposed in Ref. [19] as the convex condition of the flow potential function.

4.2 Kinetic Rate Laws. The general kinetic rate laws (Eq. (14)) yield

$$\delta\dot{\boldsymbol{\xi}} = \mathbf{G} \cdot \delta\mathbf{f} \quad \text{or} \quad \delta\dot{\xi}_\alpha = G_{\alpha\beta} \delta f_\beta \tag{41}$$

at fixed ϑ and $\boldsymbol{\xi}$. In view of Eqs. (41) and (33), the kinetic rate laws for infinitesimally constrained equilibrium states are obtained as follows:

$$\delta\dot{\boldsymbol{\xi}} = \mathbf{G}_0 \cdot \delta\mathbf{f} \quad \Rightarrow \quad \dot{\boldsymbol{\xi}} = \mathbf{G}_0 \cdot \mathbf{f} \tag{42}$$

Note that $\mathbf{G}_0 = \mathbf{H}_0$ if $\mathbf{G}$ is symmetric. Thus,

$$\delta\dot{\boldsymbol{\xi}} = \mathbf{H}_0 \cdot \delta\mathbf{f} \quad \Rightarrow \quad \dot{\boldsymbol{\xi}} = \mathbf{H}_0 \cdot \mathbf{f} \tag{43}$$

Therefore, infinitesimally constrained equilibrium states obey linear irreversible thermodynamics even if the kinetic rate laws are nonlinear. The coefficient matrix is the Hessian matrix at the equilibrium state $\mathbf{H}_0$.

4.3 Flow Potential Functions. In view of Eqs. (40) and (43),

$$\delta\mathbf{f} \cdot \delta\dot{\boldsymbol{\xi}} = \delta\mathbf{f} \cdot \mathbf{H}_0 \cdot \delta\mathbf{f} \geq 0 \tag{44}$$

at fixed ϑ. Therefore, $\mathbf{H}_0$ should be positive definite and the flow potential function is convex with respect to $\mathbf{f}$ at $\mathbf{f}=\mathbf{0}$. In view of Eqs. (20) and (18), the flow potential function has the following properties.

$$Q = Q_0 = 0, \quad \frac{\partial Q}{\partial \mathbf{f}} = \frac{1}{V}\dot{\boldsymbol{\xi}} = \mathbf{0} \quad \text{at} \quad \mathbf{f} = \mathbf{0} \tag{45}$$

The first- and second-order variations of Q are

$$\delta Q = \frac{1}{V}\left(\dot{\boldsymbol{\xi}} \cdot \delta\mathbf{f} + \int_{\mathbf{0}}^{\mathbf{f}} \delta\dot{\boldsymbol{\xi}} \cdot d\mathbf{f}\right), \quad \delta^2 Q = \frac{1}{V}\delta\dot{\boldsymbol{\xi}} \cdot \delta\mathbf{f} \tag{46}$$

In view of Eqs. (45) and (44),

$$\delta Q = 0, \quad \delta^2 Q \geq 0 \quad \text{at} \quad \mathbf{f} = \mathbf{0} \tag{47}$$

Therefore, the flow potential function Q attains its minimum at $\mathbf{f}=\mathbf{0}$. Furthermore, the flow potential function can be expanded at $\mathbf{f}=\mathbf{0}$.

$$Q = Q_0 + \delta Q + \delta^2 Q = \delta^2 Q = \frac{1}{V}\delta\mathbf{f} \cdot \delta\dot{\boldsymbol{\xi}} = \frac{1}{V}\delta f_\alpha \delta\dot{\xi}_\alpha \geq 0 \tag{48}$$

5 On Time-Independent Plasticity

The time-independent plasticity is essentially a formalism to deal with the state change induced by an infinitesimal stress or strain increment for a material sample. Consider a stress state $\boldsymbol{\sigma} = \sigma_{ij}$ on the current yield surface F, i.e.,

$$F(\boldsymbol{\sigma}, \boldsymbol{\xi}) = 0 \tag{49}$$

The initial state characterized by $(\boldsymbol{\sigma}, \boldsymbol{\xi})$ is an equilibrium state (State I). If the equilibrium state is disturbed by an infinitesimal stress increment $d\boldsymbol{\sigma}$, the disturbed state (State II) is nonequilibrium.

$$F(\boldsymbol{\sigma} + d\boldsymbol{\sigma}, \boldsymbol{\xi}) = \frac{\partial F}{\partial \boldsymbol{\sigma}} : d\boldsymbol{\sigma} > 0 \tag{50}$$

The nonequilibrium will relax to a new equilibrium state (State III).

$$F(\boldsymbol{\sigma} + d\boldsymbol{\sigma}, \boldsymbol{\xi} + d\boldsymbol{\xi}) = 0 \tag{51}$$

The plastic strain increment $d\varepsilon^p$ caused by the disturbance $d\boldsymbol{\sigma}$ is actually accumulated during the relaxation process from State II to State III. Since the initial and final states are equilibrium states and the disturbance is infinitesimal, the relaxation process of the state change can be viewed as a sequence of infinitesimally constrained equilibrium states. A well-known restriction on the plastic strain increment is imposed by Ref. [20].

$$d\boldsymbol{\sigma} : d\boldsymbol{\varepsilon}^p \geq 0 \tag{52}$$

which requires the convexity of the yield surface and leads to an associated flow rule.

$$d\boldsymbol{\varepsilon}^p = d\lambda \frac{\partial F}{\partial \boldsymbol{\sigma}} \tag{53}$$

Within the framework of Rice [1], Drucker's inequality (52) may be generalized as

$$d\boldsymbol{\sigma} : d^p\boldsymbol{\varepsilon} \geq 0 \tag{54}$$

In view of Eq. (8), the thermodynamic counterpart of Drucker's inequality is

$$d\mathbf{f} \cdot d\boldsymbol{\xi} = df_\alpha d\xi_\alpha \geq 0 \tag{55}$$

where $d\mathbf{f}$ is the conjugate force at State II, but $d\boldsymbol{\xi}$ is accumulated from State II to State III. Note that the intrinsic dissipation inequality is always imposed on a specific nonequilibrium state (see Eq. (36)). In view of Eq. (40), the intrinsic dissipation inequality for a specific infinitesimal constrained equilibrium state takes the form

$$d\mathbf{f} \cdot d\dot{\boldsymbol{\xi}} = df_\alpha d\dot{\xi}_\alpha \geq 0 \tag{56}$$

Evidently, we can not derive Eq. (55) from Eq. (56). Therefore, Drucker's inequality is not an essential thermodynamic requirement. The corollary of Drucker's inequality—the convexity of yield surfaces and associate flow rules—will be addressed in following subsections.

The issue can also be addressed in strain space. In strain space, the initial equilibrium is characterized by $(\boldsymbol{\varepsilon}, \boldsymbol{\xi})$, and the disturbance is an infinitesimal strain increment $d\boldsymbol{\varepsilon}$ and causes a plastic stress increment $d^p\boldsymbol{\sigma}$. A well-known restriction on the plastic stress increment is imposed by Il'yushin [21].

$$d\boldsymbol{\varepsilon} : d^p\boldsymbol{\sigma} \geq 0 \tag{57}$$

In view of Eq. (10), the thermodynamic counterpart of Il'yushin's restriction is also given by Eq. (55), so it is also not an essential thermodynamic requirement.

5.1 Convexity of Yield Surfaces. The state variables of the initial state are $(\boldsymbol{\sigma}, \vartheta, \boldsymbol{\xi})$ where the temperature ϑ is fixed during the process. The initial and final states are equilibrium states, so

$$Q(\boldsymbol{\sigma}, \vartheta, \boldsymbol{\xi}) = Q(\boldsymbol{\sigma} + d\boldsymbol{\sigma}, \vartheta, \boldsymbol{\xi} + d\boldsymbol{\xi}) = 0, \quad Q(\boldsymbol{\sigma} + d\boldsymbol{\sigma}, \vartheta, \boldsymbol{\xi}) \geq 0 \tag{58}$$

in view of Eqs. (45) and (48). Obviously, the flow potential function can be considered as the thermodynamic counterpart of the yield function as compared with Eqs. (49)–(51). This viewpoint is no doubt consistent with the statement by Rice [1]: "time-independent inelastic behavior may be formulated by a limiting case of the above time-dependent formulation. The yield surface may be viewed as a singular clustering of surfaces of constant flow potential." Evidently, Eq. (58) also holds in strain space.

In view of Eq. (44), the convexity of yield surfaces is required by the intrinsic dissipation inequality. It should be noted that the convexity is with respect to the conjugate forces rather than the stress or strain. The convexity may be termed *intrinsic convexity*.

5.2 Associated Flow Rule. The normality flow rule (Eq. (22)) only holds instantly. The total inelastic strain increment accumulated during the relaxation process is

$$d^p\boldsymbol{\varepsilon} = \int_0^\infty \frac{d^p\boldsymbol{\varepsilon}}{dt} dt = \int_0^\infty \frac{\partial Q}{\partial \boldsymbol{\sigma}} dt \tag{59}$$

Evidently, the relation can generally not lead to an associated flow rule.

$$d^p\boldsymbol{\varepsilon} = d\lambda \frac{\partial Q}{\partial \boldsymbol{\sigma}} \tag{60}$$

if Q is taken as yield functions, as mentioned before. Indeed, associated flow rules lead to results inconsistent with experiments, e.g., Ref. [22].

Evidently, the associated flow rule (60) can only be achieved if the direction of $(\partial Q/\partial\boldsymbol{\sigma})$ or $(d^p\boldsymbol{\varepsilon}/dt)$ is constant during the full relaxation process. Kuwabara et al. [23] reported significant vio-

lations of the associated flow rule for steels and aluminum of a different nature, following abrupt changes in strain path. Thus, the results of Ref. [23] actually imply that the abrupt changes in strain path will cause the abrupt changes in the inelastic strain rate during the relaxation process.

6 Concluding Remarks

The thermodynamics of infinitesimally constrained equilibrium states belongs to linear irreversible thermodynamics although the prescribed kinetic rate laws of internal variables may be nonlinear. The coefficient matrix is the Hessian matrix of the flow potential function at the equilibrium state. The second-order variation of the entropy production function plays a dominant role for infinitesimally constrained equilibrium states.

The process of a state change induced by an infinitesimal stress increment in time-independent plasticity can be viewed as a sequence of infinitesimally constrained equilibrium states. The thermodynamic counterpart of yield functions are flow potential functions, and their convexity is required by intrinsic dissipation inequality. Drucker and Il'yushin's inequalities are not essential thermodynamic requirements.

Acknowledgment

This work is subsidized by the special funds for major state basic research projects with Grant No. 2009CB724604 and supported by the National Natural Science Foundation of China under Project Nos. 90715041 and 50579026.

References

[1] Rice, J. R., 1971, "Inelastic Constitutive Relations for Solids: An Internal Variable Theory and Its Application to Metal Plasticity," J. Mech. Phys. Solids, **19**, pp. 433–455.
[2] Edelen, D. G. B., 1973, "Asymptotic Stability, Onsager Fluxes and Reaction Kinetics," Int. J. Eng. Sci., **11**, pp. 819–839.
[3] Edelen, D. G. B., 1972, "A Nonlinear Onsager Theory of Irreversibility," Int. J. Eng. Sci., **10**, pp. 481–490.
[4] Ziegler, H., 1977, *An Introduction to Thermomechanics*, North-Holland, Amsterdam.
[5] Moreau, J. J., 1970, "Sur les Lois de Frottement, de Viscosite et de Plasticite," C. R. Acad. Sci. Paris, Série A, **271**, pp. 608–611.
[6] Lubliner, H., 1990, *Plasticity Theory*, Macmillan, New York.
[7] Qin, Q., and Bassani, J. L., 1992, "Non-Schmid Yield Behaviour in Single Crystals," J. Mech. Phys. Solids, **40**, pp. 813–833.
[8] Collins, I. F., and Houlsby, G. T., 1997, "Application of Thermomechanical Principles to the Modelling of Geotechnical Materials," Proc. R. Soc. London, Ser. A, **453**, pp. 1975–2001.
[9] Rajagopal, K. R., and Srinivasa, A. R., 1998, "Mechanics of the Inelastic Behavior of Materials, Part II: Inelastic Response," Int. J. Plast., **14**, pp. 969–995.
[10] Maugin, G. A., 1999, *The Thermodynamics of Nonlinear Irreversible Behaviors*, World Scientific, Singapore.
[11] Houlsby, G. T., and Puzrin, A. M., 2000, "A Thermomechanical Framework for Constitutive Models for Rate-Independent Dissipative Materials," Int. J. Plast., **16**, pp. 1017–1047.
[12] Petryk, H., 2005, "Thermodynamic Conditions for Stability in Materials With Rate-Independent Dissipation," Philos. Trans. R. Soc. London, Ser. A, **363**, pp. 2479–2515.
[13] Puglisi, G., and Truskinovsky, L., 2005, "Thermodynamics of Rate-Independent Plasticity," J. Mech. Phys. Solids, **53**, pp. 655–679.
[14] Hackl, K., and Fischer, F. D., 2008, "On the Relation Between the Principle of Maximum Dissipation and Inelastic Given by Dissipation Potentials," Proc. R. Soc. London, Ser. A, **464**, pp. 117–132.
[15] Hill, R., and Rice, J. R., 1973, "Elastic Potentials and the Structure of Inelastic Constitutive Laws," SIAM J. Appl. Math., **25**, pp. 448–461.
[16] Onsager, L., 1931, "Reciprocal Relations in Irreversible Processes, I," Phys. Rev., **37**, pp. 405–406
[17] Onsager, L., 1931, "Reciprocal Relations in Irreversible Processes, II," Phys. Rev., **38**, pp. 2265–2279.
[18] Yang, Q., Tham, L. G., and Swoboda, G., 2005, "Normality Structures With Homogeneous Kinetic Rate Laws," ASME J. Appl. Mech., **72**, pp. 322–329.
[19] Yang, Q., Wang, R. K., and Xue, L. J., 2007, "Normality Structures With Thermodynamic Equilibrium Points," ASME J. Appl. Mech., **74**, pp. 965–971.
[20] Drucker, D. C., 1959, "A Definition of Stable Inelastic Material," ASME J. Appl. Mech., **26**, pp. 101–106.
[21] Il'yushin, A. A., 1961, "On a Postulate of Plasticity," J. Appl. Math. Mech., **25**, pp. 746–750.
[22] Spitzig, W. A., Sorber, R. J., and Richmond, O., 1975, "Pressure Dependence of Yielding and Associated Volume Expansion in Tempered Martensite," Acta Metall., **23**, pp. 885–893.
[23] Kuwabara, T., Kuroda, M., Tvergaard, V., and Nomura, K., 2000, "Use of Abrupt Strain Path Change for Determining Subsequent Yield Surface: Experimental Study With Sheet Metals," Acta Mater., **48**, pp. 2071–2079.

Unsteady Free-Convection Flow on a Vertical Oscillating Porous Plate With Constant Heating

C. J. Toki
Department of Ecology and Environment,
Technological Educational Institute of Ionian Islands,
Square of Kalvou,
29100, Zakynthos, Greece
e-mail: christina_toki@yahoo.com

In this paper, we consider the unsteady free-convection flows of a viscous and incompressible fluid near an oscillating porous infinite vertical plate (or wall) during the heating of the plate. The governing equations are solved in closed form by the Laplace transform technique, when the Prandtl number (Pr) of the fluid is arbitrary and the suction (or injection) is constant. This solution is applied for a special case of the constant heating effects from the harmonically oscillating plate. The resulting velocity and temperature are shown graphically and are also discussed for the case of air (Pr=0.71) or water (Pr=7.0) flows.
[DOI: 10.1115/1.2998758]

Keywords: free-convection flow, oscillating plate, thermal porous plate, exact solution

1 Introduction

Free-convection flow is encountered in cooling of nuclear reactors or in the study of environmental heat transfer processes. On the other hand from the technological point of view, the effects of the oscillatory vertical flow on free-convection are important because it has many practical applications [1].

The study of the problem of two-dimensional flow past an infinite porous plate was initiated by Lighthill [2], when the freestream oscillates in time about a constant mean. The corresponding hydromagnetic problem was solved by Debnath [3], where a general solution was derived. Extensions of these problems involving unsteady free-convection flow past an infinite or semi-infinite vertical oscillating plate were studied by various authors [4–15]. In these studies, the temperature of the plate was assumed to be constant, and when this temperature was regarded as variable, they solved the problem under specific assumptions [4,5,8]. Also, this oscillatory free-convection flow problem was solved analytically by Soundalgekar [5] and Nanousis and Tokis [6] in the absence of porosity (injection/suction).

In the present study, we consider the unsteady flows of a viscous and incompressible fluid near an infinite vertical porous oscillating plate in the presence of a constant porosity (injection/suction) of this plate. This plate is initially at rest and then suddenly oscillates harmonically with constant magnitude and frequency. Also, we let the boundary condition on the temperature of the plate to be an arbitrary time-dependent function $g(t)$ for all Prandtl numbers (Pr) of the fluid [16,17]. We regard that these temperature variations in the flow field are sufficiently large so that there is heat transfer to or from the porous plate in the flow, but small enough so that the corresponding variations in density and viscosity of the fluid can be neglected. A special case of $g(t)$ is considered when this function is equal to the step unit function $H(t)$, which corresponds to the case of constant heating of the plate [18].

The Laplace transform method is used to solve analytically this basic thermal boundary-layer problem in closed form. A new class of Laplace transforms of exponential forms is encountered [17]. Finally, the results thus obtained are discussed in Sec. 4 and the conclusions are set out in Sec. 5.

2 Mathematical Analysis of the Problem

Let us consider the two-dimensional free-convection flow of a viscous incompressible fluid near an infinite porous vertical plate (or wall). On this plate an arbitrary point was chosen as the origin of a Cartesian coordinate system with the x' axis along the plate in the upward direction and the y' axis normal to it. The flow is induced either by the motion of the plate or by heating it or both.

The plate initially at rest and at a constant temperature T'_∞ suddenly oscillates harmonically with constant magnitude and frequency, namely, with the velocity $U_0 \cos \omega' t'$, in its own plane along the x' axis. Its temperature is instantaneously increased (or decreased) by the quantity $(T'_w - T'_\infty)\ g(t)$ for $t>0$. The constant velocity U_0 is the maximum velocity of the plate, $\omega'(>0)$ is the fixed frequency of oscillations, $T'_w(\neq T'_\infty)$ is a constant temperature for the plate, and $g(t)$ is an arbitrary function of nondimensional time t (see Eq. (3*a*)).

The basic analysis on the physical grounds of the present oscillatory flow problem was made by Lighthill [2] and Soundalgekar [4,5]. As the plate is infinite in extent, the flow is independent of the distance parallel to the plate and, hence, the physical variables depend on the space coordinate y' and time t' only.

Under the above assumptions and conditions with the usual Boussinesq approximation, it can be shown that the flow is governed by the following equations.

The equation of continuity (on integration form) is

$$v' = \text{constant} = v'_0(\text{say}) \tag{1}$$

where v'_0 is the normal velocity of suction or injection at the wall at $v'_0<0$ or >0, respectively; $v'_0=0$ represents the case of a nonpermeable wall.

The remaining basic equations of energy and motion are also obtained in nondimensional form [17]

$$\frac{\partial^2 \theta}{\partial y^2} - v_0 \,\mathrm{Pr}\frac{\partial \theta}{\partial y} - \mathrm{Pr}\frac{\partial \theta}{\partial t} = 0 \tag{2a}$$

$$\frac{\partial^2 u}{\partial y^2} - v_0 \frac{\partial u}{\partial y} - \frac{\partial u}{\partial t} = -G\theta \tag{2b}$$

where the nondimensional quantities are defined as

$$y = y' U_0/\nu, \quad t = t' U_0^2/\nu, \quad u = u'/U_0, \quad v_0 = v'_0/U_0, \quad \omega = \omega' \nu/U_0^2 \tag{3a}$$

Furthermore, we have the nondimensional temperature,

$$\theta = (\mathrm{T}' - \mathrm{T}'_\infty)/(\mathrm{T}'_w - \mathrm{T}'_\infty) \tag{3b}$$

the Prandtl number,

$$\mathrm{Pr} = \mu c_P/\kappa \tag{3c}$$

the Grashot number,

$$G = \nu g \beta' (\mathrm{T}'_w - \mathrm{T}'_\infty)/U_0^3 \tag{3d}$$

where ρ denotes the fluid density, ν the kinematic viscosity, T' the temperature, g the acceleration due to gravity, β' the coefficient of volume expansion, κ the thermal conductivity, and c_P the specific heat at constant pressure.

Assuming that no slipping occurs between the plate and the fluid, the appropriate initial and boundary conditions of the system (2) of differential equations are in nondimensional form [3,17]

Contributed by the Applied Mechanics Division of ASME for publication in the JOURNAL OF APPLIED MECHANICS. Manuscript received November 23, 2007; final manuscript received July 16, 2008; published online October 31, 2008. Review conducted by Nesreen Ghaddar.

$$u(y,0^-)=0, \quad \theta(y,0^-)=0, \quad \text{for } y\geq 0 \tag{4a}$$

$$u(0,t)=\cos\,\omega t, \quad \theta(0,t)=g(t), \quad \text{for } t>0 \tag{4b}$$

$$u(\infty,t)\to 0, \quad \theta(\infty,t)\to 0, \quad \text{for } t>0 \tag{4c}$$

By applying the Laplace transform (with respect to the time t) to the system (2) of differential equations, it is found that the general solution of this system for $\theta(y,t)$ and $u(y,t)$ for $t>0$ is

$$\theta(y,t)=L^{-1}[\bar{g}(s)e^{-ry}] \tag{5a}$$

$$u(y,t)=\Phi(y,t)+A(y,\mathrm{Pr},t) \tag{5b}$$

where

$$A(y,\mathrm{Pr},t)=\frac{G\,\mathrm{Pr}}{\mathrm{Pr}-1}L^{-1}\left[\frac{\bar{g}(s)}{r^2}(e^{-qy}-e^{-ry})\right], \quad \text{for } \mathrm{Pr}\neq 1 \tag{6a}$$

$$A(y,1,t)=yGL^{-1}\left[\frac{\bar{g}(s)}{2q+\upsilon_0}e^{-qy}\right], \quad \text{for } \mathrm{Pr}=1 \tag{6b}$$

with

$$q\equiv\left(s+\frac{1}{4}\upsilon_0^2\right)^{1/2}-\frac{1}{2}\upsilon_0 \tag{7a}$$

$$r\equiv \mathrm{Pr}^{1/2}\left(s+\frac{1}{4}\upsilon_0^2\,\mathrm{Pr}\right)^{1/2}-\frac{1}{2}\upsilon_0\,\mathrm{Pr} \tag{7b}$$

and

$$\Phi(y,t)=L^{-1}\left[\frac{s}{s^2+\omega^2}e^{-qy}\right]$$

$$=\frac{y}{2\pi^{1/2}}e^{y\upsilon_0/2}\int_0^t \xi^{-3/2}e^{-(\upsilon_0^2\xi+y^2/\xi)/4}\cos\,\omega(t-\xi)d\xi \tag{8a}$$

$$=\frac{1}{4}e^{(1/2)y\upsilon_0-i\omega t}\left\{\exp\left[-y\left(\frac{1}{4}\upsilon_0^2-i\omega\right)^{1/2}\right]\mathrm{erfc}\left[\frac{y}{2t^{1/2}}-\left(\frac{1}{4}\upsilon_0^2-i\omega\right)^{1/2}t^{1/2}\right]+\exp\left[y\left(\frac{1}{4}\upsilon_0^2-i\omega\right)^{1/2}\right]\mathrm{erfc}\left[\frac{y}{2t^{1/2}}+\left(\frac{1}{4}\upsilon_0^2-i\omega\right)^{1/2}t^{1/2}\right]\right\}$$
$$+\frac{1}{4}e^{(1/2)y\upsilon_0+i\omega t}\left\{\exp\left[-y\left(\frac{1}{4}\upsilon_0^2+i\omega\right)^{1/2}\right]\mathrm{erfc}\left[\frac{y}{2t^{1/2}}-\left(\frac{1}{4}\upsilon_0^2+i\omega\right)^{1/2}t^{1/2}\right]+\exp\left[y\left(\frac{1}{4}\upsilon_0^2+i\omega\right)^{1/2}\right]\mathrm{erfc}\left[\frac{y}{2t^{1/2}}+\left(\frac{1}{4}\upsilon_0^2+i\omega\right)^{1/2}t^{1/2}\right]\right\} \tag{8b}$$

$$=\frac{1}{2}e^{(2y\upsilon_0-\upsilon_0^2t-y/t)/4}\sum_{n=0}^{\infty}\frac{(-1)^n}{\Gamma\left(\frac{n}{2}+1\right)}\left\{\left[\left(\frac{1}{16}\upsilon_0^4+\omega^2\right)^{1/2}t+c_1y+y^2/4t\right]^{n/2}\cos\,n\vartheta_1+\left[\left(\frac{1}{16}\upsilon_0^4+\omega^2\right)^{1/2}t-c_1y+y^2/4t\right]^{n/2}\cos\,n\vartheta_2\right\} \tag{8c}$$

with

$$c_{1,2}=\frac{1}{\sqrt{2}}\left[\left(\frac{1}{16}\upsilon_0^4+\omega^2\right)^{1/2}\pm\frac{1}{4}\upsilon_0^2\right]^{1/2} \tag{8d}$$

$$\tan\,\vartheta_{1,2}=c_2t^{1/2}/(\pm c_1t^{1/2}+y/2t^{1/2}), \quad \text{for } 0\leq\vartheta_{1,2}<\pi/2 \tag{8e}$$

Now, we observe that the transformed function $\bar{g}(s)$ in the expressions (5) has the known inverse function $g(t)$. So, we can consider some special cases of $g(t)$, which prescribe physically acceptable forms [16,17]. In Sec. 3 we demonstrate an application of the general results (5) in the simple case $g(t)=H(t)$, which corresponds to the case of constant heating of the plate.

3 Application of the General Formulation

The velocity field (cf. Eq. (5*b*)) consists of two parts: the first term $\Phi(y,t)$ due to the oscillation of the porous plate and the second term $A(y,\mathrm{Pr},t)$ due to the heating of this plate. The first term $\Phi(y,t)$ is unaffected by $g(t)$ and is given in Eq. (8). Then, the previous results (5) are applied to the simple case of constant heating of the plate.

In this case a constant or single heating of plate corresponds to $g(t)=H(t)$ (with $H(t)$ as the Heaviside unit function and $\bar{g}(s)=1/s$). So, the inversions of expressions (5) and (6) give the exact solutions for $\theta(y,t)$ and $u(y,t)$ for $t>0$ by

$$\theta(y,t)=F\left(y\,\mathrm{Pr}^{1/2},\frac{1}{2}\upsilon_0\,\mathrm{Pr}^{1/2},t\right) \tag{9a}$$

$$u(y,t)=\Phi(y,t)+A(y,\mathrm{Pr},t) \tag{9b}$$

where we use the abbreviation

$$F(z,b,t)\equiv\frac{1}{2}\mathrm{erfc}\left(\frac{1}{2}z/t^{1/2}-bt^{1/2}\right)+\frac{1}{2}e^{2zb}\mathrm{erfc}\left(\frac{1}{2}z/t^{1/2}+bt^{1/2}\right) \tag{10}$$

The first term of the solution (9*b*) is given by expression (8) and the second term $A(y,\mathrm{Pr},t)$ is obtained as follows:

$$A(y,\mathrm{Pr},t)=\frac{G}{\upsilon_0^3\,\mathrm{Pr}(\mathrm{Pr}-1)}L^{-1}\left\{(e^{-qy}-e^{-ry})\left[\frac{\mathrm{Pr}^2\,\upsilon_0^2}{r^3}-\frac{\mathrm{Pr}\,\upsilon_0}{r^2}+\frac{1}{r}-\frac{1}{r+\upsilon_0\,\mathrm{Pr}}\right]\right\} \tag{11a}$$

$$=\frac{G}{\upsilon_0^2(\mathrm{Pr}-1)}\left\{\exp\left(\frac{1}{2}y\upsilon_0-\frac{1}{4}\upsilon_0^2t\right)\sum_{\nu=2}^{3}\beta_\nu Ts_\nu\left(y,-\frac{1}{2}\upsilon_0\,\mathrm{Pr}^{1/2},\frac{1}{4}\upsilon_0^2(\mathrm{Pr}-1),t\right)-\exp\left(\frac{1}{2}y\upsilon_0\,\mathrm{Pr}-\frac{1}{4}\upsilon_0^2\,\mathrm{Pr}\,t\right)\sum_{\nu=2}^{3}\beta_\nu Ts_\nu\left(y\,\mathrm{Pr}^{1/2},-\frac{1}{2}\upsilon_0\,\mathrm{Pr}^{1/2},0,t\right)\right]\right\}$$
$$+\frac{G}{\upsilon_0^2\,\mathrm{Pr}(\mathrm{Pr}-1)}\left[F\left(y,\frac{1}{2}\upsilon_0,t\right)-F\left(y\,\mathrm{Pr}^{1/2},\frac{1}{2}\upsilon_0\,\mathrm{Pr}^{1/2},t\right)\right], \quad \text{for } \mathrm{Pr}\neq 1 \tag{11b}$$

$$A(y,1,t)=\frac{yG}{2\upsilon_0}\left[\mathrm{erfc}\left(\frac{1}{2}y/t^{1/2}-\frac{1}{2}\upsilon_0t^{1/2}\right)-e^{y\upsilon_0}\mathrm{erfc}\left(\frac{1}{2}y/t^{1/2}+\frac{1}{2}\upsilon_0t^{1/2}\right)\right], \quad \text{for } \mathrm{Pr}=1 \tag{11c}$$

where the inverse Laplace transforms

$$Ts_\nu(\alpha,k,\lambda,t)=L^{-1}\left\{\frac{e^{-\alpha s^{1/2}}}{[(s+\lambda)^{1/2}+k]^\nu}\right\},\quad \nu=2,3 \tag{12}$$

are expressed analytically in the work of Toki [18] and the coefficients β_ν and $\nu=2,3$ are given by

$$\beta_2=-1/\mathrm{Pr},\quad \beta_3=v_0/\mathrm{Pr}^{1/2} \tag{13}$$

Knowing the velocity field from Eq. (9), we can now calculate the skin friction of the flow at the wall of the porous plate. In nondimensional form it is given by

$$\begin{aligned}\tau&=\frac{\tau'}{\rho U_0^2}=\left.\frac{\partial u}{\partial y}\right|_{y=0}\\&=\tau_\Phi+\frac{G}{v_0^2(\mathrm{Pr}-1)}\left\{2b_1+b_2e^{-(1/4)v_0^2t}+b_3e^{-(1/4)v_0^2\,\mathrm{Pr}\,t}\right.\\&\quad+b_4e^{-(1/4)v_0^2t}M\left(1,\frac{3}{2},\frac{1}{4}v_0^2(1-\mathrm{Pr})t\right)\\&\quad\left.+\left(\frac{1}{2}v_0-b_1\right)\mathrm{erfc}\left(\frac{1}{2}v_0\,\mathrm{Pr}^{1/2}\,t^{1/2}\right)+\frac{v_0}{2\,\mathrm{Pr}}\mathrm{erfc}\left(\frac{1}{2}v_0t^{1/2}\right)\right\}\end{aligned} \tag{14}$$

where the τ_Φ expresses the skin friction due to the harmonic motion of the oscillating plate, which is given by

$$\begin{aligned}\tau_\Phi&=\left.\frac{\partial\Phi}{\partial y}\right|_{y=0}\\&=v_0\cos\omega t-\frac{2}{\pi^{1/2}}e^{-\frac{1}{4}v_0^2t}\left[\frac{1}{t^{1/2}}+\sum_{n=0}^{\infty}\frac{2^{n+1}t^{n+\frac{1}{2}}}{1\cdot3\cdots(2n+1)}\left(\frac{1}{16}v_0^4\right.\right.\\&\quad\left.\left.+\omega^2\right)^{\frac{n+1}{2}}\cos(n+1)\theta\right]\end{aligned} \tag{15}$$

with $\tan\theta=4\omega/v_0^2$, $0\le\theta<\pi/2$. The sum of the remaining terms at the right-hand side of Eq. (14) expresses the skin friction due to the free-convection currents. Moreover, in Eq. (14) the $M(1,3/2,1/4v_0^2(1-\mathrm{Pr})t)$ is the confluent hypergeometric function and the factors $b_n=b_n(t)$ and $n=1,2,3,4$ are defined by

$$\begin{aligned}b_1&=\frac{1}{2}v_0^2\,\mathrm{Pr}^{1/2}\left[\frac{1}{2}v_0\,\mathrm{Pr}\,t\left(\frac{1}{2}v_0\,\mathrm{Pr}^{1/2}\,t+1\right)+\frac{1}{2}v_0t+1\right]+\frac{1}{\mathrm{Pr}^{1/2}}\\&\quad+\frac{v_0}{2(2\,\mathrm{Pr}-1)}\left[\frac{1}{2}v_0^3\,\mathrm{Pr}^{1/2}\,t\left(\frac{1}{2}v_0\,\mathrm{Pr}\,t-1\right)+v_0^2\,\mathrm{Pr}^{1/2}\,t+\frac{1}{\mathrm{Pr}^{1/2}}\right]\\&\quad+\frac{v_0}{2(2\,\mathrm{Pr}-1)^2}\left[v_0^2\,\mathrm{Pr}\,t\left(\mathrm{Pr}^{1/2}-\frac{1}{2}\right)+\mathrm{Pr}^{1/2}(v_0-1)+4\,\mathrm{Pr}+3\right]\\&\quad+\frac{v_0(\mathrm{Pr}^{1/2}+1)}{(2\,\mathrm{Pr}-1)^3}(\mathrm{Pr}-1)(2\,\mathrm{Pr}-3)\end{aligned} \tag{16a}$$

$$\begin{aligned}b_2&=\left\{\frac{v_0(1-1/\mathrm{Pr}^{1/2})}{2(2\,\mathrm{Pr}-1)}+\frac{1}{4}v_0^4t\left(\mathrm{Pr}^{1/2}-\frac{\mathrm{Pr}}{2\,\mathrm{Pr}-1}\right)\right.\\&\quad\left.-\frac{v_0^2}{(2\,\mathrm{Pr}-1)^2}[\mathrm{Pr}(2\,\mathrm{Pr}-1)-\mathrm{Pr}^{1/2}(4\,\mathrm{Pr}-3)-1]\right\}\left(\frac{t}{\pi}\right)^{1/2}\\&\quad+\left[2(\mathrm{Pr}-1)(2\,\mathrm{Pr}-3)-1\right.\\&\quad\left.+\frac{8\,\mathrm{Pr}^3-14\,\mathrm{Pr}^2+13\,\mathrm{Pr}+6}{(2\,\mathrm{Pr}-1)^3}\right]\frac{1}{(\pi t)^{1/2}}\end{aligned} \tag{16b}$$

$$b_3=\frac{\mathrm{Pr}-1}{\mathrm{Pr}^{1/2}}\left[v_0\left(2\,\mathrm{Pr}^2-\frac{1}{2}\mathrm{Pr}+\frac{1}{2\,\mathrm{Pr}^{1/2}}-\frac{3}{2}\right)+2\,\mathrm{Pr}-3\right]+\frac{v_0^2}{(\pi t)^{1/2}} \tag{16c}$$

$$\begin{aligned}b_4&=\left\{(\mathrm{Pr}-1)\left[\frac{1}{2}v_0^2(\mathrm{Pr}-1)\left(v_0-\frac{1}{\mathrm{Pr}}\right)+2\,\mathrm{Pr}-3\right]\right.\\&\quad\left.+\frac{4}{\mathrm{Pr}^{1/2}}(2\,\mathrm{Pr}+1)\right\}\left(\frac{t}{\pi}\right)^{1/2}\end{aligned} \tag{16d}$$

We can also calculate the heat transfer coefficient in terms of the Nusselt number [14], as follows:

$$\mathrm{Nu}=x'\frac{\partial T'/\partial y'}{T'_w-T'_\infty} \tag{17a}$$

$$\frac{\mathrm{Nu}}{\mathrm{Re}}=q=\left.\frac{\partial\theta}{\partial y}\right|_{y=0}=-\frac{\mathrm{Pr}^{1/2}}{(\pi t)^{1/2}}e^{-(1/4)v_0^2t}+\frac{1}{2}v_0\,\mathrm{Pr}\,\mathrm{erfc}\left(\frac{1}{2}v_0\,\mathrm{Pr}^{1/2}\,t^{1/2}\right) \tag{17b}$$

where $\mathrm{Re}=U_0x'/\nu$ is the Reynolds number and q is the nondimensional heat transfer coefficient.

4 Discussion

The general problem of the unsteady thermal free-convection flows near an oscillating porous vertical plate was solved analytically. Its new solution was exemplified in Sec. 3 without any restrictions.

Indeed, the Grashof number G in the general solution (5) can take positive, zero, or negative values. Physically, $G<0$ corresponds to an externally heated plate as the free-convection currents are carried toward the plate. Then, $G>0$ corresponds to an externally cooled plate and $G=0$ corresponds to the absence of the free-convection currents. The result (5*b*) for the velocity is reduced to $u(y,t)=\Phi(y,t)$, when $G=0$; in this case, the velocity is independent of the Prandtl number (Pr) of the fluid and describes only hydrodynamics oscillations, which decay exponentially (cf. Eq. (8*c*)) [3].

It should be pointed out that the general solution (9) includes the case of the present problem without suction or injection at the thermal wall and the solutions for constant heating (with $g(t)=H(t)$). These results, with $v_0=0$, are exemplified in our previous paper [17]. In this case, the expression of the function $\Phi_0(y,t)$ is given in Eq. (8) with $v_0=0$.

The present results for the case of the constant heating of the plate include the results of Nanousis and Tokis [6] in the case of the absence of the magnetic field and of the suction or injection at thermal wall. The results, without suction or injection, are similar to the results of Soundalgekar [5].

It is worthwhile to point out that our solutions of the problem with porosity (injection/suction) (cf. Eq. (9)) were obtained in closed form with the Prandtl number (Pr) of the fluid different or equal to one. Indeed, for most gases Pr is between 0.7 and 0.85, whereas for liquids Pr is generally greater than 1; $\mathrm{Pr}=1$ gives the solution for very restricted classes of gas, namely, steam and ammonia.

Since the present problem arose in the study of aircraft response to atmospheric gusts, in flutter phenomena involving wings, in the flow over helicopter rotor blades, and in turbomachinery blade cascades [5,14], we applied the present results of analytical solutions for the case of flows of atmospheric air ($\mathrm{Pr}=0.71$) or water ($\mathrm{Pr}=7.0$).

Indeed, an application of the numerical values into the expression of the exact solution (cf. Eq. (9*b*)) for the case of air flow near a single heating porous plate gives velocity profiles, which are illustrated in Fig. 1 (see also the velocity profiles in the previous investigation [5] in the case of the nonporous plate). We observe that the oscillations of the porous plate will produce disturbances within a fluid in which the velocity decays almost exponentially as the distance from the plate increases.

The temperature profiles are derived from Eq. (9*a*) and are shown in Fig. 2 for air and water in the case of the single heating porous vertical plate, which oscillates harmonically. It is observed

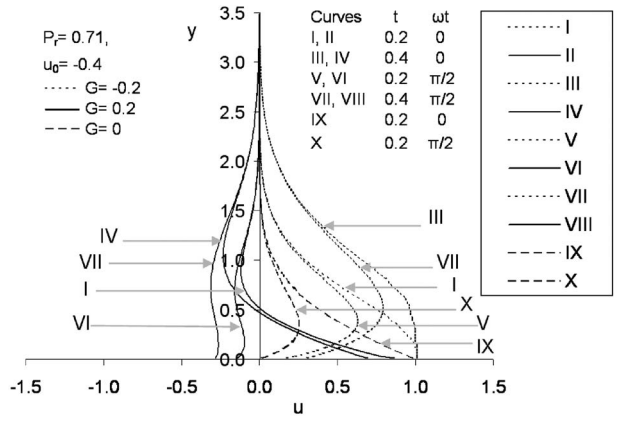

Fig. 1 Velocity profiles for the case of the air flows near the single heating ($G<0$) or cooling ($G>0$) porous vertical plate, which oscillates harmonically

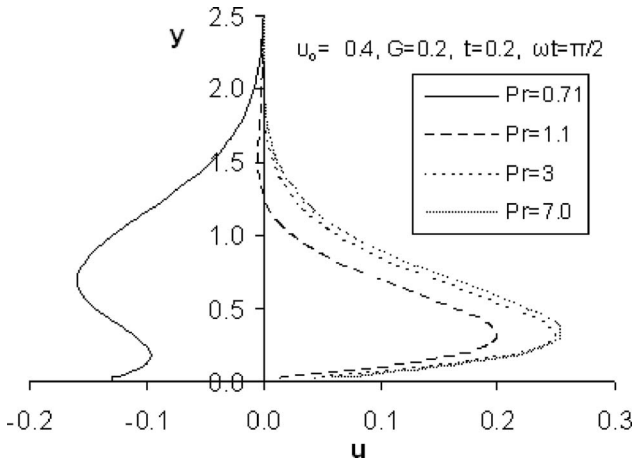

Fig. 3 Velocity profiles of the flow near the single cooling ($G>0$) porous vertical oscillating plate for varying Prandtl numbers (Pr)

that an increase in the time (t) leads to an increase in the temperature (θ) in both cases of flows of air or water. In Fig. 2, the results for the temperature of the water (Pr=7) near the porous plate are smaller than those of air (Pr=0.71).

For different values of Prandtl number (Pr), the velocity profiles of the flow near the single cooling ($G>0$) porous vertical oscillating plate are shown in Fig. 3. We observe that the velocities of all these fluids decay almost exponentially as the distance from the oscillating porous plate increases.

5 Conclusions

A general analytical solution for the problem of the unsteady free-convection flow near an oscillating porous vertical plate (or wall) was determined for an arbitrary Prandtl number (Pr).

We studied a physical example of an evaluation of the velocity and the temperature for the cases of flows of air (Pr=0.71) or water (Pr=7.0) near a vertical porous plate during constant heating. So, we deduce from the graphs that the oscillations of the porous plate will produce disturbances within a fluid in which the velocity and the temperature decay almost exponentially as the distance from the plate increases.

Finally, we note that this work gives the exact analytical solution for the free-convection flow in an oscillating and porous plate with constant heating problem, which—besides engineering applications—is interested in the study of vertical air flows into the atmosphere [1].

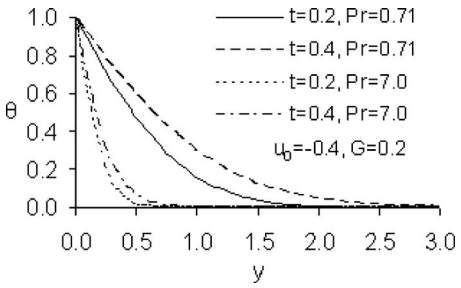

Fig. 2 Temperature profiles for the case of the air flows (Pr =0.71) and water flows (Pr=7) near the single heating porous vertical plate, which oscillates harmonically

References

[1] Gebhart, B., Jaluria, Y., Mahajan, R. L., and Sammakia, B., 1988, *Buoyancy-Induced Flows and Transport*, Hemisphere, New York, Chap. 10.

[2] Lighthill, M. J., 1954, "The Response of Laminar Skin Friction and Heat Transfer to Fluctuations in the Stream Velocity," Proc. R. Soc. London, Ser. A, **224**, pp. 1–23.

[3] Debnath, L., 1975, "Exact Solutions of the Unsteady Hydrodynamic and Hydromagnetic Boundary Layer Equations in a Rotating Fluid System," Z. Angew. Math. Mech., **55**, pp. 431–438.

[4] Soundalgekar, V. M., 1973, "Free Convection Effects on the Oscillatory Flow Past an Infinite, Vertical, Porous Plate With Constant Suction (I)," Proc. R. Soc. London, Ser. A, **333**, pp. 25–36.

[5] Soundalgekar, V. M., 1979, "Free Convection Effects on the Flow Past an Infinite Vertical Oscillating Plate," Astrophys. Space Sci., **64**, pp. 165–171.

[6] Nanousis, N. D., and Tokis, J. N., 1984, "MHD Free-Convection Flow Near a Vertical Oscillator Plate," Astrophys. Space Sci., **98**, pp. 397–403.

[7] Mansour, M. A., 1990, "Radiative and Free Convection Effects on the Oscillatory Flow Past a Vertical Plate," Astrophys. Space Sci., **166**, pp. 269–275.

[8] Soundalgekar, V. M., Pohanerkar, S. G., Lahurikar, R. M., and Birajdar, N. S., 1995, "Mass Transfer Effects on Flow Past a Vertical Oscillating Plate With Variable Temperature," Heat Mass Transfer, **30**(5), pp. 309–312.

[9] Soundalgekar, V. M., Das, U. N., and Deka, R. K., 1997, "Free Convection Effects on MHD Flow Past an Infinite Vertical Oscillating Plate With Constant Heat Flux," Indian J. Math., **39**(3), pp. 195–202.

[10] Turbatu, S., Bühler, K., and Zierep, J., 1998, "New Solutions of the II Stokes Problem for an Oscillating Flat Plate," Acta Mech., **129**, pp. 25–30.

[11] Revankar, S. T., 2000, "Free Convection Effect on Flow Past an Impulsively Started or Oscillating Infinite Vertical Plate," Mech. Res. Commun., **27**, pp. 241–246.

[12] Gupta, A. S., Misra, J. C., Reza, M., and Soundalgekar, V. M., 2003, "Flow in the Ekman Layer on an Oscillating Porous Plate," Acta Mech., **165**, pp. 1–16.

[13] Hossain, M. A., Pop, I., and Ress, D. A. S., 2000, "The Effect of Time-Periodic Surface Temperature Oscillations on Free Convection From a Vertical Surface in a Porous Medium," Transp. Porous Media, **39**, pp. 119–130.

[14] Kim, Y. J., 2000, "Unsteady MHD Convective Heat Transfer Past a Semi-Infinite Vertical Porous Moving Plate With Variable Suction," Int. J. Eng. Sci., **38**, pp. 833–845.

[15] Chaudhary, R. C., and Jain, A., 2007, "Combined Head and Mass Transfer Effects on MHD Free Convection Flow Past an Oscillating Plate Embedded in Porous Medium," Rom. J. Physiol., **52**, pp. 505–524.

[16] Kythe, P. K., and Puri, P., 1988, "Unsteady MHD Free-Convection Flows on a Porous Plate With Time-Dependent Heating in a Rotating Medium," Astrophys. Space Sci., **143**, pp. 51–62.

[17] Toki, C. J., and Tokis, J. N., 2007, "Exact Solutions for the Unsteady Free Convection Flows on a Porous Plate With Time-Dependent Heating," Z. Angew. Math. Mech., **87**(1), pp. 4–13.

[18] Toki, C. J., 2008, "Free Convection and Mass Transfer Flow Near a Moving Vertical Porous Plate: An Analytical Solution," ASME J. Appl. Mech., **75**(1), p. 011014.

Snap-Through of Shallow Elastic Arches Under End Moments

Raymond H. Plaut
Department of Civil and Environmental Engineering,
Virginia Polytechnic Institute and State University,
Blacksburg, VA 24061
e-mail: rplaut@vt.edu

Snap-through of buckled beams or shallow arches may be utilized in some MEMS devices. Such behavior can be induced by applied moments at the ends. A simply-supported uniform shallow elastic arch is analyzed. For equal end moments, the critical value is compared for arches with a sinusoidal shape, a circular shape, and a shape that maximizes the critical moment. For unequal moments, the effect of the amount of loading asymmetry on the critical value is determined for sinusoidal arches.
[DOI: 10.1115/1.3000020]

1 Introduction

Uniform shallow elastic arches with simply-supported ends are considered. A clockwise moment is applied at the left support and a counterclockwise moment at the right support. The moments may be equal or unequal. Critical values for in-plane snap-through instability are determined. Such a system may be useful for MEMS switches or micropumps [1–3].

In the analysis presented here, the unloaded arch is assumed to have a sinusoidal shape. For equal moments, the problem was treated in Ref. [4] by another procedure in which the moments were included in the equilibrium equation and the deflection was represented as an infinite series. Results obtained here are compared with those given in Ref. [5] for equal moments acting on (i) a circular arch and (ii) the arch shape that maximizes the critical moment for a given arch length and span. (Out-of-plane instability of arches subjected to end moments was investigated in Refs. [6,7] and references cited therein.)

2 Formulation

As shown in Fig. 1, the arch has a span L and total arc length S, and the moments at $X=0$ and L are $(1+\alpha)M$ and $(1-\alpha)M$, respectively, where α will be called the asymmetry parameter. The moments are equal if $\alpha=0$. The unstrained shape of the arch is denoted by $Y_o(X)$ and the loaded shape is $Y(X)$. The arch has cross-sectional area A, moment of inertia I, and modulus of elasticity E.

The analysis is carried out in nondimensional terms. The following quantities are defined:

$$x=\frac{X}{L},\quad r=\sqrt{\frac{I}{A}},\quad y=\frac{Y}{2r},\quad y_o=\frac{Y_o}{2r}$$

$$m=\frac{L^2M}{2EIr},\quad \beta^2=\frac{(S-L)AL}{2I} \tag{1}$$

The nondimensional induced thrust γ^2 and arch length parameter β are given by [5]

$$\gamma^2=2\int_0^1[(y_o')^2-(y')^2]dx \tag{2a}$$

$$\beta^2=\int_0^1(y_0')^2dx \tag{2b}$$

The equilibrium equation is

$$y''''(x)+\gamma^2y''(x)=y_o''''(x) \tag{3}$$

The boundary conditions at $x=0$ are $y=0$ and $y''-y_o''=(1+\alpha)m$, and at $x=1$ they are $y=0$ and $y''-y_o''=(1-\alpha)m$.

For the sinusoidal arch, the unstrained shape is assumed to be

$$y_o(x)=h\sin\pi x \tag{4}$$

and Eq. (2*b*) yields $\beta^2=\pi^2h^2/2$.

In terms of γ, the solution of Eq. (3) and the boundary conditions is

$$y(x)=A_1\sin\gamma x+A_2\cos\gamma x+A_3x+A_4+\frac{\pi^2h}{(\pi^2-\gamma^2)}\sin\pi x \tag{5}$$

where

$$A_1=\frac{(1+\alpha)m\cos\gamma-(1-\alpha)m}{\gamma^2\sin\gamma},\quad A_2=-\frac{(1+\alpha)m}{\gamma^2}$$

$$A_3=-\frac{2\alpha m}{\gamma^2},\quad A_4=-A_2 \tag{6}$$

Equations (4) and (5) are substituted into Eq. (2*a*), which leads to a quadratic equation in m. For given values of h (or β) and α, the solutions for m are functions of γ. If the larger solution $m(\gamma)$ exhibits a maximum between $\gamma=\pi$ and 2π, the equilibrium path has a limit point at that value of m. If $m(\gamma)$ has a maximum that occurs for $\gamma>2\pi$, the equilibrium path has a bifurcation point at $\gamma=2\pi$ and snap-through occurs then. In both cases, the critical moment is denoted m_{cr}. For extremely shallow arches, there is no critical point and the arch inverts smoothly as m is increased quasistatically (i.e., there is no sudden downward jump in deflection).

For the sinusoidal arch with equal end moments (i.e., $\alpha=0$), a limit point occurs if $1.01<h<3.27$ ($2.24<\beta<7.27$), and a bifurcation point occurs if $h>3.27$ ($\beta>7.27$). In the latter case,

$$m_{cr}=\frac{4\pi}{9}[4h+\sqrt{2(8+9\pi^2)h^2-81\pi^2}] \tag{7}$$

If the end moments are unequal, instability only occurs at a limit point.

3 Numerical Results

3.1 Equal End Moments. Figure 2 shows the dependence of m_{cr} on the arch length parameter β for the case of equal end moments. The lowest curve is for the sinusoidal arch, where the height is related to the length by $h=(\beta/\pi)\sqrt{2}$. The curve is obtained from Eq. (7) if $\beta>7.27$. In that case, the arch shape at the onset of bifurcation is given by Eq. (5) with $A_1=0$, $\alpha=0$, and $\gamma=2\pi$. The arch has a slope $y'=-\pi h/3$ at $x=0$ just before the central part of the arch jumps downward into an inverted configuration. The corresponding nondimensional horizontal length of each end portion that lies below the horizontal at this onset of snap-through is 0.093 if $\beta=10$ and 0.085 if $\beta=50$.

For a circular (or parabolic) arch with height b, one can write $y_o(x)=4bx(1-x)$ and $\beta=4b/\sqrt{3}$. Limit-point instability occurs if $0.96<b<2.49$ ($2.22<\beta<5.74$). For greater heights, m_{cr} is associated with bifurcation and is given by [5]

Contributed by the Applied Mechanics Division of ASME for publication in the JOURNAL OF APPLIED MECHANICS. Manuscript received April 11, 2008; final manuscript received September 14, 2008; published online November 5, 2008. Review conducted by Edmundo Corona.

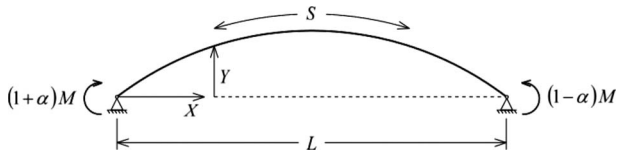

Fig. 1 Schematic of the shallow arch in dimensional form

$$m_{cr} = 2\sqrt{3}\beta + 2\pi\sqrt{2\beta^2 - 4\pi^2} \tag{8}$$

At the onset of bifurcation instability, the arch shape is

$$y(x) = \frac{(m - 8b)}{4\pi^2}[1 - \cos(2\pi x)] \tag{9}$$

so that a circular arch with $\beta > 5.74$ has a horizontal slope at its ends when snap-through occurs. The middle curve in Fig. 2 gives m_{cr} for the circular arch. For any arch length β in Fig. 2, m_{cr} for the circular arch is about 10% higher than that for the sinusoidal arch.

The top curve in Fig. 2 is for the arch shape that, for a given arch length and span, maximizes the critical moment. The results are taken from Ref. [5], which utilized the procedure described in Ref. [8]. The optimal shape depends on the value of β, and is flatter in the central region than the sinusoidal or circular shapes. Limit-point instability governs if $2.23 < \beta < 5.17$. The values of m_{cr} for the optimal arch are about 10% higher than for the circular arch.

3.2 Unequal End Moments. Results for the sinusoidal arch subjected to unequal end moments are presented in Fig. 3 for $\beta = 5$ and 10. The critical moment, normalized by its value m_o for the symmetric case $\alpha = 0$, is plotted versus the asymmetry parameter α for the range $0 \leq \alpha \leq 0.5$. The value of m_{cr} is independent of which end of the arch is subjected to the larger moment, and the moments are defined such that the sum of the magnitudes of the two end moments is the same for all values of α. For unequal moments, instability is always associated with a limit point. As the moments are increased, a small portion of the arch near the end with the larger moment displaces smoothly downward past the horizontal axis, and at m_{cr} the rest of the arch suddenly snaps downward. At the onset of instability, the nondimensional horizontal length of this portion near the end with the larger moment for the case of $\alpha = 0.5$ is 0.190 if $\beta = 5$, and 0.200 if $\beta = 10$.

For the results in Fig. 3, m_{cr} decreases as the asymmetry parameter α increases. The top curve corresponds to the arch length $\beta = 5$. In such cases in which the symmetric loading ($\alpha = 0$) leads to limit-point instability, the curve initially has zero slope, and therefore a small imperfection from symmetric loading has little effect on m_{cr}. When the symmetrically loaded arch has a bifurcation point, as with the lower curve ($\beta = 10$), there is a finite negative slope at $\alpha = 0$, and a small asymmetric imperfection in the applied end moments may induce a significant reduction in m_{cr}.

In the case of bifurcation instability, this effect of an asymmetric imperfection in the end moments is similar to that of a concentrated vertical load that is moved slightly away from the center of a symmetric arch [9,10]. The critical value of the load decreases, as does the critical moment for the case of $\beta = 10$ in Fig. 3. However, if a limit point occurs for the central vertical load, then for a range of arch lengths the critical load increases if the load is moved from the central location, whereas in Fig. 3 for $\beta = 5$, and over the whole limit-point range for symmetric loading, m_{cr} decreases as the loading becomes asymmetric.

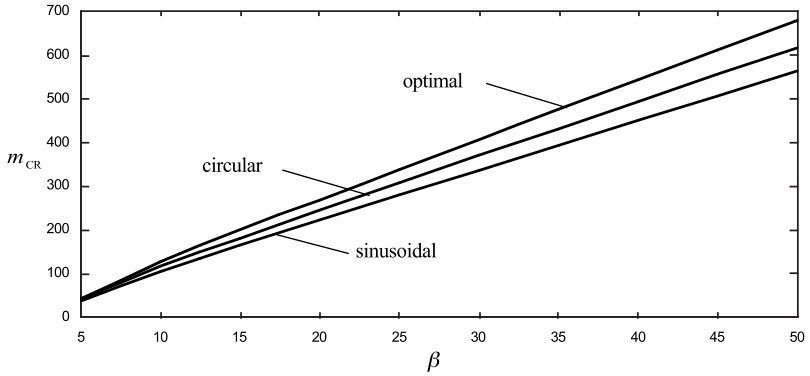

Fig. 2 Critical moment m_{cr} versus length β for equal end moments ($\alpha = 0$)

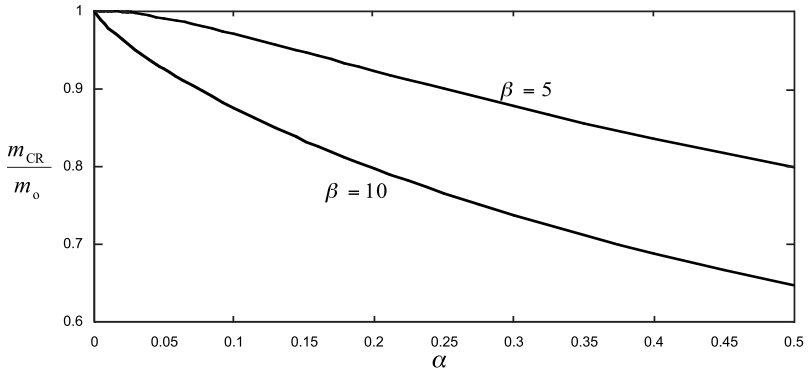

Fig. 3 Normalized critical moment m_{cr} versus the asymmetry parameter α for the sinusoidal arch

References

[1] Maurini, C., Pouget, J., and Vidoli, S., 2007, "Distributed Piezoelectric Actuation of a Bistable Buckled Beam," Eur. J. Mech. A/Solids, **26**(5), pp. 837–853.

[2] Zhang, Y., Wang, Y., Li, Z., Huang, Y., and Li, D., 2007, "Snap-Through and Pull-In Instabilities of an Arch-Shaped Beam Under an Electrostatic Loading," J. Microelectromech. Syst., **16**, pp. 684–693.

[3] Krylov, S., Ilic, B. R., Schreiber, D., Seretensky, S., and Craighead, H., 2008, "The Pull-In Behavior of Electrostatically Actuated Bistable Microstructures," J. Micromech. Microeng., **18**, p. 055026.

[4] Chen, J.-S., and Lin, J.-S., 2005, "Exact Critical Loads for a Pinned Half-Sine Arch Under End Couples," ASME J. Appl. Mech., **72**(1), pp. 147–148.

[5] Plaut, R. H., 1983, "Optimal Arch Form for Stability Under End Moments," *Developments in Mechanics, Proceedings of the 18th Midwestern Mechanics Conference*, Vol. 12, J. S. Arora, R. L. Benedict, Y. K. Liu, and V. C. Patel, eds., Iowa City, IA, May 16–18, pp. 87–89.

[6] Lim, N.-H., and Kang, Y.-J., 2004, "Out of Plane Stability of Circular Arches," Int. J. Mech. Sci., **46**(8), pp. 1115–1137.

[7] Bradford, M. A., and Pi, Y.-L., 2006, "Flexural-Torsional Buckling of Fixed Steel Arches Under Uniform Bending," J. Constr. Steel Res., **62**(1-2), pp. 20–26.

[8] Plaut, R. H., and Olhoff, N., 1983, "Optimal Forms of Shallow Arches With Respect to Vibration and Stability," J. Struct. Mech., **11**(1), pp. 81–100.

[9] Plaut, R. H., 1979, "Influence of Load Position on the Stability of Shallow Arches," Z. Angew. Math. Phys., **30**(3), pp. 548–552.

[10] Gregory, W. E., Jr., and Plaut, R. H., 1982, "Dynamic Stability Boundaries for Shallow Arches," J. Engrg. Mech. Div., **108**(EM6), pp. 1036–1050.

Three-Dimensional Elasticity Solution for Sandwich Plates With Orthotropic Phases: The Positive Discriminant Case

George A. Kardomateas
Professor
Fellow ASME
School of Aerospace Engineering,
Georgia Institute of Technology,
Atlanta, GA 30332-0150

A three-dimensional elasticity solution for rectangular sandwich plates exists only under restrictive assumptions on the orthotropic material constants of the constitutive phases (i.e., face sheets and core). In particular, only for negative or zero discriminant of the cubic characteristic equation, which is formed from these constants (case of three real roots). The purpose of the present paper is to present the corresponding solution for the more challenging case of positive discriminant, in which two of the roots are complex conjugates. [DOI: 10.1115/1.2966174]

Introduction

Elasticity solutions are significant because they provide a benchmark for assessing the performance of the various plate or shell theories or the various numerical methods such as the finite element method. For monolithic anisotropic bodies, such solutions have been developed primarily by Lekhnitskii [1]. For laminated composite or sandwich structures a few closed form solutions exist, namely, for a plate configuration by Pagano [2] for the two-dimensional case and [3] for the three-dimensional case (both under restrictive assumptions) and for a sandwich shell configuration by Kardomateas [4]. The purpose of this work is to extend the paper for the three-dimensional elastic solution by Pagano [3]. Specifically, the material constants of each phase (layer in composites or face-sheet or core in sandwich) result in a cubic characteristic equation. In Ref. [3] only the case of negative discriminant of the cubic equation, which is the case of three unequal real roots, was treated. The isotropic case, in which there are three equal real roots, was also treated. In the present paper we present the solution for the case of positive discriminant, which results in two complex conjugate roots and one real root of the cubic equation. Although the case of negative discriminant is probably more frequent with composite layers, including the transversely isotropic layers [3], the positive discriminant seems to appear frequently in sandwich construction with orthotropic cores, in which the stiffness in the transverse direction is greater than that of the in-plane directions (e.g., realistic honeycomb cores as shown in the example in the Results and Discussion section). Therefore, the solution given in the present paper completes Pagano's original work [3] for all cases of material constants.

Elasticity Formulation

We consider a sandwich plate consisting of orthotropic face-sheets of thickness f_1 and f_2 and an orthotropic core of thickness $2c$, such that the various axes of elastic symmetry are parallel to the plate axes x, y, and z (Fig. 1). The body is simply supported. A normal traction $\sigma_z = q_0(x,y)$ is applied on the upper surface but the lower surface is traction-free.

Let us denote each phase by i, where $i=f_1$ for the upper face-sheet, $i=c$ for the core, and $i=f_2$ for the lower face-sheet. Then, for each phase, the orthotropic strain-stress relations are in the same form as in Eqs. (1) and (2) of Ref. [3], with c_{ij} denoting the stiffness constants. Using the strain-displacement relations and the equilibrium relations and the simply supported plate solution for the displacements as in Eqs. (6)–(8) of Ref. [3] results in the following characteristic equation for a solution to exist in each of the sandwich phases:

$$A_0 s^6 + A_1 s^4 + A_2 s^2 + A_3 = 0 \tag{1}$$

where

$$A_0 = -c_{33}c_{44}c_{55} \tag{2a}$$

$$A_1 = p^2[c_{44}(c_{11}c_{33} - c_{13}^2) + c_{55}(c_{33}c_{66} - 2c_{13}c_{44})] + q^2[c_{55}(c_{22}c_{33} - c_{23}^2) + c_{44}(c_{33}c_{66} - 2c_{23}c_{55})] \tag{2b}$$

$$\begin{aligned} A_2 = &-p^4[c_{66}(c_{11}c_{33} - c_{13}^2) + c_{55}(c_{11}c_{44} - 2c_{13}c_{66})] \\ &+ p^2q^2[-c_{11}(c_{22}c_{33} - c_{23}^2) \\ &- 2(c_{12} + c_{66})(c_{13} + c_{55})(c_{23} + c_{44}) \\ &- 2c_{44}c_{55}c_{66} + 2c_{11}c_{23}c_{44} + c_{12}c_{33}(c_{12} + 2c_{66}) \\ &+ c_{13}c_{22}(c_{13} + 2c_{55})] - q^4[c_{66}(c_{22}c_{33} - c_{23}^2) \\ &+ c_{44}(c_{22}c_{55} - 2c_{23}c_{66})] \end{aligned} \tag{2c}$$

$$A_3 = p^6c_{11}c_{55}c_{66} + p^4q^2[c_{55}(c_{11}c_{22} - c_{12}^2) + c_{66}(c_{11}c_{44} - 2c_{12}c_{55})] + p^2q^4[c_{44}(c_{11}c_{22} - c_{12}^2) + c_{66}(c_{22}c_{55} - 2c_{12}c_{44})] + q^6c_{22}c_{44}c_{66} \tag{2d}$$

With the substitution

$$\beta = s^2 \tag{3}$$

Eq. (1), which defines the parameter s, can be written in the form of a cubic equation as

$$\beta^3 + a_1\beta^2 + a_2\beta + a_3 = 0, \quad a_i = A_i/A_0 \quad (i = 1,2,3) \tag{4}$$

This is what we would call the "characteristic equation" for the elasticity solution. Let

$$Q = \frac{3a_2 - a_1^2}{9}, \quad R = \frac{9a_1a_2 - 27a_3 - 2a_1^3}{54}, \quad D = Q^3 + R^2 \tag{5}$$

The last quantity, D, is the discriminant and determines the nature of the solution. If $D<0$, then all roots are real and unequal. This case was treated by Pagano [3]. We consider next the case of positive discriminant, which has not yet been treated.

Solution for Positive Discriminant

If $D>0$, then the cubic equation (4) has one real root and two complex conjugates.

With R and D defined in Eq. (5), we further define

$$S = \sqrt[3]{R + \sqrt{D}}, \quad T = \sqrt[3]{R - \sqrt{D}} \tag{6a}$$

Then if

$$\mu_R = -\tfrac{1}{2}(S + T) - \frac{a_1}{3}, \quad \mu_I = \tfrac{1}{2}\sqrt{3}(S - T) \tag{6b}$$

the two complex conjugate roots are

$$\beta_1 = \mu_R + i\mu_I, \quad \beta_2 = \mu_R - i\mu_I \tag{6c}$$

The real root is

Contributed by the Applied Mechanics Division of ASME for publication in the JOURNAL OF APPLIED MECHANICS. Manuscript received November 16, 2007; final manuscript received May 24, 2008; published online November 5, 2008. Review conducted by Anthony Wass.

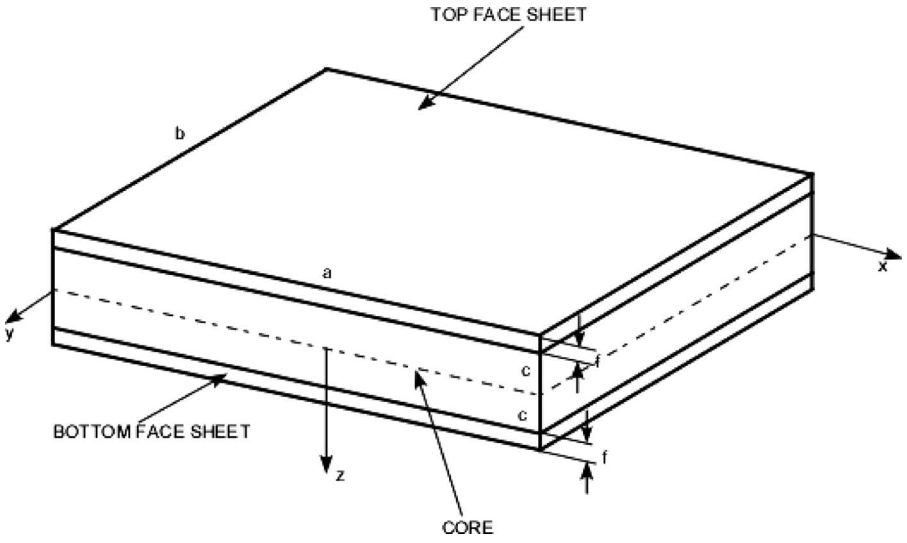

Fig. 1 Definition of the geometrical and loading configuration for the sandwich plate

$$\beta_3 = S + T - \frac{a_1}{3} \tag{6d}$$

We will consider how to deal with the complex conjugate roots first. In terms of the modulus r and amplitude θ of these complex numbers,

$$r = \sqrt{\mu_R^2 + \mu_I^2}, \quad \theta = \arctan\left(\frac{\mu_I}{\mu_R}\right) \tag{6e}$$

these roots can be set in the form

$$\beta_1 = r(\cos\theta + i\sin\theta), \quad \beta_2 = r(\cos\theta - i\sin\theta) \tag{6f}$$

From Eq. (3), we seek now the square roots of the β_is. Thus, in terms of

$$\gamma_1 = \sqrt{r}\cos\frac{\theta}{2}, \quad \gamma_2 = \sqrt{r}\sin\frac{\theta}{2} \tag{6g}$$

the corresponding roots of the sixth order equation (7), s_i, are

$$s_{1,2} = \pm(\gamma_1 + i\gamma_2), \quad s_{3,4} = \pm(\gamma_1 - i\gamma_2) \tag{6h}$$

Corresponding to these four roots, the displacement functions take the form

$$U_\eta(z) = a_{1\eta}e^{\gamma_1 z}\cos\gamma_2 z + a_{2\eta}e^{\gamma_1 z}\sin\gamma_2 z + a_{3\eta}e^{-\gamma_1 z}\cos\gamma_2 z + a_{4\eta}e^{-\gamma_1 z}\sin\gamma_2 z, \quad \eta = u,v,w \tag{7}$$

where $\eta = u,v,w$ corresponds to the U, V, W displacements and the $a_{1\eta}$ are constants. Of the 12 constants appearing in Eq. (7) only 4 are independent. The eight relations that exist among these constants are found by substituting the displacements along with Eqs. (6)–(8) of Ref. [3] into the equilibrium Eq. (3) of Ref. [3].

For convenience, let us set

$$r_1 = c_{44}(\gamma_1^2 + \gamma_2^2) + c_{66}p^2 + c_{22}q^2 \tag{8a}$$

$$r_2 = c_{44}(\gamma_1^2 + \gamma_2^2) - c_{66}p^2 - c_{22}q^2 \tag{8b}$$

$$r_3 = c_{55}(\gamma_1^2 + \gamma_2^2) + c_{11}p^2 + c_{66}q^2 \tag{8c}$$

$$r_4 = c_{55}(\gamma_1^2 + \gamma_2^2) - c_{11}p^2 - c_{66}q^2 \tag{8d}$$

and

$$e_1 = r_1(c_{13} + c_{55}) - q^2(c_{12} + c_{66})(c_{23} + c_{44}) \tag{8e}$$

$$e_2 = r_2(c_{13} + c_{55}) + q^2(c_{12} + c_{66})(c_{23} + c_{44}) \tag{8f}$$

$$e_3 = r_3(c_{23} + c_{44}) - p^2(c_{12} + c_{66})(c_{13} + c_{55}) \tag{8g}$$

$$e_4 = r_4(c_{23} + c_{44}) + p^2(c_{12} + c_{66})(c_{13} + c_{55}) \tag{8h}$$

In this way, we obtain the following relations for the coefficients in the displacement expression for $V(z)$, Eq. (7), in terms of the coefficients in the expression for $U(z)$:

$$a_{1v} = \xi_{11}a_{1u} + \xi_{12}a_{2u}, \quad a_{2v} = \xi_{21}a_{1u} + \xi_{22}a_{2u} \tag{9a}$$

$$a_{3v} = \xi_{33}a_{3u} + \xi_{34}a_{4u}, \quad a_{4v} = \xi_{43}a_{3u} + \xi_{44}a_{4u} \tag{9b}$$

where

$$\xi_{11} = \xi_{22} = \xi_{33} = \xi_{44} = \frac{q(e_1e_3\gamma_2^2 + e_2e_4\gamma_1^2)}{p(\gamma_2^2e_1^2 + \gamma_1^2e_2^2)} \tag{9c}$$

$$\xi_{12} = -\xi_{21} = -\xi_{34} = \xi_{43} = \frac{q\gamma_1\gamma_2(e_2e_3 - e_1e_4)}{p(\gamma_2^2e_1^2 + \gamma_1^2e_2^2)} \tag{9d}$$

Also, the following relations for the coefficients in the expression for $W(z)$, Eq. (7), in terms of the coefficients in the expression for $U(z)$:

$$a_{1w} = f_{11}a_{1u} + f_{12}a_{2u}, \quad a_{2w} = f_{21}a_{1u} + f_{22}a_{2u} \tag{10a}$$

$$a_{3w} = f_{33}a_{3u} + f_{34}a_{4u}, \quad a_{4w} = f_{43}a_{3u} + f_{44}a_{4u} \tag{10b}$$

where

$$f_{11} = f_{22} = -f_{33} = -f_{44} = \frac{(c_{12} + c_{66})pq\gamma_1 - r_2\gamma_1\xi_{11} - r_1\gamma_2\xi_{21}}{q(c_{23} + c_{44})(\gamma_1^2 + \gamma_2^2)} \tag{10c}$$

$$f_{12} = -f_{21} = f_{34} = -f_{43} = -\frac{(c_{12} + c_{66})pq\gamma_2 + r_2\gamma_1\xi_{12} + r_1\gamma_2\xi_{22}}{q(c_{23} + c_{44})(\gamma_1^2 + \gamma_2^2)} \tag{10d}$$

Now, coming to the real root β_3 of Eq. (4), this is treated in the same manner as in Ref. [3], i.e., if we set

$$m_3 = \sqrt{|\beta_3|} \tag{11}$$

then, if $\beta_3 < 0$, the corresponding two roots of Eq. (1) are $s_{5,6} = \pm im_3$ and the corresponding displacements can be set in the form

$$U_\eta(z) = a_{5\eta}\cos m_3 z + a_{6\eta}\sin m_3 z, \quad \eta = u,v,w \tag{12}$$

If $\beta_3 > 0$ then $s_{5,6} = \pm m_3$ and in an analogous fashion, we can set

$$U_\eta(z) = a_{5\eta} \cosh m_3 z + a_{6\eta} \sinh m_3 z, \quad \eta = u, v, w \tag{13}$$

Again, of the six unknown constants in Eq. (12) and (13) only two are independent and the four relations among them are found again by substituting these expressions into Eqs. (6)–(8) and (3) of Ref. [3].

Hence, if we consider as independent the constants a_{1u}, a_{2u}, a_{3u}, a_{4u}, a_{5u}, and a_{6u}, which we rename for convenience as g_1, g_2, g_3, g_4, g_5, and g_6, respectively, the displacement $U(z)$ is in the form

$$U(z) = d_{u1} g_1 + d_{u2} g_2 + d_{u3} g_3 + d_{u4} g_4 + d_{u5} g_5 + d_{u6} g_6 \tag{14}$$

with the z-dependent coefficients defined as

$$d_{u1} = e^{\gamma_1 z} \cos \gamma_2 z, \quad d_{u2} = e^{\gamma_1 z} \sin \gamma_2 z \tag{15a}$$

$$d_{u3} = e^{-\gamma_1 z} \cos \gamma_2 z, \quad d_{u4} = e^{-\gamma_1 z} \sin \gamma_2 z \tag{15b}$$

$$d_{u5} = \begin{cases} \cos m_3 z & \text{if } \beta_3 < 0 \\ \cosh m_3 z & \text{if } \beta_3 > 0 \end{cases} \tag{15c}$$

$$d_{u6} = \begin{cases} \sin m_3 z & \text{if } \beta_3 < 0 \\ \sinh m_3 z & \text{if } \beta_3 > 0 \end{cases} \tag{15d}$$

Similar expressions can be found for $V(z)$, $W(z)$, and the stresses.

From this analysis, we can see that within each phase (i), where $i = f_1, c, f_2$, there are six constants: $g_j^{(i)}$, $j = 1, \ldots, 6$. Therefore, for the three phases, this gives a total of 18 constants to be determined.

There are three traction conditions at each of the two core/face-sheet interfaces, giving a total of six conditions. In a similar fashion, there are three displacement continuity conditions at each of the two core/face-sheet interfaces, giving another six conditions. Finally, there are three traction boundary conditions on each of the two plate bounding surfaces, giving another six conditions, for a total of 18 equations.

Results and Discussion

As an illustration of the above, let us consider a sandwich plate with unidirectional graphite/epoxy faces and hexagonal glass/phenolic honeycomb core. Such sandwich construction is quite common in the aerospace/rotorcraft industry. The orthotropic graphite/epoxy facing moduli are (in gigapascals) as follows: $E_1^f = 181.0$, $E_2^f = E_3^f = 10.3$, $G_{23}^f = 5.96$, and $G_{12}^f = G_{31}^f = 7.17$ and facing Poisson's ratios are as follows: $\nu_{12}^f = \nu_{13}^f = 0.277$ and $\nu_{32}^f = 0.400$. The orthotropic honeycomb core moduli are (in gigapascals) as follows: $E_1^c = E_2^c = 0.032$, $E_3^c = 0.300$, $G_{23}^c = G_{31}^c = 0.048$, and $G_{12}^c = 0.013$ and core's Poisson's ratios are as follows: $\nu_{12}^c = \nu_{32}^c = \nu_{31}^c = 0.25$. The thickness of each face-sheet is $f_1 = f_2 = 2$ mm and the core $2c = 16$ mm. The plate is square with $a = b = 10 h_{\text{tot}}$, where h_{tot} is the total thickness of the plate. We further assume that a transverse loading is applied at the top face-sheet of the form represented by Eq. (25) of Ref. [3], and in the definition of p and q in Eq. (7) of Ref. [3], we further assume $m = n = 1$, i.e., the applied loading is in the form $q_0(x, y) = \sigma \sin(\pi x/a) \sin(\pi y/b)$.

Substituting the corresponding constants leads to the following βs:

Face-sheets, $D > 0$, therefore two complex conjugate roots and one real root:

$$\beta_1^f = 342.5 + i316.3, \quad \beta_2^f = 342.5 - i316.3, \quad \beta_3^f = 6150.2$$

Core, $D > 0$, therefore again two complex conjugate roots and one real root:

$$\beta_1^c = 158.9 + i49.2, \quad \beta_2^c = 158.9 - i49.2, \quad \beta_3^c = 131.6$$

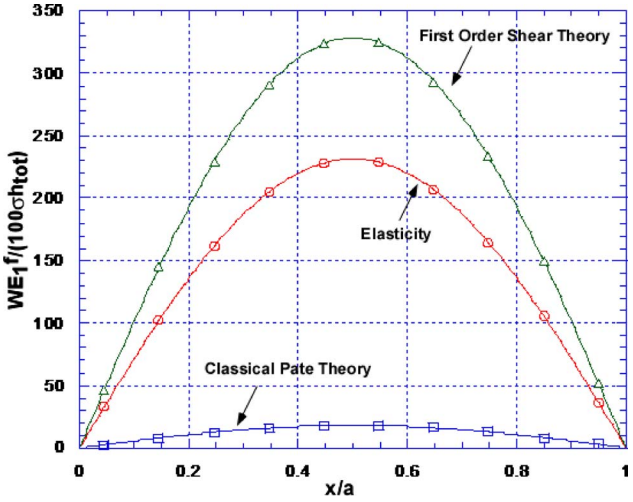

Fig. 2 Transverse displacement, *W*, at the top face-sheet and at $y = b/2$ as a function of x for $a = b = 10 h_{\text{tot}}$

Since for both the face-sheet and the core we have positive discriminant, the formulas for the coefficients in the expressions of the displacements and stresses given in the present paper are applicable. Note that if one of the phases had a negative discriminant, then we would have to use the corresponding formulas in Ref. [3].

The solution is determined by imposing the following:

(a) three traction conditions at the lower face-sheet/core interface:

$$\sigma_{zz}^{(c)} = \sigma_{zz}^{(f2)}, \quad \tau_{yz}^{(c)} = \tau_{yz}^{(f2)} \quad \text{and} \quad \tau_{xz}^{(c)} = \tau_{xz}^{(f2)} \quad \text{at } z = -c$$

(b) three displacement continuity conditions at the lower core/face-sheet interfaces:

$$U^{(c)} = U^{(f2)}, \quad V^{(c)} = V^{(f2)} \quad \text{and} \quad W^{(c)} = W^{(f2)} \quad \text{at } z = -c$$

(c) three analogous traction conditions at the upper face-sheet/core interface, $z = +c$

(d) three analogous displacement continuity conditions at the upper face-sheet/core interface, $z = +c$

(e) three traction-free conditions at the lower bounding surface:

$$\sigma_{zz} = 0, \quad \tau_{yz} = 0 \quad \text{and} \quad \tau_{xz} = 0 \quad \text{at } z = -(c + f_2)$$

and finally,

(f) three traction conditions at the upper bounding surface where the transverse load q_0 is applied:

$$\sigma_{zz} = q_0, \quad \tau_{yz} = 0 \quad \text{and} \quad \tau_{xz} = 0 \quad \text{at } z = (c + f_1)$$

Therefore, we have a system of 18 linear algebraic equations in the 18 unknowns, $g_j^{(f2)}$, $g_j^{(c)}$, and $g_j^{(f1)}$, $j = 1, 6$.

The resulting transverse displacement w at the top, i.e., at $z = c + f_1$, and at $y = b/2$ is shown in Fig. 2. In this figure, we also show the predictions of the simple classical plate theory [5,6], which does not include transverse shear.

Furthermore, the resulting displacement profile from the first order core shear theory (based on the shear being carried exclusively by the core) [5,6] is also shown in Fig. 2. It can be seen that the classical plate is too nonconservative and very inaccurate. Furthermore, the first order shear is too conservative and also quite inaccurate (although considerably better than the classical plate). Figure 3 shows the corresponding displacement profiles for a plate five times longer, i.e., with $a = b = 50 h_{\text{tot}}$. We can see that for this case of larger ratio of length over thickness, the classical and first order shear theories come closer to the elasticity, as expected; the

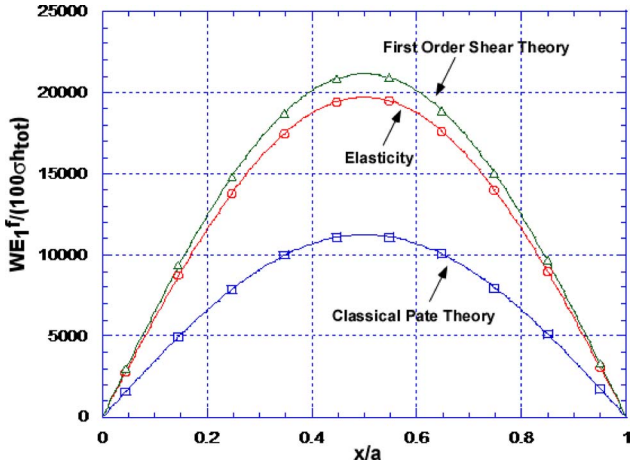

Fig. 3 Transverse displacement, W, at the top face-sheet and at $y=b/2$ as a function of x for $a=b=50h_{tot}$

classical plate is still quite inaccurate but much less so with the first order shear. These figures demonstrate clearly the large effect of transverse shear, which is an important feature of sandwich structures.

Summary

A three-dimensional elasticity solution for a rectangular sandwich plate with positive discriminant orthotropic phases is presented. This is a case frequently encountered in realistic sandwich construction. The solution is closed form. This work completes Pagano's original work [3], which was done for the negative discriminant orthotropic phases and for the isotropic phases.

Acknowledgment

The financial support of the Office of Naval Research, Grant No. N00014-07-10373, and the interest and encouragement of the Grant Monitor, Dr. Y.D.S. Rajapakse, are both gratefully acknowledged.

References

[1] Lekhnitskii, S. G., 1963, *Theory of Elasticity of an Anisotropic Elastic Body*, Holden-Day, Inc., San Francisco.
[2] Pagano, N. J., 1969, "Exact Solutions for Composite Laminates in Cylindrical Bending," J. Compos. Mater., **3**, pp. 398–411.
[3] Pagano, N. J., 1970, "Exact Solutions for Rectangular Bidirectional Composites and Sandwich Plates," J. Compos. Mater., **4**, pp. 20–34.
[4] Kardomateas, G. A., 2001, "Elasticity Solutions for a Sandwich Orthotropic Cylindrical Shell Under External Pressure, Internal Pressure and Axial Force," AIAA J., **39**(4), pp. 713–719.
[5] Vinson, J. R., 1999, *The Behavior of Sandwich Structures of Isotropic and Composite Materials*, Technomic, Lancaster, PA.
[6] Allen, H. G., 1969, *Analysis and Design of Structural Sandwich Panels*, Pergamon, Oxford, Chap. 8.

Effect of Poisson's Ratio on Three-Dimensional Stress Distribution

Z. Abdulaliyev
Metallurgical and Materials Engineering Department,
Faculty of Chemical and Metallurgical Engineering,
Istanbul Technical University,
Maslak 34469 Istanbul, Turkey
e-mail: abdulaliyev@itu.edu.tr

S. Ataoglu
Division of Mechanics,
Civil Engineering Department,
Faculty of Civil Engineering,
Istanbul Technical University,
Maslak 34469 Istanbul, Turkey
e-mail: ataoglu@itu.edu.tr

An examination of the effect of Poisson's ratio on stress distribution is important to interpret the results of a stress-strain analysis by using experimental methods because the material of the model frequently has a different Poisson's ratio from that of the prototype. In linear elasticity, the effect of Poisson's ratio on three-dimensional stress distribution is theoretically explained for simply connected bodies by using static methods in this study. It is proven that the stress components are independent from Poisson's ratio in sections of the body where the stress components arising are in equilibrium only with surface tractions. This result is useful in interpreting three-dimensional photoelasticity and other experiments and even in guiding the design. [DOI: 10.1115/1.2966218]

Keywords: experimental research, linear elasticity, Poisson's ratio, stress distribution

1 Introduction

Model and prototype, in general, have different Poisson's ratios when stress states of the structures are investigated in the models via experimental methods. The character of Poisson's ratio's effect on stress state must be known so that obtained results in the models could be correctly used in order to evaluate the strength of the prototype. It is known that the effect of this difference is not significant for the investigation of some two-dimensional problems of simply connected bodies [1,2]. In other cases, in multiply connected plane problems, this effect can be taken into account by the dislocation method [2]. In the general case of three-dimensional elasticity problems, the effect of Poisson's ratio on stress state cannot be disregarded. Different methods have been proposed in order to evaluate the effect of Poisson's ratio in the stress state of three-dimensional elasticity problems. Westergaard proposed a method to determine the necessary corrections for the prototypes using the results obtained for the solution of the problem for a specific value of Poisson's ratio [3]. However, the value of the shear modulus is considered to be equal for the materials of prototype and model in this method. In another study [4], it is proposed to follow the operations to determine the corrections with a different priority from that of the method presented by Westergaard. Another proposal states that the influence of Poisson's ratio on stress state can be determined by taking into account the application of the surface $N=\{(\nu_m-\nu_n)/((1+\nu_m)(1-2\nu_n))\}\theta_m$ and body $X_i=\{(\nu_m-\nu_n)/((1+\nu_m)(1-2\nu_n))\}\partial\theta_m/\partial x_i$ forces [5]. These forces are determined using stress components obtained in the relevant model, where $\theta_m=\sigma_{xx}+\sigma_{yy}+\sigma_{zz}$, the sum of the normal stress components in a point of the model, x_i is the coordinate of a point, and ν_m and ν_n denote the Poisson's ratios of the materials of the model and prototype, respectively. In a different work, it is shown that the difference between the solutions of elastic problems for two distinct Poisson's ratios is similar to a certain problem of thermoelasticity [6]. An experimental method, based on the application of three models set from the materials having different Poisson's ratios (ν_1, ν_2, and ν_3), is also proposed to evaluate the effect of Poisson's ratio on stress state in the application of the method of 3D photoelasticity [7]. The application of this method is not practical because it is too difficult to find three optically sensitive materials having different Poisson's ratios for the freezing method of 3D photoelasticity. The suggested methods above have theoretical and experimental restrictions for practical applications because they create new difficulties that are not only practical but also analytical.

The effect of Poisson's ratio on stress state depends on the character of examined problems since Poisson's ratio enters the equations of theory of elasticity as a parameter. Therefore, the peculiarity of the effect of Poisson's ratio on stress state is not decisively known for three-dimensional elasticity problems for a general case. Known exact solutions of problems of the theory of elasticity are the rational functions of Poisson's ratio, such as ν, $(1-\nu)$, $(1+\nu)$, $(1-\nu^2)$, $\nu/(1+\nu)$, and $(1-2\nu)$, etc. It is clear that the degree of the effect of this ratio in the examined problems depends on the appearance of the expression involving it.

The problem mathematically appears as the effect of a parameter, ν, on the general solution of the system of differential equations of elasticity. The parameter's effect may be different depending on the geometry of the examined structures, boundary conditions, and character of acting loads for each class of the problems. It may be said that it is impossible to determine the character of the mentioned effect using mathematical transformations of the differential equations of the linear theory of elasticity for a general case.

In this study, the effect of Poisson's ratio on stress state is investigated using static methods for linear elasticity problems of simply connected bodies under consideration without any body force. As is known, simply considering surface loads is enough for practical applications in the investigation of the main part of elasticity problems.

An examination of available exact solutions of three-dimensional problems of elasticity in literature [8–15] indicates that analytical expressions of stress components can be grouped according to Poisson's ratio as

$$\sigma_{ij}=f_{ij}(x_1,x_2,x_3,\dots)+\chi_{ij}(\nu)\varphi_{ij}(x_1,x_2,x_3,\dots) \tag{1}$$

where x_1, x_2, and x_3 are coordinates of a point, f_{ij} and φ_{ij} are the functions constituting the terms not involving Poisson's ratio, χ_{ij} is the multiplier expression containing only Poisson's ratio as a variable, and indices i and $j=1,2,3$.

2 Theorem

The components of stress appearing in the section of simply connected bodies subjected to the surface loads, if only in equilibrium with the system of external forces, are independent Poisson's ratio.

Let us examine the three-dimensional stress state problem of two bodies, which have the same geometry and are subjected to the identical surface loads. However, Poisson's ratios of their materials, ν_1 and ν_2 are different only.

Contributed by the Applied Mechanics Division of ASME for publication in the JOURNAL OF APPLIED MECHANICS. Manuscript received January 20, 2008; final manuscript received July 1, 2008; published online November 6, 2008. Review conducted by Zhigang Suo.

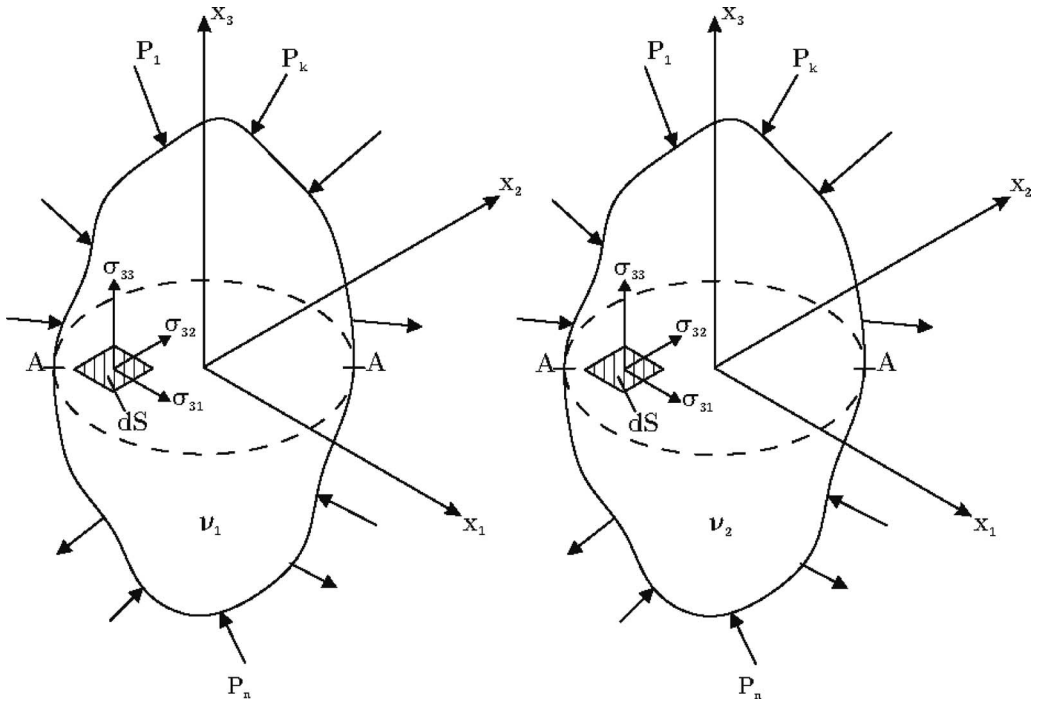

Fig. 1 Compared bodies

It is understood that analytical expressions of stress components (σ_{ij}^{I} and $\sigma_{ij}^{\mathrm{II}}$) arising in the compared bodies are only different according to the indices of Poisson's ratios

$$\sigma_{ij}^{\mathrm{I}} = F^{\mathrm{I}}(x_1, x_2, x_3, \nu_1, \dots)$$
$$\sigma_{ij}^{\mathrm{II}} = F^{\mathrm{II}}(x_1, x_2, x_3, \nu_2, \dots) \tag{2}$$

The expressions of stress components, Eq. (2), can be separated in to two groups, taking Eq. (1) into consideration (including Poisson's ratio in terms or not), as follows:

$$\sigma_{ij}^{\mathrm{I}} = f_{ij}(x_1, x_2, x_3, \dots) + \chi_{ij}(\nu_1)\varphi_{ij}(x_1, x_2, x_3, \dots)$$
$$\sigma_{ij}^{\mathrm{II}} = f_{ij}(x_1, x_2, x_3, \dots) + \chi_{ij}(\nu_2)\varphi_{ij}(x_1, x_2, x_3, \dots) \tag{3}$$

Writing the equilibrium equations for the relevant parts of the bodies, taking into consideration the stresses arising in the identical sections (A-A, Fig. 1), leads to the following formulation:

$$\sum_{j=1}^{3} \int_S \sigma_{3j}^{\mathrm{I}} dS + \sum_{k=1}^{n} P_{3k} = 0$$
$$\sum_{j=1}^{3} \int_S \sigma_{3j}^{\mathrm{II}} dS + \sum_{k=1}^{n} P_{3k} = 0 \tag{4}$$

where σ_{3j}^{I} and $\sigma_{3j}^{\mathrm{II}}$ indicate the stresses arising in the sections of the bodies, S is the area of the section, and $\Sigma_{k=1}^{n} P_{3k}$ $(k = 1, 2, \dots, n)$ is the sum of projections of the external loads to the relevant axis. It is possible to write taking into consideration equilibrium equations, Eq. (4), as

$$\sum_{j=1}^{3} \int_S \sigma_{3j}^{\mathrm{I}} dS = \sum_{j=1}^{3} \int_S \sigma_{3j}^{\mathrm{II}} dS \tag{5}$$

Equation (5) can be expressed using Eq. (3), as follows:

$$\sum_{j=1}^{3} \int_S f_{3j}(x_1, x_2, x_3, \dots) dS + \sum_{j=1}^{3} \int_S \chi_{3j}(\nu_1)\varphi_{3j}(x_1, x_2, x_3, \dots) dS$$
$$= \sum_{j=1}^{3} \int_S f_{3j}(x_1, x_2, x_3, \dots) dS + \sum_{j=1}^{3} \int_S \chi_{3j}(\nu_2)\varphi_{3j}(x_1, x_2, x_3, \dots) dS$$

This expression yields

$$\sum_{j=1}^{3} \int_S \chi_{3j}(\nu_1)\varphi_{3j}(x_1, x_2, x_3, \dots) dS = \sum_{j=1}^{3} \int_S \chi_{3j}(\nu_2)\varphi_{3j}(x_1, x_2, x_3, \dots) dS$$

Differentiating this equality with respect to dS leads to

$$\chi_{3j}(\nu_1)\varphi_{3j}(x_1, x_2, x_3, \dots) = \chi_{3j}(\nu_2)\varphi_{3j}(x_1, x_2, x_3, \dots) \tag{6}$$

To satisfy equality (6), the function $\varphi_{3j}(x_1, x_2, x_3, \dots)$ characterizing the effect of Poisson's ratio on stress state should be zero because multiplier expressions $\chi_{3j}(\nu_1)$ and $\chi_{3j}(\nu_2)$ are unequal constants. That is, Poisson's ratios do not affect arising stresses in the examined sections.

3 Conclusions

The aforesaid theorem allows us to explain the effect of Poisson's ratio on stress distribution for the known exact solutions of three-dimensional linear problems of the theory of elasticity for surface loads. In the solution of "sphere subjected to uniform pressure," stress components at any section are in equilibrium with the external forces. Moreover, it is seen that analytical expressions of stress components of this problem do not contain Poisson's ratio, as stated in the theorem. Similarly, in the solutions of problems of "related to semi-infinite" Boussinesq [10] and Love [8] (see the Appendix), the analytical expressions of stress components, arising where the sections are parallel to the boundary plane, do not even contain Poisson's ratio because the stress components arising in the sections are in equilibrium with the external forces. The examination of the three-dimensional problems of linear elasticity having exact solutions [8–15] shows that analytical expressions of stress components arising in the sections,

which correspond to the conditions indicated by the theorem, do not contain Poisson's ratio. This theorem enables the application of the results, obtained in the models with different experimental methods, to the prototypes more accurately.

Appendix

The Stress Components for a Semi-Infinite Solid by Pressure on Part of the Boundary

The formulations are

$$\sigma_{xx} = \frac{1}{2\pi}\left(\frac{\lambda}{\lambda+\mu}\frac{\partial V}{\partial z} - \frac{\mu}{\lambda+\mu}\frac{\partial^2 \xi}{\partial x^2} - z\frac{\partial^2 V}{\partial x^2}\right)$$

$$\sigma_{yy} = \frac{1}{2\pi}\left(\frac{\lambda}{\lambda+\mu}\frac{\partial V}{\partial z} - \frac{\mu}{\lambda+\mu}\frac{\partial^2 \xi}{\partial y^2} - z\frac{\partial^2 V}{\partial y^2}\right)$$

$$\sigma_{xy} = -\frac{1}{2\pi}\left(\frac{\mu}{\lambda+\mu}\frac{\partial^2 \xi}{\partial x \partial y} + z\frac{\partial^2 V}{\partial x \partial y}\right)$$

$$\sigma_{zz} = \frac{1}{2\pi}\left(\frac{\partial V}{\partial z} - z\frac{\partial^2 V}{\partial z^2}\right)$$

$$\sigma_{zy} = -\frac{1}{2\pi} z \frac{\partial^2 V}{\partial y \partial z}$$

$$\sigma_{zx} = -\frac{1}{2\pi} z \frac{\partial^2 V}{\partial x \partial z}$$

where λ and μ are Lamé's elastic constants for the material of solid, and ξ and V are the potentials of Boussinesq's three-dimensional logarithmic and Newtonian, respectively, defined as follows:

$$\xi = \int\int p \log(z+r) dx' dy'$$

and

$$V = \int\int p r^{-1} dx' dy'$$

x, y, and z are the coordinates of a point within the solid, $(x', y', 0)$ to be those of a point on the plane boundary, r denotes the distance between these points, which is given as follows:

$$r^2 = (x-x')^2 + (y-y')^2 + z^2$$

and p is the applied pressure on the plane boundary of the semi-infinite solid, which is a function of x' and y'.

It is apparent from the above expressions that the terms of the stress components $(\sigma_{zx}, \sigma_{zy}, \sigma_{zz})$—arising in the sections parallel to the boundary plane—which are in equilibrium with the external forces, do not include Poisson's ratio.

References

[1] Michell, J. H., 1899, "On the Direct Determination of Stress in an Elastic Solid, With Application to the Theory of Plates," Proc. London Math. Soc., **31**, pp. 100–124.

[2] Timoshenko, S. P., and Goodier, J. N., 1970, *Theory of Elasticity*, McGraw-Hill, New York.

[3] Westergaard, H. M., 1940, "Effects of a Change of Poisson's Ratio Analyzed by Twinned Gradients," ASME J. Appl. Mech., **62**, pp. 113–116.

[4] Fung, Y. C., 1968, *Foundations of Solid Mechanics*, Prentice-Hall, New Delhi.

[5] Beaujoint, N., Nizeri, A., and Remenieras, G., 1953, "Etude Sur Modele Re'duit des Contraintes Dans les Barrages," Ann. Ponts Chaussees, 123(4).

[6] Knops, R. J., 1959, "Method for Solving Linear Thermoelastic Problems," J. Mech. Phys. Solids, **7**, pp. 182–192.

[7] Proshko, V. M., 1958, *Voprosi Issledovaniya Napryajeniy na Obyomnix Modelyax, Polyarizasionno-Opticheskiy Metod Issledovaniya Napryajeniy*, USSR Sci. Acad., Moscow.

[8] Love, A. E. H., 1929, "The Stress Produced in a Semi-Infinite Solid by Pressure on Part of the Boundary," Philos. Trans. R. Soc. London, Ser. A, **228**, pp. 377–420.

[9] Cerruti, V., 1882, "Ricerche Intorno all'Equilibrio dei CorpiElastici Isotropi," Atti R. Accad. Naz. Lincei, Mem. Cl. Sci. Fis., Mat. Nat., **13**, pp. 81–123.

[10] Boussinesq, J., 1885, *Applications des Potentiels a l'Étude de l'Équilibre et du Mouvements de Solides Élastiques*, Gauthier-Villard, Paris.

[11] Fabrikant, V. I., Rubin, B. S., and Karapetian, E. N., 1993, "Half-Plane Crack Under Normal Load: Complete Solution," J. Eng. Mech., **119**, pp. 2238–2251.

[12] Sneddon, I. N., and Fabrikant, V. I., 1946, "Boussinesq's Problem for a Flat-Ended Cylinder," Proc. Cambridge Philos. Soc., **42**, pp. 29–39.

[13] Fabrikant, V. I., 1988, "Elastic Field Around a Circular Punch," ASME J. Appl. Mech., **56**, pp. 604–610.

[14] Abramov, V. M., 1939, "Étude d'un cas d'Action non Symetrique d'un Poincon Circulaire Appliqué à un Corps Élastique d'Epaisseur Infinie et Limité Par un Plan," C. R. Acad. Sci. URSS, **23**, pp. 759–764.

[15] Hanson, M. T., 1992, "The Elastic Field for Conical Identation Including Sliding Friction for Tranverse Isotropy," ASME J. Appl. Mech., **59**, pp. S123–S130.

Discussion: "Isotropic Clamped-Free Thin Annular Circular Plate Subjected to a Concentrated Load" (Adewale, A. O., 2006, ASME J. Appl. Mech., 73, pp. 658–663)

J. T. Chen
Department of Harbor and River Engineering,
National Taiwan Ocean University,
Keelung 20224, Taiwan, R.O.C.
e-mail: jtchen@mail.ntou.edu.tw

W. M. Lee
Department of Mechanical Engineering,
China Institute of Technology,
Taipei 11581, Taiwan, R.O.C.
e-mail: wmlee@cc.chit.edu.tw

H. Z. Liao
Department of Harbor and River Engineering,
National Taiwan Ocean University,
Keelung 20224, Taiwan, R.O.C.

1 Introduction

In this interesting paper [1], a concentrated load was applied to the clamped-free annular plate. The problem domain was divided into two parts by the cylindrical section where a concentrated load was applied. The author used the Trefftz method [2] to construct the homogeneous solution

$$u = \sum_{m=0}^{\infty} R_m(r)\cos m\theta \tag{1}$$

in each part. By substituting Eq. (1) into the governing equation, the author could determine $R_m(r)$. Mathematically speaking, the series in Eq. (1) can be seen as the summation of Trefftz bases. To simulate the concentrated force, a circularly distributed force using the Fourier series is used. Then, the author utilized two boundary conditions (BCs) in each part, two continuity, and two equilibrium conditions on the interface to determine the eight unknown coefficients. Variation of deflection coefficients, radial moment coefficients, and shear coefficients along radial positions and angles was presented. However, some results are misleading. To investigate these inconsistencies, both null-field integral formulation and finite element method (FEM) using the ABAQUS are adopted to revisit this problem. In addition, two unclear issues in Ref. [1] are discussed. One is the simulation of concentrated load and the other is the operator of shear force.

2 Concentrated Load

In Adewale's paper [1], the author expanded the concentrated load to the Fourier series

$$P \approx P\left[\frac{1}{2} + \sum_{k=1}^{\infty} \frac{2\sin\dfrac{(2k-1)\pi}{2}}{(2k-1)\pi}\cos(2k-1)\theta\right], \quad 0 \le \theta \le \frac{\pi}{2} \tag{2}$$

By summing up the series of Eq. (2), the result converges to 1 as shown in Fig. 1, which does not show the behavior of the Dirac-delta function. The Dirac-delta function $\delta(x)$ should satisfy the identity as follows:

$$\int_{-\infty}^{\infty} \delta(x)dx = 1 \tag{3}$$

Equation (2) cannot satisfy Eq. (3) such that the strength of the concentrated loading is 1. The author seems to improperly transform the concentrated load to a circularly distributed one. If this load is distributed along an angle from 0 to $\pi/2$, the results of the deflection coefficient in Fig. 5 of Ref. [1] would be untrue.

3 Definition of Shear Force

For the clamped-free annular plate problems as shown in Fig. 2, the shear force on the inner circle is zero for the free boundary. Therefore, the author obtained the shear force

$$\left(\frac{\partial^3}{\partial r^3} - \frac{1}{r^2}\frac{\partial}{\partial r} + \frac{1}{r}\frac{\partial^2}{\partial r^2} - \frac{m^2}{r^2}\frac{\partial}{\partial r}\right)R_m(r)\bigg|_{r=a} = 0 \quad \text{shear force free} \tag{4}$$

According to the displacement of Eq. (1) and the definition of shear force operator in Szilard's book [3], the shear force can be derived as

$$\frac{\partial^3 R_m(r)}{\partial r^3} - \frac{1}{r^2}\frac{\partial R_m(r)}{\partial r} + \frac{1}{r}\frac{\partial^2 R_{m(r)}}{\partial r^2} + \frac{2m^2}{r^3}R_m(r) - \frac{m^2}{r^2}\frac{\partial R_m(r)}{\partial r} + (1-\nu)\left[\frac{m^2}{r^3}R_m(r) - \frac{m^2}{r^2}\frac{\partial R_m(r)}{\partial r}\right] \quad \text{for shear force} \tag{5}$$

where ν is the Poisson ratio. Equation (4) is unreasonable since it does not involve the Poisson ratio. In literature, many articles had reported the definition of shear force operator, e.g., Refs. [1–5]. We summarized the shear force operators in Table 1. After careful comparison, Adewale's shear force operator differs from the others and consequently, this difference may cause inconsistent results.

4 Alternative Derivation of the Analytical Solution Using the Null-Field Integral Formulation

The first boundary integral equations for the domain point can be derived from the Rayleigh–Green identity as follows [5,6]:

$$8\pi u(x) = U(\zeta,x) - \int_B U(s,x)v(s)dB(s) + \int_B \Theta(s,x)m(s)dB(s) - \int_B M(s,x)\theta(s)dB(s) + \int_B V(s,x)u(s)dB(s), \quad x \in \Omega \cup B \tag{6}$$

where B is the boundary of the domain Ω; $u(x)$, $\theta(x)$, $m(x)$, and $v(x)$ are the displacement, slope, normal moment, and effective shear force; and s and x are the source point and field point, respectively. The kernel function $U(s,x)$ in Eq. (6) is the fundamental solution that satisfies

$$\nabla^4 U(s,x) = 8\pi\delta(s-x) \tag{7}$$

Therefore, the fundamental solution can be obtained as follows:

Contributed by the Applied Mechanics Division of ASME for publication in the JOURNAL OF APPLIED MECHANICS. Manuscript received July 25, 2007; final manuscript received March 25, 2008; published online November 12, 2008. Review conducted by Subrata Mukherjee.

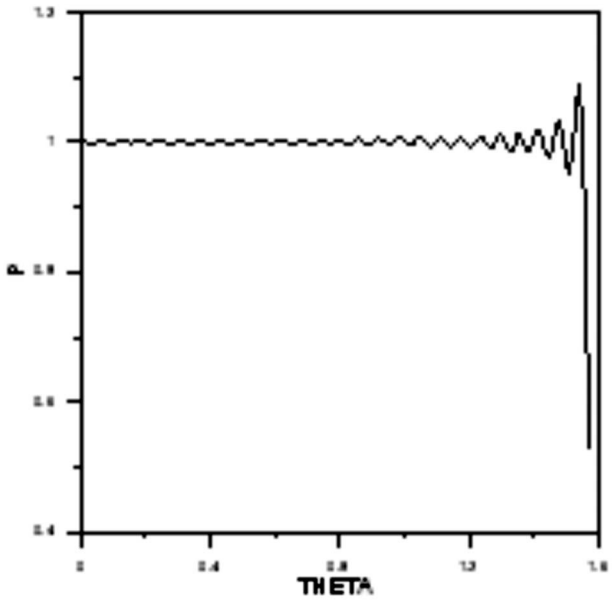

Fig. 1 Simulation of a concentrated force by Adewale's [1] (*M*=101).

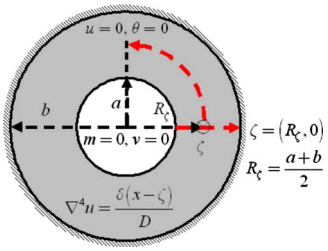

Fig. 2 Problem statement of an annular plate

$$U(s,x) = r^2 \ln r \tag{8}$$

where r is the distance between the source point s and field point x. The relationship among $u(x)$, $\theta(x)$, $m(x)$, and $v(x)$ is shown as follows:

$$\theta(x) = K_{\theta,x}(u(x)) = \frac{\partial u(x)}{\partial n_x} \tag{9}$$

Table 1 The definitions of the shear force (a) Szilard, (b) Leissa, (c) the present operator, and (d) Adewale

(a) Szilard [3]
$-D\left[\frac{\partial}{\partial r}\nabla_r^2 u + \frac{1-\nu}{r}\frac{\partial}{\partial \varphi}\left(\frac{1}{r}\frac{\partial^2 u}{\partial r \partial \varphi} - \frac{1}{r^2}\frac{\partial u}{\partial \varphi}\right)\right]$
(b) Leissa [4]
$-D\frac{\partial}{\partial r}(\nabla^2 u) + \frac{1}{r}\frac{\partial}{\partial \theta}\left[-D(1-\nu)\frac{\partial}{\partial r}\left(\frac{1}{r}\frac{\partial u}{\partial \theta}\right)\right]$
(c) Present operator [5]
$\frac{\partial \nabla_x^2 u}{\partial n_x} + (1-\nu)\frac{\partial}{\partial t_x}\left[\frac{\partial}{\partial n_x}\left(\frac{\partial u}{\partial t_x}\right)\right]$
(d) Adewale [1]
$\frac{\partial^3 R_m}{\partial r^3} - \frac{1}{r^2}\frac{\partial R_m}{\partial r} + \frac{1}{r}\frac{\partial^2 R_m}{\partial r^2} - \frac{m^2}{r^2}\frac{\partial R_m}{\partial r}$

$$m(x) = K_{m,x}(u(x)) = \nu \nabla_x^2 u(x) + (1-\nu)\frac{\partial^2 u(x)}{\partial^2 n_x} \tag{10}$$

$$v(x) = K_{v,x}(u(x)) = \frac{\partial \nabla_x^2 u(x)}{\partial n_x} + (1-\nu)\frac{\partial}{\partial t_x}\left[\frac{\partial}{\partial n_x}\left(\frac{\partial u(x)}{\partial t_x}\right)\right] \tag{11}$$

where $K_{\theta,x}(\cdot)$, $K_{m,x}(\cdot)$, and $K_{v,x}(\cdot)$ are the slope, moment, and shear force operators with respect to the point x; $\partial/\partial n_x$ is the normal derivative with respect to the field point x; $\partial/\partial t_x$ is the tangential derivative with respect to the field point x; and ∇_x^2 is the Laplacian operator. The first null-field integral equations can be derived by moving the field point x outside the domain as follows:

$$0 = U(\zeta,x) - \int_B U(s,x)v(s)dB(s) + \int_B \Theta(s,x)m(s)dB(s) - \int_B M(s,x)\theta(s)dB(s) + \int_B V(s,x)u(s)dB(s), \quad x \in \Omega^C \cup B \tag{12}$$

where Ω^C is the complementary domain of Ω. For the kernel function $U(s,x)$, it can be expanded in terms of degenerate kernel [2,5–7] in a series form as shown below:

$$U(s,x) = \begin{cases} U^I(R,\theta;\rho,\phi) = \rho^2(1+\ln R) + R^2 \ln R - \left[R\rho(1+2\ln R) + \frac{1}{2}\frac{\rho^3}{R}\right]\cos(\theta-\phi) \\ \quad - \sum_{m=2}^{\infty}\left[\frac{1}{m(m+1)}\frac{\rho^{m+2}}{R^m} - \frac{1}{m(m-1)}\frac{\rho^m}{R^{m-2}}\right]\cos[m(\theta-\phi)], \quad R \geq \rho \\ U^E(R,\theta;\rho,\phi) = R^2(1+\ln \rho) + \rho^2 \ln \rho - \left[\rho R(1+2\ln \rho) + \frac{1}{2}\frac{R^3}{\rho}\right]\cos(\theta-\phi) \\ \quad - \sum_{m=2}^{\infty}\left[\frac{1}{m(m+1)}\frac{R^{m+2}}{\rho^m} - \frac{1}{m(m-1)}\frac{R^m}{\rho^{m-2}}\right]\cos[m(\theta-\phi)], \quad \rho > R \end{cases} \tag{13}$$

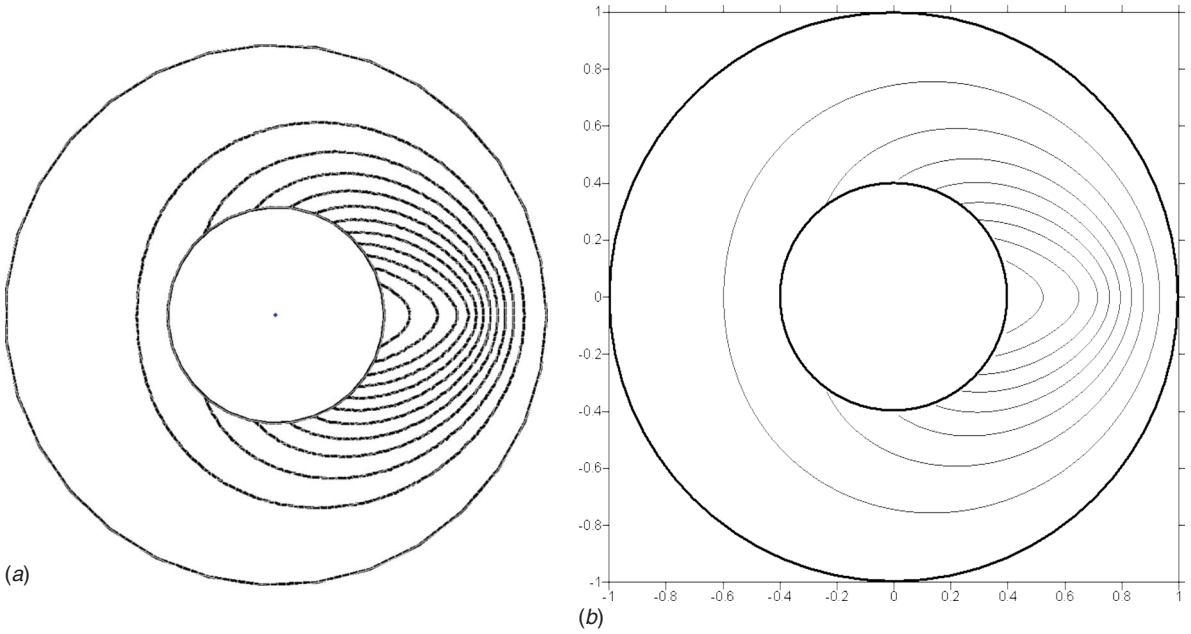

Fig. 3 Contour plots of the Green's function for the annular problem (a=0.4, b=1.0, R_ξ=0.7, D=1, ν=0.3). (a) Displacement contour by using the FEM (ABAQUS). (b) Displacement contour by using the present method (M=50).

where the superscripts I and E denote the interior and exterior cases of $U(s,x)$ kernel depending on the location of s and x. For the annular plate clamped at the outer edge and free at the inner edge, the unknown Fourier coefficients of m, v on the outer boundary and u, θ on the inner boundary can be expanded to

$$v(s) = a_0 + \sum_{n=1}^{M} (a_n \cos n\theta + b_n \sin n\theta), \quad s \in \text{outer boundary} \tag{14}$$

$$m(s) = \bar{a}_0 + \sum_{n=1}^{M} (\bar{a}_n \cos n\theta + \bar{b}_n \sin n\theta), \quad s \in \text{outer boundary} \tag{15}$$

$$\theta(s) = p_0 + \sum_{n=1}^{M} (p_n \cos n\theta + q_n \sin n\theta), \quad s \in \text{inner boundary} \tag{16}$$

$$u(s) = \bar{p}_0 + \sum_{n=1}^{M} (\bar{p}_n \cos n\theta + \bar{q}_n \sin n\theta), \quad s \in \text{inner boundary} \tag{17}$$

where a_0, a_n, b_n, $\bar{a}_0$, $\bar{a}_n$, $\bar{b}_n$, p_0, p_n, q_n, $\bar{p}_0$, $\bar{p}_n$, and $\bar{q}_n$ are the Fourier coefficients, and M is the number of Fourier series terms in real computation. By substituting all the Fourier coefficients of boundary densities and boundary conditions, the displacement field can be obtained as shown below:

$$8\pi u(x) = U(\zeta,x) - \int_B U(s,x)\left[a_0 + \sum_{n=1}^{M} (a_n \cos n\theta + b_n \sin n\theta)\right] dB(s) + \int_B \Theta(s,x)\left[\bar{a}_0 + \sum_{n=1}^{M} (\bar{a}_n \cos n\theta + \bar{b}_n \sin n\theta)\right] dB(s) - \int_B M(s,x) \times \left[p_0 + \sum_{n=1}^{M} (p_n \cos n\theta + q_n \sin n\theta)\right] dB(s) + \int_B V(s,x)\left[\bar{p}_0 + \sum_{n=1}^{M} (\bar{p}_n \cos n\theta + \bar{q}_n \sin n\theta)\right] dB(s), \quad x \in \Omega \cup B \tag{18}$$

where a_n, b_n, $\bar{a}_n$, $\bar{b}_n$, p_n, q_n, $\bar{p}_n$, and $\bar{q}_n$ (n=0,1,2,...) are solved in Ref. [7].

5 Results and Discussions

In order to verify the accuracy of Adewale's results, two alternatives, null-field approach and FEM using ABAQUS, are employed to revisit the annular problem. A concentrated load was applied at the radial center of the annular plate, as shown in Fig. 2. For the clamped-free boundary condition, Figs. 3(a) and 3(b) show the displacement contours for the Green's function by using FEM (ABAQUS) and the present method, respectively. Good agreement is obtained between our analytical solution and FEM result although Adewale [1] did not provide the displacement contour of his analytical solution. For comparison with the available results in Ref. [1], Fig. 4 shows the variation of deflection coefficients, moment coefficients, and shear force coefficients along radial positions or angles for different inner radii. It is also found that FEM results match well with our solution but deviates from Adewale's outcome [1].

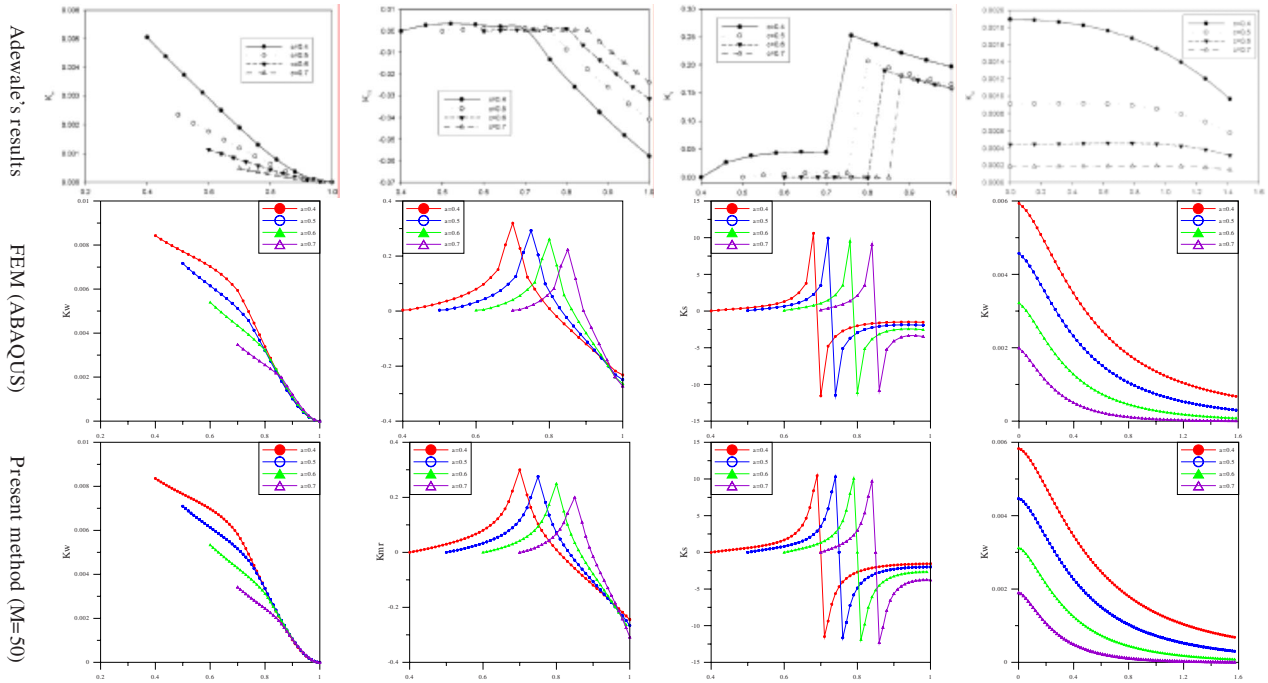

(a) Variation of deflection coefficients versus radial position

(b) Variation of moment coefficients versus radial position

(c) Variation of shear force coefficients versus radial position

(d) Variation of deflection coefficients versus radial angle

Fig. 4 Responses (b=1.0, R_ζ=0.7∼0.85, D=1, ν=0.3, $k_w = wD/P$, $k_{mr} = M_rD/P$, $k_s = M_sD/P$)

6 Concluding Remarks

To verify the accuracy of Adewale's results and to examine the response of the clamped-free annular plate subjected to a concentrated load, the null-field integral formulation was employed in solving this problem. The transverse displacement, moment, and shear force along the radial positions and angles for different inner radii were determined by using the present method in comparison with the ABAQUS data. Good agreements between our analytical results and those of ABAQUS were made but deviated from Adewale's data. The outcome of Adewale's results may not be correct.

References

[1] Adewale, A. O., 2006, "Isotropic Clamped-Free Thin Annular Circular Plate Subjected to a Concentrated Load," ASME J. Appl. Mech., **73**, pp. 658–663.

[2] Chen, J. T., Wu, C. S., and Lee, Y. T., 2007, "On the Equivalence of the Trefftz Method and Method of Fundamental Solutions for Laplace and Biharmonic Equations," Comput. Math. Appl., **53**, pp. 851–879.

[3] Szilard, R., 1974, *Theory and Analysis of Plates Classical and Numerical Methods*, Prentice-Hall, Englewood Cliffs, NJ.

[4] Leissa, A., 1993, *Vibration of Plates*, Acoustical Society of America, Melville, NY.

[5] Chen, J. T., Hsiao, C. C., and Leu, S. Y., 2006, "Null-Field Integral Approach for Plate Problems With Circular Boundaries," ASME J. Appl. Mech., **73**, pp. 679–693.

[6] Chen, J. T., Wu, C. S., and Chen, K. H., 2005, "A Study of Free Terms for Plate Problems in the Dual Boundary Integral Equations," Eng. Anal. Boundary Elem., **29**, pp. 435–446.

[7] Liao, H. Z., 2007, "Analytical Solutions for the Green's Functions of Laplace and Biharmonic Problems With Circular Boundaries," MS thesis, National Taiwan Ocean University, Taiwan.

Erratum: "Stability Analysis of an Inflatable Vacuum Chamber" [Journal of Applied Mechanics, 2008, 75(4), p. 041010]

Page 3, 2nd column, 9th line: "$E \equiv \cos(\theta/2)$" should read "$E \equiv (\cos\theta)/2$."
Page 3, 2nd column, 10th line: "$\varepsilon \equiv \sin(\theta/2)$" should read "$\varepsilon \equiv (\sin\theta)/2$."
Page 3, 2nd column, 13th line: "$-(SC+2\varepsilon RQ)$" should read "$(-SC+2\varepsilon RQ)$."
Page 4, 1st column, 2nd line: "the dagger denotes" should read "where the dagger denotes."
Page 7, last line of "Nomenclature": "$E \equiv \cos(\theta/2)$" should read "$E \equiv (\cos\theta)/2$."

